université de BORDEAUX

THÈSE PRÉSENTÉE POUR OBTENIR

LE GRADE DE

DOCTEUR DE

L'UNIVERSITÉ DE BORDEAUX

ÉCOLE DOCTORALE Sciences Physiques de l'ingénieur

SPÉCIALITÉ Mécanique

Par Youssef SLEIMAN

Etude d'un béton géopolymère écologique à ultra haute performance à base de sous-produits industriels et de matériaux recyclés

Sous la direction de : Nadia SAIYOURI

Co-directeur : Zoubir-Mehdi SBARTAÏ

Soutenue le 19/10/2026

Membres du jury :

Mme SAIYOURI, Nadia,	Professeure, Université de Bordeaux	Directrice de thèse
M. SBARTAÏ Zoubir-Mehdi	Professeur, Université de Bordeaux	Co-directeur de thèse
M. LEKLOU Ali-Nordine	Professeur, Université de Nantes	Rapporteur
Mme BIAN JIA Yun	Maîtresse de conférences HDR, Université de Lille	Rapporteure
M. AÏT-MOKHTAR Karim	Professeur, Université de La Rochelle	Président du jury
M. TAKARLI Mokhfi	Maître de conférences, Université de Limoges	Examinateur

Membres invités :

Mme ERKIZIA Edurne	Chercheuse senior, Fundación Tecnalia, Espagne	Invitée
M. UKRAINCZYK Neven	Docteur, Technical University of Darmstadt, Allemagne	Invité

Study of an eco-friendly ultra-high performance geopolymer concrete based on industrial by-products and recycled materials

Abstract

Offshore floating photovoltaic substructures are currently built in Portland-cement ultra-high-performance concrete (UHPC), whose embodied carbon sits near the upper bound of the construction sector. This thesis develops, characterizes, models, and assesses a 100% cement-free, ambient-cured Ultra-High Performance Geopolymer Concrete (GEO) as a replacement candidate, within the Horizon Europe project NATURSEA-PV. A six-stage, bottleneck-driven optimization of a GGBS and silica fume binder activated by sodium silicate and 10 M KOH, reinforced with 108 kg/m^3 of tire-derived recycled and virgin steel fibers, satisfies the five project acceptance criteria simultaneously under ambient curing: 65 MPa at 24 hours, 152 ± 5 MPa at 28 days on EN 196-1 prism halves, 208 mm slump flow, 23 min open time, and 60 wt% recycled fiber. The 28-day value is 92% of the Portland-cement reference REF, at 165 ± 4 MPa on the matched geometry. Electrochemical impedance spectroscopy from 1 to 28 days shows the optimal strength indicator to be binder-specific: the Warburg coefficient tracks GEO strength ($r = 0.983$ on log axes, $p < 0.001$), statistically indistinguishable from the gel pore resistance R2 adopted for REF ($r = 0.987$), and neither parameter serves the other binder. Acoustic emission under three-point bending identifies a cohesive, debonding-dominated fracture pathway in GEO against friction-dominated pull-out in REF. A continuum-damage model calibrated on the measured flexural response reproduces the peak load to within 2.3% but not the post-peak branch. Twelve months of sulfate and acid immersion, chloride migration, and thermal programs, and a 10-month offshore campaign at HarshLab establish superior sulfate and acid resistance, no chloride or carbonation front after real immersion, and full retention of the UHPC mechanical class in all three exposure zones. The single deficit is elevated-temperature strength retention: GEO held 36% of its ambient compressive strength at 600 °C, below the 90% of the one REF specimen that survived the exposure intact, although GEO alone kept its form at every temperature. This condition lies outside the marine service envelope. A cradle-to-grave carbon footprint assessment under EN 15804+A2 returns a 37% reduction per m^3 and 32.1% per ton against a verified third-party EPD for the reference UHPC, meeting the project carbon target, while the cost-to-strength target is not met, at 10.9% against a 35% requirement. GEO is therefore mechanically compliant, monitorable, marine-durable, and substantially lower in carbon than the UHPC it replaces.

Keywords: UHPGC; alkali activation; GGBS; recycled steel fibers; electrochemical impedance spectroscopy; acoustic emission; marine durability; life cycle assessment.

Etude D'un Béton Géopolymère Écologique À Ultra Haute Performance À Base De Sous-Produits Industriels Et De Matériaux Recyclés

Résumé

Les flotteurs photovoltaïques offshore sont aujourd'hui construits en béton fibré à ultra-hautes performances (BFUP) à base de ciment Portland, dont le carbone incorporé se situe dans la partie haute du secteur de la construction. Cette thèse développe, caractérise, modélise et évalue un béton géopolymère à ultra-hautes performances (GEO), 100 % sans ciment et à cure ambiante, comme candidat au remplacement, dans le cadre du projet Horizon Europe NATURSEA-PV. Une optimisation séquentielle en six étapes d'un liant laitier et fumée de silice, activé par silicate de sodium et KOH 10 M, renforcé par 108 kg/m^3 de fibres d'acier recyclées issues de pneus usagés et de fibres vierges, satisfait simultanément les cinq critères d'acceptation du projet en cure ambiante : 65 MPa à 24 heures, 152 ± 5 MPa à 28 jours sur demi-prismes EN 196-1, 208 mm d'étalement, 23 min de temps ouvert et 60 % en masse de fibres recyclées. Cette valeur à 28 jours représente 92 % du témoin cimentaire REF, à 165 ± 4 MPa sur géométrie appariée. La spectroscopie d'impédance électrochimique de 1 à 28 jours montre que l'indicateur optimal de résistance est propre au liant : le coefficient de Warburg suit la résistance du GEO ($r = 0,983$ en axes logarithmiques, $p < 0,001$), statistiquement indiscernable de la résistance des pores du gel R2 retenue pour REF ($r = 0,987$), et aucun des deux ne convient à l'autre liant. L'émission acoustique en flexion trois points identifie un chemin de rupture cohésif dominé par la décohésion dans le GEO, contre un arrachement frictionnel dans le REF. Un modèle d'endommagement continu calé sur la réponse en flexion mesurée reproduit la charge au pic à 2,3 % près, mais non la branche post-pic. Douze mois d'immersion sulfatique et acide, des essais de migration des chlorures et d'exposition thermique, et une campagne offshore de 10 mois à HarshLab établissent une résistance supérieure aux sulfates et aux acides, l'absence de front de chlorures et de carbonatation après immersion réelle, et le maintien intégral de la classe mécanique BFUP dans les trois zones d'exposition. Seul déficit : 36 % à 600 °C contre 90 % pour l'unique éprouvette REF survivante, le GEO restant intact à toutes les températures. Cette condition se situe hors de l'enveloppe de service marin. Une évaluation de l'empreinte carbone du berceau à la tombe selon l'EN 15804+A2 retourne une réduction de 37 % par m^3 et de 32,1 % par tonne face à une DEP vérifiée par tierce partie pour le BFUP de référence, satisfaisant l'objectif carbone du projet, tandis que l'objectif de coût rapporté à la résistance n'est pas atteint, à 10,9 % pour une exigence de 35 %. GEO est ainsi mécaniquement conforme, monitorable, durable en mer et substantiellement moins carboné que le BFUP qu'il remplace.

Mots-clés : BFUP géopolymère; activation alcaline; laitier; fibres d'acier recyclées; spectroscopie d'impédance électrochimique; émission acoustique; durabilité marine; empreinte carbone.

Research Unit



Institut de Mécanique et d'Ingénierie

CNRS, UMR 5295

http://i2m.u-bordeaux.fr

Département Génie Civil Environnemental (GCE)

351 Cours de la Libération

33405 Talence

France

Publications and Communications

Articles in peer-reviewed international journals

- Y. SLEIMAN, H. ALLAM, N. SAIYOURI, B. SOLBES, Z.M. SBARTAÏ (2026). Fracture damage mechanisms in ultra-high performance geopolymer concrete: a multi-parameter acoustic emission study. *Construction and Building Materials*, 535, 146609 (Published). https://doi.org/10.1016/j.conbuildmat.2026.146609
- Y. SLEIMAN, H. ALLAM, N. SAIYOURI, Z.M. SBARTAÏ (2026). Mechanical and electrical performances of fiber-reinforced UHPC with geopolymer and Portland cement binders. *Spectroscopy Journal*, 4(2), 11 (Published). https://doi.org/10.3390/spectroscj4020011
- Y. SLEIMAN, B. EL OIFI, C. MARTIN, N. SAIYOURI, Z.-M. SBARTAÏ (2026). Durability of a cement-free ultra-high performance geopolymer concrete: a laboratory comparison with Portland-cement UHPC validated by real marine exposure. *Case Studies in Construction Materials* (Published). https://doi.org/10.1016/j.cscm.2026.e06583
- Y. SLEIMAN, B. EL OIFI, N. SAIYOURI, Z.M. SBARTAÏ (2026). Sequential bottleneck-driven design of an ambient-cured ultra-high performance geopolymer concrete: the effect of silicate dosage on early-age strength in alkali-activated slag at low water-to-binder ratio. *Developments in the Built Environment* (Under review).
- Y. SLEIMAN, H. ALLAM, N. SAIYOURI, Z.M. SBARTAÏ (2026). Electrochemical impedance spectroscopy characterization of geopolymer ultra-high-performance concrete: microstructural evolution and strength correlation. *Journal of Building Engineering* (Under review).

Oral communications in international congresses

- Y. SLEIMAN, B. EL OIFI, N. SAIYOURI, Z.-M. SBARTAÏ (2026). Durability assessment of geopolymer ultra-high-performance concrete for marine infrastructure. *7th fib International Congress*, Lisbon, Portugal.
- Y. SLEIMAN, B. EL OIFI, Z.-M. SBARTAÏ, N. SAIYOURI (2026). Chemical resilience and thermal stability of geopolymer UHPC. *MATBUD 2026, Scientific-Technical Conference on Material Problems in Civil Engineering*, Cracow, Poland.

Communication in a national congress

- Y. SLEIMAN, N. SAIYOURI, Z.M. SBARTAÏ (2025). Development of an ultra high performance gropolymer concrete for offshore structures. Rencontres Universitaires de Génie Civil (RUGC 2025), Marseille, France.

Poster communications

- Y. SLEIMAN, N. SAIYOURI, Z.M. SBARTAÏ (2025). Optimization of an ultra high performance concrete for marine structures. *Journée de l'École Doctorale Sciences Physiques et de l'Ingénieur, Université de Bordeaux*, 28 March 2025, Talence, France.

- Y. SLEIMAN, N. SAIYOURI, Z.M. SBARTAÏ (2024). A bottleneck-driven design of an ambient-cured ultra-high performance geopolymer concrete. *EUSKAMPUS, Campus eurorégional Bordeaux-Euskampus*, Talence, France.

Other communications, competitions and prizes

- Ma Thèse en 180 secondes competition, Université de Bordeaux final, **First Jury Prize**, online: https://youtu.be/G7twdvUEuQI, 2026, Talence, France.

- Ma Thèse en 180 secondes competition, Nouvelle-Aquitaine regional final, **Third Jury Prize**, https://www.youtube.com/live/oI515_pkbIQ?si=kNZXPP6HAiJ68Ok9, 2026, Limoges, France.

“

I hope that however old we live to be,

we die young.

HENRI MATISSE

Dedication

To my parents, to my sister, my brothers, my cousins, my family members,
and to the South that raised me.

I spent three years learning how a material holds against the sea,
you spent them holding against everything else.

From afar, your courage became the foundation of every page.

This thesis carries my name, but it belongs to you.

Acknowledgments

This thesis was carried out at the Institut de Mécanique et d'Ingénierie (I2M, UMR 5295) of the Université de Bordeaux, within the European project NATURSEA-PV. Many people made it possible, and I would like to thank them here.

I first thank my supervisors, Professor Nadia Saiyouri and Professor Zoubir-Mehdi Sbartaï, for giving me the opportunity to carry out this thesis, for the trust they placed in me from the first day, and for the freedom they gave me to explore, test and sometimes fail before finding the right path.

I sincerely thank the members of my jury for the time and attention they gave to this work. I thank Professor Karim Aït-Mokhtar (Université de La Rochelle) for presiding over the jury and for examining this work. I am grateful to Professor Ali-Nordine Leklou (Université de Nantes) and Dr Yun Jia (Université de Lille) for accepting to review this manuscript, for their careful reading and for their detailed reports. I thank Dr Mokhfi Takarli (Université de Limoges) for examining this work and for the discussion during the defense. I also thank Dr Edurne Erkizia (Tecnalia) and Dr Neven Ukrainczyk (Technical University of Darmstadt), who joined the jury as invited members.

This work received funding from the European Union's Horizon Europe research and innovation programme under grant agreement No 101084348 (NATURSEA-PV). I thank all the partners of the project for three years of exchanges, and Tecnalia in particular for hosting our specimens on the HarshLab offshore platform.

I would like to thank everyone at I2M who made the experimental work of this thesis possible. I thank Bouchra El Oifi for her help in the laboratory, especially with the durability and characterization work. I am equally grateful to Bernard Solbes, always ready to help with the testing setups, including the acoustic emission campaign, and always ready for a coffee and a good discussion. I also thank Audrey Duphil and Clément for accompanying me in the tests carried out for the different chapters of this thesis, and the technical team of building A11 bis, Stéphane, Olivier and Philippe, for their help every time a machine, a mold or a press needed attention.

I sincerely thank the administration team, Sandrine, Pascal, Isabelle, Barbara and Virginie, for their availability and their patience with every form, order and mission I brought to them, and the IT team, Jean-Marc, Gilles and Clément, who were always there when a computer, a license or a server decided to stop working.

My thanks also go to Éric Lebraud (ICMCB) and Philippe Legros (PLACAMAT) for their help with the characterization of my materials, and to the TREFLE department of I2M for giving me access to its equipment, with special thanks to Cécile Gaborieau for her availability and her advice.

I also thank the professors, associate professors, postdocs and research engineers of I2M who helped me along the way. A special thank you to Hamza Allam: from the day he arrived

at the laboratory, he was always there to advise us, especially on the non-destructive testing work, and the long and deep discussions we had together taught me a great deal. Thank you so much, Hamza. I also thank Amal for her help with the modeling part of this thesis. She was always available and ready to help, even when Miral was waiting for her at the nursery. Sorry, Miral, for making your mom a little late a few times.

I was lucky to work with several interns, and each of them left a mark on this thesis. I thank Yusra for her intelligence and her scientific rigor, for the good discussions and the work we did together, and for the publication that came out of it. A special thank you goes to Ali, who arrived at a difficult time and immediately found his place: always in the right spirit, working hard and staying long hours in the concrete laboratory. Our work together on the acoustic emission results led to a fine publication, and I am grateful for the time we spent on it. I thank Baptiste for his long hours of work in the concrete laboratory, and Simube for the help he offered there as well. I thank Yan and Romain for their contribution to the modeling part, and Bland and Mohammed for the good times we spent together and the productive work we did.

Ma Thèse en 180 secondes was one of the defining challenges of this PhD. I entered the competition without a strong command of French, and I owe a great deal to my coach, Eric Drevet, whose support and technical advice guided me all the way, from the first draft of my text to the final stage. With his help, I won the First Jury Prize at the Université de Bordeaux final and the Third Jury Prize at the Nouvelle-Aquitaine regional final. I also thank the Ma Thèse en 180 secondes organizing team and the administrative staff who accompanied us throughout the competition, and all the participants with whom I shared the stage.

I want to thank, with all my heart, the PhD students of I2M with whom I shared this journey. Beyond the experiments and the deadlines, they gave me moments I will never forget, and they turned a laboratory into a place where I felt at home.

Amine, I start with you. You were my biggest supporter from the first day to the last, and you never hesitated to be by my side, whatever the moment. I shared countless laughs with you, in the lab and outside it (yes, Amine, I am always available on weekends). Thank you for your advice, often given before I even asked, and for all your jokes, even the unfunny ones. I liked them anyway. Thank you for the pranks we pulled together, for the unforgettable moments, and for that chemistry where a single look was enough to understand each other. I can truly say that you are a brother for life. (I am activatedddddddd, no card today).

Sarah, thank you for everything: for every moment and every laugh we shared, and for all the time we spent together at A8. We share the same love for our country, Lebanon, and I will never forget our salty lemon and cumin at lunch.

Maxime, I shared with you the Ma Thèse en 180 secondes adventure: the stage, the training sessions and every moment of a challenge that marked my life. Thank you for being a friend, a colleague and the best of besties. You are my motivation to do sport, and your

discipline has always influenced me positively. I am so proud of you and of everything you are achieving, and I am happy to have you as a very special person in my life.

Aurore, thank you so much for your smile, your positive vibes and the purity I always felt around you. Thank you for your support during Ma Thèse en 180 secondes: I rehearsed again and again, and you followed every rehearsal with the same attention. Thank you for the time you gave me and for correcting my French. I am proud of you.

Hamzah, thank you for all the laughs, for our “skills tools”, and for being my matte partner. Thank you for sharing everything with me, including all your technical skills. I am so happy to know you and thank you for everything.

Ali, from the APY department of I2M, you have held a special place since the very first day, and I have always seen in you the soul of my cousins. You are always the first person I call when I need something. We shared happy moments and difficult ones, when our country was going through hard times, and through all of it we stood side by side, inside the lab and outside it. You are a truly good person, and you will always be the best friend ever. I wish you all the good things life can bring, as much as you deserve them, and I am so proud of the person you are and so happy for you and your beloved wife.

Ahmad, thank you so much for being our big brother here, for all the tiramisu you made for us, and for all the moments we spent together. I wish you all the best with your wife, Batoul.

I also thank Axelle, Julian, Pierre, Timothée, David, Dylan, Sylvain, Cheima, Ali, Sarra, Lisa, Habiba, Marie, Théophile, Adrien, Lucie, Dimitri, Tuan, Marcine, Nabil, Perrine, Marion, Maria, Stefano, Nourhan, Clément, Alejandro, Asmaa, Jinxia, Xochtil, Louise, Enzo, Nour, Amr, Faustine, Ikram, Tosin, Jonathan, Sumir and Chloé for their presence, their help and the atmosphere they brought to the laboratory.

Outside the laboratory, I was lucky to be surrounded by friends who were there for the small moments and the big ones. Thank you to Mike, Jana, Sabine, Elissa, Ali, Sama, Maria, Rita, Rodolphe, Tony, Christina, Stan, Sarah, Joelle, Ayoub and to all the players of the Lebanese football team I played with.

To my uncles, Ibrahim and Saad, and to your families: you came all this way to be by my side. Far from home, you were my home. You were my greatest support, the most beautiful gift life has given me. Without you, this journey would have been far too heavy to carry. From the bottom of my heart, thank you.

To all my uncles, my cousins and all the members of the Sleiman and Saad families, and to my region: I know how hard these years have been for you. I know everything. Thank you for keeping me in your thoughts, even from far away.

Finally, the most important people in my life: Mama, Baba, my sister and my brothers.

I come from South Lebanon. From the first day of this PhD until today, the situation wasn’t stable at home. Every day, I received two kinds of messages: emails about my experiments, and news about my country. While I was here, testing how concrete resists the

sea, you were there, living through it. Being far from you during those days was the hardest part of this PhD. And yet, you were the ones giving me strength: you faced those difficult days with patience and courage, so that I could continue here. You were my motivation and the reason I never gave up. You are the source of everything in my life, and I love you with all my heart.

And to myself, I just want to say: you held on. Even on the hardest days, you did not give up, and you finished on time.

Table of Contents

Abstract…….. 2

Résumé……. 3

Research Unit……. 4

Publications and Communications 5

Dedication 8

Acknowledgments 9

Table of Contents 13

List of Figures… 19

List of Tables…. 25

List of Abbreviations 27

General Introduction

0.1 Marine renewable energy and the offshore floating PV opportunity 31

0.2 The substructure problem: from HDPE to UHPC 32

0.3 The carbon problem of conventional UHPC 33

0.4 The NATURSEA-PV framework 34

0.5 UHPGC as the cement-free route 37

0.6 Thesis objectives and central research question 39

0.7 Thesis structure 40

Chapter 1 - Formulation and Characterization

1.1 State of the art 46

1.1.1 Geopolymerization and activator chemistry 46

1.1.2 Precursor systems: GGBS, silica fume, and fly ash 49

1.1.3 Existing UHPGC formulations and what they leave open 52

1.1.4 Multi-objective optimization at UHPGC strength levels 55

1.2 Raw materials 59
1.2.1 Precursors: GGBS, silica fume, and class F fly ash 60
1.2.2 Alkali activators 60
1.2.3 Aggregates 61
1.2.4 Superplasticizer 62
1.2.5 Virgin steel fibers 62
1.2.6 Recycled tire-derived steel fibers 62

1.3 Mix design optimization protocol 62
1.3.1 Mixing Protocols 67
1.3.2 Mixers 67
1.3.3 REF protocol 68
1.3.4 PCE incompatibility 68
1.3.5 Hydroxide pre-mix 68
1.3.6 Initial UHPGC trials and protocol revision 69
1.3.7 Revised GEO protocol 69
1.3.8 Two-stage fiber addition 70
1.3.9 Visual and auditory endpoint cues 70
1.3.10 Casting and curing 70
1.3.11 Scale up 71

1.4 Characterization techniques 71
1.4.1 Fresh-state properties 73
1.4.2 Mechanical properties 74
1.4.3 Reaction kinetics 74
1.4.4 Transport properties 75
1.4.5 Phase and microstructure 77

1.5 Results 78
1.5.1 Stage 1: Effect of GGBS/FA ratio on strength and workability 79
1.5.2 Stage 2: NaOH co-activation and molarity 81
1.5.3 Stage 3: Sodium silicate dosage and binder restructuring 83
1.5.4 Stage 4: Total binder dose and NaOH molarity (G7.2SF1.8) 86
1.5.5 Stage 5: Cation replacement (NaOH to KOH) 88
1.5.6 Stage 6: Fiber incorporation and recycled-blend selection 90
1.5.7 Characterization of the optimized GEO 94

1.6 Conclusion 106
1.6.1 Limitations and perspectives 108

1.7 Transition to Chapter 2 109

Chapter 2 - Electrochemical Impedance Spectroscopy

2.1 State of the art 112
2.1.1 EIS as a microstructural probe in cementitious materials 112
2.1.2 EIS across binder chemistries 117
2.1.3 Limits of existing non-destructive methods for UHPC 120
2.1.4 Synthesis of the gap 121

2.2 Materials and methods 122
2.2.1 Mix designs 123
2.2.2 Specimen preparation and curing 124
2.2.3 EIS measurement setup 125
2.2.4 Equivalent circuit models 127
2.2.5 CNLS fitting procedure 130

2.3 Results 133
2.3.1 Microstructural baseline 133
2.3.2 Compressive strength evolution at the eight EIS ages 134
2.3.3 Nyquist evolution 136
2.3.4 Bode evolution 141
2.3.5 Fit quality and Kramers-Kronig consistency 145
2.3.6 Solution resistance Rs trajectory 150
2.3.7 Arc resistances R1, R2, and R3 154
2.3.8 CPE magnitudes and dispersion exponents 158
2.3.9 Warburg diffusion parameters 161
2.3.10 Correlation between impedance and compressive strength 164

2.4 Conclusions 169
2.4.1 Limitations and perspectives 170

2.5 Transition to Chapter 3 172

Chapter 3 - Acoustic emission and Fracture Mechanics

3.1 State of the art 174

3.1.1 Acoustic emission in cementitious materials 175
3.1.2 Acoustic emission descriptors for crack-mode classification 177
3.1.3 Acoustic emission in fiber-reinforced UHPC 181
3.1.4 Acoustic emission in alkali-activated and geopolymer composites 182
3.1.5 Research gap and chapter scope 183

3.2 Materials and methods 184
3.2.1 Mixes and specimens 184
3.2.2 Three-point bending setup 186
3.2.3 Acoustic emission acquisition 189
3.2.4 AE data processing 191

3.3 Results 192
3.3.1 Mechanical baseline: compressive strength and water porosity 193
3.3.2 Flexural response under three-point bending 194
3.3.3 Toughness and ductility 195
3.3.4 Cumulative AE activity and AE energy 197
3.3.5 Damage stage identification through b-value evolution 199
3.3.6 Crack-mode classification through RA-AF analysis 201
3.3.7 AE hit rate and damage acceleration 205

3.4 Numerical Modeling 206
3.4.1 Constitutive model and numerical implementation 207
3.4.2 Representation of the fibers and identification of the parameters 208
3.4.3 Computed flexural response 209
3.4.4 Application under direct tension 211
3.4.5 Summary and further development 213

3.5 Conclusion 213
3.5.1 Limitations and perspectives 214

3.6 Transition to Chapter 4 216

Chapter 4 - Durability and Carbon Footprint Assessment

4.1 State of the art 218
4.1.1 Marine degradation of Portland cement and the geopolymer premise 219
4.1.2 Durability of alkali-activated binders under chemical attack 221
4.1.3 Chloride transport and elevated-temperature behavior 225

4.1.4 Assessment methods and their limitations in alkali-activated systems . 227
4.1.5 Open questions on durability 231
4.1.6 The UHPC carbon benchmark and its reduction routes 232
4.1.7 Methodological dispersion and the case for like-for-like comparison .. 233
4.1.8 Open questions on the life-cycle record 234

4.2 Materials and methods 235
4.2.1 Materials 235
4.2.2 Specimen preparation and conditioning 235
4.2.3 Sulfate and acid immersion 236
4.2.4 Elevated-temperature exposure 237
4.2.5 Rapid chloride penetration..... 238
4.2.6 Electrical impedance monitoring..... 239
4.2.7 Marine exposure at HarshLab..... 240

4.3 Durability results 241
4.3.1 Sulfate and acid attack: mass change 241
4.3.2 Sulfate and acid attack: length change and phase analysis..... 243
4.3.3 Residual mechanical strength after sulfate and acid immersion..... 246
4.3.4 Impedance evolution over 365 days 250
4.3.5 Elevated-temperature resistance 252
4.3.6 Rapid chloride penetration..... 254
4.3.7 Electrical resistivity and corrosion-risk classification..... 257
4.3.8 Marine exposure at HarshLab..... 258

4.4 Goal, scope, functional unit, and system boundary 263
4.4.1 Goal of the study..... 264
4.4.2 Functional unit..... 264
4.4.3 System boundary 265
4.4.4 Impact assessment method 266
4.4.5 Data quality, cut-off, and allocation 267

4.5 Inventory 268
4.5.1 GEO mix inventory 268
4.5.2 REF-EPD mix inventory 269
4.5.3 Transport modeling..... 270
4.5.4 Data quality..... 270

4.6 Impact assessment 271
4.6.1 Headline result by EN 15804 module 271
4.6.2 Hotspot analysis of the GEO raw-materials stage 274
4.6.3 Robustness against the functional unit 275
4.6.4 End-of-life modules and method robustness 275
4.6.5 Summary of the impact assessment 276

4.7 Sensitivity analysis 277
4.7.1 Scenario design 277
4.7.2 Tornado representation and lever ranking 279
4.7.3 Robustness verdict 280

4.8 Economic analysis 281
4.8.1 Price basis, procurement tiers, and evidence quality 281
4.8.2 Cost-to-strength against KPI 2.2 283
4.8.3 Cost-carbon coupling and the path to the target 285

4.9 Conclusion 286
4.9.1 Limitations and perspectives 288

General Conclusions 291

Perspectives…… 295

References…… 297

Synthèse en langue française 311

Introduction générale 311

Résumé étendu 322

Conclusion générale et perspectives 325

List of Figures

Figure 0-1: Main current offshore floating PV technologies under field validation. (1) Ocean Sun HDPE membrane (Norway), (2) Oceans of Energy modular system (Dutch North Sea), (3) SolarDuck triangular semi-submersible (IJzendoorn, Netherlands), and (4) UHPC floaters and farm (Alqueva). **32**

Figure 0-2: NATURSEA-PV's PERT diagram. **35**

Figure 0-3: Shallow Water Basin model test of a floating PV substructure (a) and (b) the Victoria amazonica leaf that inspired the radial-rib geometry. **37**

Figure 0-4: HarshLab offshore floating laboratory operated by TEC, moored at the Biscay Marine Platform (BiMEP) in the Bay of Biscay. **37**

Figure 0-5: Graphical overview of the key points in Chapter 1. **41**

Figure 0-6: Graphical overview of the key points in Chapter 2. **42**

Figure 0-7: Graphical overview of the key points in Chapter 3. **43**

Figure 0-8: Graphical overview of the key points in Chapter 4. **44**

Figure 0-9: Architecture of the manuscript and the chained research questions across the four chapters. **45**

Figure 1-1: Compatibility regions of N-A-S-H, C-A-S-H, and coexisting gels on the CaO-Al_2O_3-SiO_2 system. Reproduced from Garcia-Lodeiro et al. (2011). **49**

Figure 1-2: Compressive strength against embodied CO_2 for UHPC and UHPGC formulations from the literature (Wang et al., 2025). **55**

Figure 1-3: Geometry and rubber-residue features of recycled tire steel fibers (RTSF) compared with virgin steel microfibers. Reproduced from Centonze et al. (2012). **57**

Figure 1-4: Flexural strength of UHPC mixes containing RTSF and RTSC at 2 to 4% fiber volume. Reproduced from Isa et al. (2020). **59**

Figure 1-5: Raw constituents used in the formulation program, as received. **60**

Figure 1-6: Particle-size distributions of the six dry constituents of the REF and GEO mixes. Powder curves from supplier datasheets by laser diffraction and sand curves from sieve analysis. **62**

Figure 1-7: Sequential optimization program schema for the GEO formulation. **66**

Figure 1-8: MATEST E094N planetary mortar mixer used for the laboratory-scale formulation work, with 4 × 4 × 16 cm^3 casting molds. **68**

Figure 1-9: Characterization equipment. (a) Flow table, (b) Vicat apparatus, (c) three-point bending rig, (d) compression press, (e) Langavant calorimeter, (f) vacuum saturation, (g) gas permeability cell, (h) mercury intrusion porosimeter, (i) X-ray diffractometer, (j) scanning electron microscope. **73**

Figure 1-10: 28-day compressive strength of the Stage 1 mixes as a function of the GGBS content of the precursor blend. Error bars denote the measured within-batch coefficient of variation. **80**

Figure 1-11: Effect of NaOH molarity on the two precursor blends of Stage 2. (a) 24-hour compressive strength, (b) 28-day compressive strength, (c) slump flow. **82**

Figure 1-12: Effect of sodium silicate dosage on G6SF1.8 at 12 M NaOH. (a) Compressive strength at 24 hours and 28 days, (b) slump flow..... **84**

Figure 1-13: Effect of NaOH molarity on G7.2SF1.8. (a) Compressive strength at 24 hours and 28 days, (b) slump flow. **87**

Figure 1-14: Effect of hydroxide cation on the G7.2SF1.8 binder at equal 10 M concentration. (a) Compressive strength at 24 hours and 28 days, (b) slump flow, (c) open time taken as the NF EN 196-3 final setting time. **89**

Figure 1-15: Compressive strength at 1 day and 28 days for the four Flexo to Spajic blends, at fiber contents of (a) 10.4 wt% and (b) 12 wt% of binder mass. **91**

Figure 1-16: Flexural strength at 1 day and 28 days for the four Flexo to Spajic blends, at fiber contents of (a) 10.4 wt% and (b) 12 wt% of binder mass. **92**

Figure 1-17: Compressive strength development of REF and GEO from 1 to 28 days on 4 × 4 × 16 cm^3 prism halves per NF EN 196-1, ambient curing (20 ± 2 °C, 50 ± 5% RH). **94**

Figure 1-18: Semi-adiabatic temperature evolution of GEO and REF over 48 hours. Single-specimen measurements per mix. The peak-temperature reproducibility was estimated at ± 2 °C from calorimeter calibration runs. **95**

Figure 1-19: Apparent nitrogen permeability Ka against inverse mean pressure at 28 days. (a) GEO, (b) REF..... **98**

Figure 1-20: Mercury intrusion porosimetry at 28 days, cumulative intruded volume against pore-entry diameter for (a) GEO and (b) REF. **100**

Figure 1-21: Mercury intrusion porosimetry at 28 days, differential distribution dV/d(log D) for (a) GEO and (b) REF, smoothed over five points. **101**

Figure 1-22: X-ray diffraction patterns at 28 days for GEO and REF, offset vertically. . **103**

Figure 1-23: SEM fracture-surface micrographs at 28 days and 350× magnification of (a) the GEO mix and (b) the REF mix. **105**

Figure 2-1: Anatomy of an impedance spectrum. (a) Nyquist plot, frequency increasing right to left. (b) Bode modulus and phase. All features are labeled on the figure and defined in Section 2.1.1. ..... **113**

Figure 2-2: The two Warburg formulations used in this chapter. (a) Finite-length short-circuit Ws for REF, closing back to the real axis at Z = Rw. (b) Semi-infinite W for GEO, rising unbounded toward low frequencies. **115**

Figure 2-3: Kramers-Kronig consistency check on a synthetic two-arc spectrum. (a) Voigt-representable spectrum with its Lin-KK residuals and (b) The same spectrum with a series inductance above 1 MHz, residuals rising sharply in the shaded band. **116**

Figure 2-4: Measurement schedule per system. **125**

Figure 2-5: EIS measurement setup. **126**

Figure 2-6: Physical interpretation of the equivalent circuit elements, mapped onto a cross-section of the UHPC microstructure between the electrodes. **128**

Figure 2-7: Equivalent circuit topologies adopted for REF. (a) Stage 1, Days 1 to 7, two arcs with a finite-length Warburg (equation 2.4). (b) Stage 2, Days 10 to 28, three arcs with the interfacial arc added (equation 2.5). **129**

Figure 2-8: Equivalent circuit topology adopted for GEO. Single-stage, two arcs with a semi-infinite Warburg (equation 2.6), applied at all eight ages. No third arc is resolved at any age. **130**

Figure 2-9: Compressive strength of REF (blue squares) and GEO (orange diamonds) over the eight EIS ages. Error bars are one standard deviation on six half-prisms per age per system. **135**

Figure 2-10: Nyquist evolution of REF over the eight curing ages, with the CNLS-fitted model overlaid. Gray circles are the measured spectra and the blue line the fitted model. Stage assignment and R^2 are given per panel. **138**

Figure 2-11: Nyquist evolution of GEO over the eight curing ages, with the CNLS-fitted model overlaid. Gray circles are the measured spectra and the orange line the fitted model. R^2 is given per panel. **140**

Figure 2-12: Age-by-age Nyquist comparison of REF and GEO. REF in blue on the lower and left axes, in kΩ, and GEO in orange on the upper and right axes, in Ω. **141**

Figure 2-13: Bode evolution of REF over the eight curing ages. (a) Impedance modulus $|Z(f)|$ and (b) Phase angle $\varphi(f)$. Curves run from Day 1 in black to Day 28 in dark red. .. **143**

Figure 2-14: Bode evolution of GEO over the eight curing ages. (a) Impedance modulus $|Z(f)|$. (b) Phase angle $\varphi(f)$. **144**

Figure 2-15: CNLS fit quality of REF across the eight curing ages. (a) Mean and maximum relative error per age, with the 5% acceptance threshold as a dashed gray line. (b) Coefficient of determination R2 per age, with the 0.99 threshold as a dashed gray line. **146**

Figure 2-16: CNLS fit quality of GEO across the eight curing ages. (a) Mean and maximum relative error per age, with the 5% acceptance threshold as a dashed gray line. (b) Coefficient of determination R2 per age, with the 0.99 threshold as a dashed gray line. **147**

Figure 2-17: Kramers-Kronig consistency of REF at the eight curing ages. Lin-KK residuals on the real part $\Delta Z'$ and imaginary part $\Delta Z''$, as percentages of $|Z|$. Dashed lines mark ±2%. **148**

Figure 2-18: Kramers-Kronig consistency of GEO at the eight curing ages. Lin-KK residuals on the real part $\Delta Z'$ and imaginary part $\Delta Z''$, as percentages of $|Z|$. Dashed lines mark ±2%. **149**

Figure 2-19: Solution resistance of REF across the eight curing ages. Filled squares are free-fit values, open squares the six ages at which the fit returns the 500 Ω cap. The gray line is the upper bound on Rs from the lowest measured Z'. **152**

Figure 2-20: Solution resistance of GEO across the eight curing ages. All eight values are free-fit. **153**

Figure 2-21: Solution resistance of REF (blue squares) and GEO (orange diamonds) across the eight curing ages. Open REF squares are at the 500 Ω cap. **154**

Figure 2-22: Arc resistances of REF across the eight curing ages. R1 (grain-boundary network), R2 (gel pore network) and R3 (interfacial arc, resolvable from Day 10), distinguished by marker. Gray shading marks the Stage 2 topology window, Days 10 to 28. ..... **156**

Figure 2-23: Arc resistances of GEO across the eight curing ages, R1 and R2 distinguished by marker. Open R1 markers at Days 2 and 14 mark ages at which the first arc lies outside the measurement window. **157**

Figure 2-24: Cross-system comparison of the arc resistances. (a) R1, grain-boundary network and (b) R2, gel pore network. **158**

Figure 2-25: Warburg amplitude Rw and time constant Tw of REF across the eight curing ages. **162**

Figure 2-26: Warburg coefficient W of GEO across the eight curing ages. Filled diamonds are accepted fits, open diamonds the two ages at which R^2 falls below 0.99. Units are $\Omega \cdot s^{-1/2}$. **163**

Figure 2-27: Correlation between REF compressive strength and the two candidate indicators across the eight curing ages. (a) Gel pore resistance R2. (b) Warburg amplitude Rw. **166**

Figure 2-28: Correlation between GEO compressive strength and the two candidate indicators across the eight curing ages. (a) Warburg coefficient W and (b) Gel pore resistance R2. ..... **167**

Figure 3-1: Schematic anatomy of an AE hit and the timing parameters that define it. .. **176**

Figure 3-2: Schematic RA-AF crack-mode classification framework. The boundary slope k is fitted independently for each specimen (Section 3.2.4). **180**

Figure 3-3: Three-point bending setup and seven-channel AE sensor array. (a) Side view to scale. (b) Front face, sensors 1 to 4. (c) Back face, sensors 5 to 7. ..... **188**

Figure 3-4: Flexural load-deflection response at 24 hours. (a) Plain matrices. (b) Fiber-reinforced composites. **195**

Figure 3-5: Flexural load-deflection response at 28 days. (a) Plain matrices. (b) Fiber-reinforced composites. **195**

Figure 3-6: Toughness decomposition into pre-peak and post-peak contributions for the cells of the design. The dotted line marks the peak-load displacement. **197**

Figure 3-7: Load, cumulative hit count, and cumulative AE energy versus mid-span deflection at 28 days. **198**

Figure 3-8: Load, cumulative hit count, and cumulative AE energy versus mid-span deflection at 24 hours. **199**

Figure 3-9: b-value evolution superimposed on the load curve at 28 days. Reference lines mark b = 1.0 and b = 1.5. ..... **200**

Figure 3-10: b-value evolution superimposed on the load curve at 24 hours. **201**

Figure 3-11: RA-AF crack-mode classification at 28 days. (a) R, (b) Rf, (c) G, (d) Gf. Percentage labels are readings at the fitted boundary and shift by 11 to 14 points under a +/- 30% change in slope (Section 3.2.4). **203**

Figure 3-12: RA-AF crack-mode classification at 24 hours. (a) R, (b) Rf, (c) G, (d) Gf. Boundary and labels as in Figure 3-11. ..... **204**

Figure 3-13: AE hit rate (hits per 0.02 mm displacement bin) versus mid-span deflection at 28 days, with the load curve overlaid. **205**

Figure 3-14: AE hit rate versus mid-span deflection at 24 hours. **206**

Figure 3-15: Finite-element discretization of the modeled specimens. (a) Three-point bending beam, (b) Fiber network of the bending specimen shown alone, (c) Uniaxial tension specimen, and (d) Fiber network of the tension specimen. **208**

Figure 3-16: Computed and measured flexural response of the fiber-reinforced geopolymer at 28 days. **210**

Figure 3-17: Computed damage field in the three-point bending specimen at three stages: (a) peak load, (b) early post-peak, and (c) end of simulation. **211**

Figure 3-18: CAST3M axial-strain (εxx) fields in the tension specimen. Perspective view of the prism and the six analyzed faces. Red indicates peak tensile strain, interpreted as cracking zones. **212**

Figure 3-19: ImageJ binary mask of the cracked region on a representative surface, obtained by isolating the high-tensile-strain (red) bands and applying morphological cleanup..... **213**

Figure 4-1: Chemical premise for the durability comparison for REF and GEO..... **221**

Figure 4-2: Position of the present work in the published durability literature on binders subjected to chemical immersion. **225**

Figure 4-3: The formation-factor concept. **229**

Figure 4-4: Position of the present work in the published life-cycle literature of ultra-high-performance concretes, plotted in strength-carbon space..... **234**

Figure 4-5: Specimens mounted in the furnace. **238**

Figure 4-6: (a) RCPT schema and (b) RCPT device. **239**

Figure 4-7: The HarshLab (Tecnalia) offshore floating facility (Biscay Marine Platform, Bay of Biscay), showing the atmospheric, splash, and immersion zones in which the GEO specimens were positioned. **241**

Figure 4-8: Mass change of (a) GEO and (b) REF specimens immersed in distilled water, Na_2SO_4, $MgSO_4$, HNO_3, and the combined magnesium-and-sodium sulfate solution over 52 weeks. **242**

Figure 4-9: Length change of (a) GEO and (b) REF specimens immersed in water, Na_2SO_4, $MgSO_4$, HNO_3, and combined Mg+Na sulfate over 52 weeks. REF blue, GEO orange. . **244**

Figure 4-10: Residual compressive strength of GEO and REF after (a) 6 and (b) 12 months of immersion in distilled water, Na_2SO_4, $MgSO_4$, HNO_3, and the combined magnesium-and-sodium sulfate solution. **248**

Figure 4-11: Residual flexural strength of GEO and REF after (a) 6 and (b) 12 months of immersion in the same five solutions. **249**

Figure 4-12: Evolution of the real component of impedance Z′ at 10 kHz for GEO and REF specimens immersed in water, Na_2SO_4, $MgSO_4$, and HNO_3 over 365 days. **251**

Figure 4-13: (a) Residual compressive and (b) flexural strength of GEO and REF after exposure to 300, 600, and 900 °C. **253**

Figure 4-14: (a) visual appearance of GEO and (b) REF specimen after exposure to 600 °C. **253**

Figure 4-15: Rapid chloride penetration results for all tested mixes (GEO, REF, CEM III/A, CEM III/B, CEM IV/A): (a) total charge passed and (b) apparent chloride diffusion coefficient. **255**

Figure 4-16: Electrical resistivity of the five mixes derived from the rapid chloride penetration measurement, $\rho = V \cdot A/(I \cdot L)$, on a logarithmic axis. **257**

Figure 4-17: Coated and uncoated Geopolymer specimens' evolution in the splash zone. **259**

Figure 4-18: Coated and uncoated geopolymer specimens' evolution on immersion zone. **260**

Figure 4-19: Residual mechanical strength of GEO after 10 months of marine exposure at HarshLab, by zone and surface condition. (a) flexural, (b) compressive. Replicate count given above each bar. **261**

Figure 4-20: Colorimetric assessment of GEO specimens after 10 months of marine exposure at HarshLab, for the seven zone and surface-condition groups. **263**

Figure 4-21: System boundary of the comparative life cycle assessment under EN 15804+A2. ..... **266**

Figure 4-22: Spatial layout of the GEO supply chain for the Valencia deployment scenario. **270**

Figure 4-23: Cradle-to-grave global warming potential by EN 15804+A2 module, per m^3. ..... **272**

Figure 4-24: Decomposition of the GEO A1 raw-materials stage by component, ranked from largest to smallest. **274**

Figure 4-25: Cradle-to-grave global warming potential of GEO decomposed by EN 15804+A2 module under two methods: EF 3.1 V1.01 (IPCC AR6 factors) and CML-IA Baseline V3.10 (IPCC AR4 factors). The two agree within 0.7% on the cradle-to-grave total, inside the expected band for cement-based products. **276**

Figure 4-26: Sensitivity tornado plot of the GEO/REF-EPD cradle-to-grave GWP delta under nine one-at-a-time perturbations from the baseline. **279**

Figure 4-27: KPI dashboard of the REF-EPD and GEO mixes in cost-to-strength versus carbon-to-strength space. **285**

List of Tables

Table 1-1: Representative formulations across the UHPC and UHPGC spectrum. **53**

Table 1-2: Chemical composition and physical properties of binder constituents and activators. **61**

Table 1-3: Optimization protocol. Each stage isolates one variable, or one defined pair, while holding the remaining parameters at the values inherited from the previous stage... **63**

Table 1-4: Mix design matrix of the GEO formulations investigated across the six optimization stages. **66**

Table 1-5: REF mixing protocol. **68**

Table 1-6: GEO mixing protocol (cement-free, alkali-activated). **70**

Table 1-7: Characterization techniques: standards, equipment, specimens, and replicates. **71**

Table 1-8: Water-accessible porosity of GEO and REF at 28 days measured per NF P18-459 on 4 × 4 × 4 cm^3 cubes. **96**

Table 1-9: Mercury intrusion porosimetry results at 28 days for GEO and REF. **101**

Table 1-10: Quantitative phase analysis of the hardened GEO at 28 days. **103**

Table 1-11: Bulk elemental composition of the GEO and REF matrices measured by map-integrated EDS on fiber-free polished regions at 28 days. **105**

Table 3-1: Steel fiber specification, declared in accordance with EN 14889-1:2006. ..... **185**

Table 3-2: Acoustic emission acquisition parameters. Physical meaning of each parameter in Section 3.1.1. ..... **189**

Table 3-3: Pencil-lead-break attenuation calibration (Hsu and Breckenridge, 1981), measured at three positions along the beam. **190**

Table 3-4: Compressive strength at 24 hours and 28 days on 100 mm cubes, and water-accessible porosity at 28 days per NF P18-459 on 40 mm cubes. **193**

Table 3-5: Mechanical and toughness values summary. **197**

Table 3-6: RA-AF crack-mode classification, median signal duration, and long-duration (>500 microseconds) event fraction. **204**

Table 3-7: Parameters of the continuum-damage model for the fiber-reinforced geopolymer at 28 days. **209**

Table 3-8: Comparison over the interval in which the computed solution is verified. **210**

Table 4-1: Published durability of alkali-activated binders under chemical immersion, with the reference binder tested in the same study (Lloyd et al., 2012). **224**

Table 4-2: Rietveld quantitative phase composition of the GEO binder. **246**

Table 4-3: Rapid chloride penetration results and apparent chloride diffusion coefficients for all tested mixes. **257**

Table 4-4: The declared functional units declared. **265**

Table 4-5: Foreground inventory of the GEO mix per m^3 of cured concrete. **268**

Table 4-6: Module-by-module cradle-to-grave global warming potential of GEO and REF, in kg CO_2-equivalent per m^3 ..... **272**

Table 4-7: Sensitivity analysis of the cradle-to-grave GEO advantage against nine one-at-a-time perturbations from the baseline of Section 4.6. ..... **278**

Table 4-8: Materials-only cost inventory of the GEO mix at industrial scale. **282**

Table 4-9: Cost-to-strength of the GEO and REF mixes against the KPI 2.2 threshold. . **284**

Table 4-10: Position of GEO against the NATURSEA-PV acceptance envelope. **286**

List of Abbreviations

AAM: Alkali-Activated Material

AAS: Alkali-Activated Slag

ACI: American Concrete Institute

AE: Acoustic Emission

AF: Average Frequency (kHz)

AFGC: Association Française de Génie Civil

AST: Automatic Sensor Test

ASTM: American Society for Testing and Materials

BGMN: Rietveld refinement software

BiMEP: Biscay Marine Energy Platform

BSE: Backscattered Electron

CEM I: Portland cement

CEM III: Blast-furnace cement

CML-IA: Centrum voor Milieukunde Leiden – Impact Assessment

CMOD: Crack Mouth Opening Displacement

CNLS: Complex Nonlinear Least-Squares

CPE: Constant Phase Element

CSIC: Consejo Superior de Investigaciones Científicas

DIC: Digital Image Correlation

DQR: Data Quality Rating

EDS: Energy-Dispersive X-ray Spectroscopy

EF: Environmental Footprint

EHU: Universidad del País Vasco

EIS: Electrochemical Impedance Spectroscopy

EPD: Environmental Product Declaration

FA: Fly Ash

FPV: Floating Photovoltaic

FPZ: Fracture Process Zone

FU: Functional Unit

GEO: Geopolymer mix

GGBS: Ground Granulated Blast-furnace Slag

GWP: Global Warming Potential (kg CO2-eq)

HDPE: High-Density Polyethylene

HDT: Hit Definition Time

HLT: Hit Lockout Time

ICDD: International Centre for Diffraction Data

IPCC: Intergovernmental Panel on Climate Change

ITZ: Interfacial Transition Zone

KPI: Key Performance Indicator

LCA: Life Cycle Assessment

LCOE: Levelized Cost of Electricity

MAR: Stichting Maritiem Research Instituut Nederland

MIP: Mercury Intrusion Porosimetry

MK: Metakaolin

MRE: Mean Relative Error

NC: Normal Concrete

NF: Norme Française

NMR: Nuclear Magnetic Resonance

OPC: Ordinary Portland Cement

OPEX: Operational Expenditure

PCE: Polycarboxylate Ether

PDT: Peak Definition Time

PE: Polyethylene

PLB: Pencil-Lead-Break

PREF: Prefabricados Supplier S.L.

PSD: Particle Size Distribution

PV: Photovoltaic

RA: Rise time to amplitude ratio (ms/V)

RA-AF: Rise time to amplitude ratio – Average Frequency

RCPT: Rapid Chloride Penetration Test

RDC: Research and Development Concretes S.L.

REF: Portland cement reference mix

RH: Relative Humidity

RILEM: International Union of Laboratories and Experts in Construction Materials, Systems and Structures

RPC: Reactive Powder Concrete

rpm: Revolutions per minute

RTSC: Recycled Tire Steel Cord

RTSF: Recycled Tire Steel Fiber

SCM: Supplementary Cementitious Material

SEM: Scanning Electron Microscopy

SF: Silica Fume

SFRC: Steel Fiber Reinforced Concrete

SH: Sodium Hydroxide

SS: Sodium Silicate

SS/SH: Sodium silicate to sodium hydroxide mass ratio

SSA: Specific Surface Area

TC: Technical Committee

TEC: Fundación Tecnalia Research and Innovation

TRL: Technology Readiness Level

TUD: Technische Universität Darmstadt

UBX: Université de Bordeaux

UCC: University College Cork

UHPC: Ultra-High Performance Concrete

UHPFRC: Ultra-High Performance Fiber-Reinforced Concrete

UHPGC: Ultra-High Performance Geopolymer Concrete

UPV: Ultrasonic Pulse Velocity

WH: Warrant Hub

WP: Work Package (NATURSEA-PV project, WP1–WP5)

XRD: X-Ray Diffraction

Chemical notation

C-S-H: Calcium silicate hydrate gel

C-(N,K)-A-S-H: Calcium (sodium, potassium) aluminosilicate hydrate gel

CO_2: Carbon dioxide

HNO_3: Nitric acid

KOH: Potassium hydroxide

N-A-S-H: Sodium aluminosilicate hydrate gel

NaOH: Sodium hydroxide

OH^-: Hydroxide ion

SO_3: Sulfur trioxide

AE notation (Chapter 3)

A: Peak amplitude of an AE hit (dB)

C: Ring-down counts

D: Signal duration of an AE hit (μs)

E: AE energy (eu)

Gf: Fracture energy from the load–CMOD curve (N/m)

GT: Total flexural toughness – area under the load–CMOD curve (J)

ℓch: Hillerborg characteristic length (mm)

Mode I: Tensile (opening) crack mode

Mode II: Shear (sliding) crack mode

Ms: Silicate modulus, SiO_2/Na_2O molar ratio of the sodium silicate activator

RT: Rise time of an AE hit (μs)

General Introduction

0.1 Marine renewable energy and the offshore floating PV opportunity

The European Union has committed to climate neutrality by 2050. The target was first set out in the European Green Deal (The European Green Deal, 2019) and given binding legal force by the European Climate Law (Regulation (EU) 2021/1119), which commits Member States to net zero greenhouse gas emissions by 2050 and to a reduction of at least 55% relative to 1990 levels by 2030 (European Climate Law, 2021). Reaching these targets requires a near-complete decarbonization of the power sector and a substantial expansion of total generation, since the strategy is to electrify transport, heating, and industrial processes currently powered by fossil fuels. Wind, hydropower, geothermal, and solar must all contribute. No single technology is sufficient at the scale and pace required. The European Commission Communication COM (2020) 741, "An EU Strategy to harness the potential of offshore renewable energy for a climate neutral future", identifies offshore renewables as essential to this trajectory (European Commission, 2020).

Solar photovoltaics (PV) face a surface-area constraint that becomes binding at continental scale. In present European climate conditions, 1 km^2 of installed PV capacity produces approximately 100 GWh per year. The total EU electricity consumption in 2019 was 2900 TWh (SAVIC). If this demand were supplied entirely by PV, an installation area of approximately 29000 km^2 would be required, comparable to the surface area of Belgium. The all-PV scenario is a thought experiment rather than a policy proposal, but it sets a useful upper bound on what ground-mounted PV alone can absorb at EU scale. Land-based deployment competes directly with agriculture, urbanization, and protected ecosystems, and the area available for new installations in Europe is intrinsically constrained by population density and biodiversity priorities. With 71% of the Earth's surface covered by water, and the EU bordered on three sides by sea, offshore solar represents the natural extension of the deployment frontier.

Floating photovoltaics (FPV) on inland water bodies are now commercially mature. Reservoirs, dam lakes, and quarry ponds host hundreds of installations worldwide, typically with floaters made of high-density polyethylene (HDPE). Offshore FPV, by contrast, remains at an early research and development stage (European Commission, 2020; Wang and Lund, 2022; Liu et al., 2024). The largest reported offshore deployment to date is a 5 MW plant in the Strait of Johor (Sunseap Group, Singapore). Pilot installations have been deployed in Norwegian waters (Ocean Sun, hydro-elastic HDPE membrane stretched on a circular tube), in the Dutch North Sea (Oceans of Energy, modular interconnected platforms), and at IJzendoorn in the Netherlands and the North Sea (SolarDuck, triangular

semi-submersible platforms with aluminum beams supported on three vertical steel cylinders) (Wang and Lund, 2022; Liu et al., 2024). Each operates at the kilowatt to low-megawatt scale, and each has reported limitations specific to its design: low scalability of compliant membranes due to mooring complexity and biofouling, structural fragility under sustained wave loading, and installation costs per m² that have so far prevented commercial-scale deployment (Liu et al., 2024). The order-of-magnitude gap between present offshore FPV deployment and the level required for a meaningful contribution to EU electricity supply remains several decades wide. Figure 0-1 shows the four main technological lines currently under field validation, including the Ultra-High-Performance Concrete (UHPC) floaters tested and installed by PREF in the Alqueva reservoir. Closing this gap is constrained less by the photovoltaic modules themselves, which are essentially the same units used onshore, than by what holds them above water. The substructure must survive open-sea conditions over a service life of decades, at a Levelized Cost of Electricity (LCOE) compatible with the targets set by the EU offshore renewable strategy (European Commission, 2020). This is the technical bottleneck on which the present thesis is anchored.

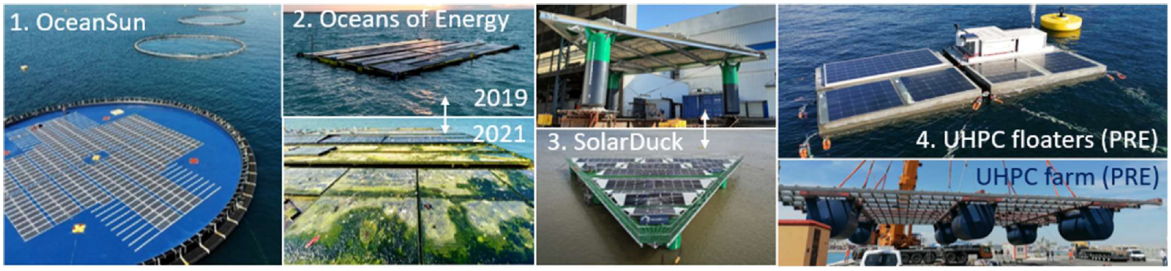

Figure 0-1: Main current offshore floating PV technologies under field validation. (1) Ocean Sun HDPE membrane (Norway), (2) Oceans of Energy modular system (Dutch North Sea), (3) SolarDuck triangular semi-submersible (IJzendoorn, Netherlands), and (4) UHPC floaters and farm (Alqueva).

0.2 The substructure problem: from HDPE to UHPC

Inland FPV substructures are dominated by HDPE. The material is inexpensive, easy to mold into modular floaters, and entirely adequate for the calm wave regimes of reservoirs and lakes. Its limits become apparent at sea. Open-sea operation requires materials capable of withstanding wind speeds above 25 m/s, currents above 1.2 m/s, and wave heights exceeding 14 m (European Commission, 2020). HDPE has neither the stiffness to maintain geometric stability under such loading nor the long-term resistance to ultraviolet exposure, oxidation, and biofouling that decade-scale offshore service demands. Its degradation under marine conditions also generates microplastic pollution, with measurable impacts on the surrounding aquatic ecosystem (Kushwaha et al., 2024).

The structural alternatives at offshore scale are limited. Steel can sustain the loads but requires periodic maintenance to prevent corrosion, increasing operational expenditure (OPEX) and reducing reliability. Aluminum, deployed in the SolarDuck pilot, faces similar corrosion-protection costs and limited fatigue performance under cyclic wave loading. Reinforced fiberglass polyester, used in the legacy mussel-farm installations of the Atlantic

basin, lacks the stiffness needed at the scale of a multi-megawatt platform (Caruso et al., 2022). The remaining candidate is concrete, but conventional reinforced concrete cannot meet the strength-to-weight ratio required for floating service.

UHPC, by contrast, satisfies the structural envelope. UHPC is approximately 40 times stiffer than HDPE and 5 times stronger (European Commission, 2020). Its compressive strength routinely exceeds 150 MPa with a tensile strength of about 10 MPa, achieved through optimized particle packing, a low water-to-binder ratio (0.16 to 0.24), high cement content, silica fume addition, and steel microfiber reinforcement at approximately 2% by volume (Richard and Cheyrezy, 1995; Shi et al., 2015). The combination of high tensile strength and low permeability allows the production of slender prestressed elements without the risk of reinforcement corrosion that conventional concrete carries in marine environments. UHPC also exhibits a strain-hardening response under tension, in which post-cracking load is transferred to the fiber network and stress is dissipated through multiple microcracks rather than a single macrocrack (Yoo and Banthia, 2016). The autogenous self-healing of crack widths up to about 50 µm under marine exposure further extends service life (Cuenca et al., 2021). Because mechanical performance per unit mass is high, the volume of material required for a given structural function is correspondingly low: a well-designed UHPC structure can be built with 50% to 70% less material than its ordinary concrete equivalent (European Commission, 2020). Lightness, in turn, reduces buoyancy demand, mooring complexity, and installation cost per m², all of which compound into a lower LCOE.

The transition from research to deployment is documented. UHPC precast components have been used in offshore aquaculture installations since 2018, replacing fiberglass-reinforced polyester floaters in mussel-farm structures exposed to waves up to 4 m (Caruso et al., 2022). In January 2022, 1450 m^2 of UHPC floaters were installed in a 5 MW FPV plant on the Alqueva reservoir (Portugal), the first reported industrial use of UHPC in offshore-class FPV substructures, with an annual production of approximately 7 GWh (European Commission, 2020). The mechanical, durability, and economic feasibility of UHPC for offshore FPV is therefore not a research hypothesis but an operational baseline.

The remaining barrier is environmental. The very feature that gives UHPC its mechanical advantage, its high cement content, drives an embodied carbon footprint that is incompatible with the decarbonization context of the EU offshore renewable strategy. Section 0.3 quantifies that incompatibility.

0.3 The carbon problem of conventional UHPC

Portland cement production accounts for approximately 8% of global anthropogenic carbon dioxide emissions (Habert et al., 2013; Sameer et al., 2019). Most of this footprint originates in the calcination of limestone at 1450 °C, which releases CO_2 both from the fuel burned and from the chemical decomposition of the carbonate raw material. UHPC concentrates the problem: cement contents in commercial UHPC mixes reach up to 1000

kg/m^3, with high-clinker type I cement typically representing up to 50% of the total mass of the binder system (Wille et al., 2011; European Commission, 2020). The embodied carbon of UHPC is correspondingly high. Cradle-to-gate assessments report values in the range 600 to 1300 kg CO_2-eq/m^3 depending on cement content, silica fume sourcing, and steel fiber origin (Yu et al., 2015). The commercial UHPC reference used in the NATURSEA-PV project, hereafter the "project reference UHPC", reports a value of approximately 930 kg CO_2-eq/m^3, near the upper bound of this range (European Commission, 2020).

This footprint scales unfavorably under the EU Green Deal trajectory. According to CEMBUREAU estimates, CO_2 emissions already account for approximately 10% of the cost of cement, driven by an increase of about 350% in CO_2 allowance prices in 2021 (CO_2 costs in cement Some calculations). As the carbon-pricing mechanism tightens through the remainder of the decade, the cost penalty on cement-intensive structural systems will compound. An FPV substructure intended to deliver decades of low-carbon electricity cannot rely on a structural material whose own carbon intensity is at the high end of the construction sector. The contradiction is structural: the offshore PV decarbonization lever, if scaled with conventional UHPC substructures, would generate a CO_2 debt at construction that erodes part of the operational climate benefit it is meant to deliver.

Decoupling the mechanical performance of UHPC from its cement-driven carbon footprint is therefore a precondition for the industrial deployment of offshore FPV at the scale that EU climate targets require. The question is whether a redesigned binder, with clinker content strongly reduced or eliminated entirely, can deliver the mechanical and durability envelope of UHPC. Two routes are open: eco-cement UHPC, in which clinker is partially substituted by industrial by-products such as GGBS or fly ash within a Portland-based binder, and Ultra-High Performance Geopolymer Concrete (UHPGC), in which Portland cement is removed entirely and replaced by an alkali-activated aluminosilicate binder. Both routes are pursued in parallel within the European project that frames this work, described in Section 0.4.

0.4 The NATURSEA-PV framework

NATURSEA-PV aims to develop novel eco-cementitious materials and components that increase the lifetime, reliability, and maintainability of offshore FPV substructures, and thereby lower their degradation rate, investment risk, and LCOE, while pursuing decommissioning, reuse, and recyclability at end of service life. The work reported in this thesis is carried out within this project, funded by the Horizon Europe program under the call HORIZON-CL5-2021-D3-03 "Sustainable, secure and competitive energy supply", grant agreement number 101084348, under the full title "Novel eco-cementitious materials and components for durable, competitive, and bio-inspired offshore FPV substructures". The consortium brings together 10 partners across 6 countries:

- Fundación Tecnalia Research and Innovation (TEC, Spain, coordinator)

- Stichting Maritiem Research Instituut Nederland (MAR, Netherlands)
- Université de Bordeaux (UBX, France)
- University College Cork (UCC, Ireland)
- Technical University of Darmstadt (TUD, Germany)
- Universidad del País Vasco (EHU, Spain)
- Consejo Superior de Investigaciones Científicas (CSIC, Spain)
- Warrant Hub (WH, Italy)
- Prefabricados Supplier S.L. (PREF, Spain)
- Research and Development Concretes S.L. (RDC, Spain)

The technical work is organized in five work packages as shown in Figure 0-2.

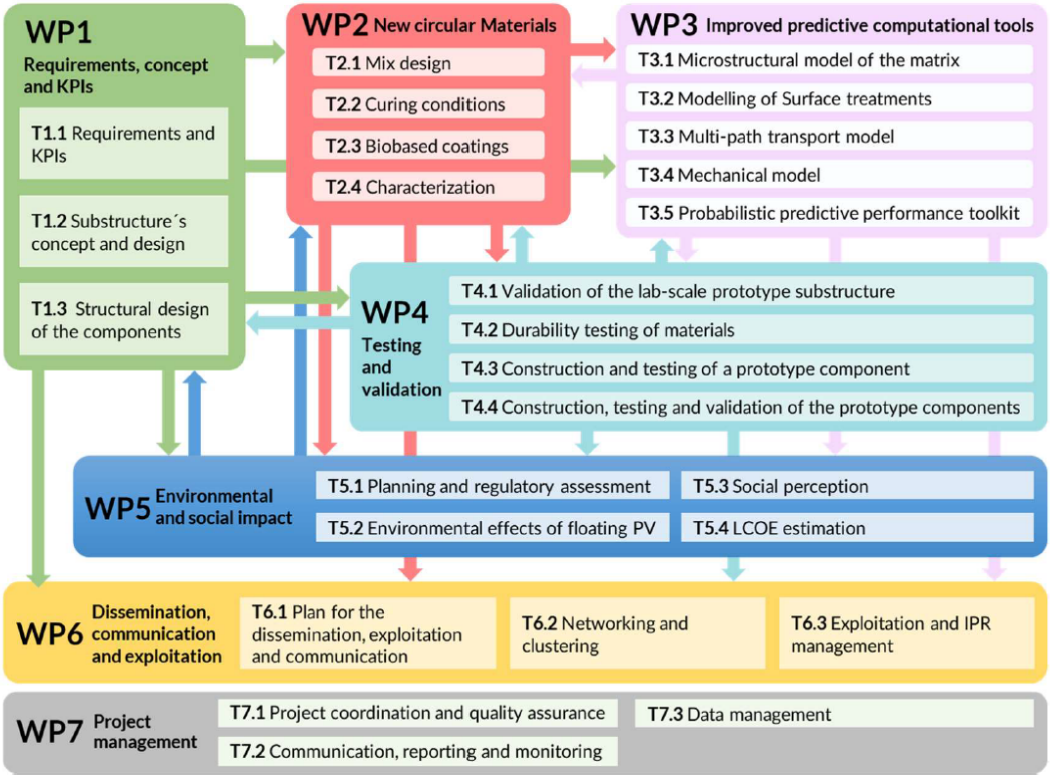

Figure 0-2: NATURSEA-PV's PERT diagram.

- WP1 covers the conceptual and structural design of the substructure, whose bioinspired geometry, derived from the radial rib architecture of the *Victoria amazonica* leaf and validated in shallow water basin model tests, sets the structural target that the WP2 materials must meet (Figure 0-3).
- WP2 develops the new circular materials and pursues the materials track of the project along two parallel binder routes: an eco-cement UHPC route, led by TEC, in which the binder is a Portland cement with high clinker substitution by industrial by-products (GGBS, CEM III type), and an alkali-activated, fully cement-free UHPGC route, led by UBX, in which the binder is GGBS and silica fume activated by alkaline solution. Both routes are evaluated against the same bounding KPIs, detailed in the third paragraph of Section 0.4, and benchmarked against the project reference UHPC,

with the offshore exposure campaign at HarshLab serving as a common validation environment. WP2 also develops bio-based protective coatings, led by EHU.

- WP3 develops the predictive computational tools, in which UBX delivers the mechanical model that feeds the chloride-ingress and durability transport model implemented by TUD.
- WP4 covers the testing and validation of materials and components, including offshore validation at HarshLab. UBX leads WP4.

- WP5 addresses life-cycle assessment, social acceptability, and regulatory questions (European Commission, 2020).

The role of UBX is therefore distributed across the materials, modeling, and validation tracks, providing direct continuity between formulation, characterization, durability, and structural simulation. Both binder routes within WP2 are bound by a set of mechanical, rheological, durability, and environmental targets derived from the project Description of Action and from internal milestone documents.

Mechanical and rheological targets specify a 24-hour compressive strength of at least 65 MPa, a 28-day compressive strength of at least 130 MPa, a slump flow between 200 and 250 mm per ASTM C1856, and an open time of at least 20 minutes. Sustainability targets specify a recycled fiber content of at least 35 wt%, a carbon footprint reduction of at least 30%, and a cost-to-strength reduction of at least 35% relative to the project reference UHPC. Durability targets specify validation at HarshLab over at least 6 months, and a service life of 50 years (European Commission, 2020). These targets together define the acceptance envelope of any material developed within WP2. The present thesis assesses the UHPGC (GEO mix) route against them, within the UBX scope of WP2 and WP4. Meeting the mechanical, rheological and recycled-content targets shows that GEO satisfies a defined laboratory specification; it does not constitute engineering validation, since long-term service life, shrinkage and drying cracking, cyclic loading, scale effects and construction variability lie outside the present demonstration.

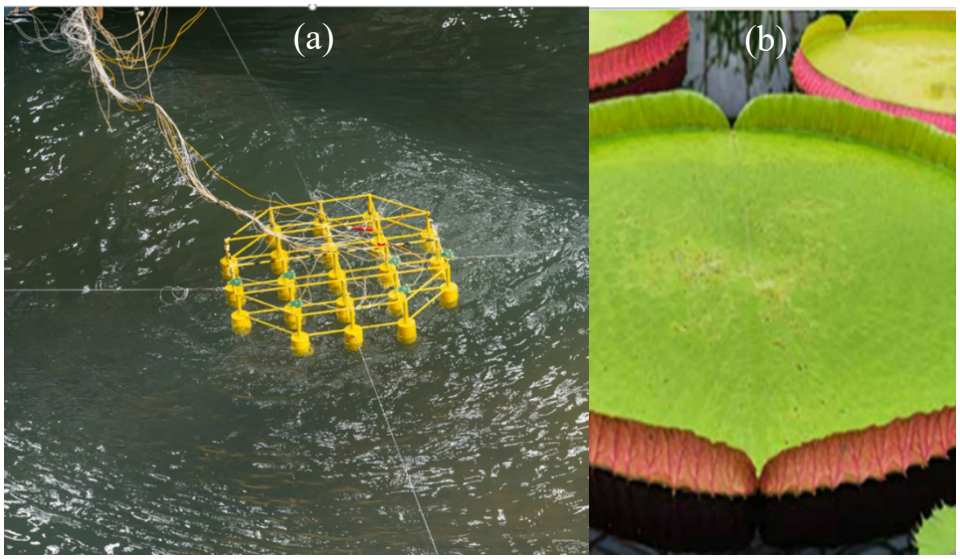

Figure 0-3: Shallow Water Basin model test of a floating PV substructure (a) and (b) the Victoria amazonica leaf that inspired the radial-rib geometry.

Marine validation is conducted at HarshLab, an offshore floating laboratory operated by TEC and moored in 2018 in the Biscay Marine Platform (BiMEP), 1.6 miles off the Basque coast in the Bay of Biscay (Spain), at a water depth of 65 m in unsheltered open sea exposed to Atlantic swells (European Commission, 2020). The 2022 upgrade increased the platform to 8.5 m diameter and 7 m height, with 120 m^2 of deck and capacity for more than 2000 specimens distributed across atmospheric, splash, and immersion zones (Figure 0-4). Within NATURSEA-PV, the materials are exposed for 10 months and assessed by visual inspection, residual mechanical testing on extracted cores, and chloride penetration depth analysis using $AgNO_3$/phenolphthalein indication.



Figure 0-4: HarshLab offshore floating laboratory operated by TEC, moored at the Biscay Marine Platform (BiMEP) in the Bay of Biscay.

Of the two binder routes bound by this acceptance envelope, the present thesis addresses the cement-free geopolymer route. Section 0.5 sets out the chemistry of alkali activation, reviews the strength levels reached in the published ultra-high-performance geopolymer literature, and identifies the issues that remain open at the formulation level.

0.5 UHPGC as the cement-free route

Geopolymerization, first formalized by Davidovits in 1975 (Davidovits, 1991), replaces the hydration chemistry of Portland cement with the alkali activation of aluminosilicate precursors. The process proceeds through three coupled stages (Shi et al., 2011; Provis and Deventer, 2014):

1. Dissolution of the precursor surface in the alkaline activator
2. Reorganization of the dissolved aluminate and silicate species
3. Polycondensation into a three-dimensional aluminosilicate network

The precursors used in cement-replacement systems are predominantly industrial by-products: ground granulated blast-furnace slag (GGBS), fly ash (FA), and silica fume (SF),

valorized at low energy cost relative to clinker production (Davidovits, 1993). The activators are alkaline solutions of sodium or potassium hydroxide combined with soluble silicates (Singh et al., 2015).

The chemistry of the resulting binding gel depends on the calcium content of the precursor system. Low-calcium fly ash and metakaolin systems form sodium aluminosilicate hydrate (N-A-S-H) gels, while high-calcium slag-based systems form calcium aluminosilicate hydrate gels that incorporate alkali ions and are designated C-(K)-A-S-H or C-(N)-A-S-H depending on the activator cation (Garcia-Lodeiro et al., 2011; Bernal et al., 2013). The slag-rich, KOH^-activated formulation developed in this thesis falls in the second category and is anchored mechanistically on a C-(N,K)-A-S-H gel, distinct from both the C-S-H plus portlandite system of Portland UHPC and the N-A-S-H gel of low-calcium geopolymers. Properly formulated, a UHPGC matches or exceeds the mechanical performance of Portland UHPC while reducing embodied carbon by 50% to 80% (Yu et al., 2015; Cai and Ye, 2021).

Recent work has progressively pushed the achievable strength and sustainability of UHPGC. Wetzel and Middendorf (2019) reached 178.6 MPa with optimized silica-fume content in an alkali-activated slag system under heat curing. Lao et al. (2022, 2023) produced strain-hardening UHPGC reaching 186 to 220 MPa using Na_2CO_3/Na_2SiO_3 activators with steel-fiber reinforcement. Liu et al. (2020b) showed that silica-fume content optimization can reduce steel-fiber consumption while preserving mechanical performance. Most recently, (Wang et al., 2025) reported a direct UHPGC against UHPC comparison with 25.7% to 61.6% higher compressive strength at 28 to 84 days, and 64.7% to 86.0% lower strength-normalized CO_2 emissions, supporting UHPGC as a viable lower-carbon alternative.

Despite this progress, four issues remain open at the formulation level for offshore-grade UHPGC and define the scope this thesis must address. **First,** most UHPGC studies optimize one or two properties in isolation, while structural deployment, particularly precast casting in complex formworks, requires strength, self-compacting flow, and open time to be controlled simultaneously (Midhin et al., 2023; Alameri et al., 2025). **Second,** the role of the alkali cation at UHPGC strength levels is essentially unexplored. KOH^-activated systems produce different gel structures and reaction kinetics than $NaOH^-$activated ones, and conventional geopolymers (20 to 60 MPa) show measurable Na^+/K^+ effects (Duxson et al., 2005; Sindhunata et al., 2006), but direct comparisons above 130 MPa have not been reported. **Third,** the behavior of the sodium silicate-to-hydroxide ratio at the low water-to-binder content characteristic of UHPGC is poorly documented. **Fourth,** the steel fibers used in published UHPGC formulations are predominantly virgin, although fibers represent a significant share of the cost and embodied carbon of the final material. Recycled tire-derived steel fibers offer a credible second-life alternative but their integration in dense matrices has not been systematically optimized (Ferdiansyah et al., 2018). None of the published UHPGC

formulations is simultaneously cement-free, ambient-cured, recycled-fiber-bearing, and validated under marine durability conditions at strength levels above 130 MPa. This is the gap this thesis addresses, within the broader NATURSEA-PV investigation of eco-cement and geopolymer binders for durable offshore service.

0.6 Thesis objectives and central research question

The present thesis develops, characterizes, models, and assesses a 100% cement-free, ambient-cured UHPGC, designated GEO, intended as a substitute for the project reference UHPC in offshore FPV substructures within the NATURSEA-PV framework. A Portland cement UHPC of equivalent mechanical class, designated REF, serves as the in-house benchmark for all comparisons. The parallel eco-cement UHPC route, pursued within the same WP2 framework by TEC and benchmarked against the same project reference UHPC, is referenced for context where it informs interpretation but lies outside the scope of this thesis. Comparisons in the present manuscript are restricted to GEO against REF. Four specific objectives structure the work and map directly onto the chapters of the manuscript. They operate at three levels: the formulation of a material satisfying coupled mechanical and rheological constraints (Objective 1), the identification of structure-property and monitoring relationships (Objective 2), and the assessment of durability and environmental performance (Objectives 3 and 4):

Objective 1. Develop and characterize a 100% cement-free, ambient-cured UHPGC based on GGBS, silica fume, and KOH/sodium silicate activation, incorporating recycled tire-derived steel fibers, that meets simultaneously the NATURSEA-PV mechanical and rheological targets. Addressed in Chapter 1.

Objective 2. Establish the multi-scale, non-destructive signatures of the GEO and REF binders by Electrochemical Impedance Spectroscopy (pore network and pore solution chemistry, Chapter 2) and by Acoustic Emission monitoring under three-point bending (fracture initiation, propagation, and energy dissipation, Chapter 3), so as to provide methodological tools for the structural health monitoring of UHPGC elements in service.

Objective 3. Quantify the long-term durability of GEO under marine-relevant chemical and thermal aggression (sulfate, acid, chloride, elevated temperature) and test the laboratory-scale outcomes in real offshore conditions at HarshLab, in order to determine whether the C-(N,K)-A-S-H gel chemistry confers a net advantage over the C-S-H plus portlandite system of REF. Addressed in Chapter 4.

Objective 4. Assess the cradle-to-grave environmental and economic performance of GEO against the project reference UHPC by Carbon Footprint Assessment, identifying the scenarios (slag allocation, recycled fiber content, transport distance and mode, silicate supply route, carbonation credit) under which the GEO system meets the NATURSEA-PV environmental and economic targets and the scenarios under which the advantage degrades. Addressed in Chapter 4.

The four objectives chain into a single argument, and the chapters follow that chain rather than the order in which the campaigns were run. Chapter 1 must succeed first, since without a mix that meets the acceptance criteria there is nothing to characterize. The microstructure it establishes then determines what the following chapters can measure. The pore network of GEO is 100-fold coarser than that of REF in dominant pore size, 700 nm against 6.2 nm (both values at a limit of the intrusion window, so they rank the two networks rather than size them), and its pore solution is dominated by residual K^+ and silicate species rather than the Ca^{2+} and OH^- pair of a portlandite-buffered Portland system. Both differences sit within the resolution of electrochemical impedance spectroscopy, which is why Chapter 2 follows.

Chapter 2 characterizes the material at rest: the impedance response is integrative and volume-averaged, reporting the net state of the matrix without resolving the discrete events by which it accumulates and releases mechanical energy. The marine substructure application subjects the material to load rather than to the quasi-equilibrium conditions of curing, so Chapter 3 observes the fiber-matrix interface directly under bending, with the fiber population held constant so that the comparison isolates the binder.

Chapters 1 to 3 together establish GEO as a distinct system, mechanically, electrochemically and in its fracture pathway, but none of them determines whether that system survives months of marine exposure or whether its carbon and cost balance justifies replacing the reference.

Chapter 4 closes both questions, and the durability and environmental balance it establishes must hold for deployment at industrial scale to be justified.

The unifying question that organizes this argument is the central research question of the thesis:

Can a 100% cement-free, ambient-cured UHPGC reach the mechanical and durability performance to survive harsh marine environments and replace conventional UHPC in offshore FPV substructures monitored by SHM?

0.7 Thesis structure

The manuscript answers this central question through four chapters in linear sequence. Each chapter opens with a focused State of the art on its own scope, is anchored by its own research question stated explicitly in the chapter's opening paragraph and answered in the chapter's Conclusion, and closes with a transition that hands off the chapter's outcome to the next. The chapter research questions are not parallel restatements of the central question. They decompose it into the specific issues that the chapter's measurements actually probe, so that no chapter overreaches beyond what its own data supports.

Chapter 1, ***Formulation and characterization***, establishes the GEO mix through a six-stage, bottleneck-driven optimization and demonstrates that the NATURSEA-PV mechanical and rheological targets can be met under ambient curing with recycled tire-derived steel fibers. The selected mix satisfies the five acceptance criteria simultaneously: 65 MPa at 24 hours, 137 MPa at 28 days on 100 mm cubes and 152 ± 5 MPa on prism halves, which is 92% of the 165 ± 4 MPa returned by REF on the matched geometry, a slump flow of 208 mm, an open time of 23 minutes, and a recycled fiber content of 60 wt %. Three findings transfer beyond this formulation: precursor calcium content rather than the activator controls the achievable strength regime, the absolute silicate dosage organizes a strength optimum, and the substitution of Na^+ by K^+ at equal molarity breaks the strength-workability trade-off that constrains NaOH-activated slag. The key points of the chapter are summarized in Figure 0-5.

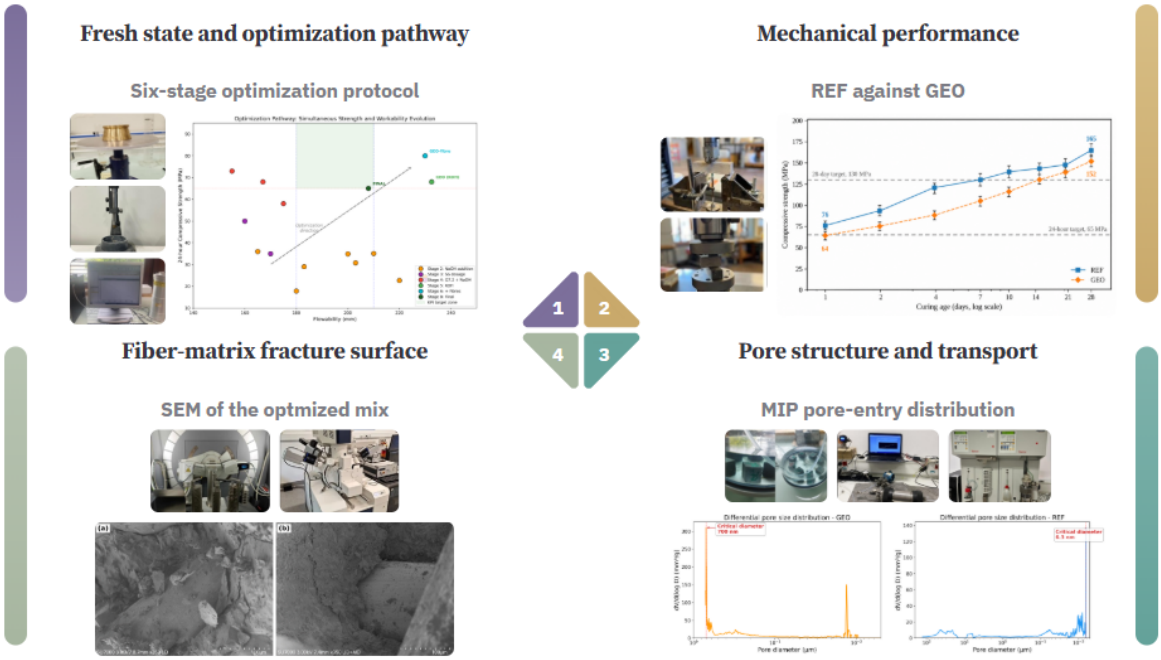

Figure 0-5: Graphical overview of the key points in Chapter 1.

Chapter 2, ***Electrochemical Impedance Spectroscopy***, characterizes the pore network and pore solution chemistry of REF and GEO from 1 to 28 days and tests whether bulk impedance can serve as a non-destructive indicator of strength development. The two binders prove electrochemically distinct on every resolved axis, and the strength indicator itself proves binder-specific: the gel pore resistance R_2 tracks REF (Pearson r = 0.987 on log axes) while the Warburg coefficient tracks GEO (r = 0.983), and neither parameter serves the other binder. A cement-free UHPC is therefore open to the same class of electrochemical quality control as conventional UHPC, provided the indicator is calibrated to the binder. The key points of the chapter are summarized in Figure 0-6.

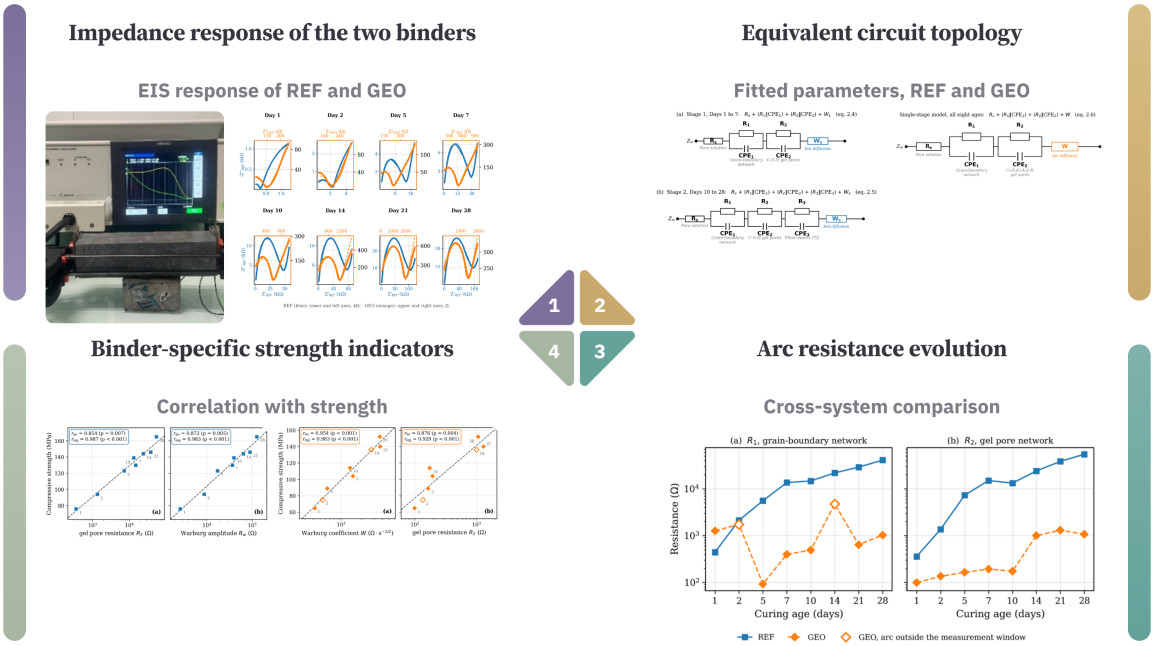

Figure 0-6: Graphical overview of the key points in Chapter 2.

Chapter 3, ***Acoustic emission and fracture mechanics***, characterizes crack initiation, propagation, and energy dissipation in plain and fiber-reinforced REF and GEO with the steel fiber type and dosage held constant. Two distinct pathways emerge: energy is dissipated through frictional fiber pull-out along the interfacial transition zone in the cementitious composite and through cohesive matrix debonding in the geopolymer. The two mature on different time scales and produce a toughness crossover, the geopolymer composite dissipating 30.20 against 25.05 J at 24 hours and 34.98 against 46.67 J at 28 days. A continuum-damage model calibrated on the measured flexural response reproduces the peak load to within 2.3% and the crack localization, but not the post-peak branch. The key points of the chapter are summarized in Figure 0-7.

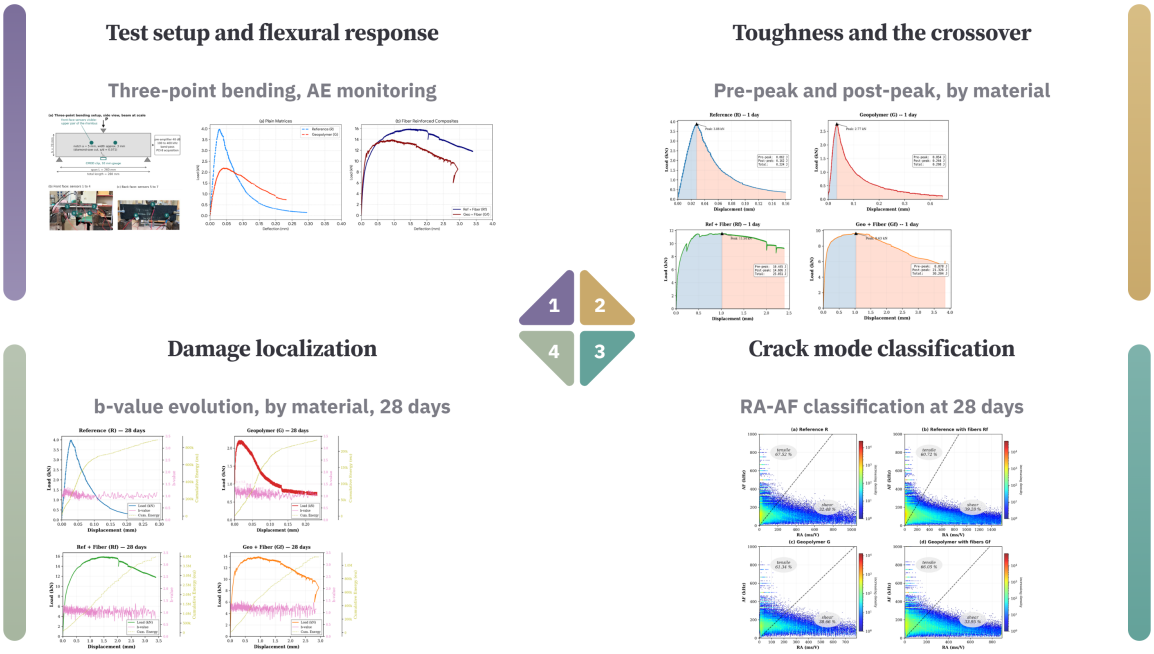

Figure 0-7: Graphical overview of the key points in Chapter 3.

Chapter 4, ***Durability and Carbon Footprint Assessment***, evaluates the resistance of REF and GEO under sulfate, acid, chloride, and elevated-temperature exposure over 12 months, with EIS monitoring across all solutions, and reports the 10-month offshore exposure campaign at HarshLab. GEO holds a decisive advantage under sulfate and acid attack, matches the reference on chloride at the level that governs marine service, and retains its full mechanical class in all three exposure zones after real immersion, with a single disadvantage at elevated temperature, 36% compressive retention at 600 °C against 90% for REF. The cradle-to-grave assessment returns a carbon reduction of 37% per m^3 and 32.1% per tonne, meeting the project carbon target, while the cost-to-strength reduction reaches 10.9% against a 35% requirement and therefore does not. The key points of the chapter are summarized in Figure 0-8.

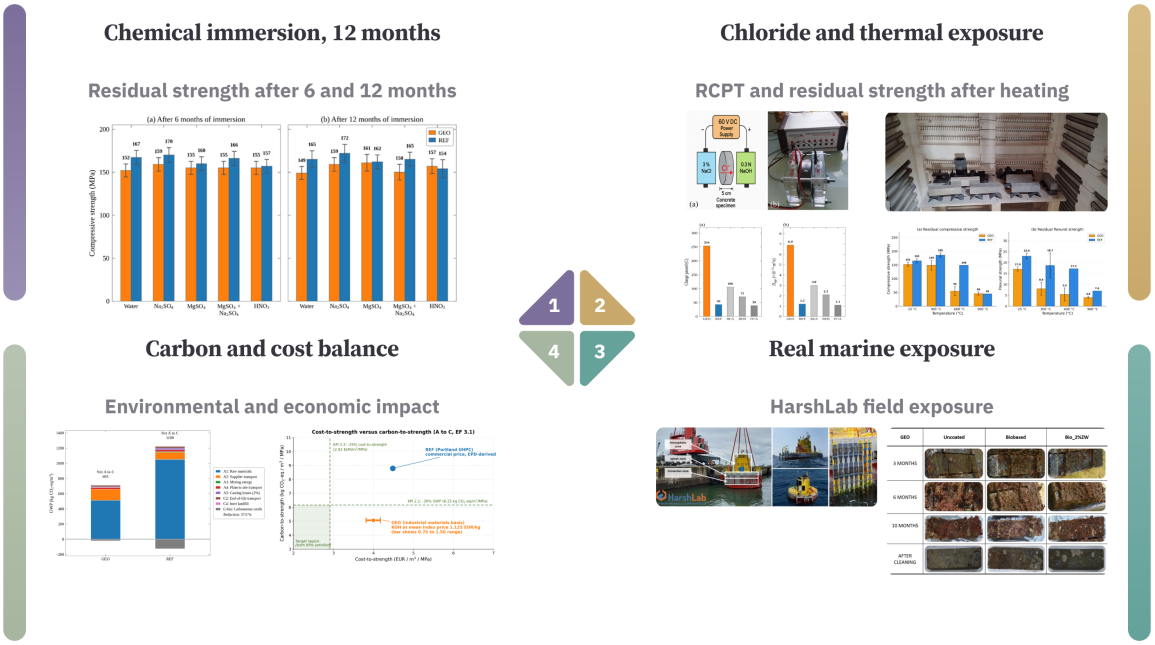

Figure 0-8: Graphical overview of the key points in Chapter 4.

The architecture of the manuscript and the chained research questions are summarized in Figure 0-9. Across the four chapters, the geopolymer and the reference systems appear under chapter-specific labels whose fiber systems differ by design and clarified in each chapter. The project reference UHPC of the carbon footprint analysis is a distinct, commercially confidential material and is listed separately.

Reporting conventions apply across the four chapters. REF designates the Portland-cement UHPC tested in the laboratory, and REF-EPD the same commercial product as described by its verified environmental product declaration, which supplies the carbon, price and declared strength used in Chapter 4; the value of approximately 930 kg CO_2-eq/m³ quoted above is the project figure (European Commission, 2020), whereas Chapter 4 uses the verified declaration. Strength is reported on two geometries: the NATURSEA-PV acceptance criteria are expressed on 100 mm cubes (NF EN 12390-3), on which GEO reaches 137 MPa at 28 days, whereas the side-by-side comparisons use EN 196-1 prism halves, on which GEO reaches 152 ± 5 MPa and REF 165 ± 4 MPa; the cost-to-strength ratio uses the declared characteristic strength of REF-EPD, 130 MPa. The fiber system differs by chapter: GEO carries 108 kg/m³ of the 60/40 recycled-virgin blend in Chapters 1, 2 and 4; REF carries virgin fibers in Chapter 2 and the same blend as GEO in Chapter 4; Chapter 3 uses 120 kg/m³ (1.5 vol%) of virgin fibers in both binders to isolate the binder effect, with the local labels R, Rf, G and Gf defined in Section 3.2.1.

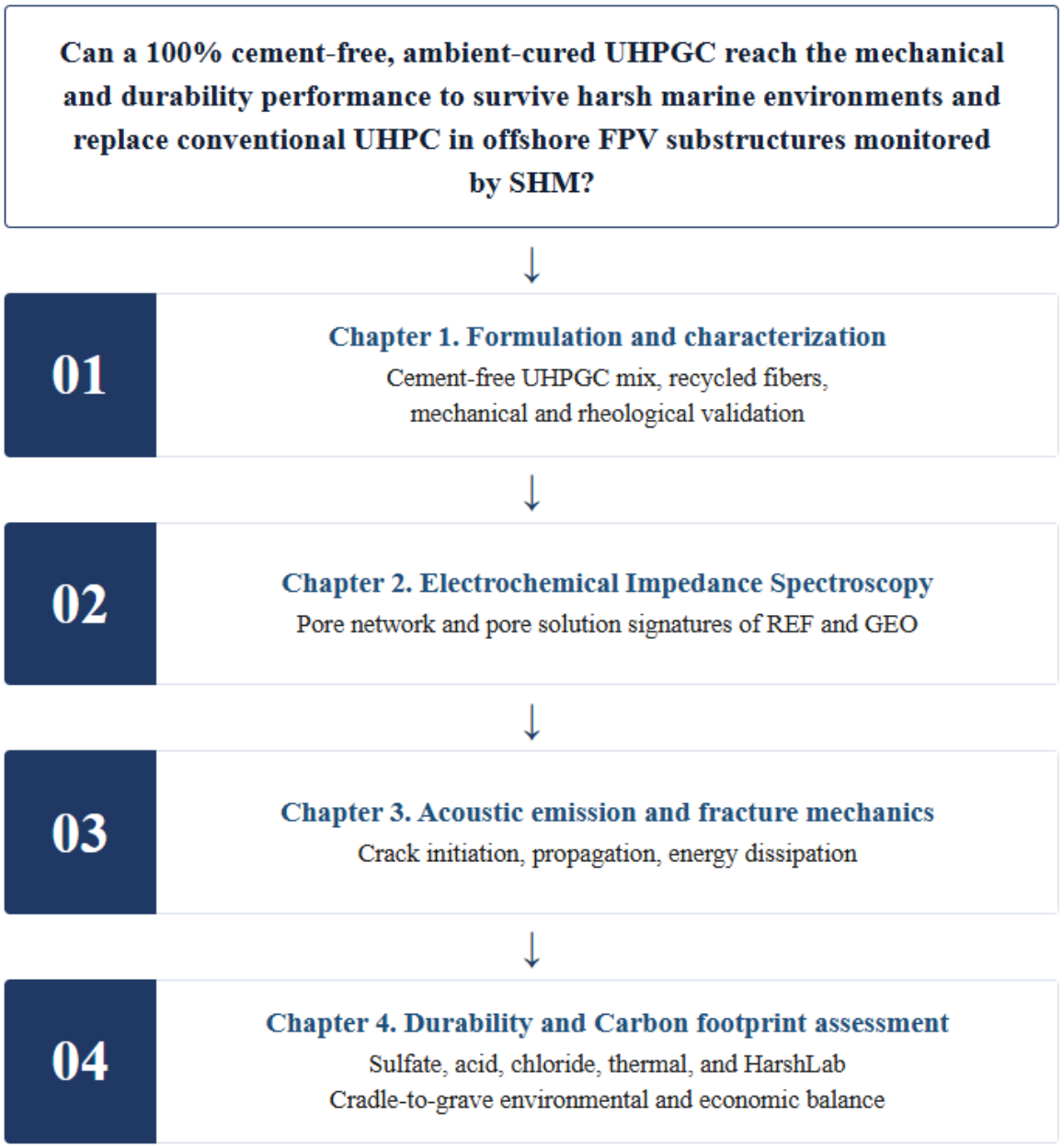

Figure 0-9: Architecture of the manuscript and the chained research questions across the four chapters.

Chapter 1 - Formulation and Characterization

UHPC has reached the structural strength required for offshore FPV substructures. However, it carries a carbon penalty of around 930 kg CO_2 per m^3 (Caruso et al., 2022), driven by an 800-1000 kg/m3 clinker content, which is incompatible with the EU Green Deal scaling trajectory (Puertas et al., 2011). UHPGC replaces Portland cement with an alkali-activated aluminosilicate binder and has demonstrated a 50-80% carbon reduction at equivalent strength (Alsalman et al., 2021). The geopolymer route, however, brings its own formulation problem: precursor blend, activator chemistry, water-to-binder ratio, fiber type, and curing regime are coupled, and the regime that delivers high strength is not always the regime that delivers acceptable workability, open time, or recycled-fiber compatibility.

Four gaps in the UHPGC literature shape this chapter's work. **First,** most studies optimize one or two properties in isolation, while structural deployment requires simultaneous control of strength, self-compacting flow, and open time. **Second,** the alkali cation effect at strength levels above 130 MPa has not been directly probed in head-to-head NaOH and KOH comparisons at fixed silicate modulus. **Third,** the behavior of sodium silicate at the low water-to-binder ratios UHPGC demands is poorly characterized. **Fourth,** recycled tire-derived steel microfibers remain virtually undocumented in dense matrices at UHPGC strength levels.

This chapter develops a 100% cement-free, ambient-cured UHPGC formulation that addresses these four gaps through a single-pass, sequential, bottleneck-driven optimization, characterizes the resulting mix mechanically, rheologically, and microstructurally, and benchmarks it against a Portland cement UHPC reference (REF) at the NATURSEA-PV target envelope.

1.1 State of the art

1.1.1 Geopolymerization and activator chemistry

The terminology of cement-free aluminosilicate binders is not yet settled, and the position adopted here bears on how the material of this thesis should be read. Provis and Deventer (2014) describe alkali activation as the umbrella term for any binder formed by the reaction of an alkaline reagent with a solid aluminosilicate precursor. Geopolymerization is then defined as a sub-case within that umbrella, distinguished by the calcium content of the precursor. Low-calcium systems yield sodium or potassium aluminosilicate hydrate gels (N-A-S-H or K-A-S-H), and high-calcium systems yield calcium aluminosilicate hydrate gels (C-A-S-H). Hence, the two coexist over an intermediate compositional band mapped in the ternary compatibility study of Garcia-Lodeiro. The structure of the two gel families is developed later in this section. In this taxonomy, geopolymerization refers to the low-

calcium branch alone, and slag-rich systems such as the binder developed here are alkali-activated materials rather than geopolymers in the strict sense.

Davidovits (1991) rejects this subordination. In his framework the alkali reagent is a hardener for an already reactive amorphous solid rather than an activator of a latent hydraulic phase, water does not participate in network structuring, and the reaction products are polymers rather than hydrates. Geopolymers therefore constitute a chemically distinct system and not a sub-category of alkali-activated materials. The binder developed in this chapter sits unambiguously on the high-calcium side of this debate. The precursor is 80 wt% GGBS carrying 43.9 wt% CaO, and the microstructural characterization identifies the binding phase as C-(N,K)-A-S-H based on XRD Rietveld refinement and gel-region EDS. According to the strict taxonomy of Provis and Deventer (2014), the material is an alkali-activated slag binder. The designations geopolymer, UHPGC and GEO are nevertheless retained throughout this thesis in the broad sense used by the NATURSEA-PV project; alkali-activated slag-based UHPC is the more precise description of the material.

The designation UHPGC is nevertheless retained throughout this manuscript, for two reasons. **First,** it is the term used consistently in the ultra-high-performance alkali-activated literature against which this chapter benchmarks, including the slag-rich systems of Wetzel and Middendorf (2019), Liu et al. (2020b), Lao et al. (2022), and Wang et al. (2025), and in the NATURSEA-PV project documentation that defines the acceptance criteria of this work.

Second, the material name is not asked to carry the chemistry. Thus, the gel designation C-(N,K)-A-S-H, used without exception hereafter, states the phase assemblage explicitly wherever the mechanism is at stake.

Whichever designation is adopted, the reaction sequence is the same three coupled steps introduced in the General Introduction: alkaline dissolution of the precursor, speciation and reorganization of the released silicate and aluminate monomers, and polycondensation into a three-dimensional network. What that sequence does not fix, and what this section addresses, is the rate at which it proceeds and the composition of the product.

The activator governs both the rate of that sequence and the chemistry of the product, since the hydroxide concentration sets the dissolution rate while the soluble silicate sets the silicon available for repolymerization, so activator dosage and modulus are the primary formulation levers (Pacheco-Torgal et al., 2008; Roy, 1999; Shi et al., 2011); (Nasir et al., 2024; Provis and Bernal, 2014). The alkalinity sets the dissolution rate and the silicate concentration of the activator, the calcium content and particle fineness of the precursor, and the available water (Duxson et al., 2005; Xu and Van Deventer, 2000); (Hajimohammadi et al., 2011; Provis and Bernal, 2014). The combined effect of silicate dosage and modulus on the cumulative heat of hydration, the setting time, and the early-age strength of alkali-activated slag was mapped by Krizan and Zivanovic (2002) and Provis and Bernal (2014).

The choice of alkali cation, sodium versus potassium, is not neutral. Na^+ (ionic radius 1.02 Å) and K^+ (1.38 Å) differ in hydration shell size, charge density, and binding affinity

to silicate oligomers (Duxson et al., 2005). The smaller, more strongly hydrated Na^+ accelerates the initial dissolution of slag but binds water tightly. This leads to a more viscous activator and a shorter open time. The larger K^+ binds water less strongly, lowering activator viscosity and extending workability while still supplying the OH^- needed for dissolution at equal molarity (Van Jaarsveld and Van Deventer, 1999; Duxson et al., 2005).

Direct comparison of NaOH and KOH activators on fly-ash geopolymers by Van Jaarsveld and Van Deventer (1999), and on waste-based inorganic polymers by Phair and Van Deventer (2001), confirmed that the cation type alters not only the reaction kinetics but also the leaching behavior and the durability of the hardened material. The cation is also incorporated into the charge-balancing sites of the gel framework, producing the C-(N)-A-S-H and C-(K)-A-S-H designations used for single-cation systems (Bernal et al., 2013; Myers et al., 2013). This direct cation effect on workability and gel composition motivates Stage 5 of the optimization protocol.

The gel chemistry of an alkali-activated binder is set principally by the calcium content of the precursor system. Low-calcium precursors, such as class F fly ash and metakaolin, produce sodium (or potassium) aluminosilicate hydrate gels (N-A-S-H or K-A-S-H) with a three-dimensional cross-linked aluminosilicate framework and limited water content (Provis et al., 2015). High-calcium precursors, predominantly ground granulated blast-furnace slag, produce calcium aluminosilicate hydrate gels (C-A-S-H) with a layered tobermorite-like structure that incorporates alkali cations in the interlayer and charge-balancing positions (Bernal et al., 2013; Myers et al., 2013). The cross-linked substituted tobermorite model of Myers et al. (2013) provides the most explicit structural description of these gels and accounts for the Si and Al NMR signatures observed in slag-rich systems. Intermediate-calcium and blended slag-fly ash systems form mixed gels in which N-A-S-H and C-A-S-H domains coexist. The proportion of each is governed by the Ca/(Si+Al) ratio of the bulk binder (Garcia-Lodeiro et al., 2011; Bernal et al., 2013; Provis and Bernal, 2014).

The ternary diagram of Garcia-Lodeiro et al. (2011) and the direct microanalysis of coexisting gel phases by Yip and Van Deventer (2003) both place the coexistence boundary in a CaO range around 10 to 30 mol% of the gel-forming system, with C-A-S-H stable above this threshold. Walkley et al. (2016) extended this picture with stoichiometrically controlled synthetic precursors, confirming that the C-(N)-A-S-H to N-A-S-H balance shifts toward the latter when alkali content rises beyond the Al-substitution capacity of the C-A-S-H gel. The slag-rich, KOH^-activated formulation developed in this chapter falls in the high-calcium regime, and its characterization tests whether a C-(N,K)-A-S-H gel is the dominant binding phase, consistent with the literature for analogous systems (see Figure 1-1).

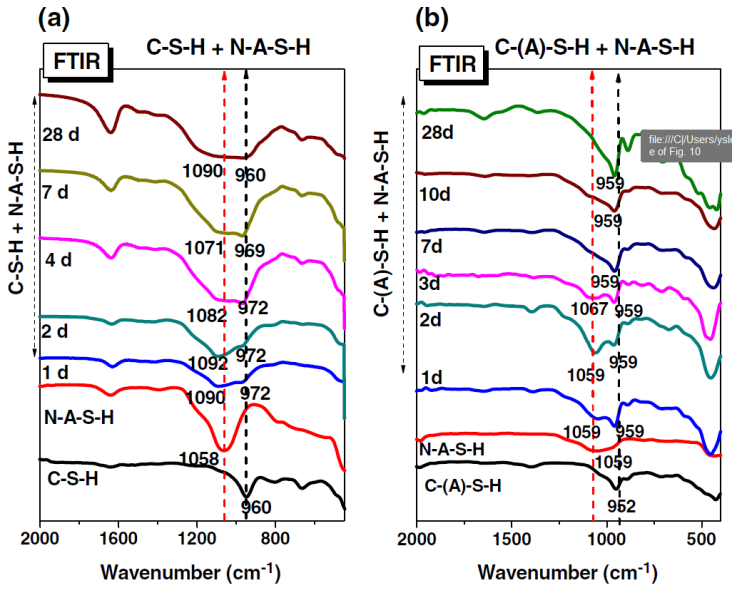

Figure 1-1: Compatibility regions of N-A-S-H, C-A-S-H, and coexisting gels on the CaO-Al_2O_3-SiO_2 system. Reproduced from Garcia-Lodeiro et al. (2011).

Three molar ratios summarize the formulation problem at the chemistry level. The Si/Al ratio sets the connectivity of the gel network and shifts the balance between sialate (Si-O-Al), sialate-siloxo (Si-O-Al-O-Si), and sialate-disiloxo (Si-O-Al-O-Si-O-Si) units (Davidovits, 2005; Provis and Bernal, 2014). The Na_2O (or K_2O) / SiO_2 ratio fixes the alkalinity available for dissolution and the silicate availability for polymerization (Duxson et al., 2005; Hajimohammadi et al., 2011). The H_2O / Na_2O (or K_2O) ratio sets the activator viscosity and dissolution rate, and its upper bound conditions the open time. These three ratios are the chemistry-level levers that the bottleneck-driven optimization manipulates, and their corresponding values are tabulated alongside the formulations.

1.1.2 Precursor systems: GGBS, silica fume, and fly ash

The cement-free UHPGC developed in this work uses three main precursors. These are: ground granulated blast-furnace slag (GGBS) as the dominant reactive aluminosilicate and calcium reservoir, silica fume (SF) as the high-pH-soluble silica source and packing densifier, and class F fly ash (FA) as a spherical low-reactivity filler tested in the Stage 1 precursor screening. The precursors used are sustainable materials derived from industrial by-products. GGBS is derived from steelmaking, silica fume from ferrosilicon production, and fly ash from coal-fired power generation. Their valorization in cementitious systems carries a lower embodied energy than clinker manufacture (Pacheco-Torgal et al., 2008). The three precursors play distinct chemical and physical roles in the alkali-activated matrix; the balance among dissolution kinetics, gel-forming capacity, and packing-density contribution determines their suitability for the strength levels demanded by UHPGC. This subsection reviews each precursor in turn and concludes on the synergies that drive the binary GGBS and SF system retained from Stage 3 of the optimization onward.

GGBS is produced by rapid quenching of blast-furnace slag in water. This freezes the aluminosilicate melt into a vitreous state with composition typically CaO 35 to 45%, SiO_2 30 to 40%, Al_2O_3 10 to 15%, and MgO 5 to 10% (Wang et al., 1994; Provis and Bernal, 2014). Its high calcium content places it in the high-Ca regime of the gel-chemistry framework discussed in Section 1.1.1. Thus, under alkali activation, it produces a calcium aluminosilicate hydrate (C-A-S-H) gel with alkali cations in the interlayer (Bernal et al., 2013; Myers et al., 2013). The mechanism is a coupled process: hydroxide ions attack the slag glass surface releasing Ca^{2+}, $Al(OH)_4^-$, and silicate monomers and oligomers, which then polymerize into a gel network. The dissolution kinetics are governed by the activator (type, concentration, modulus) and by the slag fineness, with higher Blaine values shortening the induction period and accelerating early-age strength gain (Wang et al., 1994; Shi and Day, 1995).

Wang et al. (1994) identified the dominant variables affecting AAS strength: activator type, dosage, modulus, slag fineness, water-to-slag ratio, and curing temperature. Shi and Day (1995) showed using isothermal calorimetry that the heat-release profile of alkali-activated slag deviates from that of Portland cement, with a single dominant peak typically appearing within the first few hours when sufficient hydroxide is present. The slag composition is also a primary control: Haha et al. (2011) demonstrated that increasing MgO content above ~8% in alkali-activated slag favors hydrotalcite formation alongside the C-A-S-H gel, modifying both the kinetics and the final phase assemblage. In the present work, the GGBS used conforms to NF EN 15167-1.

Silica fume, a fine particulate by-product of ferrosilicon and silicon metal production, contains more than 85% SiO_2 in amorphous form with primary particle sizes around 100 to 200 nm and a specific surface area of 15 to 25 m^2/g. In Portland UHPC, silica fume is the standard densification agent: it fills the inter-cement-grain space, reacts pozzolanically with portlandite to form additional C-S-H, and reduces the percolated capillary porosity that limits transport-property performance (Richard and Cheyrezy, 1995; Shi et al., 2015). In alkali-activated systems, the role of silica fume is two-fold.

First, under the activator's high-pH conditions, silica fume dissolves, releasing silicate monomers and oligomers that feed the gel-forming reorganization step of geopolymerization (Hajimohammadi et al., 2011).

Second, it acts as a packing densifier across the sub-micron range that GGBS particles do not cover, refining the interparticle space and raising the effective solid loading of the mix. Wetzel and Middendorf (2019) showed that silica fume at 10 to 20% of binder increases the 28-day compressive strength of an alkali-activated slag UHPGC by 30 to 40 MPa relative to the slag-only control. Aydın and Baradan (2013) reported a similar optimum near 15 to 20% for alkali-activated slag mortars, beyond which water demand outweighs the densification gain. The trade-off between dissolution contribution, packing densification, and water demand is one of the variables addressed in Stage 3 of the optimization.

Class F fly ash, the residual fine particulate from pulverized-coal combustion, is dominated by SiO_2 (50 to 60%), Al_2O_3 (20 to 30%), and Fe_2O_3 (5 to 15%), with low CaO (typically below 10%) according to ASTM C618 (Palomo et al., 1999). The spherical glassy particles, formed by rapid cooling of fly droplets, have diameters ranging from 1 to 100 µm and a surface area that is an order of magnitude lower than that of silica fume. In Portland systems, fly ash is a pozzolan that consumes portlandite slowly over months. In alkali activation, the high-pH solution dissolves the aluminosilicate glass and the released species condense to form a sodium aluminosilicate hydrate (N-A-S-H) gel (Palomo et al., 1999; Provis et al., 2015). Palomo et al. (1999) established the foundational reaction model for alkali-activated fly ash and demonstrated that the rate-limiting step at ambient temperature is the dissolution of the glassy aluminosilicate phase.

(2005) later mapped the development of the microstructure across varied activator chemistries and showed that the activator type, the activator's soluble silica content, and the curing temperature jointly govern the gel structure.

Two consequences shape the use of fly ash in UHPGC:

First, the spherical morphology confers a "ball-bearing" effect that improves fresh-state workability at a fixed water content, as observed in the Stage 1 flow data in Section 1.3.1.

Second, the slow ambient-cure kinetics, however, impose a hard upper bound on the fly-ash proportion compatible with the 24-hour strength target above 65 MPa: at room temperature and at the low water-to-binder ratios required for UHPGC strength, fly ash cannot deliver the early dissolution rate needed for rapid gel formation, and this is the reason it is screened in Stage 1 and dropped from the binary GGBS + SF system.

The three precursors span complementary particle-size scales (Figure 1-6): GGBS at 10 to 30 µm sets the dominant grain population, fly ash at 1 to 100 µm overlaps with the coarser end of GGBS and adds spherical particles in the same range, and silica fume at 0.1 to 0.3 µm fills the inter-grain space at the sub-micron scale. The combined particle-size distribution determines the maximum achievable packing density of the dry powder, which in turn sets the lower bound on water demand at fixed workability.

The chemical composition of the precursor blend, expressed as Si/Al and Ca/(Si+Al) molar ratios, also acts as a primary control on the resulting gel chemistry, biasing the system toward N-A-S-H, C-A-S-H, or a coexisting hybrid (Section 1.1.1) (Garcia-Lodeiro et al., 2011; Provis and Bernal, 2014). Lothenbach et al. (2011), surveying the broader thermodynamic literature on supplementary cementitious materials, identified the dissolution-precipitation equilibria that govern these systems and showed that small changes in precursor composition can shift the phase assemblage. In the UHPGC formulation developed here, the Stage 1 screening of GGBS/FA ratios maps directly onto this Ca/(Si+Al) axis: the high-calcium GGBS-rich compositions outperform the FA-rich compositions at ambient cure, and the screening therefore selects the GGBS + SF binary system whose properties are characterized in detail through Stages 2 to 6.

1.1.3 Existing UHPGC formulations and what they leave open

The UHPC class spans a continuum of binder chemistries. Conventional UHPC descends from the reactive powder concrete of Richard and Cheyrezy, built on a high Portland clinker content, optimized particle packing, and a very low water-to-binder ratio (Richard and Cheyrezy, 1995); they reached 200 MPa using ordinary Portland cement, silica fume, and quartz sand at a water-to-binder ratio below 0.20, with fine particle packing and pressure-and-heat curing. Subsequent work translated the RPC chemistry into industrially deployable UHPC, codified for bridge applications by Graybeal (2006) and extended to fiber-reinforced variants in the 130 to 220 MPa range by Wu et al. (2016). Eco-UHPC retains the Portland chemistry but replaces a fraction of the clinker with supplementary cementitious materials, typically slag, fly ash, or limestone, thereby achieving comparable strengths with a reduced yet still substantial clinker burden. (Yazıcı et al., 2008) showed that combinations of fly ash, GGBS, and silica fume reached a compressive strength of 178 to 195 MPa under autoclave or steam curing, reducing cement content by 20 to 60% relative to conventional RPC.

Yu et al. (2015) used the modified Andreasen and Andersen packing model to design an ambient-cured eco-UHPC with high-volume fly ash, GGBS, and limestone powder substitutions, reaching 130 to 150 MPa with reduced cement and fiber content. Tafraoui et al. (2016) explored metakaolin as a partial silica-fume replacement in UHPC and reached 250 MPa under thermal treatment with durability equivalent to the silica-fume baseline. Randl et al. (2014) developed eco-UHPC mixtures with SCM replacement levels chosen for ecological impact, reaching 130 to 160 MPa under heat curing. The results showed that packing-density gains outweigh SCM reactivity at the strength frontier.

Meng et al. (2017) formulated a cost-effective UHPC with high-volume SCMs and conventional quartz sand, reaching 125 MPa under standard curing and 168 MPa under steam curing, demonstrating that eco-UHPC can decouple strength from premium aggregates. Across the eco-UHPC family, the carbon reduction relative to conventional UHPC is typically 20 to 40%. Eco-UHPC nevertheless retains Portland clinker as the primary binder, and its carbon performance is fundamentally bounded below by the residual clinker fraction.

UHPGC removes Portland cement entirely and replaces the binder with alkali-activated aluminosilicate precursors. The literature splits into two regimes by curing temperature. Under heat curing, the strength frontier reaches 180 to 220 MPa. Wetzel and Middendorf (2019) reported 178.6 MPa on a geopolymer binder with GGBS and SF, activated by NaOH and sodium silicate at 80 °C. Lao et al. (2022) developed a strain-hardening UHPGC reaching 222 MPa with FA and GGBS, with Na2CO3 and sodium silicate activation, and steel-fiber reinforcement, the first UHPGC formulation to combine ultra-high compressive strength with tensile strain hardening. Lao et al. (2023) extended this work to PE-fiber composites with tensile strain capacity exceeding 9% at compressive strength above 180

MPa. These formulations define the upper bound of UHPGC mechanical performance, but their dependence on elevated-temperature curing constrains their compatibility with conventional precast operations.

Under ambient curing, where industrial precast deployment is realistic, the achievable strength range is narrower. Ambily et al. (2015) reported 175 MPa on a GGBS + FA + SF blend activated by NaOH and sodium silicate, with 2% virgin steel fibers. Liu et al. (2020b) developed UHPGC mixes above 120 MPa with GGBS, SF, and 2% steel fibers, showing that optimizing silica fume reduces the steel fiber demand without compromising mechanical performance.

Wang et al. (2025) presented the most recent direct comparison between UHPGC and a Portland UHPC of comparable strength class, reporting 25.7 to 61.6% higher compressive strength at 28 to 84 days for the UHPGC and 64.7 to 86.0% lower strength-normalized CO_2 emissions. This establishes that UHPGC is a suitable alternative to conventional UHPC (Figure 1-2).

The present GEO formulation falls within the ambient-cured UHPGC band, with a compressive strength of 137 MPa on 100 mm cubes, 65 MPa at 24 hours, a slump of 208 mm, an open time of 23 minutes, and a 60% recycled-fiber content. This study is distinguished from prior work in three aspects. The aspects include KOH (not NaOH) activation at a fixed silicate modulus, simultaneous satisfaction of all five NATURSEA-PV criteria, and the first systematic incorporation of tire-derived recycled steel fibers in a UHPGC matrix within the UHPC strength range (see Figure 1-4).

Table 1-1: Representative formulations across the UHPC and UHPGC spectrum.

Study	System	Binder	Activator / SCM	f'c 28d (MPa)	Curing	Fibers
Tier 1 - Conventional UHPC						
(Richard and Cheyrezy, 1995)	RPC	OPC + SF	Portland clinker, no SCM	200	Heat + pressure	None
(Graybeal, 2006)	UHPC	OPC + SF	Portland clinker	200	Steam	2% steel
(Wu et al., 2016)	UHPC	OPC + SF	Portland clinker	130-150	Ambient / steam	Varied steel
Tier 2 - Eco-UHPC						
(Yazıcı et al., 2008)	RPC + SCMs	OPC + FA + GGBS + SF	20-60% cement replacement	178-195	Autoclave / steam	3% steel

Study	System	Binder	Activator / SCM	f'c 28d (MPa)	Curing	Fibers
(Yu et al., 2015)	Eco-UHPC	OPC + FA + GGBS + LP	High-volume SCMs	130-150	Ambient	2% steel
(Tafraoui et al., 2016)	UHPC + MK	OPC + metakaolin	MK replacing SF	250	Heat	2% steel
(Randl et al., 2014)	Eco-UHPC	OPC + SCMs	SCM replacement	130-160	Heat	0.9-1.5% steel
(Meng et al., 2017)	Cost-effective UHPC	OPC + FA + slag	High-volume SCMs	125 / 168	Standard / steam	2% steel
Tier 3 - UHPGC (cement-free, alkali-activated)						
(Ambily et al., 2015)	UHPGC	GGBS + FA + SF	NaOH + sodium silicate	175	Ambient	2% virgin steel
(Wetzel and Middendorf, 2019)	UHPGC	GGBS + SF	NaOH + sodium silicate	178.6	80 °C	None
(Lao et al., 2022)	SH-UHPGC	FA + GGBS	Na_2CO_3 + sodium silicate	up to 222	80 °C	1-2% steel
(Liu et al., 2020b)	UHPGC	GGBS + SF	NaOH + sodium silicate	120+	Ambient	2% steel
(Wang et al., 2025)	UHPGC	GGBS + SF	NaOH + sodium silicate	140-160	Ambient	Not reported
This work (GEO)	UHPGC	GGBS + SF	KOH + sodium silicate	137	Ambient	1.5 vol% mixed (60/40 recycled/virgin)

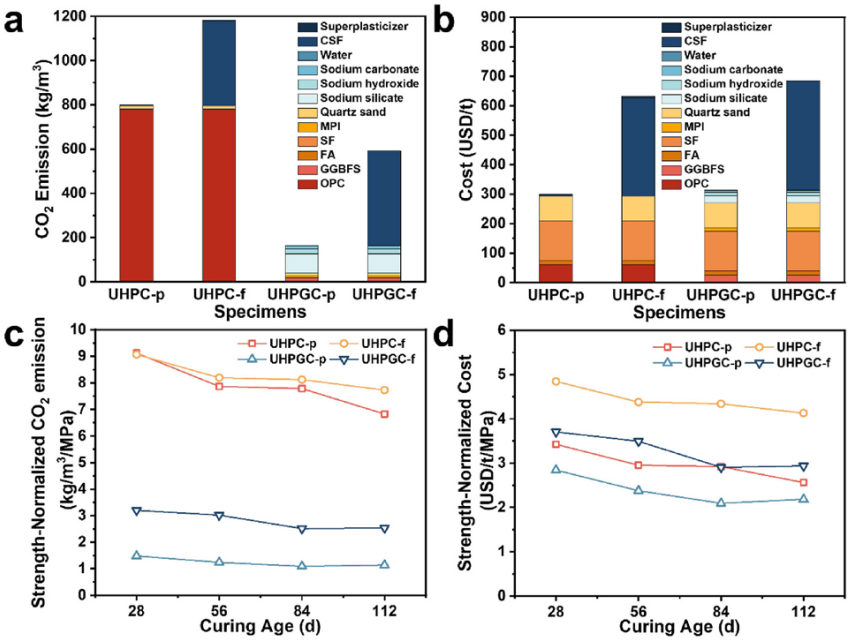

Figure 1-2: Compressive strength against embodied CO_2 for UHPC and UHPGC formulations from the literature (Wang et al., 2025).

Four issues remain open at the formulation level for offshore-grade UHPGC and define the scope addressed by the present chapter:

1. The studies compiled above optimize one or two properties in isolation, whereas structural deployment requires strength, self-compacting flow and open time to be satisfied simultaneously.
2. The effect of the alkali cation has not been probed directly above 130 MPa, where the strength and workability requirements are hardest to reconcile.
3. The behavior of sodium silicate is poorly characterized at the low water-to-binder ratios that ultra-high-performance demands, so the dosage optimum reported for conventional alkali-activated slag cannot be transferred.
4. Recycled tire-derived steel fibers remain essentially undocumented in dense matrices at this strength level, and neither their mechanical contribution nor the cost and embodied-carbon case for using them has been established. Each is treated in turn below.

1.1.4 Multi-objective optimization at UHPGC strength levels

Most UHPGC studies report performance against one or two acceptance criteria, typically compressive strength and one mechanical or transport property (Wetzel and Middendorf, 2019; Liu et al., 2020b; Lao et al., 2022). Structural deployment, particularly precast casting in complex formworks, requires simultaneous control of multiple targets that are coupled through the activator chemistry: high strength, self-compacting flow, sufficient open time, fiber dispersion, and ambient-cure compatibility. However, very few studies report this multi-target combination, and those that do tend to relax one criterion in order to satisfy the others, typically open time or recycled-fiber content.

The present chapter presents a single-pass, sequential bottleneck-driven optimization that simultaneously achieves all five NATURSEA-PV criteria and is documented in Sections 1.3 and 1.5.

1.1.4.1 Na^+ versus K^+ at UHPGC strength levels above 130 MPa

The cation effect described in Section 1.1.1 has been documented in low- and moderate-strength alkali-activated systems (Van Jaarsveld and Van Deventer, 1999; Phair and Van Deventer, 2001), but a direct comparison of NaOH and KOH at fixed modulus, fixed activator dosage, and ambient cure has not been reported at UHPGC strength levels exceeding 130 MPa. The closest precedents in the Tier 3 literature use either NaOH alone, NaOH + sodium silicate, or Na_2CO_3-based activators. KOH^-based UHPGC at this strength range is absent from the published record. The current chapter presents a direct comparison at 10 M concentration with sodium silicate held constant.

1.1.4.2 Sodium silicate behavior at low water-to-binder ratio

The sodium silicate dosage in alkali-activated slag systems has been mapped at water-to-binder (w/b) ratios above 0.30 by Krizan and Zivanovic (2002) and others, with an early-strength optimum at intermediate modulus and dosage. UHPGC operates at much lower w/b, typically below 0.22, where the silicate behavior becomes counterintuitive. The Stage 3 data show that reducing the activator-to-binder ratio from 0.50 to 0.30 and the SS/SH mass ratio from 3.0 to 2.0 more than doubles the 24-hour compressive strength of GEO. This increase in strength is due to the activator dosage, the silicate modulus, and the water-to-binder ratio decreasing together across this series. The effect is an empirical optimum in which these variables co-vary rather than an isolated single-variable mechanism. The term “silicate passivation” is retained as a working hypothesis for the low-w/b behavior. The prior literature does not characterize it as a demonstrated isolated mechanism.

1.1.4.3 Recycled steel fibers: cost and embodied-carbon rationale

Steel fibers are among the dominant contributors to the cost and embodied carbon of UHPC and UHPGC. The 2% steel-fiber content typical of ultra-high-performance fiber-reinforced concrete accounts for approximately 30% of material cost and 40% of embodied carbon, comparable to or exceeding the contribution of the binder system in life-cycle analyses (Caruso et al., 2022). Conventional UHPC and UHPGC formulations contain 2 to 4% volume of straight, uncoated, high-tensile virgin steel microfibers, typically 13 mm long and 0.2 mm in diameter, with tensile strength near 3000 MPa.

Substituting these with steel fibers recovered from end-of-life tires opens a circular-economy route: 200 to 300 million tires are discarded each year in Europe alone, and their steel cord and ply wire constitute a structural-quality stream available at low cost and with a documented carbon reduction comparable in magnitude to the cost saving. The deployability of these recycled tire steel fibers (RTSF) in dense matrices at UHPC strength levels turns on

whether their geometry, tensile-strength variability, and fiber-matrix bond can match those of virgin fibers.

Three features distinguish RTSF from virgin steel microfibers:

1. **Length variability:** The recovery process produces fibers of variable length, typically 5 to 40 mm in the bulk recovered material, with a long tail of short fragments and occasional long curls. Industrial sieving and post-processing narrow the distribution to a target band, for example 10 to 20 mm, but residual variability persists (Centonze et al., 2012).
2. **Tensile-strength scatter:** The tensile strength of RTSF is high in absolute terms, typically 2000 to 2800 MPa for steel cord wire, but more variable than that of virgin microfibers, with measured coefficients of variation typically 5 to 10 times higher (Aiello et al., 2009).
3. **Residual rubber:** Depending on the cleaning process, RTSF retain residual rubber on the fiber surface, an attribute that affects both the fiber-matrix bond and the fresh-state behavior of the concrete (Pilakoutas et al., 2004; Aiello et al., 2009; Centonze et al., 2012).

Two industrial qualities follow from the third feature: clean RTSF, obtained by mechanical or thermal processing to remove rubber, and as-recovered RTSF, which retains rubber residue and is produced at lower cost. The present work uses both, with Spajic virgin straight steel fibers as the high-bond baseline and Flexofibers as-recovered recycled fibers as the high-recycled-content alternative (Figure 1-3).

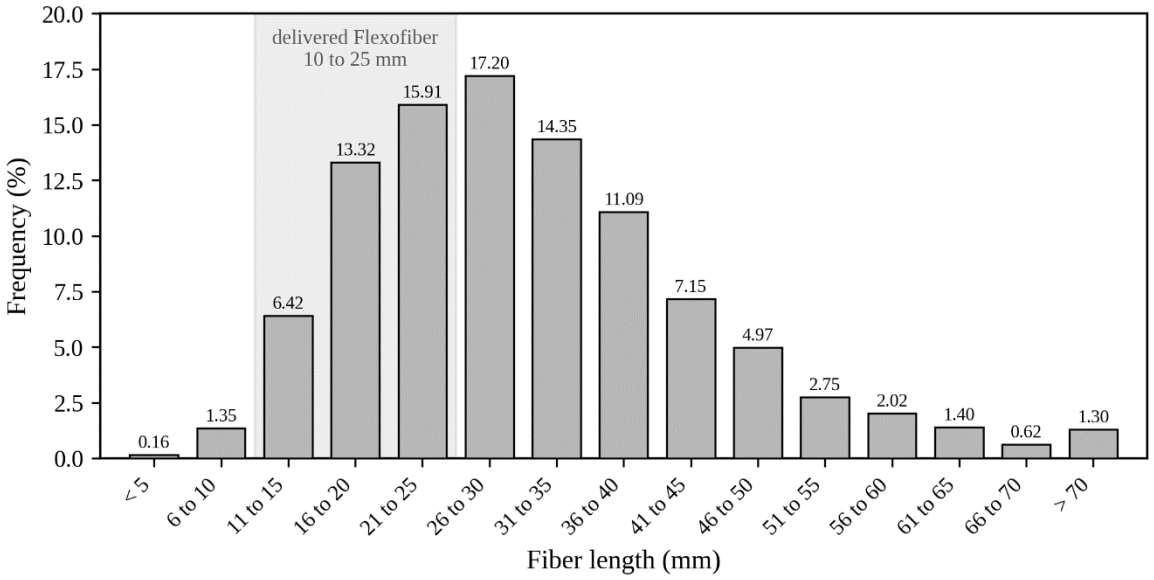

Figure 1-3: Geometry and rubber-residue features of recycled tire steel fibers (RTSF) compared with virgin steel microfibers. Reproduced from Centonze et al. (2012).

The body of work on RTSF in cementitious matrices has focused largely on normal-strength (30 to 60 MPa) and high-strength (60 to 100 MPa) concrete. Aiello et al. (2009) reported that 1 to 1.5% RTSF in normal-strength concrete delivered flexural strengths

comparable to equal-content virgin-fiber mixes, with somewhat reduced post-cracking ductility attributed to weaker fiber-matrix bond.

Centonze et al. (2012) characterized the geometry and tensile behavior of RTSF in detail and showed that the irregular shape provides mechanical anchorage that partially compensates for the bond loss from rubber residue. Pilakoutas et al. (2004) established that RTSF can serve as primary reinforcement in slabs and shotcrete, with adequate dispersion and crack resistance performance.

Caggiano et al. (2015, 2017) systematically studied the bond behavior and mechanical response of hybrid manufactured-recycled fiber concrete and showed that blending 50 to 70% RTSF with 30 to 50% virgin fibers preserves flexural strength and ductility close to those of full-virgin-fiber baselines. Martinelli et al. (2015) confirmed the same trend in post-cracking three-point-bending tests.

Hu et al. (2018) extended the comparison to high-strength concrete above 80 MPa and showed that the bond degradation from rubber residue is partially mitigated by the denser matrix. The combined evidence supports RTSF as a viable substitute or partial substitute for virgin fibers in concrete up to high-strength levels, provided that fiber cleanliness is controlled and the blend ratio is tuned to the target post-cracking behavior.

At UHPC strength levels above 130 MPa, the published literature thins to a small body of work from a single research group. Isa et al. (2020) reported the first systematic UHPC mix design with RTSF, testing 12 mixes at 2 to 4% total fiber volume with recycled tire steel cords (RTSC, long), RTSF (short), and their hybrids. The flexural strength of UHPC containing RTSF alone fell short of the virgin-fiber baseline. However, the RTSC-RTSF hybrid mixes achieved strengths comparable to those of virgin-fiber UHPC and offered substantial cost and environmental benefits. Isa et al. (2021) subsequently extended this work to ultimate-limit-state design parameters and proposed prediction models for the tensile response of eco-efficient UHPC containing recycled fibers. Zhang et al. (2022) examined the effect of fiber length on the mechanical performance of SFRC made with recycled tire fibers and confirmed the importance of length-distribution control. These studies establish that RTSF can be deployed in UHPC at fiber contents up to 4%, with three principal caveats:

1. **Rubber-residue** content must be controlled to preserve bond
2. **Hybridization** with longer recycled steel cords or virgin fibers is needed to recover flexural strength
3. **Fiber-length** distribution must be tight enough to ensure dispersion.

The UHPC matrix studied in all this work is conventional Portland-cement-based. The alkali-activated UHPGC matrix is absent from this literature (see Figure 1-4).

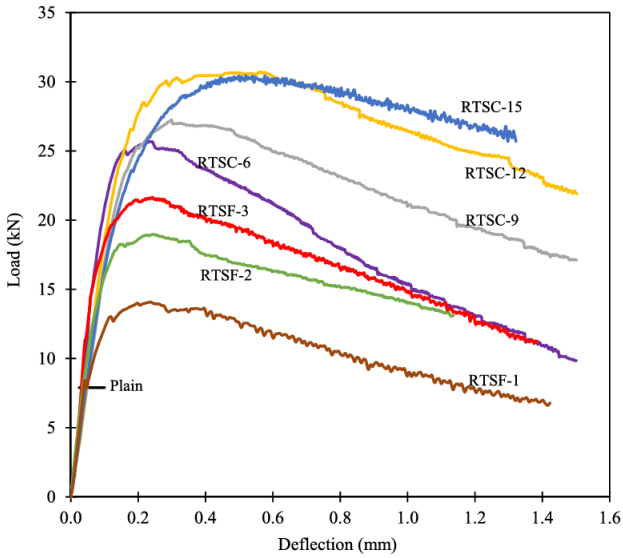

Figure 1-4: Flexural strength of UHPC mixes containing RTSF and RTSC at 2 to 4% fiber volume. Reproduced from Isa et al. (2020).

To the author's knowledge, no published study has documented the behavior of recycled tire steel fibers in a UHPGC matrix at compressive strength above 130 MPa. The UHPGC matrix differs from UHPC in three respects relevant to fiber integration: the binder gel is C-(N,K)-A-S-H rather than C-S-H plus portlandite (Section 1.1.1), the pore network is coarser at comparable compressive strength, and the activator pore solution is alkali-richer, with potential consequences for fiber-surface compatibility.

The interaction between these matrix attributes and rubber residue, as well as irregular RTSF geometry, has not been quantified. The present chapter addresses this gap through a parametric study that tests Flexo (recycled, as-recovered) and Spajic (virgin) fibers in four blend ratios at two total fiber contents in a KOH-activated GGBS and SF matrix and identifies a 60/40 Flexo/Spajic blend at 12 wt% of binder as the formulation that satisfies the NATURSEA-PV recycled-content target without compromising the four other acceptance criteria.

1.2 Raw materials

Two mixes are compared throughout this thesis. **GEO** is the UHPGC formulated in the present work, and its constituents are described individually in the subsections that follow. **REF** is the Portland cement reference: the project reference UHPC, supplied by a NATURSEA-PV project partner as a pre-blended dry premix and prepared in the laboratory by adding water and a polycarboxylate-ether superplasticizer at the dosage recommended by the supplier. Its formulation is proprietary and is not disclosed here. The binder of the premix is based on CEM I 42.5 R-SR5, a sulfate-resistant low-alkali Portland cement conforming to NF EN 197-1, as declared by the supplier.

Throughout this thesis, REF denotes this material. Its mechanical, microstructural, and durability performance was measured in the present work under curing conditions identical to those used for GEO, so that the comparison between the two binder systems is based on a single experimental campaign. The raw materials are shown in Figure 1-5.



Figure 1-5: Raw constituents used in the formulation program, as received.

1.2.1 Precursors: GGBS, silica fume, and class F fly ash

The GEO binder was formulated from three industrial by-product precursors. Their chemical compositions and physical properties are reported in Table 1-2.

GGBS was the dominant aluminosilicate precursor of the GEO binder, supplied by *Ecocem France* from the Fos-sur-Mer plant and conforming to NF EN 15167-1. Its high calcium content places it in the high-calcium regime discussed in Section 1.1.1, which biases the activated binder toward a C-A-S-H gel.

Densified SF conforming to NF EN 13263-1 was used in both REF and GEO as a sub-micron densifier and silica source.

Class F FA (Silicoline C, supplied by *Surschiste* with EN 450-1 conformity declaration) was used only in the Stage 1 precursor screening and was dropped from the optimized GEO from Stage 3 onward. The supplier's conformity declaration certifies that the oxides fall within the EN 450-1 thresholds without disclosing all raw values.

1.2.2 Alkali activators

The GEO activator system combined a **sodium silicate** solution and an alkali hydroxide. The sodium silicate was Betol 47-T (*Woellner*), used in every mix. Potassium hydroxide (KOH, ≥ 98% purity, technical grade) was used for the optimized formulation. **Sodium hydroxide** (NaOH, ≥ 98% purity, technical grade) was used in the Stage 2 to Stage 4 trials. The hydroxide solutions were prepared in deionized water (the free mixing water added at

batching was potable tap water conforming to NF EN 1008) 24 hours before mixing to allow full dissolution and to dissipate the exothermic heat of dissolution, then combined with the sodium silicate solution immediately before introduction into the mixer. The molarity range investigated was 8 M to 12 M. The optimized formulation used 10 M KOH.

Table 1-2: Chemical composition and physical properties of binder constituents and activators.

Material	SiO_2 (%)	Fe_2O_3 (%)	Al_2O_3 (%)	K_2O (%)	Na_2O (%)	MgO (%)	CaO (%)	SO_3 (%)	Density (kg/m³)	Blaine / SSA (m²/kg)
GGBS	37.6	0.33	10.26	0.26	0.22	6.93	43.9	0.03	2750	450
SF	90-95	< 1	< 1	< 4	< 4	< 3	-	< 1	2270	18500
FA	n.r.	n.r.	n.r.	2.22	0.97	n.r.	n.r.	n.r.	2110	n.r.
CEM I	n.r.	n.r.	n.r.	n.r.	n.r.	n.r.	n.r.	n.r.	3150	361
SS	27.7	-	-	-	16.72	-	-	-	1554	-

Notes: Values from manufacturers' datasheets. n.r.: not reported. Silica fume oxide ranges from supplier specification. Class F fly ash supplier reports only K_2O and Na_2O as raw values. The EN 450-1 conformity certificate confirms the remaining oxides fall within standard thresholds. Sodium silicate is supplied at 44.5% solids. Modulus Ms = SiO_2/Na_2O = 1.66. KOH and NaOH used as solid reagent grade and prepared in deionized water 24 hours before mixing, not included in this table.

1.2.3 Aggregates

Both REF and GEO used the same bimodal quartz-sand system supplied by the project reference UHPC partner. The sands had SiO_2 purity above 90 wt%, density 2.65 g/cm³, and porosity below 2%. Two grades were used, both classified by sieve analysis: a fine fraction with 90 wt% finer than 0.5 mm and 9 wt% finer than 0.125 mm, and a coarse fraction with 97 wt% finer than 1 mm, 44 wt% finer than 0.8 mm, and 12 wt% finer than 0.5 mm. The two grades were used in fixed mass proportions across all REF and GEO mixes (Table 1-4), and the total aggregate-to-binder mass ratio was held constant from Stage 3 onward to prevent aggregate effects from confounding the binder-side variables in the optimization.

The particle-size distributions of all six dry constituents are compared in Figure 1-6. The curves for GGBS, silica fume, fly ash, and CEM I are laser-diffraction data taken from the respective supplier datasheets; those for the two sand grades are derived from the sieve analyses reported above. The two measurement principles yield different equivalent diameters for irregular particles, so the comparison across the figure is indicative of the relative size scales rather than a single continuous measured gradation.

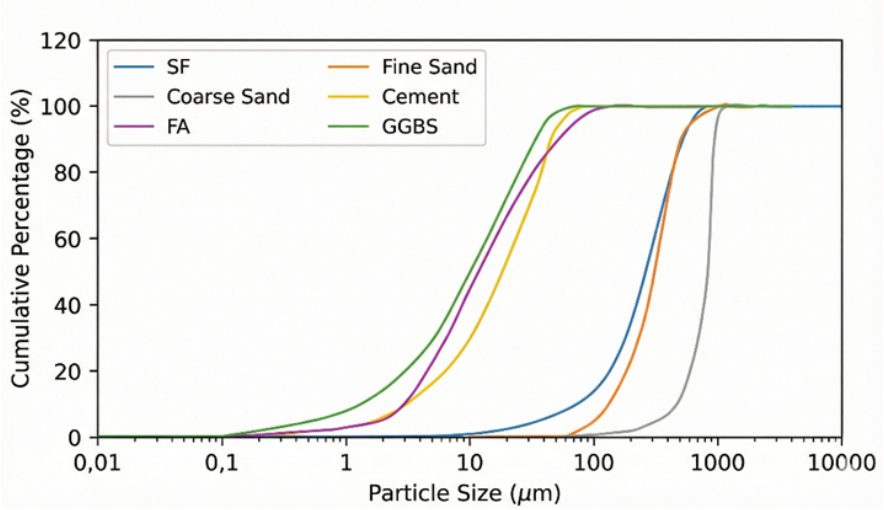

Figure 1-6: Particle-size distributions of the six dry constituents of the REF and GEO mixes. Powder curves from supplier datasheets by laser diffraction and sand curves from sieve analysis.

1.2.4 Superplasticizer

The REF mix used a third-generation polycarboxylate-ether (PCE) superplasticizer at the dosage recommended by the project reference UHPC supplier. The dosage is withheld under project confidentiality. The GEO mix used no superplasticizer. The workability target was reached through the activator chemistry alone.

1.2.5 Virgin steel fibers

Virgin straight steel fibers were supplied by Spajic, with a nominal length of 13 mm, a diameter of 0.20 mm, an aspect ratio of 65, a tensile strength of 3050 MPa, and an elastic modulus of 210 GPa. The 13 mm length matches the maximum aggregate dimension of the matrix and produces the through-fiber crack-bridging length characteristic of UHPC and UHPGC.

1.2.6 Recycled tire-derived steel fibers

Recycled fibers were Flexofibers recovered from end-of-life tires, supplied as cleaned and sieved bulk material with rubber residue partially retained on the fiber surface (Figure 1-5) (the as-recovered quality discussed in Section 1.1.4.3). The geometry was irregular, with length distribution spanning 10 to 25 mm, diameter spanning 0.15 to 0.30 mm, and a long tail of short fragments. The tensile strength of the steel cord wire is reported by the supplier as above 2000 MPa, with a substantially higher coefficient of variation than the virgin fibers.

1.3 Mix design optimization protocol

The optimization was scoped against five acceptance criteria pursued simultaneously: 24-hour compressive strength at least 65 MPa, 28-day compressive strength at least 130 MPa, slump flow of 200 to 250 mm per ASTM C1856, open time at least 20 min, and recycled tire-derived steel-fiber content at least 35 wt%.

The GEO formulation was developed through a sequential bottleneck-driven optimization in which each stage isolated and resolved the dominant limiting factor identified at the previous stage (Figure 1-7). This approach was chosen over factorial or response-surface designs for two reasons. **First**, the five criteria couple non-orthogonally to the underlying chemistry: a fractional factorial would require a prohibitive number of mixes to resolve the interactions, and a response-surface design assumes a smooth response function that the data of Section 1.5 will show is not warranted, the silicate-dosage optimum of Stage 3 being a counterexample. **Second**, the bottleneck-driven approach generates explainable mix-design decisions that map directly onto the gel chemistry described in Section 1.1.1, thereby producing a methodology transferable to other slag-rich UHPGC systems beyond the present project.

The optimization proceeded through six experimental stages, summarized in Table 1-3, with the 19 principal formulations tabulated in Table 1-4. The remainder of this section describes each stage in turn.

Table 1-3: Optimization protocol. Each stage manipulates one variable, or one defined pair, while holding the remaining parameters at the values inherited from the previous stage; co-varying quantities, such as the water-to-binder ratio, are stated in the text.

Stage	Bottleneck carried in	Variable and levels	Held constant	Measured
1. Precursor screening	entry point	GGBS to fly ash ratio, four levels: 100/0, 75/25, 50/50, 25/75	total binder mass silica fume at 15.8 wt% of binder sodium silicate alone, activator-to-binder 0.32	compressive strength at 24 h and 28 d, EN 196-1
2. NaOH co-activation and molarity	no mix reached 65 MPa at 24 h under ambient cure	NaOH molarity, three levels: 8, 10, 12 M, on two precursor blends	silicate at 300 kg/m³ precursor blend within each series	compressive strength at 24 h and 28 d slump flow, ASTM C1856
3. Silicate dosage and binder restructuring	28-day strength plateaued at 99 to 110 MPa	silicate dosage, three levels: 300, 240, 160 kg/m³ fly ash removed, silica fume raised to 22.5 wt%	NaOH at 12 M	compressive strength slump flow open time, NF EN 196-3
4. Total binder dose and NaOH molarity	neither strength criterion met, workability below the acceptance bound	NaOH molarity, three levels: 8, 10, 12 M, at 900 kg/m³ binder	silicate at 160 kg/m³	compressive strength slump flow open time
5. Cation replacement, NaOH to KOH	open time and slump flow below target at every molarity	hydroxide cation, Na^+ against K^+, at equal 10 M concentration	all other dosages at their Stage 4 values	compressive strength slump flow open time

6. Fiber incorporation and recycled-blend selection	recycled-fiber criterion not yet addressed	Flexo to Spajic blend, four levels, crossed with total dosage, two levels	matrix at its Stage 5 values	compressive and flexural strength slump flow open time

- Stage 1: Precursor screening

The program opens by fixing the precursor chemistry, since every later decision inherits it. Four GGBS to fly ash ratios were screened at constant total binder mass and constant activator, so that the strength response could be attributed to the precursor blend alone. The aggregate-to-binder ratio was not held strictly constant at this stage: the screening was designed as an initial chemistry probe, and the resulting paste-volume variation of about 10% is small against the strength differential between the extreme compositions.

- Stage 2: NaOH molarity

Stage 1 closed with no mix reaching the 24-hour acceptance value, regardless of the GGBS to fly ash ratio, which located the limit in the activator rather than in the precursor: with sodium silicate as the sole activator, no free hydroxide was available to drive rapid slag dissolution. Stage 2 therefore introduced solid sodium hydroxide as a hydroxide-alkalinity boost, at three molarities. Two precursor blends were carried forward in parallel, so that the kinetic effect of the hydroxide could be separated from the effect of the GGBS to fly ash ratio. A hydroxide-free control was cast and cured alongside each series.

- Stage 3: Sodium silicate dosage and binder restructuring

Stage 2 raised the 24-hour strength substantially but left the 28-day strength plateaued at 99 to 110 MPa across the entire molarity range, showing that the limit was no longer activation kinetics but reactive binder content. Two changes were made together. Fly ash was removed and the silica fume fraction raised to 22.5 wt% to maintain the fine-particle packing it had provided, and the silicate dosage was reduced in three steps. The reduction tested a counterintuitive hypothesis: that the silicate carried since Stage 1 was excessive and was forming a diffusion barrier on the GGBS surfaces that restricted hydroxide access to the slag. Removing the fly ash lowers the binder mass from 950 to 800 kg/m³, so holding the activator at its Stage 2 mass raises the activator-to-binder ratio to 0.50 as an arithmetic consequence rather than a design choice. The deliberate reduction proceeds from there.

- Stage 4: Total binder dose and NaOH re-optimization

Stage 3 supported the silicate hypothesis, without isolating it from the co-varying water-to-binder ratio, but left the mix short of both strength criteria and below the rheological bound, so Stage 4 addressed the two together by raising the total binder content while holding the silicate dosage in the optimum band identified at Stage 3. The hydroxide dosage was increased to activate the additional precursor, and three molarities were tested at the new binder content. The SS to SH mass ratio falls to approximately 0.89 as a consequence of fixing the silicate and raising the hydroxide, not as an independent design choice. The controlling variable identified in Stage 3 is the absolute silicate dosage, which remains in its optimum band throughout.

- Stage 5: Cation replacement, NaOH to KOH

Stage 4 reached both strength criteria but failed the slump flow and open time at every molarity tested, and the trade-off mapped across that range showed that no further tuning within the sodium-hydroxide system could close the gap. Stage 5 therefore changed the activation route rather than the dosages, replacing NaOH with KOH at equal hydroxide concentration and holding every other dosage at its Stage 4 value. The hypothesis, drawn from the cation literature of Section 1.1.1, is that the larger K^+ ion binds water and silicate species less tightly than Na^+, delaying gel nucleation and extending the workable window while supplying the same hydroxide for slag dissolution. Because a 10 M KOH solution carries more solute mass per liter than 10 M NaOH, the water-to-binder ratio co-varies with the substitution. This is stated here because it bears on the interpretation of the strength comparison.

- Stage 6: Fiber incorporation and recycled-blend optimization

With every matrix-side criterion satisfied at Stage 5, the only remaining acceptance value was the recycled-fiber content, which is a property of the fiber system rather than of the binder. Stage 6 therefore held the matrix fixed and crossed two factors: the mass ratio of recycled Flexofiber to virgin Spajic, at four levels, and the total fiber dosage, at two. Mixing followed the two-stage fiber-addition protocol of Section 1.3.8, which mitigates the dispersion difficulty caused by the rubber residue on the recycled fibers. The acceptance condition for this stage was the simultaneous satisfaction of all five criteria, with the selection among the compliant blends made on recycled content.

The complete matrix of the 19 principal formulations across the six stages is tabulated in Table 1-4. The selected GEO mix is highlighted on the last row. The Stage 6 blend-mapping series (four Flexofiber to Spajic ratios at two total dosages, Section 1.5.6) shares a single matrix composition. The table carries its two decision-relevant rows, the all-virgin bound and the selected 60/40 blend, with the full blend map reported in the Stage 6 figures. The iterative bottleneck-driven logic of the optimization, with the variable manipulated at each stage and the bottleneck identified at its close, is summarized stage by stage in Section

1.5, where the results that identified each bottleneck and motivated the transition to the next stage are reported.

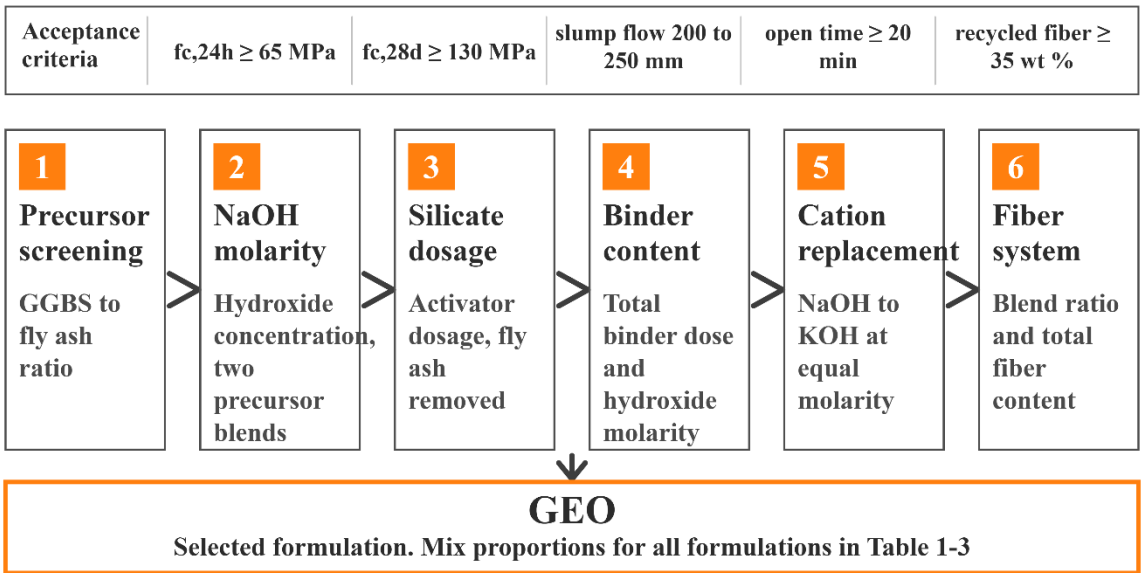

Figure 1-7: Sequential optimization program schema for the GEO formulation.

Table 1-4: Mix design matrix of the GEO formulations investigated across the six optimization stages.

Mix	Stage	GGBS (%)	FA (%)	SF (%)	SS/SH	A/b	w/b	Hydroxide
G8F0	1	84.2	0	15.8	-	0.32	0.28	-
G6F2	1	63.2	21.1	15.8	-	0.32	0.28	-
G4F4	1	42.1	42.1	15.8	-	0.32	0.28	-
G2F6	1	21.1	63.2	15.8	-	0.32	0.28	-
G4F4 + 8M NaOH	2	42.1	42.1	15.8	3.00	0.42	0.33	8 M NaOH
G4F4 + 10M NaOH	2	42.1	42.1	15.8	3.00	0.42	0.33	10 M NaOH
G4F4 + 12M NaOH	2	42.1	42.1	15.8	3.00	0.42	0.33	12 M NaOH
G6F4	2	52.2	34.8	13	-	0.26	0.26	-
G6F4 + 8M NaOH	2	52.2	34.8	13.0	3.00	0.35	0.32	8 M NaOH
G6F4 + 10M NaOH	2	52.2	34.8	13.0	3.00	0.35	0.32	10 M NaOH
G6F4 + 12M NaOH	2	52.2	34.8	13.0	3.00	0.35	0.32	12 M NaOH
G6SF1.8, SS/SH = 3.0	3	77.5	0	22.5	3.00	0.50	0.35	12 M NaOH
G6SF1.8, SS/SH = 3.0, low A/b	3	77.5	0	22.5	3.00	0.40	0.29	12 M NaOH
G6SF1.8, SS/SH = 2.0	3	77.5	0	22.5	2.00	0.30	0.24	12 M NaOH
G7.2SF1.8 + 8M NaOH	4	80.0	0	20.0	0.89	0.38	0.31	8 M NaOH
G7.2SF1.8 + 10M NaOH	4	80.0	0	20.0	0.89	0.38	0.3	10 M NaOH
G7.2SF1.8 + 12M NaOH	4	80.0	0	20.0	0.89	0.38	0.29	12 M NaOH

G7.2SF1.8 + 10M KOH	5	80.0	0	20.0	0.89	0.38	0.240.24	10 M KOH
GEO + 100% Spajic	6	80.0	0	20.0	0.89	0.38	0.24	10 M KOH
GEO (60/40, 12 wt%)	**6**	**80.0**	**0**	**20.0**	**0.89**	**0.38**	**0.24**	**10 M KOH**

Note: SS/SH is the mass ratio of sodium silicate solution to alkali hydroxide solution, A/b is the activator-solution to total-binder mass ratio, w/b is the total-water to binder mass ratio. Steel fibers are present only in the Stage 6 mixes. The selected formulation GEO is highlighted.

1.3.1 Mixing Protocols

REF and GEO required distinct mixing protocols. The reference UHPC system followed the standard sequence for Portland-cement UHPC: dry components, water with split polycarboxylate superplasticizer, high-speed activation, and fiber dispersion. The geopolymer system required adaptation in two respects. **First,** the alkaline activators must contact the GGBS and silica fume surfaces before the aggregate-borne water phase, otherwise dilution outpaces dissolution and the early geopolymerization is incomplete. **Second,** the polycarboxylate superplasticizer used in REF is incompatible with the high-alkalinity activator solution and must be omitted from GEO. The 24-hour pre-mixing of the hydroxide solution is a further GEO-specific requirement that does not exist for REF. This subsection describes both protocols and the rationale for the GEO-side adaptations.

1.3.2 Mixers

The laboratory mixing was performed in a MATEST E094N planetary mortar mixer with a 4 L pan volume and a maximum working batch size of 1 L of UHPC. The mixer has two rotational speeds (60 rpm and 120 rpm) and can accommodate aggregates up to 3 mm and a fiber content up to 2.5% by volume. The mixer is shown in Figure 1-8. For the scale-up verification described in Section 1.3.11, mixes were transferred to a Forced Action Mixer XM 2-650 (Collomix) with a 20 L working capacity and a single rotational speed.





Figure 1-8: MATEST E094N planetary mortar mixer used for the laboratory-scale formulation work, with 4 × 4 × 16 cm^3 casting molds.

1.3.3 REF protocol

The reference UHPC was mixed according to the sequence summarized in Table 1-5. Dry components (premix powders, fine sand, and coarse sand) were combined and mixed at 60 revolutions per minute (rpm) for 1.5 min. Mixing water and the first half of the polycarboxylate superplasticizer (MC-Power Flow 3095, dosed at 30 kg/m^3 on a solution-mass basis) were added at 60 rpm for 1 min, followed by a 1-min pause to allow water-cement contact and admixture diffusion. The remaining superplasticizer was added at 60 rpm and the mix was continued for 3.5 min, during which the consistency progressed from dry through plastic to fluid. High-speed mixing at 120 rpm followed for 2 min to homogenize the fluid mortar (Camacho Torregrosa, 2013). Steel fibers were finally added at 60 rpm for 3 min to ensure dispersion without clumping. Total mixing time was 12 minutes.

Table 1-5: REF mixing protocol.

Time (min)	Process	Speed	Mix aspect
0 to 1.5	Dry components: Binder, fine sand, & coarse sand	60 rpm	Dry
1.5 to 2.5	Add water + 50% polycarboxylate superplasticizer	60 rpm	Dry
2.5 to 3.5	Pause	0 rpm	Dry
3.5 to 7	Add remaining 50% superplasticizer	60 rpm	Dry
7 to 9	High-speed homogenization	120 rpm	Dry → plastic → fluid
9 to 12	Add steel fibers (single stage)	60 rpm	Fluid

1.3.4 PCE incompatibility

Polycarboxylate superplasticizers degrade in pore solutions above pH ~13 through hydrolysis of the carboxylate side chains, thereby removing the steric stabilization that produces the water-reducing effect (Palacios and Puertas, 2005; Kim et al., 2024). The GEO activator solutions are at pH ~14 to 14.5 (10 M alkali hydroxide), well into the regime where PCE molecules lose function. The GEO mixes therefore used no superplasticizer. The required workability was achieved solely through the activator chemistry: KOH at 10 M produces an activator solution with lower viscosity and a longer open time than NaOH at the same molarity (Section 1.1.1, quantified in Section 1.5.5).

1.3.5 Hydroxide pre-mix

The hydroxide solution (NaOH for Stages 1 to 4, KOH for Stage 5 onward) was prepared 24 hours in advance in deionized water at the target molarity. The dissolution of solid

hydroxide in water is strongly exothermic, with adiabatic temperature rises of up to ~60 K observed at 12 M; the 24-h pre-mix allows the solution to dissipate this heat and reach room temperature before contact with the binder, thereby eliminating thermal disturbance during early geopolymerization. The sodium silicate solution (Betol 47-T) was used as supplied at room temperature. The hydroxide and silicate solutions were combined in the mixer in two-stage additions, as described below, rather than pre-blended off-line. Pre-blending the two activator solutions produces a viscous, opalescent silicate gel that is difficult to dose accurately and can locally pre-react, reducing activator efficiency.

1.3.6 Initial UHPGC trials and protocol revision

The first UHPGC trials applied the REF sequence with the activator solutions substituted for the water-and-PCE phase: dry components → activator + 50% hydroxide → pause → remaining hydroxide → high-speed → fibers. This protocol did not deliver the targeted performance. The activator solutions, introduced together with the aggregates after the dry-binder phase, did not contact the GGBS and silica fume particles long enough for dissolution and early geopolymerization to proceed before the aggregate-borne water was distributed across the mix. Setting was inconsistent across batches, early-age strength varied by more than 15% within nominally identical mixes, and the measured water-accessible porosity was around 12% (compared with 8.25% achieved with the revised protocol). Mixing procedures reported for alkali-activated concrete vary, and many follow the Portland practice of combining precursor and aggregate in the dry phase before adding the activator. Where the sequence has been tested directly, however, pre-contacting the precursor with the activator solution ahead of the remaining constituents has been found to raise the compressive strength, an effect attributed to more complete activation of the slag (Kim and Kang, 2021). The protocol was revised on that basis and on the mechanistic reasoning above: the activator must reach the binder at full concentration before the aggregate-borne dilution occurs.

1.3.7 Revised GEO protocol

The revised GEO mixing sequence is summarized in Table 1-6. The binder (GGBS, silica fume, and in Stage 1 also fly ash) was mixed dry at 60 rpm for 1 min. The sodium silicate solution and 50% of the hydroxide solution were then added together at 60 rpm for 1 min, allowing the activator phase to wet the binder surfaces and initiate slag dissolution before the aggregates enter. The mixer was brought to 120 rpm for 1 min of high-speed homogenization of the activated slurry. The aggregates (fine and coarse sands) and the remaining 50% of the hydroxide solution were then added at 60 rpm for 1 min, followed by 4 min of high-speed mixing at 120 rpm during which the consistency progressed through dry, plastic, and fluid states. The steel fibers were added at 60 rpm for 2 min in the two-stage sequence described below. Total mixing time was 10 minutes.

Table 1-6: GEO mixing protocol (cement-free, alkali-activated).

Mixing time (min)	Process	Speed	Mix aspect
0 to 1	Dry binder: GGBS + silica fume	60 rpm	Dry
1 to 2	Add sodium silicate solution + 50% KOH solution	60 rpm	Dry
2 to 3	High-speed homogenization of activated slurry	120 rpm	Dry
3 to 4	Add aggregates (fine + coarse sand) + remaining 50% hydroxide solution	60 rpm	Dry → moist
4 to 8	High-speed mixing	120 rpm	Dry → plastic → fluid
8 to 9	Add first half of steel fibers	60 rpm	Fluid
9 to 10	Add remaining half of steel fibers	60 rpm	Fluid

1.3.8 Two-stage fiber addition

Steel fibers were added in two stages to mitigate dispersion difficulties caused by rubber residue on the Flexofibers. Half of the total fiber mass was added first, and the mix was run for 1 min at 60 rpm. The remaining half was then added, and the mix was run for a further 1 min. The two-stage addition prevents the formation of fiber clumps that single-step addition produces in mixes with high recycled-fiber content. The two-stage addition was found to be necessary even at 10.4 wt% fiber content. At 12 wt%, single-step addition of the 100% Flexofibers mix produced visible clumping within the first 30 seconds.

1.3.9 Visual and auditory endpoint cues

Two operator-level cues complement the time-based protocol of Table 1-6. The consistency transition from dry to plastic occurs between minutes 4 and 5 of the high-speed mixing phase, marked by a drop in motor pitch as the slurry becomes self-mobile and the mixer load decreases. The plastic-to-fluid transition occurs between minutes 6 and 7, marked by a second pitch shift as the matrix coalesces around the aggregates. If the dry-to-plastic transition is not heard within minute 5, the mix is short of activator-borne water and a small adjustment (~2% of activator mass) is added before high-speed mixing continues. If the plastic-to-fluid transition is not heard by minute 7, the mix is over-activated and the slump flow will exceed the upper bound of 250 mm.

1.3.10 Casting and curing

Casting began immediately after fiber dispersion to take advantage of the 20-to-23-minute open time. The standard molds used for the optimization work were 4 × 4 × 16 cm^3 prisms per NF EN 196-1 for compressive and flexural strength testing. The final optimized

GEO mix and the REF reference were also cast in 10 × 10 × 10 cm^3 cubes per NF EN 12390-3 to verify scale-up. Specimens were cast without vibration, the mixes being self-compacting at the target slump flow. Curing was performed at 20 ± 2 °C and 50 ± 5% RH for the first 24 hours under sealed conditions. Specimens were then demolded and stored under the same conditions until testing.

1.3.11 Scale up

Scale-up trials in the 20 L Forced Action Mixer XM 2-650 followed the same staged-addition protocol with one operational difference: the second-speed function of the laboratory MATEST mixer is not available on the Forced Action Mixer, so the entire mix was performed at the single available speed and the total mixing time was extended by 2 min to compensate for the slower energy input. The dry-component order was also adjusted: a thin layer (~2 mm) of coarse sand was poured first to prevent the binder from caking at the bottom of the vessel, followed by the GGBS, silica fume, fine sand, and remaining coarse sand. Approximately 10% of the activator-borne water was reserved for the late-stage mixing for operator-level workability adjustment, since the larger thermal mass of the 20 L mix produces rheological behavior that differs marginally from that of the 1 L laboratory batch.

1.4 Characterization techniques

The optimized GEO and the REF reference were characterized across five property domains. Two techniques address the **fresh state**, where the acceptance criteria of Section 1.3 are defined. Two address the **mechanical performance** that the optimization targets. One resolves the **reaction kinetics** that distinguish an alkali-activated binder from a Portland one. Three characterize the **transport properties** of the pore network, and two the **phase composition and microstructure** that explain the mechanical result and set the durability question carried into Chapter 4. The subsections that follow are grouped accordingly.

All specimens were cast and cured as described in Section 1.3.10, and all reported ages are counted from the end of mixing. The standards, equipment, specimen geometries, and replicate numbers for each technique are summarized in Table 1-7 and the photographs are in Figure 1-9. Unless stated otherwise, compressive strengths reported for the optimization stages were measured on prism halves.

Gas permeability and mercury intrusion porosimetry were performed at the I2M laboratory, TREFLE department, the permeability measurements with assistance from Audrey Duphil; X-ray diffraction at the ICMCB laboratory, with assistance from Eric Lebraud; and scanning electron microscopy with energy-dispersive X-ray spectroscopy at Placamat (Plateforme Aquitaine de Caractérisation des Matériaux, Université de Bordeaux), with assistance from Philippe Legros.

Table 1-7: Characterization techniques: standards, equipment, specimens, and replicates.

Property	Standard	Equipment	Specimen	n
Slump flow	ASTM C1856	Truncated cone Ø100 × Ø70 × 50 mm	Single batch	2 orthogonal measurements
Open time	NF EN 196-3, Vicat, final setting	Vicat apparatus, 1.13 mm needle, 300 g moving mass	Paste	1 per mix
Compressive strength (prisms)	NF EN 196-1, 50 ± 10 N/s	Hydraulic press	4 × 4 × 16 cm^3 prism halves	≥ 3 per age
Compressive strength (cubes)	NF EN 12390-3	Hydraulic press	10 × 10 × 10 cm^3 cubes	≥ 3 per age
Flexural strength	NF EN 196-1, three-point bending, span 100 mm	Hydraulic press	4 × 4 × 16 cm^3 prisms	≥ 3 per age
Semi-adiabatic calorimetry	NF EN 196-9 (Langavant)	Langavant calorimeter, Ø 85 × 150 mm steel container, type-K thermocouple	≈ 1.5 kg fresh mix	1 per mix
Water-accessible porosity	NF P18-459	Vacuum desiccator (25 mbar, 4 h), 105 °C oven	4 × 4 × 4 cm^3 cubes	3 per mix
Nitrogen gas permeability	Cembureau method	Triaxial cell, 2.5 bar lateral confinement, six differential pressures 12.8 to 59.6 kPa	Ø 35 × 60 mm cylinder, dried at 60 °C to constant mass	1 (+1 check)
Mercury intrusion porosimetry	Internal protocol, Washburn equation	Pascal 440 porosimeter (REF 0.009 to 201 MPa, GEO 1.75 to 251 MPa)	≈ 1 cm^3 chips, dried at 60 °C	1 per mix
X-ray diffraction with Rietveld	Internal protocol, ICDD PDF-4+	Bruker D8 Advance + LynxEye XE, Cu Kα	Ground powder, back-loaded	1 per mix
SEM and EDS	Internal protocol	HITACHI SU7000 and Zeiss EVO 50, 10 to 20 kV, BSE and SE, EDS	3 × 2 × 1 cm^3 chips, Pt-coated 5 nm	1 per mix, multiple fields

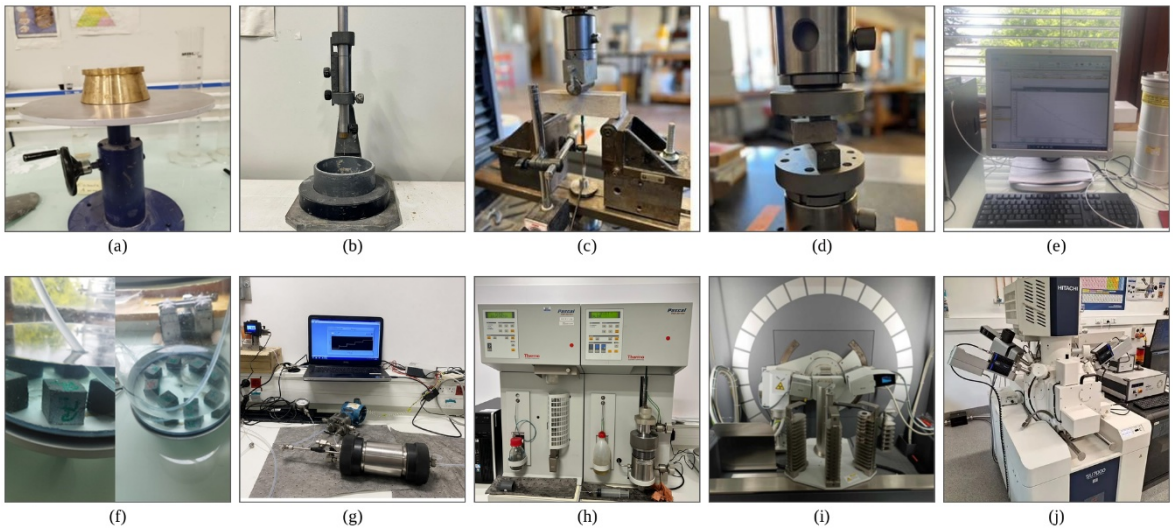

Figure 1-9: Characterization equipment. (a) Flow table, (b) Vicat apparatus, (c) three-point bending rig, (d) compression press, (e) Langavant calorimeter, (f) vacuum saturation, (g) gas permeability cell, (h) mercury intrusion porosimeter, (i) X-ray diffractometer, (j) scanning electron microscope.

1.4.1 Fresh-state properties

Two properties define the fresh-state acceptance window of Section 1.3: the **slump flow**, which measures the self-compacting consistency at the end of mixing, and the **open time**, which bounds the interval over which the mix can still be placed under gravity. The two are measured by different methods and are reported separately.

Flowability was measured (Figure 1-9a) per ASTM C1856/C1856M using a truncated cone mold (base Ø 100 mm, top Ø 70 mm, height 50 mm). The mold was placed on a flat, leveled, dry plate and filled in a single layer without tamping. After lifting the mold vertically, the mix was allowed to spread freely for 2 min ± 5 s, and the average flow diameter was recorded as the mean of two orthogonal measurements. Acceptance was 200 to 250 mm for the NATURSEA-PV self-compacting target.

Open time was determined separately by Vicat needle penetration (Figure 1-9b) following NF EN 196-3. A sample of the binder paste was placed in the standard conical mold immediately after mixing, and the penetration of the 1.13 mm needle under a total moving mass of 300 g was recorded at intervals until penetration ceased.

Open time is reported here as the NF EN 196-3 final setting time, that is, the elapsed time from the end of mixing at which the needle penetrates no more than 0.5 mm into the specimen. This operational definition is adopted because it bounds the interval over which the self-compacting mix can still be placed in formwork under gravity. It is an upper bound measured on paste: it does not show that the complete fiber-reinforced concrete keeps its slump flow throughout that interval, which flow-retention measurements or rheometry on the concrete would establish. It is stated explicitly because NF EN 196-3 also defines an initial setting time, which is not the quantity reported here.

1.4.2 Mechanical properties

The **compressive strength** is the primary acceptance criterion at both 24 hours and 28 days, and the **flexural strength** characterizes the contribution of the fiber system introduced at Stage 6. Both are measured on the same prism specimens, the flexural test preceding the compressive test on the resulting halves.

Compressive strength was measured at 1 day and 28 days (Figure 1-9d). During the optimization stages 1 to 5, the test was performed on 4 × 4 × 16 cm^3 prism halves obtained as the fragments from the flexural test, following NF EN 196-1, at a loading rate of 50 ± 10 N/s. The compressive strength was computed as:

$$f_c = \frac{F}{A} \quad \textbf{(1.1)}$$

where F is the maximum load at failure (N) and A the loaded cross-sectional area (mm^2). For the final GEO and REF mixes, the test was repeated on 10 × 10 × 10 cm^3 cubes per NF EN 12390-3 to verify the scale dependence and to permit benchmarking against the NATURSEA-PV target envelope, which is expressed in cubic-specimen units.

Flexural strength was obtained by three-point bending (Figure 1-9c) on the same 4 × 4 × 16 cm^3 prisms used for the compressive test, following NF EN 196-1, with a span of 100 mm. The flexural strength was computed as:

$$f_f = \frac{3FL}{2bd^2} \quad \textbf{(1.2)}$$

where F is the maximum load at fracture (N), L is the loaded span (mm), and b and d are the width and depth of the specimen cross-section (mm). All strength results are the arithmetic mean of at least three replicates per mix per age. Standard deviations were computed with n-1 weighting and reported alongside the means.

1.4.3 Reaction kinetics

Semi-adiabatic calorimetry resolves the **temperature response** of the two binders over the first 48 hours. The technique distinguishes the rapid, uninterrupted reaction of an alkali-activated slag from the dormant period and delayed acceleration of Portland hydration, and it is the measurement that explains the rheological behavior reported in Section 1.5.5.

The thermal response of the optimized GEO and the REF reference was monitored under semi-adiabatic conditions (Figure 1-9e) following the NF EN 196-9 (Langavant method). Approximately 1.5 kg of fresh mix was placed in a sealed cylindrical steel container (Ø 85 × 150 mm) immediately after the end of mixing. The container was inserted into an insulated Langavant calorimeter, and the centerline temperature was recorded for 48 hours at 5-minute intervals via a centrally embedded type-K thermocouple, along with the room ambient temperature recorded in parallel.

Two deviations from the standard are declared. The tests were performed on the actual REF and GEO mixes rather than on the standard mortar prescribed by NF EN 196-9, so that the thermal profiles correspond to the materials characterized elsewhere in this chapter. The baseline was taken as the recorded ambient temperature rather than an inert reference specimen of equivalent heat capacity, so the temperature difference reported here is the specimen-to-room difference rather than the specimen-to-reference difference defined by the standard.

The temperature difference relative to the baseline was computed as:

$$\theta(t) = T_s(t) - T_a(t) \quad \textbf{(1.3)}$$

The temperature excursion is reported as:

$$\Delta\theta = \theta_{max} - \theta(0) \quad \textbf{(1.4)}$$

where $\Delta\theta$ is the difference between the maximum of θ and its value at the start of acquisition. Referring the excursion to $\theta(0)$ rather than to zero accounts for the elevated initial temperature of the GEO specimen, which entered the calorimeter already above ambient. The rate of temperature change was obtained as the numerical derivative dTs/dt of the measured series, smoothed with a five-point centered moving average corresponding to a 25-minute window.

NF EN 196-9 derives the cumulative heat of reaction from the same temperature record as:

$$Q(t) = \frac{c}{m}\theta(t) + \frac{1}{m}\int \alpha\theta(\tau)\, d\tau \quad \textbf{(1.5)}$$

in which the first term is the heat stored in the calorimeter and specimen and the second the heat lost through the calorimeter walls, with c the total heat capacity of calorimeter and specimen (J K−1), α the total heat-loss coefficient of the apparatus (J h−1 K−1), and m the binder mass (g).

Over a 48-hour window the loss term dominates, accounting for approximately 90% of Q(48 h) for the GEO specimen across the plausible range of α. Since α was not independently calibrated on the present apparatus, the computed heat would restate that assumed coefficient rather than a measured quantity, and Q(t) is therefore not reported. The technique resolves the difference in reaction kinetics between the rapid alkali-activated geopolymerization and the slower Portland-cement hydration.

1.4.4 Transport properties

Three techniques characterize the pore network and its connectivity. The **water-accessible porosity** gives the total volume of connected pore space, the **apparent gas permeability** gives the ease with which a fluid traverses it, and mercury intrusion porosimetry resolves the **pore-entry diameter distribution** within it. Taken together they

separate the amount of porosity from its size and connectivity, a distinction that carries the microstructural argument of Section 1.5.7.

Water porosity was measured (Figure 1-9f) following NF P18-459 on 4 × 4 × 4 cm^3 cubes cut from the same casting as the strength-test prisms. The specimens were saturated under vacuum at 25 mbar for 4 hours, after which the saturated mass m_a (air-weighed) and the hydrostatic mass mw (suspended in water) were recorded. The specimens were then dried at 105 °C in a forced-air oven to constant mass m_d. The water-accessible porosity P_w was calculated as:

$$P_w = \frac{m_a - m_d}{m_a - m_w} \times 100 \quad \textbf{(1.6)}$$

Each reported value is the mean of three replicate specimens. Drying at 105 °C coarsens the gel-pore network of alkali-activated systems by removing structural water from the C-(N,K)-A-S-H interlayer; the porosity values reported here therefore correspond to a fully dried state of the GEO transport network rather than the in-service moisture condition, and the implications are discussed with the durability assessment of Chapter 4.

Gas permeability was measured at 28 days (Figure 1-9g) on Ø 35 × 60 mm cylindrical specimens cored from the same casting as the porosity cubes. Specimens were dried at 60 °C to constant mass and tested in a Cembureau-style triaxial cell with 2.5 bar lateral confinement and downstream pressure equal to atmospheric pressure. Six differential pressures across the specimen (12.8, 24.7, 35.4, 45.4, 55.0, and 59.6 kPa) were applied in succession to capture the Klinkenberg slip effect. At each differential pressure, the steady-state volumetric flow rate was measured and the apparent permeability Ka was computed using Darcy's law for compressible gas flow. Where the Klinkenberg slip dependence

$$K_a = K_v\left(1 + \frac{\beta}{P_m}\right) \quad \textbf{(1.7)}$$

was followed, the intrinsic (liquid-equivalent) permeability Kv was extracted by linear regression of Ka against the inverse mean pressure 1/Pm, with Kv as the y-intercept and β as the gas-slip coefficient characteristic of the pore-gas system. Each reported value is obtained from a single specimen, with the six Ka measurements serving as internal pressure-replicate points.

The mean gas pressure accessible with the applied differential pressures spans a narrow range, from approximately 108 to 131 kPa, so the regression baseline in 1/Pm covers only 7.6 to 9.3 MPa^{-1} and the extrapolation to 1/Pm = 0 extends well beyond the measured interval. For REF, Ka varied by 3.6% across the six steps, and the Klinkenberg regression yielded an intercept that coincided with the mean apparent permeability, so the mean values of Kv and Ka are numerically identical for that mix.

For GEO, Ka did not follow the Klinkenberg slip dependence, so no intercept could be extracted and the value is reported as the mean apparent permeability $K_{a,mean}$ over the six pressure steps. Because Kv and $K_{a,mean}$ are not in general the same quantity, the

comparison between the two mixes in Section 1.5 is drawn on the Ka,mean basis. Reproducibility was checked on a second specimen per mix, with agreement within 6% at each pressure point.

MIP was performed at 28 days on a Pascal 440 high-pressure porosimeter (Figure 1-9h). Representative sub-samples of approximately 1 cm^3 were cut from the core of cubic specimens, oven-dried at 60 °C to constant mass, and degassed under vacuum before intrusion. The pore-entry diameter d corresponding to each applied mercury pressure P was computed from the Washburn equation:

$$d = -\frac{4\gamma \cos \theta}{P} \quad \textbf{(1.8)}$$

where $\gamma = 0.485$ N/m is the surface tension of mercury and $\theta = 130°$ the mercury-pore-wall contact angle. The REF specimen was analyzed over the full instrument pressure range (0.009 to 201 MPa, pore-entry diameters from 139 µm to 6.2 nm). The GEO specimen could not complete the low-pressure stage due to rapid mercury uptake by the coarser pore network and was therefore analyzed on the high-pressure stage only (1.75 to 251 MPa, 0.7 µm to 5.0 nm). Pore entries above 0.7 µm in GEO, spanning the upper part of the coarse capillary range and the whole of the macro-pore range, are not resolved by the present measurement.

The capillary and gel-pore ranges that govern transport and mechanical performance are fully captured, and the comparison between REF and GEO is reported within the jointly resolved window of 6 to 712 nm, bounded below by the finest pore entry resolved for REF (6.2 nm at 201 MPa) and above by the coarsest resolved for GEO (0.71 µm at 1.75 MPa). Cumulative intrusion V(d) and the differential pore-size distribution dV/d(log d) were derived from the raw intrusion data. The dominant pore-entry diameter was identified as the peak of the differential distribution, equivalently the steepest slope of the cumulative curve. Where that peak lies at a limit of the measurement window it is reported as a bound rather than as a resolved peak.

1.4.5 Phase and microstructure

Two techniques characterize what the binder is made of and how it is arranged. **X-ray diffraction (XRD) with Rietveld refinement** gives the crystalline phase assemblage and, by difference, the amorphous fraction. **Scanning electron microscopy (SEM)** with **energy-dispersive spectroscopy (EDS)** gives the gel composition and the morphology of the fiber-matrix interface. The two are complementary: diffraction identifies phases but cannot locate them, while microscopy locates features but identifies them only by elemental ratio.

The phase assemblage of the optimized GEO and the REF reference was characterized at 28 days by XRD on a Bruker D8 Advance diffractometer (Figure 1-9i) with a LynxEye XE position-sensitive detector. The radiation was Cu Kα ($\lambda = 1.5406$ Å), the tube was operated at 40 kV and 40 mA, and the patterns were recorded from $2\theta = 6°$ to 100° with a step size of 0.017° and a counting time of 1 s per step. Specimens were prepared by gentle

dry-grinding of representative chips taken from the core of cubic specimens and back-loaded into the sample holder to minimize preferred orientation.

Crystalline phases were identified against the ICDD PDF-4+ database. Quantitative phase analysis of the GEO pattern was performed by Rietveld refinement in the BGMN software using a fundamental-parameters approach. No crystalline internal standard was added to the powder, so the refinement returns relative crystalline-phase abundances only. Absolute weight fractions were recovered by mass balance against the quartz aggregate, which is the only source of crystalline quartz in the hardened specimen and whose mass fraction is fixed by the mix design.

The supplier reports the sand to be above 90 wt% SiO_2, and the aggregate was assumed not to have dissolved measurably during the 28-day ambient cure. The powder was sieved below 63 µm, and the aggregate-to-binder ratio of the sieved fraction was bracketed at 1.03 to 1.22 relative to the bulk mix. This range propagates into the uncertainties reported in Table 1-10.

The amorphous C-(N,K)-A-S-H fraction was obtained by difference. The weighted-profile residual was $R_{wp} = 21.3\%$, consistent with a pattern dominated by a broad amorphous scattering contribution rather than by well-resolved crystalline reflections, and the phase fractions are therefore reported as semi-quantitative. The REF pattern was interpreted qualitatively and was not refined.

The local-scale **microstructure** of the optimized GEO and the REF reference was examined at 28 days by SEM (Figure 1-9j) on prismatic sub-samples of approximately 3 × 2 × 1 cm^3 cut from the core of cubic specimens. Specimens were dried at 60 °C for at least 24 hours, mounted on aluminum stubs, and sputter-coated with a 5 nm platinum layer to prevent the accumulation of static charge.

Imaging was performed on a HITACHI SU7000 and Zeiss EVO 50 in backscattered-electron and secondary-electron modes at accelerating voltages between 10 and 20 kV, at magnifications spanning 100× (matrix, aggregate and fiber overview) to 10000× (gel morphology). EDS point and area analyses were used to map the local elemental composition of the gel phase, with particular attention to the Ca/Si and Al/Si ratios that distinguish the C-(N,K)-A-S-H gel of GEO from the C-S-H gel of REF.

1.5 Results

This section reports the formulation development and characterization of the GEO mix, following the bottleneck-driven structure. The mix-design optimization walks through six experimental stages, each isolating one compositional variable and identifying the limiting factor that triggers the next stage: GGBS/FA ratio (Section 1.5.1), NaOH addition and molarity (Section 1.5.2), sodium silicate dosage (Section 1.5.3), total binder content and NaOH dosage (Section 1.5.4), alkali cation type Na^+ vs K^+ (Section 1.5.5), and incorporation

of recycled steel fibers (Section 1.5.6). Section 1.5.7 then reports the multi-technique characterization of the optimized mix (semi-adiabatic calorimetry, water-accessible porosity, nitrogen gas permeability, mercury intrusion porosimetry, X-ray diffraction with Rietveld refinement, and SEM/EDS), benchmarked against the Portland-cement reference REF at matched fiber dosage.

The five NATURSEA-PV acceptance criteria defined in Section 1.5 of the General Introduction are tracked stage by stage so that the convergence on the target envelope is visible in the data, not only in the conclusion. The 19 mixes investigated across the six stages are summarized in Table 1-4. The compressive strengths reported in Section 1.5 were measured on 4 × 4 × 16 cm^3 prism halves in accordance with NF EN 196-1 and are means of three specimens per age, reported to the nearest MPa. Stages 1 to 5 were conducted on the unreinforced binder matrix, so the strengths reported for those stages are matrix values as steel fibers were introduced only at Stage 6.

1.5.1 Stage 1: Effect of GGBS/FA ratio on strength and workability

The six optimization stages and their outcomes are summarized in Figures 1-9 through 1-16, with each stage reporting the matrix-side acceptance variable (compressive strength or slump flow) against the variable manipulated at that stage. The stages are read in sequence: each closes by identifying the bottleneck that motivates the next stage. The intermediate-mix mechanical and rheological data underlying these figures are tabulated in Table 1-4 of Section 1.3.

The objective of Stage 1 was to identify, at fixed activator chemistry and a constant total binder content, the GGBS-to-FA mass ratio that yields the highest 28-day compressive strength under ambient curing conditions. Four mixes (G2F6, G4F4, G6F2, G8F0 in Table 1-4, rows 1 to 4) varied the GGBS content from 200 to 800 kg/m^3 in 200 kg/m^3 steps, with fly ash correspondingly reduced from 600 to 0 kg/m^3. Silica fume was held at 150 kg/m^3 across all four mixes (15.8 wt% of binder). The activator was sodium silicate solution alone (Betol 47-T), with no alkali hydroxide added at this stage, at an activator-to-binder mass ratio of 0.32 and a water-to-binder ratio of 0.28.

The sand grading and the fine-to-coarse proportion were held identical in all the optimization stages, although the aggregate-to-binder ratio varied with the binder composition (Section 1.3). The compositional excursion was therefore restricted to the precursor chemistry, captured by the molar Ca/(Si+Al) ratio of the precursor blend, which rose monotonically with the GGBS fraction to reach 0.70 in the fly-ash-free G8F0.

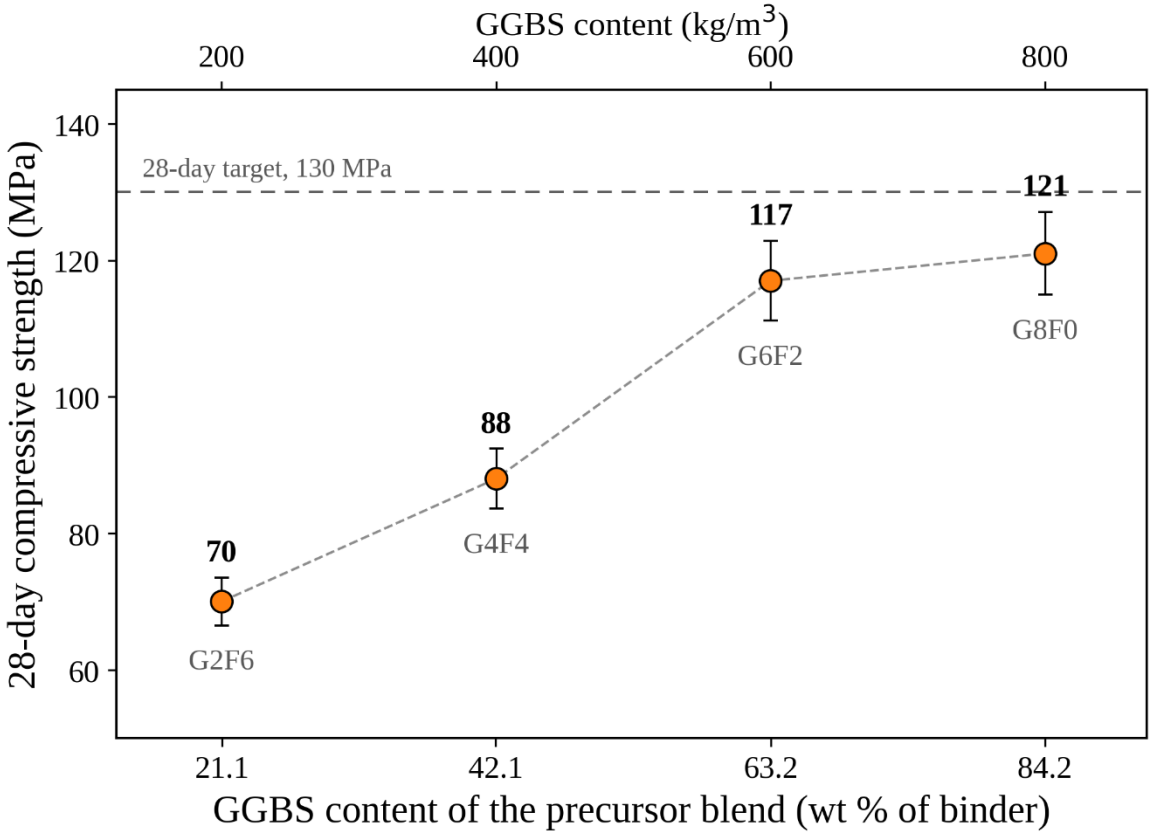

Figure 1-10: 28-day compressive strength of the Stage 1 mixes as a function of the GGBS content of the precursor blend. Error bars denote the measured within-batch coefficient of variation.

The 28-day compressive strength rose monotonically with GGBS content from 70 MPa at G2F6 to 88 MPa at G4F4, 117 MPa at G6F2, and 121 MPa at G8F0 (Figure 1-10). The increase was not linear with composition. The 0 to 50% GGBS substitution band (G2F6 to G4F4) contributed 18 MPa, the 50 to 75% band (G4F4 to G6F2) contributed 29 MPa, and the 75 to 100% band (G6F2 to G8F0) contributed only 4 MPa. The strength response therefore saturated above approximately 600 kg/m^3 GGBS at this activator chemistry, indicating that beyond G6F2 the calcium reservoir of the precursor is no longer the rate-limiting variable.

The correlation with the calcium (Ca) content of the precursor is consistent with the calcium-driven gel-formation argument of Section 1.1.1: GGBS contributes 43.9 wt% CaO and drives the gel chemistry into the C-A-S-H domain of the ternary diagram (Garcia-Lodeiro, with a cross-linked, tobermorite-like layered structure of higher intrinsic stiffness. The fly ash used here declares only 1.60 wt% total CaO and favors an N-A-S-H gel of lower cross-link density and lower mechanical performance (Garcia-Lodeiro et al., 2011; Provis and Deventer, 2014).

As GGBS replaces fly ash, the gel composition shifts from a sodium-balanced low-calcium aluminosilicate toward the calcium-balanced regime that supports ultra-high strength, with diminishing returns above approximately 600 kg/m^3 of GGBS.

Slump flow at the end of mixing tracked the same particle-morphology shift. The fly-ash-rich G2F6 reached 210 mm, just inside the 200 to 250 mm acceptance band, while the GGBS-rich G8F0 fell to 185 mm, below the lower bound. The ball-bearing effect of the spherical fly-ash particles, well documented in cementitious systems (Yazıcı et al., 2008), reduces the water demand of the fresh paste at fixed activator dose. Replacing fly ash with the irregular, sub-100-µm GGBS particles removes this lubrication and raises the water demand of the binder, producing the observed flow loss.

Two bottlenecks were identified at the end of Stage 1:

- **First,** the 24-hour compressive strength of all four mixes remained below 30 MPa, far below the 65 MPa acceptance value. With sodium silicate as the sole activator, the only alkalinity available was that carried by the silicate solution itself, and no free hydroxide was supplied to drive rapid slag dissolution within the first day. The deficit was present across the full compositional range, so it could not be resolved by precursor selection.

- **Second,** even the strongest mix (G8F0) plateaued at 121 MPa at 28 days, 7% below the 130 MPa target, and its slump flow dropped below the rheological acceptance lower bound. The dominant limiting factor was therefore the activator chemistry, specifically the hydroxide alkalinity available for slag dissolution, not the precursor selection.

Stage 1 closed with two operational decisions: G2F6 was dropped from further investigation given its low 28-day strength, and the 24-hour strength deficit was carried into Stage 2 for resolution through NaOH co-activation at increasing molarity, with G4F4 and a workability-corrected version of G6F2 (designated G6F4 with FA raised from 200 to 400 kg/m^3) tested in parallel to verify that the kinetic effect of NaOH is independent of the GGBS/FA ratio.

1.5.2 Stage 2: NaOH co-activation and molarity

Stage 2 introduced solid sodium hydroxide into the activator system as a hydroxide-alkalinity boost, while the silicate dosage was held at 300 kg/m^3 (the Stage 1 value). The two precursor blends were tested in parallel: G4F4 (400 GGBS + 400 FA + 150 SF) and G6F4 (600 GGBS + 400 FA + 150 SF), the latter created by doubling the fly-ash content of the Stage 1 G6F2 mix to recover the workability lost when GGBS reached 600 kg/m^3.

Three NaOH molarities (8 M, 10 M, 12 M) were investigated at 100 kg/m^3 of NaOH solution. A hydroxide-free control was cast and cured alongside each series for internal comparison. For G4F4 this control is the Stage 1 mix of identical composition. G6F4 has no Stage 1 counterpart, so a dedicated control was batched. Adding the alkaline solution raised the activator-to-binder ratio from 0.32 to 0.42 for G4F4 and from 0.26 to 0.35 for G6F4, and the water-to-binder ratio from 0.28 to 0.33 for G4F4 and from 0.28 to 0.32 for G6F4. Both controls are therefore drier than the molarity series they anchor, so the strength gains reported below understate the effect of the hydroxide addition.

The 24-hour compressive strength of G4F4 rose from 17.9 MPa with no NaOH to 22.6, 24.3, and 34.9 MPa at 8, 10, and 12 M, a 95% gain at the highest molarity (Figure 1-11a). The 28-day strength followed the same trend but with a much smaller relative gain, rising from 88.0 MPa with no NaOH to 93.4, 97.3, and 99.5 MPa at the three molarities, an increase of 13% at 12 M (Figure 1-11b).

The 24-hour response is resolved well beyond the measurement scatter, whereas the increments between consecutive molarities at 28 days lie at or within one standard deviation, so only the full span from the hydroxide-free control to 12 M is resolvable at that age. The asymmetric early-versus-late response is the kinetic signature of accelerated slag dissolution: NaOH at high molarity raises the pore-solution hydroxide concentration, shortens the induction period, and accelerates the dissolution-precipitation cycle that builds the early-age C-A-S-H scaffold (Shi and Day, 1995; Provis and Deventer, 2014). Nevertheless, it does not alter the final gel assemblage, which is set by the precursor chemistry at later ages (Fernández-Jiménez and Palomo, 2005; Haha et al., 2011).

The same asymmetry was observed on G6F4, with 24-hour strength rising from 29.0 to 30.8, 35.1, and 36.0 MPa at the three molarities and 28-day strength rising from 102.0 to 105.0, 108.0, and 110.0 MPa. The G6F4 early-age values exceeded those of G4F4 by 8 to 11 MPa at 0, 8, and 10 M, reflecting both the higher GGBS content and the larger total binder mass, 1150 against 950 kg/m^3, and consistent with the calcium-driven mechanism of Stage 1. The two blends converge at 12 M, where the difference falls to 1.1 MPa, indicating that the advantage of the richer precursor is progressively offset once the hydroxide concentration is sufficient to drive dissolution in the leaner blend.

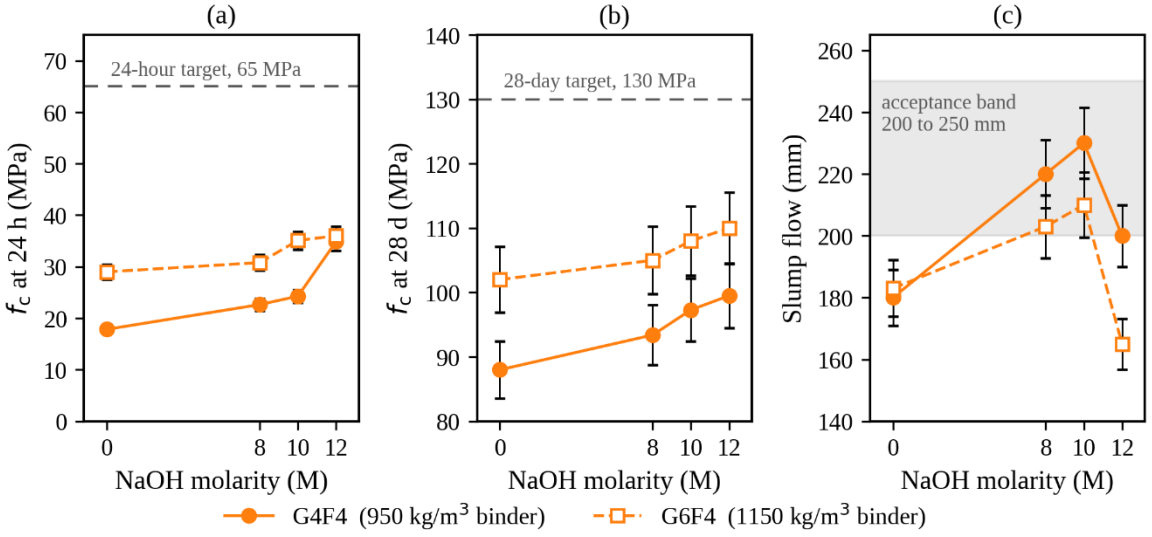

Figure 1-11: Effect of NaOH molarity on the two precursor blends of Stage 2. (a) 24-hour compressive strength, (b) 28-day compressive strength, (c) slump flow.

Slump flow tracked the activator dose. For G4F4, flow rose from 180 mm with no NaOH to 220 mm at 8 M and 230 mm at 10 M, then fell to 200 mm at 12 M, remaining inside the acceptance band at all three molarities and peaking at 10 M. For G6F4, flow rose from 183

to 203 and 210 mm at 8 and 10 M, then dropped sharply to 165 mm at 12 M, below the 200 mm lower bound. The drop is consistent with the increased ionic strength of the activator solution and accelerated early gel nucleation at high Na^+ concentration, which together raise the apparent viscosity of the fresh paste in the high-GGBS, high-NaOH regime (Wetzel and Middendorf, 2019) (see Figure 1-11c).

Stage 2 left two findings on the record:

First, NaOH co-activation accelerated the 24-hour strength gain but did not unlock the 65 MPa target: the highest 24-hour value across the six mixes was 36 MPa (G6F4 + 12 M NaOH), still 45% below the acceptance value.

Second, the 28-day strength of the FA-bearing blends plateaued at 99 to 110 MPa across the NaOH molarity range, well below the 130 MPa target. The kinetic bottleneck of Stage 1 was therefore alleviated, but not resolved, by the NaOH addition.

The limiting factor had shifted from activation kinetics to total reactive-binder content, as observed by Wetzel and Middendorf (2019) on closely related alkali-activated UHPC systems. Stage 2 closed with the decision to eliminate fly ash entirely in Stage 3, redistribute the freed binder mass to silica fume and GGBS, and increase the silica-fume fraction from 15.8 wt% of binder (Stage 1 and 2 baseline) to approximately 22.5 wt% to maintain the fine-particle packing previously provided by the spherical fly ash.

Removing the fly ash lowers the binder mass from 950 to 800 kg/m^3, so holding the activator at its Stage 2 mass of 400 kg/m^3 raises the activator-to-binder ratio to 0.50 as an arithmetic consequence rather than a design choice. From that starting point the activator dosage was deliberately reduced to 0.40 and 0.30, to test the counterintuitive hypothesis that the silicate dosage carried since Stage 1 was excessive and passivating the slag dissolution front. That hypothesis is tested directly in Stage 3.

The molarity ranking established here applies to the fly-ash-bearing blends of Stage 2 and does not transfer directly to the fly-ash-free binder introduced in Stage 3. On the restructured binder of Stage 4 the 28-day ranking inverts, and the molarity carried into the final formulation is determined there.

1.5.3 Stage 3: Sodium silicate dosage and binder restructuring

Stage 2 closed with a 28-day plateau at 99 to 110 MPa across the NaOH molarity range (8 to 10 M), indicating that the limiting factor had shifted from activation kinetics to total reactive-binder content.

Stage 3 addressed this through two changes implemented simultaneously: fly ash was eliminated from the binder, and the silica-fume fraction was raised from 15.8 to 22.5 wt% of binder to maintain the fine-particle packing previously provided by the spherical fly-ash

particles. The reformulated binder, designated G6SF1.8, consisted of 620 kg/m^3 of GGBS and 180 kg/m^3 of silica fume (77.5 wt% GGBS, 22.5 wt% SF, total binder 800 kg/m^3).

At the same time, the activator dosage was systematically reduced to test the silicate-passivation hypothesis introduced in Section 1.1.4.2: that the high silicate dosage carried through Stages 1 and 2 (300 kg/m^3 of sodium silicate solution in both, with SS/SH = 3.0 once NaOH was introduced in Stage 2) was forming a diffusion barrier on the GGBS particle surfaces that restricted hydroxide-ion access to the slag and capped the gel-formation rate.

Three G6SF1.8 mixes were tested at 12 M NaOH held constant, with the activator-to-binder mass ratio reduced from 0.50 to 0.30 in two steps and the SS/SH mass ratio reduced from 3.0 to 2.0: G6SF1.8-S300 (SS = 300 kg/m^3, NaOH solution = 100 kg/m^3, SS/SH = 3.0, AA/B = 0.50), G6SF1.8-S240 (SS = 240, NaOH = 80, SS/SH = 3.0, AA/B = 0.40), and G6SF1.8-S160 (SS = 160, NaOH = 80, SS/SH = 2.0, AA/B = 0.30). The water-to-binder ratio fell from 0.35 to 0.24 across the three mixes as a direct consequence of the reduced liquid volume.

The results, presented in Figure 1-12, revealed a counter-intuitive trend. As the activator dose was reduced, the 24-hour compressive strength more than doubled, rising from 23 MPa at S300 through 35 MPa at S240 to 50 MPa at S160. The 28-day compressive strength rose monotonically from 80 MPa at S300 through 115 MPa at S240 to 127 MPa at S160, an increase of 59% across the same compositional excursion. The slump flow tracked the opposite direction, falling from 230 mm at S300 (well inside the 200 to 250 mm acceptance band) to 170 mm at S240 and 160 mm at S160 (both below the rheological lower bound).

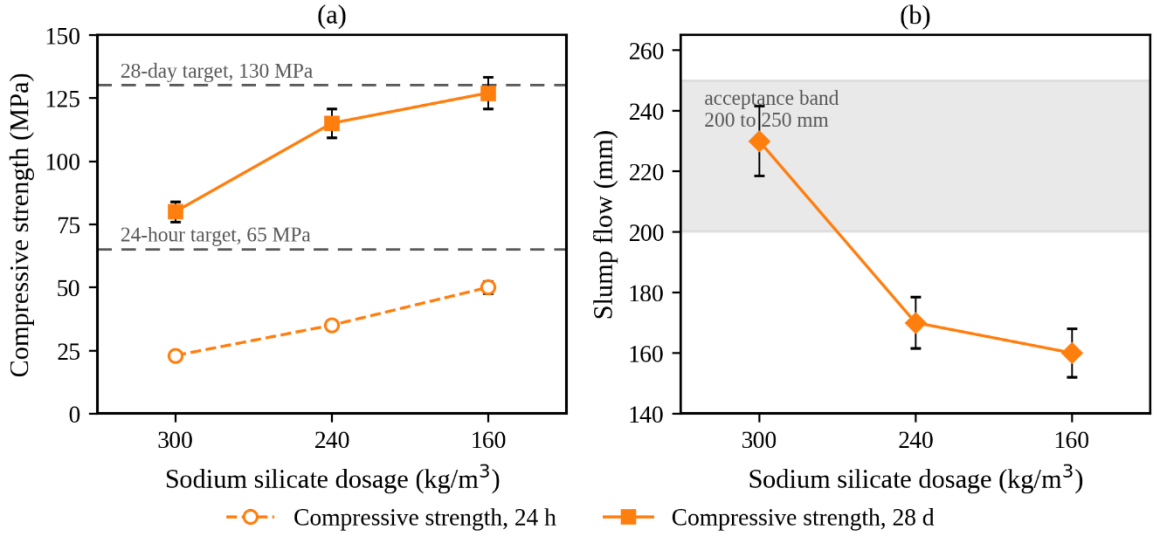

Figure 1-12: Effect of sodium silicate dosage on G6SF1.8 at 12 M NaOH. (a) Compressive strength at 24 hours and 28 days, (b) slump flow.

The 24-hour strength gain at lower silicate dose is consistent with the proposed silicate-passivation mechanism. In that reading, dissolved silicate species adsorbing on freshly exposed GGBS surfaces form a diffusion barrier that restricts hydroxide access to the underlying slag and retards the dissolution-precipitation cycle that builds the early-age

C-A-S-H scaffold. Reducing the absolute silicate dose lowers the surface coverage and frees the dissolution pathway (Hajimohammadi et al., 2011).

The activator modulus offers no explanation for the first and larger step of the series. Because the silicate and hydroxide doses were scaled together from S300 to S240, while holding SS/SH at 3.0, the SiO_2/Na_2O ratio of the combined activator remains unchanged at 1.08 across that step, yet the 28-day strength increases by 35 MPa. The modulus falls only at the third mix, to 0.92 at S160, where the 28-day gain is a smaller 12 MPa.

Over that step the mapping of Krizan and Zivanovic (2002), which places an optimum at intermediate modulus and dosage for alkali-activated slag systems, becomes relevant. The water-to-binder ratio, by contrast, falls at every step, from 0.35 through 0.29 to 0.24, so the strength gain cannot be attributed to the silicate dosage alone: a w/b reduction of this magnitude is itself one of the strongest strength levers available in a UHPC binder.

The G6SF1.8 trajectory from S300 to S160 therefore identifies an empirical optimum in which absolute silicate dosage and w/b co-vary throughout, with the activator modulus varying only over the final step. The reading is consistent with silicate passivation but is not an isolated demonstration of it. For this 12 M NaOH activator and 620 kg/m^3 GGBS precursor the optimum band lies at approximately 160 to 190 kg/m^3 of sodium silicate solution.

A second observation deserves emphasis. The design variable that controls passivation behavior is the absolute sodium silicate dosage (kg/m^3), not the SS/SH mass ratio. The two mixes G6SF1.8-S240 and G6SF1.8-S160 differ in SS/SH ratio (3.0 versus 2.0) only because the NaOH solution dose was held constant at 80 kg/m^3 while the silicate was reduced.

The underlying physical mechanism is the silicate surface coverage on the slag, captured by the absolute silicate concentration in the activator solution. This distinction matters for the trajectory from Stage 3 to Stage 4: Stage 4 increased the total binder content and raised the hydroxide dosage simultaneously, dropping SS/SH to approximately 0.89 even though the absolute silicate dosage was held in the same 160 to 190 kg/m^3 band identified at the end of Stage 3. Reading Stages 3 and 4 in absolute rather than ratio-based terms therefore reconciles the trajectory as a single optimization controlled by the absolute silicate dosage, not as a change in design strategy.

Stage 3 closed with an empirical optimum consistent with the silicate-passivation hypothesis, though not isolated from the concurrent w/b and modulus reduction, and one bottleneck was identified. The strength performance of G6SF1.8-S160 (50 MPa at 24 hours, 127 MPa at 28 days) approached but did not meet the two strength acceptance values (65 MPa and 130 MPa). More importantly, the slump flow of both S240 and S160 mixes dropped below the rheological acceptance lower bound, driven by the reduction in total activator-solution volume that was necessary to realize the strength gain.

The Stage 3 conclusion is therefore that the silicate-passivation reading is supported but not conclusive, that the resulting binder is workability-limited at the strength optimum, and that the total binder content may need to be raised to close the residual 24-hour and 28-day strength gaps. These two issues are addressed jointly in Stage 4 by increasing the total binder content to 900 kg/m^3 (720 GGBS + 180 SF) within the optimum absolute silicate band of approximately 160 to 190 kg/m^3, while raising the hydroxide dosage to activate the additional precursor.

1.5.4 Stage 4: Total binder dose and NaOH molarity (G7.2SF1.8)

Stage 3 left the optimization at G6SF1.8-S160, which was consistent with the silicate-passivation reading and approached the strength targets (50 MPa at 24 hours, 127 MPa at 28 days) but failed the rheological acceptance bound (slump flow 160 mm). Two adjustments were made simultaneously for Stage 4:

First, the total binder content was raised from 800 to 900 kg/m^3 to provide additional aluminosilicate reactants

Second, and the GGBS/SF mass ratio was set at 4:1 (720 GGBS + 180 SF, 80 wt% GGBS and 20 wt% SF of binder).

The absolute sodium silicate dosage was held at 160 kg/m^3, within the optimum band identified at the end of Stage 3, while the hydroxide dosage was raised to 180 kg/m^3 of NaOH solution to activate the additional precursor. The resulting SS/SH mass ratio fell to 0.89 as a direct consequence of the increased hydroxide, rather than as an independent design choice; the absolute silicate dose, identified in Stage 3 as the controlling variable, remained within the optimum band. The activator-to-binder ratio settled at 0.38 and the water-to-binder ratio at 0.29 to 0.31 across the three NaOH molarities. The reformulated binder is designated G7.2SF1.8.

Three NaOH molarities were tested in parallel: 8 M, 10 M, and 12 M, with all other parameters held constant. The 28-day acceptance criterion of 130 MPa was met at 10 M NaOH, with a 24-hour strength of 68 MPa, also above the 65 MPa acceptance value (Figure 1-13).

The 8 M mix reached 58 MPa at 24 hours and 118 MPa at 28 days, falling short of both targets by 11% and 9% respectively. The 12 M mix reached 73 MPa at 24 hours (12% above the 24-hour target) but only 127 MPa at 28 days (2% below the 28-day target). The 28-day strengths at 10 M and 12 M differ by 3 MPa, less than one standard deviation at the measured scatter, so the series is best read as a plateau above 10 M rather than as a genuine reversal.

The absence of any further gain is itself informative: beyond 10 M the additional hydroxide no longer converts into 28-day strength, consistent with reports that excess alkali disrupts later-age polycondensation in alkali-activated slag systems by over-driving the gel

reorganization step and producing a more open, less cross-linked network (Fernández-Jiménez and Palomo, 2005).

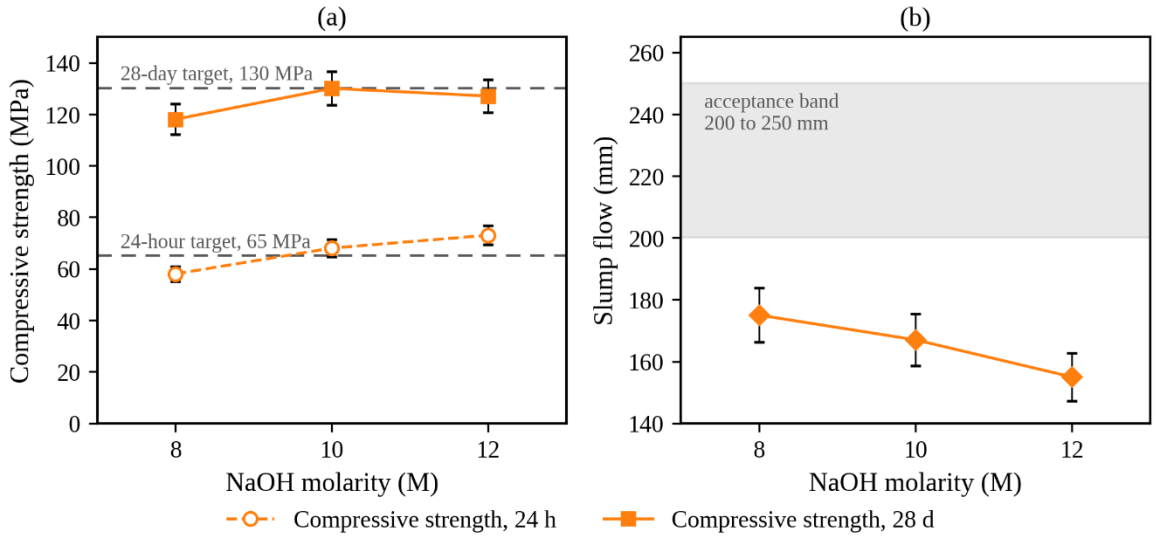

Figure 1-13: Effect of NaOH molarity on G7.2SF1.8. (a) Compressive strength at 24 hours and 28 days, (b) slump flow.

The slump flow followed a monotonic decreasing trend across the molarity range, falling from 175 mm at 8 M to 167 mm at 10 M and 155 mm at 12 M. All three values sat below the 200 mm rheological acceptance lower bound. The Vicat open-time measurements (Section 1.4.1) gave NF EN 196-3 final-setting times below 20 minutes for all three NaOH molarities, failing the open-time acceptance criterion. The strength-workability trade-off characteristic of alkali-activated slag with sodium hydroxide is therefore active across the full molarity range tested (Wang et al., 1994; Shi and Day, 1995): the higher the Na^+ concentration, the more rapid the gel nucleation and the shorter the open window.

This trade-off cannot be resolved within the $NaOH^-$activator framework by further compositional tuning, because the 10 M mix already sits at the strength optimum and lower molarities sacrifice the 28-day target while higher molarities compromise both the workability and the long-term strength.

The 130 MPa achieved at 10 M NaOH on G7.2SF1.8 is the first formulation in the optimization program to satisfy both compressive-strength acceptance criteria, and it does so under ambient cure and without fly ash, a combination that distinguishes this binder from the bulk of the UHPGC literature compiled in Table 1-1. The same Table 1-1 entries reach 130 MPa or higher either through heat curing or through high-volume fly-ash blends. The present G7.2SF1.8 + 10 M NaOH formulation reaches the target under ambient cure on a binary GGBS + SF binder.

Stage 4 closed with two findings. The strength acceptance criterion is satisfied for 10 M NaOH on G7.2SF1.8 with 24-hour and 28-day compressive strengths of 68 and 130 MPa. The workability and open-time acceptance values are not satisfied at any of the three

molarities, and the strength-workability trade-off mapped in Stage 4 indicates that further compositional tuning within the $NaOH^-$activator system cannot close this gap.

The bottleneck identified at the end of Stage 4 is therefore not on the strength side but on the rheology and reaction-kinetics side, and its resolution required a change in activation strategy rather than a further tuning of dosages. Stage 5 tested the hypothesis that this trade-off can be broken by replacing the Na^+ activator cation with K^+ at equal molarity, exploiting the difference in ionic size and hydration-shell binding energy to extend the open time without sacrificing the strength established in Stage 4.

1.5.5 Stage 5: Cation replacement (NaOH to KOH)

Stage 4 closed with the strength targets met at G7.2SF1.8 + 10 M NaOH (68 MPa at 24 hours, 130 MPa at 28 days) but the rheological and open-time targets were not met across the full NaOH molarity range. Stage 5 tested the cation-substitution hypothesis introduced in Section 1.1.1: that the strength-workability trade-off observed across the NaOH molarity sweep is driven by the small, high-charge-density Na^+ cation, and that replacing Na^+ with the larger K^+ at equal molarity should preserve the hydroxide alkalinity (and therefore the gel chemistry and strength) while extending the open time and increasing the slump flow.

The composition was held identical to G7.2SF1.8 + 10 M NaOH across all dosages, except for the hydroxide solute: KOH replaced NaOH at the same volumetric concentration (10 M), using the same hydroxide solution at 180 kg/m³. One consequential co-variation must be stated: at equal molarity, a 10 M KOH solution carries approximately 40% more solute mass per liter than 10 M NaOH (about 561 against 400 g/L), so the same mass of hydroxide solution delivers less water, and the water-to-binder ratio fell slightly, from 0.29 in the Stage 4 NaOH mix to 0.28 in the KOH mix (Table 1-4). The change is too small to account for the rheological response reported below.

The KOH solution was prepared in deionized water 24 hours before mixing to allow the strongly exothermic dissolution to dissipate before contact with the binder (Section 1.3.5) and was combined with the sodium-silicate solution immediately before introduction into the mixer. The activator-to-binder ratio remained at 0.38, the sodium-silicate dosage at 160 kg/m^3, the SS/SH mass ratio at 0.89, and the water-to-binder ratio settled at 0.28, against 0.29 for the 10 M NaOH baseline. The resulting binder is the matrix-optimized GEO.

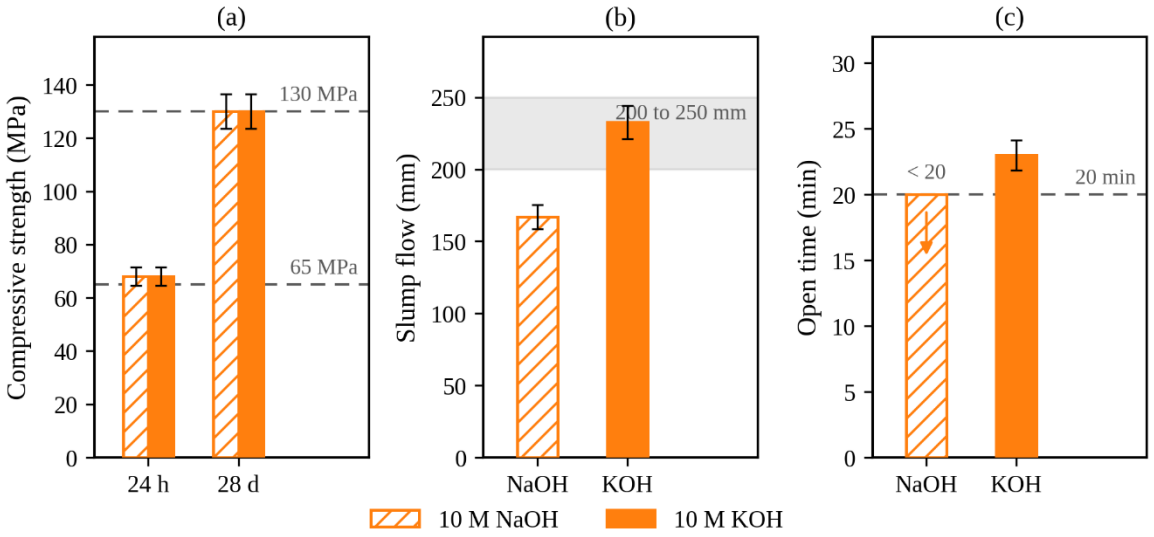

Figure 1-14: Effect of hydroxide cation on the G7.2SF1.8 binder at equal 10 M concentration. (a) Compressive strength at 24 hours and 28 days, (b) slump flow, (c) open time taken as the NF EN 196-3 final setting time.

The matrix-side results, shown in Figure 1-14 against the corresponding NaOH baseline for Stage 4, showed unchanged compressive strength alongside a markedly improved rheology.

The compressive strength was unchanged: the KOH mix reached 68 MPa at 24 hours and 130 MPa at 28 days, matching the 10 M NaOH baseline of Stage 4 to the nearest MPa at both ages. The two activation routes are therefore indistinguishable in compressive strength at the precision reported here. This is consistent with the hydroxide alkalinity, which is identical at 10 M in both systems, controlling slag dissolution and the resulting C-A-S-H scaffold. No strength-determining cation contribution is resolvable at this molarity.

The rheological properties, by contrast, improved dramatically. The slump flow rose from 167 mm with NaOH to 232.5 mm with KOH, an increase of 39% moving the formulation from below the 200 mm acceptance lower bound to the upper half of the 200 to 250 mm target band. The NF EN 196-3 final-setting time (the operational open time defined in Section 1.4.1) extended from below 20 minutes with NaOH to 23 minutes with KOH, meeting the 20-minute acceptance value for the first time in the optimization program.

The proposed mechanism, an interpretation drawn from the literature rather than isolated here since the water-to-binder ratio co-varies slightly with the cation, rests on the differences in ionic size (Na+: 1.02 Å, K+: 1.38 Å) and the resulting differences in ion-silicate binding strength. The smaller, higher-charge-density Na^+ cation forms stronger ion pairs with the dissolved silicate and aluminate species in the activator solution, accelerating early gel nucleation and producing a rapid viscosity build-up that shortens the open time and lowers the slump flow (Van Jaarsveld and Van Deventer, 1999; Phair and Van Deventer, 2001).

The larger K^+ cation binds water and silicate species less tightly, delays the onset of gel nucleation, and extends the open time at equal hydroxide concentration. K^+ is also a more effective structure-directing cation in the polycondensation step: it stabilizes larger silicate cages, including D4R units, producing a more ordered aluminosilicate network at later ages and partially compensating for the slower initial kinetics (Walkley et al., 2016).

The result is a binder that preserves the strength of the $NaOH^-$activated system at 28 days while resolving the rheological bottleneck at the fresh state. To the author's knowledge, this is the first direct Na^+ to K^+ comparison reported above 130 MPa in a UHPGC system. It extends the cation-effect observations from conventional geopolymers to the ultra-high-performance domain.

Stage 5 closed with all four matrix-side acceptance criteria satisfied simultaneously: 24-hour compressive strength of 68 MPa (target ≥ 65), 28-day compressive strength of 130 MPa (target ≥ 130), slump flow of 232.5 mm (target 200 to 250), and open time of 23 minutes (target ≥ 20). The bottleneck identified at this stage was no longer on the matrix side. The remaining acceptance criterion of the NATURSEA-PV envelope, the recycled fiber content ≥ 35 wt%, is a fiber-system criterion that was addressed in Stage 6 by introducing the recycled tire-derived steel fibers alongside the virgin Spajic baseline.

1.5.6 Stage 6: Fiber incorporation and recycled-blend selection

Stage 6 added steel fibers to the matrix-optimized GEO binder. The two design variables were the fiber composition (recycled Flexofibers versus virgin Spajic) and the total fiber dosage. The matrix composition was held at the Stage 5 final values (G7.2SF1.8 + 10 M KOH). Two total fiber dosages were tested, 10.4 and 12 wt% of binder mass, corresponding to 94 and 108 kg/m^3 (approximately 1.2 and 1.4 vol% of the total mix at a steel density of 7850 kg/m^3). At each dosage, four Flexo to Spajic mass blends were investigated: 100/0, 60/40, 50/50, and 0/100.

The 10.4 wt% series at four blend ratios is shown in Figure 1-15 (lower-dose bars). The 28-day compressive strength rose monotonically with the virgin-Spajic fraction: 129 MPa at 100% Flexo (recycled), 135 MPa at 60/40 Flexo/Spajic, 136 MPa at 50/50, and 145 MPa at 100% Spajic (virgin). The 28-day flexural strength differentiated the fiber types more strongly (Figure 1-16): 13.0 MPa at 100% Flexo, 17.0 MPa at 60/40, 19.0 MPa at 50/50, and 25.0 MPa at 100% Spajic. The compressive-strength response is dominated by the matrix and the fiber volume fraction, both held nearly constant across the four blends, with a secondary contribution from fiber confinement that scales with fiber tensile strength.

The flexural-strength response is dominated by fiber pull-out and bond, which depend strongly on fiber geometry, surface condition, and rubber-residue interference at the fiber-matrix interface. Recycled tire steel fibers carry rubber residue from the shredding process that weakens the bond with the surrounding gel (Centonze et al., 2012; Caggiano et al., 2015), and their geometry is irregular and length-distributed rather than uniform,

lowering the achievable bridging stress at a given fiber dosage (Aiello et al., 2009; Isa et al., 2020).

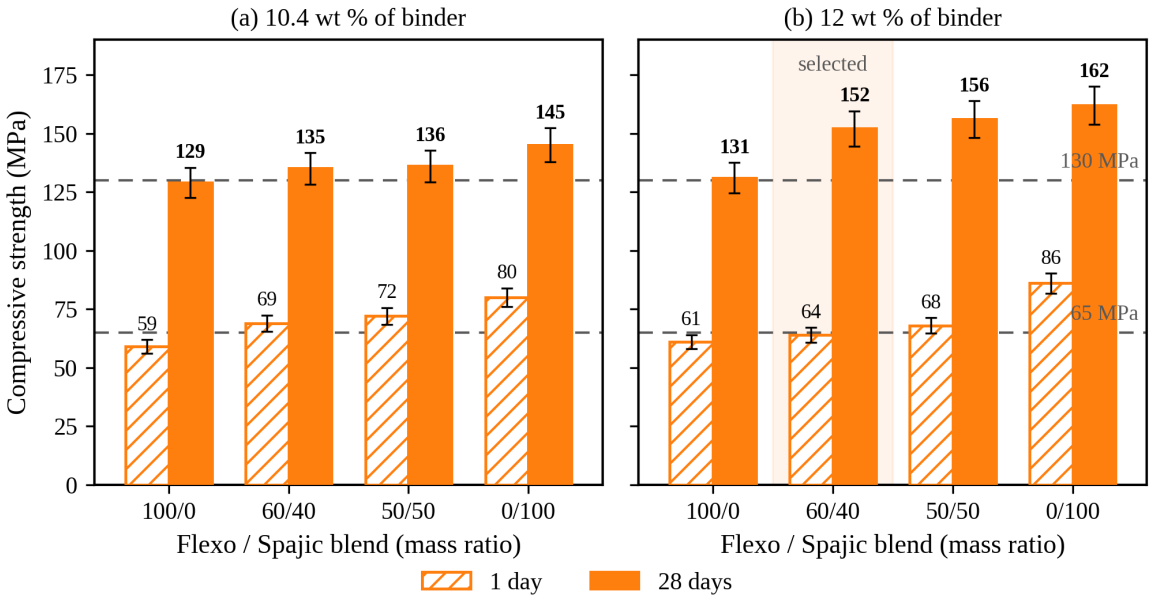

Figure 1-15: Compressive strength at 1 day and 28 days for the four Flexo to Spajic blends, at fiber contents of (a) 10.4 wt% and (b) 12 wt% of binder mass.

At the higher 12 wt% fiber content (108 kg/m^3, 1.4 vol%), the same blend-ratio hierarchy was preserved with all values systematically higher, reflecting the additional fiber-confinement contribution at the higher dosage. The 28-day compressive strength reached 131 MPa at 100% Flexo, 152 MPa at 60/40 Flexo/Spajic, 156 MPa at 50/50, and 162 MPa at 100% Spajic (Figure 1-15). The 28-day flexural strength at the same blends was 15 MPa, 17 MPa, 18 MPa, and 27 MPa respectively (Figure 1-16).

The flexural response remained bond-limited, with only the 100% Spajic mix showing a substantial dosage-driven gain (25 to 27 MPa) and the 60/40 blend unchanged at 17 MPa from the lower dosage. Slump flow declined with both fiber content and recycled-fiber proportion: at 12% the 60/40 blend reached 208 mm, the 100% Flexo mix dropped to 195 mm, and the 100% Spajic mix recorded 225 mm. The recycled-fiber effect on workability is attributed to rubber residue on the Flexofiber surfaces, which increases inter-fiber friction in the fresh paste (Isa et al., 2020). Of the four blends tested at 12 wt%, two are eliminated by the acceptance criteria.

The 0/100 Spajic mix, although the strongest of the series, contains no recycled fiber and fails the 35 wt% recycled-content criterion outright. The 100/0 Flexo mix satisfies that criterion most aggressively at 100 wt% recycled, but fails two others: its slump flow of 195 mm falls below the 200 mm rheological bound, and its 24-hour compressive strength of 61 MPa falls below the 65 MPa acceptance value.

The two intermediate blends, 60/40 and 50/50, satisfy all five criteria. The 50/50 blend performs marginally better mechanically, with 68 MPa at 24 hours and 156 MPa at 28 days on prism halves, compared to 64 MPa at 24 hours and 152 MPa at 28 days.

The 60/40 blend was nevertheless selected, because the 35 wt% recycled-content requirement is a floor rather than a target and the objective of the formulation program was to maximize the recycled fraction subject to the mechanical and rheological constraints. At 60 wt% recycled the selected blend contains 71% more recycled tire-derived fiber than the minimum specification while still meeting all acceptance values.

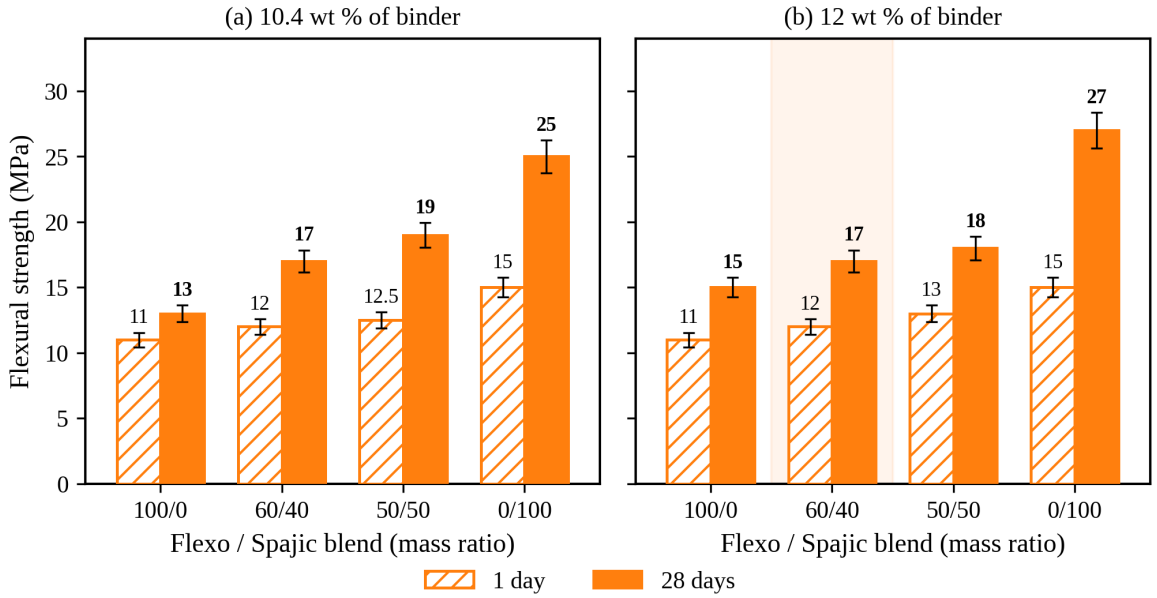

Figure 1-16: Flexural strength at 1 day and 28 days for the four Flexo to Spajic blends, at fiber contents of (a) 10.4 wt% and (b) 12 wt% of binder mass.

On the 10 × 10 × 10 cm^3 cube geometry (NF EN 12390-3), which is the basis on which the NATURSEA-PV envelope is expressed, the selected mix achieves a 24-hour compressive strength of 65 MPa and a 28-day compressive strength of 137 MPa, meeting the 65 MPa and 130 MPa acceptance values with margins of 0 and 5% respectively.

On the 4 × 4 × 16 cm^3 prism halves used throughout the optimization, the same mix gives 65 MPa at 24 hours and 152 MPa at 28 days, together with a 28-day flexural strength of 17.0 MPa (NF EN 196-1, three-point bending, span 100 mm). The prism value of 152 MPa is carried forward as the cross-test reference for the side-by-side characterization of REF and GEO in Section 1.5.7 and for the durability, electrochemical, and acoustic-emission studies of Chapters 2 to 4, where both mixes are tested at the same EN 196-1 geometry.

The two compressive values describe the same mix at the same age. The 11% excess of the prism-half result over the cube result at 28 days is the expected direction and magnitude of the specimen-geometry effect in UHPC: the smaller loaded volume of the prism half contains fewer critical flaws, and its 40 mm loaded face is more strongly confined

by the testing platens than the 100 mm face of the cube, both of which raise the apparent strength (Graybeal and Davis, 2008; Kusumawardaningsih et al., 2015).

After 24 hours, the two geometries returned the same value, 65 MPa. The size effect scales with the brittleness of the material and is therefore weaker at 65 MPa than at 150 MPa, and it is further offset at that age by the greater heat retention of the cube, which presents 0.060 mm-1 of surface per unit volume against 0.113 mm-1 for the prism and is consequently marginally further advanced in reaction (Section 1.5.7). The difference between the two geometries at 24 hours is in any case smaller than the measurement scatter.

The 24-hour criterion is therefore satisfied without margin on either geometry, and the early-age performance of the selected mix should be regarded as meeting the acceptance value rather than exceeding it.

Slump flow at 208 mm and an NF EN 196-3 final-setting open time of 23 minutes complete the acceptance set. The 60/40 blend at 12 wt% binder mass is therefore the operating point that satisfies all five NATURSEA-PV acceptance criteria while maximizing recycled fiber content.

Stage 6 closed the optimization. The final GEO mix proportions are reported in Table 1-4, and the matrix-and-fiber system characterized in Section 1.5.7 alongside the Portland-cement reference REF. The six stages presented in Figures 1-9 through 1-15 trace the resulting trajectory from a fly-ash-rich, sodium-silicate-dominated alkali-activated binder of 70 MPa compressive strength through six bottleneck-driven decisions to a binary GGBS + SF, KOH^-activated, recycled-fiber-bearing UHPGC of 137 MPa cube and 152 MPa prism-half compressive strength, 17.0 MPa flexural strength, 208 mm slump flow, 23-minute open time, and 60 wt% recycled fiber content. Each transition resolves one bottleneck and inherits the others. The final mix is the intersection of all five NATURSEA-PV acceptance constraints.

The Portland-cement reference REF, cast and cured under identical ambient conditions (20 ± 2 °C, 50 ± 5% RH) at the same steel-fiber dosage of 108 kg/m^3 and tested on the same 4 × 4 × 16 cm^3 prism geometry per NF EN 196-1, reached a 28-day compressive strength of 165 ± 4 MPa, against 152 ± 5 MPa for the selected GEO mix on the matched geometry. The 24-hour compressive strength was 76 ± 6 MPa for REF and 65 ± 4 MPa for GEO. The complete strength-development curves from 1 to 28 days are shown in Figure 1-17. GEO exhibited an early-age strength deficit at 24 hours (86% of REF) that narrowed progressively over the curing window, reaching 92% of REF at 28 days. Both binders crossed the NATURSEA-PV 28-day acceptance threshold of 130 MPa: REF at 7 days, GEO at 14 days. The microstructural origin of this convergence pattern, and of the residual 8% strength gap at 28 days, is the subject of Section 1.5.7.

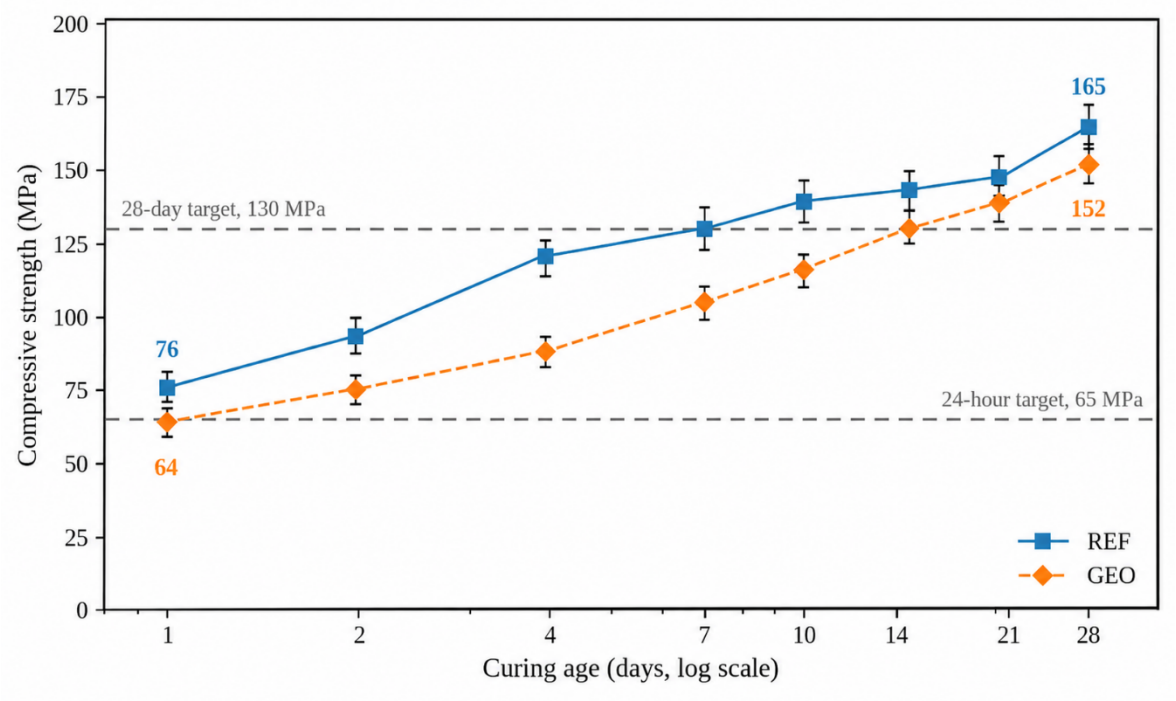

Figure 1-17: Compressive strength development of REF and GEO from 1 to 28 days on 4 × 4 × 16 cm^3 prism halves per NF EN 196-1, ambient curing (20 ± 2 °C, 50 ± 5% RH).

1.5.7 Characterization of the optimized GEO

This section reports the multi-technique characterization of the optimized GEO mix at the 28-day benchmark, compared with the Portland-cement reference REF on companion specimens cast from the same batches and cured under identical ambient conditions (20 ± 2 °C, 50 ± 5% RH). The six techniques converge on a single mechanistic picture: the 8% prism-basis strength gap and the 22-fold gap in mean apparent gas permeability between GEO and REF share a common microstructural origin in the absence of an induction period during the geopolymerization reaction, which locks GEO into a coarse capillary pore network at 700 nm before the slow refinement processes of Portland systems can take place. The gel chemistry of GEO partly offsets this coarser pore structure, GEO retaining 92% of the REF compressive strength despite a 72% higher gravimetric porosity. Methodology details for each technique are reported in Section 1.4.

1.5.7.1 Semi-adiabatic calorimetry

GEO and REF exhibited fundamentally different reaction kinetics over the first 48 hours after mixing. The temperature evolution and its time derivative are reported in Figure 1-18. REF followed the classical multi-stage Portland-cement hydration: the specimen remained below 30 °C for the first 24.7 hours, a dormant period during which the anhydrous phases dissolved slowly through a passivating C-S-H layer, before rising at up to 3.9 K/h to a maximum of 57.5 °C at 38.2 hours, driven by the C_3S hydration of the alite phase identified in the XRD analysis below. GEO, by contrast, showed no discernible induction period. Its

temperature was already elevated at 31.8 °C at the start of acquisition, against 24.9 °C for REF, indicating that the reaction had begun during mixing itself. It then rose at up to 14.9 K/h to a maximum of 63.2 °C within 5.6 hours, reaching its exotherm nearly 7 times sooner than REF.

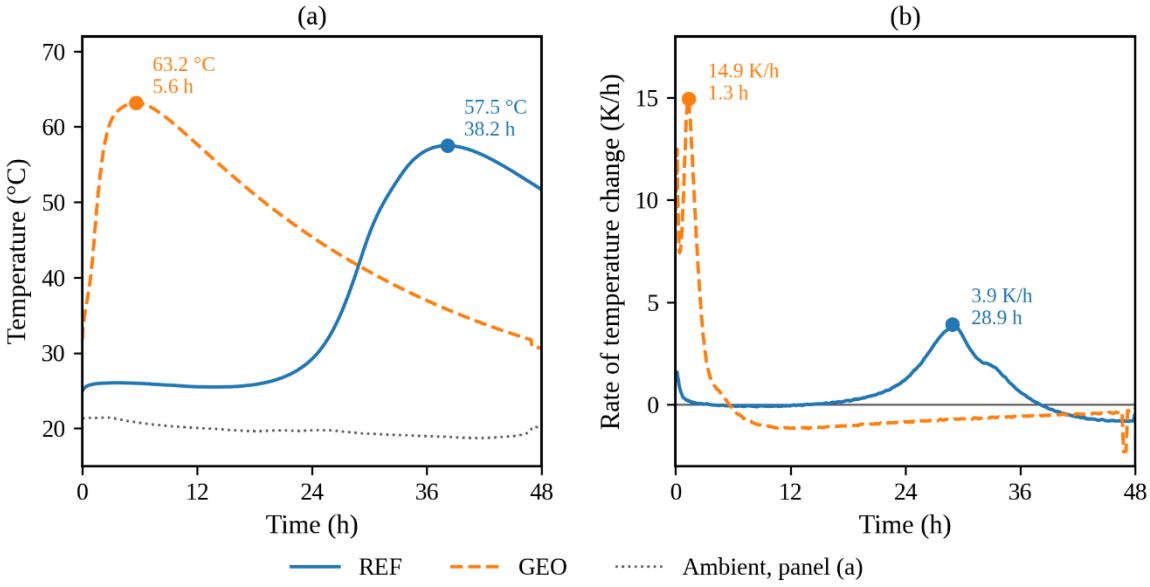

Figure 1-18: Semi-adiabatic temperature evolution of GEO and REF over 48 hours. Single-specimen measurements per mix. The peak-temperature reproducibility was estimated at ± 2 °C from calorimeter calibration runs.

The magnitude of the thermal response was comparable in the two binders, but its temporal distribution was not. Measured above their respective initial states, the temperature excursions were 32.0 K for GEO and 35.1 K for REF, so the two mixes differ in the rate at which heat is released rather than in the temperature rise attained. GEO completed 90% of its excursion within 3.0 hours, whereas REF required 33.6 hours to reach the same fraction. At the end of the 48-hour window GEO had returned to its initial thermal state, 10.4 K above ambient, while REF remained 31.4 K above ambient, indicating that the REF reaction was still in progress when acquisition stopped and that its total heat release is therefore not captured within the measurement window

This behavior is characteristic of alkali-activated slag systems, where the high alkalinity of the KOH activator at 10 M (pH above 14) causes immediate dissolution of the slag glass network through the rupture of Si-O-Si and Al-O-Si bonds by hydroxide ions (Wang et al., 1994; Shi and Day, 1995; Provis and Deventer, 2014), with water participating both as a transport medium and, through incorporation into the C-(N,K)-A-S-H gel, as a structural component of the reaction product. The absence of an induction period is consistent with quasi-instantaneous nucleation, in which the dissolved Ca, Si, and Al species precipitate without the inhibitory passivation that characterizes Portland-cement hydration. The semi-adiabatic configuration does not resolve the initial dissolution peak of either

binder, nor a distinct polycondensation shoulder in GEO. Resolving those features would require isothermal calorimetry.

These calorimetric data explain the rheology observed in Section 1.5.5. The absence of a dormant period limits the GEO open time to 23 min, against the longer window characteristic of polycarboxylate-stabilized Portland UHPC. The K^+ cation moderates the initial dissolution rate relative to Na^+ (Section 1.5.5), which is why KOH extends the open time without reducing the 28-day strength: the substitution redistributes the reaction in time rather than altering its extent, and the 28-day mechanical performance, which depends on the gel formed over the full curing period rather than on the rate of its early formation, is unaffected.

1.5.7.2 Water-accessible porosity

The GEO porosity sat within the 6 to 12% range reported for UHPGC, while REF at 4.80% fell below the 6 to 9% range quoted for ambient-cured UHPC (Wille et al., 2011), consistent with the dense particle packing achieved by the polycarboxylate superplasticizer in the reference premix. Wang et al. (2025) reported 7.4% for an ambient-cured UHPGC at w/b = 0.22. The present GEO value of 8.25% is 11% higher, consistent with the slightly higher water-to-binder ratio of the formulation developed here.

Table 1-8: Water-accessible porosity of GEO and REF at 28 days measured per NF P18-459 on 4 × 4 × 4 cm^3 cubes.

Property	Unit	REF	GEO
m_{sat} (saturated mass in air)	g	150.14	149.89
m_{hyd} (hydrostatic mass)	g	89.00	83.12
m_{dry} (oven-dried mass)	g	147.18	144.47
Water porosity P_w	%	**4.80 ± 0.18**	**8.25 ± 0.32**
Bulk dry density	kg/m^3	2403 ± 12	2164 ± 14

The 10% bulk-density gap between the two mixes can be decomposed into a porosity contribution and a particle-density contribution. The dry solid density (excluding pores), $\rho_{solid} = \rho_{bulk} / (1 - P_w)$, is 2524 kg/m^3 for REF and 2359 kg/m^3 for GEO, so the GEO binder solid is 6.5% less dense than the REF binder solid at zero porosity. Of the total 239 kg/m^3 bulk-density gap between the two mixes, approximately 87 kg/m^3 (3.6 percentage points of REF density) is attributable to the higher GEO porosity and 152 kg/m^3 (6.4 percentage points) to the lower particle density of the geopolymer binder. The particle-density contribution dominates and reflects the lower mean atomic mass of the C-(N,K)-A-S-H gel relative to the C-S-H plus portlandite assemblage of REF, which retains a denser residual anhydrous fraction: unhydrated clinker at 3100 to 3200 kg/m^3 in REF against unreacted GGBS at 2750 to 2900 kg/m^3 in GEO.

Three factors explain the higher GEO porosity:

- First, no effective superplasticizer is available for the GEO mix: polycarboxylate-ether admixtures, standard in Portland UHPC, degrade in the high-alkalinity activator solution (pore-solution pH above 13) through hydrolysis of the carboxylate side chains (Plank et al., 2015), removing the steric stabilization that produces the water-reducing effect. The GEO workability target is therefore reached through the KOH activator chemistry alone (Section 1.5.5, Stage 5), without the dense particle packing that a superplasticizer enables in REF.

Second, the rapid setting documented above by calorimetry traps air that would otherwise escape during an OPC-style induction period.

Third, polycondensation likely releases water as a by-product (Si-OH + HO-Si → Si-O-Si + H_2O), which may create additional capillary voids. In contrast, the balance in OPC hydration is net consumption of water.

The first two factors are documented mechanisms. The third is hypothesized and would require complementary nuclear magnetic resonance imaging or thermogravimetric analysis to quantify directly.

The GEO bulk dry density of 2164 kg/m^3 sat just below the lower end of the published range for ambient-cured slag-based UHPGC, typically 2200 to 2350 kg/m^3 (Wang et al., 2025). The 10% gap against REF is mechanistically expected for a fully KOH^- activated, calcium-substituted aluminosilicate binder: as decomposed above, two thirds of the gap come from the lower density of the GEO solid phase, dominated by the difference between residual GGBS and residual clinker, and one third from the higher accessible porosity.

For the NATURSEA-PV application, the lower density is an advantage: with GEO meeting the 130 MPa structural target with a 5% margin on the cube basis on which the criterion is defined (Section 1.5.6), the 10% bulk-density reduction translates directly into a lighter floating substructure and a smaller ballast mass for stability.

Despite the 72% higher gravimetric porosity, GEO still reached 92% of the REF compressive strength at 28 days (152 ± 5 against 165 ± 4 MPa on 4 × 4 × 16 cm^3 prism halves, Section 1.5.7). This decoupling between total porosity and mechanical performance indicates a different pore morphology, with voids that increase gravimetric porosity without forming a connected pore network capable of propagating microcracks under load. Wang et al. (2025) reported a similar finding on directly comparable UHPGC and UHPC systems. The mercury-intrusion data presented below support this interpretation by resolving the pore-size distribution of the two materials at radically different length scales while accommodating comparable intruded volumes in the jointly resolved 6 to 700 nm range.

1.5.7.3 Nitrogen gas permeability

The mean apparent nitrogen gas permeability of GEO at 28 days was $K_{a,mean}$ = 4.96 × 10^{-16} m^2 compared with 2.22 × 10^{-17} m^2 for REF, a 22-fold ratio. Apparent permeabilities measured at six differential pressures between 12.8 and 59.6 kPa ranged from 3.82 to 6.01 × 10^{-16} m^2 for GEO and 2.18 to 2.26 × 10^{-17} m^2 for REF. Neither series followed the Klinkenberg dependence over the accessible pressure range: the model requires a positive slope of K_a against 1/Pm, and both fitted slopes were negative.

The accessible mean pressure spanned only 107 to 131 kPa, a factor of 1.22, so extrapolating to 1/Pm = 0 extends 4.6 times beyond the measured interval. The pressure range was therefore too narrow to resolve a slip coefficient reliably in either material. For GEO the trend was strong and systematic (r^2 = 0.98). For REF it was not resolvable (r^2 = 0.21, with a spread of 3.6% about the mean). No intrinsic permeability was therefore extracted for either mix, and both values are reported as mean apparent permeabilities over the six pressure steps.

Apparent permeability against inverse mean pressure is plotted for both mixes in Figure 1-19. Each value is from a single specimen, with a second specimen per mix used as a reproducibility check, which agrees within 6% at each pressure point.

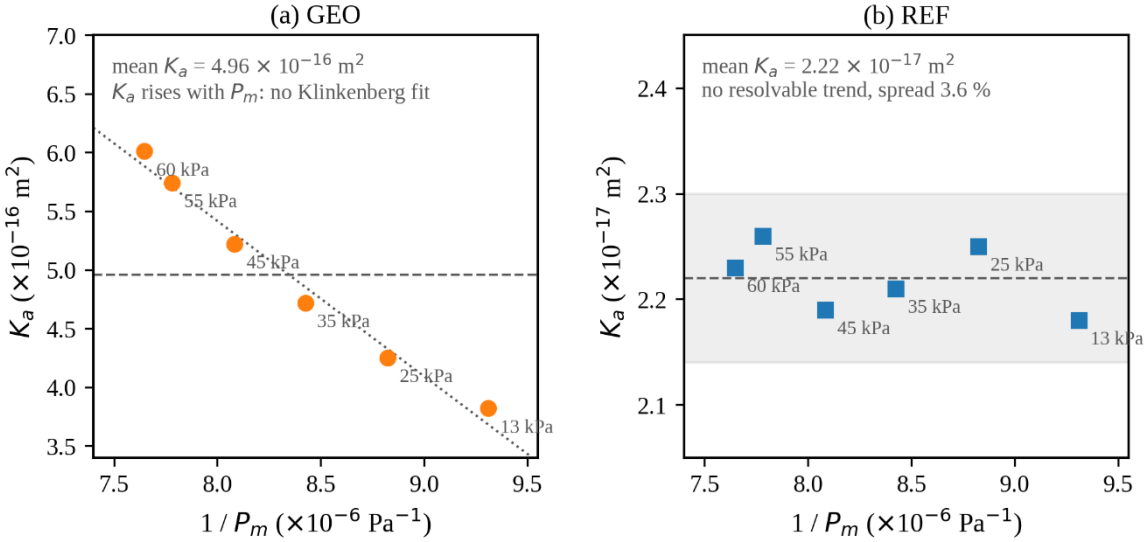

Figure 1-19: Apparent nitrogen permeability Ka against inverse mean pressure at 28 days. (a) GEO, (b) REF.

GEO fell within the 10^{-16} to 10^{-15} m^2 range reported for alkali-activated systems (Wang et al., 2020) and agreed with (Wang et al., 2025), who reported 3.1 to 5.8 × 10^{-16} m^2 for ambient-cured UHPGC. REF at 2.22 × 10^{-17} m^2 sat slightly above the 10^{-18} to 10^{-17} m^2 range quoted for Portland UHPC (Fehling et al., 2014).

The permeability ratio of 22 was greater than the porosity ratio of 1.72. For identical pore geometry (that is, identical tortuosity τ and pore-wall specific surface S), the Kozeny-Carman equation predicts the permeability ratio to scale as the cube of the porosity ratio, giving $(0.0825 / 0.0480)^3 \approx 5.1$. The experimentally measured permeability ratio was approximately 22, roughly 4 times the Kozeny-Carman prediction. The conclusion is not

sensitive to the upper-bound caveat discussed below: taking the lowest measured GEO value rather than the mean still leaves an excess of a factor of three. This fourfold gap indicates that the two materials cannot share the same pore geometry: the excess GEO permeability must arise from a lower tortuosity and/or a coarser characteristic pore size, a hypothesis examined directly by the mercury-intrusion data presented in the next subsection.

The two materials showed distinct pressure dependences (Figure 1-19). GEO showed a spread of 44% about the mean, rising monotonically from 3.82 to 6.01 × 10^{-16} m^2 as mean pressure increased, whereas REF varied by only 3.6%. The sweep also confirms that the measurements lie in the laminar regime, since inertial departure would produce a decrease in apparent permeability with increasing flow rate, which was not observed in either mix.

Two factors are consistent with this behavior:

First, slip is expected to be weak in GEO: the nitrogen mean free path near atmospheric pressure is of the order of 65 nm, an order of magnitude below the 700 nm dominant pore-entry diameter measured by mercury intrusion, so the slip contribution should be small in a pore network this coarse.

Second, the lateral confinement of 2.5 bar leaves an effective confining stress that decreases as the upstream pressure rises across the series, which can promote progressive gas bypass at the specimen-sleeve interface in a specimen of markedly higher permeability. The GEO value is therefore treated as an upper bound.

Drying at 60 °C, while standard for nitrogen permeability measurement, is known to coarsen the gel-pore network of alkali-activated materials by removing structural water from the C-(N,K)-A-S-H interlayer; the GEO values reported here therefore correspond to a fully dried, upper-bound state of the transport network rather than the in-service moisture condition. The 22-fold higher mean apparent gas permeability of GEO relative to REF is the principal durability-relevant signal in the present microstructural dataset and must be flagged before any structural-deployment claim, but gas permeability alone is only a partial proxy for service durability:

- The value represents an upper-bound transport state.
- It does not by itself predict the service-relevant ingress modes (chloride and sulfate diffusion in saturated conditions, carbonation in unsaturated conditions), each of which interacts differently with the C-(N,K)-A-S-H gel chemistry (Wang et al., 2020).
- The KOH pore solution maintains pH above 13, favorable for steel-fiber passivation, but raises the question of carbonation buffering in the absence of portlandite.

The microstructural results of the present chapter are therefore explicitly framed as material-characterization findings rather than as a structural-durability assessment. A

dedicated durability evaluation of the optimized GEO formulation under chloride migration, sulfate exposure, seawater immersion, and elevated-temperature exposure is reported in Chapter 4.

1.5.7.4 Mercury intrusion porosimetry

Pore sizes are classified throughout this work as gel pores below 10 nm, fine capillaries from 10 to 100 nm, coarse capillaries from 0.1 to 1 µm, and macro-pores above 1 µm. The classification refers to pore-entry diameters as resolved by mercury intrusion and is applied identically to both mixes.

GEO exhibited a dominant pore-size peak at 700 nm with 78.4% of the resolved intruded volume in the coarse capillary range of 0.1 to 1 µm, together with a secondary maximum at 13 nm accounting for the 20.6% held between 10 and 100 nm (Figure 1-20 and Figure 1-21). REF showed its highest resolved dV/d(log D) at 6.2 nm, with the remaining volume distributed across gel pores below 10 nm (18.1%), fine capillaries between 10 and 100 nm (35.4%), coarse capillaries between 0.1 and 1 µm (10.6%), and macro-pores above 1 µm (35.1%). Both maxima lie at a limit of their respective measurement windows and are therefore lower bounds: the GEO peak at 700 nm against a coarse limit of 712 nm, and the REF peak at 6.2 nm against a fine limit of 6.2 nm. The contrast in dominant pore size is nevertheless 100-fold. Total intruded volumes within the jointly resolved 6 to 712 nm range were comparable, 14.18 against 13.87 mm^3/g. The full curves are reported in Figures 1-19 and 1-20 and the numerical summary in Table 1-9.

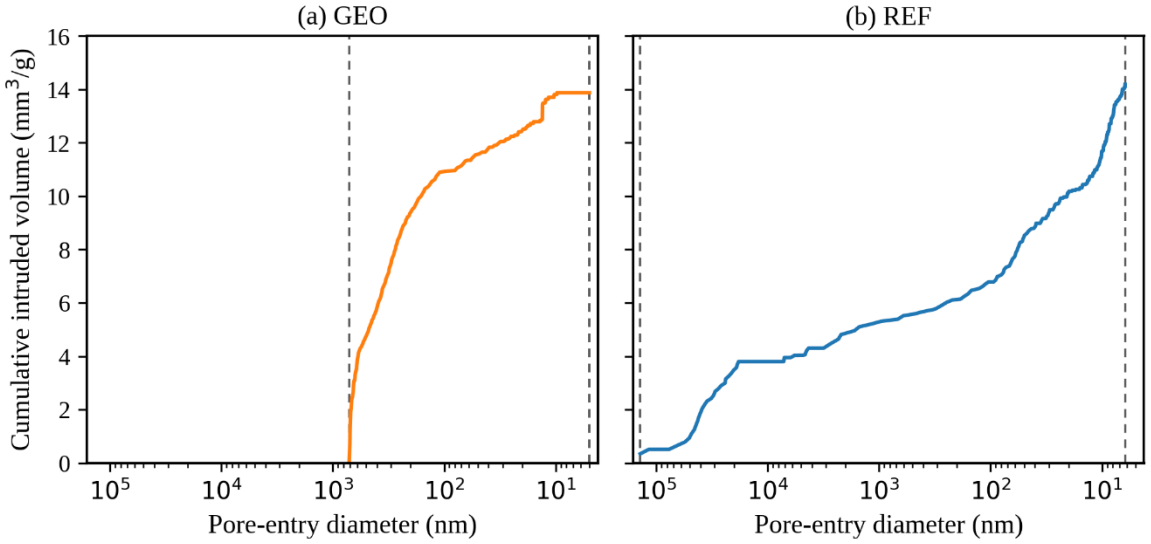

Figure 1-20: Mercury intrusion porosimetry at 28 days, cumulative intruded volume against pore-entry diameter for (a) GEO and (b) REF.

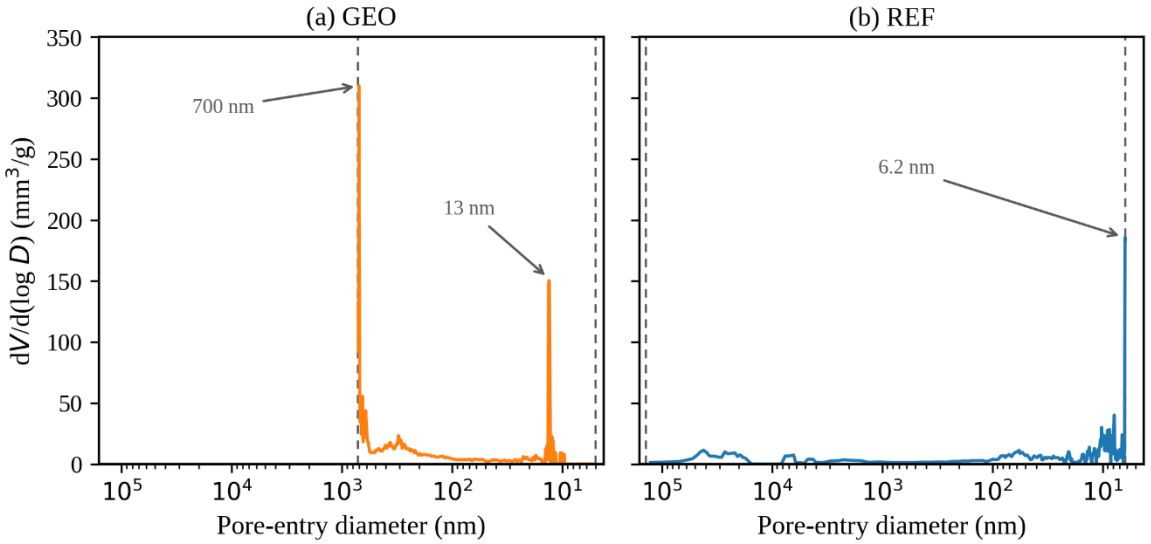

Figure 1-21: Mercury intrusion porosimetry at 28 days, differential distribution dV/d(log D) for (a) GEO and (b) REF, smoothed over five points.

Table 1-9: Mercury intrusion porosimetry results at 28 days for GEO and REF.

Property	Unit	REF	GEO
Measurement range	MPa	0.009 to 201	1.75 to 251
Total intruded volume	mm^3/g	14.18	13.87
Critical pore / dominant peak	nm	6.3	700
Gel pores (< 10 nm)	%	18.1	0.5
Fine capillary (10 to 100 nm)	%	35.4	20.6
Coarse capillary (0.1 to 1 µm)	%	10.6	78.4

The coarse, bimodal GEO pore network, with a dominant peak at 700 nm and a secondary maximum at 13 nm, is the microstructural signature of the rapid gelation identified by the calorimetry above: the absence of an induction period locks the capillary network into a coarse configuration before the pore-refinement processes of Portland systems can operate, as also reported by Bernal et al. (2013) for ambient-cured alkali-activated slag. The REF distribution is characteristic of a mature C-S-H gel in which prolonged hydration has shifted the dominant pore population toward nanometric dimensions (SAVIC.).

Mercury intrusion resolves only part of the pore space in either mix, and a larger part in GEO. The intruded volumes correspond to 3.00% porosity for GEO and 3.41% for REF at their respective bulk densities, against water-accessible porosities of 8.25% and 4.80%. Two thirds of the GEO porosity therefore lies outside the resolved window, against under a third for REF, the GEO shortfall sitting principally above 712 nm where the low-pressure stage did not reach. The comparison between the two mixes is accordingly confined to the jointly

resolved 6 to 712 nm band, within which the intruded volumes are similar, 13.87 against 14.18 mm^3/g; any unresolved GEO macro-porosity would add to the GEO value alone.

This contrast explains why GEO is 22 times more permeable to nitrogen while being only 1.72 times more porous, a ratio some four times the Kozeny-Carman porosity-only prediction of approximately 5. Transport is governed by the connected pathway rather than by total porosity, and the two materials differ in which population provides it. The macro-pores above 1 µm in REF cannot: treated as a connected network under the tortuosity that reproduces the GEO permeability, they would predict 3 to 6 × 10^{-16} m^2, fifteen to twenty-five times the measured value, so they must be isolated, consistent with entrapped air voids. The same treatment applied to the 0.1 to 1 µm band reproduces the measured permeability of both mixes at a pore diameter near 700 nm. Transport is therefore carried by pores of comparable size in each material and differs mainly in the volume available, 0.36% of the specimen in REF against 2.35% in GEO.

The MIP-accessible gel-pore fraction of GEO, 0.5%, is two orders of magnitude below the 18.1% of REF. Two readings are consistent with this: the C-(N,K)-A-S-H gel pores may lie below the 5 nm resolved at maximum intrusion pressure, or the gel may be more densified at the gel scale than the REF C-S-H. Bernal et al. (2013) report C-A-S-H gel pores typically below 3 nm by small-angle scattering, and Puertas et al. (2011) report higher cross-linking in alkali-activated slag than in C-S-H, so the first reading carries the greater weight with a possible minor contribution from the second. The picture is consistent with the fiber-matrix adhesion reported by SEM below: a dense gel skeleton coexisting with a coarse inter-particle void network.

1.5.7.5 X-ray diffraction with Rietveld refinement

The crystalline assemblages of GEO and REF at 28 days differ in two respects. REF contains quartz (SiO_2, ICDD 01-086-1629) from the aggregate and residual unhydrated alite (Ca3SiO5, ICDD 00-042-0551), with the C-S-H gel raising the baseline between 25 and 35° 2θ without producing peaks. GEO contains quartz, calcite and ettringite over a broad amorphous hump centered near 29° 2θ that corresponds to the C-(N,K)-A-S-H gel. Portlandite was detected in neither: in REF its diagnostic (001) reflection at 18.0° reaches only 28% of the intensity the 34.1° feature would require, so that feature is attributed to alite, and the absence is consistent with the silica fume content of the reference premix, at which near-complete pozzolanic consumption by 28 days is expected.

The diffraction patterns are reported in Figure 1-22, and the Rietveld-quantified GEO phase composition in Table 1-10.

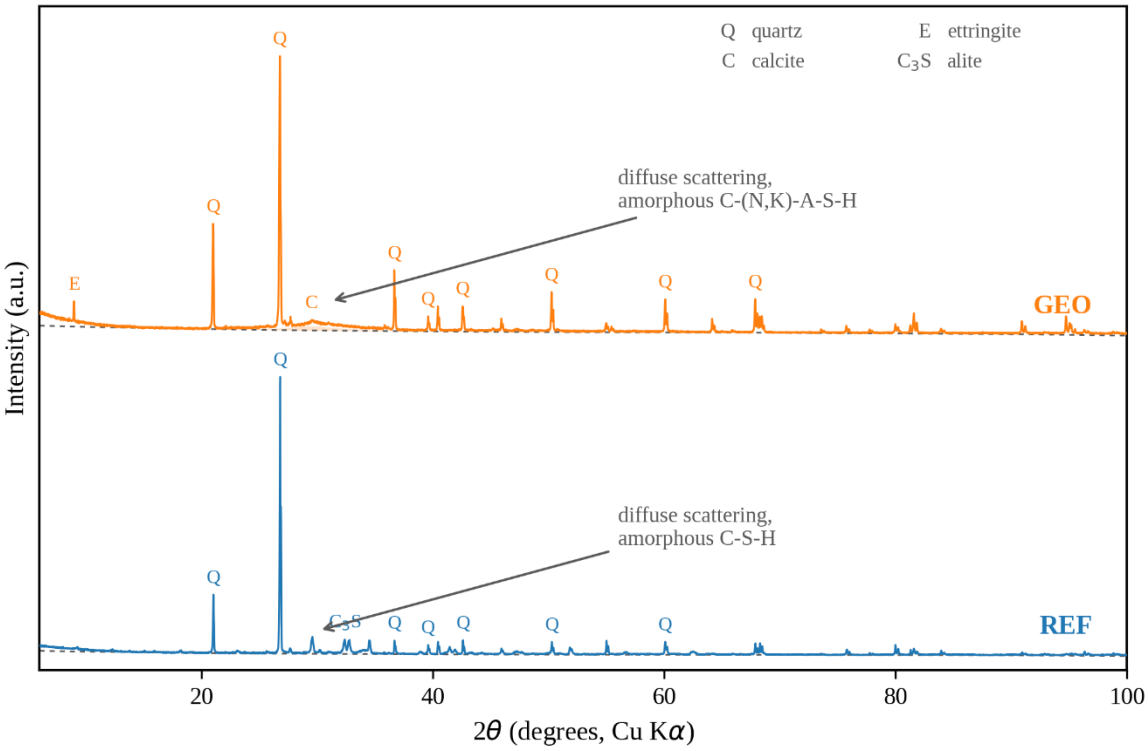

Figure 1-22: X-ray diffraction patterns at 28 days for GEO and REF, offset vertically.

Table 1-10: Quantitative phase analysis of the hardened GEO at 28 days.

Phase	ICDD code	Weight fraction (%)
Quartz (SiO_2)	01-086-1629	48.5 ± 4.0
Calcite ($CaCO_3$)	00-005-0586	7.1 ± 0.6
Zeolite (tentative, K-faujasite)	00-039-0219 (Na-form)	3.7 ± 0.9
Ettringite	00-016-0695	1.1 ± 0.4
Amorphous total (gel plus unreacted glass)	–	39.5 ± 4.0

The refinement returned Rwp = 21.3%, above the sub-10% target of fully crystalline systems but within the 18 to 25% range reported by Bernal et al. (2013) for alkali-activated slag, where a broad unfittable scattering background constrains the achievable fit. They discuss the same difficulty and the role of an internal standard in recovering the amorphous fraction. The recovered quartz fraction of 48.5 wt% falls inside the 42 to 50 wt% implied by the design aggregate content and the sieving bracket. Since the aggregate anchors the mass balance, this is a sampling check rather than an independent validation of the quantification.

Calcite at 7.1 wt% holds 30% of the calcium in the mix and is attributed to carbonation of the gel over the 28-day cure at 50 ± 5% RH in air, with no portlandite reserve available in either binder to buffer the pore solution. Ettringite at 1.1 wt% requires more sulfate than the 0.03 wt% SO_3 declared for the GGBS, which would predict only 0.04 wt%. The discrepancy is consistent with the sulfide fraction of the slag, which blast-furnace conditions

favor and which NF EN 15167-1 limits separately from SO3; commercial GGBS carries 0.5 to 1.5 wt% S_2^-, whose progressive oxidation would supply the shortfall. Verification against the S2- line of the supplier conformity certificate is flagged.

Two phases expected in such a system were sought and not found. A faujasite-type zeolite was initially fitted at 3.7 wt%, but its diagnostic (111) reflection near 6.2° reaches a signal-to-noise ratio of 4.9 against 38.5 for the ettringite main line at 1.1 wt%, and the REF pattern shows a stronger feature at the same position; the phase is therefore not reported and its intensity is retained in the amorphous fraction. Hydrotalcite, the usual magnesium sink in alkali-activated slag, would represent approximately 8.7 wt% if it took up all the 2.1 wt% MgO supplied by the GGBS, and no reflection of that intensity is present. Both absences are consistent with the chemistry: calcium competes for the aluminosilicate to form C-A-S-H, and the magnesium is taken to be incorporated in the gel.

The amorphous fraction is approximately 40 wt% of the whole sample, or 77 wt% of the non-aggregate mass. This is an upper bound on the gel content, since diffraction cannot separate the gel from unreacted GGBS and silica fume: at a slag reaction degree of 50 to 60%, typical at 28 days, unreacted glass would account for roughly a third of it, and selective dissolution or 29Si MAS NMR would be required to resolve the two. With that caveat the value sits within the 60 to 80 wt% range reported for mature alkali-activated slag systems (Bernal et al., 2013; Myers et al., 2013).

Neither binder carries a portlandite reserve at 28 days: none forms in GEO, and in REF it has been consumed pozzolanically. Pore-solution alkalinity therefore rests on the alkalis and the C-S-H in REF, and on the residual KOH and sodium silicate in GEO, a mixed potassium-sodium reservoir in a molar ratio of approximately 1.4 to 1. Neither is buffered as a portlandite reserve would be, so the carbonation resistance of both materials depends on the gel chemistry. This is examined under controlled exposure in Chapter 4.

1.5.7.6 SEM and bulk EDS

The fiber-matrix interface of GEO at 28 days showed a cohesive-failure morphology, with a substantial layer of adhering matrix along the fiber and fractured gel fragments bridging the fiber-matrix contact (Figure 1-23a). The fracture preferentially propagated through the matrix rather than along the interface, indicating strong adhesion between the C-(N,K)-A-S-H gel and the uncoated steel surface. REF, in contrast, showed an adhesive-failure pull-out signature: a clean, striated pull-out void with the matrix peeled back as a distinct fracture plane, with the interfacial transition zone acting as the preferred crack path (Figure 1-23b). The micrographs shown are representative of three companion specimens examined per mix. The cohesive-vs-adhesive signature was consistent across all three pairs and is consistent with the flexural results of Section 1.5.6 (Stage 6), where the matrix-bond mechanism dominates the energy-dissipation budget.

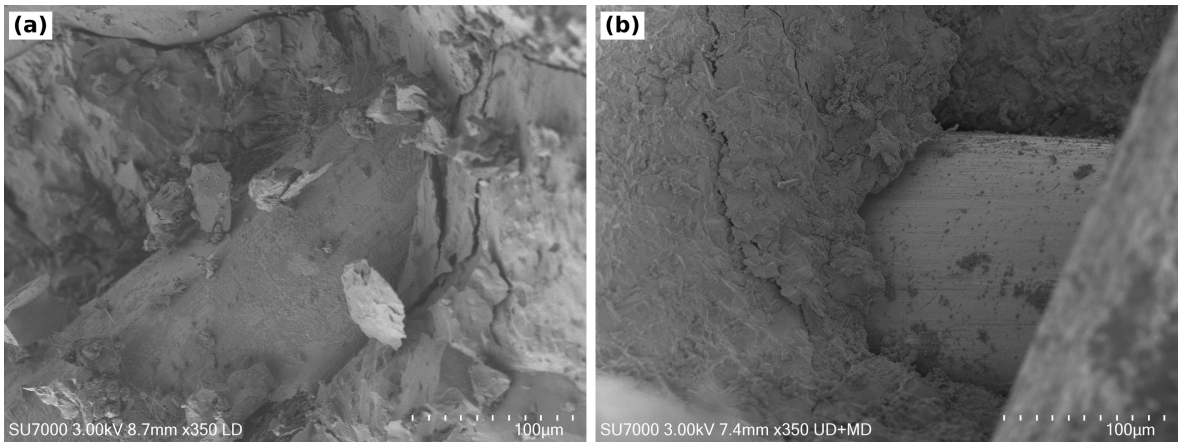

Figure 1-23: SEM fracture-surface micrographs at 28 days and 350× magnification of (a) the GEO mix and (b) the REF mix.

Table 1-11: Bulk elemental composition of the GEO and REF matrices measured by map-integrated EDS on fiber-free polished regions at 28 days.

Element	REF (wt%)	GEO (wt%)
Calcium (Ca)	23.8	8.1
Silicon (Si)	13.1	23.4
Aluminum (Al)	1.3	5.8
Potassium (K)	0.6	7.3
Sodium (Na)	0.5	3.5

Note: Acquired at 15 kV, mean of three map regions per specimen. The five elements shown are those that differentiate the two binders; oxygen and minor constituents are omitted. Values integrate gel and residual unhydrated grains over the analyzed area and are therefore qualitative at the phase level.

The bulk EDS composition (Table 1-11) documents the activator signature and the calcium inversion between the two binders. GEO contained 7.3 wt% K and 3.5 wt% Na against 0.6 and 0.5 wt% in REF, reflecting residual KOH and sodium silicate from the activator together with sodium silicate-derived Na retained in the pore solution and bound in the gel framework. Aluminum was 4.5 times higher in GEO than in REF (5.8 against 1.3 wt%), and silicon was roughly 1.8 times higher (23.4 against 13.1 wt%), consistent with the incorporation of both elements into the C-(N,K)-A-S-H network. Calcium was almost 3 times higher in REF (23.8 against 8.1 wt%), consistent with C-S-H as the dominant binder in a Portland system. Expressed as molar ratios (the conventional EDS reporting basis), the bulk Ca/Si ratio was 1.27 for REF and 0.24 for GEO. The bulk Al/Si ratio was 0.10 for REF and 0.26 for GEO.

Point-EDS measurements on gel-clean polished regions, selected by BSE contrast to exclude residual GGBS or CEM I grains (n = 2 spots per mix), directly characterized the gel phase. The REF gel returned a mean Ca/Si molar ratio of 1.72 (individual spots 1.27 and

2.17) and an Al/Si of 0.10, with K and Na below the detection limit. This is the signature of a high-calcium C-S-H gel typical of mature Portland UHPC. The GEO gel returned a mean Ca/Si of 0.39 (spots 0.24 and 0.54), an Al/Si of 0.21, and K/Si and Na/Si of approximately 0.20 each. With two gel-clean spots per mix, the individual ratios carry substantial scatter, and the values are therefore treated as indicative rather than quantitative. The contrast between the two binders is nonetheless unambiguous, since the two ranges do not overlap. The GEO value lies below the 0.7 to 1.5 range typical of C-A-S-H in $NaOH^-$activated slag (Walkley et al., 2016), and above the low-calcium N-A-S-H domain, placing the gel in the coexistence region of the ternary compatibility diagram of Garcia-Lodeiro et al. (2011). The presence of both K (from KOH) and Na (from sodium silicate) at comparable molar fractions in the gel framework, with K/Si ≈ Na/Si ≈ 0.20, justifies the C-(N,K)-A-S-H notation used throughout this chapter rather than the simpler C-(K)-A-S-H that would apply to a KOH^- only activator. The Al/Si gel ratio of 0.21 fell within the 0.20 to 0.30 range reported by Myers et al. (2013) and Puertas et al. (2011) for tetrahedral-Al substitution in C-A-S-H, confirming framework substitution rather than interlayer-cation behavior for the aluminum.

The bulk-to-gel difference in Ca/Si (bulk 0.24 against gel 0.39 for GEO; bulk 1.27 against gel 1.72 for REF) reflects what each measurement integrates. The bulk EDS includes residual GGBS or CEM I grains and the quartz aggregate within the analyzed area, both of which dilute or skew the gel chemistry. The point-EDS values are the gel-only composition. The consistent direction of the bulk-to-gel shift in both materials (lower bulk than gel) is consistent with quartz-aggregate dilution of Ca and enrichment of Si in the bulk reading, which is the expected geometric effect of including the 42 to 50 wt% quartz aggregate content of the analyzed powder. These observations close the chain of evidence linking the XRD-identified C-(N,K)-A-S-H amorphous phase to the bulk-EDS activator signature and the gel-EDS chemistry descriptors.

1.6 Conclusion

The chapter asked whether a 100% cement-free, ambient-cured UHPGC based on GGBS, silica fume, and sodium silicate plus KOH activation, incorporating recycled tire-derived steel fibers, can meet the NATURSEA-PV mechanical and rheological targets simultaneously. The answer is yes.

The optimized mix, designated G7.2SF1.8 with 10 M KOH and a 60/40 Flexo to Spajic fiber blend at 12 wt% of binder mass, delivers a 28-day compressive strength of 137 MPa on 10 × 10 × 10 cm^3 cubes, a 5% margin above the 130 MPa target. Slump flow is 208 mm, inside the 200 to 250 mm band, and the NF EN 196-3 final-setting open time is 23 minutes. Recycled fiber content reaches 60 wt%, well above the 35 wt% target. The 24-hour compressive strength of 65 MPa meets the early-age criterion exactly, without margin.

The formulation was reached through six bottleneck-driven stages, each isolating and resolving the limiting factor identified at the previous one (Section 1.3). Precursor screening

established that the calcium content of the blend controls the 28-day strength, and fly ash was removed. Hydroxide co-activation raised the 24-hour strength but left the 28-day value plateaued, locating the limit in reactive binder content rather than in kinetics.

Reducing the absolute silicate dosage, with the water-to-binder ratio falling at the same time, then doubled the 24-hour strength, and raising the binder content to 900 kg/m³ brought both strength criteria within reach, at the cost of workability at every NaOH molarity tested. Replacing NaOH with KOH at equal molarity resolved that trade-off, extending the slump flow from 167 to 232.5 mm and the open time beyond 20 minutes without loss of strength. Fiber blending then satisfied the recycled-content criterion at the selected 60/40 ratio.

Multi-technique characterization at 28 days locates the origin of the residual 8% strength gap relative to REF (Section 1.5.7). GEO shows no induction period, reaching its exotherm at 5.6 hours against 38.2 hours for REF and completing 90% of its temperature excursion within 3.0 hours against 33.6.

That rapid gelation locks in a coarse capillary network before the pore-refinement processes of Portland systems can operate. The water-accessible porosity is 1.72 times that of REF and the mean apparent gas permeability 22 times higher, with mercury intrusion resolving a dominant pore-entry diameter of 700 nm in GEO against 6.2 nm in REF; both values sit at a limit of the intrusion window, so they rank the two pore networks rather than size them. Transport in both materials is nevertheless carried by pores of comparable size, differing mainly in the volume available.

The binder itself is a C-(N,K)-A-S-H gel of Ca/Si 0.39 against 1.72 for the REF C-S-H, with potassium and sodium at comparable molar fractions in the framework. The fracture surface shows cohesive failure through the matrix in GEO against interfacial pull-out in REF.

Three findings emerge that are transferable beyond the present project.

First, the calcium content of the precursor blend is the controlling descriptor at ultra-high-performance levels. Raising the GGBS fraction from 21 to 84 wt% of binder lifted the 28-day strength from 70 to 121 MPa under identical activation, with the gain saturating above approximately 600 kg/m³ of GGBS.

Second, the absolute sodium silicate dosage, rather than the SS/SH mass ratio, organizes an empirical strength optimum at low water-to-binder ratio. The behavior is consistent with a silicate-passivation regime, though not isolated from the co-varying water-to-binder ratio and activator modulus, and the optimum lies in the 160 to 190 kg/m³ band for the binder contents tested.

Third, the Na^+ to K^+ substitution at equal hydroxide molarity extends the rheological window without sacrificing strength, breaking a trade-off characteristic of NaOH-activated slag. The cation mechanism invoked for it, a weaker ion pairing of K^+ that delays gel nucleation, is an interpretation consistent with the literature rather than an isolated demonstration, since the water-to-binder ratio co-varies slightly with the cation.

To the author's knowledge, this is the first reported UHPGC formulation combining ambient cure, a binary GGBS and silica fume binder without fly ash, KOH activation above 130 MPa, and over 60 wt% recycled tire-derived steel fibers in a single mix design. It is also the first direct Na^+ to K^+ comparison reported above 130 MPa in an ambient-cured cement-free system, with the substitution understood as an activation-route comparison in which the water-to-binder ratio co-varies with the cation.

1.6.1 Limitations and perspectives

Three limitations bound the microstructural results.

First, the gas permeability, mercury intrusion, and calorimetry were each carried out on a single specimen per mix, so batch-to-batch reproducibility of those descriptors is not quantified.

Second, the gel-phase EDS rests on two gel-clean spots per mix. The individual atomic ratios therefore carry substantial scatter and are reported as indicative; the contrast between the binders is unambiguous only because the two ranges do not overlap.

Third, the amorphous fraction returned by the Rietveld refinement comprises both the C-(N,K)-A-S-H gel and the unreacted GGBS and silica fume, which diffraction cannot separate. It is therefore an upper bound on the gel content.

Three measurement windows further constrain the interpretation. Absolute heats of reaction are not reported, since the loss coefficient of the calorimeter was not independently calibrated and dominates the heat balance over 48 hours (Section 1.4.3). The mercury-intrusion maxima of both mixes lie at a limit of their respective windows and are lower bounds, so the pore-size contrast can only be larger than measured. And the accessible gas pressure range was too narrow to resolve a slip coefficient in either mix, so permeabilities are reported on a mean apparent basis.

Each has a defined remedy. Selective dissolution or ^{29}Si MAS NMR would separate the gel from the unreacted precursor and convert the amorphous fraction into a measured gel content. Isothermal calorimetry would resolve the early dissolution peak that the semi-adiabatic configuration cannot, and an independently calibrated loss coefficient would restore the heat quantification.

Completing the low-pressure mercury-intrusion stage on GEO would bound the macro-porosity above 712 nm that currently lies outside the window, and a wider gas-pressure range would permit a Klinkenberg extrapolation on a defensible lever arm. A larger number of gel-clean EDS spots, or nanoindentation coupled to compositional mapping, would constrain the gel stoichiometry and its mechanical contribution together.

Two further limitations bound the compliance claims, and a third the formulation itself. The open time is the NF EN 196-3 final setting time measured on paste, an upper bound on the placement window; it does not show that the fiber-reinforced concrete keeps its slump flow over that interval, which flow-retention measurements or rheometry on the complete

concrete would establish. The 24-hour criterion is met by the mean of three specimens, exactly at the threshold, so production-level compliance would require a characteristic value, the mean minus a margin set by the batch scatter, and therefore a higher mean or a faster early reaction. Finally, several optimization stages changed more than one quantity at a time, the water-to-binder ratio co-varying with the silicate dose in Stage 3 and slightly with the cation in Stage 5, and the mix was produced from a single lot of each raw material: the results establish the performance of the combined formulations rather than the isolated effect of each variable, and the robustness of the mix to the variability of the slag, the silica fume and the recycled fibers is not quantified.

The chapter establishes the formulation, the mechanical and rheological compliance, and the microstructural baseline of GEO at 28 days. It does not establish whether these gains translate into a net durability advantage over the Portland reference in the marine environment of an offshore floating photovoltaic substructure, nor does it quantify the fracture behavior across the loading history. Those questions are addressed in the chapters that follow.

1.7 Transition to Chapter 2

The optimization and characterization reported in this chapter resolved the formulation and the microstructural baseline of GEO at 28 days through six destructive techniques on companion specimens. The microstructural picture that emerged carries two features of direct relevance to electrochemical characterization. **First,** the pore network of GEO is 100-fold coarser than REF in dominant pore size (700 nm against 6.2 nm), so the electrolyte path length, the tortuosity, and the pore connectivity that govern bulk ionic transport differ between the two materials by orders of magnitude. **Second,** the pore-solution chemistry of GEO is dominated by residual K^+ and silicate species rather than the Ca^{2+} and OH^- pair of a portlandite-buffered Portland system, so the ionic mobilities, the matrix-electrolyte interfacial polarization, and the steel-fiber double-layer response differ by binder type. Both features sit within the resolution of electrochemical impedance spectroscopy.

Chapter 2 reports the EIS characterization of REF and GEO from 1 to 28 days under identical ambient curing. The chapter addresses two questions: whether the pore network and pore-solution chemistry of GEO produce an EIS signature that is distinguishable from REF across the curing window, and whether the parameters of an equivalent-circuit fit to the impedance spectrum can serve as non-destructive indicators of the strength development reported in this chapter. The frequency-domain methodology and the equivalent-circuit selection are reported in Section 2.2. The time evolution of the fitted circuit parameters and the resulting fingerprint of each binder system are reported in Section 2.3, and the cross-correlation against the compressive-strength data of Section 2.3.2 is reported in Section 2.3.10, establishing the conditions under which EIS parameters can be used as proxy indicators of strength gain in a cement-free UHPC.

Can a 100% cement-free, ambient-cured UHPGC reach the mechanical and durability performance to survive harsh marine environments and replace conventional UHPC in offshore FPV substructures monitored by SHM?

↓

01

Chapter 1. Formulation and characterization

Cement-free UHPGC mix, recycled fibers,
mechanical and rheological validation

↓

02

Chapter 2. Electrochemical Impedance Spectroscopy

Pore network and pore solution signatures of REF and GEO

↓

03

Chapter 3. Acoustic emission and fracture mechanics

Crack initiation, propagation, energy dissipation

↓

04

Chapter 4. Durability and Carbon footprint assessment

Sulfate, acid, chloride, thermal, and HarshLab
Cradle-to-grave environmental and economic balance

Chapter 2 - Electrochemical Impedance Spectroscopy

Chapter 1 established that the GEO mix meets the NATURSEA-PV mechanical and rheological targets under ambient curing and reaches 92% of the REF compressive strength at 28 days on the prism-half geometry used throughout this chapter. The two binders are not microstructural equivalents that happen to converge in compressive strength. The GEO pore network is roughly two orders of magnitude coarser than REF at comparable total intruded volume, with the dominant resolved peak at 700 nm against 6.2 nm for REF. Both values sit at a limit of the joint intrusion window, so they rank the two pore networks rather than measure a critical pore diameter in either. The GEO pore solution is alkali-dominated (Na^+ and K^+ retained from the KOH and sodium silicate activator) without the portlandite buffer that maintains the Ca^{2+}/OH^- chemistry of REF. The gel itself is a calcium-poor C-(N, K)-A-S-H of Ca/Si ≈ 0.39 against 1.72 for REF, with both Na and K bound in the gel framework at K/Si ≈ Na/Si ≈ 0.20. These contrasts in pore network geometry, pore solution chemistry, and gel composition are the structural facts that motivate the present chapter.

Whether and how these contrasts translate into the in-service behavior of an offshore FPV substructure cannot be answered by mechanical characterization alone. An offshore substructure is a thick-walled concrete element exposed to seawater, splash, and atmospheric zones across a service life that NATURSEA-PV targets at several decades. Strength development under such conditions cannot be monitored by repeated destructive sampling, and the formulation has to be qualified by methods that can be applied non-destructively on the cast element. Electrochemical Impedance Spectroscopy (EIS) is the natural tool for this question because it decomposes the bulk electrical response into the pore solution conductivity, the gel and interfacial phases, and the long-range ionic diffusion, each of which can be tracked independently as a function of curing age.

Two questions follow. **First,** do the pore network and pore solution contrasts identified in Chapter 1 produce an electrochemical signature that distinguishes GEO from REF across the curing window? **Second,** can a parameter of that signature serve as a non-destructive proxy for strength development, so that the same measurement supports both formulation qualification and in-service monitoring of a structural element? The two questions are coupled: a distinguishable signature alone is not sufficient if no parameter of it tracks strength gain, and a strength correlation that holds for REF does not transfer to GEO if the underlying microstructural process is fundamentally different.

Chapter research question: Does the pore network and pore solution chemistry of GEO produce a distinguishable electrochemical signature from REF, and can EIS parameters serve as non-destructive indicators of strength development in a cement-free UHPC?

2.1 State of the art

Electrochemical Impedance Spectroscopy (EIS) is the extraction of frequency-resolved electrical information from a material under small-amplitude alternating voltage when the multiple electrochemical processes within it respond at their characteristic timescales. In a saturated cementitious matrix the responding processes are the conduction of ions through the continuously connected pore solution, the polarization of charge at the gel-solid interfaces, and the long-range diffusion of ions through the connected pore network (Macdonald and Johnson, 2005; Orazem, 2008). An impedance analyzer applied to two electrodes coupled to the specimen faces converts the resulting current response into a complex impedance spectrum that is parameterized and stored alongside the curing record. The technique therefore delivers a frequency-resolved microstructural fingerprint that single-frequency resistivity measurements alone cannot produce. The price for that resolution is a list of acquisition and processing choices, each of which must be defended in the methods section: frequency band, electrode configuration, contact correction, equivalent circuit topology, fitting weighting, Kramers-Kronig validation, and parameter bounds. This section defines every term that appears in the rest of the chapter, introduces the equations behind each impedance descriptor, summarizes what is known about EIS in Portland cement, UHPC, and alkali-activated systems, and ends by isolating the gap that the present chapter is designed to close.

2.1.1 EIS as a microstructural probe in cementitious materials

2.1.1.1 Physical origin of an EIS signal

A small-amplitude alternating voltage applied across a saturated cementitious specimen drives a current response whose phase and magnitude depend on frequency. The characteristic frequency range for the processes that matter in cementitious matrices is 1 Hz to 1 MHz, with the upper limit set in practice by parasitic lead inductance and the lower limit by the duration over which the curing state can be considered stationary (McCarter et al., 2003). The acquisition window used in this chapter, 4 Hz to 5 MHz, brackets this range on both sides. The decade below 4 Hz is excluded to keep the acquisition time per specimen short enough that the curing state does not change during the sweep, and the band above 1 MHz is acquired for diagnostic purposes but excluded from the fit, for the reason given in Section 2.2.3. The complex impedance $Z(\omega)$, measured as the ratio of voltage to current at angular frequency ω, separates the contributions of the pore solution, the solid-pore interfaces, and the long-range diffusion into distinct spectral features. The two standard representations used throughout this chapter are the Nyquist plot, in which the negative imaginary part is plotted against the real part with frequency as an implicit parameter, and the Bode plot, in which the impedance modulus and the phase angle are plotted separately against the logarithm of frequency. Figure 2-1 introduces both representations for an

idealized two-arc cementitious spectrum and labels every feature that the rest of this chapter refers to.

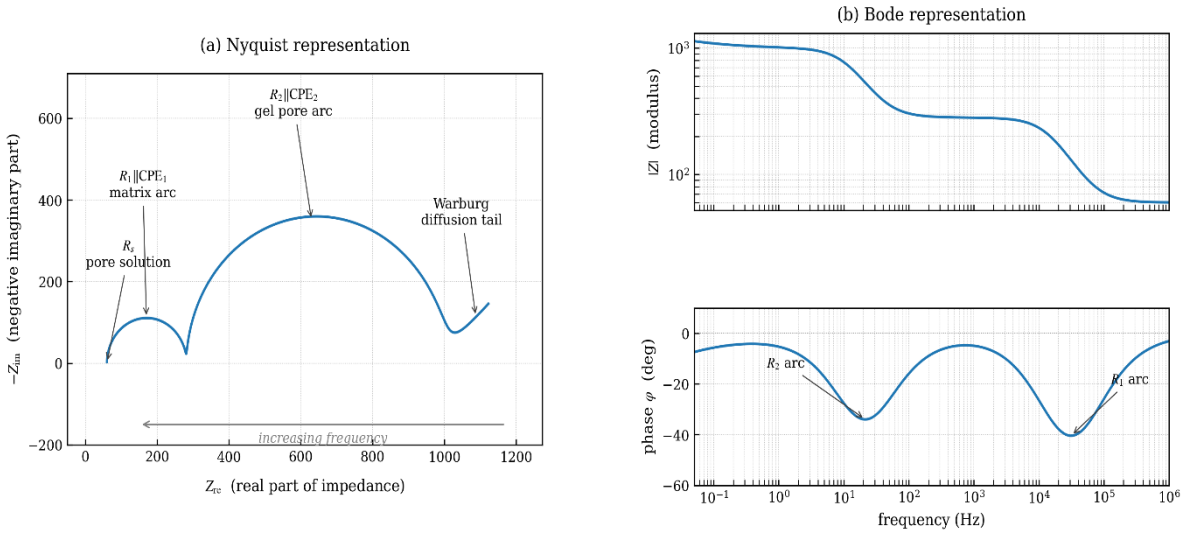

Figure 2-1: Anatomy of an impedance spectrum. (a) Nyquist plot, frequency increasing right to left. (b) Bode modulus and phase. All features are labeled on the figure and defined in Section 2.1.1.

2.1.1.2 Spectrum versus parameter set

Two terms are used throughout the cementitious EIS literature and they are not interchangeable. A spectrum is the full set of complex impedance measurements at every probed frequency. A parameter set is the small ordered list of values extracted from the spectrum by complex nonlinear least-squares (CNLS) fitting against an equivalent circuit model. Cross-system and cross-age comparisons in this chapter are made at the parameter level (Rs, R1, R2, R3, Q1, Q2, Q3, n1, n2, n3, Rw or W), following the convention of cementitious EIS studies on hydrating and polycondensing systems (Christensen et al., 1994; Song, 2000). Spectrum-level statistics appear only in the Kramers-Kronig validation of Section 2.2.5 and in the qualitative Nyquist evolution of Section 2.3.3.

2.1.1.3 Solution resistance Rs (Ω)

Rs is the real-axis intercept of the Nyquist plot at the high-frequency limit. Physically, Rs represents the bulk ionic conductivity of the continuously connected pore solution. Its magnitude is governed by the concentration and mobility of the dissolved species: Ca2+ and OH- in Portland systems buffered by portlandite, Na+ and K+ retained from the activator in alkali-activated systems. Because Rs reports bulk pore-solution conductivity rather than interfacial polarization, it is the most attenuation-insensitive parameter of the spectrum, and its evolution tracks the consumption of free ions as the matrix densifies (McCarter et al., 2003).

2.1.1.4 Charge-transfer resistance Ri (Ω) and constant phase element

Each R || CPE arc on the Nyquist plot captures the polarization of charge at one distinct microstructural interface. The resistance Ri is the diameter of the arc on the real axis, and the constant phase element CPEi parameterizes the dielectric character of the interface through a magnitude Qi (units $F \cdot s^{n-1}$) and an exponent ni (dimensionless, typically between 0.5 and 1.0 in cementitious systems). The CPE impedance is defined as

$$Z_{CPE}(\omega) = \frac{1}{Q\,(j\omega)^n} \tag{2.1}$$

where j is the imaginary unit and ω the angular frequency. The CPE replaces the ideal capacitor of textbook RC circuits because real cementitious interfaces are distributed in geometry and orientation, so the dielectric response is not characterized by a single relaxation time but by a distribution of relaxation times (Brug et al., 1984). The exponent n encodes the degree of dispersion of the interface: n = 1 corresponds to an ideal capacitor, n = 0.5 to a Warburg-type diffusion limit, and intermediate values to interfaces of intermediate disorder. Values approaching 1.0 therefore indicate a more homogeneous interface and lower values a more dispersive one. Figure 2-1a locates the R || CPE arcs within the full spectrum, and Figure 2-2 gives the two Warburg signatures in isolation.

2.1.1.5 Finite-length short-circuit Warburg Rw (Ω) and Tw (s) for REF

At the low-frequency end of the spectrum, the impedance is governed by the long-range diffusion of ions across the connected pore network. For REF, this diffusion takes place through a bounded pore network that terminates at the densely packed unreacted grain-boundary network, and the appropriate Warburg formulation is the finite-length short-circuit form Ws. The Ws impedance is defined as

$$Z_{Ws}(\omega) = R_w \frac{\tanh\sqrt{j\omega\,T_w}}{\sqrt{j\omega\,T_w}} \tag{2.2}$$

where Rw is the diffusion resistance with units of Ω and Tw is the diffusion time constant with units of s. The Nyquist signature of Ws is a 45-degree rise at the high-frequency end of the diffusion region that bends back to the real axis at the low-frequency limit Z = Rw. Figure 2-2a illustrates this signature.

2.1.1.6 Semi-infinite Warburg W ($\Omega \cdot s^{-1/2}$) for GEO

For GEO, the diffusion takes place through a coarser pore network that does not terminate within the measurement window, and the appropriate Warburg formulation is the semi-infinite form W. The W impedance is defined as

$$Z_W(\omega) = W(1 - j)\frac{1}{\sqrt{\omega}} \tag{2.3}$$

where W is the Warburg coefficient with units of $\Omega \cdot s^{-1/2}$. The Nyquist signature of W is a 45-degree rise that continues unbounded toward low frequencies. Throughout this work, the REF Warburg amplitude is denoted Rw and the GEO Warburg coefficient is denoted W, reflecting their distinct mathematical forms, units, and physical meanings.

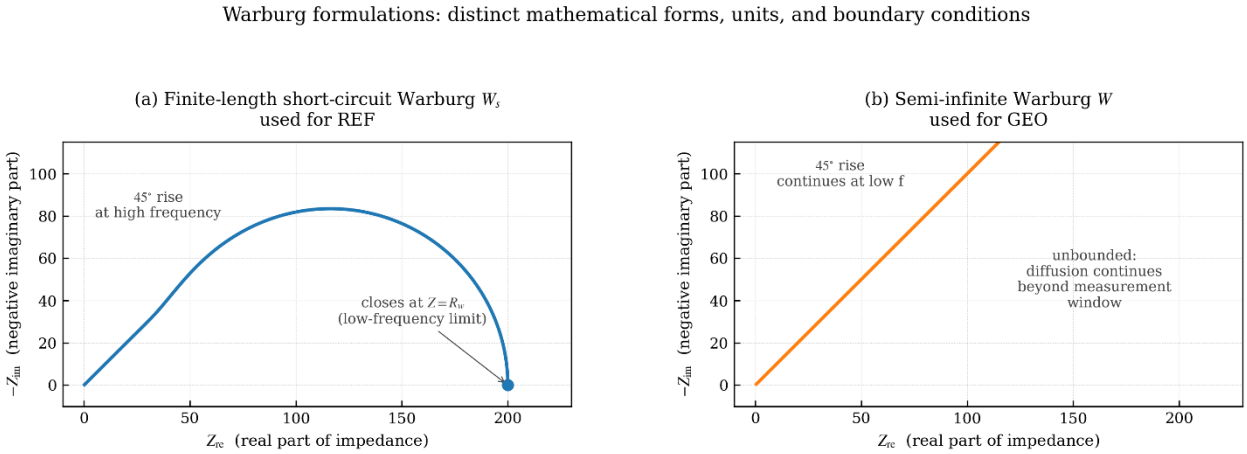

Figure 2-2: The two Warburg formulations used in this chapter. (a) Finite-length short-circuit Ws for REF, closing back to the real axis at Z = Rw. (b) Semi-infinite W for GEO, rising unbounded toward low frequencies.

2.1.1.7 Equivalent circuit topologies for REF and GEO

The full equivalent circuit topologies adopted for the two systems are introduced below and defended in Section 2.2.4. For REF during early hydration (Days 1 to 7), a two-arc topology with a finite-length short-circuit Warburg is sufficient:

$$Z(\omega) = R_s + (R_1 \parallel CPE_1) + (R_2 \parallel CPE_2) + W_s \quad \textbf{(2.4)}$$

From Day 10 onward, a third arc emerges in the REF Nyquist plots and is attributed to the steel fiber-matrix interfacial transition zone. The REF topology extends to:

$$Z(\omega) = R_s + (R_1 \parallel CPE_1) + (R_2 \parallel CPE_2) + (R_3 \parallel CPE_3) + W_s \quad \textbf{(2.5)}$$

For GEO, a single-stage topology with a semi-infinite Warburg is applied across the full 28-day window:

$$Z(\omega) = R_s + (R_1 \parallel CPE_1) + (R_2 \parallel CPE_2) + W \quad \textbf{(2.6)}$$

2.1.1.8 Topology selection criteria

Equivalent circuit modeling translates the measured spectrum into the smallest set of these elements that reproduces the data within an accepted tolerance. The strength of the method is that each element has an unambiguous physical assignment and a measurable temporal trajectory. The weakness is that any spectrum admits more than one circuit topology if the goodness-of-fit threshold alone is the selection criterion. Cementitious EIS practice therefore combines three concurrent requirements: a numerical goodness-of-fit threshold (typically $R2 > 0.99$ and a mean relative error below 5%), the physical plausibility

of the fitted parameter values (CPE exponents within the dispersive range and resistances strictly positive), and the rejection of competing topologies that yield non-identifiable parameters or violate physical bounds (Boukamp, 1995; Schönleber et al., 2014). The implementation for REF and GEO, including the parameter intervals actually imposed, is reported in Sections 2.2.4 and 2.2.5.

2.1.1.9 Kramers-Kronig consistency check

A separate consistency check is applied to the measured spectra before any circuit fitting is attempted. The Kramers-Kronig (KK) relations are integral transforms that connect the real and imaginary parts of any causal, linear, time-invariant impedance function. A spectrum that satisfies these conditions can therefore be fitted by a linear Kramers-Kronig transform, a sequence of RC circuits, with small residuals across the band (Boukamp, 1995; Schönleber et al., 2014). A spectrum containing a contribution the Voigt basis cannot represent, for example a series lead inductance, produces residuals that diverge above the frequency band where the inductance becomes significant. Figure 2-3 illustrates the principle on two synthetic spectra, one KK-compliant and one corrupted by a small inductive contribution above 1 MHz, and shows how the Lin-KK residuals separate the two cases. The figure also shows the rationale for excluding the band above 1 MHz from CNLS fitting in the present work. The residual threshold adopted here is stated once, with the acceptance criteria, in Section 2.2.5.

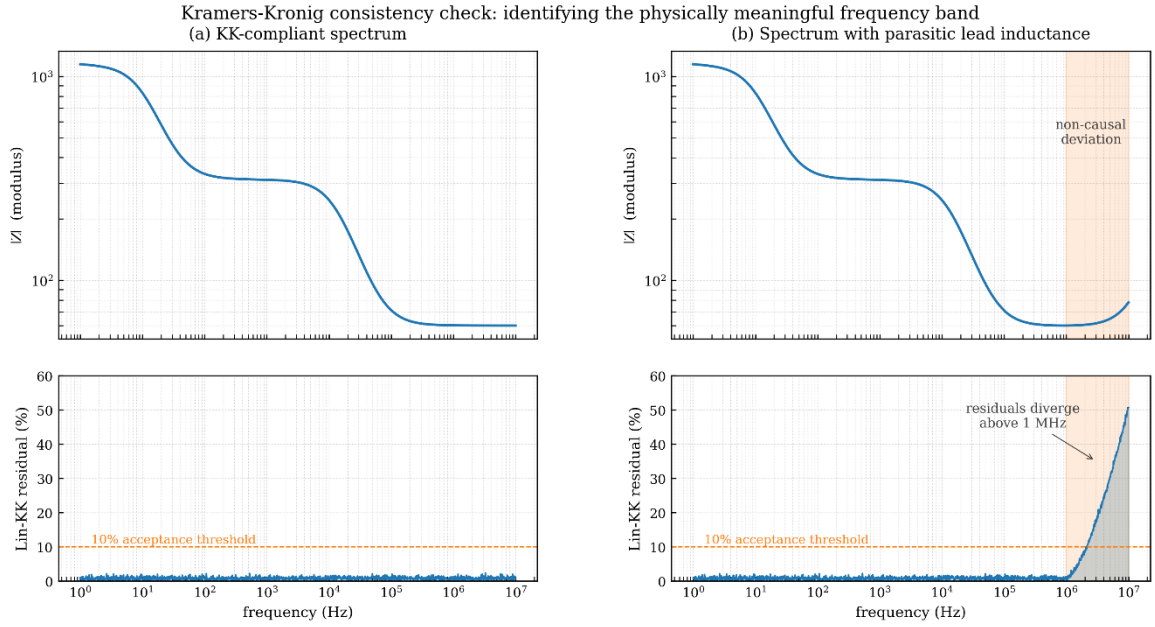

Figure 2-3: Kramers-Kronig consistency check on a synthetic two-arc spectrum. (a) Voigt-representable spectrum with its Lin-KK residuals and (b) The same spectrum with a series inductance above 1 MHz, residuals rising sharply in the shaded band.

2.1.1.10 Goodness-of-fit metrics: R^2 and MRE

Two quantitative metrics are used jointly in this chapter to assess the goodness of each CNLS fit at each age and for each system. The coefficient of determination R2 quantifies the fraction of the variance in the complex impedance explained by the fitted model, computed on the complex residual so that error in the phase is penalized alongside error in the magnitude. The mean relative error MRE is defined as

$$\mathrm{MRE} = \frac{1}{N}\sum_{i}\frac{|Z_{\mathrm{meas}}(f_i) - Z_{\mathrm{fit}}(f_i)|}{|Z_{\mathrm{meas}}(f_i)|} \times 100\% \quad \textbf{(2.7)}$$

where N is the number of frequency points over which the metric is evaluated. The acceptance thresholds, and the frequency band over which R2, MRE, and the maximum relative error are evaluated, are stated in Section 2.2.5. The maximum relative error per spectrum is also reported alongside MRE in Section 2.3.5, in order to surface any localized misfit at the frequency extremes.

2.1.1.11 Attenuation insensitivity of impedance parameters

Unlike acoustic emission, where attenuation between source and sensor limits the comparability of absolute amplitudes across binders, EIS parameters are intrinsically attenuation-insensitive once the contact impedance correction described in Section 2.2.3 is applied. The fitted Rs, Ri, Qi, ni, Rw and W values represent volume-averaged properties of the cementitious matrix that are independent of the geometric coupling between the electrodes and the specimen surface. This insensitivity is a methodological advantage of EIS over impedance-adjacent techniques such as single-frequency resistivity, in which moisture and surface effects perturb the measured value without a frequency-resolved means of separating them. The implication for cross-binder claims in this chapter is that the impedance parameters reported below need no geometric or coupling correction before REF and GEO are compared. Parameters that converge to a limit of the fitting interval are a separate matter and are identified where they occur.

2.1.2 EIS across binder chemistries

2.1.2.1 What the impedance spectrum reports in Portland cement systems

EIS has been applied to Portland cement systems for more than three decades, establishing the now-standard reading of the spectrum in which the high-frequency intercept reports the pore solution and the successive arcs report the polarization of the solid-liquid interfaces as hydration densifies the matrix (Christensen et al., 1994). They established the relationship between impedance arcs and the developing microstructure of hydrating cement paste, showing that the high-frequency arc corresponds to bulk pore solution conduction while lower-frequency features reflect the developing solid phases. McCarter and Brousseau (1990) characterized the AC response of hardened cement paste and identified the frequency dependence of the dielectric constant as a microstructural indicator. Gu et al. (1992, 1993)

proposed equivalent circuit models for hydrating Portland cement and reported that the circuit parameters evolve systematically with hydration degree, with the gel-arc resistance growing by more than two orders of magnitude during the first 28 days at ambient temperature. Song (2000) consolidated these models into a general equivalent circuit framework for AC impedance spectroscopy of concrete.

Later work moved from description to quantitative correlation, relating impedance parameters to porosity, chloride diffusivity, and compressive strength. Dong et al. (2015) extended impedance interpretation to blended fly-ash slag cement systems, showing that supplementary cementitious materials shift the temporal evolution of the gel arc without changing its qualitative behavior. Park et al. (2022) combined EIS with artificial neural networks for water-to-cement ratio estimation, opening the use of EIS as an input to data-driven quality-control tools. Embedded resistivity sensors combined with EIS have been proposed for real-time strength estimation in cement paste during the first 24 hours (Cabeza et al., 2002).

Two methodological issues recur:

- The contact impedance introduced by the electrode arrangement, which the two-electrode configuration cannot separate from the specimen response,
- The choice of frequency window, which determines which relaxations are captured at all (Keddam et al., 1997).

At the ultra-high-performance strength class the literature remains scarce, and the few available studies concern Portland-based UHPC rather than cement-free systems (Sánchez et al., 2008); (McCarter et al., 2003; Chi et al., 2019); (Christensen et al., 1994; Dotelli and Mari, 2001). The ultra-low porosity of UHPC implies that the dominant resistive phases in the impedance response are the densely packed unreacted grain-boundary network and the gel pore layer, rather than the large capillary pore system that dominates ordinary concrete (Nóvoa, 2026). The incorporation of steel micro-fibers introduces additional electrochemical interfaces, specifically the fiber-matrix interfacial transition zone, which may manifest as a distinct impedance arc requiring a dedicated circuit element (Nóvoa, 2026).

2.1.2.2 What changes in alkali-activated systems

The application of EIS to alkali-activated and geopolymer materials is comparatively recent and substantially narrower in scope. It is dominated by applications rather than by microstructural interpretation: moisture and strain sensing that exploits the high ionic conductivity of the matrix, and microstructural characterization of fly-ash and metakaolin systems. Biondi et al. (2019) exploited the ionic conductivity of fly-ash geopolymer matrices to develop embedded moisture sensors for reinforced concrete health monitoring, using impedance spectroscopy and equivalent circuit models to optimize the sensor response across a range of saturation states. Criado et al. (2010) used impedance spectroscopy to track the activation kinetics of fly ash, identifying distinct conduction regimes associated with the

dissolution and polycondensation stages of the alkali-activation reaction. Pouhet and Cyr (2016) characterized the mesoporosity of metakaolin-based geopolymers through intrinsic ionic conductivity measurements obtained from complex impedance spectroscopy, confirming that charge transport occurs primarily through the connected mesopore network saturated with the residual activator solution (Alexander, 2026).

Two limits of this body of work matter for the present chapter:

First is that no study has attempted to establish a quantitative correlation between impedance parameters and compressive strength in an alkali-activated system. The predictors validated in the Portland cement literature were derived from, and remain physically tied to, the monotonic densification of C-S-H gel, so their transfer to a binder that forms its gel by dissolution and polycondensation is an assumption rather than a result. The alkali-activated studies reviewed above were moreover designed around the state of the pore solution, which is the quantity that moisture and corrosion sensing target, whereas compressive strength is carried by the solid skeleton. The literature has therefore optimized for a different observable than the one a strength indicator requires.

The second limit is that no study has compared the two binder chemistries within a single experimental framework. Published values for the same nominal parameter originate from specimens that differ in water-to-binder ratio, aggregate skeleton, electrode configuration, frequency window, and equivalent circuit topology, so a cross-study comparison cannot separate a binder effect from a protocol effect. The difficulty is compounded if the two chemistries require different circuit topologies, in which case a resistance labeled R2 in a two-arc model and a resistance labeled R2 in a three-arc model are not the same physical quantity and should not be compared at all.

2.1.2.3 The ultra-high-performance strength class

At the ultra-high-performance strength class both literatures thin sharply, and they do so asymmetrically. EIS work at this scale is scarce, and what exists has been performed on ordinary cement pastes at water-to-binder ratios of 0.35 to 0.50, where the pore structure and the ionic environment differ markedly from an ultra-dense fiber-reinforced matrix. Their common finding is that the ultra-low water-to-binder ratio changes which phases dominate the impedance response: with the large capillary pore system of ordinary concrete largely eliminated, the dominant resistive phases become the densely packed unreacted grain-boundary network and the gel pore layer (Nóvoa, 2026). A second consequence follows from the fiber reinforcement that defines the class. Steel micro-fibers introduce additional electrochemical interfaces, and the fiber-matrix interfacial transition zone may manifest as a distinct impedance arc requiring a dedicated circuit element (Torrents et al., 2000).

For cement-free UHPC no EIS study is available at all. The alkali-activated work reviewed above concerns pastes and mortars at ordinary water-to-binder ratios, where both the pore network and the ionic environment differ from an ultra-dense fiber-reinforced

matrix by orders of magnitude. The two bodies of work therefore stop short of each other. The Portland side reaches the strength class but not the binder chemistry, and the alkali-activated side reaches the binder chemistry but not the strength class. Neither offers a basis for predicting which impedance parameter tracks strength development in a cement-free UHPC, or whether the two binders require the same equivalent circuit topology at all.

2.1.2.4 Reaction mechanism and the expected impedance trajectory

The reason to expect a difference is mechanistic. Where Portland cement produces semicrystalline C-S-H gel through the unidirectional and essentially irreversible hydration of alite and belite clinker phases, alkali-activated slag undergoes dissolution of the glassy precursor in the alkaline medium followed by polycondensation of a calcium-bearing aluminosilicate hydrate gel whose composition depends on the calcium content of the precursor and on the alkali cation of the activator (. For low-calcium fly-ash or metakaolin systems activated by sodium hydroxide or sodium silicate, the gel is commonly described as N-A-S-H. For the high-calcium slag-rich system activated by potassium hydroxide and sodium silicate used in this thesis, the sodium-bearing form C-(N)-A-S-H is the closest analogue described in the literature (Garcia-Lodeiro et al., 2011; Myers et al., 2013). The additional binding of potassium in the gel framework, giving C-(N,K)-A-S-H, is established here from the XRD Rietveld refinement and gel-region EDS reported in Chapter 1 (Section 1.5.7) rather than imported from the literature.

This mechanistic difference is expected to produce qualitatively different impedance trajectories in time. C-S-H gel growth is monotonic. C-(N,K)-A-S-H gel formation involves multiple overlapping dissolution-reprecipitation equilibria as residual slag particles continue to be attacked by the activator solution at rates that depend on particle size and local chemical environment (. Whether this difference produces measurable departures from monotonicity in the impedance trajectories of GEO, and whether such departures invalidate the use of impedance parameters as strength predictors, are questions that the present chapter addresses directly.

2.1.3 Limits of existing non-destructive methods for UHPC

2.1.3.1 Non-destructive monitoring during early-age curing

Non-destructive monitoring of compressive strength development during early-age curing is essential for optimizing demolding, transport, and post-tensioning schedules in concrete construction (Sant et al., 2008), and is a direct prerequisite for any in-service quality-control protocol on a cast offshore element. Three established techniques frame the case for EIS, and each is limited in a different way.

Ultrasonic pulse velocity relates wave speed to the elastic modulus and correlates only indirectly with strength, losing sensitivity once the matrix has percolated (Malhotra and Carino, 2003). Hassan and Jones (2012) assessed the feasibility of ultrasonic and resonant

frequency testing on ultra-high-performance fiber-reinforced concrete specifically and identified the limitation that matters here: in a matrix of this density the elastic modulus stabilizes well before the compressive strength does, so the property the measurement reports and the property of interest decouple over precisely the window in which the monitoring is required.

The maturity method infers strength from the time-temperature history through a calibration that is specific to one mix and does not transfer to a different binder chemistry (Malhotra and Carino, 2003). For a comparison between a Portland cement and an alkali-activated system this is disqualifying by construction. Two separate calibrations would be required, and any difference observed between the two systems would then rest on the two calibrations rather than on the measurement. Single-frequency resistivity is simple and rapid but returns a single scalar in which pore geometry and pore-solution conductivity are inseparably combined (Rajabipour and Weiss, 2007; Spragg et al., 2013). That combination is the specific obstacle for the present work, because the two systems differ in both quantities at once and in opposite directions. GEO has both the coarser pore network and the more conductive pore solution, so a single resistivity reading cannot say which of the two is responsible for the value it returns.

2.1.3.2 The case for EIS

Electrochemical Impedance Spectroscopy separates what a single-frequency measurement combines. By probing across several frequency decades, it resolves the pore solution conductivity, the interfacial polarization, and the long-range ionic diffusion into distinct spectral features, each with its own temporal trajectory. This is what makes EIS a candidate where the other three techniques fall short. It does not depend on the elastic modulus, it requires no mix-specific calibration, and it does not collapse pore geometry and pore-solution chemistry into a single number. Whether EIS delivers on this candidacy for the REF and GEO systems of this thesis, and which specific impedance parameter best tracks the strength development of each binder, are the operational questions that the present chapter addresses.

2.1.4 Synthesis of the gap

2.1.4.1 The gap

Three conclusions follow from the literature reviewed above. The EIS interpretation framework for Portland cement is mature and supports a quantitative correlation between gel-arc resistance and compressive strength, but it has been established on ordinary pastes and mortars and has not been extended to the ultra-high-performance strength class. The alkali-activated literature has not attempted a strength correlation at all, in any binder of that family, at any water-to-binder ratio. And no published work has compared the EIS response of a Portland cement UHPC against an alkali-activated UHPC within a unified experimental

framework, or asked whether the same impedance parameter serves as a reliable strength predictor for both binder chemistries.

2.1.4.2 Why the gap matters for UHPGC

This gap matters because the differences between the two systems in pore solution ionic strength, gel structure, reaction kinetics, and fiber-matrix interaction may require not only different circuit topologies but different predictor parameters, and neither possibility can be assessed by studying either system in isolation. Each of the three contrasts established in Chapter 1 has a direct and separable expected signature on the impedance response. The pore network geometry should act on the long-range diffusion path, and therefore on the Warburg parameters Rw and W. The pore solution chemistry should act on the bulk ionic conductivity, and therefore on the solution resistance Rs. The gel composition should act on the polarization of the gel-solid interface, and therefore on the gel pore resistance R2. Because the two systems differ in all three at once, the combined effect on the strength correlation cannot be predicted from any one of them and can only be measured by side-by-side EIS characterization under a single protocol.

2.1.4.3 Chapter objectives

The present chapter addresses this gap by investigating REF and GEO under identical EIS protocols and curing conditions, with four objectives. The first is to establish physically motivated equivalent circuit topologies for each system and to validate their adequacy through Kramers-Kronig consistency checks and quantitative goodness-of-fit metrics. The second is to quantify the evolution of all circuit parameters and to interpret their trajectories in terms of the microstructural processes specific to each binder. The third is to compare the impedance signatures of REF and GEO within a unified experimental framework and to identify the asymmetries that distinguish C-S-H densification from C-(N,K)-A-S-H polycondensation. The fourth is to evaluate the candidacy of selected EIS parameters as non-destructive indicators of compressive strength development in each system, and to assess the practical implications of binder-specific indicator selection for the deployment of EIS in offshore FPV substructure construction.

2.2 Materials and methods

This section describes the two cementitious systems compared in this chapter, the specimen geometry and curing protocol, the EIS measurement chain, the equivalent circuit models adopted for each system, and the CNLS fitting procedure that converts the measured spectra into the parameter trajectories used in Section 2.3. The two systems and their mix proportions are inherited from Chapter 1. Only the parameters that condition the EIS interpretation of the present chapter are restated here. All experimental work was conducted at the I2M laboratory of the University of Bordeaux.

2.2.1 Mix designs

2.2.1.1 Two systems under identical EIS protocols

Two UHPC systems are compared in this chapter. The reference system (REF) is a Portland cement UHPC. The alternative system (GEO) is the alkali-activated geopolymer UHPC formulated in Chapter 1, in the deployment form selected at the close of the optimization, including its recycled fiber blend. Both systems use the same granular skeleton of high-purity quartz sand, the same polycarboxylate-ether superplasticizer family, and the same steel fiber dosage of 108 kg/m^3. The systems differ in binder chemistry and, as a consequence of testing the deployment mix, in the composition of the fiber population. Section 2.2.1.3 sets out what this means for the interpretation of the results.

2.2.1.2 REF and GEO binder chemistries

The two binders contrast fundamentally in their reaction chemistry. REF develops a portlandite-buffered Ca^{2+} and OH^- pore solution and produces semicrystalline C-S-H gel as the principal hydration product. GEO develops an alkali-dominated Na^+ and K^+ pore solution, retained from the 10 molar KOH and sodium silicate activator, with no portlandite buffering. Its principal polycondensation product is a calcium-bearing aluminosilicate hydrate gel of the form C-(N,K)-A-S-H, characterized in Chapter 1 (Section 1.5.7) by XRD Rietveld refinement and gel-region EDS analysis. This binder-chemistry contrast is the structural fact that the present chapter probes through EIS.

2.2.1.3 Steel fiber reinforcement

Steel fiber dosage is held constant across REF and GEO at 12 weight percent of binder, corresponding to 108 kg/m^3 and 1.4% by volume of the total mix at a steel density of 7850 kg/m^3. The fiber type is not. REF carries 100% virgin straight uncoated steel micro-fibers of 13 mm length and 0.20 mm diameter. GEO carries the recycled blend selected in Chapter 1 (Section 1.5.6), 60% recycled tire-derived Flexofiber and 40% virgin fiber by mass, which meets the NATURSEA-PV recycled-content target and which is therefore the fiber population of the deployed material. The recycled fraction differs from the virgin fiber in three respects established in Chapter 1 (Section 1.2.1): a length distribution spanning 10 to 25 mm rather than a uniform 13 mm, a diameter distribution spanning 0.15 to 0.30 mm rather than a uniform 0.20 mm, and rubber residue partially retained on the fiber surface from the recovery process.

This is a deliberate choice and it carries a cost. The choice is deliberate because the purpose of the chapter is to qualify the material that will be cast into an offshore substructure, and that material contains recycled fiber. The cost is that binder chemistry and fiber population change together between the two systems, so any observable that depends on the fiber-matrix interface is confounded. The bulk parameters of the impedance spectrum, the

solution resistance, the gel pore resistance, and the long-range diffusion terms, are governed by the pore solution and the pore network rather than by the fiber surface, and the comparison of those parameters between REF and GEO remains a binder comparison. The interfacial parameter is a different matter, and the consequences for the third arc of the REF equivalent circuit are set out in Section 2.2.4 and revisited in Section 2.3.7.

The acoustic emission campaign of Chapter 3 is a separate casting series at a different fiber dosage, 120 kg/m^3 and 1.5% by volume, with a virgin fiber population in both systems. The two chapters are therefore not comparable on fiber content and are not intended to be.

2.2.2 Specimen preparation and curing

2.2.2.1 Casting and demolding

Prismatic specimens of dimensions 4 × 4 × 16 cm^3 were cast for both REF and GEO. A single batch was prepared per system to ensure consistent material properties across all measurement ages within each system. The mixing protocol differs between REF and GEO to account for their fundamentally different rheology and reaction kinetics: GEO requires pre-blending of the activator solution prior to addition of the dry precursors to control the rapid initial dissolution reaction. All specimens were demolded at 24 hours.

2.2.2.2 Ambient curing regime

After demolding, all specimens were stored at ambient temperature (22 ± 2 °C) and relative humidity (50 ± 5%) without any additional thermal or moist-curing treatment. This ambient curing regime was deliberately adopted to evaluate the feasibility of GEO for in-situ construction of offshore FPV substructures, where heat curing is impractical, and to provide a direct comparison with REF under identical environmental conditions (Provis and Deventer, 2014). The ambient regime also discriminates against geopolymer systems that require elevated-temperature curing to develop strength, which is one of the operational constraints of the NATURSEA-PV deployment.

2.2.2.3 Eight-age EIS measurement schedule

From each batch, three prismatic specimens were dedicated exclusively to non-destructive EIS measurements. These three specimens were remeasured at each of the eight curing ages (1, 2, 5, 7, 10, 14, 21, and 28 days), with the copper-plate electrodes reattached at each measurement age to ensure consistent contact conditions (Figure 2-4). The eight-age schedule was selected to resolve the early-age microstructural development (Days 1, 2, 5, 7) at higher temporal resolution than the four-age formulation campaign reported in Chapter 1, while extending the observation window to the 28-day standard maturity. The lower temporal resolution beyond Day 14 reflects the slower rate of microstructural change in the post-percolation regime of both binders, where additional intermediate ages would not have added information commensurate with the measurement effort.

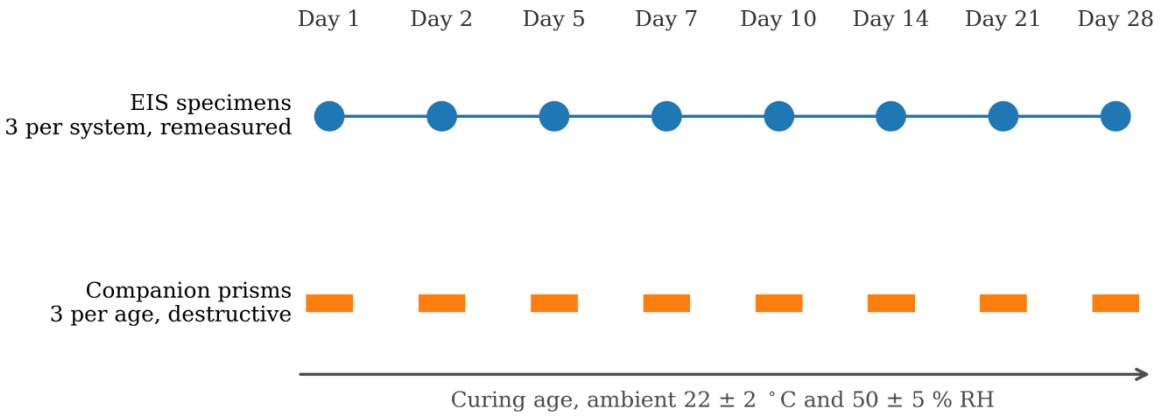

Figure 2-4: Measurement schedule per system.

2.2.2.4 Companion prisms for destructive mechanical testing

A separate set of 24 companion prisms per mix was reserved for destructive mechanical testing, with three specimens dedicated to each of the eight measurement ages. At each age, the three companion prisms were first loaded to failure in three-point bending following EN 196-1, after which the two intact halves of each broken prism were tested in compression on the 40 × 40 mm cross-section. Compressive strength results are therefore reported as the mean and standard deviation of six half-prism measurements per age per mix. Flexural strength results, reported in Chapter 1 (Section 1.5.7) for the 28-day age only, are not repeated in this chapter since the present analysis correlates EIS parameters with compressive strength specifically.

2.2.3 EIS measurement setup

2.2.3.1 Instrument and frequency window

Impedance spectra were acquired with a HIOKI IM3570 impedance analyzer at each of the eight curing ages (Figure 2-5). The frequency window extends from 4 Hz to 5 MHz, with a sinusoidal excitation voltage of 0.1 V rms. The excitation amplitude is small enough to maintain a linear response (verified by Kramers-Kronig pre-validation, Section 2.2.5) and large enough to keep the signal-to-noise ratio acceptable across the impedance range of the two systems, which spans almost four orders of magnitude between GEO at Day 1 (≈ 100 Ω baseline) and REF at Day 28 (> 100 kΩ). Each sweep comprises 401 logarithmically spaced frequency points, approximately 66 points per decade across the 6.1 decades of the window. All measurements were performed in a controlled-temperature laboratory at 22 ± 2 °C to minimize the thermal sensitivity of the pore solution conductivity, which dominates the high-frequency real-axis intercept (McCarter and Brousseau, 1990; McCarter et al., 2003).

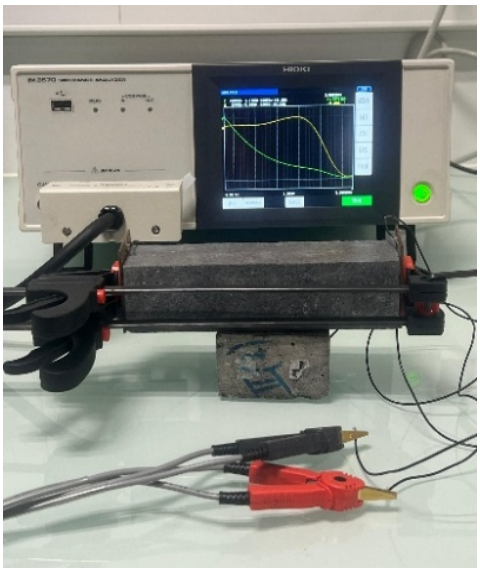

Figure 2-5: EIS measurement setup.

2.2.3.2 Electrode configuration

The measurement configuration used two copper plate electrodes of dimensions 40 × 40 mm, affixed to the two opposing end faces of each prism to ensure full-face electrical contact across the specimen cross-section. A water-based conductive paint (Bare Conductive Electric Paint) was applied at the electrode-specimen interface at each measurement age. The conductive paint serves three functions: it lowers the contact resistance between the copper plate and the specimen surface, it accommodates the surface roughness of the demolded prism by deforming into the surface asperities, and it ensures reproducible electrical coupling on successive electrode reattachments. The same electrode geometry, paint formulation, and contact pressure were used for all 48 measurement events (two systems times eight ages times three specimens per age).

2.2.3.3 Two-electrode limitation

The two-electrode configuration was selected because the same specimens are remeasured non-destructively at eight curing ages, which precludes any arrangement requiring an embedded reference electrode, and it is the configuration used in the majority of cementitious EIS studies of recent years (Cabeza et al., 2002; Chi et al., 2019). Two limitations follow. The measured impedance includes a contact contribution at the electrode-specimen interface, which overlaps in frequency with the low-frequency arcs of the matrix and would bias the fitted parameters if left uncorrected. The contact correction procedure described below addresses it. The contact contribution is also frequency-dependent and largest at the low-frequency end, which is where the diffusion features of both systems sit, so the Warburg parameters carry more of this uncertainty than the arc resistances do. A three-electrode arrangement is preferred below approximately 1 kHz, and a four-electrode arrangement would eliminate the contact contribution entirely (Nóvoa, 2026), but neither is compatible with repeated non-destructive measurement on the same specimens.

2.2.3.4 Contact impedance correction

To isolate the intrinsic impedance response of the cementitious matrix from electrode and contact artifacts, a blank calibration measurement was performed by recording the impedance of the two copper plates in direct contact (Z_{plates}) immediately before each measurement session. For each system and each age, three prismatic specimens were measured independently, and their complex impedance spectra were averaged point-by-point across frequency to obtain a mean spectrum (Z_{av}). The corrected spectrum submitted to CNLS fitting was then computed as

$$Z_{corrected}(f) = Z_{av}(f) - Z_{plates}(f) \quad \textbf{(2.8)}$$

This subtraction protocol is consistent with the contact-impedance correction methodology proposed by Keddam et al. (1997) and applied by Sánchez et al. (2008), and ensures that the fitted equivalent circuit parameters reflect the bulk dielectric and conductive properties of the cement or geopolymer matrix exclusively, without contamination from electrode polarization effects.

2.2.3.5 Frequency band considerations

Two practical points on the frequency window are worth stating explicitly. First, at frequencies above approximately 1 MHz, the measured impedance shows an upward deviation in the modulus that the equivalent circuit does not represent. This deviation is attributed to parasitic inductance in the measurement leads and electrode connections and is not a property of the cementitious matrix (McCarter et al., 2003; Macdonald, 2006). The 46 points above 1 MHz are retained in the recorded spectrum and in the goodness-of-fit statistics, but the fitting procedure described in Section 2.2.5 gives the residuals below 1 MHz the dominant weight, so the fitted parameters are determined by the physically meaningful band.

2.2.4 Equivalent circuit models

2.2.4.1 Element-by-element physical assignment

The physical interpretation of EIS spectra in cementitious systems rests on the assignment of each circuit element to a specific microstructural feature (Gu et al., 1992; Song, 2000; McCarter et al., 2003). For the present work, the assignment introduced in Section 2.1.1 is applied to both systems. The solution resistance Rs represents the bulk ionic conductivity of the continuously connected pore solution, whose magnitude is governed by the concentration and mobility of the dissolved species. Each parallel R || CPE arc captures the dielectric relaxation of a distinct microstructural phase. The first arc (R1 || CPE1) is associated with the percolating inter-particle matrix network. At the ultra-low water-to-binder ratios characteristic of UHPC (below 0.20), the large capillary porosity that dominates the impedance response of ordinary cement paste is largely eliminated, and the dominant

resistive phase of the matrix network is the densely packed boundary between unreacted precursor grains (Olson et al., 1995; Sant et al., 2008). The second arc (R2 || CPE2) is associated with the gel pore network and the resistive layer formed by the principal reaction product: C-S-H for REF and C-(N,K)-A-S-H for GEO (Song, 2000; Provis and Deventer, 2014). The physical correspondence between these elements and the UHPC microstructure is summarized in Figure 2-6.

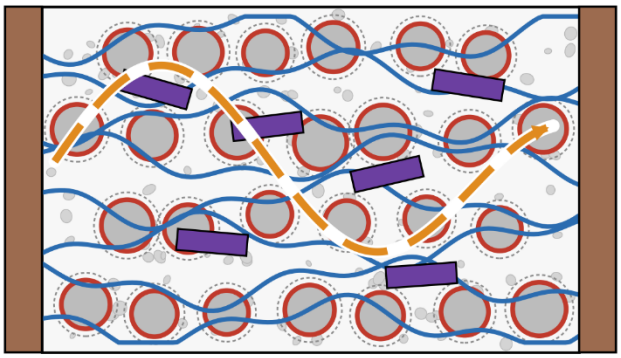

Figure 2-6: Physical interpretation of the equivalent circuit elements, mapped onto a cross-section of the UHPC microstructure between the electrodes.

2.2.4.2 Stage-dependent topology for REF

For REF, a stage-dependent circuit topology was adopted based on the qualitative evolution of the Nyquist spectra. During early hydration (Days 1, 2, 5, and 7), a two-arc topology Rs + (R1 || CPE1) + (R2 || CPE2) + Ws (equation 2.4) is sufficient to reproduce the measured response within the goodness-of-fit thresholds defined in Section 2.2.5. From Day 10 onward, a third arc emerged in the Nyquist plots at intermediate frequencies, and the topology was extended to Rs + (R1 || CPE1) + (R2 || CPE2) + (R3 || CPE3) + Ws (equation 2.5). The third arc is attributed to the progressive development of an electrochemical double layer at the steel fiber-matrix interfacial transition zone, where the densifying C-S-H gel establishes intimate electrical contact with the uncoated fiber surface (Torrents et al., 2000; Suryanto et al., 2016). The timing of this topology transition is consistent with the percolation threshold of the C-S-H gel network reported at 7 to 10 days for Portland cement systems at ambient temperature (Christensen et al., 1996; Sant et al., 2008).

The series arrangement of the elements follows the physical current path from one electrode to the other: through the pore solution (Rs), across the inter-particle grain boundaries (R1 || CPE1), through the gel layer (R2 || CPE2), and, from Day 10 onward, across the fiber-matrix double layer (R3 || CPE3), before the long-range ionic diffusion captured by the finite-length Warburg element (Ws). The two REF topologies are shown in Figure 2-7.

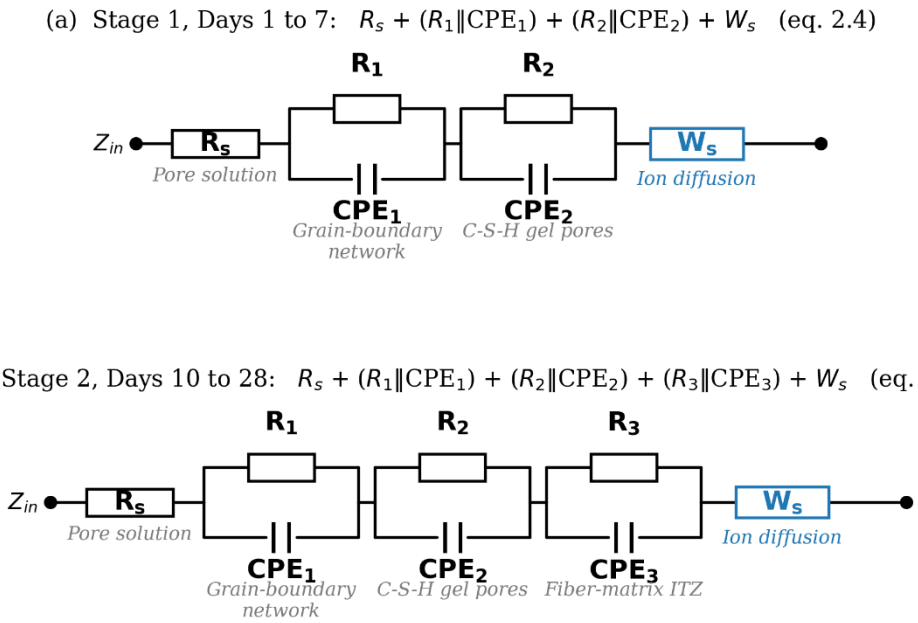

Figure 2-7: Equivalent circuit topologies adopted for REF. (a) Stage 1, Days 1 to 7, two arcs with a finite-length Warburg (equation 2.4). (b) Stage 2, Days 10 to 28, three arcs with the interfacial arc added (equation 2.5).

2.2.4.3 Single-stage topology for GEO

For GEO, a single-stage topology Rs + (R1 || CPE1) + (R2 || CPE2) + W (equation 2.6) was applied across all eight measurement ages. The absence of a third arc throughout the 28-day window admits four concurrent explanations, which the present experiment cannot separate. The first is the fiber population. The third arc is assigned to the double layer that forms where the gel makes intimate electrical contact with an uncoated steel surface, and 60 weight percent of the GEO fiber population carries rubber residue retained from tire recovery, an insulating layer that would suppress precisely that response. The remaining three are properties of the binder. The lower overall impedance magnitude of the GEO matrix limits the resolution of additional features close to the noise floor. The alkali-dominated pore solution produces ionic conductivities one to two orders of magnitude higher than mature Portland cement pore solutions, reducing the contrast between the bulk pore solution and the fiber-matrix interface. And the slower polycondensation kinetics of C-(N,K)-A-S-H relative to early-age C-S-H precipitation would delay any fiber-matrix arc beyond the 28-day observation window (Wang and Scrivener, 1995; Provis and Deventer, 2014).

Distinguishing the fiber explanation from the three binder explanations would require a GEO series cast with the virgin fiber population, which is identified as a perspective in Section 2.5. The adequacy of the single-stage GEO topology is verified by the goodness-of-fit metrics reported in Section 2.3.5 and by the Kramers-Kronig consistency check applied to the corrected spectra. The GEO topology is shown in Figure 2-8.

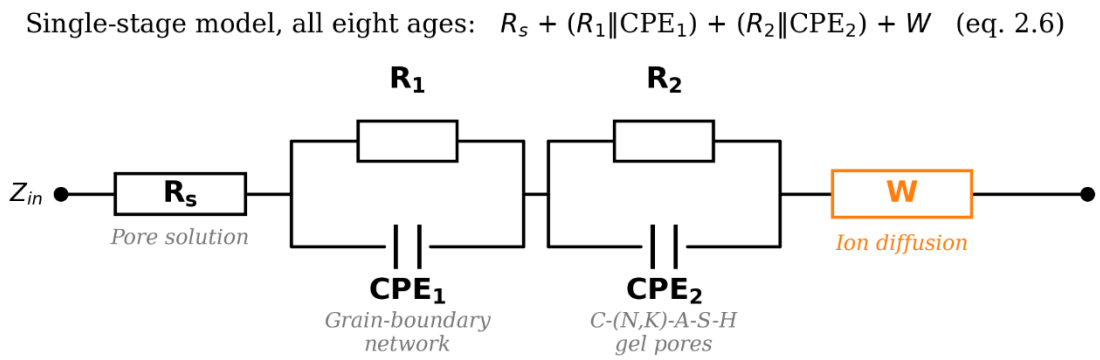

Figure 2-8: Equivalent circuit topology adopted for GEO. Single-stage, two arcs with a semi-infinite Warburg (equation 2.6), applied at all eight ages. No third arc is resolved at any age.

2.2.4.4 Alternative topologies tested and rejected

Alternative topologies were tested before fixing the two adopted models. For REF, a single-stage three-arc topology applied uniformly across Days 1 to 28 was rejected because the third-arc parameters at Days 1 to 7 collapsed onto the second-arc parameters, leaving R3 and CPE3 non-identifiable. A two-arc topology applied uniformly across Days 10 to 28 was rejected because it left a systematic residual structure at intermediate frequencies that the two-arc form cannot reproduce at any parameter set. For GEO, a two-stage topology mirroring REF was tested and rejected because the second stage produced R3 values below the noise floor and CPE3 magnitudes outside the physical bound. A three-arc topology with two interfacial arcs and no Warburg element was also rejected because it produced spurious high-frequency arcs at the longest curing ages. The selection of the two adopted topologies therefore satisfies the three concurrent requirements introduced in Section 2.1.1: numerical goodness-of-fit threshold met, fitted parameters within physical bounds, and competing topologies rejected on identifiability or bound-violation grounds.

2.2.5 CNLS fitting procedure

2.2.5.1 Weighted least-squares objective

Equivalent circuit parameters were extracted from the corrected impedance spectra by complex nonlinear least-squares (CNLS) fitting implemented in MATLAB. The optimization minimizes the sum of squared weighted complex residuals

$$S = \sum_{i} [w_i^2 \, |Z_{meas}(f_i) - Z_{model}(f_i)|^2] \quad \textbf{(2.9)}$$

where the proportional weight $w_i = 1 / |Z_{meas}(f_i)|$ is applied to both the real and imaginary components simultaneously. The proportional weighting scheme ensures an equal relative contribution from all frequency decades to the residual sum, preventing the low-frequency high-impedance region from dominating the fit at the expense of the high-frequency arcs. Equal relative weighting is the standard choice for cementitious systems whose impedance

varies by three to four orders of magnitude across the measurement window (Van Westing et al., 1994).

2.2.5.2 Logarithmic parameterization

To improve the numerical conditioning of the optimization, all positive-definite circuit parameters (Rs, Ri, Qi, Rw, W) were optimized in logarithmic space. The CPE dispersion exponents ni were optimized in linear space because they are dimensionless and confined to a narrow physical band, and a logarithmic transform on a bounded variable adds no conditioning benefit. The choice of logarithmic space also reflects the physical fact that the parameters in question span several orders of magnitude across the eight curing ages, while the ni exponents move within a narrow band.

2.2.5.3 Levenberg-Marquardt solver and evolutionary chaining

The Levenberg-Marquardt algorithm was used as the nonlinear solver through MATLAB's lsqnonlin function, with the optimization tolerance set to a relative parameter change of 10^{-8} and a maximum of 5000 function evaluations per fit. Initial parameter estimates at Day 1 were determined by visual inspection of the Nyquist and Bode plots, guided by the physical element assignments described in Section 2.2.4. For all subsequent ages, an evolutionary chaining strategy was adopted: the converged parameter set from age t serves as the initial estimate for age t + 1. This approach reduces the sensitivity of the optimizer to local minima arising from the non-convexity of the CNLS objective function, enforces continuity of the fitted parameter trajectories across curing ages, and reflects the continuous and irreversible nature of cement hydration and geopolymer polycondensation. For REF, the topology transition from the two-arc Stage 1 (Days 1 to 7) to the three-arc Stage 2 (Days 10 to 28) was handled by initializing the Day 10 fit with the converged Day 7 Stage 1 parameters for Rs, R1, CPE1, R2, CPE2, and Rw, while R3 and CPE3 are seeded from the shoulder emerging in the Day 10 Nyquist plot. This initialization protocol preserves the continuity of the Stage 1 parameters across the topology change.

2.2.5.4 Parameter constraints and known saturation artifacts

Physical constraints were imposed throughout the optimization. All resistances and CPE magnitudes were constrained to strictly positive values, and the CPE dispersion exponents to the physically admissible interval between the Warburg-like limit and the ideal-capacitor limit. Perturbation testing of the converged fits, reported in Section 2.3.8, confirms that no exponent reached a limit of its interval at any age in either system: every fitted exponent sits at an interior minimum of the objective function. Several converged values fall on round numbers, which reflects the convergence tolerance applied to the exponents rather than any constraint.

Two constraints did bind and produce saturation artifacts in the reported parameter trajectories:

First, an upper bound on Rs of 500 Ω is reached in the REF fit from Day 5 onward, where six consecutive fits returned the bound value of exactly 500 Ω. The consequences are developed in Section 2.3.6, where the solution resistance is shown to be an extrapolated rather than a measured quantity in both systems.

Second, in the three-arc Stage 2 topology adopted for REF at Days 10 to 28, the exponents n1 and n2 were held fixed at 0.88 rather than fitted, in order to keep a 12-parameter model well-conditioned, leaving 10 of the 12 parameters free. No REF exponent trajectory is therefore available beyond Day 7.

2.2.5.5 Acceptance criteria for fitted spectra

Fitting quality at each age was assessed by two complementary metrics introduced in Section 2.1.1: the coefficient of determination R2 computed on the complex impedance, and the mean relative error MRE defined in equation (2.7). Both are evaluated over the full measured spectrum of 401 frequency points, including the band above 1 MHz that carries the parasitic inductance contribution and that the weighting scheme suppresses in the fit itself. A fit is considered acceptable when $R2 > 0.99$ and $MRE < 5\%$. The maximum relative error per spectrum is also reported alongside the mean relative error in Section 2.3.5. Because the metrics span the full spectrum while the fit is dominated by the band below 1 MHz, the maximum relative error is expected to fall in the inductance band and to exceed the mean by a wide margin. It is reported as a diagnostic of where the residual sits rather than as an acceptance criterion

2.2.5.6 Kramers-Kronig pre-validation by the Lin-KK method

Before the CNLS fitting is applied, the corrected spectra were subjected to a Kramers-Kronig consistency check using the linear Kramers-Kronig method of Boukamp (1995), in the robust formulation of Schönleber et al. (2014) (the Lin-KK method). The Lin-KK test fits a sequence of RC circuits to the measured spectrum and reports the residuals in real and imaginary components separately. The criterion adopted here is stated on the mean absolute residual, which is required to remain below 2% across the fit band. Maxima are reported descriptively together with their frequency localization rather than as pass or fail, because they are isolated points at the band edges where the Voigt expansion loses support and are not indicative of a causality violation. This is a stricter test than a 5 or 10% bound applied to isolated maxima, and it is applied to the more meaningful statistic.

For all 16 spectra reported in this chapter, two systems times eight ages, the mean residuals lie between 0.22 and 1.08%, so every spectrum passes with at least twofold margin. The detailed Lin-KK residual tables are presented in Section 2.3.5.

2.3 Results

This section reports the electrochemical impedance characterization of REF and GEO across the eight curing ages, benchmarked on companion specimens cast from the same batches and cured under identical ambient conditions (Section 2.2.2). Section 2.3.1 recapitulates the microstructural baseline established in Chapter 1 (pore network, pore solution chemistry, and gel composition) that conditions the impedance interpretation, and Section 2.3.2 reports the compressive strength evolution of the two systems over the same eight ages, which serves as the dependent variable for the correlation analysis. Sections 2.3.3 to 2.3.5 then present the measured spectra and their fitting: the Nyquist evolution (Section 2.3.3), the Bode evolution (Section 2.3.4), and the quality of the complex nonlinear least-squares fit together with its Kramers-Kronig validation (Section 2.3.5). Sections 2.3.6 to 2.3.9 develop the extracted equivalent-circuit parameters one family at a time, tracing the temporal trajectory of each and interpreting it against the microstructural processes specific to each binder: the solution resistance (Section 2.3.6), the charge-transfer resistances (Section 2.3.7), the constant-phase-element exponents (Section 2.3.8), and the Warburg diffusion element (Section 2.3.9). Section 2.3.10 evaluates the correlation between the EIS parameters and compressive strength and identifies the optimal strength indicator for each system. Throughout, the contrast between REF and GEO in the bulk parameters is read as an effect of binder chemistry, since the granular skeleton, the fiber dosage, and the curing regime are held constant between the two systems. The fiber population is not, and the parameters affected by that difference are identified where they arise (Section 2.2.1).

2.3.1 Microstructural baseline

Before the impedance results are presented, the microstructural baseline that grounds their interpretation is recapitulated from Chapter 1. The full mercury intrusion porosimetry data, the XRD Rietveld refinement, and the SEM-EDS analysis on which this baseline is built are reported in Chapter 1 (Section 1.5.7), on specimens cast from the same optimized GEO mix used here.

Three numerical facts established in that chapter condition the EIS interpretation of the present chapter and are restated for clarity.

First, the pore network of GEO is approximately two orders of magnitude coarser than REF at comparable total intruded porosity, as measured by MIP at 28 days. The dominant resolved pore-size peak is 6.2 nm for REF and approximately 700 nm for GEO. Both values sit at a limit of the joint intrusion window, the fine limit for REF and the coarse limit for GEO, so they rank the two pore networks against each other rather than measure a critical pore diameter in either (Chapter 1, Section 1.5.7). The 700 nm peak of GEO is characteristic of the mesoporous network of slag-based geopolymers, in which the C-(N,K)-A-S-H gel envelops larger residual capillary voids, while the 6.2 nm peak of REF is characteristic of the gel-pore network of mature C-S-H. The water-accessible porosity is 4.80% for REF and

8.25% for GEO, and the mean apparent gas permeability differs by a factor of approximately 22 between the two systems, 2.22×10^{-17} m² for REF against 4.96×10^{-16} m² for GEO. Neither permeability series followed Klinkenberg behavior, so these are apparent rather than intrinsic values and are used here only as a ranking. Taken together, these pore-network metrics predict that the long-range ion diffusion features of the impedance spectrum should be substantially faster for GEO than for REF, and that the Warburg formulation appropriate for GEO is the semi-infinite limit rather than the finite-length limit adopted for REF.

Second, the pore solution chemistry of the two systems is structurally different. REF is buffered by the dissolution of portlandite $Ca(OH)_2$ and contains predominantly Ca^{2+} and OH^- species. GEO contains no portlandite, none being detected by XRD, and retains a significant fraction of Na^+ and K^+ from the activator solution. The bulk alkali content measured by EDS in Chapter 1 is 7.3 weight percent K and 3.5 weight percent Na for GEO, against 0.6 and 0.5 weight percent for REF (Section 1.5.7). Since the gel-region EDS returns K/Si and Na/Si of approximately 0.20 each, the excess bulk potassium is not bound in the gel framework and is therefore carried in the pore solution, which makes K^+ the principal mobile alkali of the GEO system. The higher ionic strength of the GEO pore solution predicts a lower solution resistance Rs for GEO than for REF at comparable maturity. The extent to which the present measurements can test that prediction is set out in Section 2.3.6, where the identifiability limits of Rs are established.

Third, the principal reaction product of REF is semicrystalline C-S-H gel with a calcium-to-silicon ratio Ca/Si of approximately 1.72 from gel-region EDS, while the principal reaction product of GEO is an amorphous C-(N,K)-A-S-H gel with a Ca/Si of approximately 0.39, an Al/Si of approximately 0.21, and K/Si and Na/Si of approximately 0.20 each. Both Na and K are bound in the GEO gel framework. The amorphous fraction of GEO is 77 weight percent on a reacted-binder basis, which is an upper bound, since XRD cannot distinguish reacted gel from unreacted glassy precursor. This dominant amorphous fraction is consistent with the leading role of the gel pore network in the overall electrochemical response. These three facts, the pore network geometry, the pore solution chemistry, and the gel composition, are the structural anchors against which the impedance trajectories presented in Sections 2.3.3 to 2.3.9 are interpreted.

2.3.2 Compressive strength evolution at the eight EIS ages

The compressive strength of the companion prisms was measured at each of the eight curing ages on six half-prism specimens per age per system, following the EN 196-1 procedure described in Section 2.2.2. The results are reported in Figure 2-9 as mean and standard deviation and span the full 28-day window. The REF system reached a 28-day compressive strength of 165 ± 4 MPa, and the GEO system reached 152 ± 5 MPa. Both systems exceeded the NATURSEA-PV 28-day target of 130 MPa established in Chapter 1, with margins of 27% (REF) and 17% (GEO). The compressive strength values across all

eight ages are shown in Figure 2-9. It is this prism-half series, measured on the companion specimens cast from the same batches as the EIS prisms, that is correlated with the impedance parameters in Section 2.3.10.

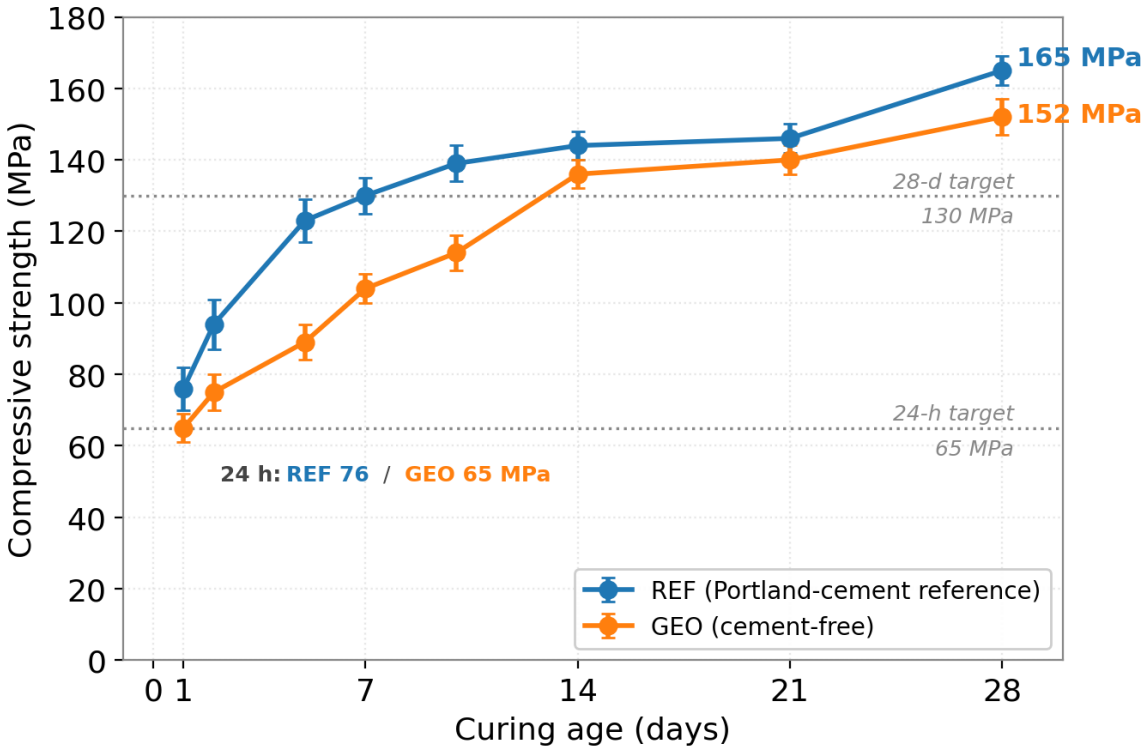

Figure 2-9: Compressive strength of REF (blue squares) and GEO (orange diamonds) over the eight EIS ages. Error bars are one standard deviation on six half-prisms per age per system.

Four kinetic features of the compressive strength trajectories are relevant to the interpretation of the impedance evolution that follows.

First, both systems reached the NATURSEA-PV 24-hour target of 65 MPa at Day 1, with REF at 76 ± 6 MPa and GEO at 65 ± 4 MPa. The early dominance of REF over GEO of approximately 17% at Day 1 reflects the rapid hydration kinetics of the high-alite Portland cement clinker, which produces a significant fraction of C-S-H gel within the first 24 hours. The slower early strength gain of GEO reflects the slower kinetics of alkali-activation of slag and silica fume under ambient curing, in which the dissolution of the precursor and the polycondensation of the C-(N,K)-A-S-H gel proceed in parallel and require more time to develop the connected gel network.

Second, the REF strength gain followed a smooth quasi-logarithmic trajectory from Day 1 to Day 21, with the strength increasing from 76 MPa to 146 MPa over this window. The standard deviation of REF compressive strength rose from 6 MPa at Day 1 to 7.5 MPa at Day 2, then fell steadily to 4 MPa from Day 21 onward, the early peak reflecting the sensitivity of the measurement to small differences in hydration state while the matrix is still developing, and the later decline reflecting the convergence of that state across the three companion prisms as densification proceeds. The corresponding trajectory for GEO from Day 1 to Day 21 increased from 65 MPa to 140 MPa, with a slightly higher relative

variability that decreased from a coefficient of variation of 6% at Day 1 to 3% at Day 21. The GEO trajectory showed a more pronounced acceleration between Day 7 (104 MPa) and Day 14 (136 MPa), consistent with a step in the densification of the C-(N,K)-A-S-H gel network in this age window, a feature that is revisited in Section 2.3.7 when the R2 trajectory is presented.

Third, both systems showed a substantial strength gain between Day 21 and Day 28. The REF strength increased from 146 to 165 MPa (13% gain over 7 days), and the GEO strength increased from 140 to 152 MPa (9% gain over the same window). The Day 28 acceleration of REF is consistent with the late pozzolanic reaction of silica fume, which continues past Day 21 as the calcium hydroxide produced by primary cement hydration is progressively consumed by the silica-fume secondary reaction to form additional C-S-H gel (Gu et al., 1993; Taylor, 1997). The Day 28 acceleration of GEO is consistent with the continued slow polycondensation and densification of the C-(N,K)-A-S-H gel as residual slag particles continue to dissolve and contribute to the gel network beyond Day 21 (Wang and Scrivener, 1995). Both acceleration mechanisms are slow chemical processes that operate over weeks under ambient curing and that the eight-age EIS schedule of this chapter is designed to resolve.

Fourth, the REF and GEO strength curves converged over the 28-day window, with the REF-to-GEO ratio decreasing from 1.17 at Day 1 to 1.09 at Day 28, a residual difference of 9%.

2.3.3 Nyquist evolution

The Nyquist spectra of REF and GEO over the eight curing ages are presented in Figure 2-10 and Figure 2-11, and overlaid on a common age-by-age basis in Figure 2-12. Both systems share one qualitative trend: the impedance locus expands systematically toward higher real-axis values as curing advances, reflecting the progressive densification of the pore network and the reduction in ionic mobility as reaction products occupy the pore space (Gu et al., 1992; Christensen et al., 1994; Cabeza et al., 2002). Beyond this common direction of travel, the two systems differ in three respects that the remainder of this section develops in turn: the absolute impedance magnitude, the morphology of the spectrum, and the topological evolution of the equivalent circuit required to describe it.

In every panel of Figures 2-10 to 2-12, the markers are the measured impedance and the continuous line is the model response, computed from the equivalent circuit assigned to each system in Section 2.2.4 (equation 2.4 or 2.5 for REF, equation 2.6 for GEO) and evaluated at the parameter set returned by the complex nonlinear least-squares fit of Section 2.2.5. The full fitted parameter values for all eight ages are reported in the parameter-trajectory analysis of Sections 2.3.6 to 2.3.9. Goodness of fit is summarized here by the coefficient of determination quoted in each panel title. The formal Kramers-Kronig consistency check and the residual analysis that justify the fitting window are reported in Section 2.3.5. The

measured response above approximately 1 MHz carries a parasitic lead-inductance contribution that the equivalent circuit does not represent (Section 2.2.3). These points were retained in the fit and in the goodness-of-fit statistics.

2.3.3.1 Nyquist evolution of REF

At Day 1, the REF spectrum (Figure 2-10) displayed a single shallow depression followed by a rising diffusion tail, with the locus reaching approximately 2 kΩ on the real axis. The two-arc topology was required by the fit rather than resolved by eye at this age. This early-age morphology is consistent with a well-connected capillary pore network and a nascent C-S-H gel that has not yet percolated (Christensen et al., 1994; Olson et al., 1995). The two-arc model of Stage 1 ($Rs + R_1 \parallel CPE_1 + R_2 \parallel CPE_2 + W_s$, equation 2.4) reproduced the measured locus with a coefficient of determination of 0.9996 at Day 1, confirming that two relaxation processes are sufficient at this age.

Between Days 1 and 7, the real-axis span increased by approximately one order of magnitude, reaching on the order of 35 kΩ at Day 7. This expansion is driven by the rapid consumption of mixing water and the formation of C-S-H gel, which displaces the conductive pore solution and raises the resistance of every conduction path through the matrix (Gu et al., 1992, 1993). Throughout this window the two-arc topology remained adequate, with the coefficient of determination staying above 0.998 at every age (0.9987, 0.9994, and 0.9993 at Days 2, 5, and 7 respectively).

A qualitative change in morphology occurred at Day 10. A third arc emerged on the low-frequency side of the locus, and the two-arc model no longer reproduced the measured response without systematic residuals. The topology was therefore extended to the three-arc model of Stage 2 (Rs + R1 ∥ CPE1 + R2 ∥ CPE2 + R3 ∥ CPE3 + Ws, equation 2.5), which reproduced the Day 10 locus with a coefficient of determination of 0.9995. The characteristic frequency of the new arc is 4.2 kHz at Day 10, falling to 801 Hz at Day 28, which places it below both existing arcs at every age and establishes it as a distinct relaxation rather than a reparameterization of the second.

The onset at Day 10 coincides with the C-S-H gel percolation threshold reported at 7 to 10 days for Portland systems at ambient temperature (Christensen et al., 1996; Sant et al., 2008). On that basis the arc is interpreted as the electrochemical double layer at the steel fiber-matrix interfacial transition zone, which becomes electrically resolvable once the densifying gel establishes intimate contact with the fiber surface (Torrents et al., 2000; Suryanto et al., 2016). This interpretation is contingent on the fiber population, and the two systems do not share one. REF carries virgin steel fiber and GEO carries the recycled blend described in Section 2.2.1, so the appearance of the arc in REF and its absence in GEO cannot be assigned to binder chemistry on the present evidence. The emergence of the arc at Day 10 and its subsequent growth are observations. The assignment to the fiber-matrix

interface is an interpretation, and Section 2.2.4 sets out the four explanations the experiment cannot separate.

From Day 10 to Day 28 the third arc grew progressively and the total real-axis span reached 178 kΩ at Day 28, with the coefficient of determination remaining at or above 0.999 across all eight ages (0.9995, 0.9995, 0.9993 and 0.9992 at Days 10, 14, 21 and 28). The frequency ordering of the three arcs is preserved throughout, with the first arc above the second and the second above the third at every Stage 2 age, so each fitted resistance corresponds to the same physical feature across the series. The smooth, strictly rightward growth of the locus is consistent with the unidirectional densification of Portland cement hydration and supports the adequacy of the stage-dependent topology (Gu et al., 1992; Christensen et al., 1994).

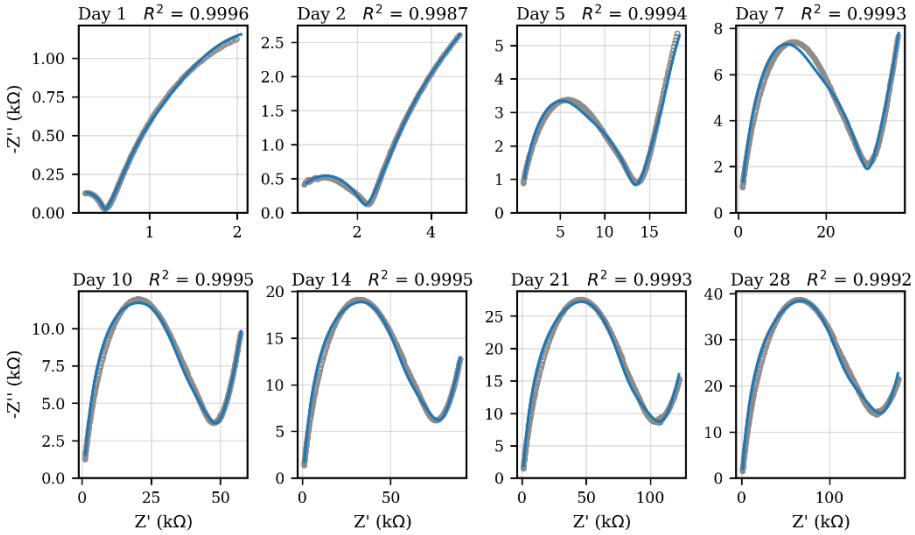

Grey circles: measured. Blue line: CNLS-fitted model. Days 1 to 7: Stage 1, two-arc model (eq. 2.4). Days 10 to 28: Stage 2, three-arc model (eq. 2.5).

Figure 2-10: Nyquist evolution of REF over the eight curing ages, with the CNLS-fitted model overlaid. Gray circles are the measured spectra and the blue line the fitted model. Stage assignment and R^2 are given per panel.

2.3.3.2 Nyquist evolution of GEO

The GEO spectra (Figure 2-11) differ from REF in two defining respects:

First, the impedance magnitude was markedly lower at every age. At Day 1 the real-axis span reached only about 230 Ω, against approximately 2 kΩ for REF, and at Day 28 the maximum real-axis value was on the order of 2.5 kΩ, against approximately 160 kΩ for REF. The contrast was therefore close to one order of magnitude at Day 1 and widened to nearly two orders by Day 28. This lower and more slowly growing magnitude reflects the high ionic conductivity of the alkali-dominated pore solution of GEO, in which residual Na^+ and K^+ from the activator sustain a conductive pore fluid that the densifying C-(N,K)-A-S-H gel does not fully obstruct (Song, 2000; Provis and Deventer, 2014).

Second, the single-stage two-arc topology (Rs + R1 ∥ CPE1 + R2 ∥ CPE2 + W, equation 2.6) was maintained across all eight ages without any topological transition. No third arc emerged at any age.

Four explanations are consistent with this observation and the present experiment cannot separate them:

- The recycled fraction of the GEO fiber population, which carries retained rubber residue at the interface where the REF arc is assigned
- The low overall impedance magnitude of the geopolymer matrix, which limits the resolution of an additional interfacial contribution above the dominant pore-solution conduction
- The high ionic conductivity of the alkali pore solution, which reduces the contrast between bulk and interface
- The slower polycondensation kinetics of the gel, which would delay any such arc beyond the observation window (Berrocal et al., 2018).

The semi-infinite Warburg element, rather than the finite-length form adopted for REF, was retained throughout, consistent with the faster and less bounded ion diffusion expected in the high-mobility alkali pore solution (Section 2.2.4).

Fit quality for GEO was high from Day 5 onward, with the coefficient of determination at or above 0.995 at every age beyond Day 2 (0.9976, 0.9973, 0.9960, 0.9951, and 0.9951 at Days 5, 7, 10, 21, and 28). It was lower at the two earliest ages, 0.9922 at Day 1 and 0.9835 at Day 2. The reduced early-age fit quality is attributable to the compressed impedance response: at low absolute magnitude, the arcs occupy a narrow region of the complex plane and their resolution is more sensitive to measurement noise (McCarter et al., 2003).

A further feature, visible in the Day 14 and Day 21 panels, is a slight non-monotonic perturbation of the first arc, in which the arc amplitude decreases marginally before recovering. This behavior is absent in REF and has direct consequences for the choice of strength predictor in Section 2.3.10. It is examined there alongside the full parameter trajectories. A second feature of the GEO fits is that the frequency ordering of the two arcs is not preserved across the series. At Days 7 and 10 the first arc lies above the second in characteristic frequency, whereas at the remaining six ages the ordering is reversed. The R1 and R2 trajectories reported in Section 2.3.7 are therefore indexed by fitted position rather than by physical identity, and are read as a pair rather than individually. Neither is used as a strength indicator for GEO.

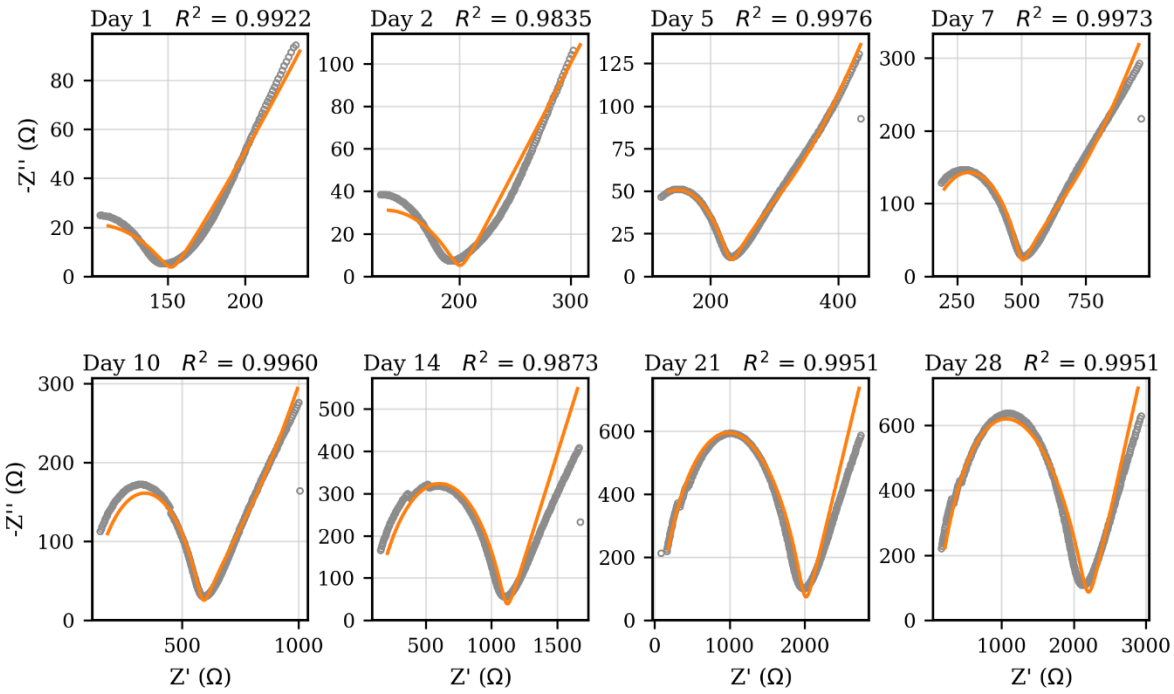

Grey circles: measured. Orange line: CNLS-fitted model. Single-stage two-arc model (eq. 2.6) at all eight ages.

Figure 2-11: Nyquist evolution of GEO over the eight curing ages, with the CNLS-fitted model overlaid. Gray circles are the measured spectra and the orange line the fitted model. R^2 is given per panel.

2.3.3.3 Cross-system comparison

Figure 2-12 overlays the REF and GEO loci age by age, with the REF impedance read on the left and lower axes in kΩ and the GEO impedance on the right and upper axes in Ω. The dual-axis presentation is necessary precisely because the two systems differ by one to two orders of magnitude in impedance, and a shared linear axis would compress the GEO locus to an unreadable point near the origin. Read in this way, the figure consolidates the three contrasts established above. The REF locus is one to two orders larger and grows the faster of the two. The REF locus acquires its third arc from Day 10 while the GEO locus retains two resolved arcs plus a diffusion tail throughout. And the two systems converge in neither magnitude nor morphology over the 28-day window.

The Nyquist evolution answers the first half of the chapter research question in the affirmative. The pore network and pore solution chemistry of GEO produce an electrochemical signature distinguishable from REF not by a single parameter but by the joint behavior of magnitude, morphology, and topology. The lower magnitude tracks the conductive alkali pore solution and the coarser pore network established in Chapter 1, and the single-stage topology is itself a fingerprint of the system, since the REF topology transition at Day 10 has no counterpart in GEO (Provis and Deventer, 2014). The absence of a resolvable third arc in GEO is part of that fingerprint, but it is a joint property of the binder and the fiber population and is not attributable to the binder alone. Whether these distinguishable signatures also serve as quantitative indicators of strength development, the

second half of the chapter research question, is addressed through the parameter trajectories and the correlation analysis of Sections 2.3.6 to 2.3.10.

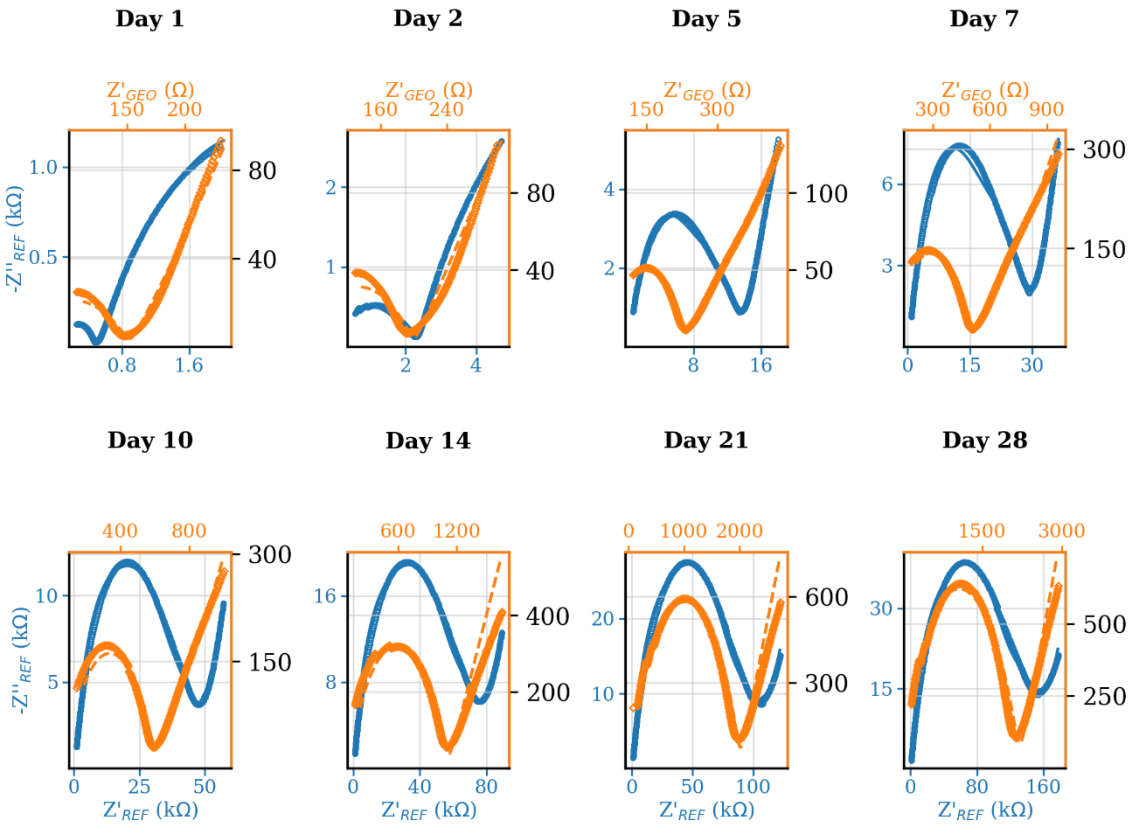

REF (blue): lower and left axes, kΩ. GEO (orange): upper and right axes, Ω.

Figure 2-12: Age-by-age Nyquist comparison of REF and GEO. REF in blue on the lower and left axes, in kΩ, and GEO in orange on the upper and right axes, in Ω.

2.3.4 Bode evolution

The Bode representations of REF and GEO over the eight curing ages are presented in Figure 2-13 (REF) and Figure 2-14 (GEO). Each Bode pair separates the impedance into its frequency-resolved modulus |Z(f)| and phase angle φ(f). The Bode representation is complementary to the Nyquist plots of Section 2.3.3: the Nyquist view emphasizes the morphology of the impedance locus in the complex plane and the order of the relaxations, while the Bode view localizes those same relaxations on the frequency axis and quantifies their migration with curing age (Gu et al., 1992, 1993). For the present chapter, the Bode evolution is the natural representation for two questions that the Nyquist view answers only qualitatively: how the characteristic relaxation frequencies of each system shift with age, and how the high-frequency real-axis intercept Rs evolves at the frequency band where it is most reliably read.

As in Section 2.3.3, the response above approximately 1 MHz, shaded gray in both figures, carries a parasitic lead-inductance contribution that the equivalent circuit does not represent (Section 2.2.3). These points are retained in the fit and in the goodness-of-fit

statistics, and the shading marks the band in which the model is known to be incomplete rather than a band that was removed.

2.3.4.1 Bode evolution of REF

Figure 2-13 presents the Bode response of REF across the eight ages. Three features of the REF evolution stand out. **First,** the low-frequency modulus |Z(4 Hz)| increased by approximately two orders of magnitude across the 28-day window, from on the order of 2 kΩ at Day 1 to on the order of 200 kΩ at Day 28. This widening tracked the rightward growth of the Nyquist locus reported in Section 2.3.3 and reflects the progressive densification of the C-S-H gel network and the closure of the percolating pore network as hydration advances (Gu et al., 1992; Olson et al., 1995).

Second, the high-frequency modulus did not reach a plateau at any age. The real part Z′ continued to decrease across the whole upper decade, falling from 4.2 kΩ at 1 MHz to 1.1 kΩ at 5 MHz at Day 28, and from 417 Ω to 261 Ω at Day 1.

In every one of the 16 spectra of this chapter, the minimum of Z′ occurs at the top frequency of the sweep. The high-frequency real-axis intercept, which is the solution resistance Rs, therefore lies beyond the 5 MHz ceiling of the instrument and is not reached by the measurement. This is consistent with the characteristic frequency of the first REF arc, which is 5.79 MHz at Day 1 and remains above 90 kHz at Day 28: the arc has not closed onto the real axis by the end of the window. What the Bode modulus does provide is a rigorous upper bound on Rs at each age, since Z′ decreases monotonically with frequency and Rs is its limit. Those bounds and their consequences are developed in Section 2.3.6.

Third, and most informative for the kinetic interpretation, the phase response shows a maximum, that is a least negative excursion of φ, whose position migrated by 2.7 orders of magnitude across the eight ages. At Day 1 this maximum sat at 31.9 kHz with a value of −3.05 degrees, reflecting a still-fluid pore network in which long-range ionic transport dominates. It fell to 2.38 kHz by Day 2, 345 Hz by Day 5, and 59.7 Hz by Day 28, where the maximum value had deepened to −5.13 degrees. The phase minima, by contrast, sit at the two edges of the measurement band at every age and are not relaxation features. This downward migration of the phase maximum is the frequency-domain signature of the slowing of charge-storage processes as gel densification reduces the mobility of polarizable species. The same shift, expressed as the migration of the characteristic frequency $f_c = \frac{1}{2\pi(RQ)^{1/n}}$ of each modeled relaxation, is quantified from the fitted parameters in Section 2.3.7 (Christensen et al., 1994).

The qualitative change in the Bode shape between Day 7 and Day 10 also corroborates the topology transition documented in Section 2.3.3. From Day 10 onward, the phase response developed a shoulder at intermediate frequencies (approximately 10^2 to 10^4 Hz) that is absent in the Day 1 to Day 7 traces. This shoulder is the frequency-domain counterpart of the third Nyquist arc and is consistent with the assignment of that arc to the fiber-matrix

interfacial transition zone, subject to the fiber-population qualification of Section 2.3.3 (Torrents et al., 2000; Suryanto et al., 2016).

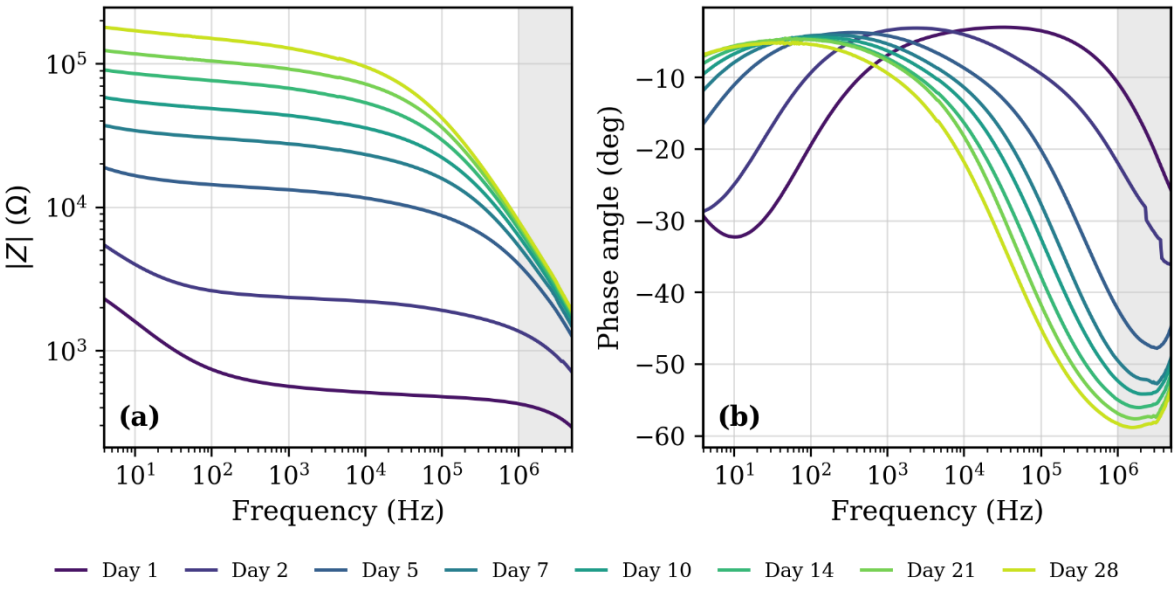

Grey band above 1 MHz: the unmodeled inductive contribution (Section 2.2.3).

Figure 2-13: Bode evolution of REF over the eight curing ages. (a) Impedance modulus |Z(f)| and (b) Phase angle φ(f). Curves run from Day 1 in black to Day 28 in dark red.

2.3.4.2 Bode evolution of GEO

Figure 2-14 presents the Bode response of GEO across the eight ages. The GEO evolution differs from REF on every axis. The low-frequency modulus |Z(4 Hz)| increased from on the order of 220 Ω at Day 1 to on the order of 3.5 kΩ at Day 28, a widening of approximately one order of magnitude, against approximately two orders for REF. The Rs plateau in the 105 to 10^6 Hz band rose from on the order of 150 Ω at Day 1 to on the order of 500 Ω at Day 28. The Rs evolution is therefore visible and continuous in GEO, whereas in REF it is modest relative to the bulk impedance growth. The persistence of a low and slowly evolving Rs in GEO is the direct frequency-domain expression of the alkali-dominated pore solution chemistry established in Chapter 1: the residual K^+ and Na^+ from the activator sustain a conductive pore fluid that the densifying C-(N,K)-A-S-H gel does not fully obstruct (Olson et al., 1995; Provis and Deventer, 2014).

The phase response of GEO shows a markedly different behavior. The principal phase maximum sat at 18.2 kHz at Day 1 and migrated to 1.26 kHz by Day 28, a shift of 1.2 orders of magnitude against 2.7 orders for REF. Its value stayed between −2.0 and −3.1 degrees throughout the 28-day window. The shape of the phase curve broadened with age, with the high-frequency rolloff steepening from −5.7 degrees at 1 MHz on Day 1 to −40.9 degrees at the same frequency on Day 28, but the maximum did not collapse toward the low-frequency end of the spectrum as it did for REF.

Two factors account for this contrast. **First,** the GEO pore solution remains conductive throughout the 28-day window because the activator-derived alkalis are not consumed by

reaction in the way that calcium and hydroxide are consumed in Portland cement hydration. The characteristic frequency of the bulk pore-solution relaxation therefore stays high. **Second,** the polycondensation of C-(N,K)-A-S-H proceeds without producing a discrete gel-percolation transition in the 28-day window, so the second arc, even as it grows in resistance, does not generate the same downward migration of the phase trough that the C-S-H gel imposes on REF (Olson et al., 1995; Provis and Deventer, 2014). The absence of a third arc in the Nyquist plots of GEO is mirrored in the Bode response by the absence of any intermediate-frequency phase shoulder. The GEO phase curve at Day 28 is qualitatively the same shape as at Day 1, only translated downward.

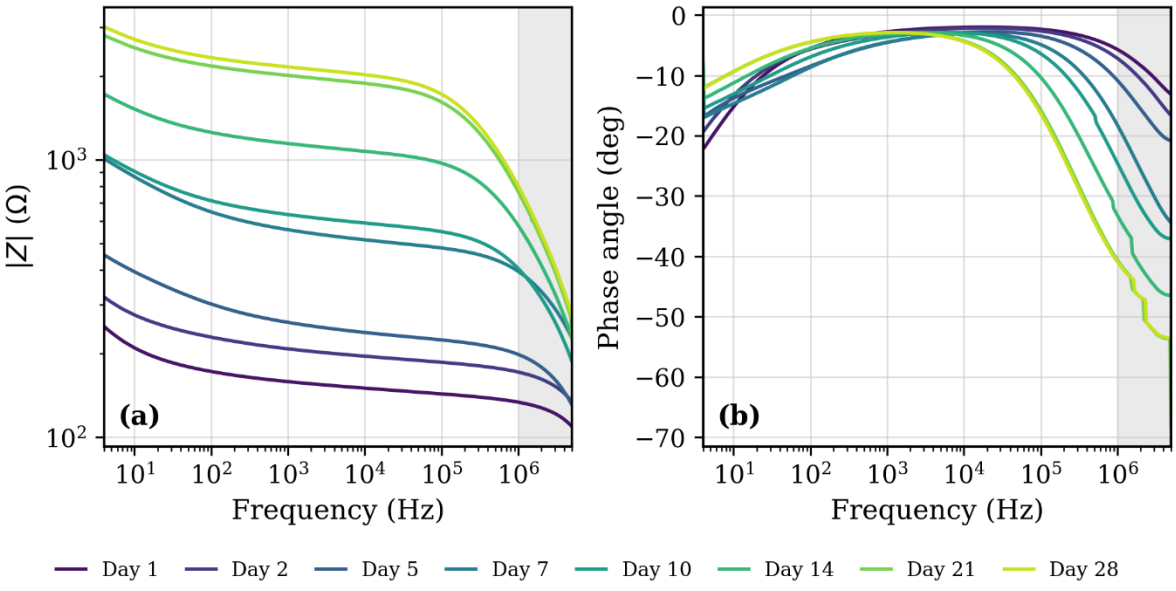

Grey band above 1 MHz: the unmodeled inductive contribution (Section 2.2.3).

Figure 2-14: Bode evolution of GEO over the eight curing ages. (a) Impedance modulus |Z(f)|. (b) Phase angle φ(f).

2.3.4.3 Cross-system comparison

Three contrasts emerge between the REF and GEO Bode trajectories that the Nyquist view of Section 2.3.3 did not resolve quantitatively. **First**, the magnitude of the modulus growth at low frequency: approximately two orders for REF against approximately one order for GEO across the same 28-day window. The REF system widens its impedance range faster than GEO, even though the two systems converge in compressive strength (Section 2.3.2, residual 9% difference at Day 28). The impedance growth and the strength growth therefore decouple in GEO in a way that they do not in REF, a result that is fully developed in the parameter-trajectory analysis of Sections 2.3.6 to 2.3.9 and in the strength correlation of Section 2.3.10.

Second, the migration of the principal phase feature: 2.7 orders of magnitude for REF, 1.2 orders for GEO. This contrast is the clearest single-spectrum kinetic fingerprint of the binder system. For REF, the time constant shifts by 2.7 orders of magnitude as the C-S-H gel densifies. For GEO, the corresponding time constant stays close to its Day 1 value. This

is consistent with the picture, developed in Section 2.3.3, in which the GEO impedance signature is dominated by the alkali-conductive pore solution throughout the 28-day window, while the REF signature progressively shifts from a pore-solution-dominated regime to a gel-controlled regime as hydration consumes the conductive species (Gu et al., 1992; Christensen et al., 1994).

Third, the high-frequency limit is reached in neither system. In all 16 spectra the real part Z' continues to decrease to the top frequency of the sweep, so the real-axis intercept that defines the solution resistance lies beyond the 5 MHz ceiling of the instrument at every age. The two systems differ in how far from that limit the measurement stops. At Day 28 the REF modulus at 5 MHz is 1.1 kΩ against a low-frequency value of 179 kΩ, so the measurement terminates while still two orders above the intercept, whereas the GEO modulus falls from 3.0 kΩ to 164 Ω over the same window and terminates within a factor of a few. The consequence is that the pore-solution contribution is closer to being resolved in GEO than in REF, but is quantified in neither. What the Bode modulus yields at each age is an upper bound on Rs rather than a value, and those bounds are developed in Section 2.3.6.

The Bode evolution, in turn, refines the answer to the first half of the chapter research question. The pore network and pore solution chemistry of GEO produce a Bode signature that is distinguishable from REF not only in absolute magnitude (as established in Section 2.3.3) but also in the frequency-domain kinetics of every relaxation feature: the low-frequency modulus widens an order of magnitude less, and the high-frequency limit, though unreached in both systems, is approached far more closely in GEO. Whether these frequency-domain contrasts also translate into quantitative correlations with strength development is examined in Sections 2.3.6 to 2.3.10.

2.3.5 Fit quality and Kramers-Kronig consistency

Before the fitted parameter trajectories of Sections 2.3.6 to 2.3.9 are presented, the adequacy of the CNLS fit and the causal consistency of the measured spectra are reported. Two complementary tests are applied at every age. **First,** the goodness-of-fit metrics defined in Section 2.2.5, the coefficient of determination R2 computed on the impedance modulus and the mean and maximum relative errors on the real and imaginary parts (MRE and max RE), are reported per age and per system. **Second,** the Kramers-Kronig consistency of each measured spectrum is verified by an independent Lin-KK procedure that fits a series of Voigt elements to the data and reports the residuals as a percentage of the measured impedance magnitude (Boukamp, 1995; Schönleber et al., 2014). The two tests are complementary: the goodness-of-fit metrics quantify how well the assigned equivalent circuit reproduces the data, while the Kramers-Kronig check probes whether the data themselves are physically valid impedance measurements that respect the causality and linearity assumptions of the underlying integral relations (Christensen et al., 1996).

2.3.5.1 CNLS goodness-of-fit

Figure 2-15 reports the CNLS goodness-of-fit metrics for REF. All three metrics are evaluated over the full measured spectrum of 401 frequency points, including the band above 1 MHz that carries the unmodeled inductive contribution, as set out in Section 2.2.5. The mean relative error remained below the 5% acceptance threshold at every age, rising from 1.06% at Day 1 to 4.50% at Day 28 with a single reversal at Day 5, where it fell to 1.53% from 1.74% at Day 2. The coefficient of determination stayed at or above 0.9987 at every age, with the Day 1 fit reaching 0.9996 and the Day 2 fit, the lowest of the eight, reaching 0.9987. The maximum relative error exceeded 5% at every age including Day 1, climbing from 7.5% to 27.9% at Day 28. That the maximum is large while the mean is small is expected under a full-spectrum evaluation, and the next paragraph shows where the maximum sits. On the joint criterion of R2 above 0.99 and mean relative error below 5%, the REF fit is acceptable at every age.

The localization of the maximum relative errors is uniform across the eight ages: in every case the maximum falls in the band above approximately 1 MHz, where the parasitic lead inductance produces a modulus deviation that the equivalent circuit does not represent. The 46 points above 1 MHz constitute 11% of the spectrum, so their contribution to the mean is bounded, but they set the maximum at every age. Restricted to the band below 1 MHz, the maximum relative error falls from 27.9 to 13.4% at Day 28 and from 21.1 to 7.4% at Day 7. The maximum is therefore reported as a diagnostic of where the residual sits rather than as an acceptance criterion.

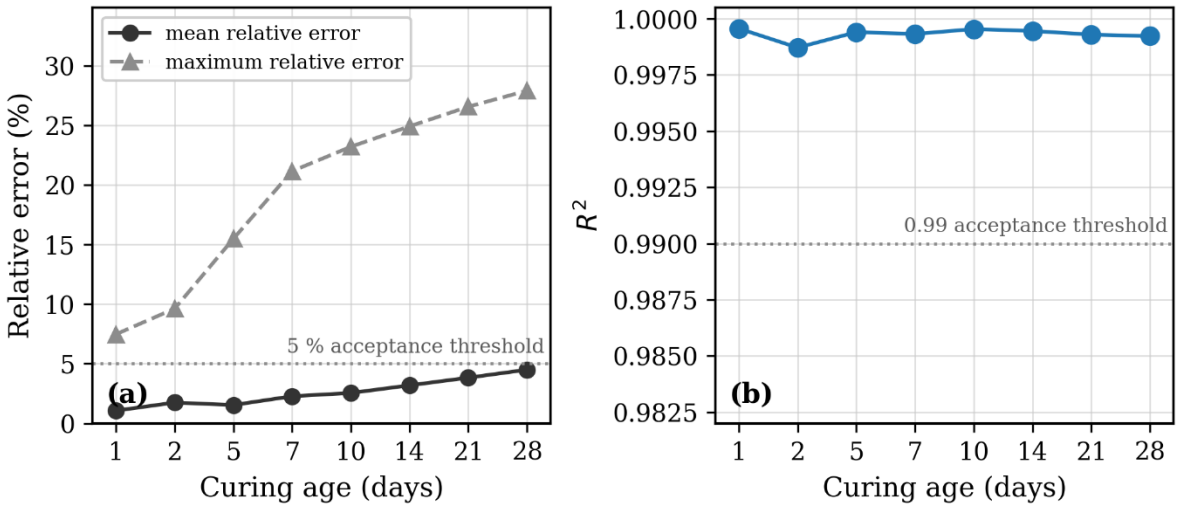

Figure 2-15: CNLS fit quality of REF across the eight curing ages. (a) Mean and maximum relative error per age, with the 5% acceptance threshold as a dashed gray line. (b) Coefficient of determination R2 per age, with the 0.99 threshold as a dashed gray line.

Figure 2-16 reports the same metrics for GEO. The mean relative error remained below 5% at every age, bounded between 1.08% at Day 5 and 3.65% at Day 14. The coefficient of determination varied more across ages than for REF and fell below 0.99 at two ages, 0.9835 at Day 2 and 0.9873 at Day 14. At the six remaining ages it stayed at or above 0.9922 and reached 0.9976 at Day 5. The maximum relative error exceeded 5% at every age and reached

43.0% at Day 21, with the other seven ages bounded between 6.2 and 23.5%. As for REF, these maximum-error points lie predominantly in the high-frequency band.

The two below-threshold ages have a common cause that is independent of the fit statistics. At both Day 2 and Day 14 the first-arc CPE magnitude Q1 is unconstrained by the data. Varying it by a factor of 16 about its converged value changes the sum of squared relative residuals from 0.2655 to 0.2651, a variation in the fourth decimal, and the associated exponent n1 is equally unconstrained (Section 2.3.8).

The characteristic frequency of an R || CPE arc is $f_c = \frac{1}{2\pi(RQ)^{1/n}}$, so a bounded Q1 at these magnitudes places the first arc at 9.2 × 10⁻⁵ Hz at Day 2 and 3.3 × 10⁻⁵ Hz at Day 14, four orders of magnitude below the 4 Hz lower limit of the measurement window. The first arc is therefore not resolved at these two ages, and the fitted R1 and Q1 values are constraint artifacts rather than measurements. This is consistent with the compressed impedance response at Day 2, where the entire Nyquist locus spans approximately 230 Ω, and with the transient perturbation of the first arc visible at Day 14 in Figure 2-11. The mean relative error at both ages remains below the 5% ceiling, 2.47% at Day 2 and 3.65% at Day 14, so the discrepancy is not driven by a small number of grossly misfit points but by an unresolved relaxation. Days 2 and 14 are excluded from the interpretation of the GEO first arc in Section 2.3.7.

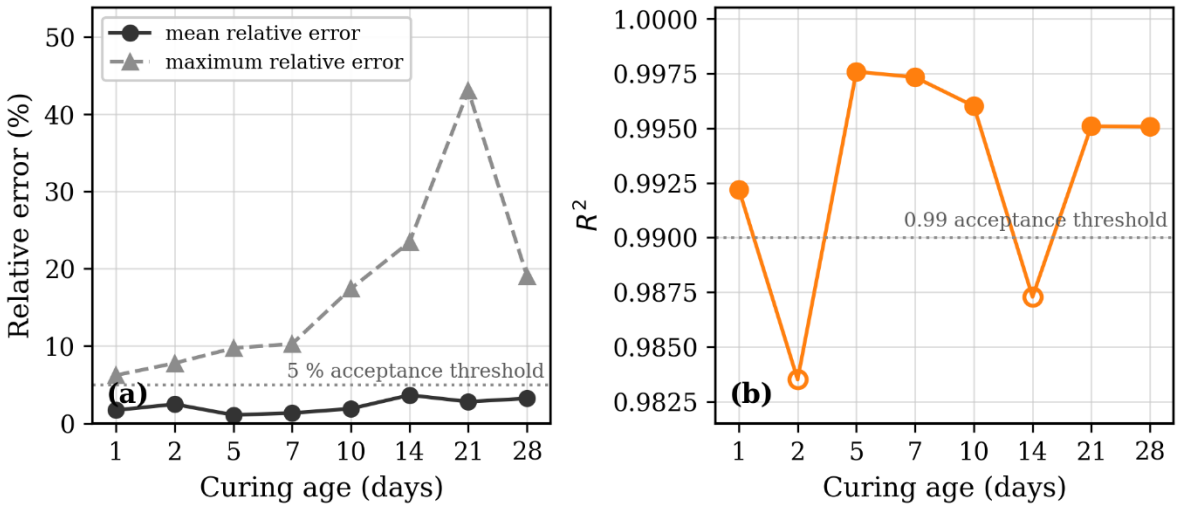

Figure 2-16: CNLS fit quality of GEO across the eight curing ages. (a) Mean and maximum relative error per age, with the 5% acceptance threshold as a dashed gray line. (b) Coefficient of determination R2 per age, with the 0.99 threshold as a dashed gray line.

2.3.5.2 Lin-KK consistency check

Figure 2-17 reports the Kramers-Kronig consistency of the measured REF spectra. The Lin-KK residuals on the real part $\Delta Z'$ and on the imaginary part $\Delta Z''$ are reported as percentages of the measured impedance magnitude across the eight ages. The criterion adopted in this work is stated on the mean absolute residual and requires it to remain below 2% across the fit band (Section 2.2.5). For REF the mean stayed between 0.27% at Day 1

and 1.08% at Day 28, increasing monotonically with curing age and passing the criterion at every age with at least twofold margin.

The maximum residual within the fit band stayed below 5% at Days 1 through 10 and reached 5.5, 7.6 and 9.7% at Days 14, 21 and 28. These maxima are concentrated in a localized feature in $\Delta Z'$ centered near 5×10^5 Hz, at the upper edge of the fit band immediately adjacent to the inductive region, and the residuals outside this feature remained within ±2% at every age. They are reported descriptively rather than as pass or fail, because a maximum taken over a Voigt expansion at the edge of its support is not a test of causality. Judging the validation on the mean rather than on isolated maxima is the stricter of the two available criteria, since a 2% bound on the mean is tighter than the 5 or 10% bounds conventionally applied to maxima and it is applied to the more informative statistic.

Above approximately 10^5 to 10^6 Hz both $\Delta Z'$ and $\Delta Z''$ diverge sharply, with full-range maximum residuals climbing from 3.2% at Day 1 to 62% at Day 28. This divergence is the frequency-domain signature of the parasitic lead inductance described in Section 2.2.3. The equivalent circuit contains no inductive element and the Lin-KK basis is composed of Voigt elements, which cannot represent one either, so the divergence reflects the incompleteness of both representations in that band rather than a violation of causality by the measurement. A series inductance is itself causal and Kramers-Kronig compliant. The Kramers-Kronig consistency of REF is therefore confirmed at every age on the mean criterion, and the excursions of the maximum residual are localized in a narrow band at the upper edge of the fit window and do not affect the lower-frequency parameters that carry the interpretive load of this chapter.

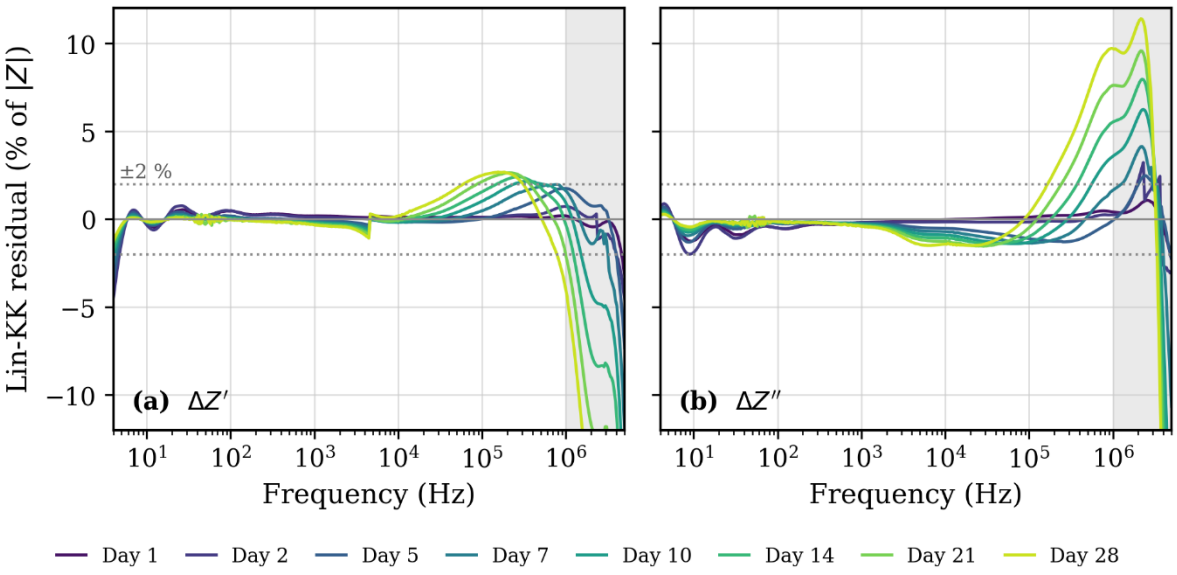

Grey band above 1 MHz: the unmodeled inductive contribution, which the Voigt basis cannot represent either.

Figure 2-17: Kramers-Kronig consistency of REF at the eight curing ages. Lin-KK residuals on the real part $\Delta Z'$ and imaginary part $\Delta Z''$, as percentages of $|Z|$. Dashed lines mark ±2%.

Figure 2-18 reports the equivalent check for GEO. The mean of the absolute Lin-KK residuals within the fit band is markedly tighter than for REF, staying between 0.22% at Day

21 and 0.32% at Day 28 at every age, against 0.27 to 1.08% for REF. The maximum residual within the fit band stayed below 5% at Days 1, 2 and 21, at 5.10, 4.45 and 2.33% respectively, and ranged between 8.0 and 10.8% at the remaining five ages, with the largest excursions at the lowest measured frequencies. These low-frequency excursions are edge effects of the Voigt expansion at the limit of the measurement band rather than inconsistencies of the measured spectrum (Schönleber et al., 2014). Above approximately 10^5 Hz the GEO residuals diverge for the same reason as the REF residuals, and the divergence is more pronounced at Days 14 to 28 than at earlier ages.

Taken together, the Lin-KK validation of GEO is at least as strong as that of REF within the fit band, with mean absolute residuals 3 to 5 times smaller at every age. This tighter envelope is consistent with the lower absolute impedance magnitude of GEO documented in Section 2.3.3: at lower |Z| the relative weight of measurement noise on the residual percentage is smaller, and the Voigt representation captures the spectrum more cleanly. The Kramers-Kronig consistency of GEO is confirmed at every age on the mean criterion.

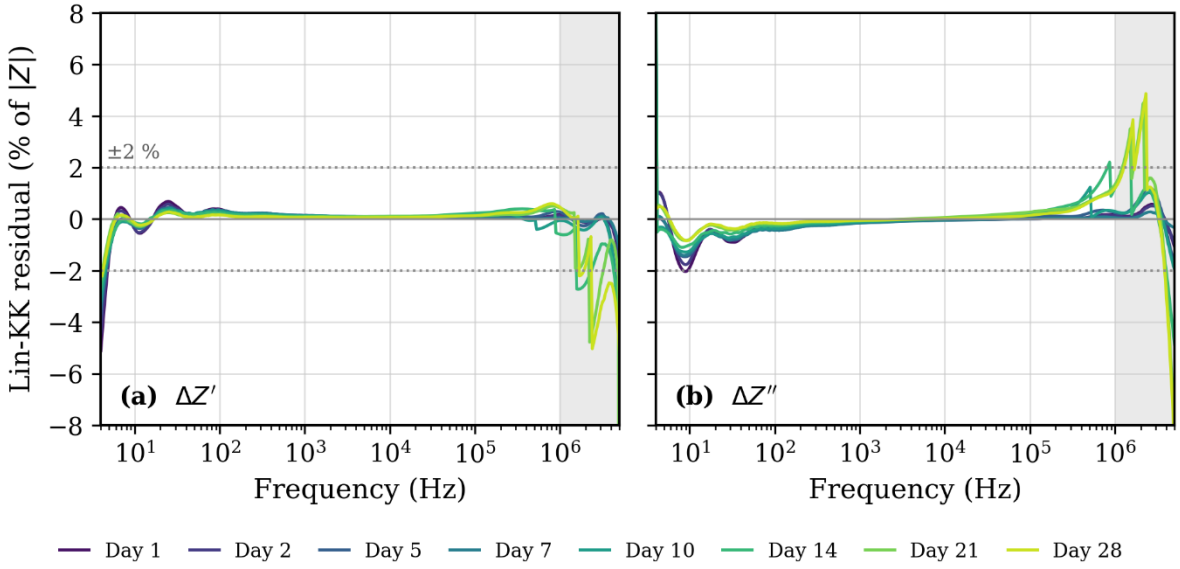

Grey band above 1 MHz: the unmodeled inductive contribution, which the Voigt basis cannot represent either.

Figure 2-18: Kramers-Kronig consistency of GEO at the eight curing ages. Lin-KK residuals on the real part ΔZ′ and imaginary part ΔZ″, as percentages of |Z|. Dashed lines mark ±2%.

2.3.5.3 Synthesis

The two validation tests, applied jointly, support the use of the fitted parameter trajectories of Sections 2.3.6 to 2.3.9 for the cross-system comparison and for the strength correlation of Section 2.3.10. The REF CNLS fit meets the R2 and mean relative error thresholds at every age. The GEO fit meets the mean relative error threshold at every age and the R2 threshold at six of the eight ages, the two exceptions being Day 2 and Day 14, where the first arc lies outside the measurement window and is excluded from interpretation. The Lin-KK check confirms the Kramers-Kronig consistency of every measured spectrum on the mean-residual criterion, with mean absolute residuals below 1.1% for REF and below

0.4% for GEO at every age. The divergence above approximately 10^5 Hz is attributed to a parasitic lead inductance that neither the equivalent circuit nor the Voigt basis represents, and it is confined to a band that carries none of the parameters interpreted in this chapter. The combined validation justifies the parameter-level comparison of REF and GEO across the eight curing ages.

2.3.6 Solution resistance Rs trajectory

2.3.6.1 Methodological note on the CNLS parameter set

Before the fitted parameter trajectories are reported, three limitations of the CNLS optimization documented in Section 2.2.5 are stated once and applied to all parameter-trajectory sections of this chapter.

The first concerns the constraints applied during optimization. All resistances and CPE magnitudes were constrained to strictly positive values and the CPE exponents to the physically admissible dispersion interval. Perturbation testing of the converged fits (Section 2.3.8) confirms that no exponent reached a limit of that interval at any age, so the fitted exponents are measurements rather than constraints. Two constraints did bind: the solution resistance of REF was capped at 500 Ω, and the Stage 2 exponents n1 and n2 were held fixed at 0.88 rather than fitted, leaving 10 of the 12 Stage 2 parameters free. The consequences of the Rs cap are the subject of the present section.

The second concerns the two GEO ages at which the coefficient of determination falls below 0.99, Day 2 and Day 14. As established in Section 2.3.8, the first-arc parameters at these ages are not constrained by the data at all: the objective function is invariant to a sixteenfold change in Q1 and to the full range of n1. The relaxation the element represents lies four orders of magnitude below the measurement window, so it is not sampled. The GEO first-arc parameters at these two ages are excluded from interpretation throughout the chapter, although they are retained on the plots for visual continuity.

The third limitation is the subject of the present section and concerns the solution resistance of both systems.

2.3.6.2 Identifiability of the solution resistance

The solution resistance is defined as the high-frequency limit of the real part of the impedance, reached once every parallel R || CPE branch has collapsed. Whether a measurement can determine it therefore depends on whether the arcs have closed onto the real axis within the acquisition window.

In all 16 spectra of this chapter the minimum of Z' occurs at the top frequency of the sweep. Z' falls from 4223 Ω at 1 MHz to 1123 Ω at 5 MHz for REF at Day 28, and from 417 Ω to 261 Ω at Day 1, with the same pattern in GEO at every age. The locus has not closed by the end of the window, so the intercept lies beyond the 5 MHz ceiling of the instrument

and Rs is an extrapolated parameter rather than a measured one in both systems and at every age.

The cause is quantitative. The characteristic frequency of an R || CPE arc is $f_c = \frac{1}{2\pi(RQ)^{1/n}}$. For REF the first arc lies at 5.79 MHz at Day 1, above the ceiling, and falls to 90 kHz by Day 28. For GEO the fastest arc lies at 9.12 MHz at Day 1 and at 5.94 and 3.51 MHz at Days 2 and 5, remaining at or above the ceiling for the first three ages and reaching 0.52 MHz by Day 28. In both systems the relaxation that must collapse before Rs is exposed sits at the top of the window or beyond it, and the measurement stops before the collapse is complete.

What the measurement does provide is a rigorous upper bound. Since Z' decreases monotonically with frequency and Rs is its limit, Rs is smaller than the lowest measured Z' at every age: 261, 569, 887, 956, 1048, 1098, 1107 and 1123 Ω for REF, and 107, 129, 122, 188, 150, 157, 85 and 164 Ω for GEO, at Days 1 to 28.

Three consequences follow for what this chapter can claim. Rs is not interpreted as a physical quantity in either system. The 500 Ω cap on the REF fit is below the measured bound from Day 5 onward, so from that age the constraint that determines the fitted value is the cap and not the data. And refitting is not a remedy: re-optimizations of the REF Day 28 spectrum under a raised cap return values between 500 and 2497 Ω depending on the configuration, with the coefficient of determination changing only in the fifth decimal, which is non-identifiability demonstrated rather than a value awaiting a better fit. Extending the acquisition ceiling above 10 MHz is identified as a perspective in Section 2.5.

2.3.6.3 Rs trajectory of REF

Figure 2-19 reports the fitted Rs of REF against the upper bounds established above. Two ages are free-fit, at 45.7 Ω on Day 1 and 94.4 Ω on Day 2, and both lie well inside their bounds of 261 and 569 Ω. From Day 5 onward the converged value is exactly 500 Ω at six consecutive ages, reproducing the upper bound of the parameter interval to the last decimal. This is the signature of a constraint, not of convergence.

The rise between Day 1 and Day 2 is the only movement in the REF series that the fit determines freely, and it is consistent with the rapid consumption of free water and of dissolved Ca^{2+} and OH^- by the accelerating alite hydration of the Portland clinker, which reduces both the volume and the ionic strength of the percolating pore solution (McCarter et al., 2003; Sant et al., 2008; Provis and Deventer, 2014). Beyond Day 2 the fitted series carries no information about the pore solution. What can be stated is that Rs remains below 887 Ω at Day 5 and below 1123 Ω at Day 28, and that a value of two to three kilohms, which an earlier reading of the Bode modulus appeared to support, is excluded by the bound.

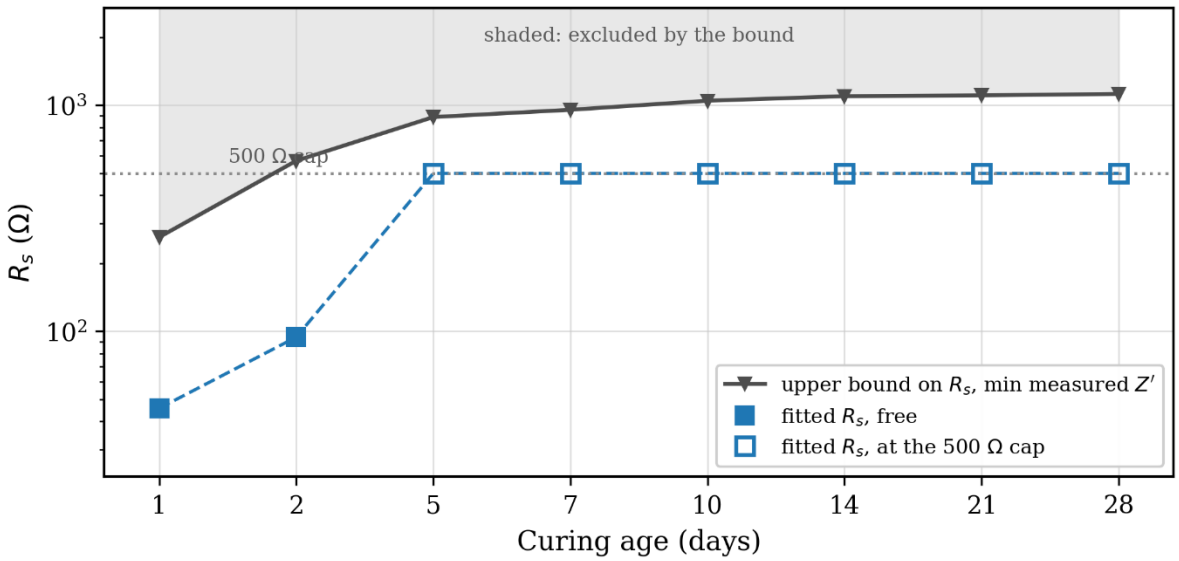

Figure 2-19: Solution resistance of REF across the eight curing ages. Filled squares are free-fit values, open squares the six ages at which the fit returns the 500 Ω cap. The gray line is the upper bound on Rs from the lowest measured Z′.

2.3.6.4 Rs trajectory of GEO

Figure 2-20 reports the fitted Rs of GEO. Unlike REF, no age is bound-affected: the fitted values are 53.3, 64.4, 64.9, 93.9, 93.4, 100.6, 46.3 and 83.0 Ω, all interior to the parameter interval and all between one third and two thirds of their respective upper bounds. The extrapolation from the last measured point to the fitted intercept is therefore shorter for GEO than for REF, consistent with the arc frequencies of Section 2.3.6.2, but it remains an extrapolation and the same caution applies.

Read subject to that caution, the GEO series stays within a 46 to 101 Ω band across the full 28-day window, against an upper bound that never exceeds 188 Ω. The absence of any order-of-magnitude excursion is itself informative: it is consistent with the alkali activator being redistributed between the pore solution and the gel framework rather than stoichiometrically consumed, so that the conductive pool is not depleted as the calcium and hydroxide of REF are (Wang and Scrivener, 1995; Provis and Deventer, 2014). The Day 21 value of 46.3 Ω is the lowest of the series and falls to less than half the Day 14 value before recovering at Day 28. This excursion has support outside the fit. The lowest measured Z′ at Day 21 is 85 Ω, against 157 Ω at Day 14 and 164 Ω at Day 28, so the raw high-frequency response is anomalously low at that age independently of any model. Whether this reflects a transient release of alkali from continued slag dissolution, reported in alkali-activated slag systems beyond the first two weeks (Wang and Scrivener, 1995), or a measurement condition specific to that session, cannot be resolved from the present data. The excursion is recorded and is not used to support any conclusion.

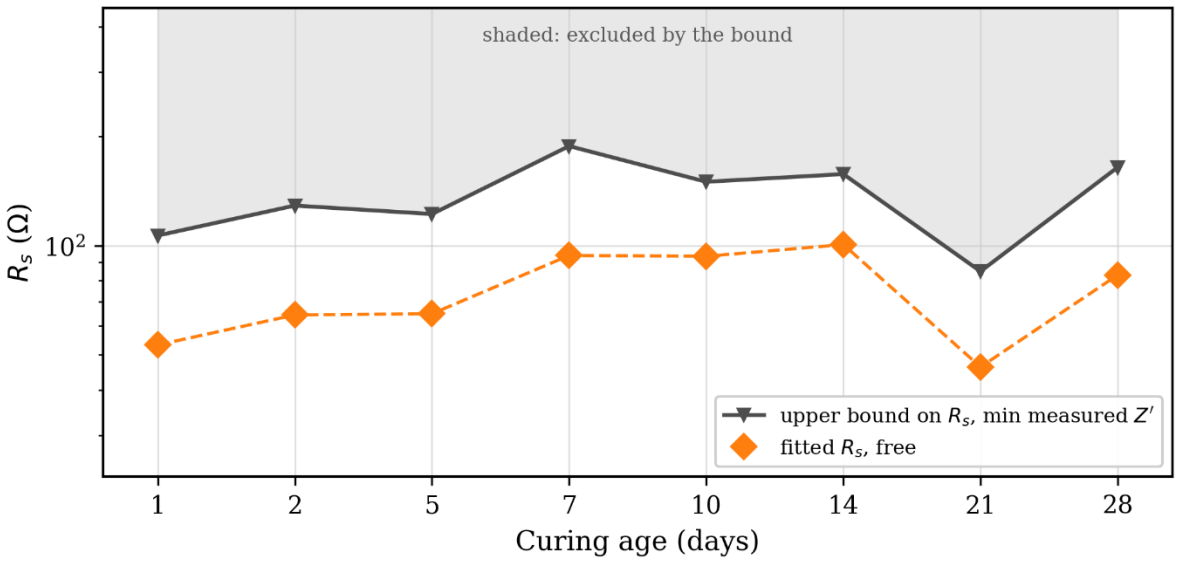

Figure 2-20: Solution resistance of GEO across the eight curing ages. All eight values are free-fit.

2.3.6.5 Cross-system comparison

Figure 2-21 overlays the two systems. The comparison that survives the identifiability limits is bounded but not empty.

At Day 1, where both systems are free-fit and both bounds are tightest, the two values are comparable, 45.7 Ω for REF against 53.3 Ω for GEO. The as-cast pore-solution conductivity of the two systems is therefore of the same order despite their different chemistries, which is consistent with comparable volumetric ion concentrations at the same ultra-low water-to-binder ratio, one dominated by Ca^{2+} and OH^- and the other by K^+ and Na^+.

Beyond Day 1 the systems separate in a way that the bounds establish without needing the fitted values. The REF upper bound rises by a factor of 4.3 across the eight ages, from 261 to 1123 Ω, while the GEO upper bound rises by a factor of 1.5, from 107 to 164 Ω. Since these bounds are read directly from the measured Z' at the top of the window, the divergence is a property of the measurement rather than of the model. It is the parameter-level expression of the contrast already established in the Nyquist and Bode evolutions: the high-frequency response of REF grows steadily with hydration while that of GEO changes little, which is what an alkali pool that is redistributed rather than consumed predicts.

What cannot be stated is the size of the mature-age separation. The chapter's earlier expectation, set out in Section 2.3.1, was that Rs would be substantially lower for GEO than for REF throughout the window. The bounds are consistent with that expectation from Day 2 onward, since the GEO bound never exceeds 188 Ω while the REF bound exceeds 880 Ω from Day 5, but they do not quantify it, and at Day 1 the two systems are indistinguishable.

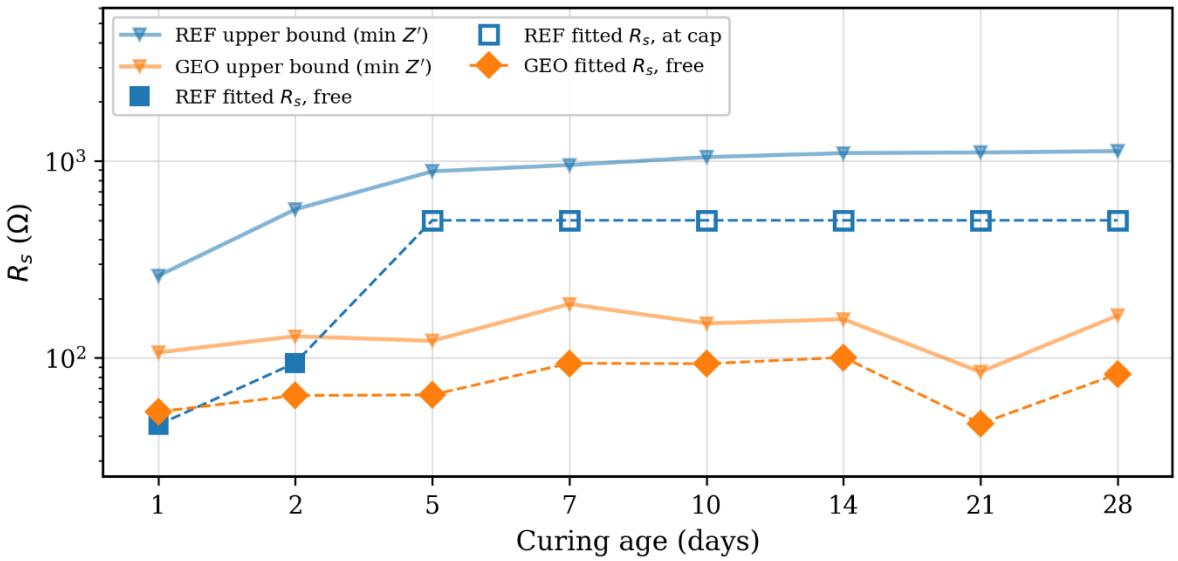

Figure 2-21: Solution resistance of REF (blue squares) and GEO (orange diamonds) across the eight curing ages. Open REF squares are at the 500 Ω cap.

The Rs trajectories together support a coherent picture of asymmetric pore-solution evolution between the two systems. The REF pore solution depletes rapidly in the first five days of curing as Ca^{2+} and OH^- are consumed by C_3S hydration, reaching a plateau no less than 500 Ω by Day 5 that persists through Day 28. The exact mature-age value cannot be resolved from the present fit and is identified as a perspective for future work. The GEO pore solution sustains an alkali-conductive composition throughout the 28-day window, with a modest densification-driven rise from approximately 50 Ω at Day 1 to approximately 80 to 100 Ω at Day 28, punctuated by a transient Day 21 dip whose physical interpretation is developed in Section 2.3.10. The order-of-magnitude separation between the two trajectories at mature ages confirms the fundamentally different pore-solution chemistry of the two binder systems and provides the first parameter-level signature, in this chapter, of the binder asymmetry established structurally in Chapter 1.

2.3.7 Arc resistances R1, R2, and R3

The arc resistances R1, R2, and R3 quantify the resistive contribution of each microstructural phase identified in Section 2.2.4: R1 the grain-boundary network around unreacted precursor grains, R2 the gel pore network, and R3 the interfacial arc that develops in REF from Day 10. Unlike the solution resistance of Section 2.3.6, these resistances are determined by spectral features that lie inside the measurement window at every age, and they carry the bulk of the interpretable signal of this chapter.

Their magnitudes are nonetheless coupled to the unresolved solution resistance, since Rs and the arc resistances are frequency-flat real contributions in a series chain. Re-optimizing the REF spectra with the Rs cap removed moves R1 by up to 21%, R2 by up to 37% and R3 by up to 30%, with the coefficient of determination changing only in the fifth decimal. Within the Stage 2 window the R2 shift is far more uniform, at 1.37, 1.32, 1.27 and 1.26 times the reported value across Days 10 to 28, a coefficient of variation of 3.9%. The

absolute magnitudes below are therefore reported as the values returned by the adopted fit, and the trajectory shapes rather than the absolute levels carry the interpretation.

2.3.7.1 Resistance trajectories of REF

Figure 2-22 reports the evolution of R1, R2, and R3 for REF. Both R1 and R2 rise by more than two orders of magnitude over the 28-day window, from 443 Ω and 360 Ω at Day 1 to 40 853 Ω and 54 641 Ω at Day 28. During Stage 1 the two are close, rising together from approximately 350 to 450 Ω at Day 1 to approximately 13 600 to 15 000 Ω at Day 7, which reflects the simultaneous densification of the inter-particle grain boundaries and the growing C-S-H gel layer during the acceleration period of Portland cement hydration (Gu et al., 1993, 1992; Taylor, 1997).

R1 rises monotonically at every age. R2 does not: it falls from 14 980 Ω at Day 7 to 13 225 Ω at Day 10, a reduction of 11.7%, before resuming its rise. This is the only reversal in the REF series and it coincides exactly with the Stage 1 to Stage 2 topology transition. The interpretation is a redistribution rather than a physical decrease. The third arc enters at Day 10 carrying 20 584 Ω, and the sum R2 + R3 at Day 10 is 33 809 Ω, which continues the Day 5 to Day 7 progression without discontinuity. What the two-arc model had assigned to R2 at Day 7 is divided between two elements from Day 10, and R2 alone therefore steps down at the transition. The reversal is a property of the model change and not of the matrix.

The two resistances cross three times across the series. R1 exceeds R2 at Days 1, 2 and 10, and R2 exceeds R1 at Days 5, 7, 14, 21 and 28, reaching 1.34 times R1 at Day 28. The crossings do not disturb the identity of either parameter: the characteristic frequency of the first arc lies above that of the second at all eight ages, from 5.79 MHz against 12.8 Hz at Day 1 to 90.2 kHz against 15.9 kHz at Day 28. The magnitude crossings are therefore a real observation about the relative growth of the two resistive phases and not an artifact of the fit labeling. The sustained excess of R2 over R1 from Day 14 indicates that the gel pore network becomes the dominant resistive phase as the C-S-H gel fills the remaining capillary porosity, while the grain-boundary network, largely densified by the end of Stage 1, contributes a progressively smaller share (.

The third resistance appears at 20 584 Ω at Day 10 and rises to 64 508 Ω at Day 28, exceeding both R1 and R2 at all four Stage 2 ages, and its characteristic frequency falls from 4.2 kHz to 801 Hz over the same window, below both other arcs throughout. The resulting hierarchy at Day 28 is R3 > R2 > R1 in resistance and $f_{c1} > f_{c2} > f_{c3}$ in frequency. If the assignment of R3 to the fiber-matrix interfacial transition zone is correct, this hierarchy is consistent with that interface presenting the highest charge-transfer barrier of the three phases (Torrents et al., 2000; Suryanto et al., 2016). That assignment remains contingent on the fiber-population question set out in Section 2.2.1, and nothing in this chapter depends on it.

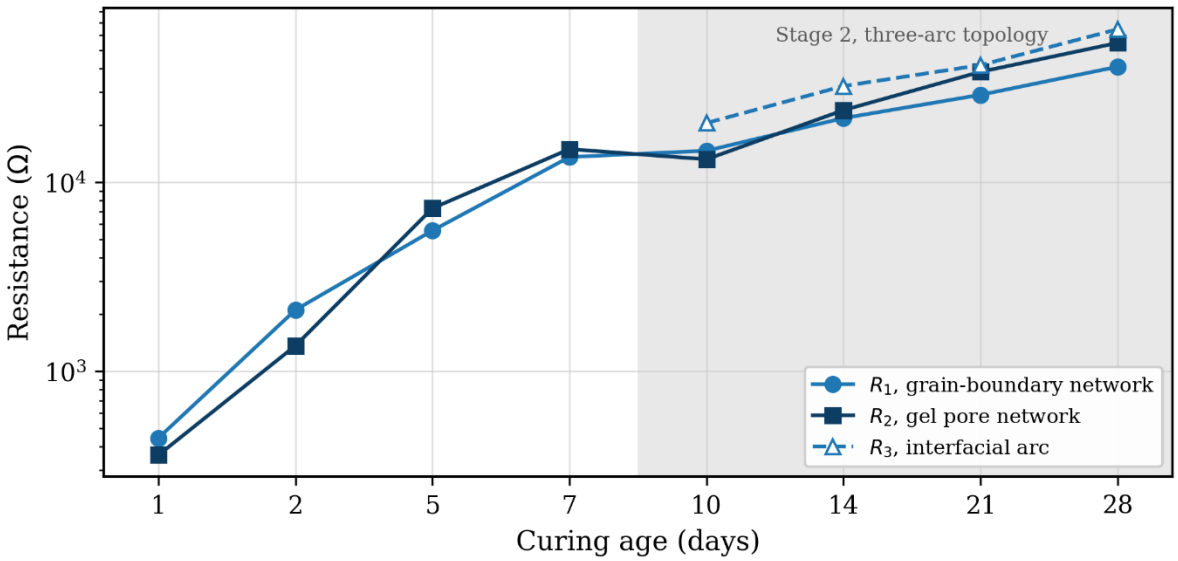

Figure 2-22: Arc resistances of REF across the eight curing ages. R1 (grain-boundary network), R2 (gel pore network) and R3 (interfacial arc, resolvable from Day 10), distinguished by marker. Gray shading marks the Stage 2 topology window, Days 10 to 28.

2.3.7.2 Resistance trajectories of GEO

Figure 2-23 reports R1 and R2 for GEO. No third arc is resolved at any age. The GEO resistances are smaller than the REF resistances at almost every age and follow a less regular trajectory.

R2 rose from 99 Ω at Day 1 to 193 Ω at Day 7, held near 174 Ω at Day 10, then stepped to 1005 Ω at Day 14 and 1299 Ω at Day 21 before settling at 1069 Ω at Day 28. The overall rise of approximately one order of magnitude reflects the progressive densification of the C-(N,K)-A-S-H gel pore network as polycondensation advances (Wang and Scrivener, 1995; Provis and Deventer, 2014). The step occurs between Day 10 and Day 14, a factor of 5.8 in four days, and is followed by a fall of 17.7% between Day 21 and Day 28 during which the compressive strength rises from 140 to 152 MPa. That terminal reversal is what disqualifies R2 as a strength indicator for GEO, and it is developed in Section 2.3.10.

R1 is non-monotonic, and it is not determined by the data at two of the eight ages. The values at Days 1, 5, 7, 10, 21 and 28 are 1261, 92, 400, 490, 641 and 1027 Ω. At Days 2 and 14 the fitted values of 1737 and 4754 Ω are not interpretable: perturbation testing (Section 2.3.8) shows the objective function to be invariant to a sixteenfold change in the associated CPE1 magnitude, and the first-arc characteristic frequencies of 9.2×10^{-5} and 3.3×10^{-5} Hz lie four orders of magnitude below the measurement window, so the arc is not sampled at those ages. Excluding them, the remaining six values define a band between 92 and 1261 Ω with no monotonic trend, in contrast to the two-order monotonic rise of the REF grain-boundary resistance.

A further constraint applies to both GEO resistances. The frequency ordering of the two arcs is not preserved across the series. At Days 7 and 10 the first arc lies above the second in characteristic frequency, at 2.06 and 1.14 MHz against 95 and 47 Hz, whereas at Days 21

and 28 the ordering is reversed, at 128 and 130 kHz against 518 and 523 kHz. The fitted R1 and R2 of GEO are therefore indexed by position in the parameter vector rather than by physical identity, and neither is read as a single continuous physical quantity across the window. This is why neither is adopted as a strength indicator for GEO, and it distinguishes the GEO case from REF, where the ordering holds at every age.

Read subject to that constraint, the GEO grain-boundary resistance shows none of the monotonic two-order rise seen in REF. This is consistent with the picture established in Chapter 1 of a geopolymer matrix whose transport properties are governed primarily by the gel phase rather than by the inter-particle grain boundaries (Provis and Deventer, 2014).

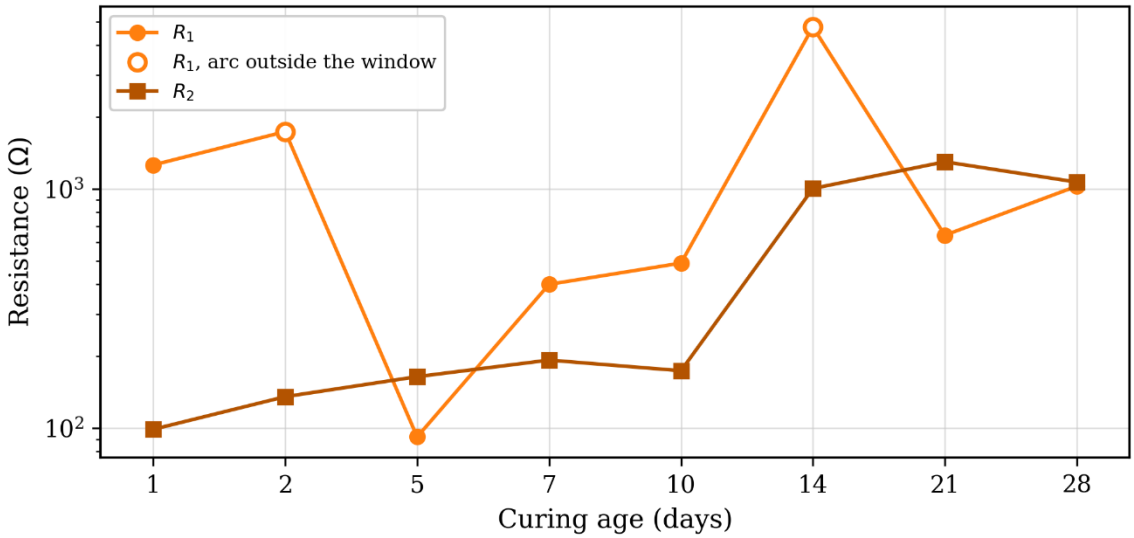

Figure 2-23: Arc resistances of GEO across the eight curing ages, R1 and R2 distinguished by marker. Open R1 markers at Days 2 and 14 mark ages at which the first arc lies outside the measurement window.

2.3.7.3 Cross-system comparison

Figure 2-24 compares the two systems in separate panels. Two contrasts dominate. First, the magnitude separation. For the gel pore resistance R2, REF exceeds GEO at every age, from a factor of 3.6 at Day 1 to a factor of 51 at Day 28, where REF reaches 54 641 Ω against 1069 Ω. For the grain-boundary resistance R1 the separation is not present at Day 1, where GEO exceeds REF at 1261 against 443 Ω, and establishes itself from Day 2 onward, reaching a factor of 40 at Day 28. The R2 separation mirrors the impedance-magnitude difference established in the Nyquist and Bode evolutions and reflects the higher gel-phase resistivity and lower connected porosity of the densifying C-S-H matrix relative to the more open, alkali-conductive C-(N,K)-A-S-H matrix (Gu et al., 1992; Provis and Deventer, 2014).

Second, the trajectory shape. The REF resistances rise across the full window with a single reversal in R2 at the topology transition, which is a model artifact rather than a physical feature. The GEO R2 rises in one step at Days 10 to 14 and then reverses at the terminal interval, and the GEO R1 is neither monotonic nor consistently identified. The

contrast is the parameter-level expression of the difference in reaction mechanism, the continuous precipitation of C-S-H in REF against the dissolution and polycondensation of C-(N,K)-A-S-H in GEO (Taylor, 1997; Provis and Deventer, 2014). REF also develops a resolvable hierarchy of three resistive phases with a stable frequency ordering, which GEO does not within the present measurement window.

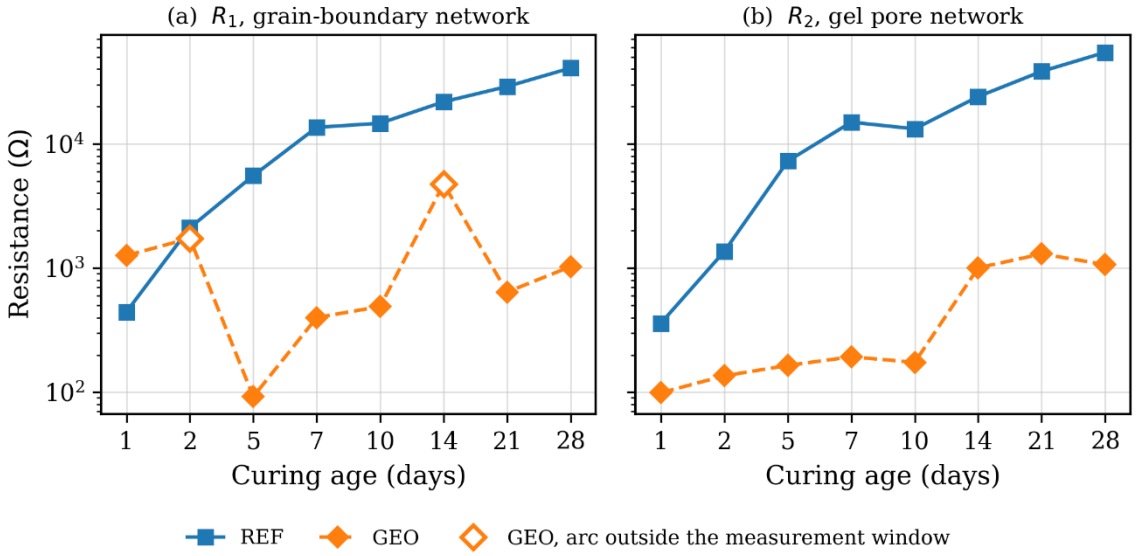

Figure 2-24: Cross-system comparison of the arc resistances. (a) R1, grain-boundary network and (b) R2, gel pore network.

Taken together, the arc resistance trajectories provide the clearest parameter-level distinction between the two binder systems in this chapter. The REF resistances rise monotonically over two orders of magnitude, develop a $R_3 > R_2 > R_1$ hierarchy in Stage 2, and confirm the progressive densification of a multi-phase C-S-H matrix with a resolvable fiber-matrix interface. The GEO resistances are smaller, follow a less regular trajectory dominated by the gel pore resistance R_2, show no resolvable fiber-matrix arc, and carry the same Day 14 to Day 21 perturbation seen in the other observables. The magnitude separation and the difference in trajectory shape together indicate, at the level of the fitted circuit parameters, different microstructural evolution pathways: C-S-H densification in REF and, as an interpretation not confirmed here, a reorganization of the C-(N,K)-A-S-H gel in GEO. The correlation of these resistance trajectories with the compressive strength development of the two systems is examined in Section 2.3.10.

2.3.8 CPE magnitudes and dispersion exponents

The constant phase elements CPE1, CPE2, and CPE3 replace ideal capacitors in the equivalent circuits of Section 2.2.4 to account for the distributed relaxation behavior of each microstructural interface. Each is parameterized by a magnitude Q and a dispersion exponent n, with n = 1 corresponding to an ideal capacitor and n = 0.5 to a diffusion-controlled response.

Two properties of the fitted CPE set condition what can be read from it. In the Stage 2 topology adopted for REF at Days 10 to 28, the exponents n1 and n2 were fixed at 0.88 rather than fitted, in order to keep a 12-parameter model well conditioned, so no REF exponent trajectory is available beyond Day 7. And the sensitivity of the objective function to the CPE parameters varies by orders of magnitude between ages. Where the associated arc lies inside the measurement window, the exponent is determined to better than 0.02. Where it does not, the parameter is unconstrained and its fitted value carries no information. The distinction is established below by direct perturbation of the converged fits.

2.3.8.1 Identifiability of the fitted CPE parameters

The identifiability of each CPE parameter was tested by perturbing it about its converged value with all other parameters held fixed, and recomputing the sum of squared relative residuals. A parameter that the data determines produces a minimum, with the objective rising in both directions. A parameter that the data does not determine leaves the objective unchanged.

All fitted exponents pass this test at the ages where the corresponding arc lies inside the measurement window. The response is sharp. For REF n1 at Day 2 the objective takes the values 22.53, 6.17, 0.84, 0.19, 0.86 and 5.82 as the exponent moves from 0.54 to 0.63, a well-conditioned minimum spanning two orders of magnitude over a range of 0.09 in n. Comparable curvature is found for REF n2 at Day 5, REF n3 at Day 14, GEO n1 at Day 5, and GEO n2 at Day 7. Several converged values fall on round numbers, 0.500 and 0.600 in particular, which reflects the convergence tolerance applied to the exponents rather than any constraint: at each of these the objective rises on both sides, so the value is an interior optimum determined to within the tolerance step.

Two GEO ages fail the test outright. At Day 2 the first-arc magnitude Q1 can be varied by a factor of 16, from a quarter to 4 times its converged value, while the objective changes from 0.2655 to 0.2651, a variation in the fourth decimal. The exponent n1 at the same age is equally unconstrained, with the objective invariant to four decimals across the whole interval from 0.94 to 1.03. Day 14 behaves identically. At these two ages the first arc is therefore not merely poorly resolved but absent from the objective function, and the reported R1, Q1 and n1 are arbitrary within wide limits.

The cause is the one identified in Section 2.3.5. At Days 2 and 14 the first-arc characteristic frequency, $f_c = \frac{1}{2\pi(RQ)^{1/n}}$, evaluates to 9.2×10^{-5} and 3.3×10^{-5} Hz, four orders of magnitude below the 4 Hz lower limit of the measurement window. The relaxation the element represents is not sampled, so the fit has nothing to constrain it against. This is a stronger and more specific statement than the coefficient of determination alone supports, and it is the ground on which the GEO first-arc parameters at Days 2 and 14 are excluded from interpretation throughout this chapter.

2.3.8.2 REF CPE

For REF the fitted exponents are those of Stage 1. The first-arc exponent n1 takes 0.668, 0.600, 0.870 and 0.840 at Days 1, 2, 5 and 7, and the second-arc exponent n2 takes 1.000, 1.000, 0.600 and 0.601. Both are determined at every age. The n1 series rises from 0.67 to 0.87 and settles at 0.84, indicating a first-arc response that becomes less dispersive as the grain-boundary network densifies during the acceleration period of hydration.

The n2 series traverses a wider range, from the ideal-capacitor limit at Days 1 and 2 to 0.60 at Days 5 and 7. Since both endpoints are determined rather than imposed, this is a measurement: the second arc is close to ideally capacitive at the earliest ages and becomes markedly dispersive by the end of the first week. That is consistent with a gel pore interface that is initially simple and becomes geometrically distributed as the C-S-H network develops and its pore size distribution broadens.

The third-arc exponent n3, the only Stage 2 exponent that was fitted, takes 0.500, 0.500, 0.500 and 0.520 at Days 10 to 28. It sits close to the Warburg-like limit of 0.5 throughout, which is the value expected for a diffusion-controlled interfacial response, and rises slightly at the last age. The CPE magnitudes fall by roughly two orders of magnitude across the window, Q1 from 2.0×10^{-8} to 2.1×10^{-10} F · s^{n-1} and Q2 from 3.5×10^{-5} to 7.3×10^{-10} F · s^{n-1}, consistent with the reduction in effective interfacial capacitance as the conductive pore network is progressively obstructed by hydration product. Neither is strictly monotonic: Q1 rises between Days 1 and 2 and again between Days 5 and 7, and Q2 rises marginally between Days 21 and 28.

2.3.8.3 GEO CPE

For GEO both exponents were fitted at every age. The first-arc exponent n1 takes 1.000, 1.000, 0.500, 0.784, 0.736, 0.993, 0.722 and 0.664, and the second-arc exponent n2 takes 0.511, 0.546, 0.698, 0.500, 0.515, 0.725, 0.750 and 0.776. The Day 2 and Day 14 values of n1 are excluded for the reason established above.

Read over the remaining six ages, n2 rises from 0.51 at Day 1 to 0.78 at Day 28, a trend toward less dispersive behavior consistent with the densification of the C-(N,K)-A-S-H gel pore network. It sits near the Warburg-like limit of 0.5 at the three earliest ages and at Day 7, indicating a second-arc interface whose response is close to diffusion-controlled during the first week of ambient curing, in contrast to REF, whose second arc is near-ideal at the same ages. This is the most direct expression in the CPE family of the binder contrast the chapter is built on.

The magnitudes span a wide range, Q1 from 6.6×10^{-9} to 4.5×10^{-3} F · s^{n-1} over the six interpretable ages, and Q2 from 8.2×10^{-9} to 3.1×10^{-4} F · s^{n-1}. Neither is read as a capacitance trajectory.

The magnitudes do carry one unambiguous structural signal. At Days 7 and 10, Q1 falls to 6.6×10^{-9} and 1.8×10^{-8} while Q2 rises to 2.1×10^{-4} and 3.1×10^{-4}, so the two parameters exchange their magnitude ranges by roughly four orders relative to every other age. These are the same two ages at which the arc characteristic frequencies invert, as reported in Section 2.3.7. The exchange is therefore visible in two independent parameter families and confirms that the fitted first and second arcs of GEO correspond to different physical features at different ages. This is the principal structural result of the present section and the reason neither GEO arc parameter is adopted as a strength indicator in Section 2.3.10.

In summary, the CPE parameters are determined by the data wherever the corresponding arc lies inside the measurement window, and the exponents are resolved to within the convergence tolerance at those ages. Three limits apply. The REF Stage 2 exponents are imposed rather than fitted, so no REF exponent trajectory extends beyond Day 7. The GEO first-arc parameters at Days 2 and 14 are unconstrained, with the objective function invariant to a sixteenfold change in Q1, because the relaxation they describe lies four orders below the measurement window. And the GEO magnitudes exchange ranges at Days 7 and 10, which establishes the arc-identity problem developed in Section 2.3.7. Subject to these, the exponents support two substantive readings: the REF second arc moves from near-ideal to markedly dispersive across the first week, while the GEO second arc begins near the diffusion-controlled limit and becomes progressively less dispersive through Day 28.

2.3.9 Warburg diffusion parameters

The Warburg element captures the long-range ionic diffusion impedance within the connected pore network and is a direct probe of the tortuosity and connectivity of that network as it evolves with curing age. As established in Section 2.2.4, the two systems require different Warburg formulations. For REF, a finite-length short-circuit Warburg W_s is used, appropriate for a bounded pore network in which ion diffusion terminates at an impermeable boundary, a condition physically consistent with the dense, low-porosity C-S-H matrix. It is parameterized by the diffusion amplitude Rw. For GEO, a semi-infinite Warburg W is used, reflecting the faster and less constrained ion diffusion sustained by the alkali-rich pore solution, in which the high K^+ and Na^+ mobility maintains active diffusion across the full specimen thickness even as the gel densifies (Barsoukov, 2005; Diard et al., 2008). Both parameters are free-fit at every age in their respective systems, with no bound hits. Because the two formulations differ in mathematical form, units and physical meaning, the REF and GEO diffusion parameters are presented separately and compared qualitatively rather than by direct numerical overlay.

2.3.9.1 Diffusion amplitude of REF

Figure 2-25 reports the REF Warburg amplitude Rw. It rises monotonically from 2610 Ω at Day 1 to 127 165 Ω at Day 28, spanning nearly two orders of magnitude, with the steepest rise during Stage 1, from 2610 to 36 688 Ω between Day 1 and Day 7, continuing at a shallower logarithmic rate through Stage 2. The associated finite-length time constant Tw runs 0.13, 0.43, 0.25, 0.46, 0.38, 0.57, 0.77 and 0.81 s across the eight ages: the endpoints rise by a factor of six but the series is not monotonic, with reversals at Days 5 and 10. Both parameters are subject to the same identifiability limit as the solution resistance of Section 2.3.6, and more severely. Rw and Rs are both frequency-flat real contributions in a series chain, so the value the fit assigns to one depends on what it assigns to the other. Re-optimizing the REF spectra with the Rs cap removed moves Rw by up to 184% and Tw by up to 486%, with the coefficient of determination changing only in the fifth decimal. At Day 28 the same spectrum admits Rw values from 47 000 to 342 500 Ω across configurations that fit equally well. Restricted to the Stage 2 window, the spread is 41.6% for Rw and 71.9% for Tw, against 3.9% for the gel pore resistance R2 over the same ages.

The consequence is that the REF diffusion parameters are reported but not interpreted quantitatively. The monotonic rise of Rw is a robust feature of the trajectory shape and is consistent with the progressive obstruction of long-range diffusion pathways as the C-S-H gel fills the capillary porosity and the connected pore network becomes more tortuous (Gu et al., 1992; Olson et al., 1995; Taylor, 1997). Its absolute magnitude at any age is not determined by the present fit, and neither is the effective diffusion path length that Tw would otherwise give. Rw is not adopted as a strength indicator for REF, and the reason is not that it correlates poorly. Its logarithmic correlation with compressive strength is 0.978, close to that of R2. The reason is that an indicator whose value cannot be stated to better than a factor of three cannot be calibrated, and calibration is what a non-destructive indicator is for.

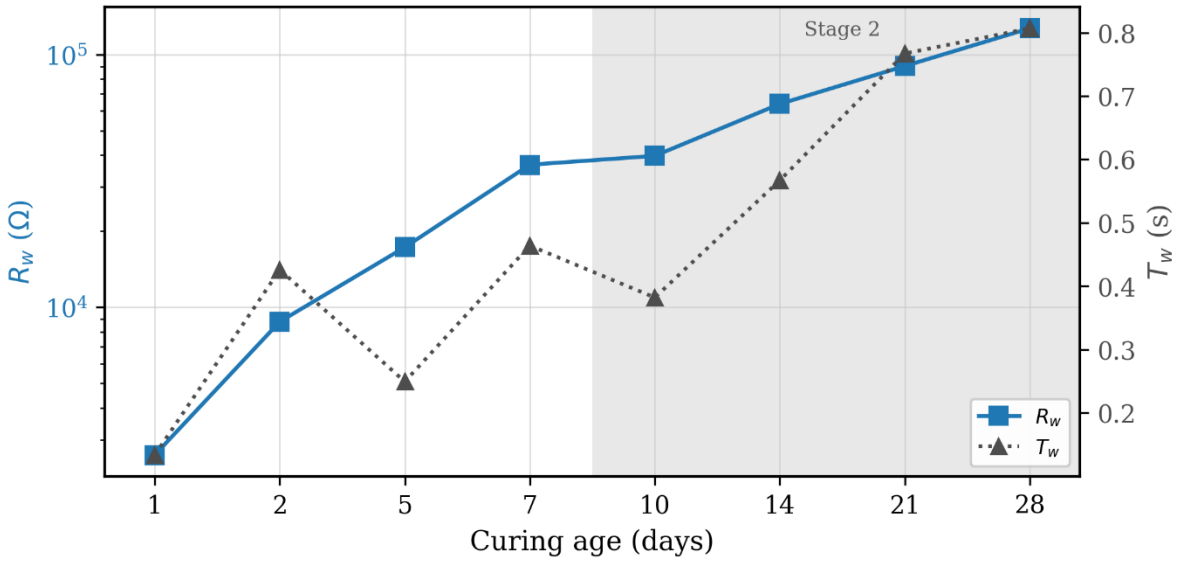

Figure 2-25: Warburg amplitude Rw and time constant Tw of REF across the eight curing ages.

2.3.9.2 Warburg coefficient of GEO

Figure 2-26 reports the GEO Warburg coefficient W. As an impedance amplitude with units $\Omega \cdot s^{-1/2}$ rather than a diffusion coefficient in the Fickian sense (Section 2.1.1), it rises from 416 to 3638 $\Omega \cdot s^{-1/2}$ between Day 1 and Day 28, approximately one order of magnitude against nearly two for the REF amplitude. The trajectory is smooth through Day 5, at 416, 545 and 633 $\Omega \cdot s^{-1/2}$, steps up to 1492 at Day 7, falls 9.4% to 1351 at Day 10, rises to 2745 at Day 14, and settles at 3682 and 3638 at Days 21 and 28. The overall rise reflects the progressive densification of the C-(N,K)-A-S-H gel pore network and the associated increase in diffusion impedance as polycondensation advances.

Two features of this trajectory bear on the indicator selection of Section 2.3.10. The Day 7 to Day 10 reversal of 9.4% is not unique to W: the gel pore resistance R2 falls by 9.7% over the same interval, so the two parameters share this feature and it does not distinguish them. The terminal interval does. Between Day 21 and Day 28, W changes by 1.2% while the compressive strength rises from 140 to 152 MPa, whereas R2 falls by 17.7% over the same interval. It is the fidelity of W at the terminal age, not the smoothness of its trajectory, that makes it the usable indicator for GEO.

Unlike Rw, the GEO coefficient is not coupled to an unresolved parameter. The GEO solution resistance is free-fit at every age with no bound hits, the semi-infinite formulation carries no time constant, and refitting W under the alternative band restriction moves it by a mean factor of 0.950 with a coefficient of variation of 6.4% across the eight ages. That shift is near-uniform, so it leaves the correlation coefficients unchanged, and W is therefore both interpretable in magnitude and stable under refitting.

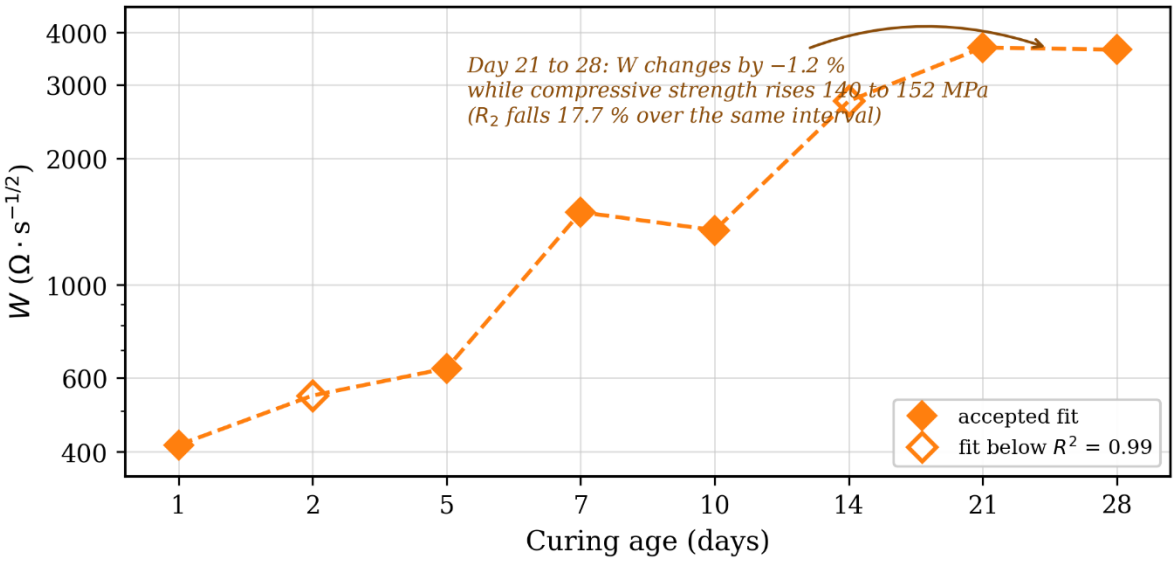

Figure 2-26: Warburg coefficient W of GEO across the eight curing ages. Filled diamonds are accepted fits, open diamonds the two ages at which R^2 falls below 0.99. Units are $\Omega \cdot s^{-1/2}$.

2.3.9.3 Cross-system comparison

The two diffusion parameters cannot be overlaid directly because they parameterize different Warburg formulations: the finite-length amplitude Rw for REF and the semi-infinite coefficient W for GEO. Their trajectories nonetheless support a coherent contrast.

First, the magnitude: at every age the REF diffusion parameter exceeds the GEO parameter, and the separation widens with curing as REF rises nearly two orders of magnitude against approximately one for GEO. **Second,** the choice of Warburg formulation itself distinguishes the systems: the bounded finite-length response of REF reflects diffusion terminating at the dense, low-porosity C-S-H boundary, while the semi-infinite response of GEO reflects diffusion sustained across the full specimen thickness by the alkali-conductive pore solution. **Third,** the trajectory shape. The REF amplitude rises monotonically at every age, the signature of unidirectional pore-network densification, while the GEO coefficient carries a step at Days 10 to 14 and a reversal at Days 7 to 10. The contrast in shape is real, but the comparison is asymmetric in reliability: the REF amplitude is monotonic and unidentifiable in magnitude, while the GEO coefficient is irregular and well determined. Trajectory shape is therefore compared here, and absolute magnitudes are not.

Taken together with the resistive trajectories of Section 2.3.7, the Warburg parameters complete the picture of the pore-network evolution of the two systems. The REF amplitude Rw and the resistances R1, R2 and R3 all rise over nearly two orders of magnitude, a self-consistent signature of the progressive densification and tortuosity increase of the C-S-H matrix. The GEO coefficient W and the gel pore resistance R2 both rise about one order of magnitude and both carry the Day 10 to Day 14 step, a self-consistent signature of a more open C-(N,K)-A-S-H network whose evolution is irregular in the Day 10 to Day 21 window. On the basis of these trajectories, the gel pore resistance R2 of REF and the Warburg coefficient W of GEO are carried forward as the candidate non-destructive indicators examined in Section 2.3.10. For REF, R2 is selected over Rw not on correlation strength, which is comparable, but because its magnitude is determined to within 4% across the Stage 2 window while that of Rw is not. For GEO, W is selected over R2 because R2 reverses by 17.7% at the terminal interval while the strength rises, and because the identity of the GEO arc parameters is not stable across the series (Section 2.3.8).

2.3.10 Correlation between impedance and compressive strength

The preceding sections established the evolution of the individual circuit parameters. This section evaluates the practical objective of the chapter: whether any of these parameters can serve as a non-destructive indicator of compressive strength development, and whether the same indicator applies to both binder systems. The compressive strength data are those reported in Section 2.3.2, measured on companion prisms at the eight EIS ages following EN 196-1, with REF rising from 76 to 165 MPa and GEO from 65 to 152 MPa over the 28-day window.

Both strength curves rise monotonically at every age. This sets the criterion against which a candidate indicator is judged: not that the indicator itself be monotonic, since none of the fitted parameters is, but that it should not move against the strength at any interval, and above all not at the terminal one, where a monitoring application would be calibrated.

2.3.10.1 Correlation method

Each candidate impedance parameter is correlated against the compressive strength across the eight curing ages using the Pearson correlation coefficient r. All correlations are computed on the eight curing-age points (n = 8, six degrees of freedom), and the two-tailed significance is reported with each coefficient. Because the impedance parameters span one to two orders of magnitude while the strength varies over a factor of approximately two, two correlation measures are reported for each parameter: the linear coefficient r_{lin} computed on the raw parameter values, and the coefficient r_{log} computed against the base-ten logarithm of the parameter. The logarithmic measure is the more physically appropriate of the two, because the impedance of a densifying porous matrix grows multiplicatively with the degree of pore-network refinement rather than additively, so a log-linear relationship between strength and impedance is expected on mechanistic grounds (Gu et al., 1994; Cosoli et al., 2020). The linear coefficient is reported alongside for continuity with the impedance-strength literature, which conventionally cites linear Pearson coefficients. Two candidate parameters are evaluated for each system: the gel pore resistance R2 and the Warburg diffusion parameter, the amplitude Rw for REF and the coefficient W for GEO. These four were selected from the parameter trajectories of Sections 2.3.7 and 2.3.9 as the only ones whose physical identity is stable across the full series in their respective systems.

2.3.10.2 Strength indicator for REF

Figure 2-27 reports the correlation of the REF compressive strength against both candidates. The gel pore resistance R2 gives $r_{lin} = 0.854$ ($p = 0.007$) and $r_{log} = 0.987$ ($p < 0.001$). The Warburg amplitude Rw gives $r_{lin} = 0.872$ ($p = 0.005$) and $r_{log} = 0.983$ ($p < 0.001$). On the logarithmic measure, which is the physically appropriate one, the two are effectively indistinguishable, and correlation strength alone does not separate them. In both panels the same eight ages fall on the same log-linear trend, which is itself informative: in REF the gel pore resistance and the long-range diffusion impedance track the same underlying process, the progressive densification of the C-S-H matrix.

One feature of panel (a) is worth naming, because a reader encounters it before any explanation. The Day 10 point at 139 MPa lies to the left of the Day 7 point at 130 MPa, so the two ages are inverted with respect to R2. This is the 11.7% step down in R2 at the Stage 1 to Stage 2 topology transition described in Section 2.3.7, where the third arc enters carrying 20 584 Ω and the resistance that the two-arc model assigned to R2 alone is divided between two elements. It is a property of the model change and not of the matrix, and the same two ages are correctly ordered in panel (b), where the Warburg amplitude is unaffected by the transition.

Identifiability separates the two candidates where correlation does not. As established in Sections 2.3.7 and 2.3.9, the fitted magnitudes of both are coupled to the unresolved solution resistance, but by very different amounts. Across re-optimizations that fit equally

well, the Stage 2 values of R2 shift by 1.37, 1.32, 1.27 and 1.26 times the reported value, a coefficient of variation of 3.9%, while those of Rw shift by 41.6% and its time constant by 71.9%. A near-uniform shift leaves the Pearson coefficient unchanged, which is why the correlation of Rw survives its own indeterminacy, but it does not leave a calibration intact. An indicator whose value at a given age can be stated only to within a factor of three cannot convert a measured impedance into an estimated strength.

R2 is therefore adopted as the strength indicator for REF, on the ground that it is both the marginally stronger correlator and the only one of the two whose magnitude is determined. Rw is reported but not adopted.

The scope of the claim follows from the same numbers. R2 supports quantitative strength estimation from Day 10 onward, where its value is determined to within 4% across the admissible parameter family. At the four earlier ages the shift is larger and less uniform, at 0.66, 1.90, 0.94 and 0.94 times the reported value, so R2 tracks strength there but does not calibrate. This restriction is not added after the fact: Day 10 is the Stage 1 to Stage 2 topology boundary that Section 2.2.4 defends independently, and it is the age from which the three-arc model resolves the gel pore arc separately from the interfacial arc.

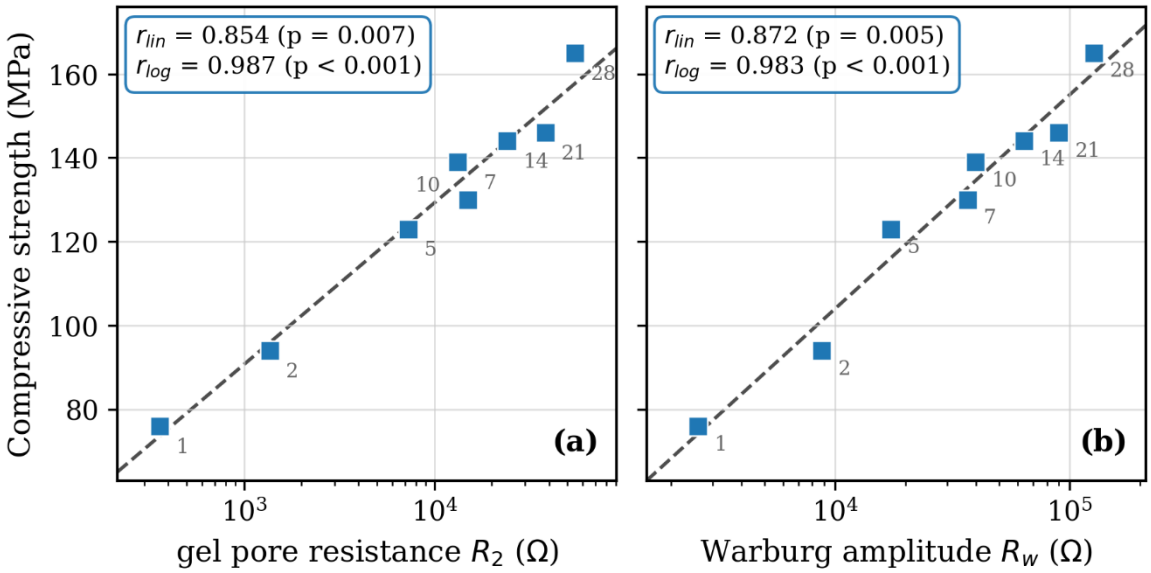

Figure 2-27: Correlation between REF compressive strength and the two candidate indicators across the eight curing ages. (a) Gel pore resistance R2. (b) Warburg amplitude Rw.

2.3.10.3 Strength indicator for GEO

Figure 2-28 reports the equivalent correlation for GEO. The Warburg coefficient W gives $r_{lin} = 0.954$ ($p < 0.001$) and $r_{log} = 0.983$ ($p < 0.001$), the strongest linear correlation of any parameter in either system. The gel pore resistance R2 gives $r_{lin} = 0.876$ ($p = 0.004$) and $r_{log} = 0.929$ ($p < 0.001$).

The reason for the difference is specific, and it is not the one a smoothness argument would give. Both parameters reverse between Day 7 and Day 10, W by 9.4% and R2 by 9.7%, so that feature is common to them and separates nothing. They differ at the terminal

interval. Between Day 21 and Day 28 the compressive strength rises from 140 to 152 MPa, a gain of 8.6%. Over the same interval W changes by 1.2%, which is a plateau, while R2 falls by 17.7%, which is a reversal against the strength. The consequence is visible in panel (b), where the Day 28 point sits to the left of the Day 21 point: the specimen is 12 MPa stronger and its gel pore resistance is lower. Panel (a) shows the same two ages in the correct order.

This reversal falls at the mature age where a monitoring calibration would be anchored, which is why it disqualifies R2 rather than merely weakening it.

The Warburg coefficient is adopted as the strength indicator for GEO. Two further properties support it. Its magnitude is not coupled to an unresolved parameter, unlike the REF Warburg amplitude, since the GEO solution resistance is free-fit at every age and the semi-infinite formulation carries no time constant. And its physical identity is stable across the series, whereas the identity of the GEO arc parameters is not: as established in Section 2.3.8, the first and second arcs exchange both their characteristic frequencies and their CPE magnitude ranges at Days 7 and 10, so the GEO R2 trajectory does not represent a single physical feature across the eight ages. That alone would disqualify R2 for GEO independently of its terminal behavior.

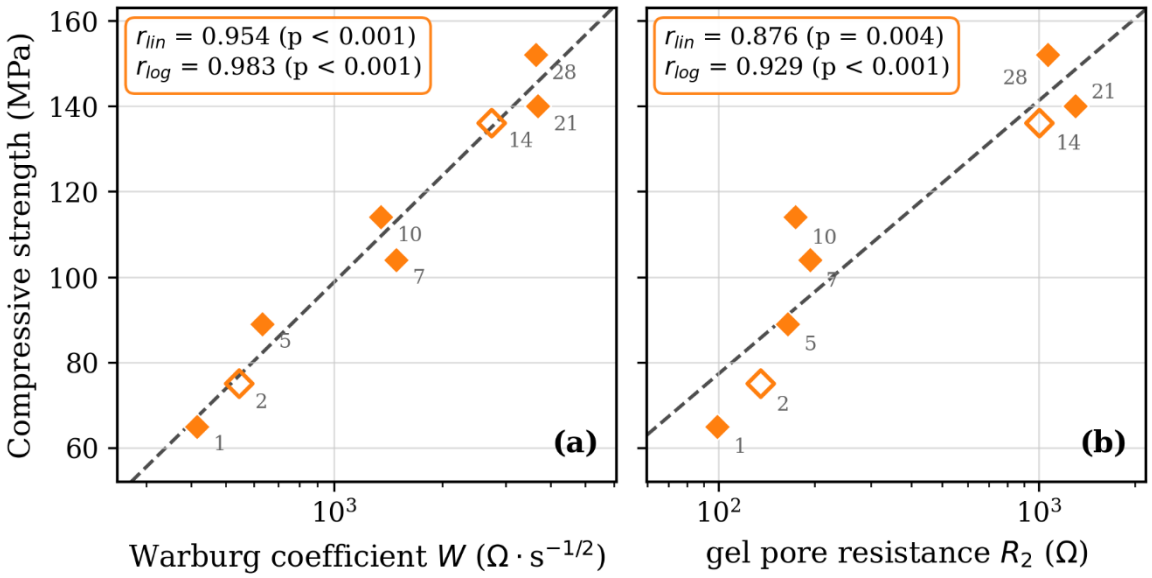

Figure 2-28: Correlation between GEO compressive strength and the two candidate indicators across the eight curing ages. (a) Warburg coefficient W and (b) Gel pore resistance R2.

2.3.10.4 Robustness

Both selections were tested against the fitting choices that produced them. Re-optimizing the REF spectra with the solution resistance freed, and recomputing the correlation on the resulting parameter family, moves r_{log} for R2 from 0.987 to 0.974, with p below 0.0001 throughout. Refitting the GEO spectra over the reduced frequency band and recomputing moves r_{log} for W from 0.983 to 0.990. Neither selection changes.

The two indicators were also tested against the exclusion of their problematic ages, and the exclusion grounds differ by system. GEO has two ages at which the fit falls below the acceptance threshold, Day 2 and Day 14, shown as open markers in Figure 2-29. Dropping both takes r_{log} for W from 0.983 to 0.978 on six points. REF has no such age, its lowest coefficient of determination being 0.9987, and Day 2 is set aside on a different ground, that the solution resistance goes negative there when the cap is freed. Dropping it takes r_{log} for R2 from 0.987 to 0.984 on seven points. For completeness, dropping Day 1 as well takes it to 0.930, so the earliest age carries substantial leverage in a correlation spanning two decades of impedance, and no ground exists for excluding it.

2.3.10.5 The Day 10 to Day 21 irregularity in GEO

The GEO trajectories are collectively irregular between Day 10 and Day 21, and the irregularity appears in several parameters at neighboring rather than identical ages. The first Nyquist arc perturbs at Days 14 and 21 (Section 2.3.3), the coefficient of determination falls below threshold at Day 14 (Section 2.3.5), the fitted solution resistance dips at Day 21 (Section 2.3.6), the gel pore resistance steps between Day 10 and Day 14 (Section 2.3.7), and the Warburg coefficient steps over the same interval (Section 2.3.9). No comparable clustering appears anywhere in the REF series.

Two of these have identified proximate causes that are not physical. The Day 14 coefficient of determination falls because Q1 reaches its upper bound, placing the first arc four orders of magnitude below the measurement window, and the Day 21 solution resistance dip has support in the raw spectrum, where the lowest measured Z' is 85 Ω against 157 and 164 Ω at the neighboring ages. The remaining three are trajectory features of free-fit parameters.

The most consistent physical interpretation, supported by the alkali-activated slag literature, is a delayed reorganization of the C-(N,K)-A-S-H gel between two and three weeks of ambient curing, in which an initially open and highly connected gel densifies and compartmentalizes as residual slag continues to dissolve and reprecipitate (Wang and Scrivener, 1995; Provis and Deventer, 2014). Such a reorganization would redistribute the gel pore network and alter the connectivity of the diffusion path while the compressive strength continued to rise, which is what is observed. The present dataset cannot confirm it. The evidence is a clustering of irregularities in a three-age window, two of which have fitting explanations, and time-resolved microstructural characterization would be required to establish the mechanism. It is identified as a perspective in Section 2.5.

2.3.10.6 Binder-specific indicator selection

The central practical finding of this chapter is that the two binder systems require different EIS strength indicators. For REF the gel pore resistance R2 is the indicator, at r_{log} = 0.987, calibrated from Day 10 onward. For GEO the Warburg coefficient W is the indicator, at r_{lin} = 0.954 and r_{log} = 0.983 across the full window. Neither parameter serves

the other system: the REF Warburg amplitude is indeterminate in magnitude, and the GEO gel pore resistance both reverses against strength at the terminal interval and fails to represent a single physical feature across the series.

The asymmetry is not a measurement inconvenience but a consequence of the different microstructural evolution pathways established through this chapter. The unidirectional densification of C-S-H in REF makes densification-sensitive parameters good strength proxies, so that either candidate would correlate and the choice falls to identifiability. The irregular intermediate-age behavior of the C-(N,K)-A-S-H gel in GEO leaves only the integrative diffusion parameter robust, and the choice is forced by the data. Impedance-based strength monitoring of UHPC therefore cannot rely on a single universal parameter and must be calibrated to the binder chemistry.

This result answers the research question posed at the opening of the chapter. The pore network and pore solution chemistry of GEO do produce a distinguishable electrochemical signature from REF, expressed in the order-of-magnitude lower impedance magnitude, the sustained low solution resistance, the absence of a resolvable fiber-matrix interfacial arc, and the non-monotonic intermediate-age response interpreted as a gel reorganization, none of which appear in REF. And EIS parameters can serve as non-destructive indicators of strength development in a cement-free UHPC: the Warburg coefficient W predicts the GEO compressive strength with a logarithmic correlation of 0.983 across the full 28-day window, a predictive quality equal to the best REF indicator. The cement-free geopolymer UHPC is therefore not only of the same mechanical class as the Portland cement reference, at 92% of its compressive strength (Chapter 1), but is also amenable to the same class of non-destructive electrochemical monitoring, provided the indicator parameter is selected to match the binder chemistry.

2.4 Conclusions

Electrochemical impedance spectroscopy was applied to the non-destructive characterization of the two UHPC systems across eight curing ages from Day 1 to Day 28. Spectra were acquired from 4 Hz to 5 MHz on 401 logarithmically spaced points, corrected for electrode and contact contributions, validated by Kramers-Kronig consistency checks, and fitted by complex nonlinear least-squares to physically motivated equivalent circuits. REF required a stage-dependent topology, two arcs during the first week and three from Day 10 with the emergence of an interfacial arc, while GEO was described by a single-stage two-arc model throughout. The fit met the acceptance criteria at every age for REF and at six of eight ages for GEO, and the Lin-KK mean residuals stayed below 1.1% for REF and below 0.4% for GEO.

The two systems evolve along different microstructural pathways. The REF impedance magnitude exceeded that of GEO by one to two orders of magnitude at every age. The REF arc resistances and Warburg amplitude rose by nearly two orders across the window, the

signature of unidirectional C-S-H densification, with a single reversal in R2 at the topology transition attributable to the redistribution of resistance to the third arc. The GEO parameters were smaller, rose by about one order, and were collectively irregular between Day 10 and Day 21. The GEO first and second arcs also exchange their characteristic frequencies and CPE magnitude ranges at Days 7 and 10, so neither represents a single physical feature across the series.

The research question asked whether the pore network and pore solution chemistry of GEO produce a distinguishable electrochemical signature from REF, and whether EIS parameters can serve as non-destructive indicators of strength development in a cement-free UHPC. **Both parts are answered affirmatively.**

GEO is electrochemically distinct from REF on every axis the measurement resolves. Its impedance magnitude is one to two orders lower. Its topology is single-stage rather than stage-dependent, with no resolvable third arc at any age. Its intermediate-age parameter behavior is irregular where that of REF is not. And its upper bound on the solution resistance rises by a factor of 1.5 across the window against 4.3 for REF, a divergence read directly from the measured spectra rather than from the fit. These are the electrochemical expression of the binder chemistry established structurally in Chapter 1.

On the practical question, the analysis identified **binder-specific strength indicators**. For REF the gel pore resistance R2 correlates with compressive strength at a logarithmic coefficient of 0.987 and supports quantitative estimation from Day 10 onward, where its value is determined to within 4% across the admissible parameter family. For GEO the Warburg coefficient W correlates at 0.954 linear and 0.983 logarithmic across the full window.

The two selections rest on different grounds. For REF both candidates correlate almost identically and the choice falls to identifiability, R2 shifting by 3.9% across the Stage 2 window against 41.6% for the Warburg amplitude. For GEO the choice is forced by the data, R2 falling 17.7% between Day 21 and Day 28 while the strength rises from 140 to 152 MPa. Both selections were tested against the fitting choices that produced them and neither changed, the REF coefficient moving from 0.987 to 0.974 under a freed solution resistance and the GEO coefficient from 0.983 to 0.990 under a restricted fitting band.

The central qualification is that the optimal indicator is binder-specific. Impedance-based monitoring of UHPC cannot rely on a single universal parameter and must be calibrated to the binder chemistry. For the NATURSEA-PV application this establishes that the cement-free geopolymer UHPC is amenable to the same class of non-destructive electrochemical quality control as conventional UHPC, a prerequisite for its deployment in offshore FPV substructures where in-situ strength verification during ambient curing is operationally valuable.

2.4.1 Limitations and perspectives

Six limitations of the present analysis are acknowledged and define perspectives for future work.

First, the solution resistance was not measured in either system. In all 16 spectra the real part of the impedance is still decreasing at the top of the acquisition window, and the characteristic frequency of the fastest arc is 5.79 MHz for REF and 9.12 MHz for GEO at Day 1. Extending the acquisition ceiling above 10 MHz, or adopting a four-terminal fixture, would bring the intercept inside the window. This limit also propagates to the REF Warburg parameters, which share the same frequency-flat character.

Second, the GEO first-arc parameters at Days 2 and 14 are not constrained by the data. The objective function is invariant to a sixteenfold change in the associated CPE magnitude and to the full range of its exponent, because the corresponding relaxation lies four orders of magnitude below the 4 Hz lower limit of the measurement window. These two ages are excluded from the interpretation of the GEO first arc throughout the chapter. Extending the acquisition floor below 4 Hz would test whether the relaxation is physical or an artifact of the two-arc topology applied to a system that may not require it at early ages.

Third, the fiber population differs between the two systems. REF carries virgin steel fiber and GEO the recycled blend of the deployment mix, at matched dosage but not matched type. Any observable that depends on the fiber-matrix interface is confounded between binder and fiber, and the third arc of the REF circuit is such an observable. The acoustic emission campaign of Chapter 3 holds the fiber type constant across both systems and therefore addresses this confound for the mechanical observables, though not for the impedance response, which would still require a GEO series cast with virgin fiber and measured by EIS.

Fourth, the irregularity of the GEO trajectories between Day 10 and Day 21 could not be mechanistically confirmed. Two of the five affected observables have identified fitting causes rather than physical ones, and the remaining three are consistent with a delayed gel reorganization but do not establish it. Time-resolved microstructural characterization across that window, by in-situ X-ray diffraction or nuclear magnetic resonance, would settle it.

Fifth, the fitting configuration constrained part of the parameter set. The REF Stage 2 exponents were fixed rather than fitted, and the REF solution resistance reached its 500 Ω cap at six consecutive ages. A refit under a raised cap, together with the extended frequency window identified above, would establish how much of the residual uncertainty is a property of the material and how much of the configuration.

Sixth, all spectra come from a single batch of each mix, and the two calibrations are specific to these mixes: the rule for selecting an indicator transfers to other binders, the calibration curves do not. Validation on additional batches and mixes is required before the indicators are used for quality control, and circuit-free analyses of the full spectrum, such as the distribution of relaxation times or a principal component analysis across ages, would

extend the single-parameter indicators toward a multidimensional maturation signature; sixteen spectra are too few for statistical learning.

2.5 Transition to Chapter 3

This chapter characterized the two systems through their bulk electrochemical response, establishing how the pore network evolves with curing and how that evolution tracks compressive strength. The impedance response is an integrative, volume-averaged probe: it reports the net state of the matrix but does not resolve the discrete events by which the material accumulates and releases mechanical energy under load. Yet the marine substructure application of NATURSEA-PV subjects the material not to the quasi-equilibrium conditions of curing but to mechanical loading, in which fracture initiation, crack propagation, and the bridging action of the steel fibers govern the structural performance and the durability of the cracked state.

The chapter also left one question open that a mechanical probe can address. The third arc of the REF circuit was assigned to the fiber-matrix interfacial transition zone. REF and GEO carry the same fiber dosage but not the same fiber type, REF being reinforced with virgin uncoated steel and GEO with the recycled blend of the deployment mix, on which retained rubber residue covers part of the fiber surface. The electrochemical evidence therefore cannot separate a binder effect from a fiber effect at that interface. The acoustic emission campaign of the next chapter is cast with the same virgin fiber population in both systems, so the fiber is held constant there and the comparison isolates the binder. It also observes the interface directly under load rather than through its dielectric response.

The next chapter therefore turns from the electrochemical to the mechanical, and from the volume-averaged to the event-resolved. Chapter 3 applies multi-parameter acoustic emission monitoring under three-point bending to four configurations, the two matrices in plain and steel-fiber-reinforced format 24 hours and 28 days, resolving fracture into matrix cracking, fiber-matrix debonding, and frictional pull-out. That campaign is a separate casting series at a fiber dosage of 120 kg/m^3 with a virgin fiber population in both systems, so it is not comparable to the present chapter on fiber content and is not intended to be. Where the present chapter distinguished the binders through the slow evolution of their pore networks, the next distinguishes them through the energy-dissipation pathway their fracture engages.

Can a 100% cement-free, ambient-cured UHPGC reach the mechanical and durability performance to survive harsh marine environments and replace conventional UHPC in offshore FPV substructures monitored by SHM?

↓

01

Chapter 1. Formulation and characterization

Cement-free UHPGC mix, recycled fibers,
mechanical and rheological validation

↓

02

Chapter 2. Electrochemical Impedance Spectroscopy

Pore network and pore solution signatures of REF and GEO

↓

03

Chapter 3. Acoustic emission and fracture mechanics

Crack initiation, propagation, energy dissipation

↓

04

Chapter 4. Durability and Carbon footprint assessment

Sulfate, acid, chloride, thermal, and HarshLab
Cradle-to-grave environmental and economic balance

Chapter 3 - Acoustic emission and Fracture Mechanics

Chapter 2 established that the REF and GEO mixes of the thesis carry distinguishable bulk electrochemical signatures, with EIS resolving the pore network and pore solution differences predicted by the microstructural baseline of Chapter 1. The EIS response, however, probes the undisturbed material. It does not describe how the two binders behave once the matrix is forced to crack. The next question shifts from non-destructive monitoring of an intact specimen to the dynamics of failure: under load, how do the two binders initiate cracks, propagate them, and dissipate energy, and does the binder difference identified in Chapters 1 and 2 carry through to the fracture process. Chapter 1 (Section 1.5.7) already provided a first qualitative answer in the form of two distinct fracture surface morphologies in fiber pull-out, with cohesive failure observed through the geopolymer matrix and adhesive failure observed along the Portland-cement interfacial transition zone. Chapter 3 turns this qualitative observation into a quantitative, time-resolved description by coupling three-point bending of notched prismatic specimens with multi-parameter acoustic emission monitoring, on a 2 × 2 experimental design in binder chemistry and fiber inclusion. For clarity within this chapter, the four configurations are designated R (Portland-cement reference without fibers), Rf (R with fibers), G (geopolymer matrix without fibers), and Gf (G with fibers). The relationship between this notation and the thesis-wide REF and GEO labels is detailed at the start of Section 3.2.1. The four configurations are tested at two curing ages of 24 hours and 28 days. The fiber type and volume fraction are held constant across Rf and Gf to isolate the contribution of binder chemistry to the fracture response. The chapter is a case study using virgin straight steel fibers (SPAJIC OL 13/.20, NV Bekaert SA, EN 14889-1:2006 compliant) and does not address the recycled tire-derived steel fiber formulation developed for the NATURSEA-PV substructure application, which is treated in Chapter 1. The conclusions drawn here therefore apply to the specific binder pair tested with this fiber geometry, and their transfer to recycled fibers and to other precursor systems is discussed in the chapter Conclusion and in the General Conclusion of the thesis. Chapter 3 characterizes this fracture experimentally, through multi-parameter acoustic emission. The research question it addresses is stated formally in Section 3.1.5, once the relevant background and the gap have been established.

3.1 State of the art

Acoustic emission (AE) is the release of transient elastic waves from a material under stress when local strain energy is suddenly redistributed by a damage event. In concrete-like materials the events are microcrack nucleation, microcrack coalescence, interfacial debonding, frictional sliding on existing crack faces, and fiber pull-out (Aggelis, 2011; Behnia et al., 2014). Piezoelectric transducers coupled to the specimen surface convert the surface motion produced by these waves into a voltage signal that is sampled, parameterized,

and stored alongside the mechanical loading record. The technique therefore delivers a time-resolved damage record that load-displacement curves alone cannot produce. The price for that resolution is a list of acquisition and processing choices, each of which must be defended in the methods section: threshold, frequency band, sensor type, hit timing parameters, sliding-window length for the b-value, slope of the RA-AF classifier, attenuation-sensitive versus attenuation-insensitive descriptors. This section defines every term that appears in the rest of the chapter, introduces the equations behind each descriptor, summarizes what is known about AE in fiber-reinforced UHPC and in alkali-activated composites, and ends by isolating the gap that the present chapter is designed to close.

Two conventions govern the acquisition and are used throughout. A hit is one sensor's record of a signal that crossed the detection threshold, whereas an event is the set of hits attributed to a single source, so hit counts reflect sensor coverage as well as source activity. All parametric statistics in this chapter are computed at the hit level, the standard convention in AE fracture studies on concrete (Ohtsu et al., 2007.; Aggelis, 2011). The waveform recorded at the sensor is not the waveform at the source: the detection threshold, the sensor frequency response, and the three timing windows that segment the continuous signal into hits (peak definition, hit definition, and hit lockout time) all shape what is recorded (Behnia et al., 2014; Grosse et al., 2021). The values adopted in this work, and the rationale for each, are reported with the acquisition chain in Section 3.2.3.

3.1.1 Acoustic emission in cementitious materials

A damage event releases part of the stored elastic strain energy as an elastic wave. In cementitious matrices the characteristic frequency content of these sources lies between 20 kHz and 1 MHz, well above structural vibration and most environmental noise, which is what makes AE usable on a specimen during an active mechanical test (Behnia et al., 2014; Grosse et al., 2021). What reaches the sensor, however, is shaped by four acquisition choices, each defended below.

3.1.1.1 Detection threshold

The threshold is the voltage level, expressed in dB relative to 1 µV at the sensor output, above which the acquisition system begins to record a hit. Below it the signal is discarded as background noise. A threshold set too low inflates the hit count with electrical and mechanical noise, and one set too high suppresses low-energy damage events and biases the population toward high-amplitude sources (Aggelis, 2011).

3.1.1.2 Sensor selection and frequency band

Resonant sensors have a strong response peak near a single central frequency and a higher signal-to-noise ratio in that band. Broadband sensors trade sensitivity for a flatter response across a wider window. For concrete fracture studies the resonant type with a 150

kHz central frequency is the standard choice, because the dominant frequency content of microcracking in cementitious matrices sits in this band and the signal-to-noise gain over a broadband sensor is decisive at the low thresholds used in laboratory AE (Muralidhara et al., 2010; Behnia et al., 2014).

3.1.1.3 Hit timing parameters: PDT, HDT, HLT

Three timing parameters segment the continuous signal stream into discrete hits. The peak definition time is the window opened after the first threshold crossing within which the peak amplitude is searched, and it must exceed the rise time of the slowest physically meaningful source, or a short burst following the first crossing will be locked in as the true peak. The hit definition time is the window opened after the most recent crossing within which the system waits for the next one, and if none occurs the hit is closed at the last crossing. It must therefore be long enough to capture the natural ring-down of the sensor and short enough to separate two genuinely distinct hits. The hit lockout time is the dead time after a hit closes, during which reflections of the same source are prevented from being recorded as new hits. The three timers are shown acting on a single signal in Figure 3-1, alongside the waveform quantities they govern. They must be tuned to the sensor resonance, the specimen geometry, and the expected source frequency. The values adopted here and their justification are given in Section 3.2.3.

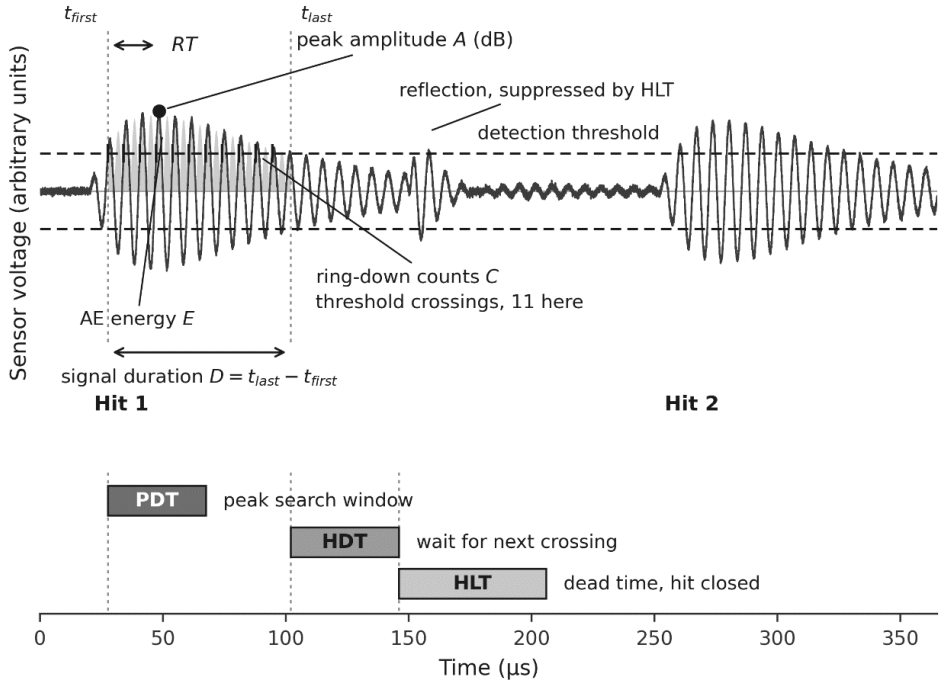

Figure 3-1: Schematic anatomy of an AE hit and the timing parameters that define it.

3.1.1.4 Attenuation, propagation and the limits of cross-material comparison

An AE signal recorded at the sensor is not the signal at the source. Between the source and the sensor, the wave loses amplitude through geometric spreading, scattering on

heterogeneities (aggregates, pores, fibers), and intrinsic material damping. Attenuation in concrete-like materials is in the range of 1 to 5 dB/cm and is strongly dependent on porosity (Shiotani et al., 2001; Ospitia et al., 2023). The more porous of the two binders tested here reaches the top of that range and, in its fiber-reinforced form, slightly exceeds it, as reported with the attenuation calibration in Section 3.2.3. The implication for the present chapter is that the cementitious matrix and the more porous geopolymer matrix do not attenuate equally, and absolute AE amplitude and absolute AE energy cannot be compared between binders without explicit attenuation calibration. Pencil-lead-break (PLB) tests following the Hsu-Nielsen protocol provide a reproducible artificial source for that calibration (Hsu and Breckenridge, 1981). PLB-derived attenuation values for the four configurations are reported in Section 3.2.3, and the consequences for the interpretation of cross-binder claims are discussed in Section 3.4.

A useful taxonomy follows from the attenuation argument. Parameters that depend on absolute amplitude or absolute signal energy (peak amplitude, signal duration in absolute terms, ring-down counts, AE energy, cumulative AE energy) are attenuation-sensitive. Parameters defined as ratios or shape descriptors of within-specimen distributions (RA, AF, b-value, tensile-to-shear ratio) are largely attenuation-insensitive. Cross-binder claims in this chapter are restricted to the second class, while the first class is reported for within-binder comparisons across ages. This distinction is the single most important methodological choice in the chapter.

3.1.2 Acoustic emission descriptors for crack-mode classification

The chapter uses eight descriptors, defined below. Five are read directly from each hit, two are ratios derived from them, and the b-value is computed from the amplitude distribution across a population of hits. Two aggregate measures of the loading history, the hit rate and the cumulative sums, close the section.

3.1.2.1 Peak amplitude A (dB)

The peak amplitude is the maximum value of the rectified voltage signal during the hit. It is expressed in decibels relative to a 1 µV reference at the sensor output:

$$A(dB) = 20 \log_{10} \left(\frac{V_{peak}}{V_{ref}}\right) \quad \textbf{(3.1)}$$

with V_{ref} = 1 µV at the sensor output. Peak amplitude is the most direct measure of source intensity, and it belongs to the attenuation-sensitive class defined above.

3.1.2.2 Signal duration D (µs)

The signal duration is the time interval between the first and the last threshold crossing of the hit:

$$D = t_{last} - t_{first} \quad \textbf{(3.2)}$$

D ranges from a few tens of microseconds for short, brittle events (rapid matrix cracking with a fast ring-down) to several milliseconds for long, sustained events (frictional sliding, fiber pull-out, or post-peak crack-face interaction where the source continues to radiate over an extended time). The literature commonly uses a cut-off near 500 μs to separate short from long events, and the fraction of hits above this cut-off is used as a proxy for the contribution of frictional mechanisms to the damage process (Muralidhara et al., 2010; Li et al., 2022).

3.1.2.3 Rise time RT (μs)

The rise time is the interval from the first threshold crossing to the time of peak amplitude:

$$RT = t_{peak} - t_{first} \quad \textbf{(3.3)}$$

RT is one of the two inputs to the RA descriptor defined below, where its physical mapping onto crack mode is set out.

3.1.2.4 Ring-down counts C

The ring-down count is the number of positive threshold crossings within the hit. C is an integer with no physical units. It correlates with both the signal duration and the amplitude, since a longer or higher hit will produce more crossings before the signal decays back below the threshold. C is one of the inputs to the AF descriptor defined below (Aggelis, 2011; Grosse et al., 2021).

3.1.2.5 AE energy E (energy units, eu)

AE energy is the time integral of the squared (or, in the convention adopted here, rectified) voltage signal over the duration of the hit:

$$E = \int_{t_{first}}^{t_{last}} |V(t)|dt \quad \textbf{(3.4)}$$

The integral is computed in arbitrary units called energy units (eu) rather than joules, because the absolute conversion to joules requires sensor calibration and coupling correction that are typically not performed in laboratory AE on concrete. Within a single instrumented test, cumulative AE energy is a robust measure of total damage-related energy release. Landis and Baillon demonstrated that, for fine-grained cementitious matrices, the cumulative AE energy correlates strongly with the mechanical fracture energy G_f, enabling AE energy to serve as a proxy for fracture energy in within-material comparisons (Landis and Baillon, 2002). The correlation weakens in heterogeneous materials and across material families due to silent dissipation mechanisms that do not radiate detectable high-frequency waves, which places cumulative AE energy in the attenuation-sensitive class.

3.1.2.6 RA value: rise time scaled by amplitude

RA combines rise time and peak amplitude into a single descriptor that captures the "shape" of the hit:

$$RA = \frac{RT\ (\mu s)}{1000\ x\ A\ (V)} \quad \textbf{(3.5)}$$

RA is expressed in ms/V, the factor of 1000 converting the rise time from microseconds to milliseconds. To use Equation 3.5, the peak amplitude must be converted from dB back to volts via $V = V_{ref} \cdot 10^{(A/20)}$, with Vref = 1 µV. Low RA values correspond to short rise times relative to amplitude, characteristic of fast tensile crack opening. High RA values correspond to long rise times relative to amplitude, characteristic of slow shear-dominated mechanisms. RA is the horizontal axis of the RA-AF classification plane (Figure 3-2) and is one of the two descriptors used to assign each hit to a crack-mode class.

3.1.2.7 Average frequency AF: counts per unit duration

AF is the average crossing rate during the hit, expressed in kilohertz:

$$AF = \frac{C}{D\ (ms)} \quad \textbf{(3.6)}$$

High AF values indicate that many threshold crossings occur in a short duration, characteristic of high-frequency content and a fast-oscillating signal (tensile cracking). Low AF values indicate fewer crossings per unit time, characteristic of low-frequency content and a slower oscillation (shear sliding, fiber pull-out). AF is the vertical axis of the RA-AF classification plane (Ohno and Ohtsu, 2010; Aggelis et al., 2013a).

3.1.2.8 RA-AF crack-mode classification

The RA-AF plane is the standard tool for assigning each hit to a crack mode (Figure 3-2). Tensile (Mode I) events cluster at low RA and high AF. Shear (Mode II) events cluster at high RA and low AF. The two populations are separated by a boundary line whose slope k has units of kHz · V / ms. RILEM TC 212-ACD recommends fitting the slope to the data for each material system rather than imposing a universal value (Ohtsu, 2010).

The reason the slope must be fitted rather than imported is that RA is a ratio of a time to a voltage, so its numerical scale depends on the amplitude reference, the pre-amplification, and the sensor sensitivity of the chain that produced it. A slope calibrated on one acquisition chain carries no meaning on another unless both are first reduced to a common convention. Matrix properties compound this, since attenuation shifts the amplitude distribution, and with it the RA distribution, between a dense low-porosity matrix and a more porous one. A data-driven boundary, fitted independently for each specimen by unsupervised clustering on the angular distribution of events in the RA-AF plane, removes the dependence on an imported constant while preserving the physical interpretation of the two regions (Chen et al., 2022). The approach used in this chapter applies K-means clustering (k = 2) to the

angular distribution θ = arctan (AF/RA) and fits the boundary slope independently for each specimen.

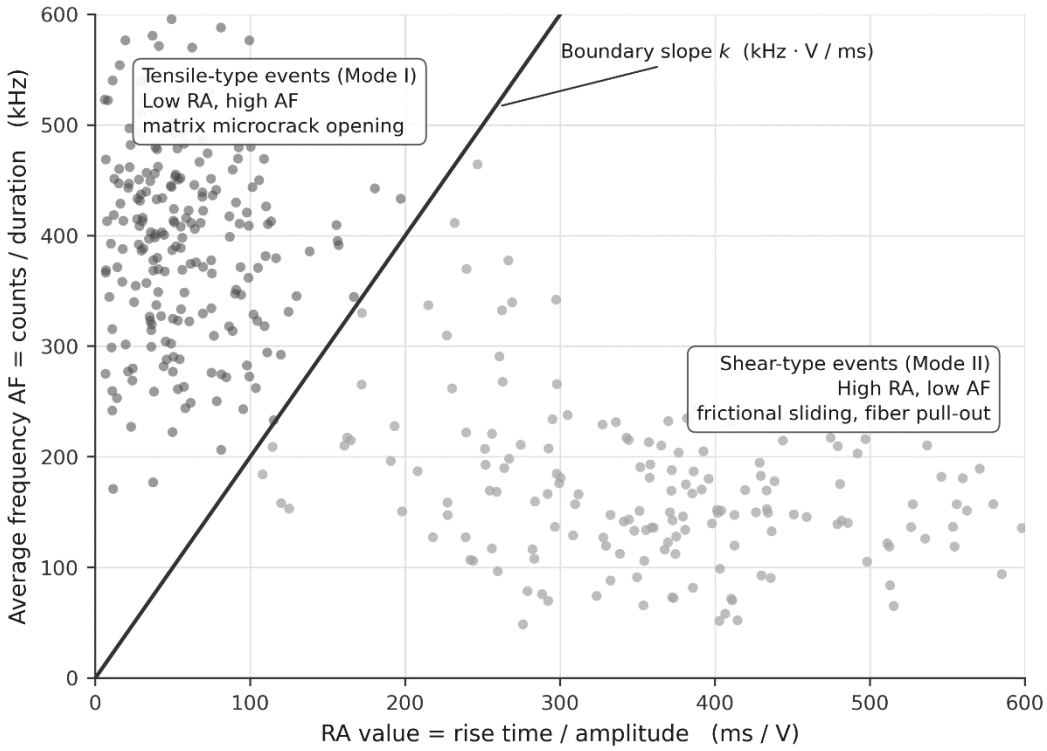

Figure 3-2: Schematic RA-AF crack-mode classification framework. The boundary slope k is fitted independently for each specimen (Section 3.2.4).

3.1.2.9 b-value: shape of the amplitude distribution

The b-value is borrowed from seismology, where the Gutenberg-Richter law relates the cumulative number N of earthquakes with magnitude greater than or equal to M to the magnitude itself:

$$\log_{10} N(\geq M) = a - b \cdot M \tag{3.7}$$

In the AE adaptation, the seismic magnitude is replaced by half the dB amplitude:

$$M_{AE} = \frac{A(dB)}{20} \tag{3.8}$$

The b-value is estimated by maximum likelihood following Aki (1965):

$$b = \frac{N \log_{10} e}{\sum_i (M_i - M_{min})} \tag{3.9}$$

where N is the number of hits in the window, M_i is the AE magnitude of hit i obtained from Equation 3.8, and M_{min} is the magnitude corresponding to the detection threshold. For the 35 dB threshold used here, $M_{min} = 1.75$.

The interpretation is direct. A b-value above 1.5 indicates an amplitude distribution dominated by low-amplitude events, characteristic of distributed microcracking ahead of any

macro-crack. A b-value between 1.0 and 1.5 indicates a mixed regime. A b-value below 1.0 indicates a distribution dominated by high-amplitude events, characteristic of macro-crack propagation with localized damage. Whether the fiber-reinforced geopolymer at 24 hours sustains a b-value above the localization threshold through the whole loading history, and how it compares with its cementitious counterpart, is the most directly testable claim in Chapter 3 and is addressed in Section 3.3.5.

3.1.2.10 Hit rate and damage acceleration

The hit rate is the number of hits per unit displacement (hits/mm) or per unit time (hits/s). Computed in displacement bins of 0.02 mm, the hit rate locates the periods of intense damage activity. Two archetypes are diagnostic of the failure mode. A sharp narrow peak at or just before the peak load is characteristic of quasi-brittle failure: microcracks nucleate, coalesce, and a single macro-crack forms in a short displacement window. A broad plateau extending through the deflection-hardening and post-peak regimes is characteristic of fiber-bridged composites: damage events are continuously generated at fiber-bridging sites throughout the post-peak softening branch (Schechinger and Vogel, 2007; Gao and Tian, 2025). The displacement location and shape of the hit-rate profile are therefore a fingerprint of the failure mode.

3.1.2.11 Cumulative descriptors: hit count and energy

Two running sums complete the descriptor list. The cumulative hit count $N(\delta)$ is the total number of hits recorded up to displacement δ. The cumulative AE energy $E_{cum}(\delta)$ is the corresponding running sum of E. Both quantities follow a sigmoidal trajectory in quasi-brittle matrices, with a slow elastic build-up, a sharp acceleration near peak load, and a plateau after failure. In fiber-reinforced composites, the trajectories are quasi-linear well beyond the peak load, reflecting sustained energy release through fiber debonding and pull-out (Landis and Baillon, 2002; Aggelis et al., 2013b). Both are attenuation-sensitive descriptors, in the sense defined in Section 3.1.1.

3.1.3 Acoustic emission in fiber-reinforced UHPC

UHPC is characterized by a dense, low-porosity binder, a continuous granular skeleton, and compressive strengths above 130 MPa (Yoo and Banthia, 2016; Amran et al., 2022). Steel fibers at typical volume fractions of 1 to 3 vol% convert the inherently brittle matrix into a strain-hardening composite, dissipating energy through matrix microcracking, fiber debonding, and frictional pull-out. AE monitoring of fiber-reinforced UHPC under flexural loading has consolidated around four recurring observations.

Yang et al. studied rapid-hardening UHPC modified with C-S-H seeds and sulfo-aluminate cement under three-point bending. The proportion of shear-type events and the total AE energy increased with the activity of the early-strength agents, consistent with a

denser ITZ and enhanced frictional fiber pull-out (Yang et al., 2023). Gao and Tian extended this framework to lightweight UHPC modified with recycled powder and identified three AE damage stages by combining b-value analysis with energy parameters: elastic flexural hardening, deflection hardening, and flexural softening, each with a characteristic b-value range and energy release rate (Gao and Tian, 2025). Chen et al. combined AE with digital image correlation in fiber-reinforced cementitious composites and applied K-means clustering to AE descriptors. They separated matrix failure from fiber-matrix debonding, with debonding events characterized by amplitudes above 60 dB, and they validated the AE-derived FPZ evolution against DIC strain maps (Chen et al., 2022). Li et al. monitored UHPC-NC composite beams under bending and demonstrated that the b-value trajectory provides a quantitative early-warning indicator of crack propagation across the bond interface (Li et al., 2021).

Three AE signatures recur across these studies. Cumulative AE energy continues to rise well beyond peak load, attributed to progressive fiber pull-out and crack-face friction. The RA-AF distribution carries a measurable shear component, typically 15 to 25% of the event population, attributed to frictional sliding at a dense fiber-matrix interfacial transition zone (Yang et al., 2021; Chen et al., 2022). The b-value typically drops below unity during the post-peak regime, marking damage localization into one or more dominant cracks bridged by the fiber population (Li et al., 2021; Gao and Tian, 2025). Fiber geometry and surface treatment modulate these signatures: hooked-end and twisted fibers, relying on mechanical anchorage rather than interfacial friction, produce different shear-to-tensile balances than straight fibers (Ranjbar et al., 2016).

3.1.4 Acoustic emission in alkali-activated and geopolymer composites

Alkali-activated and geopolymer binders bind aluminosilicate precursors (slag, fly ash, metakaolin, calcined clays) into a three-dimensional gel network through a polycondensation reaction triggered by a high-pH activator (Duxson et al., 2005; Provis and Deventer, 2014). The gel chemistry depends on the precursor and the activator. Slag-rich systems activated by sodium silicate plus potassium hydroxide, as used in the present work, form a calcium-bearing aluminosilicate gel of the C-(N,K)-A-S-H type, distinct from the low-calcium N-A-S-H gel characteristic of fly-ash or metakaolin geopolymers (Garcia-Lodeiro et al., 2011; Bernal et al., 2013). The denser packing of the C-(N,K)-A-S-H network, the presence of residual unreacted slag grains, and the absence of portlandite produce a microstructure that differs from C-S-H-based binders in pore size distribution, gel chemistry, and fracture surface morphology (Palomo et al., 1999; Abdellatief et al., 2023).

Two fracture-mechanical features recur in the geopolymer literature. Pan et al. (2011) measured the Hillerborg characteristic length of fly-ash geopolymer concrete and reported values approximately 3 times smaller than those of ordinary Portland cement concrete of comparable compressive strength, the difference arising from a tensile splitting strength

higher by about 28%, an elastic modulus lower by about 22%, and a fracture energy lower by about 24%. A shorter characteristic length implies a smaller fracture process zone and a more brittle response. That comparison, however, is between a heat-cured fly-ash geopolymer and a normal-strength Portland concrete, both in plain form. It is routinely carried forward as a general property of alkali-activated binders, but neither of its two terms is the material of the present chapter, which is an ambient-cured slag-based system at ultra-high strength for which the appropriate comparator is cementitious UHPC rather than normal-strength concrete. The threefold figure is therefore an upper bound on the brittleness penalty rather than a value transferable to the present binder pair. Liu et al. (2020a) studied steel-fiber-reinforced UHPGC and reported that the fracture energy gain from fiber addition is comparable in magnitude to cementitious UHPC but with a different post-peak softening shape, suggesting a different fiber-matrix interaction mode.

AE monitoring of geopolymer composites is at an earlier stage of development. Ranjbar et al. (2016) characterized the interfacial bond mechanisms of steel and polypropylene fibers in geopolymer composites, establishing that the fiber-matrix interface in alkali-activated systems differs in failure mode from its cementitious counterpart (Ranjbar et al., 2016). Korniejenko et al. (2022) investigated long-fiber-reinforced geopolymer composites at different operating temperatures and reported AE-derived damage stages consistent with those observed in cementitious systems.

None of these AE studies on geopolymer composites includes a direct comparison with a Portland-cement reference of comparable mix design, fiber type, and curing regime, instrumented with the same sensors and processed with the same descriptors. The available evidence therefore characterizes geopolymer fracture in isolation but does not isolate the contribution of binder chemistry to the AE signature.

3.1.5 Research gap and chapter scope

The preceding sections identify one gap that the present chapter is designed to close. The acoustic emission literature has characterized the fracture of cementitious and, more recently, of fiber-reinforced geopolymer composites, but no study has used real-time acoustic emission to compare the operative damage mechanisms of a cementitious and a geopolymer UHPC under identical loading, geometry, and fiber conditions (Section 3.1.4). The distinction in fracture pathway between the two binder chemistries therefore remains inferred from global mechanical response rather than resolved from the damage record itself.

This gap is addressed here for the specific binder pair established earlier in the thesis. Chapter 1 identified, from the fiber pull-out surfaces of the optimized geopolymer, two distinct fracture morphologies: cohesive failure through the geopolymer matrix, against adhesive failure along the interfacial transition zone of the Portland-cement reference. Chapter 2 established, through electrochemical impedance spectroscopy, that the two binders are distinguishable in pore network and pore solution chemistry. What neither

chapter resolved is how this binder distinction expresses itself in the dynamics of failure, when the material is loaded to fracture, and whether the resulting crack can be described numerically well enough to feed the durability analysis of Chapter 4. The first question is the object of the present chapter. The numerical description is reported in Section 3.4.

Chapter 3 accordingly addresses the following research question: at 24 hours and 28 days, how does the binder system, cementitious against geopolymer, shape the initiation, propagation, and energy dissipation of fracture under three-point bending, in both plain and fiber-reinforced conditions, with the steel fiber type and volume fraction held constant? The question is answered experimentally through multi-parameter acoustic emission, and the answer is stated in the chapter Conclusion.

The experimental program is a two-by-two case study in binder chemistry and fiber inclusion, restricted to virgin straight steel micro-fibers.

3.2 Materials and methods

Section 3.2 specifies the experimental program used to answer the chapter research question stated in Section 3.1.5. The program comprises four UHPC configurations (R, G, Rf, Gf), tested under three-point bending at two curing ages (24 hours and 28 days) with simultaneous seven-channel acoustic emission monitoring. The full mix design rationale, the fresh-state characterization, and the microstructural baseline of the four binders are covered in Chapter 1. This section reports only what is required to defend the fracture and AE measurements presented in Sections 3.3 and 3.4.

Chapter 3 is a case study restricted to virgin straight steel fibers (SPAJIC OL 13/.20, NV Bekaert SA, EN 14889-1:2006 compliant). The recycled tire-derived steel fiber formulation developed for the NATURSEA-PV substructure application is treated in Chapter 1 and is not used here. The fracture-pathway conclusions drawn in Sections 3.3 and 3.4 therefore apply to the binder pair tested with this fiber geometry, and their transfer to recycled fiber composites and to other precursor systems is discussed in Section 3.5 and in the General Conclusion of the thesis.

3.2.1 Mixes and specimens

3.2.1.1 Sample naming convention specific to Chapter 3:

In this chapter the reference Portland-cement mix without fibers is designated R, and the same mix with fibers is designated Rf. Likewise, the alkali-activated geopolymer mix without fibers is designated G, and the same mix with fibers is designated Gf. The suffix "f" denotes the addition of straight steel micro-fibers at 1.5 vol%. The fiber type and volume fraction are identical for Rf and Gf, so the experimental design is a 2 × 2 factorial in binder chemistry (R vs G) and fiber inclusion (plain vs fiber-reinforced). This shorthand matches

the published acoustic emission article on which this chapter is based and is used in every figure caption and table of Chapter 3.

3.2.1.2 Cross-chapter clarification:

Chapter 1 reports the formulation work on a single optimized geopolymer composite that includes the steel fibers. That composite is labeled "GEO" in Chapter 1. In the Chapter 3 notation, the Chapter 1 "GEO" mix corresponds to Gf (geopolymer with fibers). The Chapter 3 symbol G denotes the same geopolymer matrix without fibers, introduced here to enable the 2 × 2 fracture-mechanics comparison. R is the plain reference UHPC without fibers, and Rf denotes the same reference tested with the steel micro-fibers designated REF in Chapters 1, 2, and 4.

Two chemically distinct UHPC systems were compared in four configurations. R is the project reference UHPC, the commercial Portland-cement UHPC tested in the project and designated REF elsewhere in this thesis. Its detailed formulation is proprietary and is not disclosed. G is the cement-free alkali-activated binder developed in the present work, synthesized from a binary precursor of ground granulated blast-furnace slag (GGBS) and silica fume, activated by a combined sodium silicate plus 10 M potassium hydroxide solution with a silicate modulus Ms = SiO_2/Na_2O of 1.0 to 1.5 and a total alkali content of 6 to 8% by precursor mass. The reference was received as a supplied premix, mixed in the laboratory according to the supplier's instructions, and tested in two conditions: without fibers (R), and with the same steel micro-fibers and dosage as Gf introduced during mixing (Rf). Full precursor compositions, particle-size distributions, mixing protocols, fresh-state properties, and patent status are reported in Section 1.2.1.

The fiber-reinforced conditions Rf and Gf were obtained by adding straight, uncoated, cold-drawn steel micro-fibers to the corresponding plain matrix at a dosage of 120 kg/m^3 (1.5 vol%). The fiber type and dosage are identical for the two reinforced conditions, so that any difference observed between Rf and Gf in the fracture or AE response can be attributed to the binder rather than to the reinforcement. The fiber properties declared by the manufacturer in accordance with EN 14889-1:2006 are summarized in Table 3-1.

Table 3-1: Steel fiber specification, declared in accordance with EN 14889-1:2006.

Product identifier	**SPAJIC OL 13/.20**
Manufacturer	NV Bekaert SA, Zwevegem, Belgium
Fiber shape	Straight, cold-drawn steel wire
Coating	uncoated
Length L (mm)	13
Diameter d (mm)	0.20
Aspect ratio L / d	65
Tensile strength (N/mm^2)	3050
Modulus of elasticity (GPa)	210

Harmonized standard	EN 14889-1:2006, System 1 conformity, CE marked

Specimens were cast in single-use steel molds of internal dimensions 7 × 7 × 28 cm^3, treated with a thin film of mineral release agent prior to filling. The fresh material was placed in a single lift without external vibration, finished flush with the top of the mold, and covered with a vapor-tight polyethylene film to prevent surface drying. All specimens were cured in ambient laboratory conditions at 20 ± 2 °C and 50 ± 10% relative humidity until the designated testing age of 24 hours or 28 days. No heat curing and no water curing were applied. This regime was selected to evaluate the feasibility of the G mix under in-situ casting conditions, where heat curing is not practical, and to keep R and G under identical thermal and hygric histories.

3.2.1.3 Replicate count and AE-detailed specimen selection

Two specimens per configuration per age (n = 2) were prepared and tested under simultaneous mechanical loading and AE acquisition. Across all eight cells of the design (four configurations × two ages), the coefficient of variation of peak load remained below 8% and the coefficient of variation of total toughness remained below 12% for the four fiber-reinforced cells. The unreinforced cells showed comparable peak-load agreement and a slightly higher toughness dispersion consistent with the shorter post-peak softening branch.

Multi-parameter AE post-processing (b-value evolution, RA-AF classification, hit-rate profiling) was performed on one specimen per cell (n = 1 AE-detailed), selected from the two replicates through a two-step technical pre-screen. (1) Step 1: instrumentation integrity. Both replicates were required to pass the Automatic Sensor Test (AST) of the AEwin software with greater than 95% amplitude recovery across all seven channels, and the Hsu-Nielsen pencil-lead-break (PLB) calibration with a near-field amplitude greater than 80 dB at every channel (Section 3.2.3). (2) Step 2: peak load and below 12% on total toughness, and every AE conclusion is a comparison between cells rather than an absolute value. The full mechanical response of both replicates is reported in Table 3-5 (Section 3.3.3).

This pre-screen is a technical rule rather than an aesthetic selection. It is consistent with established practice in AE fracture studies on cementitious composites, where the stochastic nature of AE waveforms precludes meaningful event-by-event averaging across specimens (Muralidhara et al., 2010; Behnia et al., 2014). The constraint on inferential power is acknowledged explicitly in the limitations subsection (Section 3.4): AE-derived percentages and trajectories are reported with the understanding that they identify a fracture pathway qualitatively, and that confidence-interval estimation on AE descriptors requires future campaigns with larger replicate numbers.

3.2.2 Three-point bending setup

Flexural fracture behavior was evaluated by three-point bending on notched prismatic specimens of dimensions 7 × 7 × 28 cm^3, using a 100 kN servo-hydraulic testing machine and a clear support span of 260 mm. The geometry, loading configuration, and instrumentation are shown in Figure 3-3.

A transverse notch of depth a = 5 mm and width approximately 3 mm was cut at mid-span on the tensile face of each beam with a diamond saw before testing, yielding a notch-to-depth ratio a/d = 0.071. This relatively shallow notch was a deliberate choice for the fiber-reinforced configurations. The deeper notch recommended by RILEM TC 162-TDF for plain concrete (a/d = 0.3 to 0.5) would sever the fiber-bridging zone immediately above the notch tip, pre-determine the crack path, and suppress the matrix-dominated crack-initiation phase that is of primary interest in the present comparative study (RILEM TC 162-TDF, 2002). The 5 mm notch is sufficient to localize the fracture plane at mid-span while preserving full engagement of the fiber-reinforced zone above the notch. The same notch geometry was applied to the plain matrices to keep the configurations directly comparable.

Crack mouth opening displacement (CMOD) was measured with a clip-on extensometer mounted across the notch mouth with a 10 mm gauge length. Loading was applied under CMOD closed-loop feedback control at a constant rate of 0.0013 mm/s for the entire test, in line with the recommendations of RILEM TC 162-TDF (2002) for stable crack propagation through the softening branch. Load was recorded by the load cell of the testing machine and mid-span deflection was recorded by the internal displacement transducer of the actuator. Load, CMOD, and mid-span deflection were sampled synchronously at 10 Hz, giving a displacement resolution of the order of 0.001 mm per data point.

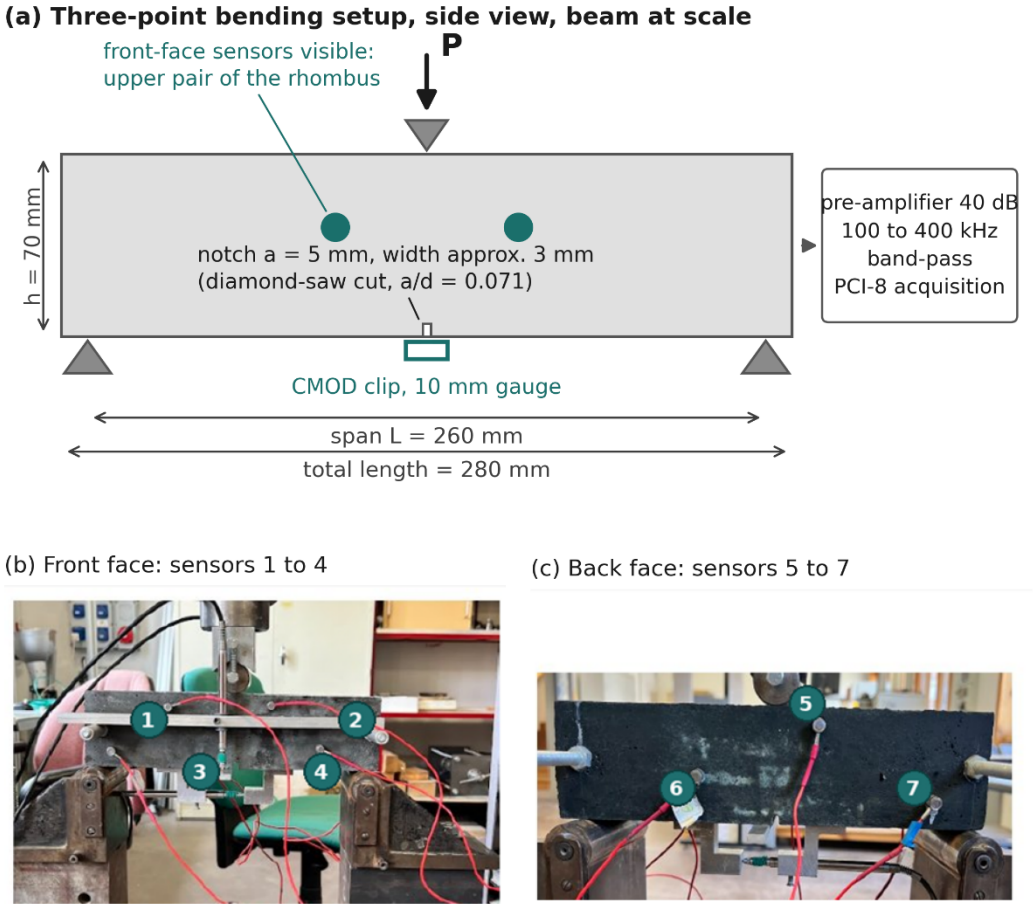

Figure 3-3: Three-point bending setup and seven-channel AE sensor array. (a) Side view to scale. (b) Front face, sensors 1 to 4. (c) Back face, sensors 5 to 7.

3.2.2.1 Toughness and ductility integration protocol

Total flexural toughness G_T was computed as the area under the load-versus-mid-span-deflection curve using the trapezoidal rule, integrated from zero displacement to the maximum recorded displacement at test termination, where test termination was defined as the point at which the residual load fell below 0.5% of the peak load or at which the actuator reached its stroke limit. CMOD-based integration is the reference choice for absolute fracture energy because it isolates crack-related deformation from elastic beam bending and support settlement. In the present test, the CMOD signal carried small but visible feedback oscillations in the post-peak regime that precluded reliable area integration over the full softening branch. Load-deflection integration was therefore adopted as a comparative measure across configurations and ages.

The non-crack deformations included in the mid-span signal are small relative to the total deflection for the fiber-reinforced specimens, where total displacements reach several millimeters, and they affect all four configurations similarly, preserving the validity of the comparative toughness ranking. For the unreinforced specimens, where total deflections are at most a few tenths of a millimeter, the relative overestimation is proportionally larger. Reported toughness values for R and G plain matrices are therefore comparative within the

precision allowed by the integration choice, and the plain-matrix toughness comparison is interpreted with that caveat throughout Sections 3.3 and 3.4.

The toughness was decomposed into pre-peak and post-peak contributions to separate the matrix-dominated and the fiber-bridging-dominated phases. The ductility index was defined as the ratio of the displacement at test termination to the displacement at peak load, providing a single dimensionless measure of post-peak deformation capacity.

3.2.3 Acoustic emission acquisition

Acoustic emission was acquired simultaneously with mechanical loading using a PCI-8 multi-channel data acquisition system and seven R15-type resonant piezoelectric transducers with a 150 kHz central frequency. The seven sensors were arranged asymmetrically on the two longitudinal faces of the specimen, with the layout chosen to maximize coverage of the fracture process zone at and around the mid-span notch. Four sensors were mounted on the front face in a rhombus pattern centered on the notch and the loading axis: two sensors (1 and 2) above mid-height, flanking the loading nose on either side, and two sensors (3 and 4) below mid-height, flanking the notch on either side. Three sensors were mounted on the back face in a downward-pointing triangle: a single sensor (5) at the top edge directly above the notch, and two sensors (6 and 7) near the bottom edge close to the supports. The schematic layout and the corresponding laboratory installation are shown in Figure 3-3.

Raw analog signals were pre-amplified at 40 dB gain and filtered with a 100 to 400 kHz band-pass to suppress low-frequency mechanical noise from the loading frame and high-frequency electronic interference. A fixed amplitude threshold of 35 dB was applied uniformly across all seven channels. The hit-timing parameters of the acquisition system were set to peak definition time PDT = 100 µs, hit definition time HDT = 200 µs, and hit lockout time HLT = 400 µs, with a maximum hit duration of 1000 ms and a waveform sampling rate of 1 MHz. The physical meaning of PDT, HDT, and HLT, and the rationale for their tuning, are given in Section 3.1.1. Table 3-2 summarizes the complete acquisition configuration.

Table 3-2: Acoustic emission acquisition parameters. Physical meaning of each parameter in Section 3.1.1.

Parameter	Value
Acquisition system	Mistras PCI-8 multi-channel
Sensor type	R15 resonant piezoelectric, 150 kHz central frequency
Number of channels	7 (4 front face + 3 back face, asymmetric)
Pre-amplification gain	40 dB
Band-pass filter	100 to 400 kHz
Detection threshold	35 dB (fixed, uniform across all channels)

Peak Definition Time (PDT)	100 µs
Hit Definition Time (HDT)	200 µs
Hit Lockout Time (HLT)	400 µs
Maximum hit duration	1000 ms
Waveform sampling rate	1 MHz
Effective dynamic range	35 to 99 dB at the sensor (after 40 dB pre-amp and 5 dB cable loss)
Software	AEwin (Mistras Group)

3.2.3.1 Sensor coupling verification and PLB attenuation calibration

Before each test, sensor coupling was verified by the Automatic Sensor Test (AST) of the AEwin software, which injects a known excitation through each sensor in turn and measures the response at the others. Coupling was accepted only when every channel showed an amplitude recovery greater than 95%. In parallel, three Hsu-Nielsen pencil-lead-break (PLB) calibration sources (Hsu and Breckenridge, 1981) were applied with a 2H 0.5 mm graphite lead at three positions along the beam (notch mouth, quarter-span, and near a support). PLB sources provide a reproducible artificial AE event whose location and amplitude are known to within a tolerance of a few decibels, and they serve here both as a final coupling check (every sensor was required to register an amplitude greater than 80 dB at the near-field source) and as a characterization of the attenuation profile of each specimen.

The PLB-derived attenuation values for the four configurations are summarized in Table 3-3. The cementitious configurations R and Rf showed attenuation in the range of 2.1 to 3.8 dB/cm, while the geopolymer configurations G and Gf showed attenuation in the range of 3.5 to 5.2 dB/cm, consistent with the higher water-accessible porosity of the latter (Section 3.3.1). The within-binder variation across replicates is small relative to the cross-binder difference, which supports treating attenuation as a binder property rather than a specimen artifact, and which is the measured basis for the descriptor taxonomy of Section 3.1.1. No path-length correction was applied to the parametric AE data.

Table 3-3: Pencil-lead-break attenuation calibration (Hsu and Breckenridge, 1981), measured at three positions along the beam.

Configuration	Attenuation range (dB/cm)	Comment
R	2.1 to 3.4	Dense Portland-cement matrix, lowest signal loss
Rf	2.5 to 3.8	Slightly higher, fiber inclusion increases scattering
G	3.5 to 4.5	Higher porosity ~6% (Section 3.3.1)
Gf	4.0 to 5.2	Highest porosity + fiber scattering combined

3.2.4 AE data processing

Seven descriptors were extracted from the parametric AE record, all defined in Section 3.1.2: peak amplitude A, signal duration D, rise time RT, ring-down counts C, AE energy E, and the two derived ratios RA and AF. The processing choices that operationalize these descriptors are reported below. The physical meaning of each parameter is not repeated here.

3.2.4.1 b-value evolution

The b-value was estimated through the Aki maximum-likelihood estimator (Section 3.1.2) on chronologically ordered hits, using a sliding window of 500 consecutive hits stepped by 50 hits, yielding a continuous b-value trajectory as a function of CMOD. The 500-hit window length was selected to balance statistical stability of the Gutenberg-Richter linear regression against temporal resolution. Robustness was verified by repeating the analysis with window sizes of 300 and 700 hits: the b-value transitions identified in Section 3.3.5, including the sustained $b > 1.0$ trajectory of Gf at 24 hours, remained consistent across all three window sizes. The standard error of each b-value estimate, computed as $\sigma_b = b / \sqrt{N}$, was typically ±0.09 to 0.13 for the 500-hit window, smaller than the b-value transitions characteristic of damage-stage changes ($\Delta b \approx 0.3$ to 0.5). The detection threshold of 35 dB corresponds to a minimum AE magnitude $M_{min} = 1.75$ in the Aki framework. The upper limit of the dynamic range (99 dB at the A/D converter) was never reached, the maximum recorded amplitude in the campaign being 96 dB on a Rf specimen at 28 days. No signal saturation was observed.

3.2.4.2 RA-AF crack-mode classification

Each hit was placed in the RA-AF plane following the descriptor definitions of Section 3.1.2. The classification boundary, which separates the tensile cluster at low RA and high AF from the shear cluster at high RA and low AF, was determined individually for each specimen by K-means clustering with $k = 2$ on the one-dimensional angular distribution $\theta = \arctan(AF/RA)$. The boundary slope k_b was taken as the tangent of the bisector angle between the two cluster centroids and is expressed in kHz·V/ms. The clustering was run from a fixed random seed so that the fitted boundaries are reproducible. The mean silhouette score across the eight specimens of the campaign was 0.61 ± 0.07, indicating a moderate but physically meaningful cluster separation.

Two sensitivity tests were applied to confirm that the reported tensile and shear percentages are not artifacts of the classification choice. **First,** the detection threshold was varied by ±5 dB (30 and 40 dB) and the K-means classification re-run. The tensile and shear percentages varied by less than ±2.5 percentage points for every specimen, well below the cross-binder differences reported in Section 3.3.6. **Second,** the fitted boundary slope was varied by ±30% for every specimen and the classification recomputed. The absolute tensile

and shear percentages shift by 11 to 14 percentage points across that range and are therefore reported as readings at the fitted boundary rather than as absolute values. The comparisons the chapter draws from them are unaffected: the shear fraction of Rf exceeds that of Gf at both ages and at every slope tested, and the change in shear fraction produced by adding fibers is positive in the cementitious system and negative or negligible in the geopolymer system at both ages and at every slope tested. The recommendation of RILEM TC 212-ACD is itself to fit the boundary to the material system rather than to impose a universal value (Ohtsu, 2010), which is the approach followed here and justified on physical grounds in Section 3.1.2.

All recorded hits carried finite, positive RA and AF and were therefore classifiable. No hits were excluded from the crack-mode analysis.

3.2.4.3 AE hit rate

The hit rate was computed by binning the hits into displacement windows of width 0.02 mm and counting the number of hits whose associated mid-span displacement fell within each bin. The bin width was chosen as the smallest value that gives at least one hit per bin in the post-peak regime for the fiber-reinforced configurations, ensuring a well-resolved profile without introducing artificial spikes in the unreinforced cases. The resulting histogram was smoothed with a 3-bin moving average for visualization only. All reported peak positions and peak magnitudes refer to the unsmoothed distribution.

3.2.4.4 Long-duration event fraction

The long-duration event fraction was defined as the percentage of hits whose signal duration D exceeded 500 µs, the literature cut-off associated with frictional sliding and post-peak crack-face interaction (Landis and Baillon, 2002). Following the attenuation taxonomy of Section 3.1.1, the long-duration fraction is interpreted as a relative indicator within each material system, and cross-binder comparisons are made cautiously, acknowledging that signal duration is influenced both by the source mechanism and by sensor resonance, specimen geometry, and material-dependent attenuation. The systematic difference in long-duration fraction between Rf and Gf reported in Section 3.3, measured with identical sensors and an identical specimen geometry, supports its interpretation as a binder-dependent fracture signature.

3.3 Results

Section 3.3 reports the experimental observations from the program defined in Section 3.2 and the interpretation that follows directly from each descriptor. Subsections 3.3.1 to 3.3.7 are organized by descriptor, from the mechanical baseline to the AE-derived parameters. Each closes with the short interpretive step that the data on the page supports. The multi-parameter integration that identifies the binder-specific fracture pathway, the

cross-anchor to Chapter 2 EIS, and the methodological limitations are gathered in Section 3.4. Each numerical claim is anchored to a specific figure or table.

3.3.1 Mechanical baseline: compressive strength and water porosity

Table 3-4 reports the compressive strength of the four configurations at 24 hours and 28 days, measured on 100 mm cubes, together with the water-accessible porosity at 28 days measured on 40 mm cubes according to NF P18-459. All values are means of three specimens, reported with the standard deviation. Both binder systems reached the strength range expected of ultra-high-performance matrices once fiber-reinforced (Yoo and Banthia, 2016), while the plain geopolymer matrix at 112 MPa sits below the 130 MPa threshold conventionally applied to this class. At 28 days the Portland-cement reference R reached 130 MPa, while the alkali-activated reference G reached 112 MPa, leaving a strength gap of 18 MPa (14%) between the two binders. The introduction of steel fibers at 1.5 vol% added 15 to 28 MPa to the 28-day compressive capacity, lifting Rf to 145 MPa and Gf to 140 MPa. At 24 hours the same hierarchy held, with a wider relative gap between the plain matrices: R reached 58 MPa and G 49 MPa, a difference of 9 MPa or 16%. The fiber contribution at this age was larger in the geopolymer, 21 MPa against 16 MPa, bringing Rf and Gf to 74 and 70 MPa, a gap of only 5%. The two fiber composites therefore entered the flexural tests at 24 hours with closely matched compressive capacity. These values are not directly comparable with the 28-day compressive strengths reported for REF and GEO in Chapter 1. Those were determined on prism halves following EN 196-1, on specimens carrying the recycled tire-derived fiber blend of the NATURSEA-PV formulation rather than the virgin straight fibers used here. Both the specimen geometry and the fiber system differ.

Water-accessible porosity followed the inverse hierarchy. The Portland-cement matrix R was the densest at 3.2% and the alkali-activated matrix G was twice as porous at 6.4%. Adding steel fibers increased porosity in both systems by entrapped air and by the formation of a more porous interfacial transition zone around the fibers: Rf reached 4.8% and Gf reached 8.25%.

Together these two measurements set the baseline against which the AE descriptors must be interpreted. R was denser and stronger, whereas G was more porous and weaker. The porosity gap, a factor of two between the matrices, is the structural origin of the attenuation gap reported in Table 3-3 for the plain matrices (R: 2.1 to 3.4 dB/cm; G: 3.5 to 4.5 dB/cm) and is the reason why cross-binder comparisons of absolute AE amplitude and AE energy must be qualified, per Section 3.1.1. Whether that strength and porosity hierarchy carries through to fracture energy is the first question the flexural results address.

Table 3-4: Compressive strength at 24 hours and 28 days on 100 mm cubes, and water-accessible porosity at 28 days per NF P18-459 on 40 mm cubes.

Mix	24 h compressive strength (MPa)	28 d compressive strength (MPa)	28 d water-accessible porosity (%)

R	58 ± 4	130 ± 3	3.2 ± 0.2
Rf	74 ± 6	145 ± 4	4.8 ± 0.35
G	49 ± 5	112 ± 4	6.4 ± 0.28
Gf	70 ± 4	140 ± 5	8.25 ± 0.4

3.3.2 Flexural response under three-point bending

Load-deflection curves at 24 hours are shown in Figure 3-4 and at 28 days in Figure 3-5, in each case split into plain matrices (panel a) and fiber-reinforced composites (panel b). The peak load, the displacement at peak load, and the maximum displacement at test termination are listed in Table 3-5.

The plain matrices exhibited the quasi-brittle response expected from notched UHPC specimens: a sharp linear rise to peak load followed by a fast load drop. At 24 hours R reached 3.88 kN at 0.03 mm and G reached 2.77 kN at 0.03 mm (Figure 3-4a). At 28 days R reached 3.99 kN and G reached 2.19 kN at comparable peak displacements (Figure 3-5a). The plain geopolymer was the only configuration whose peak flexural load fell between the two ages, from 2.77 to 2.19 kN, over a period in which its compressive strength rose from 49 to 112 MPa. Increasing matrix stiffness with continued geopolymerization raises the stress concentration at the notch tip without a matching gain in fracture surface energy, so the notched flexural capacity does not follow the compressive gain. The same divergence appears in the toughness data of Section 3.3.3, where the two plain matrices converge despite an 18 MPa compressive gap.

The fiber-reinforced composites transformed the response into deflection-hardening with a broad post-peak softening branch. At 24 hours Rf attained 11.54 kN at 1.02 mm and Gf attained 9.63 kN at 1.03 mm. Gf sustained load up to 3.85 mm of mid-span deflection, the largest maximum displacement observed for any specimen in the campaign (Figure 3-4b). At 28 days Rf reached 15.91 kN at 1.50 mm and Gf reached 13.93 kN at 0.95 mm (Figure 3-5b). The peak-load gap between the cementitious and the geopolymer composite is 17% at 24 hours and 12% at 28 days.

The fiber addition multiplied the peak flexural load by a factor of 3.0 to 6.4, the largest gain being that of the geopolymer at 28 days. The peak-load hierarchy R > G under compression carried through to Rf > Gf under flexure, but the displacement at peak load and the maximum displacement at test termination told a different story: Gf reached the largest maximum displacement of the campaign at 24 hours (3.85 mm), suggesting that the geopolymer composite engages its post-peak fiber-bridging capacity earlier and more extensively than the cementitious composite at this age. At 28 days the pattern reversed: Gf reached its peak load at 0.95 mm against 1.50 mm for Rf, so the geopolymer composite peaked earlier but the cementitious composite sustained load over a longer deflection.

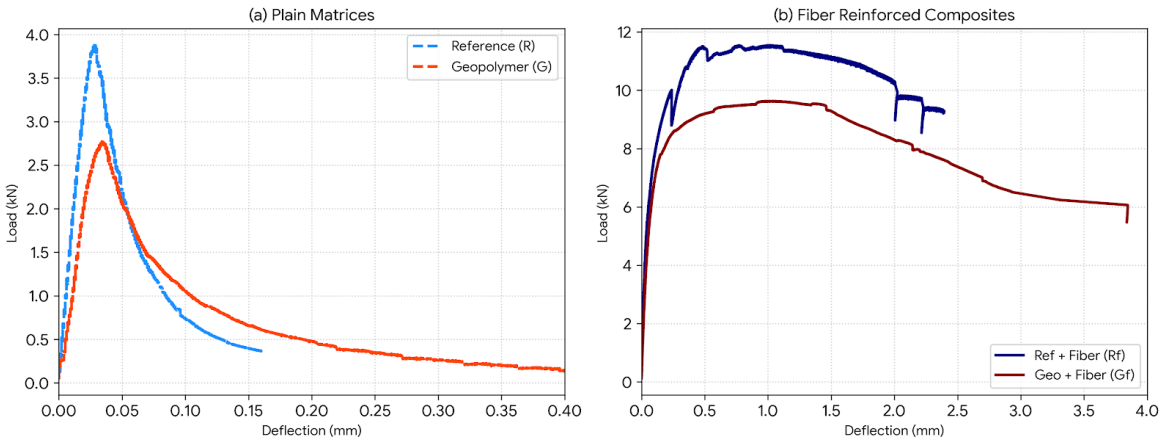

Figure 3-4: Flexural load-deflection response at 24 hours. (a) Plain matrices. (b) Fiber-reinforced composites.

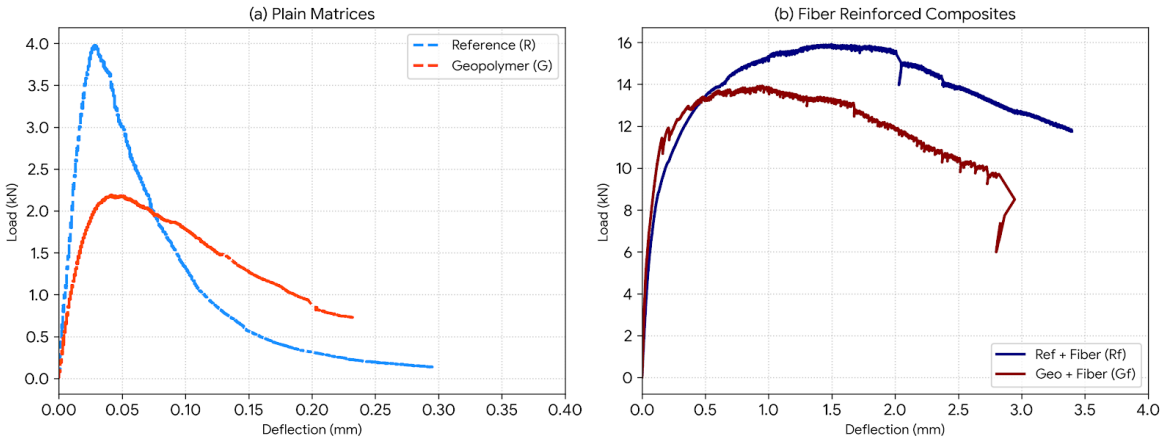

Figure 3-5: Flexural load-deflection response at 28 days. (a) Plain matrices. (b) Fiber-reinforced composites.

3.3.3 Toughness and ductility

Total flexural toughness G_T, defined in Section 3.2.2 as the area under the load-versus-mid-span-deflection curve, is the integrated measure of energy absorption capacity across the test. Values for the eight cells of the design are reported in Table 3-5 and visualized panel by panel in Figure 3-6, with pre-peak and post-peak contributions shaded separately.

The plain matrices exhibited very low total toughness at both ages, dominated by the post-peak contribution. At 24 hours R reached 0.224 J (pre-peak 0.062 J, post-peak 0.162 J) and G reached 0.298 J (pre-peak 0.054 J, post-peak 0.244 J). At 28 days the two plain matrices reached almost identical total toughness, 0.334 J for R and 0.336 J for G, in spite of the 18 MPa compressive strength gap. Within the precision allowed by the load-deflection integration used here (Section 3.2.2, toughness integration protocol), the two plain matrices dissipated comparable energy in fracture at 28 days.

The fiber-reinforced composites were two orders of magnitude tougher. At 28 days Rf reached 46.67 J and Gf reached 34.98 J, corresponding to a 140-fold increase over R for Rf

and a 104-fold increase over G for Gf. At 24 hours the order was reversed: Gf reached 30.20 J while Rf reached 25.05 J, a difference of 5.15 J in favor of the geopolymer composite. The toughness crossover between Gf and Rf therefore occurred between the 24-hour and the 28-day test. Between 24 hours and 28 days, Rf gained 21.62 J in total toughness (+86%) while Gf gained only 4.78 J (+16%).

The ductility index, defined in Section 3.2.2 as the ratio of the displacement at test termination to the displacement at peak load, captures the post-peak deformation capacity. Plain matrices had ductility indexes in the range 5.7 to 13.2, dominated by the very small displacement at peak. The two plain matrices moved in opposite directions between the ages. R rose from 5.71 to 10.54 as its maximum displacement grew from 0.16 to 0.30 mm, while G fell from 13.21 to 5.66 as its maximum displacement contracted from 0.45 to 0.23 mm. The plain geopolymer therefore lost both peak flexural load and post-peak deformation capacity over the same period, two independent expressions of the embrittlement noted in Section 3.3.2. Fiber-reinforced composites had lower ductility indexes (2.27 to 3.73) because their displacement at peak is larger, but they sustained load over a much wider absolute displacement range. Gf consistently had the highest ductility index among the fiber composites (3.73 at 24 hours and 3.10 at 28 days), consistent with the extended post-peak softening visible in Figure 3-4b and Figure 3-5b.

The toughness crossover warrants an interpretive step here. The 86% gain of Rf between 24 hours and 28 days is much larger than the 16% gain of Gf over the same period. The most plausible mechanism is differential maturation of the fiber-matrix interfacial transition zone. Continued Portland-cement hydration between 24 hours and 28 days densifies the ITZ around the fibers in Rf, increasing frictional resistance during pull-out and lifting post-peak toughness from 14.61 J to 26.65 J (+82%). The geopolymer matrix in Gf, whose alkali-activation reaction is substantially complete at 24 hours under ambient curing, gains less ITZ stiffness over the same period. The post-peak toughness increases more modestly, from 21.33 J to 23.36 J (+10%). This hypothesis is consistent with the b-value, RA-AF, and duration evidence reported in Subsections 3.3.5 to 3.3.8 and is consolidated in Subsection 3.3.9.

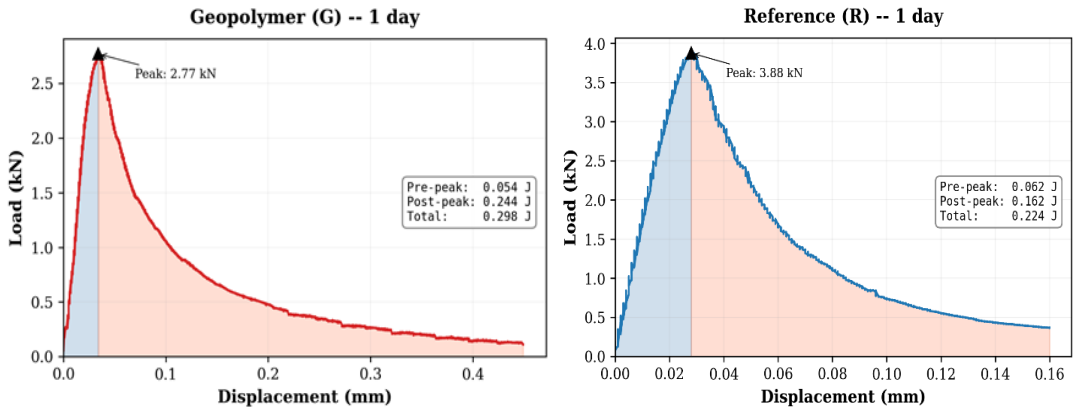

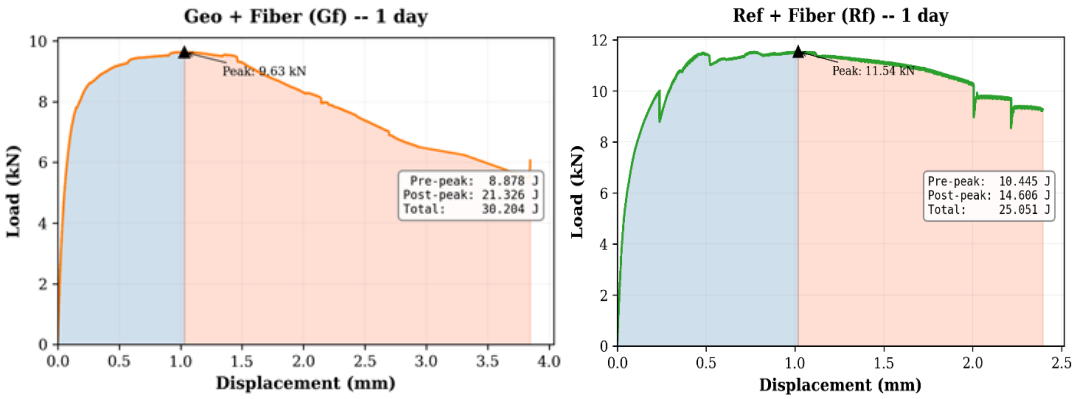

Figure 3-6: Toughness decomposition into pre-peak and post-peak contributions for the cells of the design. The dotted line marks the peak-load displacement.

Table 3-5: Mechanical and toughness values summary.

Mix	Age	Peak Load (kN)	Peak Disp (mm)	Max Disp (mm)	Pre-Peak Toughness (J)	Post-Peak Toughness (J)	Total Toughness (J)	Ductility Index
R	24 h	3.88	0.03	0.16	0.062	0.162	0.224	5.71
Rf	24 h	11.54	1.02	2.39	10.44	14.61	25.05	2.35
G	24 h	2.77	0.03	0.45	0.054	0.244	0.298	13.21
Gf	24 h	9.63	1.03	3.85	8.88	21.33	30.20	3.73
R	28 d	3.99	0.03	0.30	0.068	0.266	0.334	10.54
Rf	28 d	15.91	1.50	3.40	20.02	26.65	46.67	2.27
G	28 d	2.19	0.04	0.23	0.062	0.274	0.336	5.66
Gf	28 d	13.93	0.95	2.95	11.62	23.36	34.98	3.10

3.3.4 Cumulative AE activity and AE energy

The cumulative hit count $N(\delta)$ and the cumulative AE energy $E_{cum}(\delta)$ are running sums computed up to the mid-span displacement δ, as defined in Section 3.1.2. Both descriptors are attenuation-sensitive (Section 3.1.1) and are therefore reported here primarily for within-binder comparisons across ages. Cross-binder comparisons of absolute values are qualified by the attenuation calibration of Table 3-3. Trajectories are shown at 28 days in Figure 3-7 and at 24 hours in Figure 3-8.

At 28 days the plain matrix R produced a total of 221368 hits and a cumulative AE energy of 53.4×10^6 eu, while the plain matrix G produced 123025 hits and 28.1×10^6 eu (Figure 3-7, top row). The two plain matrices showed sigmoidal cumulative trajectories: slow build-up during the elastic phase, sharp acceleration near peak load, and a plateau shortly after failure. The fiber composites Rf and Gf reached almost identical total hit counts at 28 days, 493340 hits for Rf and 492626 hits for Gf, and almost identical cumulative AE energies, 118.5×10^6 eu for Rf and 114.6×10^6 eu for Gf. The cumulative trajectories for the fiber composites were quasi-linear well beyond peak load, in contrast to the sharp saturation of the plain matrices (Figure 3-7, bottom row).

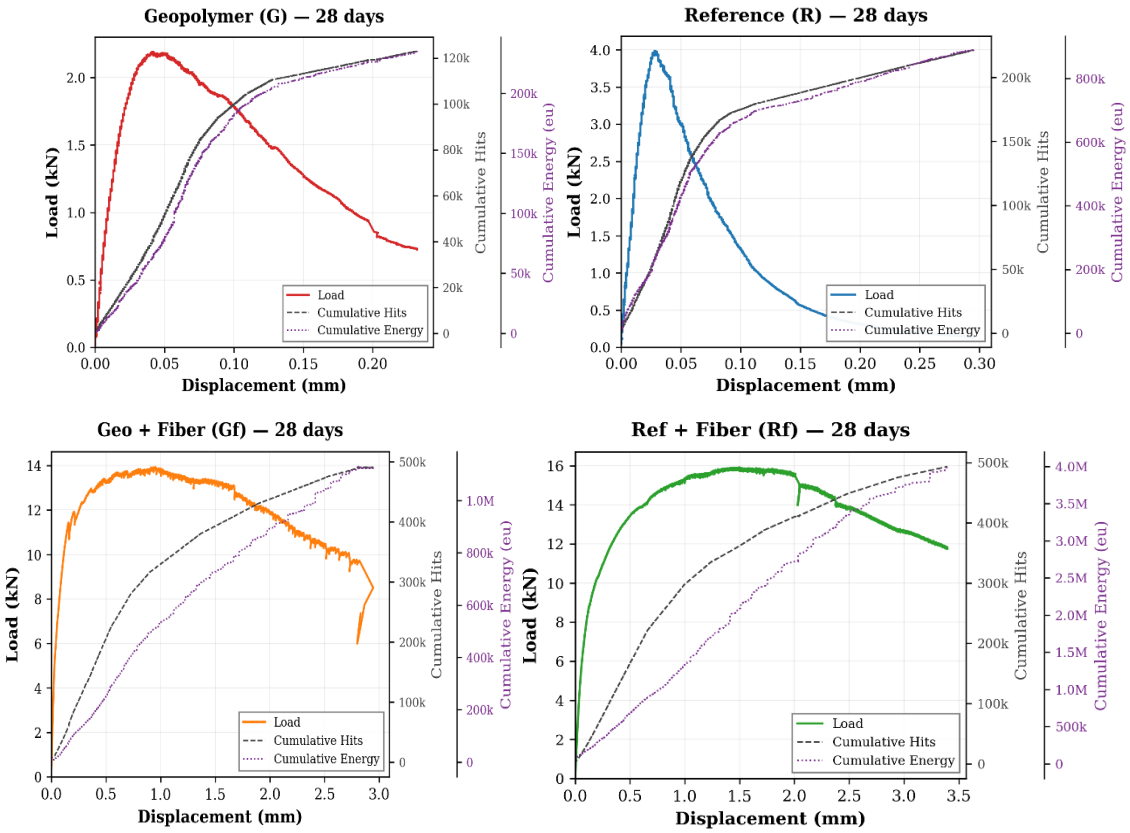

Figure 3-7: Load, cumulative hit count, and cumulative AE energy versus mid-span deflection at 28 days.

At 24 hours the picture was different. R produced 38636 hits and 9.2 × 10^6 eu. G produced 25141 hits and 5.7 × 10^6 eu (Figure 3-8, top row). The fiber composites diverged sharply at 24 hours: Rf produced 313370 hits and 69.8 × 10^6 eu, while Gf produced only 41146 hits and 9.2 × 10^6 eu, a ratio of approximately 7.6 to 1 in both hit count and cumulative energy (Figure 3-8, bottom row).

The 7.6:1 ratio at 24 hours collapsed to almost 1:1 by 28 days, a within-binder maturation signature that is not predictable from the mechanical response alone. The hit-rich 24-hour signature of Rf indicates that the cementitious fiber composite is already generating a high frequency of damage events during deflection hardening, with the population dominated by short-duration matrix microcracking. The hit-poor 24-hour signature of Gf reflects a smaller population of individually more energetic dissipation events rather than a suppression of distributed damage: Gf absorbed 30.20 J of mechanical energy against 25.05 J for Rf while recording one seventh as many hits, so each recorded event in the geopolymer composite corresponds to substantially more dissipated work. The cross-binder comparison of absolute hit counts is qualified by the higher attenuation in the geopolymer matrix (Table 3-3). That qualification does not account for the 24-hour gap, however, because the same attenuation difference applies at 28 days, where Rf and Gf record 493340 and 492626 hits respectively. An attenuation contrast that leaves the hit counts within 0.15% of each other at one age cannot produce a 7.6-fold separation at the other. The 24-hour divergence is therefore a property of the damage process, not of the propagation path.

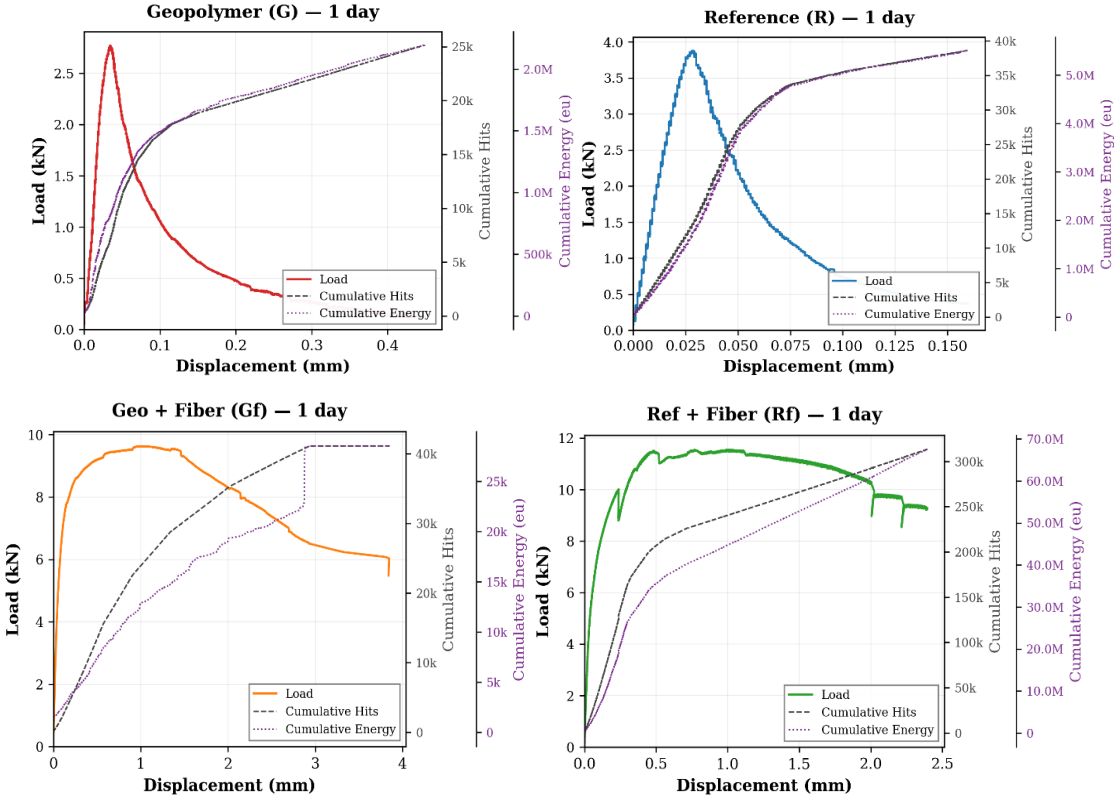

Figure 3-8: Load, cumulative hit count, and cumulative AE energy versus mid-span deflection at 24 hours.

3.3.5 Damage stage identification through b-value evolution

The b-value, computed through the Aki maximum-likelihood estimator on a sliding window of 500 hits stepped by 50 hits (Section 3.2.4, Eqs. 3.7-3.9), is the shape descriptor of the within-window AE amplitude distribution. Values above 1.5 indicate distributed microcracking. Values below 1.0 indicate macro-crack localization. The b-value evolution along the loading history is shown superimposed on the load curve at 28 days in Figure 3-9 and at 24 hours in Figure 3-10.

At 28 days the plain matrices showed a b-value drop close to peak load. R started at an initial value of 1.07 with a mean of 1.05 and reached a minimum of 0.73 in the post-peak regime (Figure 3-9). G showed a higher initial b-value of 1.19 with a mean of 1.11 and a minimum of 0.81 (Figure 3-9). The fiber composites at 28 days reached lower minimum b-values than the plain matrices: Rf dropped to 0.54 (mean 1.05) and Gf dropped to 0.53 (mean 1.18) (Figure 3-9). The two fiber composites were indistinguishable at this age, with minima of 0.54 and 0.53, against a separation of 0.29 at 24 hours. The b-value is therefore the third descriptor, after cumulative hit count and cumulative AE energy, to show Rf and Gf converging between the two ages.

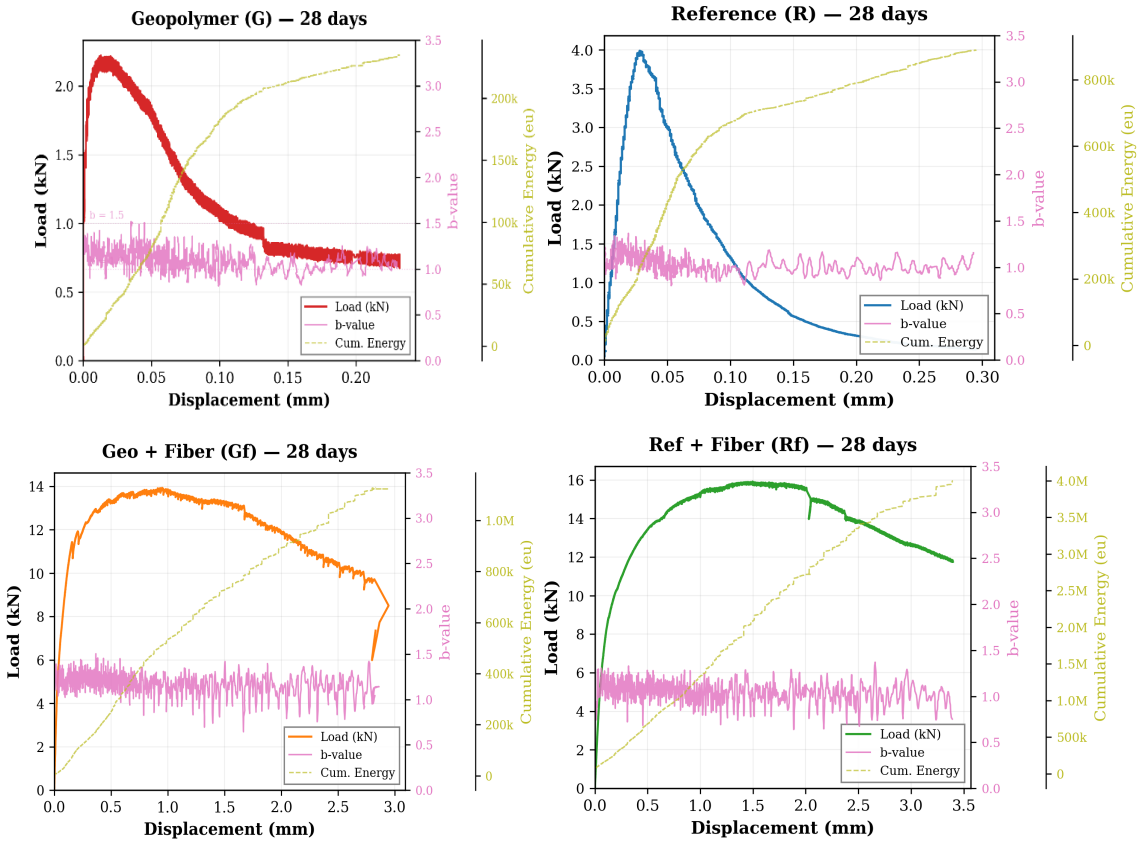

Figure 3-9: b-value evolution superimposed on the load curve at 28 days. Reference lines mark b = 1.0 and b = 1.5.

At 24 hours the b-value behavior diverged between the configurations (Figure 3-10). R had an initial b-value of 1.42 and reached a minimum of 0.89. Rf started at 1.22 with a minimum of 0.71. G started at 1.05 with a minimum of 0.82. Gf was the singular case: it had the highest initial b-value of 1.56, the highest mean of 1.53, and a minimum of 1.00, the only specimen in the campaign whose b-value did not drop below 1.0 at any point (Figure 3-10).

The minimum of 1.00 sits at the boundary of the localization band, and the standard error of ±0.09 to 0.13 reported in Section 3.2.4 straddles that boundary, so the absolute statement that Gf never localized is at the resolution limit of the estimate. The comparison between specimens is what the data supports firmly. The minimum b-value of Gf at 24 hours exceeds that of its cementitious counterpart Rf by 0.29, about 2.5 times the standard error, and its mean of 1.53 is the highest recorded in the campaign. The geopolymer composite therefore sustained a markedly less localized damage process than the cementitious composite at the same age, with microcracking distributed across a fracture process zone rather than channeled into a single dominant crack. Because the b-value is a shape descriptor of the within-specimen amplitude distribution, this conclusion is independent of the attenuation contrast between the two binders. In combination with the high toughness of Gf at this age (30.20 J, the highest value at 24 hours in Table 3-6), this is the first piece of evidence that the early-age geopolymer fiber composite dissipates energy through distributed micro-mechanisms rather than through localized macro-crack propagation.

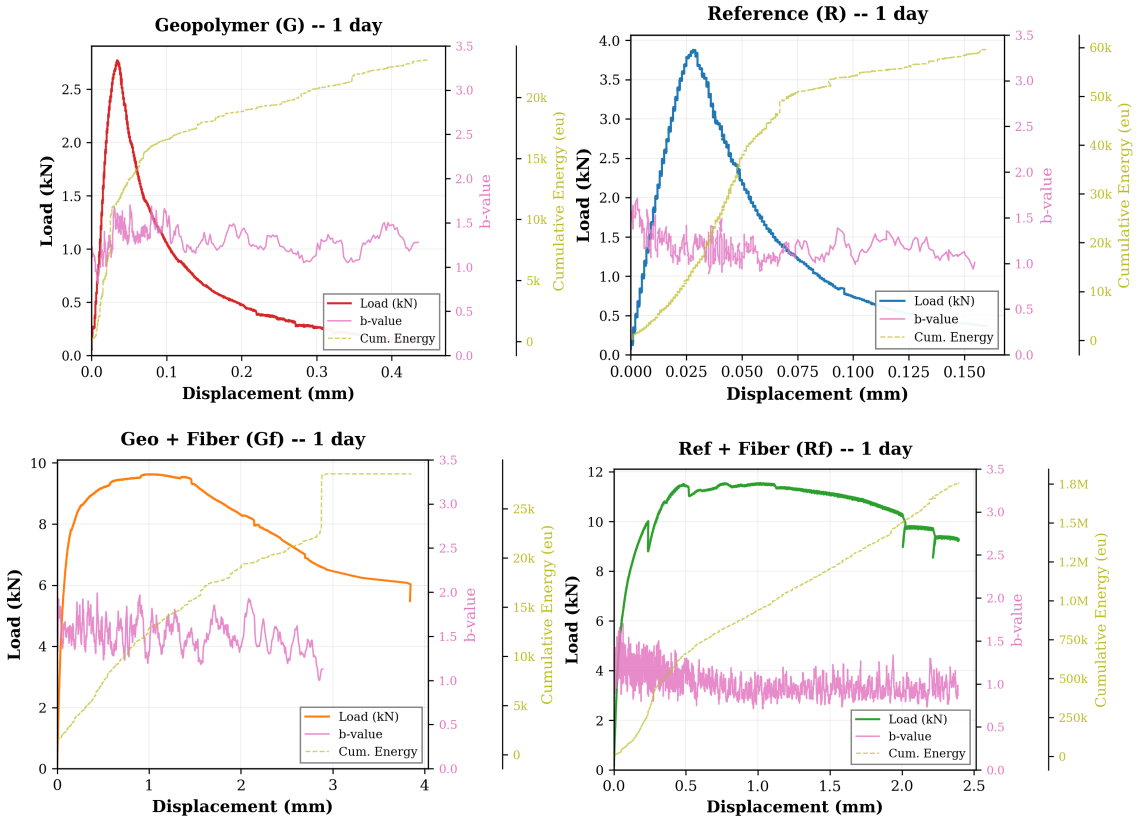

Figure 3-10: b-value evolution superimposed on the load curve at 24 hours.

Comparing the two ages, three of the four configurations moved toward a more localized damage process. The initial b-value fell from 1.42 to 1.07 for R, from 1.22 to 1.07 for Rf, and from 1.56 to 1.23 for Gf, and the minimum fell in each case, most steeply for Gf, from 1.00 to 0.53. Progressive matrix stiffening concentrates stress at the crack tip instead of redistributing it, so a given loading history produces proportionally fewer small events as the material matures. The plain geopolymer G was the exception: its initial b-value rose from 1.05 to 1.19 while its minimum was essentially unchanged, 0.82 against 0.81. That change is confined to the pre-peak regime and does not indicate a less localized failure, since the mechanical data of Sections 3.3.2 and 3.3.3 show G losing both peak flexural load and post-peak deformation capacity over the same period. The steep fall of the Gf minimum is not in conflict with the limited toughness gain reported in Section 3.3.3. The compressive strength of the geopolymer matrix more than doubled between the two ages, from 49 to 112 MPa, so the matrix stiffened considerably even where the fiber-matrix interface, which governs pull-out dissipation, did not.

3.3.6 Crack-mode classification through RA-AF analysis

The RA-AF plane assigns each hit to a tensile or shear class against a boundary fitted independently for that specimen (Section 3.2.4). Percentages are reported in Table 3-6 and the distributions at 28 days and 24 hours, respectively, in Figure 3-11 and Figure 3-12. Two properties of the descriptor govern how the values below are read. The absolute percentages shift by 11 to 14 points when the fitted boundary is varied by ±30%, so they are readings at

a particular boundary and not absolute mode fractions. Comparisons between specimens, and changes within a specimen between ages, are stable across that range and are what the following discussion relies on.

The shear fraction rose in all four cells between 24 hours and 28 days: R from 25.70 to 32.48%, Rf from 36.48 to 39.28%, G from 30.13 to 38.66%, and Gf from 29.19 to 33.95%. The fitted boundary became shallower in every cell over the same interval, a change that by itself reduces the shear fraction, so the physical increase is larger than the tabulated one. Maturation therefore shifts every configuration toward a higher proportion of shear-type sources, and does so more strongly than the numbers alone suggest.

The clearest signal in the classification is the effect of adding fibers, because it compares each composite against its own matrix and therefore removes the binder baseline. In the cementitious system the fibers raised the shear fraction, by 10.8 points at 24 hours and 6.8 points at 28 days. In the geopolymer system they did not: the shear fraction fell by 0.9 points at 24 hours and by 4.7 points at 28 days. The sign of the fiber contribution differs between the two binders at both ages and at every boundary slope tested across the ±30% range, and the separation between the two effects lies between 10.2 and 11.9 points at every one of those six points. Fibers introduced into the Portland-cement matrix create a population of shear-type sources. The same fibers introduced into the geopolymer matrix do not. This is consistent with the fracture-surface morphologies observed independently in Chapter 1, where the geopolymer fracture ran cohesively through the matrix while the cementitious fracture followed the interfacial transition zone.

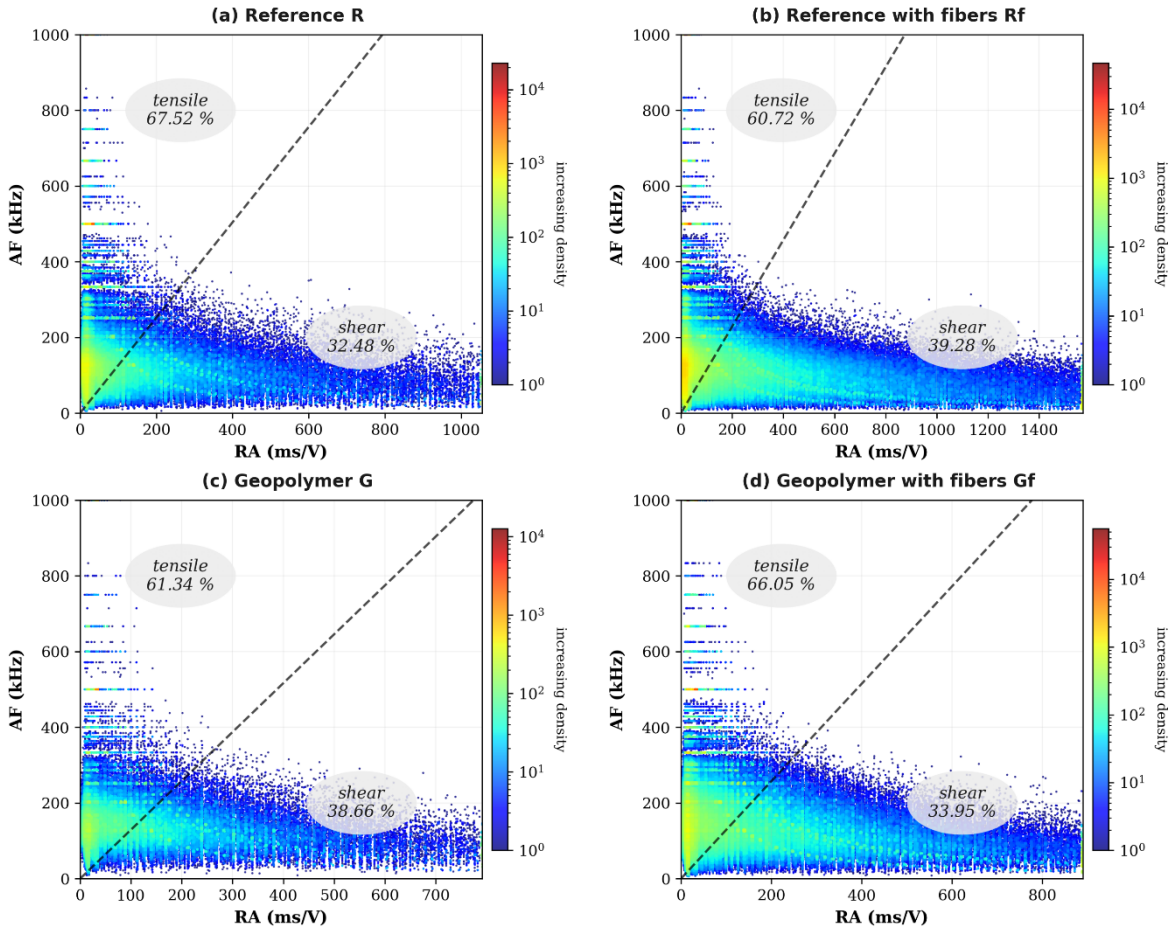

Figure 3-11: RA-AF crack-mode classification at 28 days. (a) R, (b) Rf, (c) G, (d) Gf. Percentage labels are readings at the fitted boundary and shift by 11 to 14 points under a +/-30% change in slope (Section 3.2.4).

Between the two fiber composites, Rf carried the higher shear fraction at both ages, 36.48 against 29.19% at 24 hours and 39.28 against 33.95% at 28 days. The ordering holds at every slope tested, but the separation is a few percentage points against an 11-to-14-point sensitivity to boundary placement, so the crack-mode classification establishes the direction of the difference and not its magnitude. The duration statistics reported below carry that magnitude on an independent basis. Applying the same classification to a sliding window rather than to the full record shows the shear fraction of the cementitious systems rising through the post-peak regime while the geopolymer systems hold a lower and flatter profile, consistent with the cumulative values. The windowed percentages are not reported here, since their movements are smaller than the sensitivity of the classification to boundary placement.

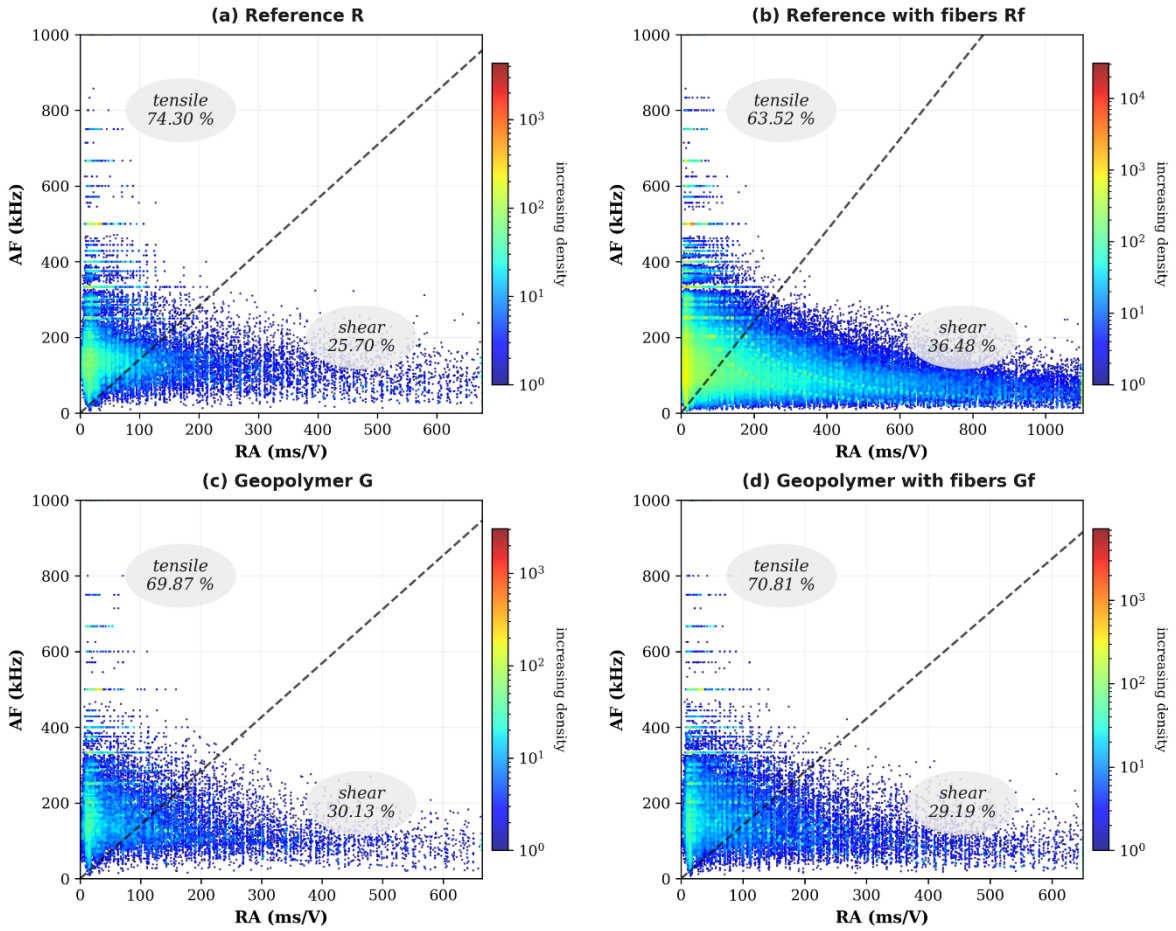

Figure 3-12: RA-AF crack-mode classification at 24 hours. (a) R, (b) Rf, (c) G, (d) Gf. Boundary and labels as in Figure 3-11.

Table 3-6: RA-AF crack-mode classification, median signal duration, and long-duration (>500 microseconds) event fraction.

Mix	Age	Tensile (%)	Shear (%)	Median duration (µs)	Long duration > 500 µs (%)
R	24 h	74.3	25.7	68	5.2
Rf	24 h	63.52	36.48	98	9.9
G	24 h	69.87	30.13	43	1.2
Gf	24 h	70.81	29.19	36	0.7
R	28 d	67.52	32.48	147	16.7
Rf	28 d	60.72	39.28	168	18.4
G	28 d	61.34	38.6636.66	82	3.3
Gf	28 d	66.05	33.95	72	3.6

Median signal duration and the fraction of long-duration events (>500 µs, Section 3.2.4) provide a complementary axis on the same classification (Table 3-6). At 28 days Rf had the longest median duration (168 µs) and the highest long-duration fraction (18.4%) of the campaign, while Gf at the same age had a median duration of 72 µs and a long-duration fraction of only 3.6%. The Rf-to-Gf ratio of long-duration events at 28 days was 5.1 to 1. At 24 hours the same ranking held but at lower absolute values: Rf at 9.9% and Gf at 0.7% long-

duration, an Rf-to-Gf ratio of 14 to 1. Long signal durations are characteristic of frictional sliding mechanisms where the source continues to radiate over an extended time window (Aggelis et al., 2013a; Carpinteri et al., 2013). The systematic divergence between Rf and Gf, measured with identical sensors and an identical specimen geometry, is the second independent indicator of the frictional-vs-cohesive pathway distinction introduced above.

3.3.7 AE hit rate and damage acceleration

The AE hit rate, computed on 0.02 mm displacement bins (Section 3.2.4), locates the periods of intense damage activity. Profiles are shown at 28 days in Figure 3-13 and at 24 hours in Figure 3-14, with the load curve overlaid in each panel.

The plain matrices showed a sharp narrow peak in the hit rate at the peak load displacement. At 28 days R peaked at approximately 0.028 mm and G peaked at approximately 0.041 mm. In both cases the hit rate fell sharply after the peak load was reached (Figure 3-13). At 24 hours the same sharp-peak pattern appeared, R peaking at approximately 0.028 mm and G at approximately 0.034 mm (Figure 3-14). This profile is the AE signature of localized quasi-brittle failure as defined in Section 3.1.2.

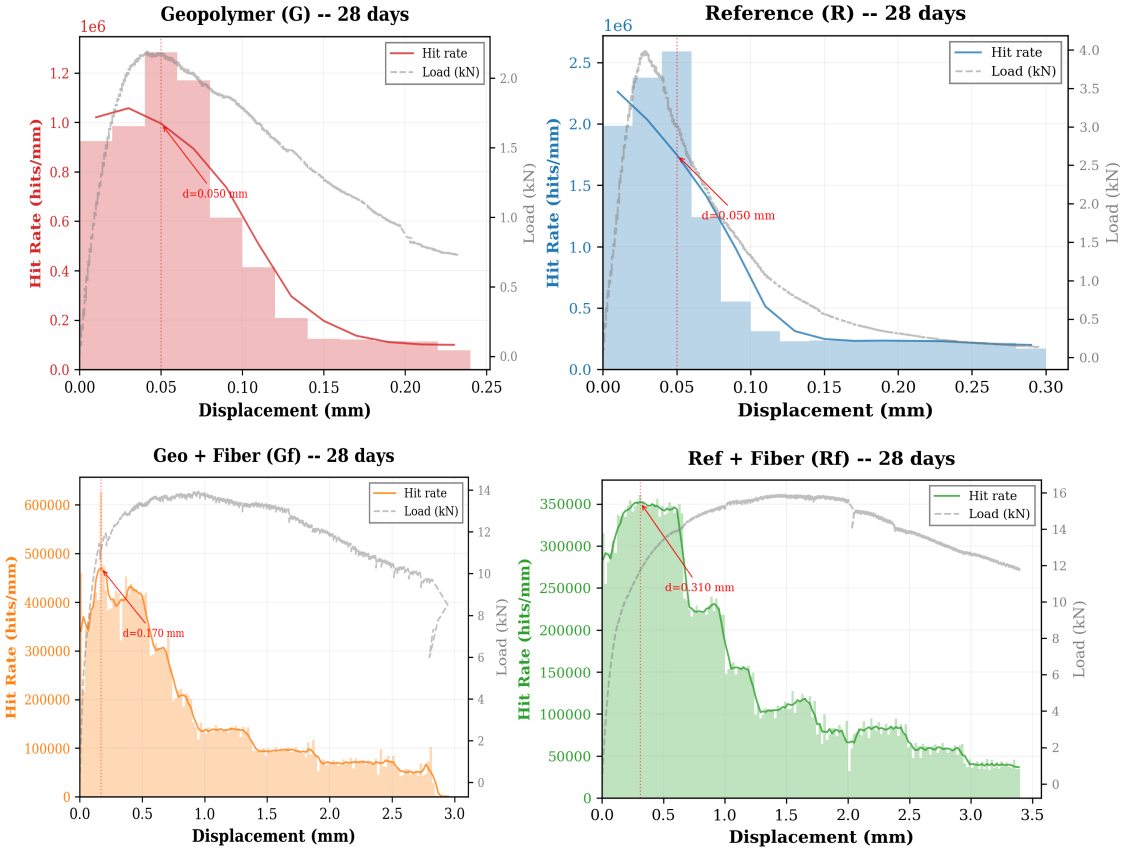

Figure 3-13: AE hit rate (hits per 0.02 mm displacement bin) versus mid-span deflection at 28 days, with the load curve overlaid.

The fiber composites showed a broad plateau in the hit rate that extended through the deflection-hardening regime and into the post-peak softening branch. At 28 days the Rf hit rate peaked at the peak-load displacement, within the 0.02 mm bin resolution, and remained elevated until approximately 2 mm of deflection. At 28 days Gf showed a broader and lower

plateau, sustained from approximately 0.5 mm to beyond 2 mm of deflection (Figure 3-13). At 24 hours the difference in absolute hit rate between Rf and Gf was the most pronounced of the campaign (Figure 3-14), consistent with the 7.6:1 ratio in cumulative hits reported in Section 3.3.4. As argued there, the same attenuation contrast leaves the two composites within 0.15% of each other in total hit count at 28 days, so the 24-hour separation is not a propagation artifact. The Gf profile at 24 hours was the broadest and lowest of the campaign, with activity sustained to 3.85 mm of deflection, the largest maximum displacement recorded in any test. A low-intensity profile spread across a wide displacement window is the hit-rate expression of the result reported in Section 3.3.3: Gf absorbed 30.20 J against 25.05 J for Rf at this age while generating one seventh as many hits, because its damage events were distributed over a displacement range more than one and a half times wider rather than concentrated near peak load.

The hit-rate profile is therefore a fingerprint of failure mode at the binder-system level: sharp narrow peak for quasi-brittle plain matrices, broad plateau for fiber-bridged composites, with Gf showing the broadest and flattest plateau at both ages and Rf showing a more concentrated plateau around the peak. The Gf profile is consistent with damage events spread across a wide displacement window, the Rf profile with damage events more concentrated around the maximum-load phase.

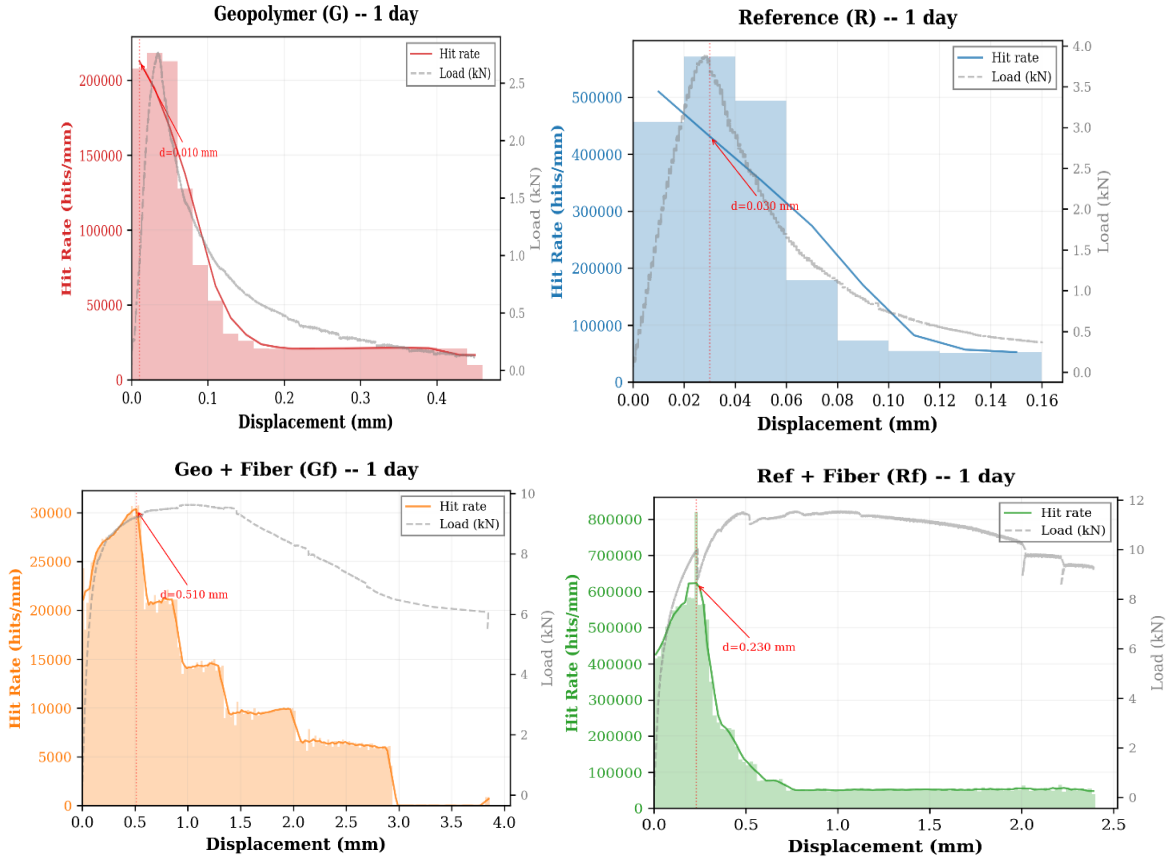

Figure 3-14: AE hit rate versus mid-span deflection at 24 hours.

3.4 Numerical Modeling

A complementary numerical study of the fracture of the fiber-reinforced geopolymer was carried out as part of the mechanical-modeling activity of the NATURSEA-PV project (WP3). Its object is a calibrated description of the fracture of the material and, from it, a representative cracked geometry for the project transport modeling, in which chloride ingress through a damaged microstructure is evaluated. The formulation is set out in Section 3.4.1, the identification of the parameters in Section 3.4.2, the computed flexural response in Section 3.4.3, and the application under direct tension in Section 3.4.4.

3.4.1 Constitutive model and numerical implementation

The fracture of the matrix was described by the isotropic scalar damage model of Fichant, La Borderie, and Pijaudier-Cabot (1999), of the class introduced for concrete by Mazars (1986). A single damage variable D, bounded between zero in the intact material and unity at complete loss of stiffness, degrades the elastic tensor through the effective-stress relation

$$\sigma = (1 - D)\, E_0 : \varepsilon \tag{3.10}$$

in which σ is the stress tensor, ε the strain tensor and E_0 the elastic stiffness of the intact material. The growth of damage is driven by an equivalent strain built from the positive part of the principal strains,

$$\tilde{\varepsilon} = \sqrt{\sum_{i=1}^{3} \langle \varepsilon_i \rangle^2} \tag{3.11}$$

where the Macaulay brackets retain only the tensile principal strains, so that degradation is governed by local extension and the dissymmetry of concrete-like materials between tension and compression is respected. Damage initiates when the equivalent strain reaches the threshold

$$\varepsilon_0 = f_t / E_0 \tag{3.12}$$

and evolves thereafter through an exponential softening law governed by the tensile strength and the fracture energy. The formulation is appropriate to the Mode I tensile fracture that develops at mid-span in a notched beam, and an anisotropic description would introduce parameters that a single localized crack plane cannot identify. The computations were performed with the finite-element code CAST3M (Verpeaux et al., 1989).

The three-point bending specimen was reproduced at full scale with the geometry of the experimental campaign: a prism of 70 × 70 × 280 mm³, a clear span of 260 mm between supports, and a transverse notch 5 mm deep at mid-span on the tensile face. The domain was discretized with tetrahedral elements refined to approximately 1 mm in the central zone above the notch, where the crack was expected to localize, and coarsened toward the supports and the loading point. Softening was regularized by the crack-band approach of Hillerborg

et al. (1976), the band width being derived element-wise from the element volume so that the energy dissipated per unit crack area is preserved and the computed response is objective with respect to the discretization. Loading was applied at mid-span as a monotonically increasing imposed displacement, and the reaction at the loading line was integrated at each increment.

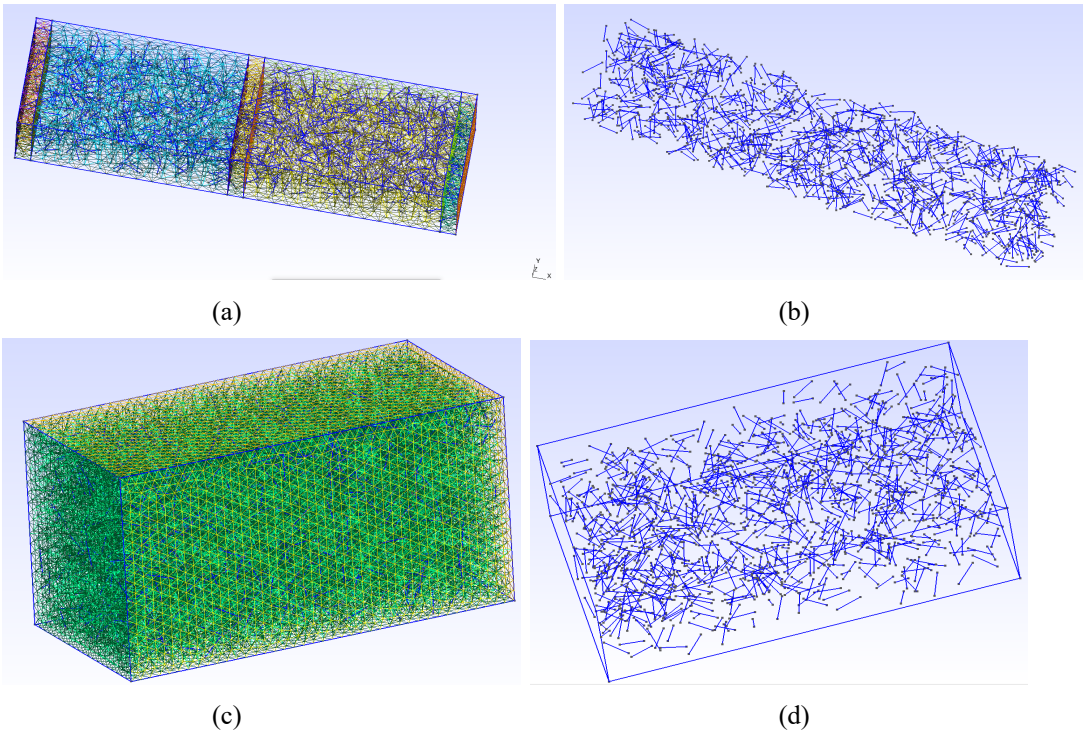

Figure 3-15: Finite-element discretization of the modeled specimens. (a) Three-point bending beam, (b) Fiber network of the bending specimen shown alone, (c) Uniaxial tension specimen, and (d) Fiber network of the tension specimen.

3.4.2 Representation of the fibers and identification of the parameters

An explicit representation of the fiber content of the physical mix is not attainable within a finite-element discretization. The 1.5 percent volume fraction of 13 mm by 0.20 mm micro-fibers corresponds to some fifty thousand fibers in a specimen of this size, against the order of one thousand that can be meshed and coupled to the matrix within the memory and solution-time limits of the computation. This constraint is recognized in the literature on explicit fiber modeling, where coupling fiber and matrix through shared nodes requires node-coincident meshes that are impractical to generate for large fiber populations (Cunha et al., 2012; Pros et al., 2012). Comparison of computations performed with and without the bar elements confirms that at attainable fiber density their direct contribution to the computed capacity is negligible.

The constitutive parameters are therefore effective properties of the composite rather than of the matrix, and were identified on the measured flexural response of the fiber-reinforced geopolymer at 28 days. Two parameters govern that response. The tensile strength f_t sets the level of the computed curve, while the characteristic crack opening w_1, the ratio of

the fracture energy to the tensile strength, sets its shape. Because the correction term in the crack-band expression is four orders of magnitude smaller than the fracture energy, the softening modulus is inversely proportional to w_1 to within 0.01 percent, so the identification proceeds along a shape-preserving direction: w_1 is fixed by the form of the measured response and f_t then scales it. The identified values are given in Table 3-7.

Table 3-7: Parameters of the continuum-damage model for the fiber-reinforced geopolymer at 28 days.

Symbol	Description	Value	Unit
E_0	Elastic modulus	34 500	MPa
ν	Poisson ratio	0.20	–
ρ	Density	2 390	kg/m³
f_t	Effective composite tensile strength	5.5	MPa
G_f	Crack-band fracture energy	4.70	N/mm
$w_1 = G_f / f_t$	Characteristic crack opening	0.85	mm
α	Softening shape coefficient	1.5	–

Note: The elastic modulus is taken as consistent with values reported for steel-fiber ultra-high-performance geopolymer concrete, 27 to 35 GPa (Liu et al., 2020).

The identified values are physically consistent with the material. An effective tensile strength of 5.5 MPa lies below the 10 to 13 MPa reported for Portland-matrix ultra-high-performance fiber-reinforced concrete, which is consistent with the weaker fiber-matrix interfacial zone of the alkali-activated binder. A characteristic crack opening of 0.85 mm is a plausible scale for fibers of 13 mm length whose embedded ends pull out over distances of up to half that length. The crack-band fracture energy of 4.70 N/mm falls below the apparent work of fracture obtained by dividing the measured toughness by the ligament area, as expected for a deflection-hardening composite in which the toughness integral contains substantial bulk deformation energy alongside the energy consumed within the crack band.

3.4.3 Computed flexural response

The computed and measured responses are compared in Figure 3-16 and Table 3-8. The computation was verified by repeating it with forced acceptance of non-converged increments disabled. The two runs agree to within the resolution of the recorded output at every increment up to 1.620 mm of mid-span deflection, which establishes that no increment in that interval had been accepted without satisfying the residual tolerance. Beyond that deflection the Newton scheme ceases to converge, the tangent stiffness of the fully damaged band approaching zero on the load plateau, and the computed response is not verified further. Deflections are resolved to the imposed increment of 0.020 mm.

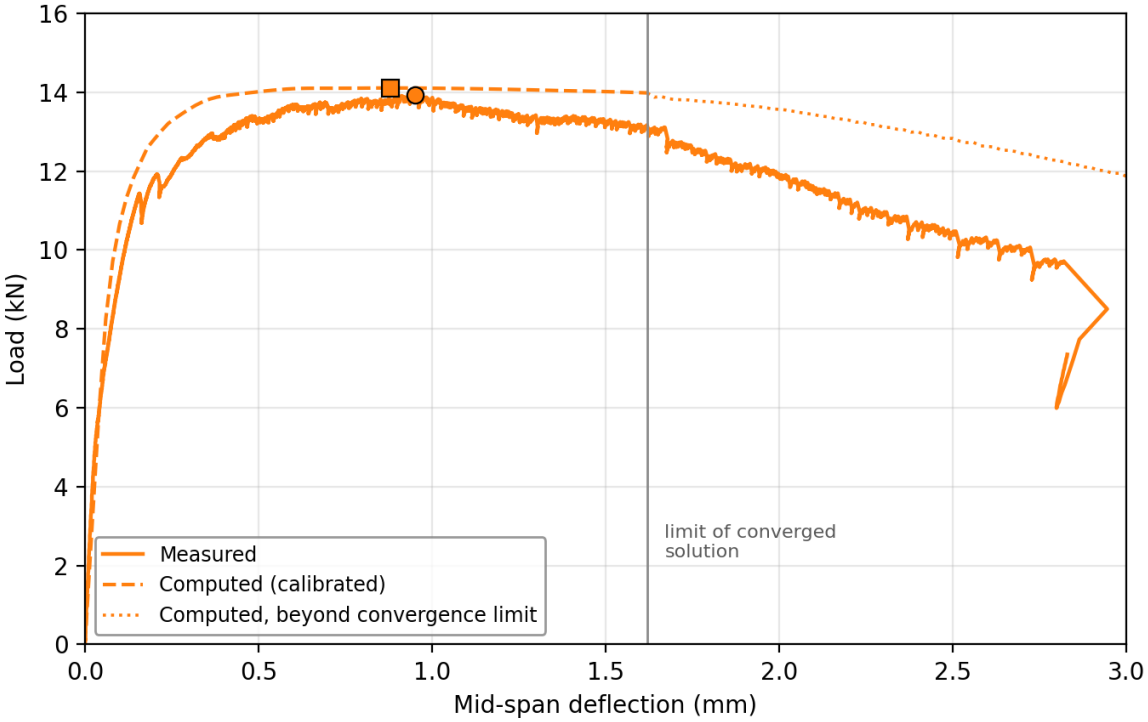

Figure 3-16: Computed and measured flexural response of the fiber-reinforced geopolymer at 28 days.

Table 3-8: Comparison over the interval in which the computed solution is verified.

Quantity	Computed	Measured	Difference
Peak load	14.11 kN	13.93 kN	+1.3 %
Deflection at peak	0.880 mm	0.950 mm	-7.4 %
Load at 1.620 mm	13.98 kN	13.03 kN	+7 %
Toughness, 0 to 1.620 mm	21.69 J	20.61 J	+5.2 %

The status of this agreement is stated precisely. The model is calibrated, not independently validated. The tensile strength was set by the load level and the characteristic crack opening by the shape of the response, so the peak load and the deflection at peak are fit residuals rather than predictions. The load at 1.620 mm and the toughness were not targeted, and although they derive from the same test they are the only entries whose agreement is not guaranteed by construction. Since the softening modulus is inversely proportional to w_1, the identified pair is one admissible set rather than a unique identification, the tensile strength and the fracture energy trading off along a shape-preserving direction. The model has not been tested against a second geometry, a second age, or a notch-depth series. Beyond the peak the computed load decays too slowly: within the verified interval the divergence is established but modest, the computed load exceeding the measured by 7 percent at 1.620 mm against 1.3 percent at the peak, while the unverified continuation shows the excess growing to 29 percent by 2.750 mm. The mechanism is that exponential softening cannot represent the accelerating loss of bridging as fibers pull out over several millimeters

of crack opening. No mesh-convergence study is reported; the crack-band regularization limits mesh dependence but does not replace such a study. The coincidence between the convergence limit and a load step in the measured record at the same deflection is fortuitous, the computation being independent of the measured record.

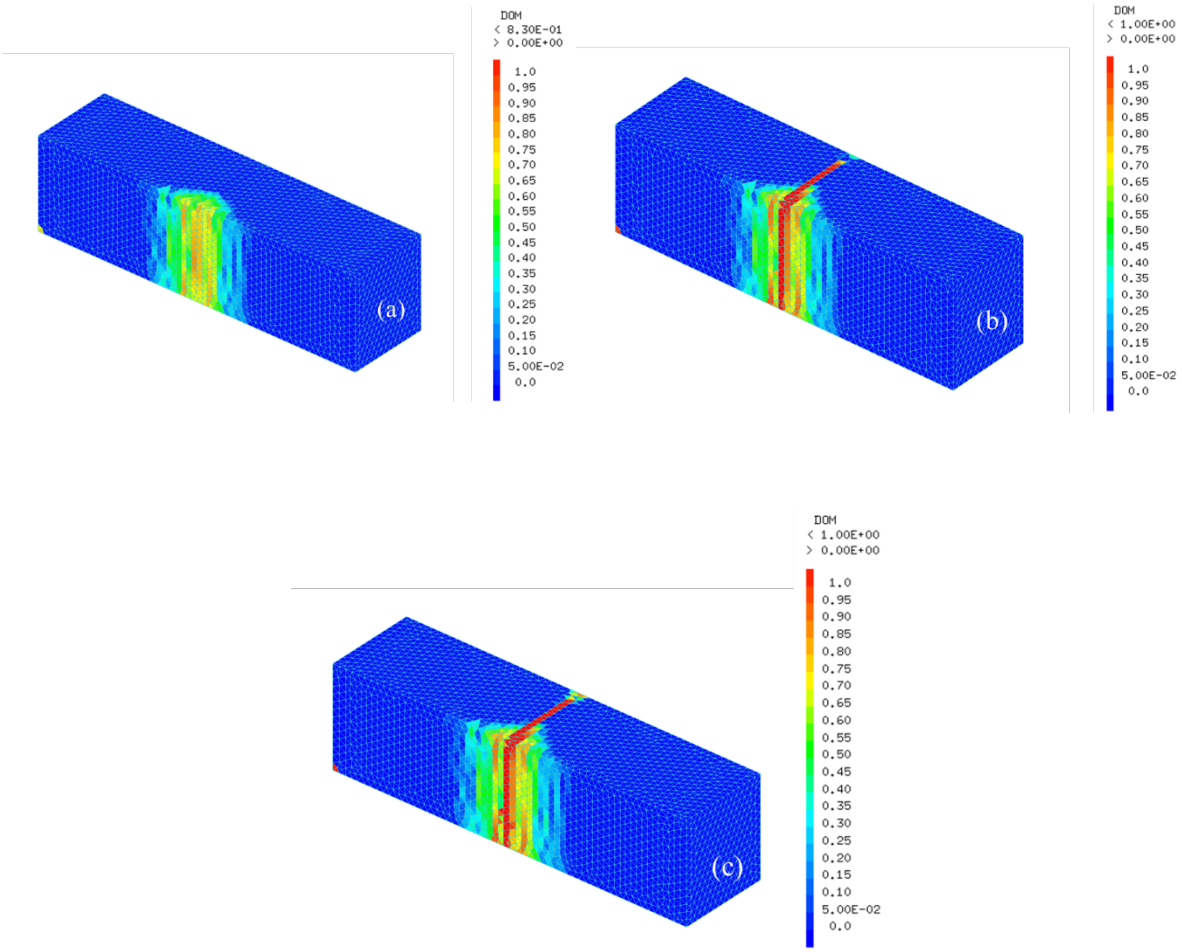

Figure 3-17: Computed damage field in the three-point bending specimen at three stages: (a) peak load, (b) early post-peak, and (c) end of simulation.

3.4.4 Application under direct tension

The transport modeling of the project requires a representative cracked geometry: a domain in which the crack pattern produced by tensile loading is available for the simulation of ingress through the damaged microstructure. The model was applied under direct tension for that single objective, performed within the project modeling task at an earlier stage. The specimen was modeled as a rectangular prism of 200 × 100 × 100 mm³ loaded along its axis, discretized with quadratic tetrahedral elements of approximately 3 mm refined to 1 mm in the central gauge region, one end fixed and an axial displacement imposed at the opposite end under displacement control. Consistent with the purpose of the application, the load-displacement response is not reported as a result. The quantities of interest are the crack pattern and its extent.

To visualize the tensile-damage localization, six representative surfaces of the specimen were exported as maps of the axial strain, in which the highest tensile strains, interpreted as the cracking zones, appear in red and the elastic regions in blue (Figure 3-18). The maps show the emergence and coalescence of vertical macro-cracks with secondary branches, the strain bands aligned with the loading direction. Consistent with the stochastic placement of the fibers, the pattern is a network of parallel transverse cracks rather than a single plane, which provides a more realistic transport geometry than an idealized single crack.

To isolate the high-strain bands for inspection, on each of the six surfaces the high-tensile-strain region was converted to a binary mask by thresholding and morphological cleanup in ImageJ (Figure 3-19). The areal extent of the cracking was measured from the resulting objects, but the calibration of the image analysis could not subsequently be re-established, and the measurement is therefore not reported.

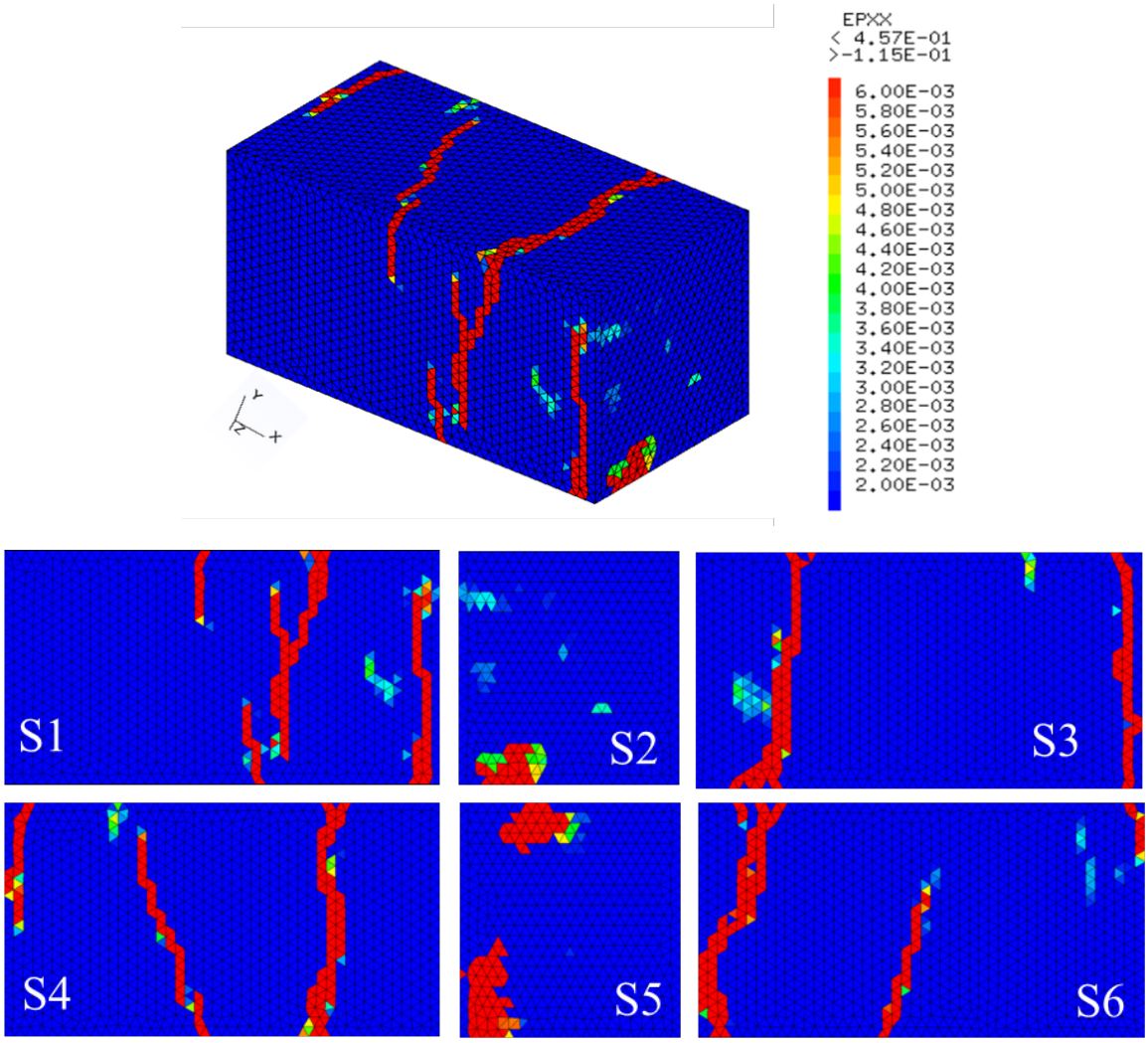

Figure 3-18: CAST3M axial-strain (εxx) fields in the tension specimen. Perspective view of the prism and the six analyzed faces. Red indicates peak tensile strain, interpreted as cracking zones.

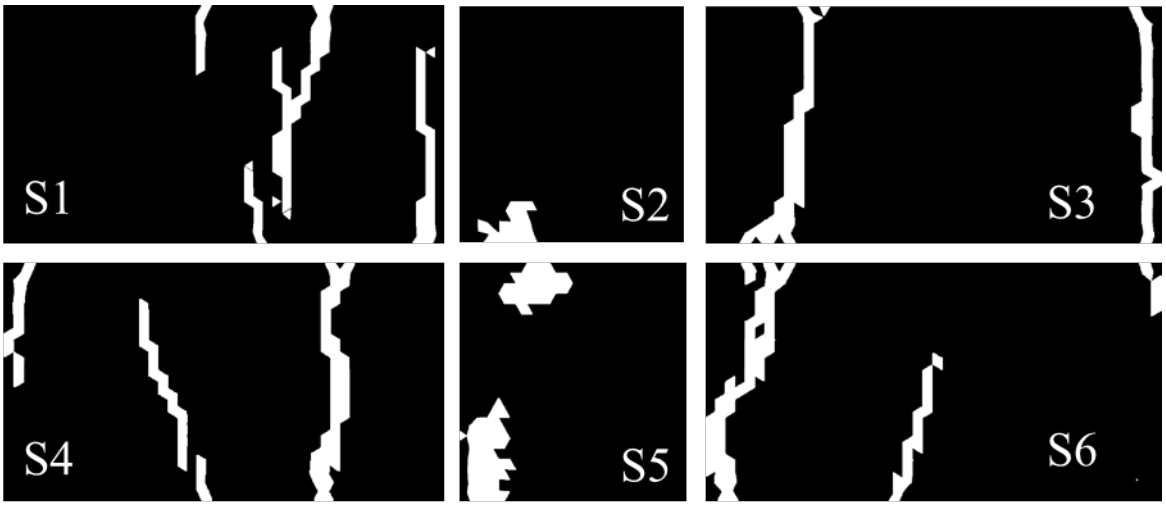

Figure 3-19: ImageJ binary mask of the cracked region on a representative surface, obtained by isolating the high-tensile-strain (red) bands and applying morphological cleanup.

The cracking is described here by its pattern rather than its extent. The variation reflects the heterogeneous development of strain localization across the faces of the specimen, cracking initiating in localized regions before coalescing into a continuous fracture band. The mean crack width and the crack path length, which together with the cracked area govern the rate of ingress through a crack, were likewise not established. Their measurement from the same binary objects by morphological analysis is a direct extension of the procedure used here. The cracked geometry so established provides the domain from which the transport-relevant crack parameters can subsequently be measured.

3.4.5 Summary and further development

A continuum-damage model calibrated on the measured flexural response of the fiber-reinforced geopolymer reproduces the peak flexural capacity of the material within 1.3 percent and the work of deformation within 5.2 percent over the interval in which the solution is verified, and localizes damage into the crack plane observed experimentally. Applied under direct tension it generates a physically plausible and quantifiable cracked geometry for the project transport modeling. Its principal limitation is the representation of the fibers, which at attainable density contribute negligibly and whose bridging is therefore carried by the calibrated matrix parameters rather than resolved. The replacement of that treatment by an explicit fiber-matrix interface law, in which the bridging stress is a function of the local crack opening and is calibrated against single-fiber pull-out tests, together with the extraction of the crack width and path length from the computed field, are identified in the Perspectives of the thesis as the directions for the further development of the model.

3.5 Conclusion

Multi-parameter acoustic emission was applied to the fracture characterization of the two UHPC systems under three-point bending, on a two-by-two design in binder chemistry and fiber inclusion at 24 hours and 28 days. Notched prismatic specimens of 7 × 7 × 28 cm^3 were loaded to failure under CMOD closed-loop control at 0.0013 mm/s over a 260 mm span, with seven resonant transducers recording the emission through a 100 to 400 kHz band at a 35 dB threshold. Eight descriptors were extracted from the parametric record, together with the hit rate and the cumulative sums. Attenuation was calibrated by pencil-lead break on every specimen and ranged from 2.1 to 3.8 dB/cm in the cementitious matrices against 3.5 to 5.2 dB/cm in the geopolymer matrices, so cross-binder claims were restricted to descriptors insensitive to that difference.

The descriptors separate the two fiber composites into two fracture pathways. Rf engages a friction-dominated pathway: it carries the highest shear fraction of the campaign at both ages, adding fibers to the cementitious matrix raises that fraction by 6.8 points at 28 days and 10.8 points at 24 hours, its median signal duration is the longest at 168 µs and its long-duration fraction the highest at 18.4%, and its b-value falls below unity in the post-peak regime at both ages. Gf engages the opposite pathway: adding the same fibers to the geopolymer matrix lowers the shear fraction, by 4.7 points at 28 days and 0.9 points at 24 hours, its median duration is 72 µs and its long-duration fraction 3.6%, falling to 0.7% at 24 hours, and its b-value at 24 hours reaches a minimum of 1.00 against 0.71 for Rf, the highest in the campaign. **These signatures indicate that energy is dissipated in Rf through frictional pull-out along the fiber-matrix interface and in Gf through distributed matrix microcracking and cohesive debonding**, reproducing the two fracture-surface morphologies observed independently in Chapter 1.

The two pathways mature on different time scales, and that is what produces the toughness crossover. At 24 hours the cementitious interfacial transition zone is only partially developed under ambient curing and Rf reaches 25.05 J, while the geopolymer matrix has substantially completed its alkali-activation reaction, the cohesive debonding pathway is already fully engaged, and Gf delivers 30.20 J. Between 24 hours and 28 days continued hydration densifies the Rf interface and Rf gains 21.62 J, an increase of 86%, while Gf gains 4.78 J, an increase of 16%, consistent with a mechanism already largely engaged at 24 hours. Cumulative AE activity converges over the same interval while its distribution in time does not: the 7.6 to 1 ratio of cumulative hits and energy at 24 hours falls to approximately 1 to 1 at 28 days, where the two composites record 493340 and 492626 hits, but Rf releases that total through long-duration interfacial events and Gf through short ones distributed through the matrix.

3.5.1 Limitations and perspectives

Four limits of the measurement were established.

First, the replicate count is two specimens per cell with multi-parameter post-processing on one, so the AE percentages and trajectories identify a fracture pathway qualitatively and do not support confidence-interval estimation.

Second, total flexural toughness is integrated on mid-span deflection rather than on CMOD, because the CMOD signal carried feedback oscillations in the post-peak regime, so the ranking of the four configurations is preserved but the absolute magnitudes carry that caveat.

Third, the crack-mode classification is inferential rather than calibrated against Mode I and Mode II references, and varying the fitted boundary slope through ±30% moves the absolute percentages by 11 to 14 points while preserving every comparison drawn from them, so the classification supports the direction of the differences and not their magnitude.

Fourth, the fiber type and dosage are held constant at 1.5% by volume of straight uncoated micro-fibers, so the pathway conclusions do not transfer directly to other fiber geometries, to the recycled tire-derived fibers of the NATURSEA-PV application treated in Chapter 1, or to fly-ash and metakaolin precursor systems with different gel chemistry. In particular, the campaign used 120 kg/m³ of virgin fibers rather than the 108 kg/m³ recycled-virgin blend of the deployed GEO, so the transfer of the fracture conclusions to the final formulation remains to be demonstrated.

These limits define the next campaign: at least three specimens per cell with AE analysis on all of them, the 60/40 recycled blend in place of the virgin fiber, tests at 90 days and one year to establish whether the toughness hierarchy observed at 28 days is stable, direct characterization of the fiber-matrix interface after failure (single-fiber pull-out, SEM-EDS line scans or nanoindentation) to test the pathways inferred from the AE descriptors, and impedance measurements before and after load steps to couple the two non-destructive methods.

The research question asked how the binder system shapes fracture initiation, propagation, and energy dissipation under three-point bending, in plain and fiber-reinforced conditions at two ages, with the steel fiber type and volume fraction held constant. **It is answered through the mode of the fiber-matrix interface.** The binder determines whether the interface fails by frictional sliding or by cohesive matrix debonding, the two modes produce internally coherent signatures across descriptors that probe different aspects of damage, and they mature on different time scales, so that a friction-dominated system gains with the binder while a debonding-dominated system does not. These pathways are consistent with the electrochemical distinction of Chapter 2, which probes the same two materials undisturbed at the micro-pore scale where acoustic emission probes them at the fracture-event scale during active failure. Under three-point bending the geopolymer composite reaches 88% of the peak load and 75% of the total flexural toughness of the cementitious composite at 28 days and exceeds it in toughness at 24 hours; the difference in mechanism is not a deficit but a different mode of dissipation, fully engaged at early age;

whether the hierarchy observed at 28 days persists at later ages was not tested. Whether it survives sulfate attack, chloride ingress, thermal cycling, and acid exposure is the subject of Chapter 4. The numerical description of the same fracture, by a calibrated continuum-damage model, is reported in Section 3.4.

3.6 Transition to Chapter 4

Chapters 1, 2, and 3 together establish the geopolymer system as mechanically and electrochemically distinguishable from the cementitious reference, with a coherent fracture signature under bending. The three chapters have probed the material in its undisturbed state (Chapter 2 EIS), under load until failure (Chapter 3 AE under bending), and in terms of its formulation and fresh-state properties (Chapter 1). What they have not addressed is the question that ultimately decides the NATURSEA-PV application: how the material performs over months and years of exposure to the offshore marine environment.

The marine environment imposes four distinct aggressions on a structural concrete: sulfate attack from sulfate-rich seawater, chloride ingress that drives steel reinforcement corrosion, thermal cycling at the air-water interface, and acid exposure from biofouling-related metabolic activity. The cementitious reference UHPC is the established benchmark in marine durability standards and has been validated over decades of field service. The geopolymer system has no comparable field history at this scale, and the fundamental question is whether the binder chemistry that supports the Chapter 3 fracture-pathway distinction also supports a durability profile at least equivalent to that of the cementitious reference.

Chapter 4 addresses this question through a campaign of durability tests designed around the marine aggressions listed above, performed on the REF and GEO systems established in Chapters 1 to 3. Sulfate attack is evaluated through long-term immersion in sodium sulfate solutions, chloride ingress through rapid chloride penetration testing per ASTM C1202 and through long-term ponding, acid resistance through immersion in dilute acid baths, and thermal performance through cyclic temperature exposure. The chapter answers the following research question: does the distinct binder chemistry of GEO (cement-free, no portlandite, calcium-rich aluminosilicate matrix) confer net durability advantages over REF under marine-relevant aggression, or are gains in chemical resistance offset by losses in thermal performance? The answer is essential to the central research question of the thesis, and frames the life-cycle assessment of Chapter 4.

Can a 100% cement-free, ambient-cured UHPGC reach the mechanical and durability performance to survive harsh marine environments and replace conventional UHPC in offshore FPV substructures monitored by SHM?

↓

01

Chapter 1. Formulation and characterization

Cement-free UHPGC mix, recycled fibers,
mechanical and rheological validation

↓

02

Chapter 2. Electrochemical Impedance Spectroscopy

Pore network and pore solution signatures of REF and GEO

↓

03

Chapter 3. Acoustic emission and fracture mechanics

Crack initiation, propagation, energy dissipation

↓

04

Chapter 4. Durability and Carbon footprint assessment

Sulfate, acid, chloride, thermal, and HarshLab
Cradle-to-grave environmental and economic balance

Chapter 4 - Durability and Carbon Footprint Assessment

Chapter 3 established how the binder system governs fracture in REF and GEO: where REF dissipates energy at the fiber-matrix interface, the C-(N,K)-A-S-H gel of GEO carries the dominant crack-arrest mechanism in the matrix bulk. That behavior, however, was characterized on sound material. An offshore floating substructure spends its service life under chemical and physical aggression that no laboratory mechanical test reproduces, and the question that decides whether GEO can replace conventional UHPC offshore is not how it breaks when intact, but whether it stays intact, and at what environmental and economic cost over the service life that durability secures.

This chapter therefore addresses one compound question: does the distinct binder chemistry of GEO confer net durability advantages over REF under marine-relevant aggression (sulfate, acid, chloride, and elevated temperature), or are the gains offset by losses in thermal performance, and does the resulting material deliver the carbon and cost-to-strength advantages needed to justify replacing conventional UHPC? The durability assessment occupies the first part of the chapter and establishes whether GEO is fit for the marine service, including whether it satisfies the 50-year design life targeted by the project. The carbon footprint assessment that follows then compares GEO and REF on time-independent functional units. The two parts connect through durability adequacy, not through a service-life normalization.

4.1 State of the art

The durability of a marine concrete is governed by the chemistry of its binder, because the classical degradation mechanisms of Portland cement concrete are, almost without exception, reactions that target specific hydration phases. When those phases are absent or chemically reorganized, the corresponding degradation pathway is closed. The gel chemistry of GEO, a calcium aluminosilicate hydrate incorporating both sodium and potassium and designated C-(N,K)-A-S-H, was established in Chapter 1. As fundamentally different from the calcium silicate hydrate and portlandite assemblage of Portland cement, this section examines the consequences that difference is expected to have under marine exposure, and the carbon cost it carries.

The section is devided in two parts:

- The first sets out the degradation mechanisms of Portland systems and the chemical premise for a geopolymer advantage, then assembles the published benchmark against which the exposures examined in this chapter are interpreted, then the limitations that each measurement method inherits in an alkali-activated pore solution.

- The second turns to the life cycle: the carbon benchmark of the ultra-high-performance class and the methodological dispersion that makes published reductions difficult to compare.

Each part closes by stating what its own literature leaves open, and the compound gap that the present chapter fills is stated in the chapter framing paragraph above.

4.1.1 Marine degradation of Portland cement and the geopolymer premise

Three degradation routes govern the Portland assemblage and set the premise this chapter tests: expansive sulfate attack, acid dissolution of the portlandite reserve, and chloride ingress to the reinforcement.

4.1.1.1 Degradation routes in the Portland assemblage

Sulfate attack proceeds through the reaction of penetrating sulfate with the aluminate phases and the portlandite reserve to form expansive ettringite and gypsum (Mehta, 1983). Both products occupy substantially more solid volume than the phases they replace, so their formation inside a confined, already-hardened pore structure generates internal crystallization pressure. That pressure, rather than any loss of chemical bonding, is the proximate cause of the damage: it drives expansion, opens internal microcracks that admit further sulfate, and progressively dismantles the cohesion of the matrix (Neville, 1963; Mehta, 1983). The ettringite considered here is the external route, formed from sulfate penetrating a hardened matrix. The internal route, delayed ettringite formation, is excluded on both sides of the comparison and for different reasons. It requires sustained curing above approximately 65 °C (Taylor et al., 2001).

The semi-adiabatic peak measured in Chapter 1 reached 57.5 °C for REF, which was cured at ambient temperature throughout. GEO reached a higher peak, 63.2 °C, but holds neither the reactive aluminate nor the portlandite that the delayed route consumes, so the mechanism has no substrate in that binder at any temperature. Delayed ettringite formation is therefore outside the scope of the present comparison. Its relevance at substructure scale, where the section-scale exotherm exceeds the small-specimen value, is raised in the Perspectives.

The identity of the attacking cation changes the picture in a way that matters directly for a seawater environment. Sodium sulfate attacks almost entirely through the aluminate and portlandite routes described above, so its aggressiveness scales with the reactive-aluminate and portlandite content of the binder. Magnesium sulfate is more damaging, and damaging through an additional pathway: beyond forming ettringite and gypsum, the magnesium ion exchanges with calcium in the calcium silicate hydrate itself, decalcifying the principal binding gel and replacing it with non-cementing magnesium silicate hydrate, while precipitating a brucite surface layer (Bonen and Cohen, 1992).

Seawater carries both sulfate cations at once, together with chloride, so the marine condition is inherently a combined-cation attack rather than either single-salt laboratory case.

Acid attack is governed by the same portlandite reserve, which buffers the pore solution at high pH but dissolves readily on contact with an acid front, leaving a leached and progressively deepening degraded skin (Bakharev, 2005).

Chloride ingress is the governing durability concern for reinforced or fiber-bearing marine concrete, since chloride reaching the steel depassivates it and initiates corrosion (Provis et al., 2012). The Portland assemblage, however, carries a partial defense of its own. The aluminate phases that make it vulnerable to sulfate also react with penetrating chloride to precipitate Friedel's salt, a layered calcium aluminate chloride hydrate that removes free chloride from the pore solution and fixes it in the solid phase.

The binding capacity scales with the reactive aluminate content of the binder, so the same C_3A and AFm reserve that opens the sulfate pathway closes part of the chloride one (Suryavanshi et al., 1996). That dual role sets the terms of the comparison developed below: a binder that eliminates reactive aluminate in order to defeat sulfate attack necessarily forfeits the chloride binding that the aluminate provides.

The reactive aluminate and the portlandite that drive all of these routes are abundant in a Portland binder. They are precisely the two phases that the alkali-activated binder either reorganizes into its gel or omits altogether, which is the basis of the premise developed in the following subsection.

4.1.1.2 The chemical premise for a geopolymer advantage

The alkali-activated binder of GEO holds its aluminum in a fundamentally different state. Rather than existing as discrete, reactive aluminate hydrate phases, the aluminum is incorporated substitutionally at bridging tetrahedral sites within the cross-linked calcium aluminosilicate hydrate gel, the layered, tobermorite-like C-(N,K)-A-S-H framework characterized in Chapter 1, where it is structurally bound and not available to nucleate ettringite (Komljenović et al., 2013; Ismail et al., 2014).

At the same time the binder contains no portlandite at all, the gel having formed by alkali activation rather than by the hydration of calcium silicates that liberates free lime. These two facts, aluminum locked in the gel and portlandite absent, are the chemical premise of the whole durability comparison, summarized in Figure 4-1. They predict that the two pathways most damaging to Portland concrete in a marine environment, expansive sulfate attack and acid dissolution of portlandite, should be closed or strongly suppressed in GEO.

The premise cuts both ways, and the chapter is built around that tension rather than around an assumption of geopolymer superiority. The same absence of reactive aluminate that prevents ettringite formation also removes the Friedel's-salt chloride-binding capacity

that aids Portland concrete, so GEO must resist chloride by pore structure alone. And the pore structure is the weaker side of the ledger: Chapter 1 established that GEO carries a markedly coarser capillary network than REF, with a dominant pore-size peak near 700 nm against 6.2 nm and a mean apparent gas permeability 22 times higher.

The chemical advantage under sulfate and acid is therefore set against a transport disadvantage under chloride, and, as Section 4.1.3 will argue, against an expected disadvantage under elevated temperature that follows from the high calcium content of the same gel. Three of these aggressors, sulfate, acid, and chloride, act within the marine service envelope. Elevated temperature is included as a project-required screening condition that lies outside it, and is treated on that basis throughout. Whether the chemical gains outweigh the transport and thermal penalties across the four, taken together, is the question this chapter exists to answer.

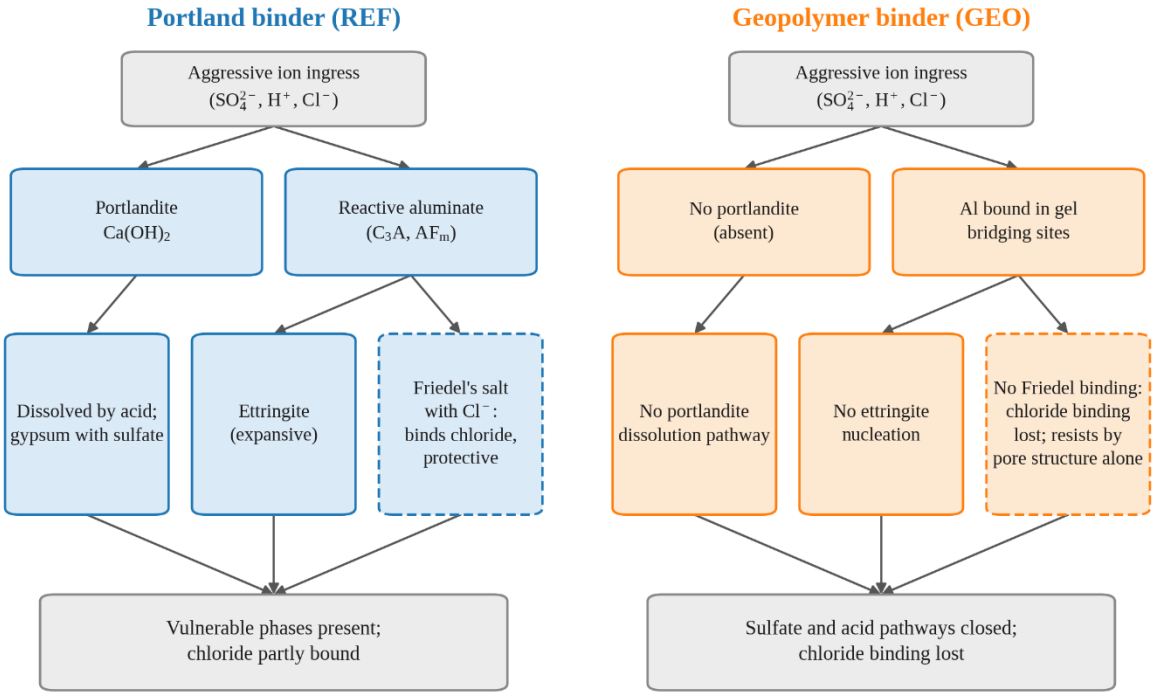

Figure 4-1: Chemical premise for the durability comparison for REF and GEO.

4.1.2 Durability of alkali-activated binders under chemical attack

The published record on alkali-activated slag broadly confirms the advantage that the preceding subsection predicts: with no portlandite and aluminum bound within the gel framework, the classical expansive sulfate route is largely closed, and acid exposure attacks a binder holding no comparable dissolvable calcium reserve (Bakharev, 2005; Lloyd et al., 2012; Ismail et al., 2014; Aiken et al., 2018). The record is not uniform, however, and the two aggressors diverge sharply in how far they have been characterized. Sulfate resistance rests on a small number of studies whose mechanistic explanation is precisely the one

advanced above. Acid resistance rests on a larger body of work that agrees on direction while disagreeing on severity. Neither reaches the strength class of the present material. The studies that report a quantitative outcome together with the Portland binder tested alongside are assembled in Table 4-1 and placed against the present work in Figure 4-2.

4.1.2.1 Sulfate resistance and the role of the gel cation

The mechanism set out in Section 4.1.1 has been measured directly rather than merely inferred. Komljenović et al. (2013) exposed sodium-silicate-activated slag mortar and a Portland-slag cement of comparable consistency to a 5% sodium sulfate solution over 90 days and found that the two materials diverged rather than degrading at different rates.

The alkali-activated mortar gained strength throughout, reaching a relative strength index of 1.11 in compression and 1.12 in flexure, while the benchmark cement declined to 0.90 and 0.91 as ettringite and gypsum formed in its pore structure. Their microstructural analysis attributed the divergence to precisely the two features identified above: the absence of portlandite, and the unavailability of aluminum for reaction with sulfate because it is held within the C-A-S-H and hydrotalcite gels rather than as a discrete reactive phase. Alkali-activated slag under sodium sulfate does not merely resist attack. Within the duration studied it continues to mature while the Portland comparator loses cohesion.

The identity of the attacking cation is expected to modulate that outcome, and to modulate it unfavorably in the chemistry that seawater actually presents. Sodium sulfate attacks principally through the aluminate and portlandite routes, both weak or absent in the alkali-activated binder, which is why the divergence reported above is as clean as it is.

Magnesium sulfate operates through an additional pathway that the geopolymer cannot close, since the magnesium ion exchanges with calcium in the binding gel itself, destabilizing the principal binding phase and precipitating a surface brucite layer whose net effect depends on its adherence (Bonen and Cohen, 1992; Komljenović et al., 2013). A calcium-rich C-(N,K)-A-S-H gel is exposed to that route in a way that the low-calcium aluminosilicate frameworks of fly-ash systems are not. No study in the reviewed record, however, reports magnesium sulfate exposure of an alkali-activated binder at ultra-high-performance strength level, so the expectation rests on mechanism rather than on a measured comparison.

The consequence for a marine assessment is more restrictive still. Seawater carries both sulfate cations simultaneously, together with chloride, and the net effect of that combination on a slag-based binder cannot be obtained by superposing two single-salt results when one of those results is itself unmeasured. The reviewed literature contains no exposure of an alkali-activated binder to a combined magnesium-and-sodium sulfate solution. This is the specific deficiency that the 12-month single-cation and combined-cation campaign of the present chapter addresses, and it is reported here without a published comparator.

4.1.2.2 Acid resistance, the corroded layer, and the mobility of the alkali

The acid record is the most developed of the exposures examined in this chapter and is consistent in direction across binder chemistries, exposure severities, and measurement conventions. Fly-ash geopolymer pastes exposed to 5% acetic acid at pH 2.4 for 6 months lost 38 to 60% of their strength depending on activator, against 91% for the Portland paste tested alongside (Bakharev, 2005).

Fly-ash and slag geopolymer mortars exposed to 5% sulfuric acid for 56 days showed mass changes between a slight gain and a 7.6% loss, against 28.3 and 34.6% for the Portland mortars of comparable strength (Aiken et al., 2018). A comparison carried to 24 months at pH 3 found the geopolymer to lose 1% of its compressive strength in hydrochloric acid where Portland cement lost 20% and high-alumina cement 68% (Vafaei et al., 2018). Across three binder families, four acids, and durations spanning two months to two years, the ranking does not reverse.

The severity, by contrast, is disputed, and the mechanism by which the geopolymer resists has been read more optimistically than the evidence supports. The dealuminated, silica-enriched residue left at an attacked surface is denser than the bulk gel and impedes further ingress, and this has been described as rendering the attack self-limiting. Measurements of corroded depth rather than mass or strength show that the arrest is partial (Lloyd et al., 2012). The fitted corrosion law for nitric acid at pH 3, the aggressor adopted in the present campaign, yields a corroded depth of approximately 0.45 mm at 85 days and advances linearly rather than asymptotically. The broader methodological finding of that study also bears on how the present results are read: mass loss is an unreliable indicator for these materials, because acid attack leaves an apparently intact but structurally weak residue that continues to contribute mass, so that a specimen may lose performance while gaining weight.

Two features of that record apply directly to the binder examined here:

First is that acid attack on an alkali-activated system is a leaching process as much as a dissolution one. The composition across an attacked zone, resolved by energy-dispersive analysis, showed that 96% of the sodium, 98% of the calcium, and 79% of the aluminum had left the corroded layer, in a two-stage alkali-leaching sequence in which weakly bound alkali departs first and structurally bound alkali follows (Vafaei et al., 2018). For a potassium-activated binder the mobile alkali is therefore a principal reactant rather than a spectator, and the residue is alkali-depleted as well as dealuminated.

Second is that the activator cation has been reported to matter, and to matter adversely. Among the three fly-ash systems examined under sulfuric acid at pH 0.8 (Bakharev, 2005), the system activated by a sodium and potassium hydroxide mixture lost 89% of its strength

where the sodium-hydroxide system lost 17.5% and then stabilized, a difference attributed to a coarser average pore diameter, 116 Å against 45 Å, and to active sites created on the gel surface by the potassium ion. A study isolating alkali type from other compositional factors found no significant effect (Lloyd et al., 2012).

The two findings are not necessarily in conflict, since the cation effect reported by Bakharev (2005) was inseparable from a pore-structure effect, but the disagreement is unresolved and it concerns the activator adopted in the present work. Both studies were conducted on low-calcium fly-ash pastes, and the second at a pH more than two orders of magnitude below the exposure applied here, so neither transfers directly to a slag-based binder at pH 3. The result is recorded because it is the most adverse published finding for a potassium-activated system, and because silence about it would be the weaker position.

A further limitation follows from the same coupling. Because alkali departure and gel densification both proceed at an attacked surface, and because both raise the electrical impedance of a specimen, impedance alone cannot separate a protective surface layer from a pore solution depleted of its charge carriers. That ambiguity governs the interpretation of the acid results in Section 4.3 and is developed in Section 4.1.4.

Table 4-1: Published durability of alkali-activated binders under chemical immersion, with the reference binder tested in the same study (Lloyd et al., 2012).

Study	Alkali-activated binder	Reference binder	Aggressor	Duration	Alkali-activated outcome	Reference outcome
Komljenović et al. (2013)	Slag, sodium silicate	CEM II/A-S 42.5N	5% Na_2SO_4	90 d	Strength index 1.11 comp., 1.12 flex.	0.90 comp., 0.91 flex.
Bakharev (2005)	Fly ash, NaOH	OPC paste	5% acetic, pH 2.4	180 d	−40%	−91%
Bakharev (2005)	Fly ash, NaOH + KOH	OPC paste	5% acetic, pH 2.4	180 d	−38.3%	−91%
Bakharev (2005)	Fly ash, NaOH	OPC paste	5% sulfuric, pH 0.8	120 d	−17.5%, then stable	destroyed at 30 d
Bakharev (2005)	Fly ash, NaOH + KOH	OPC paste	5% sulfuric, pH 0.8	60 d	−89%	destroyed at 30 d
Lloyd et al. (2012)	Fly ash / GGBS	OPC, CAC pastes	HNO_3, pH 3	85 d	0.45 mm corroded depth	not reported at pH 3
Aiken et al. (2018)	Fly ash / slag, 0 to 70% slag	CEM I mortars	5% H_2SO_4	56 d	mass change −0.1 to 7.6%	28.3 and 34.6%
Vafaei et al. (2018)	Waste glass / CAC	Portland, high alumina	pH 3 HCl	730 d	−1%	−20%, −68%

Vafaei et al. (2018)	Waste glass / CAC	Portland, high alumina	pH 3 H_2SO_4	730 d	−64%	−100% both, at 540 and 450 d
Kong and Sanjayan (2010)	Fly ash, silicate + KOH	none	800 °C, 1 h	1 h	paste −73.4%, mortar −100%, concrete −58.4%	-
Li et al. (2020)	not covered	Portland UHPC	high sulfate	365 d	-	≈ −12%
Graybeal and Tanesi (2007)	not covered	Portland UHPC	ASTM C1202	28, 56 d	-	18 to 360 C by curing
This work	GEO	Project reference UHPC, 165 MPa	Na_2SO_4, $MgSO_4$, combined, HNO_3	365 d	Section 4.3	

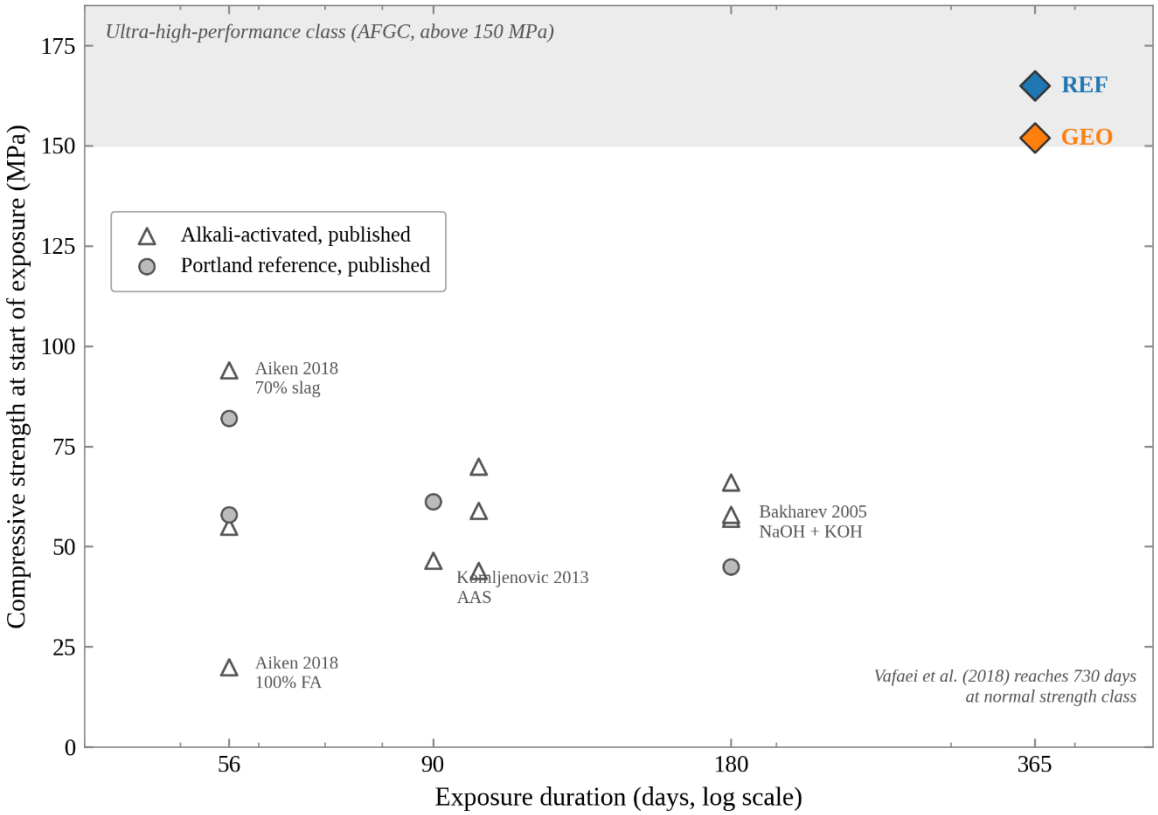

Figure 4-2: Position of the present work in the published durability literature on binders subjected to chemical immersion.

4.1.3 Chloride transport and elevated-temperature behavior

The two mechanisms that run against the geopolymer are treated together, because both trace to the composition of the same gel: the aluminum locked into its framework, which

closes the sulfate pathway but forfeits chloride binding, and the calcium that fills it, which delivers ambient strength but sets the thermal ceiling.

UHPC of either binder class sits at the favorable extreme of the chloride transport scale, so the comparison conducted here is between two already excellent materials rather than between a good and a poor one (Graybeal and Tanesi, 2007; Li et al., 2020). The scale on which any binder difference must be read is established by measurements of the charge passed under ASTM C1202 on a single commercial UHPC subjected to four curing regimes (Graybeal and Tanesi, 2007).

Steam curing at 90 °C produced 18 C, tempered steam at 60 °C produced 39 C, and the same material cured under ambient laboratory conditions produced 360 C at 28 days, falling to 76 C by 56 days as hydration continued. One material, one mix design, a twentyfold range governed by thermal treatment alone. Any charge difference attributed to binder chemistry has to be weighed against a within-material variance of that magnitude, and against the fact that both materials examined here were cured at ambient temperature and therefore occupy the least favorable end of that range by construction.

Two effects nonetheless separate the binders:

First is a material property and works against the geopolymer: the Friedel's-salt mechanism that chemically binds chloride in Portland systems depends on the calcium aluminate hydrates that the alkali-activated binder does not form in the same way, so a larger share of the chloride inventory remains free in the pore solution (Provis et al., 2012).

Second is not a transport property at all but an artifact of how transport is measured, since the standard migration test records total ionic current rather than chloride flux and the alkali-activated pore solution carries a far higher mobile-ion content than a Portland one. Part of any charge difference therefore reflects pore-solution conductivity rather than chloride mobility. That confound governs the reading of every chloride result in this chapter and is developed in Section 4.1.4.

Elevated temperature is the one mechanism where the geopolymer literature predicts an advantage, on the basis of low-calcium fly-ash and metakaolin systems whose aluminosilicate network survives dehydration far better than a calcium silicate hydrate (Kong and Sanjayan, 2010; Lahoti et al., 2018).

GEO is not a low-calcium system, and that is decisive. Its binder is a high-calcium C-(N,K)-A-S-H gel formed from a GGBS-dominant precursor, structurally a layered, tobermorite-like calcium aluminosilicate hydrate rather than a cross-linked aluminosilicate framework, whose compositional domain is distinguished from the low-calcium gels in Figure 1-1. Its thermal decomposition pathway is therefore expected to resemble that of a calcium-rich hydrate, closer to the C-S-H of Portland cement than to the N-A-S-H of fly-ash geopolymers. The thermal behavior of potassium-activated slag systems specifically has been little characterized, most published work having addressed $NaOH^-$activated or sodium-

silicate-activated systems, so the magnitude of the effect for this chemistry is not established (Guerrieri and Sanjayan, 2010; Rashad, 2014).

The published expectation is further conditioned by specimen form in a way that is rarely carried into the comparison. A fly-ash geopolymer activated by sodium silicate and potassium hydroxide, the same activator pair adopted here, was heated as paste, mortar, and concrete to 800 °C under a controlled ramp (Kong and Sanjayan, 2010). A 25 mm paste cube gained 6.4% of its strength. The identical paste cast as a 100 × 200 mm cylinder lost 73.4%. The mortar retained no measurable strength and split into two halves at 600 °C. The concrete lost 58.4%.

The size dependence was attributed to thermal gradients that steepen as the section grows, and the mortar and concrete losses to thermal incompatibility between the geopolymer matrix and the aggregate. The reputation of geopolymers for thermal stability therefore rests on small paste specimens and does not survive the addition of aggregate and section, which is the form in which any structural material is used.

Strength retention and structural integrity must also be distinguished, because the pore network bears on them differently. UHPC is more prone to explosive spalling than conventional or high-performance concrete, precisely because the virtual absence of capillary porosity and the low free-water content raise vapor pressure during heating, and hybridization of steel with polypropylene fibers is the established mitigation (Li et al., 2020). Permeability is protective under thermal loading rather than adverse, and on that basis the 22-fold difference in mean apparent gas permeability established in Chapter 1 would relieve pressure more readily in the geopolymer.

The controlled regime adopted here, 5 °C/min to target with a two-hour hold and furnace cooling, drives most free water out well below the target temperatures and therefore weakens the pressure-driven route relative to a fire curve, so permeability is expected to be a contributing rather than a governing factor. The chapter reports strength retention and specimen integrity separately, to 900 °C, and softens neither, because an honest account of the mechanism where the geopolymer is disadvantaged is what gives the favorable mechanisms their credibility.

4.1.4 Assessment methods and their limitations in alkali-activated systems

Three measurement families carry the durability argument of this chapter: migration, the electrical methods of impedance and resistivity, and colorimetry. Each is set out below with the limitation it inherits in an alkali-activated pore solution, and the subsection closes on the reason the laboratory campaign is paired with a field one.

4.1.4.1 Migration theory and the apparent diffusion coefficient

Chloride transport resistance is screened by the rapid chloride penetration test (ASTM C1202), which reports the total charge passed under an applied potential as a penetrability proxy, with the standard itself cautioning that the charge is an indication of penetrability rather than a direct diffusion measurement, a limitation examined in detail elsewhere (Joshi et al., 2000). To convert the migration measurement into a transport coefficient, the apparent chloride diffusion coefficient is recovered through the Nernst-Planck relation, which links the steady-state ionic flux under an applied field to the diffusion coefficient, the ion valency, the bulk concentration, and the cell geometry (Andrade, 1993).

The derivation assumes the measured current is carried predominantly by the ion of interest, an assumption that is only approximate in the high-ionic-strength pore solutions characteristic of alkali-activated systems, and corrections for Joule heating and the associated temperature rise over the test duration refine the estimate (Julio-Betancourt and Hooton, 2004; Ghosh et al., 2011). For the low charge values characteristic of UHPC these corrections are small and do not alter the penetrability classification, a point the results return to when reconciling the present uncorrected coefficients against the corrected values reported in the literature (Hasan et al., 2024).

Coupled electrical and hydraulic drivers can accelerate chloride transport in ultra-high-performance concrete well beyond diffusion-controlled rates (Chen et al., 2025), a condition that does not arise in a floating photovoltaic substructure, where no stray current is present and hydrostatic pressure is negligible.

4.1.4.2 Impedance, resistivity, and the formation factor

Electrical impedance spectroscopy probes the same transport network non-destructively and continuously, which makes it the natural tool for tracking microstructural change over a 12-month exposure. The bulk resistance is extracted from the real component of impedance in a frequency window where electrode polarization is minimal and the response is dominated by conduction through the connected pore solution. It scales jointly with the connected pore volume, the conductivity of the pore solution, and the tortuosity of the network (McCarter et al., 2003).

The rigorous durability descriptor, however, is not the bulk resistance itself but the formation factor, the ratio of bulk resistivity to pore-solution resistivity, which divides out the pore-solution chemistry and isolates the pore-structure geometry (Snyder et al., 2000) (Figure 4-3).

This distinction is decisive for the present comparison, and getting it wrong would invert the conclusion. Because the alkali-activated pore solution of GEO is intrinsically far more conductive than a Portland pore solution, GEO will show a lower bulk impedance than REF even if its pore structure is of comparable or only moderately inferior quality.

The low impedance reflects the mobile-ion content of the pore liquid, not necessarily a poor pore network (Provis, 2018). A correct reading therefore requires either the formation factor or an explicit acknowledgment that the bulk values are confounded.

The formation factor requires extraction of the pore solution, which was not performed in the present work, so the impedance results of this chapter are read as a within-mix temporal indicator of microstructural stability, whether each material's pore structure is refining, stable, or degrading over time, rather than as a between-mix measure of pore quality. This limitation is stated again in Section 4.3.4, where the impedance data are interpreted, so that the comparison is not over-read.

Electrical resistivity, recoverable from the same measurements, is widely used as a corrosion-risk indicator through empirical thresholds calibrated on field and laboratory concrete: resistivity above roughly 200 Ω·m corresponds to negligible corrosion likelihood, with progressively higher risk at lower values (Song and Saraswathy, 2007; Broomfield, 2023). These thresholds were established largely on Portland systems and inherit the same pore-solution confound as the bulk impedance, so for an alkali-activated material with a highly conductive pore solution they tend to place the material in a higher apparent risk band than its pore structure warrants.

The present chapter applies them in that spirit, as a conservative bound on corrosion risk rather than as a direct measure of pore quality, and reads any threshold crossing with that caveat attached.

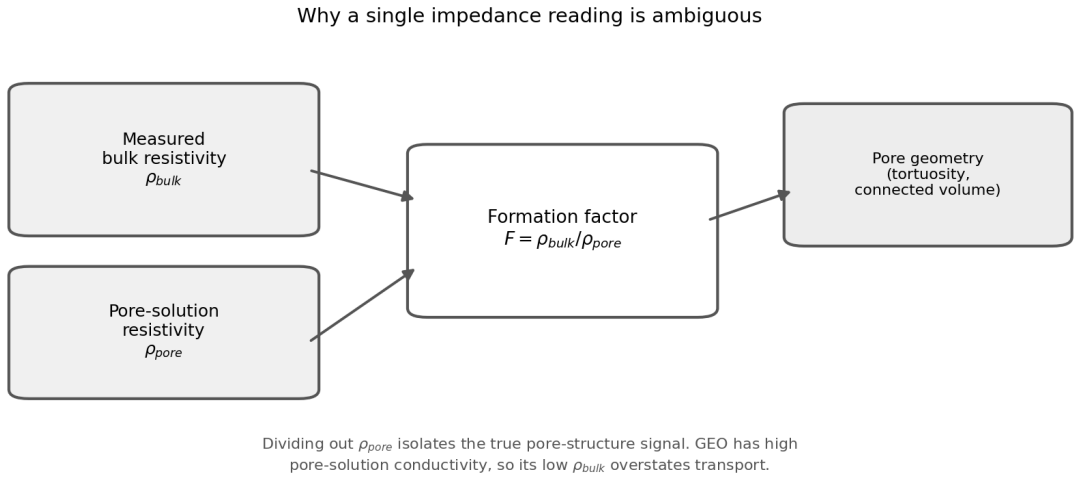

Figure 4-3: The formation-factor concept.

4.1.4.3 Colorimetric front detection

After marine exposure, the carbonation and chloride fronts are read directly on freshly fractured faces with two colorimetric sprays, a simple and robust complement to the electrical methods, applied to the marine-exposed specimens in Section 4.3.8.

Phenolphthalein develops a pink-violet color where the matrix retains a pore-solution pH above roughly 9 and remains colorless where the alkalinity has been neutralized, so the boundary between colored and colorless regions maps the depth of alkalinity loss (EN 14630).

Silver nitrate precipitates white silver chloride where free chloride is present above a low threshold and develops a brown silver-oxide color in chloride-free regions, delineating the chloride penetration front.

Both sprays carry limitations in an alkali-activated system. The silver nitrate reading is confounded by carbonation rather than by chloride, because the brown reference color requires free hydroxide: a carbonated but chloride-free zone never develops it and reads as though chloride were present, which is why the phenolphthalein result must be read alongside it (Pontes et al., 2021). The present chapter applies both sprays to the same fracture surfaces for this reason. The phenolphthalein limitation is the more consequential of the two.

The indicator reports pore-solution alkalinity, not carbonate content, and in this binder the two demonstrably coexist: Chapter 1 measured 7.1 wt% calcite in GEO after a 28-day ambient cure at 50 ± 5% relative humidity, in a material whose KOH^--activated pore solution remains strongly alkaline. Alkali-activated slag carbonates more readily than a Portland system because it holds no portlandite to buffer the pore solution (Bernal et al., 2013), so a uniformly pink phenolphthalein result cannot be read as an absence of carbonate.

The colorimetric result of this chapter is therefore reported as retained alkalinity, which is the property governing passivation of the embedded steel fibers, and not as a measurement of carbonate content, which was not determined on the exposed specimens.

4.1.4.4 Laboratory acceleration against real marine exposure

Accelerated laboratory immersion isolates a chosen aggressor at fixed concentration and answers mechanistic questions cleanly, but it cannot reproduce the coupled wetting and drying, the biofouling, the temperature cycling, and the combined-ion chemistry of a real marine environment, nor the alternation of exposure conditions along the tidal column that a real structure experiences.

Field exposure supplies that realism, at the cost of experimental control and of time. The HarshLab floating facility in the Bay of Biscay provides exposure in three zones, an atmospheric zone above the waterline, a splash zone subject to cyclic wetting and wave action at the tidal interface, and a permanently immersed zone, allowing laboratory-derived mechanisms to be checked against the service environment they are intended to predict.

The present chapter pairs the two deliberately. The laboratory program is fully comparative: 12 months on both binders, in single-salt solutions and in the combined magnesium-and-sodium sulfate condition representative of seawater, with continuous impedance monitoring throughout.

The field program is not, and that is its one limitation: the 10-month HarshLab campaign reported here covers GEO across the three zones, the project reference UHPC having been tested in parallel by a project partner outside the scope of this work. The field results therefore do not extend the binder comparison. What they test is whether the behavior predicted for GEO from accelerated laboratory exposure holds, overstates, or understates what a real marine environment produces, and that is the question they are used to answer here.

4.1.5 Open questions on durability

Four boundaries limit what the published record can predict for the present material, and each falls on a different one of the exposures examined in this chapter.

First is strength class, and it applies to the chemical attack literature as a whole. Every alkali-activated study assembled in Table 4-1 was conducted below 95 MPa, and the majority on pastes or mortars between 40 and 70 MPa, whereas the binder examined here reaches 152 MPa on prism halves at 28 days. Pore structure, identified as the controlling variable for acid resistance (and for penetration depth (Aiken et al., 2018), is precisely the property that separates an ultra-high-performance matrix from a normal-strength one, so extrapolation across that boundary is not a matter of degree.

Second is exposure chemistry. Magnesium sulfate has not been applied to an alkali-activated binder at ultra-high-performance strength level, and the combined magnesium-and-sodium condition representative of seawater has not been applied at all. The expectation that a calcium-rich gel is exposed to the magnesium exchange route therefore rests on mechanism rather than on a measured comparison, and the seawater-representative condition is reported in this chapter without a published comparator.

Third concerns the two mechanisms that run against the geopolymer, and it takes a different form in each. For chloride, the published record shows that curing regime moves a single UHPC across a twentyfold range of migration charge, so no meaningful binder comparison can be drawn from studies that do not hold curing constant, and none exists at this strength class for a cement-free binder. For elevated temperature, the geopolymer advantage is documented on low-calcium fly-ash and metakaolin systems, on paste specimens, and it does not survive the addition of aggregate or an increase in section. The behavior of a potassium-activated, calcium-rich slag binder is essentially uncharacterized.

Fourth is methodological and it conditions all of the above. The non-destructive descriptors on which a modern durability assessment depends, the migration charge and the bulk impedance, are both inflated by the high ionic strength of an alkali-activated pore solution, and the formation factor that would divide that effect out requires a pore-solution extraction that the prior UHPGC durability literature does not report. A comparison drawn from bulk electrical values alone can therefore invert its own conclusion.

Finally, the alkali-activated durability record is largely accelerated and laboratory-based, a limitation its own authors state: the data available to them derived from laboratory testing because field performance data were not publicly available (Lloyd et al., 2012).

4.1.6 The UHPC carbon benchmark and its reduction routes

That closes the durability half of the review. The second half turns from whether the material survives marine service to what producing it costs, because a binder that endures but carries no environmental advantage over the reference it replaces answers none of the questions this thesis asks.

UHPC is the highest-strength member of the cement-based family and also the most carbon-intensive per unit volume, since its performance is bought with a high binder content. Published cradle-to-gate values cluster between roughly 600 and 1300 kg CO_2-equivalent per m^3 (Wille et al., 2011; Yoo and Banthia, 2016). Its mechanical density derives from a discontinuous granular skeleton packed at low water-to-binder ratios, with Portland cement contents that commonly fall in the 800 to 1000 kg per m^3 range and supplementary silica fume contents of 150 to 250 kg per m^3 (Habert et al., 2013). Because strength rises faster than carbon across the family, the per-MPa functional unit used later in this chapter reports the comparison on a performance rather than a volume basis (Habert et al., 2013; Stengel and Schießl, 2014; Sameer et al., 2019).

Two generations of reduction strategy are distinguishable. First-generation strategies substitute part of the clinker with industrial by-products, typically slag, fly ash, or limestone, and reach reductions of the order of a third while retaining a Portland binder (Habert et al., 2013; Yu et al., 2015; Caruso et al., 2022). Second-generation strategies remove the clinker altogether, activating aluminosilicate by-products with an alkaline solution. Transposed to the ultra-high-performance strength class, this is the UHPGC route to which the present work belongs (Provis and Deventer, 2014; Yu et al., 2015). The published UHPGC benchmark is set by a strain-hardening formulation at approximately 480 kg CO_2-equivalent per m^3 (Lao et al., 2023), a reduction of 52 to 60% relative to the conventional Portland range of Table 4-2.

That benchmark does not, however, bracket the result obtained here, and the reason is chemical rather than methodological. The activator dominates the cradle-to-gate burden of any alkali-activated binder, and its contribution depends on which activator is chosen (Provis and Deventer, 2014; Habert and Ouellet-Plamondon, 2016). The published benchmark was activated by sodium carbonate. The formulation examined here uses sodium silicate together with potassium hydroxide, selected in Chapter 1 for the rheology and early strength that the ultra-high-performance target requires. As Section 4.6 shows, that choice places roughly 69% of the A1 burden in the activator, of which the potassium hydroxide alone accounts for about 60%. The present mix therefore sits above the best published UHPGC and level with

the best eco-UHPC, and the carbon assessment of this chapter is framed accordingly: the question is not whether removing clinker reduces carbon, which is established, but whether the reduction survives the activator burden that a UHPGC-grade activator imposes.

4.1.7 Methodological dispersion and the case for like-for-like comparison

The comparability of published life-cycle results in the UHPC and UHPGC family is hampered by methodological dispersion. Studies report results on widely different functional units, one m^3, one ton, one MPa of strength, or one m^2 of structural element. They apply inconsistent system boundaries, cradle-to-gate or cradle-to-grave, with or without the use module and with or without carbonation crediting, and they select impact-assessment methods of different vintages, principally CML 2001 and the successive Environmental Footprint releases (Provis and Deventer, 2014; Habert and Ouellet-Plamondon, 2016).

The shift from the IPCC AR4 to the AR6 hundred-year global-warming characterization factors, embedded in the EF 3.1 method, introduces a 5 to 8% systematic shift in the cradle-to-gate global warming potential of cement-based products relative to older CML-based studies, which complicates direct numerical comparison across the literature.

The Environmental Product Declaration framework codified in EN 15804+A2 was designed to address this fragmentation by imposing a uniform declared unit, module-by-module reporting, and a fixed cut-off rule. Nonetheless, declaration coverage of UHPC remains thin, and supplier-specific verified declarations are rare in the academic literature. The present work uses one such declaration as the data source for the REF mix and mirrors its system boundary and declared unit in the GEO inventory, ensuring a like-for-like comparability that most published comparative studies cannot claim.

Table 4-2 summarizes the published cradle-to-gate global warming potential of representative formulations across the binder generations identified above, on the per-cubic-meter functional unit common to all entries. The GEO mix of the present work is included on its cradle-to-gate basis, modules A1 to A3, for direct comparability with the cited studies.

Two patterns emerge. **First,** the spread within each generation is substantial: conventional Portland UHPC spans 1000 to 1200 kg CO_2-equivalent per m^3, a factor of 1.2 across studies of nominally similar mixtures, reflecting the methodological dispersion described above more than any real difference in binder chemistry. **Second,** the gap between generations is consistent in direction, Portland UHPC above eco-UHPC above UHPGC, but quantitatively variable: the best eco-UHPC formulation (Yu et al., 2015) reaches a footprint comparable to the higher UHPGC formulations, indicating that the binder-substitution gain saturates well before the cement-free threshold. Figure 4-4 places these values in two-dimensional strength-carbon space, with the present GEO mix marked against the mechanical target.

A further axis of dispersion concerns the strength value against which carbon is normalized. The compressive strengths reported in Table 4-2 derive from different specimen geometries and standards, and the source studies rarely state which, so a per-MPa comparison inherits an uncontrolled variance from the mechanical side as well as the environmental one. The value entered for the present work, 152 MPa, is the 28-day compressive strength measured on prism halves following EN 196-1, the basis used consistently throughout this thesis.

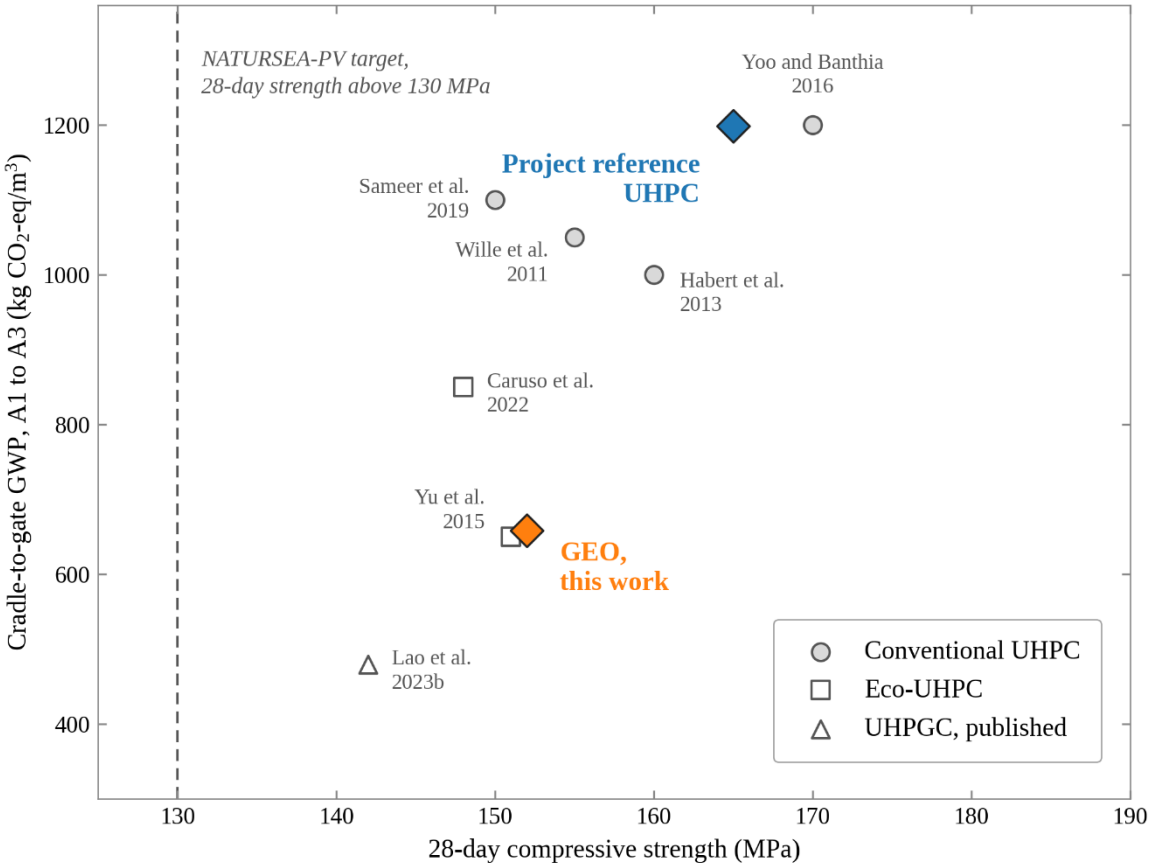

Figure 4-4: Position of the present work in the published life-cycle literature of ultra-high-performance concretes, plotted in strength-carbon space.

4.1.8 Open questions on the life-cycle record

Three limitations follow:

First is that no published comparison of a UHPGC against a Portland UHPC of the same mechanical class is drawn from a single, internally consistent inventory: the two sides are almost always taken from separate studies with separate boundaries and separate impact methods, so the reported difference conflates binder chemistry with methodological choice.

Second is that the activator burden, which the preceding subsection identifies as the dominant term for any cement-free binder, is reported inconsistently and often at a level of

aggregation that prevents the individual activator components from being resolved, so the sensitivity of the result to activator selection cannot be recovered from the published record.

Third is that the durability of the compared materials almost never enters the life-cycle assessment at all, whether through a service-life assumption, a maintenance scenario, or a use-phase module, so a material with a superior environmental profile and an inferior service life is credited on the first without being charged for the second.

The present chapter addresses the first two directly, through a single inventory and a disaggregated sensitivity analysis, and addresses the third by placing the durability assessment ahead of the life-cycle assessment within the same chapter.

4.2 Materials and methods

This section specifies the two mixes and the durability test program applied to them. The mix designs and raw materials are reported in Chapter 1 and are not reproduced here. The material properties restated in Section 4.2.1 are those used by the test protocols and the analysis of Section 4.3. Each subsequent subsection describes one exposure or measurement program, giving the governing standard, the specimen geometry, the exposure conditions, the number of specimens prepared, and the quantities measured.

4.2.1 Materials

The two mixes are the Portland cement reference (REF) and the cement-free geopolymer (GEO) established and characterized in Chapters 1 to 3. Both carry the fiber system selected in Chapter 1: 108 kg/m^3 of a 60/40 blend of Flexo recycled tire-derived and Spajic virgin steel fibers, corresponding to 1.4% by volume of the total mix, of which 60% by weight is recycled. The 1.5% by volume system of straight uncoated fibers used in Chapter 3 belongs to a separate specimen series prepared for the acoustic emission campaign and is not used in the present chapter.

The material properties to which the following protocols and the analysis of Section 4.3 refer are those determined in Chapter 1 and are restated here for reference. At 28 days, the age at which the laboratory exposures began, the compressive strength determined on prism halves following EN 196-1 was **152 MPa for GEO** and **165 MPa for REF**. The water-accessible porosity was 8.25% for GEO and 4.80% for REF. The dominant pore-size peak was near 700 nm for GEO and 6.2 nm for REF, and the mean apparent gas permeability of GEO was 22 times that of REF. The binder of REF is a calcium silicate hydrate and portlandite assemblage. That of GEO is the C-(N,K)-A-S-H gel characterized in Chapter 1, and contains no portlandite.

4.2.2 Specimen preparation and conditioning

Prismatic specimens of 4 × 4 × 16 cm^3 were cast for the sulfate immersion, the acid immersion, the electrical impedance monitoring, the elevated-temperature exposure, and the marine exposure. Cylindrical specimens of 100 mm diameter and 50 mm thickness were cast for the rapid chloride penetration test. All specimens were demolded 24 hours after casting and then stored at 20 ± 2 °C and 50 ± 5% relative humidity until the age of 28 days, matching the ambient curing regime under which the two mixes were characterized in Chapter 1.

The rapid chloride penetration specimens were cast without steel fibers, following the caution given in ASTM C1202 that an embedded electrically conductive material inflates the charge passed and invalidates the penetrability reading. All other specimens contained the fiber system described in Section 4.2.1. Every mix entering the chloride comparison was cast fiber-free and tested under identical conditions.

The laboratory immersion, elevated-temperature, and chloride programs began at a specimen age of 28 days. The marine exposure campaign described in Section 4.2.7 began at 90 days, the additional period covering transport to and installation at the offshore facility.

4.2.3 Sulfate and acid immersion

Specimens were immersed at 20 ± 2 °C for 12 months, that is 52 weeks, in five solutions: distilled water as the control, a 5% sodium sulfate solution, a 5% magnesium sulfate solution, a nitric acid solution maintained at pH 3, and a combined magnesium-and-sodium sulfate solution at 10% total concentration, made up of the two salts at 5% each. Each cation in the combined solution is therefore present at the same 5% concentration as in its own single-salt bath, so that the variable distinguishing the combined condition from the two single-salt conditions is the presence of the second cation rather than a change in the concentration of the first; the total sulfate content of that bath is correspondingly twice that of the single-salt baths. All solutions were renewed every four weeks to hold the concentration constant. The nitric acid bath was checked weekly and readjusted with concentrated acid to maintain pH 3 ± 0.2 against the buffering action of the dissolving matrix.

The protocol follows the practice established for alkali-activated systems rather than a single standard, because no standard covers 12-month immersion of an ultra-high-performance alkali-activated binder. The 4 × 4 × 16 cm^3 prism geometry, the 5% sodium sulfate concentration, the monthly renewal of the aggressive solution, and the use of a relative strength criterion follow (Komljenović et al., 2013), who adopted them for alkali-activated slag against a Portland-slag benchmark after finding the conditions recommended in CEN/TR 15697 unsuitable for that binder class.

The nitric acid exposure at pH 3, maintained by periodic addition of concentrated acid, follows (Lloyd et al., 2012; Vafaei et al., 2018), who applied the same acid at the same pH to inorganic polymer and geopolymer binders. The general framework for chemical

resistance assessed by mass change and residual strength is that of ASTM C267, applied by (Aiken et al., 2018; Vafaei et al., 2018) to the same binder class.

Nine prisms of each mix were immersed in each solution, giving 30 specimens in total. At weeks 0, 1, 2, 3, 4, 5, 8, 12, 16, 20, 26, and 52, each specimen was removed from solution, surface-dried with a damp cloth to a saturated surface-dry condition, weighed to the nearest 0.01 g on an analytical balance, and measured along its long axis to the nearest 0.01 mm with a digital caliper, corresponding to a length-change resolution of approximately 60 µm/m over the 160 mm gauge length.

Mass change and length change were computed for each specimen against its own week-0 value, so that inter-specimen variability is removed from the reported change:

$$\Delta m = 100 \frac{m_t - m_0}{m_0} \quad \textbf{(4.1)}$$

$$\Delta l = 100 \frac{l_t - l_0}{l_0} \quad \textbf{(4.2)}$$

where m_t and l_t are the mass in grams and the length in millimeters at the measurement age, m_0 and l_0 the corresponding values at week 0, Δm the mass change in percent, and Δl the length change in µm/m.

At 12 months the three prisms of each mix in each solution were tested in three-point bending over a 100 mm span, and the six resulting halves were tested in compression, both following EN 196-1. The design therefore yields three flexural and six compressive determinations per mix per solution.

4.2.4 Elevated-temperature exposure

Six prisms of each mix were prepared for each of three target temperatures, 300, 600, and 900 °C. Specimens were heated in an electric furnace at 5 °C/min to the target temperature, held at that temperature for two hours to bring the full cross-section to thermal equilibrium and then allowed to cool inside the furnace to ambient temperature without forced ventilation, so that the additional cracking associated with rapid quenching was avoided. The specimen arrangement in the furnace is shown in Figure 4-5. The visual condition of every specimen was recorded photographically after cooling and before mechanical testing.

After cooling, residual flexural strength was determined by three-point bending over a 100 mm span and residual compressive strength on the recovered halves, both following EN 196-1, so that the design yields six flexural and 12 compressive determinations per mix per temperature.

The unheated reference values are the 28-day strengths given in Section 4.2.1, determined on the Chapter 1 series of three prisms and six halves per mix. The number of specimens actually tested at each temperature is reported with the results in Section 4.3.



Figure 4-5: Specimens mounted in the furnace.

4.2.5 Rapid chloride penetration

The rapid chloride penetration test followed ASTM C1202, using the cell arrangement shown in Figure 4-6. Cylindrical specimens were vacuum-saturated and tested at 28 days. One face of the test cell was held in a 3% sodium chloride solution serving as the cathode and the other in a 0.3 N sodium hydroxide solution serving as the anode. A potential of 60 V was applied for six hours and the current logged at one-minute intervals, the total charge passed being obtained by integration of the current-time curve.

Five mixes were tested: REF, GEO, and three blended Portland cements of types CEM III/A, CEM III/B, and CEM IV/A. The blended-cement specimens were prepared by a project partner and tested in the present laboratory under the protocol described above, having been conditioned to 28 days under the same regime of 20 ± 2 °C and 50 ± 5% relative humidity as the REF and GEO specimens. Three specimens of each of the five mixes were tested.

The test cell exposes 95 mm of the 100 mm cast face, giving an exposed area A of 7.09 × 10^{-3} m^2 over a specimen thickness L of 0.05 m. Because the exposed diameter equals the reference diameter of ASTM C1202, the diameter correction specified in the standard reduces to unity and no adjustment to the measured charge is required.

The total charge passed was obtained by numerical integration of the logged current over the six-hour test:

$$Q = \int_0^t I \, dt \tag{4.3}$$

where Q is the charge in coulombs, I the current in amperes, and t the elapsed time. ASTM C1202 prescribes a trapezoidal summation of readings taken at 30-minute intervals. The one-minute logging interval used here allows direct numerical integration of the current-time curve and gives a closer estimate of the charge passed.

The apparent chloride diffusion coefficient was derived from the migration current through the Nernst-Planck relation introduced in Section 4.1.4 (Andrade, 1993):

$$D_{app} = \frac{R\,T\,L\,I}{z^2 F^2\,A\,E\,C_0} \tag{4.4}$$

where R is the universal gas constant, T the absolute temperature taken as 293 K, I the average current over the six-hour test, z the chloride valency of 1, F the Faraday constant, E the applied potential of 60 V, C0 the chloride concentration of the catholyte at 513 mol/m^3, and A and L as defined above.

The electrical resistivity was obtained from the same measurement, on the same specimens at 28 days:

$$\rho = \frac{V\,A}{I\,L} \tag{4.5}$$

where ρ is the resistivity in Ω·m, V the applied potential of 60 V, and I the average current over the six-hour test.

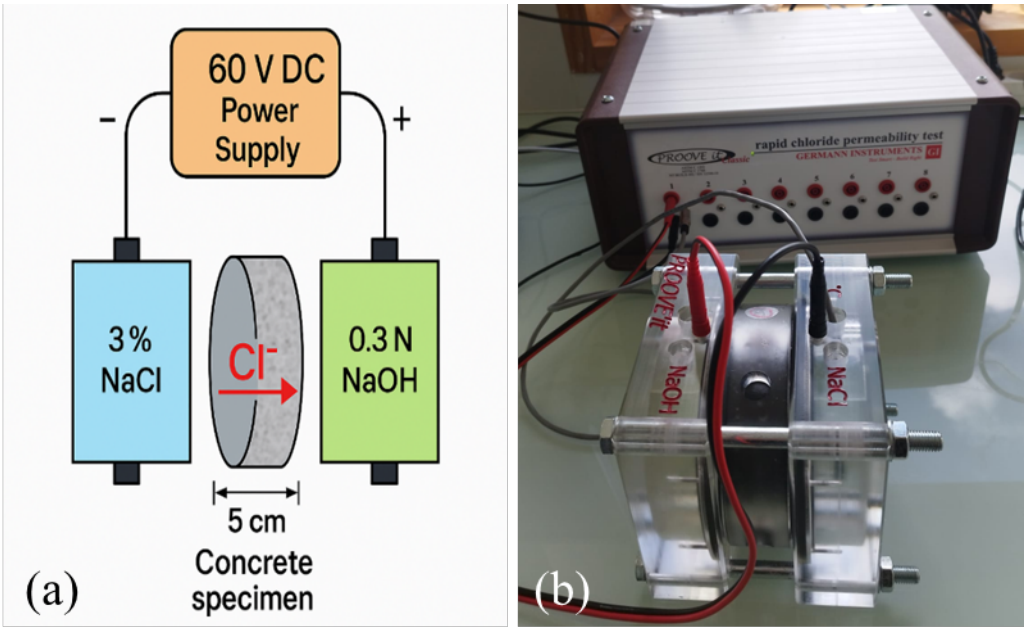

Figure 4-6: (a) RCPT schema and (b) RCPT device.

4.2.6 Electrical impedance monitoring

The pore structure of the immersed prisms was monitored by electrical impedance spectroscopy over the 12-month exposure. A two-electrode uniaxial configuration was used, with copper plate electrodes pressed against the two 40 × 40 mm^2 end faces of each prism through conductive sponge contacts. Spectra were acquired on a HIOKI IM3536 impedance analyzer from 4 Hz to 5 MHz at an excitation amplitude of 100 mV, at 12 intervals between Day 1 and Day 365. Specimens were removed from solution and surface-dried to a saturated surface-dry condition for each measurement and returned immediately afterwards, so that the record is a periodic series of measurements on the same specimens rather than a continuous one.

The bulk resistance was taken from the real component of the impedance at 10 kHz, the frequency at which electrode polarization is minimal and the response is dominated by conduction through the connected pore network. One REF and one GEO specimen were instrumented in each of the five solutions, giving 10 impedance time series and no replicate within any condition. In accordance with the limitation established in Section 4.1.4, the bulk resistance of an alkali-activated material is depressed by the ionic strength of its pore solution, and the pore-solution extraction required to compute a formation factor was not performed. The impedance data are therefore treated throughout as a within-mix indicator of change over time and not as a between-mix measure of pore quality.

4.2.7 Marine exposure at HarshLab

In parallel with the laboratory program, prismatic GEO specimens of the same 4 × 4 × 16 cm^3 geometry were deployed at the HarshLab floating facility in the Bay of Biscay and positioned in the three exposure zones of the structure: an atmospheric zone above the waterline, a splash zone subject to cyclic wetting, drying, and wave action at the tidal interface, and a fully immersed zone permanently submerged in Atlantic seawater (Figure 4-7).

Within the splash and immersed zones, three surface conditions were compared: an uncoated specimen, a specimen treated with a bio-based zwitterionic coating (Coat1), and a specimen treated with a second bio-based coating (Coat2), both coatings developed within the project and documented in deliverables D2.2 and D4.2. The atmospheric zone carried uncoated specimens only.

The project reference UHPC was tested in parallel at the same facility by a project partner, outside the scope of the present work, so only the GEO field results are reported in this chapter.



Figure 4-7: The HarshLab (Tecnalia) offshore floating facility (Biscay Marine Platform, Bay of Biscay), showing the atmospheric, splash, and immersion zones in which the GEO specimens were positioned.

Exposure began at a specimen age of 90 days and continued for 10 months. On retrieval, each specimen was first tested in three-point bending over a 100 mm span for residual flexural strength, and the two fragments from that test were then tested in compression for residual compressive strength, so that each prism yields one flexural and two compressive determinations. The number of specimens per exposure zone and surface condition is reported with the results in Section 4.3.

Immediately after fracture, the fresh internal faces were sprayed with phenolphthalein and with 0.1 M silver nitrate to reveal the alkalinity and free-chloride fronts by the colorimetric procedure described in Section 4.1.4, phenolphthalein developing a pink-violet color where the matrix remains alkaline, and silver nitrate developing a brown silver-oxide color where chloride is absent and a white silver-chloride precipitate where chloride has penetrated.

4.3 Durability results

This section reports the durability program in the order set out in the methods: the sulfate and acid immersion first, by mass change, dimensional change, and phase analysis, then the elevated-temperature response, then chloride transport by the rapid chloride penetration test, the derived resistivity, and the year-long impedance evolution, and finally the marine exposure at HarshLab, by residual mechanical performance and colorimetric front detection. Each subsection closes with a short interpretive paragraph. The consolidated synthesis, the limitations, and the service-life projection that carries into the life-cycle assessment close each subsection.

4.3.1 Sulfate and acid attack: mass change

The mass response over 52 weeks (Figure 4-8) separates the two binders, but not along the axis the chemistry alone would predict. GEO gains more mass than REF in the

magnesium-bearing solutions and behaves differently from it in acid, while the two are closely comparable in sodium sulfate and in the water control.

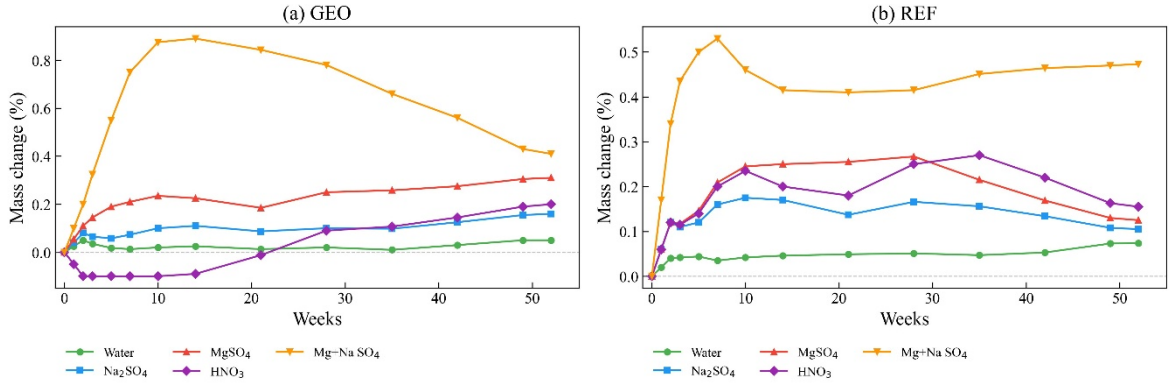

Figure 4-8: Mass change of (a) GEO and (b) REF specimens immersed in distilled water, Na_2SO_4, $MgSO_4$, HNO_3, and the combined magnesium-and-sodium sulfate solution over 52 weeks.

For **GEO**, the combined magnesium-and-sodium sulfate solution dominates the response. Mass rose steeply over the first 12 weeks to a peak near 0.89%, then declined steadily over the remainder of the exposure to about 0.41% at week 52, losing more than half of the accumulated gain.

Magnesium sulfate produced a smaller but sustained gain, rising to roughly 0.23% by week 12, dipping to 0.19% near week 21, and then increasing progressively to about 0.31% at week 52 without any sign of stabilizing.

Sodium sulfate produced a modest and stable gain, reaching about 0.08% by week 5 and a maximum near 0.11% by week 13, holding close to that level thereafter. The distilled-water control varied little, remaining between zero and 0.05% throughout with a slight increase toward the end of the exposure.

Nitric acid produced the only reversal in the program. GEO lost mass over the first 14 weeks, reaching about −0.10% between weeks 7 and 14, before crossing zero near week 20 and gaining steadily to roughly 0.20% at week 52. The early loss may be attributed to the leaching of soluble alkaline species during the initial stages of acid attack, the alkali that charge-balances the aluminum in the gel framework being the most mobile constituent available to an acid front. The subsequent gain is consistent with the accumulation of reaction products outpacing dissolution of the matrix. Neither mechanism was directly quantified, since neither the pore solution nor the leachate was analyzed.

REF gained mass in every solution and at no point lost any. The combined sulfate solution again produced the largest response, rising sharply to a peak near 0.53% by week 8, falling to about 0.41% by week 20, and then recovering to roughly 0.47% at week 52. **Magnesium sulfate** rose to about 0.24% by week 10, held to week 28 where it reached a secondary maximum near 0.27%, and then declined to about 0.13% at week 52. Nitric acid followed a similar shape, rising to 0.21% by week 8, peaking near 0.27% at week 36, and

falling to about 0.16% by week 52. Sodium sulfate rose to about 0.17% between weeks 10 and 14 and declined gradually to 0.11%. The water control gained about 0.07%, the signature of continued hydration in a Portland system.

Two features of the comparison are worth isolating:

First is that GEO gains more mass than REF in both magnesium-bearing baths, by a factor of roughly 1.7 at the combined-solution peak and by more than a factor of two at week 52 in magnesium sulfate. That runs against the expectation set out in Section 4.1.1, where the absence of portlandite and of reactive aluminate in GEO closes the routes that add solid volume in a Portland matrix. If those routes are indeed closed, another mass-adding process must be operating, and it operates only where magnesium is present. This is consistent with the magnesium-specific pathway identified by Bonen and Cohen (1992): precipitation of a brucite surface layer together with magnesium-for-calcium exchange in the calcium-bearing gel, forming non-cementing magnesium silicate hydrate. Neither product requires the phases GEO lacks. Neither was identified in the present specimens, however, since the quantitative phase analysis reported in Section 4.3.2 was performed on unexposed material.

Second is that the two binders differ in the direction of the late-stage trend rather than in the early response. GEO holds or increases its mass toward the end of the exposure in magnesium sulfate, sodium sulfate, and acid, whereas REF declines after an intermediate peak in all three. In a Portland matrix the decline may be related to progressive surface deterioration, in which material added by expansive product formation is subsequently removed by dissolution or by loss of degraded surface layers, following the sequence described by Mehta (1983). In GEO the absence of that decline is consistent with the deposited product remaining attached over the exposure period. Surface deterioration was not quantified in the present study.

The magnitudes throughout are small. No specimen of either binder changed mass by more than 0.9% at any point, and all but the combined-solution series remained within 0.35% at week 52. Values of this order do not in themselves indicate structural damage, and Section 4.3.3 confirms that they are not accompanied by loss of compressive strength: magnesium sulfate produced the highest residual compressive strength recorded for GEO in any solution.

4.3.2 Sulfate and acid attack: length change and phase analysis

The dimensional response (Figure 4-9) separates the two binders more sharply than the mass response, and it separates them in opposite directions depending on the aggressor. Each binder has one solution in which it is dimensionally unstable, and they are not the same solution.

GEO expanded in both magnesium-bearing baths. The combined solution produced a rapid expansion to a peak near 0.29% by week 7, followed by partial relaxation to about 0.20% by week 21 and stability thereafter, ending near 0.21% at week 52.

Magnesium sulfate produced a similar but smaller response, reaching about 0.18% between weeks 7 and 10, relaxing to 0.15% near week 21, rising again to a secondary maximum near 0.20% around week 42, and closing at about 0.17%. In the two solutions without magnesium the behavior inverts.

Sodium sulfate produced an early contraction to about −0.13% by week 4, a partial recovery, a second decline to −0.08% between weeks 21 and 28, and a final value near −0.05%.

Nitric acid contracted to about −0.12% by week 4, recovered through zero near week 15 to a maximum of 0.04% at week 21, then returned to a stable −0.03 to −0.04%. The water control varied little, reaching −0.06% at week 4 and settling near −0.02%.

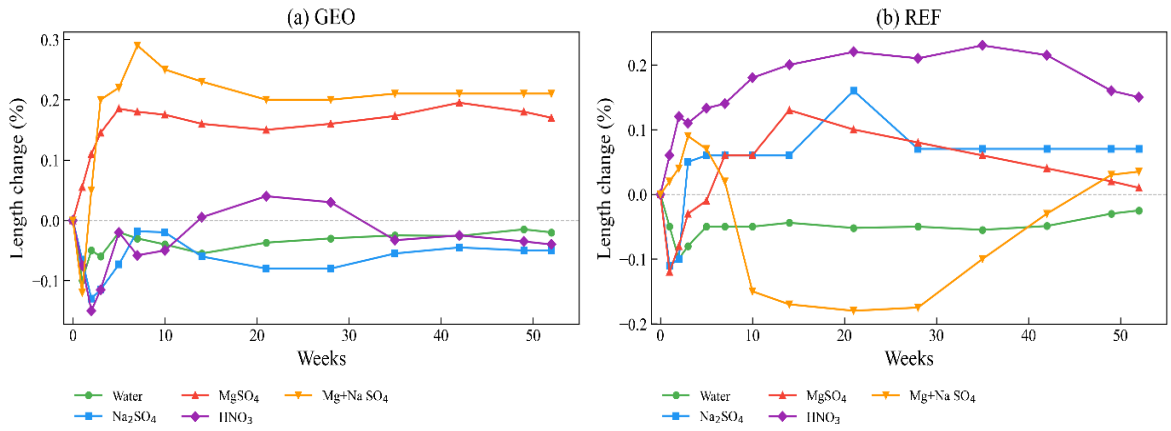

Figure 4-9: Length change of (a) GEO and (b) REF specimens immersed in water, Na_2SO_4, $MgSO_4$, HNO_3, and combined Mg+Na sulfate over 52 weeks. REF blue, GEO orange.

The **REF** pattern is close to the mirror image.

Nitric acid produced its largest and most sustained expansion, rising to 0.12% by week 3 and continuing to a plateau of 0.22 to 0.23% between weeks 21 and 36 before relaxing to about 0.15%.

Sodium sulfate fluctuated early, reaching 0.10% at week 3, falling to −0.02% by week 6, then rising to a maximum of 0.16% at week 21 and stabilizing near 0.07% from week 35.

Magnesium sulfate contracted to about −0.12% in the first three weeks, expanded to a peak of 0.13% by week 13, and then declined steadily to close near 0.01%. The combined solution behaved unlike any other series in the program: after an initial expansion to about 0.10% by week 4 it contracted strongly, reaching a minimum near −0.18% between weeks 21 and 28, and recovered only slowly to about 0.03% at week 52. The water control remained near −0.05%, recovering slightly to −0.03%.

The comparison inverts between the two aggressors that matter most. Under the combined solution representative of seawater, GEO expands by 0.29% while REF contracts by 0.18%. Under nitric acid, REF expands by 0.23% while GEO returns to within 0.04% of its original length. Expansion and contraction of comparable magnitude are not equivalent processes: expansion in a sulfate environment is consistent with internal product formation generating pressure, whereas contraction is consistent with removal of solid material, whether by leaching or by decalcification of the binding phase. Neither process was directly quantified here.

The magnitude of the GEO expansion under magnesium-bearing solutions deserves to be stated plainly. ASTM C1012 adopts 0.10% expansion as the criterion distinguishing sulfate-resistant behavior, and GEO exceeds that value in both magnesium baths, reaching twice it at the combined-solution peak. The comparison is indicative rather than formal, since the present specimens are 4 × 4 × 16 cm^3 prisms measured by caliper rather than the gauge-stud mortar bars the standard prescribes, and the exposure regime differs. It nevertheless places the GEO dimensional response under magnesium sulfate in the range that would fail a conventional sulfate-resistance screening, and it is the least favorable dimensional result recorded for GEO.

That result stands against the compressive data of Section 4.3.3, where magnesium sulfate produced the highest residual compressive strength recorded for GEO, an index of 1.06 against its 28-day value. Expansion of 0.2% accompanied by a 6% strength gain can be interpreted as deposition of reaction product within the pore space, generating dimensional change without disrupting the load-bearing skeleton, though the phase assemblage responsible was not resolved. The mass data support that reading, GEO gaining mass steadily in the same baths and continuing to gain to week 52. Whether the balance holds beyond the exposure window cannot be determined from these data, and it is the principal reason the dimensional result is carried into the service-life discussion rather than set aside.

The quantitative phase analysis of the as-cured material provides part of the explanation. Rietveld refinement (Table 4-2) found the GEO matrix dominated by an amorphous calcium aluminosilicate hydrate gel at 39.5 wt%, with no detectable portlandite and only trace ettringite at 1.1 wt%. The absence of portlandite removes the phase that acid attacks first in a Portland system (Bakharev, 2005), and the negligible ettringite, together with the aluminum held in the gel rather than in reactive aluminate phases, is the direct microstructural evidence for the gel-binding mechanism that (Komljenović et al., 2013) inferred indirectly from expansion data alone.

The refinement returned a high weighted-profile residual (R_{wp} = 21.3%), reflecting the predominantly amorphous, multi-phase matrix. The amorphous fraction was recovered by mass balance against the quartz aggregate rather than by direct refinement, so the phase fractions are reported as semi-quantitative.

Table 4-2: Rietveld quantitative phase composition of the GEO binder.

Phase	ICDD code	Weight fraction (%)
Quartz (SiO_2)	01-086-1629	48.5 ± 4.0
Calcite ($CaCO_3$)	00-005-0586	7.1 ± 0.6
Zeolite (tentative)	00-039-0219 (Na-form)	3.7 ± 0.9
Ettringite	00-016-0695	1.1 ± 0.4
Amorphous C-(N,K)-A-S-H	–	39.5 ± 4.0

One limitation of that analysis must be stated. The quantitative phase analysis characterizes the as-cured material at 28 days and was not repeated on the exposed specimens. The phase assemblage responsible for the dimensional response under magnesium-bearing solutions therefore remains unresolved, and identifying it, in particular whether brucite and magnesium silicate hydrate form at the exposed surface as the literature on Portland systems would predict, would require post-exposure diffraction and microscopy that fall outside the present program.

4.3.3 Residual mechanical strength after sulfate and acid immersion

The mass and dimensional records of the preceding subsections track the progress of chemical activity but do not establish whether that activity costs the material its load-bearing capacity. Residual compressive and flexural strength were therefore measured on the immersed specimens at two ages, six and 12 months, in each of the five solutions.

Testing at two ages rather than one answers a question the endpoint alone cannot: whether any change observed at 12 months was still developing when the exposure ended. Three prisms of each mix were tested per solution at each age, giving three flexural and six compressive determinations per cell. The reference values throughout are the 28-day strengths at the start of exposure, 152 MPa for GEO and 165 MPa for REF in compression, and 17.0 and 23.0 MPa in flexure.

4.3.3.1 Compressive strength

After 6 months, both binders retained their full ultra-high-performance class in every solution (Figure 4-10). GEO held between 152 and 159 MPa and REF between 157 and 170 MPa, all values well above the 130 MPa threshold that defines the class. Relative to their own 28-day strengths the two binders had already begun to diverge. GEO equaled or exceeded its 152 MPa reference in every solution, reaching 159 MPa in sodium sulfate and 155 MPa in magnesium sulfate, the combined solution, and nitric acid alike. REF exceeded its 165 MPa reference in water, sodium sulfate, and the combined solution, but fell below it in magnesium sulfate at 160 MPa and more clearly in nitric acid at 157 MPa.

After 12 months the picture is unchanged in every material respect. GEO held between 149 and 161 MPa and REF between 154 and 172 MPa, again with no value approaching the 130 MPa threshold. Every cell lies within one standard deviation of its 6-month value: the largest single change in either binder is the GEO strength in magnesium sulfate, from 155 to 161 MPa, against a measured standard deviation of 9.7 MPa on that cell. Nothing in the compressive response continued to develop between the two ages.

Two features are worth isolating:

First is that GEO ends above its 28-day reference in three of the five solutions, at 159 MPa in sodium sulfate, 161 MPa in magnesium sulfate, and 157 MPa in nitric acid, and marginally below it in water at 149 MPa and in the combined solution at 150 MPa. Continued maturation of a binder still reacting at 28 days accounts for those gains more readily than any strengthening effect of the aggressor, and the pattern is in any case not statistically resolved: the two sulfate gains sit at 1.6 and 1.8 standard errors against the 28-day value, short of the conventional threshold at the replicate count used here. Read against the same-age water-immersed control rather than the 28-day value, which removes the effect of continued maturation, no GEO compressive value in an aggressive bath falls below the 149 MPa of the water control at 12 months.

Second is the acid result, which is the only significant compressive change in the dataset. REF fell from 165 MPa at 28 days to 157 MPa at 6 months and 154 MPa at 12, a loss of 6.7% and the single comparison in the compressive program that clears two standard errors. GEO in the same bath moved the other way, from 152 to 155 to 157 MPa. The direction of that contrast is consistent with the acid literature reviewed in Section 4.1.2, where the geopolymer ranking above the Portland comparator does not reverse across three binder families and four acids, and it is reproduced here at a strength class none of those studies reached.

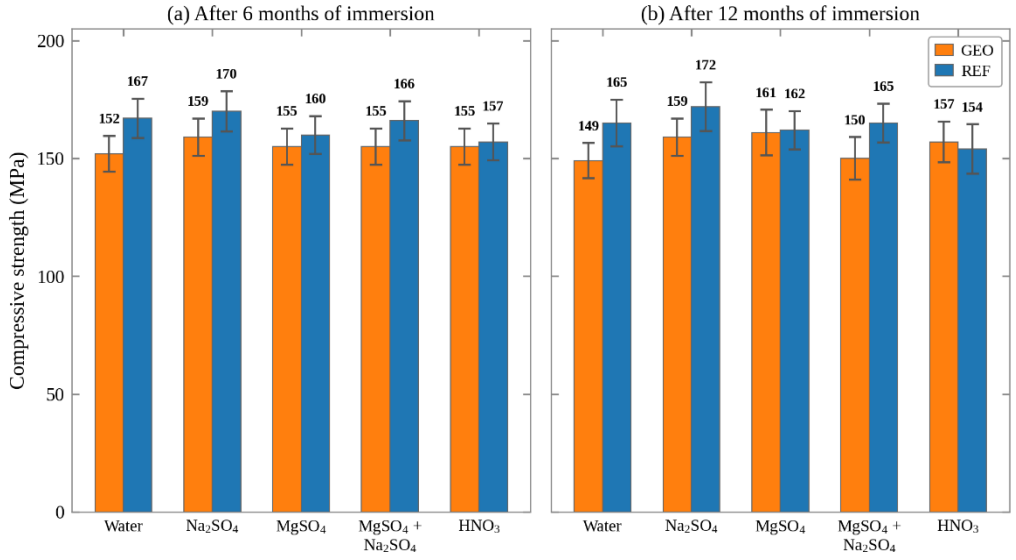

Figure 4-10: Residual compressive strength of GEO and REF after (a) 6 and (b) 12 months of immersion in distilled water, Na_2SO_4, $MgSO_4$, HNO_3, and the combined magnesium-and-sodium sulfate solution.

4.3.3.2 Flexural strength

The flexural response (Figure 4-11) separates the two binders in the opposite direction, and it does so consistently across the five solutions.

After 6 months, GEO held between 15 and 17 MPa against its 17.0 MPa reference, at or below that value in every solution and lowest in the combined bath at 15 MPa. REF held between 23 and 25 MPa against its 23.0 MPa reference, at or above that value in every solution and highest in sodium sulfate at 25 MPa. After 12 months, GEO held between 16.0 and 16.6 MPa and REF between 24.0 and 27.0 MPa, preserving the same signs: every GEO value at or below 17.0 MPa, every REF value at or above 23.0 MPa.

As in compression, almost nothing changed between the two ages. The exception is REF in magnesium sulfate, which rose from 24 to 27 MPa, a gain of about two standard errors and the only cell in the flexural programs where the second 6 months differ materially from the first. That cell is also the only flexural comparison in the dataset that is statistically significant against its own 28-day reference, at 17.4% above 23.0 MPa. None of the GEO reductions reaches significance: the largest, 5.9% in magnesium sulfate, in the combined solution and in nitric acid alike, sits at 1.5 standard errors.

The consequence for the ratio between the two binders should be stated carefully, because the obvious reading is the wrong one. GEO stood at 74% of the REF flexural strength before exposure. After 12 months it stands between 59 and 67%, so the gap widened in every solution. That widening is not principally GEO degrading. In magnesium sulfate, where the ratio falls furthest, GEO loses 5.9% while REF gains 17.4%. In water, sodium sulfate, and nitric acid the REF gain likewise exceeds the GEO loss. What the flexural data record is that REF continued to develop under immersion while GEO did not, a difference in maturity rather than a durability failure.

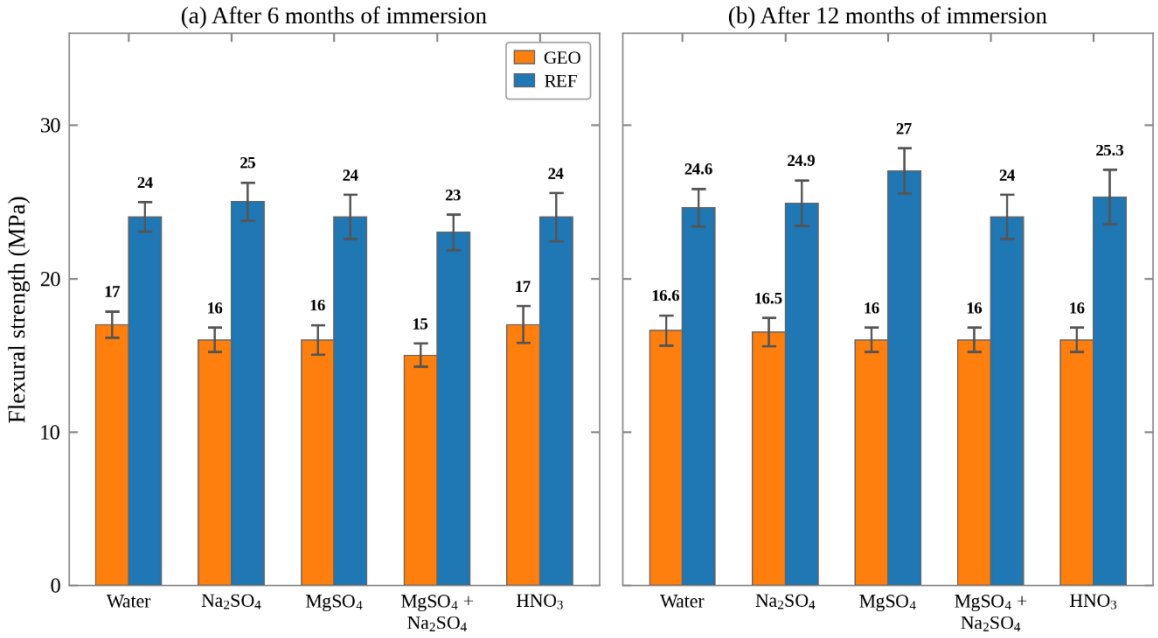

Figure 4-11: Residual flexural strength of GEO and REF after (a) 6 and (b) 12 months of immersion in the same five solutions.

Read together, the two figures show the binders behaving differently in a way neither measure reveals alone. Expressed as a fraction of its own 28-day value, **GEO** ends above unity in compression and below unity in flexure in all four aggressive solutions, while the two measures agree to within 0.4 percentage points in the water control. The divergence is 7.5 percentage points in sodium sulfate, 11.8 in magnesium sulfate, 9.2 in nitric acid, and 4.6 in the combined solution.

REF shows no such split, ending above unity on both measures in three solutions and below unity on both in acid. Compressive strength in a fiber-reinforced matrix is governed by the matrix itself, whereas flexural strength depends additionally on stress transfer across the fiber-matrix interface, so a binder whose matrix is unaffected while its flexural capacity falls is behaving as though the aggressor reaches the interface rather than the matrix. That reading is supported by the water control, where no aggressor is present and the two measures move together, and by the consistency of the pattern across four different chemistries.

It is not supported by any individual significant comparison, since at three prisms per cell none of the GEO flexural reductions is resolved against its own scatter. Confirming it would require direct characterization of the fiber-matrix interface after exposure, which was not performed here.

What the two ages do establish, with one exception in the REF flexural response to magnesium sulfate, is that every cell in both programs lies within one standard deviation of its 6-month value: whatever the aggressors did to either binder, they did within the first 6 months. A single 12-month endpoint would have left open the possibility that degradation

was still advancing when the exposure ended, and it is on the closure of that possibility, rather than on the 12-month values themselves, that any statement about behavior beyond the test window rests.

4.3.4 Impedance evolution over 365 days

The year-long impedance record (Figure 4-12) tracks how each pore structure evolved under sustained immersion. Across all four monitored solutions, REF held a bulk resistance one to two orders of magnitude above GEO throughout. In the water control, REF rose from about 4 000 Ω at Day 1 to 70 000 Ω by Day 120 and stabilized near 70 000 to 80 000 Ω, while GEO rose from about 200 Ω to 3 000 Ω over the same period. As Section 4.1.4 sets out, this absolute separation is governed largely by the higher mobile-ion content of the KOH^-activated pore solution and the finer pore network of REF rather than by any degradation of GEO.

Two durability-relevant patterns emerge, and both align with mechanisms reported in the literature:

First, both mixes showed a generally rising impedance across all solutions over the year, indicating that neither underwent progressive microstructural degradation. The rise is consistent with continued pore refinement through ongoing hydration in REF and continued geopolymerization in GEO. A transient dip near Day 250 appeared simultaneously in all 10 series, in both binders and in every solution. A chemical origin would not act on two distinct binder systems in four different solutions at the same moment, so the dip is read as a common-mode measurement effect rather than a material response. Ambient temperature was not logged over the campaign, so the specific cause could not be identified; bulk resistance in a saturated specimen is sensitive to both temperature and electrode contact, and either would act on all series simultaneously. The values recovered to the pre-dip trend by Day 365 in every series, and the affected point is excluded from the trend reading while the underlying data are retained.

Second, the per-solution sensitivity is diagnostic and is consistent with the sulfate and acid mechanisms proposed earlier in this chapter. The GEO impedance in the sulfate solutions tracked its own water control closely, both reaching roughly 2 000 to 4 000 Ω at Day 365, consistent with no measurable effect of sulfate ingress on its pore structure, the conclusion (Komljenović et al., 2013) reached for alkali-activated slag, obtained here from a non-destructive electrical signal rather than from expansion. REF, by contrast, showed a reduced impedance in sodium sulfate relative to its own water control, which is consistent with the early sulfate ingress that drives the ettringite expansion described by Mehta (1983).

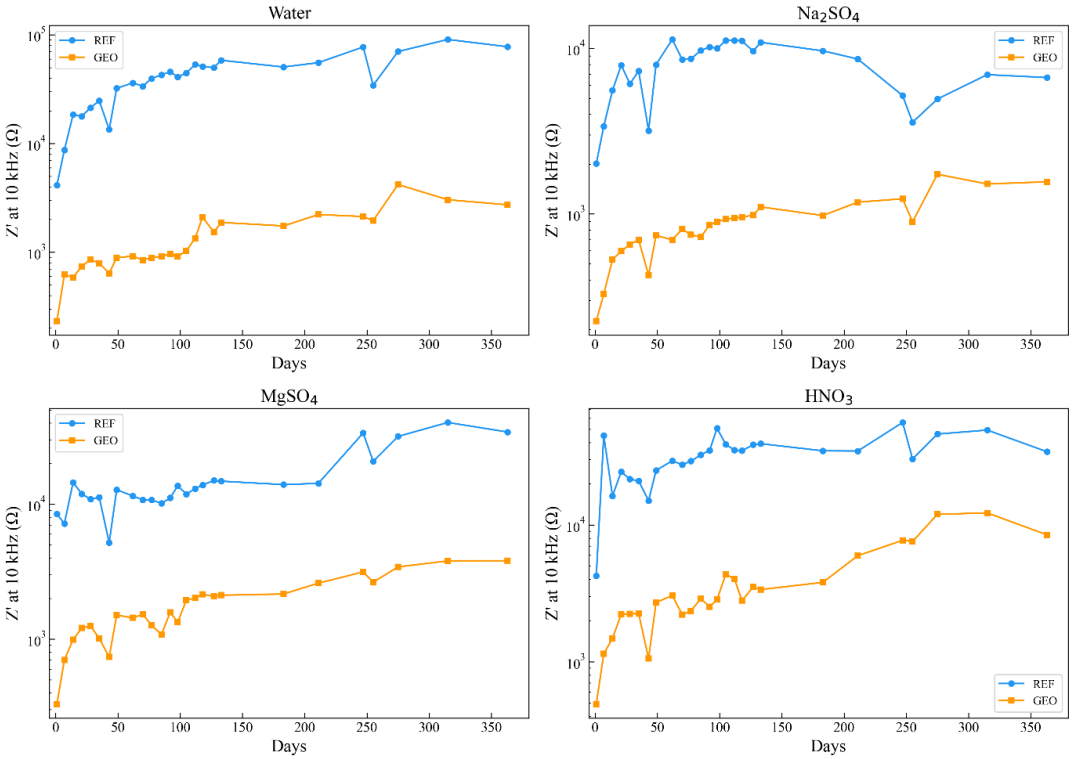

Figure 4-12: Evolution of the real component of impedance Z′ at 10 kHz for GEO and REF specimens immersed in water, Na_2SO_4, $MgSO_4$, and HNO_3 over 365 days.

In nitric acid, GEO rose to about 10 000 Ω, the highest final value among its specimens, consistent with the densified, dealuminated surface layer that (Bakharev, 2005; Vafaei et al., 2018) describe for geopolymers under acid. REF in acid reached 30 000 to 50 000 Ω with periodic fluctuations, consistent with alternating precipitation and dissolution at the acid-concrete interface over an otherwise intact bulk. The impedance record thus reproduces, non-destructively and over the full exposure, the same binder-specific mechanisms that the literature established by destructive means.

Two limits bound this reading:

- The record comprises one specimen per mix per solution, 10 series in all, so the trajectories are read as trends rather than as replicated measurements, and no scatter can be attached to any individual value.

- And because the pore solution was not extracted, the formation factor is not available, so the impedance magnitudes are interpreted within each mix over time rather than as a pore-structure property deconvolved from pore-solution conductivity.

The year-long trends within each binder are therefore robust. Any cross-binder comparison of the absolute magnitudes remains qualitative.

4.3.5 Elevated-temperature resistance

This is the one mechanism where GEO underperforms REF, and the result runs against the prevailing expectation for geopolymers. It is reported here in full, with its statistical caveat given equal weight to the headline numbers, because the credibility of the favorable findings elsewhere in the chapter depends on the unfavorable one being stated without softening.

At ambient temperature the mixes measured 165 MPa (REF) and 152 MPa (GEO) in compression (Figure 4-13).

At 300 °C, REF rose to 186 MPa, a 13 % increase attributable to capillary drying and accelerated pozzolanic reaction between silica fume and portlandite, while GEO held 149 MPa, a marginal 2 % decrease as the onset of gel dehydration was partly offset by continued geopolymerization. At 600 °C the measured values diverged: the single surviving REF specimen gave 149 MPa, 90 % of ambient, while GEO fell to 55 ± 16.6 MPa, 36 % of ambient, across 6 specimens that all remained intact. At 900 °C both mixes had lost most of their strength, GEO retaining 46 MPa, 30 % of ambient, and the single surviving REF specimen 45 MPa, 27 %.

The flexural results followed the same overall ranking with a steeper relative loss for GEO: from 17.0 MPa ambient to 8.0 MPa at 300 °C (47 %), 5.4 MPa at 600 °C (32 %), and 4.0 MPa at 900 °C (24 %), against REF's 23.0 MPa ambient, 18.7 MPa at 300 °C (81 %), 17.2 MPa at 600 °C (75 %), and 7.0 MPa at 900 °C (30 %). The REF value at 300 °C carries the largest scatter in the thermal program, and the 81 % retention should be read with that in mind. The REF flexural values at 600 and 900 °C derive from the same single surviving specimens and carry the limitation set out below.

Specimen survival bears directly on the comparison above 300 °C. At both 600 and 900 °C only one REF specimen survived heating in testable condition, giving 149 and 45 MPa respectively; the remaining REF specimens fractured during or immediately after heating. Every GEO specimen remained intact and was tested at all three temperatures, the 600 °C cell giving a mean of 55 MPa with a standard deviation of 16.6 MPa. The REF retentions of 90 % at 600 °C and 27 % at 900 °C each rest on a single specimen and are not statistically representative means. They are reported because the survival pattern is itself an outcome, but the REF-GEO gap at 600 °C and the apparent convergence at 900 °C should not be read as measured differences between comparable population means.

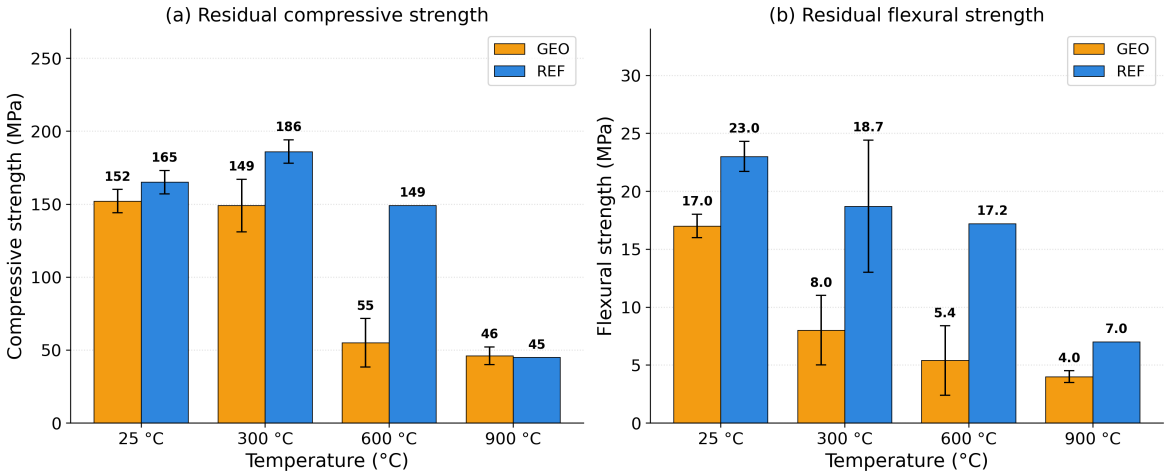

Figure 4-13: (a) Residual compressive and (b) flexural strength of GEO and REF after exposure to 300, 600, and 900 °C.

The visual record reinforces this (Figure 4-14): GEO held its prismatic form at every temperature without explosive spalling, undergoing only a progressive color change, whereas REF fractured during or immediately after heating at both 600 and 900 °C in all but one specimen, showing through-cracking with loss of section and exposed steel fibers at 900 °C.

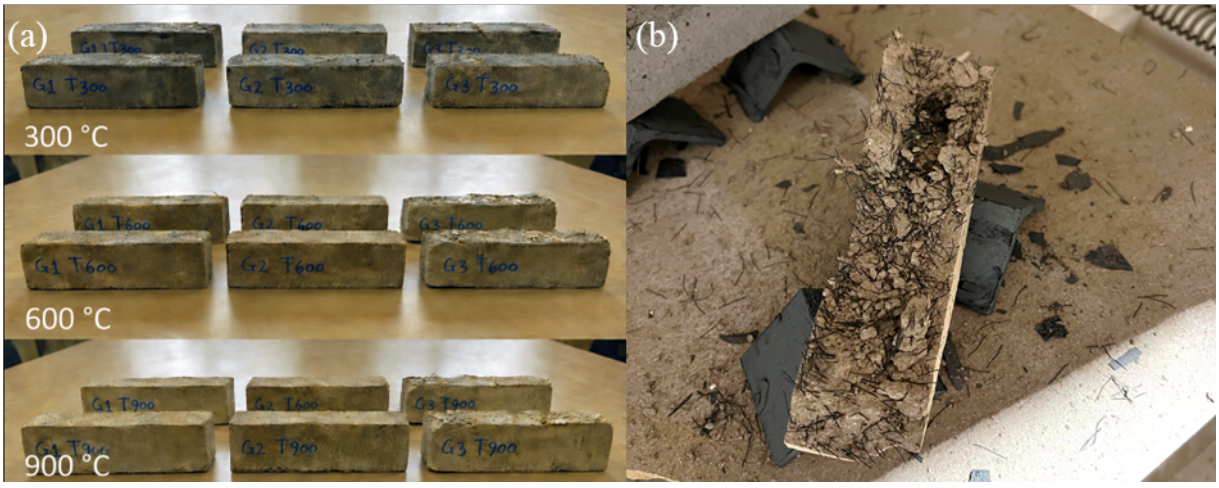

Figure 4-14: (a) visual appearance of GEO and (b) REF specimen after exposure to 600 °C.

Read against the literature, the result is not a contradiction of the geopolymer thermal advantage but a clarification of its boundary. The 36 % compressive retention of GEO at 600 °C falls far below the more than 50 % that (Kong and Sanjayan, 2010; Lahoti et al., 2018) report for low-calcium, fly-ash-based geopolymers at the same temperature, the very studies that established the refractory reputation of geopolymers.

The deficit has an identifiable origin in the binder chemistry characterized in Chapter 1. The GEO gel carries a calcium-to-silicon ratio of about 0.39, against 1.72 for the REF C-S-H, with potassium and sodium in the framework, and the mix carries a water-accessible porosity of 8.25 % against 4.80 % for REF, in a capillary network whose dominant resolved

pore entry is approximately 700 nm against 6.2 nm. The advantage reported by those authors derives from the low-calcium N-A-S-H gel, a three-dimensional aluminosilicate network structurally close to a ceramic, whereas GEO is a high-calcium C-(N,K)-A-S-H gel formed from a GGBS-dominant precursor, structurally a layered calcium aluminosilicate hydrate whose decomposition resembles the C-S-H of Portland cement more than the N-A-S-H of fly-ash systems. GEO is therefore expected to track the dehydration behavior of a calcium-rich hydrate rather than the ceramic-like retention of the fly-ash systems, which is what the data show, with its higher porosity compounding the loss of load-bearing section as the gel dehydrates while acting in the opposite sense on integrity. The thermal stability reported in the geopolymer literature is a property of the low-calcium gel specifically, and a calcium-rich slag system should not be expected to inherit it. The present dataset cannot separate the contributions of gel stability, total porosity, and pore-size distribution, since the three co-vary across the mixes and no thermal series was run with porosity held constant; thermogravimetric analysis of the exposed material, high-temperature X-ray diffraction, and mercury intrusion porosimetry before and after heating would separate them.

The discrepancy is explained by gel chemistry rather than contradicting those authors: their advantage derives from the low-calcium N-A-S-H gel, a three-dimensional aluminosilicate network structurally close to a ceramic, whereas GEO is a high-calcium C-(N,K)-A-S-H gel formed from a GGBS-dominant precursor, structurally a layered calcium aluminosilicate hydrate whose decomposition resembles the C-S-H of Portland cement more than the N-A-S-H of fly-ash systems.

Two further points bound the finding. The deficit is one of strength retention, not structural integrity: GEO held its prismatic form without explosive spalling at every temperature, whereas REF fractured during heating at 600 and 900 °C and spalled with exposed fibers, so on integrity the ranking reverses. The present data do not resolve why. The 22-fold permeability difference would favor GEO on the thermo-hydral route (Kalifa et al., 2000), but the slow heating regime makes that route secondary, and no post-exposure phase analysis was performed that would identify the decomposition products responsible for the REF damage, so the integrity asymmetry is reported as observed rather than explained. Sustained exposure to 600 °C is also not a marine service condition, so the result defines a known limit of the formulation, addressable through partial precursor substitution, refinement of the capillary network, and thermally stable fiber systems as set out in the Perspectives, rather than a barrier to its intended offshore use.

4.3.6 Rapid chloride penetration

Both mixes resisted chloride transport at the level expected of UHPC, with GEO higher than REF but still far inside the favorable range (Figure 4-15). GEO recorded a mean charge passed of 254 Coulombs, classified as Very Low penetrability under ASTM C1202, while

REF recorded 43 Coulombs, classified as Negligible. Both lie well below 1000 Coulombs, the upper bound of the Very Low class. For context, normal-strength concrete registers 2000 to 4000 Coulombs under the same test. The apparent chloride diffusion coefficient, obtained from the migration current through the Nernst-Planck relation, was 6.9×10^{-13} m^2/s for GEO and 1.2×10^{-13} m^2/s for REF, roughly a 6-fold difference.

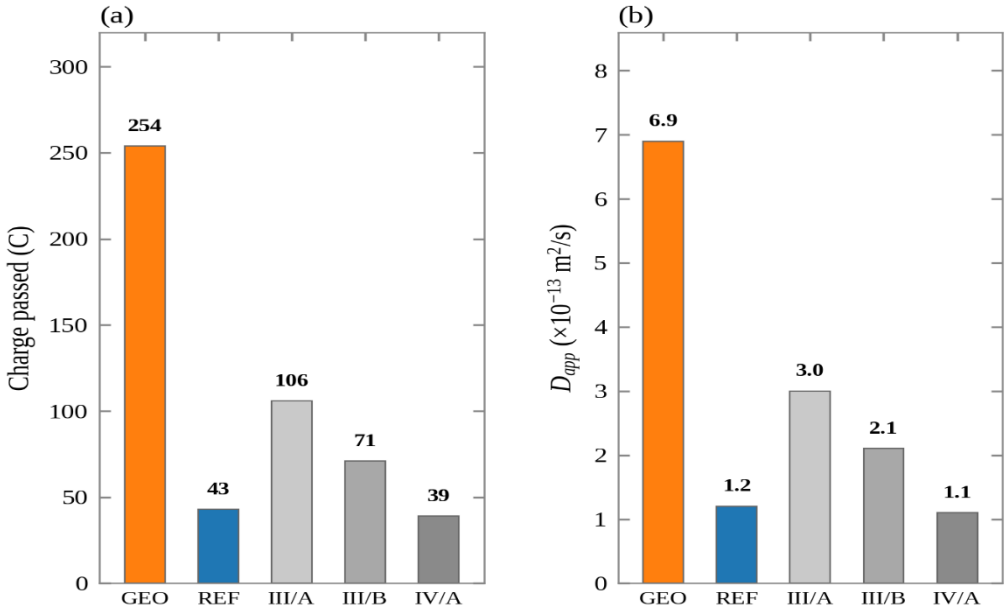

Figure 4-15: Rapid chloride penetration results for all tested mixes (GEO, REF, CEM III/A, CEM III/B, CEM IV/A): (a) total charge passed and (b) apparent chloride diffusion coefficient.

To place the two project mixes in context, three blended-cement concretes were tested under identical conditions, with results in Table 4-3. Four of the five mixes fell within a narrow band between 39 and 106 C, CEM IV/A at 39 C, REF at 43 C, CEM III/B at 71 C, and CEM III/A at 106 C, differences of an order that the test does not reliably resolve at these low charge levels. GEO at 254 C recorded the highest charge of the five and was the only mix to separate clearly from that band, while remaining within the Very Low category. The ranking shows that a fully cement-free geopolymer UHPC achieves chloride resistance better than conventional concrete, though it does not match the very lowest permeabilities of optimized Portland or blended-cement UHPC.

All apparent diffusion coefficients fall in the 10^{-13} m^2/s range characteristic of UHPC, two to three orders of magnitude below the 10^{-11} to 10^{-12} m^2/s of conventional C30 to C50 concrete.

Both mixes sit at the favorable extreme of the UHPC chloride scale that the literature describes, and the comparison sharpens once the test artifact is accounted for. Both values sit inside the range published for UHPC, and the comparison is sharper than a band alone conveys. (Graybeal and Tanesi, 2007; Li et al., 2020) measured one commercial UHPC under four curing regimes and obtained 18 C after steam curing and 360 C at 28 days with no thermal treatment.

Both mixes of the present work were cured at ambient temperature and therefore correspond to the least favorable of those regimes, yet GEO at 254 C falls below the 360 C recorded for the ambient-cured commercial material and REF at 43 C falls near the steam-cured value. Against conventional concrete at 2000 to 4000 C, both are two orders of magnitude lower.

Two points qualify the GEO-versus-REF difference:

First is physical: GEO's transport porosity is both coarser and more abundant than that of REF. Flow in both materials is carried by the 0.1 to 1 µm band, which occupies 2.35% of the GEO specimen against 0.36% in REF. The macro-porosity above 1 µm in REF is isolated rather than percolating, since treating it as a connected network would predict a permeability 15 to 25 times the measured value (Section 1.5.7).

Total porosity alone does not account for the difference: on a Kozeny-Carman porosity-only basis the 1.72-fold porosity ratio predicts a factor of about five, against the measured 22-fold ratio in mean apparent gas permeability (4.96×10^{-16} against 2.22×10^{-17} m^2). The residual factor of about four is carried by the two-order-of-magnitude contrast in dominant pore size, permeability being governed by the size and connectivity of the largest interconnected pathway rather than by total porosity. A genuinely higher charge is expected on the same basis.

Second concerns the measurement and is the more important, and it is the limitation the standard itself notes and that (Provis, 2018) emphasizes for alkali-activated materials specifically: the rapid chloride penetration test records the total ionic current, not the chloride flux, and the KOH-activated pore solution of GEO carries far more mobile potassium and hydroxide than a Portland pore solution, so part of the higher charge reflects pore-solution conductivity rather than chloride mobility, and the 5.8-fold charge ratio overstates the true transport difference.

The charge passed, the apparent diffusion coefficient and the resistivity reported below are three outputs of the same current record, not three independent measurements. The Nernst-Planck calculation of the apparent coefficient further assumes that chloride carries a defined share of the current; in the highly alkaline KOH-activated pore solution of GEO, hydroxide and potassium ions carry most of it, so the apparent coefficient overestimates the chloride mobility of GEO and is conservative.

The field colorimetry of Section 4.3.8, which detected no chloride front even under permanent immersion, supports reading the GEO charge as conservative. On the absolute diffusion coefficient, (Hasan et al., 2024) reported values two orders of magnitude lower for non-proprietary UHPC after Joule and Arrhenius corrections. For the low charges recorded here (all below 300 C) those corrections are below 5% and do not change the penetrability class, so the uncorrected coefficients are reported directly, with the caveat that they are upper bounds.

Table 4-3: Rapid chloride penetration results and apparent chloride diffusion coefficients for all tested mixes.

Mix	Charge passed (C)	Classification	D_{app} (m^2/s)
GEO	254	Very Low	6.9×10^{-13}
REF	43	Negligible	1.2×10^{-13}
CEM III/A	106	Very Low	3.0×10^{-13}
CEM III/B	71	Negligible	2.1×10^{-13}
CEM IV/A	39	Negligible	1.1×10^{-13}

4.3.7 Electrical resistivity and corrosion-risk classification

The electrical resistivity derived from the rapid chloride penetration current places all five mixes in the negligible-corrosion-risk band (Figure 4-16). REF measured 4274 Ω·m and GEO 724 Ω·m. Among the blended cements, CEM IV/A reached 4712 Ω·m, CEM III/B 2588 Ω·m, and CEM III/A 1734 Ω·m. Under a widely used classification, resistivity above 200 Ω·m corresponds to negligible corrosion likelihood, 100 to 200 Ω·m to low risk, and below 100 Ω·m to high risk (Song and Saraswathy, 2007; Broomfield, 2023). All five mixes exceed the 200 Ω·m threshold, GEO at 724 Ω·m sitting more than 3 times above it and roughly an order of magnitude above the 50 to 100 Ω·m of saturated normal-strength concrete that those same sources place at or below the high-risk boundary.

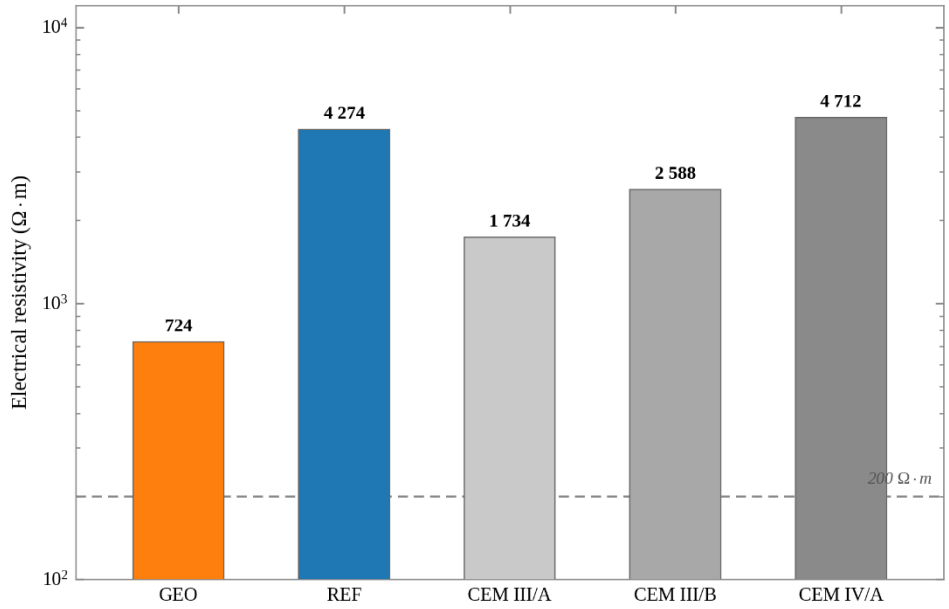

Figure 4-16: Electrical resistivity of the five mixes derived from the rapid chloride penetration measurement, $\rho = V \cdot A/(I \cdot L)$, on a logarithmic axis.

The lower resistivity of GEO relative to the Portland-based mixes does not indicate an inferior pore structure. As Section 4.1.4 sets out and (Provis, 2018) emphasizes for alkali-

activated materials, it reflects the high mobile-ion content of the KOH^--activated pore solution, which raises conductivity independently of pore geometry.

The thresholds were calibrated on Portland systems and therefore place an alkali-activated material conservatively, in a higher apparent risk band than its pore structure warrants. Read with that caveat, the resistivity confirms that GEO provides robust protection against chloride-induced reinforcement corrosion despite its higher total porosity, in agreement with the diffusion coefficient of Section 4.3.6.

4.3.8 Marine exposure at HarshLab

4.3.8.1 Residual mechanical performance

The 10-month HarshLab campaign is assessed here first by the visual condition of the specimens and then by their residual mechanical strength. The visual record was documented at three, six, and 10 months and after cleaning, for the uncoated, Coat1, and Coat2 surface conditions in both the splash and immersed zones. Figure 4-17 shows the evolution in the splash zone and Figure 4-18 in the permanently immersed zone.

In the splash zone, light rust staining appeared on all specimens within the first three months and did not progress significantly through 10 months. Its origin is the oxidation of steel fibers exposed at the cut surface, and it is the only adverse observation of the field campaign. Because it is confined to fibers intersecting a cut face, it does not indicate ingress to the fiber population within the matrix. It does, however, identify the fiber-matrix interface as the element of the composite that the marine environment reaches first, which is consistent with the divergence between compressive and flexural behavior reported in Section 4.3.3. No systematic difference in surface condition emerged between the uncoated specimens and either coating, and both bio-based coatings remained adhered for the full exposure period.

GEO	Uncoated	Biobased	Bio_2%ZW
3 MONTHS			
6 MONTHS		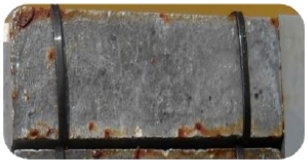	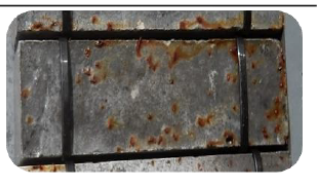
10 MONTHS		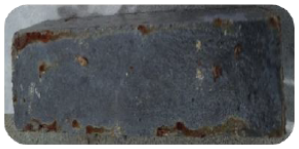	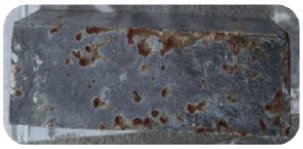

Figure 4-17: Coated and uncoated Geopolymer specimens' evolution in the splash zone.

In the immersed zone, the specimens followed the biofouling trajectory typical of submerged concrete in productive coastal water, from light algal colonization at three months to substantial fouling coverage by 10 months across all three surface conditions, with surface marks comparable to the reference specimens after cleaning. In neither zone was there any visible sign of matrix deterioration, spalling, or cracking. The specimens whose residual strength is reported below are the same specimens shown here.

GEO	Uncoated	Biobased	Bio_2%ZW
3 MONTHS			
6 MONTHS			
10 MONTHS			
AFTER CLEANING			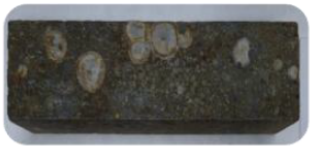

Figure 4-18: Coated and uncoated geopolymer specimens' evolution on immersion zone.

After 10 months at the HarshLab floating facility, the GEO specimens retained their full mechanical class in every zone and surface condition (Figure 4-19). The residual flexural strength ranged only from 14 to 17 MPa across all seven groups: the atmospheric-zone specimen, labeled Air in Figure 4-19, held 17 MPa, matching the 28-day reference of 17.0 MPa. The splash-zone uncoated, Coat1, and Coat2 groups gave 16, 15, and 16 MPa, and the immersed-zone counterparts gave 16, 14, and 15 MPa. The residual compressive strength told the same story, every group exceeding 150 MPa: the Air group recorded 164 MPa, the splash-zone groups 155, 150, and 157 MPa, and the immersed-zone groups 157, 167, and 158 MPa.

The replicate counts vary between groups and are given above each bar in Figure 4-19. Flexural results rest on one to three prisms per group and compressive results on the corresponding half-prisms, so the compressive count is twice the flexural count in every group. The splash-zone Coat2 group comprises a single prism, and its flexural value therefore carries no measured scatter.

Two readings of these numbers must be distinguished. The **first** is that no group fell outside the range spanned by the others on either measure, so no effect of exposure zone or of coating is resolvable at these replicate counts. That is not the same as demonstrating that neither has an effect: with one to three specimens per group in flexure, a difference of the order of 10 percent would not be detected. The **second** concerns the comparison against the laboratory reference. The marine specimens were 90 days old at deployment and approximately 13 months old at retrieval, whereas the 152 MPa reference is a 28-day value, and no companion specimens were aged unexposed over the same period. The compressive values therefore bound any degradation attributable to marine exposure rather than demonstrating a gain from continued geopolymerization, and the 167 MPa recorded for the immersed Coat1 group should be read in that light.

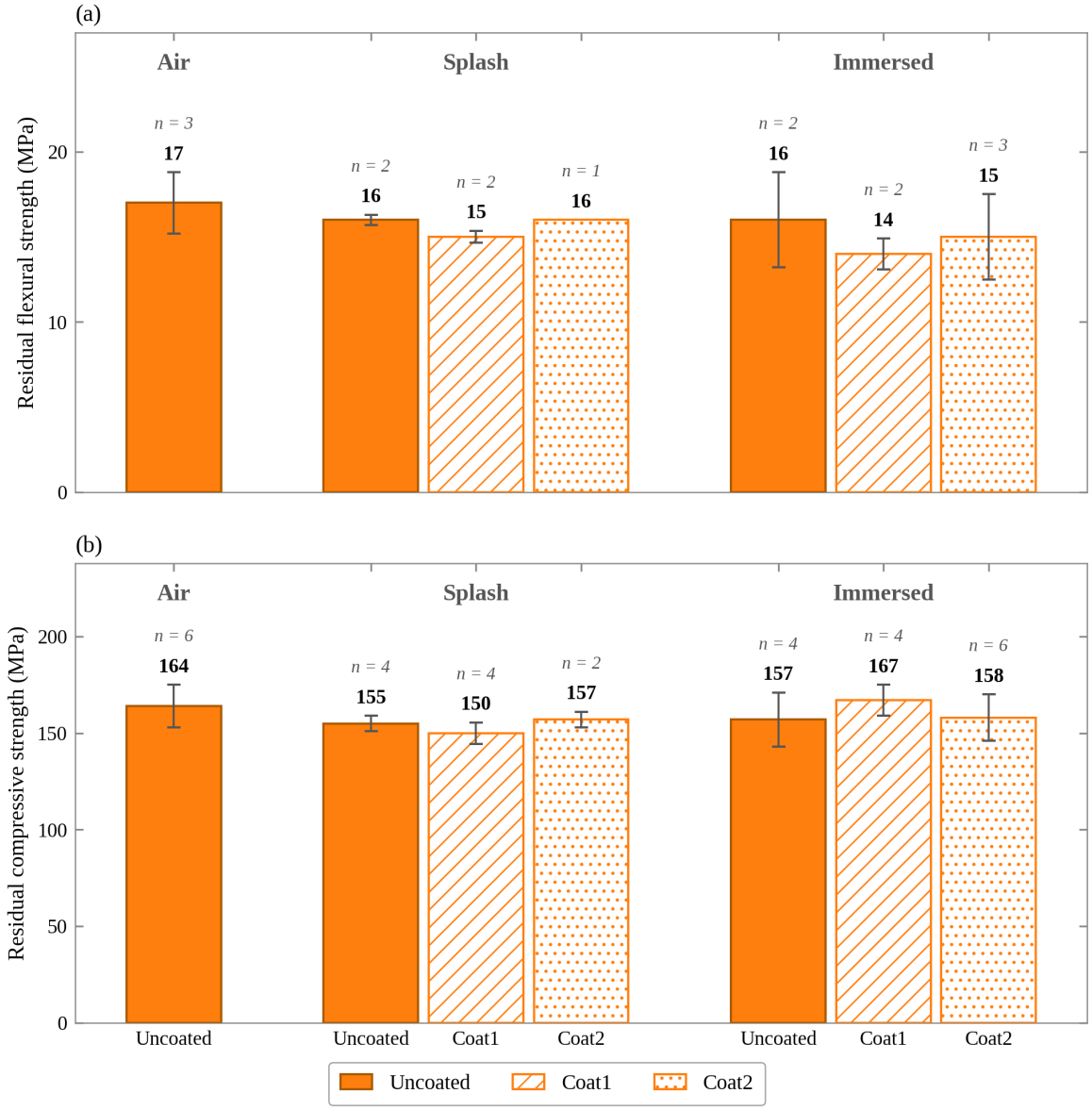

Figure 4-19: Residual mechanical strength of GEO after 10 months of marine exposure at HarshLab, by zone and surface condition. (a) flexural, (b) compressive. Replicate count given above each bar.

Within those limits, the field result is the most direct durability evidence in the chapter. A comprehensive review of UHPC durability covers permeability, chloride ingress, reinforcement corrosion, carbonation, freeze-thaw, chemical attack, alkali-silica reaction, and fire resistance without addressing alkali-activated binders in any of them (Li et al., 2020), while the alkali-activated durability record does not reach this strength class and derives, as its own authors state, largely from accelerated laboratory testing because field performance data are not publicly available (Lloyd et al., 2012). Ten months in the Bay of Biscay across atmospheric, splash, and immersed zones, with full retention of mechanical class in all three, is direct evidence where the published record offered laboratory inference. It is consistent with the chemical stability of the C-(N,K)-A-S-H gel inferred from the

laboratory sulfate and chloride results over the ten months tested; with one to three prisms per group and no same-age unexposed controls, it supports performance retention over that period, not a fifty-year service life.

4.3.8.2 Carbonation and chloride ingress

The colorimetric assessment of the retrieved specimens detected no carbonation front and no chloride front in any zone (Figure 4-20). Phenolphthalein produced a uniform pink-violet color across the full cross-section of every specimen, in all three zones and for all surface conditions, with no colorless rim at the exposed faces. The matrix therefore retained its alkalinity throughout, with no loss of pore-solution pH detectable by the indicator after 10 months of exposure.

Silver nitrate produced a predominantly brown silver-oxide color across the fractured faces, with no continuous white silver-chloride front penetrating from the surfaces, indicating that free chloride was not present at concentrations sufficient to precipitate silver chloride within the bulk, even under permanent immersion. The method reveals free chloride only above a threshold concentration, so the absence of a continuous front means that no front was detected, not that no chloride entered; chloride profiles by titration would quantify the ingress. Localized orange-brown staining on some faces was traced to oxidation of the cut steel fibers at the fracture surface, not to the chloride indicator, and does not correspond to a chloride front.

Two limits bound what the phenolphthalein result establishes. The indicator reports **pore-solution alkalinity**, not carbonate content, and the two can coexist: Chapter 1 measured 7.1 wt% calcite in GEO after a 28-day ambient cure, in a material whose KOH^- activated pore solution remains strongly alkaline. **A uniform pink-violet** response therefore establishes that the alkalinity governing passivation of the embedded steel fibers was retained, which is the property that matters for the reinforcement, but it is not a measurement of carbonate content and the carbonation state of the exposed specimens was not determined.

The silver nitrate result carries the complementary limitation set out in Section 4.1.4: the brown reference color requires free hydroxide, so a carbonated but chloride-free zone would read as though chloride were present. Here the two sprays agree, the matrix being alkaline throughout, so that failure mode does not arise.

The absence of a detectable carbonation front and chloride front under real seawater immersion is consistent with the transport measurements. It agrees with the very low diffusion coefficient of Section 4.3.6 and with the rising impedance of Section 4.3.4. Those are electrical measurements and they share the pore-solution confound established in Section 4.1.4, so their agreement alone would not settle the question.

The colorimetry does not share that confound: it reads the front directly on a fractured face, and it detected none. The chloride conclusion therefore rests on the agreement of the

electrical family with an independent field observation, which is the multi-method, laboratory-plus-field consistency that the prior UHPGC durability literature reviewed in Section 4.1 did not assemble. Within the detection limit of the method, GEO resisted chloride ingress over the ten months of marine exposure despite its higher total porosity relative to REF, and the conservative reading of the rapid chloride charge flagged in Section 4.3.6 is supported by the field result.

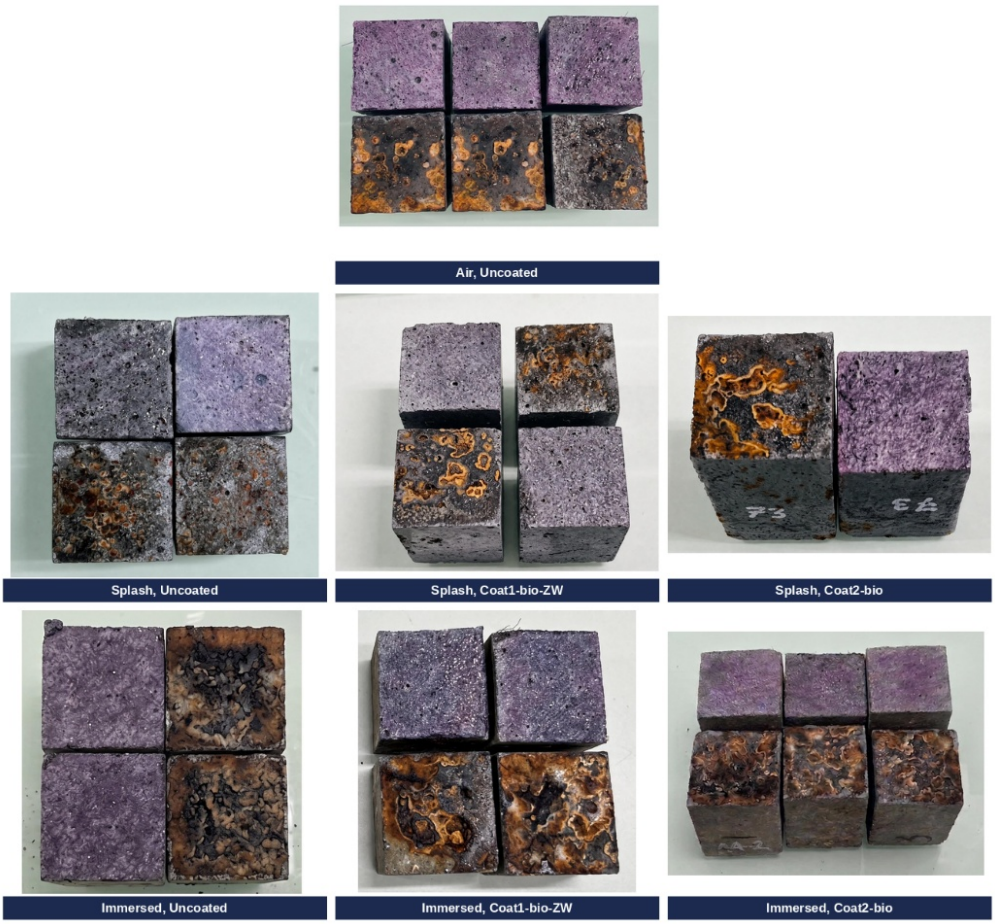

Figure 4-20: Colorimetric assessment of GEO specimens after 10 months of marine exposure at HarshLab, for the seven zone and surface-condition groups.

4.4 Goal, scope, functional unit, and system boundary

The chapter turns from the durability of GEO to its environmental and economic performance. From this point through the economic analysis and the KPI verdict, the comparator is the reference UHPC, whose impacts are drawn from a verified third-party Environmental Product Declaration. This section sets out the goal and scope of the assessment, defines the functional units, specifies the system boundary under EN 15804+A2, and states the cut-off, allocation and data-quality rules applied throughout. Two requirements constrain these choices: comparability with the verified declaration, which fixes the declared unit, the boundary and the indicator set, and consistency with the

predecessor assessment by Monteiro (2023), which established the methodological precedent for cement-substitute binders within the same research group.

4.4.1 Goal of the study

The assessment has three aims. The first is to quantify the cradle-to-grave global warming potential of the geopolymer mix developed in Chapters 1 to 3 and to compare it against the reference UHPC. The second is to test how far that comparison depends on the inventory data and the methodological choices behind it, through a structured sensitivity analysis. The third is to position both mixes against the two binding environmental and economic targets of the NATURSEA-PV project: a carbon reduction above 30% and a cost-to-strength reduction above 35%, both measured against the reference.

The study follows ISO 14040 and ISO 14044 and uses conventional Portland UHPC as the reference scenario. It is not intended to support an Environmental Product Declaration for GEO, since the precursor data available at this stage do not meet the verification requirements of EN 15804+A2. The assessment quantifies a single impact category, global warming potential, following ISO 14040 and ISO 14044 and the module structure of EN 15804+A2. It is a comparative carbon footprint rather than a full life cycle assessment.

4.4.2 Functional unit

Two declared units are used in parallel, and the use of more than one is deliberate, because the choice of reporting basis is itself a known lever in green-concrete assessment (Habert and Ouellet-Plamondon, 2016).

The primary unit is one m^3 of cured UHPC. It is chosen because volume, not mass, governs the design of a floating substructure: the section geometry and the displaced volume set the buoyancy, and the quantity a designer specifies is a volume of concrete. It is not the unit on which the reference declaration reports, so the reference impacts are converted to a volumetric basis through the reference density.

The second unit is one ton of concrete, and this is the declared unit of the reference Environmental Product Declaration. Because it requires no density conversion, the comparison on this basis is direct on both sides. It is reported alongside the volumetric result so that the effect of the conversion is visible rather than absorbed into a single headline.

The two units do not give the same answer, and the difference is physical. GEO is the lighter material: its batched mass is 2234 kg/m^3, in which sodium silicate is counted as solids following the life cycle inventory of Table 4-5, against a measured bulk dry density of 2403 ± 12 kg/m^3 for the reference (Table 1-8). The reference declaration states no density, so the measured value is used for the conversion. The difference of roughly 7% is a consequence of the lower specific gravity of the cement-free binder. On a volumetric basis that lightness

counts in GEO's favor, since less material fills the same m^3. On a mass basis it does not count at all. The volumetric result therefore combines the binder chemistry with the density advantage, while the mass result isolates the chemistry alone, and both are reported throughout on the same system boundary.

Two conventions in that comparison are conservative and are stated here rather than left implicit. The reference density adopted is the bulk dry value. The as-produced density implied by the saturated masses of Table 1-8 is approximately 2451 kg/m^3, and using it would raise the volumetric reduction by 1.2 percentage points. On the GEO side, the per-ton comparison divides by the inventory mass of 2234 kg/m^3 rather than the physical as-batched mass of 2323 kg/m^3 obtained by counting the sodium silicate as delivered solution (Table 4-9). Using the physical mass would raise the per-ton reduction from 32.1 to 34.7%. Both choices reduce the reported advantage of GEO. The two units are summarized in Table 4-4.

Table 4-4: The declared functional units declared.

Functional unit	Declared quantity	Question it answers	Density basis
Primary (FU1)	1 m^3 of cured UHPC	what it costs in carbon to build a given volume of structure	reference impacts converted at 2403 kg/m^3, measured (Table 1-8)
Secondary (FU2)	1 ton of cured UHPC	what the material costs per unit mass, independent of density	GEO at 2234 kg/m^3 inventory mass (Table 4-5), reference as declared, no conversion

The parallel use of two functional units follows the recommendation of Habert and Ouellet-Plamondon (2016) for green-concrete assessments, which notes that mass-based and volume-based units systematically disadvantage Portland-based mixtures relative to alkali-activated alternatives by failing to account for differences in declared strength. Reporting on all three in parallel quantifies the magnitude of this functional-unit dependence rather than concealing it behind a single choice, and the impact-assessment results in Section 4.6 confirm that the headline finding holds across all three units.

4.4.3 System boundary

The system boundary is cradle-to-grave under the EN 15804+A2 module nomenclature, shown in Figure 4-21. The production-stage modules A1, A2, and A3 are included for both mixes. The construction-stage modules A4 and A5 are included with project-symmetric assumptions: a transport distance of 50 km from plant to deployment site and a casting-loss factor of 2% by mass for both mixes, consistent with the reference declaration. The end-of-life modules C2 and C4 are included. Modules C1 and C3 are screened in both mixes under the cut-off rule of EN 15804+A2 clause 6.3.7, because no matching Ecoinvent 3.9.1 dataset exists for the demolition and crushing of UHPC and a generic structural-concrete proxy

would introduce an uncontrolled bias. Module D is reported as a memo item but excluded from the headline figure, consistent with the conservative practice of the reference declaration.

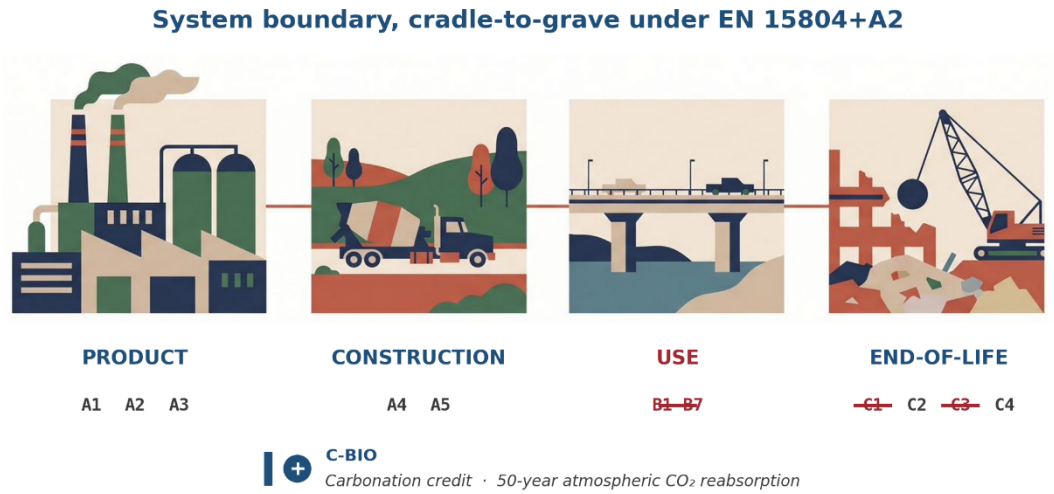

Figure 4-21: System boundary of the comparative life cycle assessment under EN 15804+A2.

The use stage, modules B1 to B7, is excluded entirely, and the exclusion follows the reference declaration itself. That declaration reports on a declared unit rather than a functional unit, states no reference service life, and excludes the use stage on that basis. Under EN 15804+A2 these follow from one another, since a declared unit is used where the function of the product in the works is not specified. Mirroring that boundary is what makes the two systems comparable.

Beyond this formal symmetry, nothing in the durability assessment of Section 4.3 distinguishes the two mixes in a way that would produce different use-stage burdens, and the operational and maintenance burdens of a floating substructure are in any case dominated by the photovoltaic modules rather than by the concrete.

A carbonation-uptake credit is applied to both mixes to account for atmospheric CO_2 reabsorption by the cured matrix, computed as 12% of the A1 carbon stock for the reference following Souto-Martinez et al. (2018) and 4% for GEO following the geopolymer-specific model of Stripple and Gustafsson (2018); the lower factor for GEO reflects the lower calcium content of the matrix and the reduced thermodynamic driving force for carbonation in an alkali-activated binder. The asymmetry works against GEO: removing the credit entirely from both mixes would raise the reported reduction from 37 to 41.8%, so the headline result is obtained despite a credit structure that favors the Portland comparator by a factor of three.

4.4.4 Impact assessment method

The primary impact-assessment method is the European Commission Environmental Footprint method, version 3.1, as implemented in SimaPro 9.6.0.1. It was selected for three reasons: it is the method mandated by EN 15804+A2 for declarations issued or revised after July 2022, which makes it the natural basis for comparison against the REF-EPD declaration. It incorporates the IPCC AR6 hundred-year global-warming characterization factors, the current consensus that superseded the earlier AR4 factors used by the CML-IA baseline, and it covers 19 impact categories in one framework, including the four required by EN 15804+A2 (global warming potential split into total, fossil, biogenic, and land-use-change components) and 15 further indicators for completeness.

An independent cross-check on the global-warming indicator is performed with the CML-IA baseline method, version 3.10, in the same installation, reported per module in Section 4.6. Its purpose is to quantify the dispersion between the AR4-based CML method and the AR6-based EF 3.1 method on the present inventory and to confirm that the headline result is not an artifact of the method choice, an expected residual difference of order 0.5 to 1% on cement-based products being the test of method-robustness (Andrade and Sanjuán, 2018).

4.4.5 Data quality, cut-off, and allocation

Three rules govern the inventory:

The cut-off rule covers at least 99% of the mass of each mix on the cubic-meter basis, per EN 15804+A2 clause 6.3.7: all components above 1% of mix mass are inventoried explicitly, and components below that threshold are omitted unless their carbon intensity is exceptionally high, which arises in neither mix.

The treatment of the GGBS precursor requires a separate statement, because it is the single inventory choice to which the result is most sensitive. The emission factor adopted, 15.7 kg CO_2-eq per t, is taken from the DIOGEN database via the Ecocem Fos-sur-Mer entry, the same source used by Monteiro (2023). The allocation rule declared by that entry could not be verified from the documentation available. Its magnitude indicates a cut-off treatment, in which no share of the ironmaking burden is allocated to the slag and only the processes converting it to a usable precursor are counted. That convention is contested. Habert and Ouellet-Plamondon (2016) observe that the European end-of-waste directive means blast furnace slag can no longer be classified as waste in Europe but as a by-product, so that an allocation is in principle required, and they report, citing Van den Heede and de Belie, that allocating as little as 2% of steel production to the slag already yields 0.13 kg CO_2-eq per kg. The consequences of that range for the present result are quantified in Section 4.7 rather than resolved here.

All other allocation in the inventory is mass-based and applied uniformly to both mixes. Data quality is assessed against the matrix of EN 15804+A2 Annex E, with separate technological, geographical, and temporal scores.

4.5 Inventory

The GEO mix design was described in Chapters 1 to 3 and is not repeated here. The REF-EPD comparator is imported from its verified declaration (Section 4.5.2). This section sets out how those designs are translated into a life cycle inventory: which background process represents each component, how the activator is handled on a dry-mass basis, how transport to the Valencia plant is modeled, and how the REF-EPD data are imported from the supplier declaration. It closes with the data-quality assessment that supports the comparative assertion.

4.5.1 GEO mix inventory

The GEO mix is a fiber-reinforced UHPGC of nine components, with a total mass of 2234.2 kg per m^3 and a density of 2234 kg/m^3. The binder is alkali-activated, with ground granulated blast-furnace slag and silica fume as the aluminosilicate precursors and potassium hydroxide combined with sodium silicate as the activator. The fiber system is hybrid: 60% of the fiber mass is recycled steel (Dapcons Flexofibers) and 40% is virgin steel microfiber (Spajic). The mix proportions, suppliers, transport distances, and background processes are given in Table 4-5.

Table 4-5: Foreground inventory of the GEO mix per m^3 of cured concrete.

Component	Mass (kg/m^3)	% mass	Supplier (origin)	Distance (km)	Background process
GGBS	720.0	32.2	Ecocem Iberia (Spain)	700	GGBS, Diogen supplier-specific (15.7 kg CO_2-eq/t)
Silica fume	180.0	8.1	Ferroglobe Sabón (Spain)	800	Silica fume, market, RER
Sodium silicate (Betol 47-T, dry)	71.2	3.2	Xatico (Spain)	350	Sodium silicate, solid, market, GLO
KOH (dry)	64.8	2.9	Ercros Tarragona (Spain)	280	Potassium hydroxide, market, GLO
Tap water	115.2	5.2	Municipal (Valencia)	0	Tap water, market, Europe
Fine quartz sand	435.0	19.5	Local quarry (Valencia)	50	Silica sand, market, RER

Component	Mass (kg/m^3)	% mass	Supplier (origin)	Distance (km)	Background process
Coarse quartz sand	540.0	24.2	Local quarry (Valencia)	50	Silica sand, market, RER
Recycled tire steel fibers (Flexofibers)	64.8	2.9	Dapcons (Spain)	280	Steel reinforcement, recycled, market, RER
Virgin steel microfibers	43.2	1.9	Sisak (Croatia)	200+1900+50	Steel reinforcement, primary, market, RER

Note: Mass percentages are on the total-mass basis. Transport distances are one-way truck routes from each supplier to the Valencia plant, except the multimodal Spajic microfiber route detailed in the text. Background processes are from Ecoinvent 3.9.1 cut-off. The GGBS process uses a supplier-specific Diogen value (Section 4.5.4). Check Section 4.5.3 for the mode of the transport.

Two features of the inventory warrant emphasis, and both are decisive for the result that follows.

First, the activator subsystem (sodium silicate, potassium hydroxide, and dilution water) is only 11.3% of the mass but contributes a disproportionate share of the cradle-to-gate global warming potential, because of the high specific carbon intensity of chlor-alkali production, exactly the activator-dominance that Provis and Deventer (2014) identified as the controlling burden of alkali-activated binders and that Habert and Ouellet-Plamondon (2016) placed at 60 to 85% of binder emissions. The present inventory is therefore structured to expose this contribution rather than bury it, and Section 4.6 quantifies it.

Second, the methodology follows the predecessor assessment by Monteiro (2023) in three respects: the same Diogen dataset for GGBS, the same Ecoinvent processes for sodium silicate and potassium hydroxide, and the same allocation convention across the activator subsystem. The geographic anchoring differs (Monteiro used Ecocem Fos-sur-Mer for a Bordeaux deployment; the present work uses Ecocem Iberia for Valencia), but the shared database conventions let the activator inventory be considered methodologically anchored against an independent prior study, a comparability rarely available in this literature.

4.5.2 REF-EPD mix inventory

The REF-EPD mix is imported directly from a verified Environmental Product Declaration certified under EN 15804+A2 and authenticated by AENOR in March 2024. No SimaPro modeling is performed on the REF-EPD side: the cradle-to-gate impact values on all 19 EF 3.1 indicators and on the CML-IA cross-check, the system boundary, the declared characteristic strength above 130 MPa, and the supplier-gate cost (583 EUR/m^3, used in Section 4.8) are read from the declaration. The per-component composition of the REF-EPD mix is supplier-confidential and is not disclosed. The comparison is conducted on the

declared module-by-module impact values, and no part of the method requires the underlying component masses. The methodological strength of this arrangement is that the REF-EPD uncertainty is bounded by third-party verification under EN 15804+A2 rather than by a literature regression of typical UHPC values, the standard fallback in published comparative UHPC assessments, which carries uncertainty bands of 20% or more.

4.5.3 Transport modeling

Transport in module A2 is modeled per component and aggregated. The road segment uses the Ecoinvent process for a EURO6 16-to-32-ton lorry (European fleet average). The sea segment of the Spajic supply uses the container-ship process. Most precursors are sourced within the Iberian Peninsula, with road distances between 280 km (KOH, Ercros Tarragona) and 800 km (silica fume, Ferroglobe Sabón), favorable against the Northern-European supply chains common in published comparative assessments.

The single intercontinental segment is the Spajic microfiber leg, decomposed as 200 km road from Sisak to Rijeka, 1900 km sea from Rijeka to Valencia, and 50 km road from port to plant. Despite being only 1.9% of the mix mass, this leg accounts for roughly one-third of the total A2 carbon, through the high mass-distance integral of the sea segment. The asymmetry is examined in the sensitivity analysis. Figure 4-22 shows the supply-chain layout.

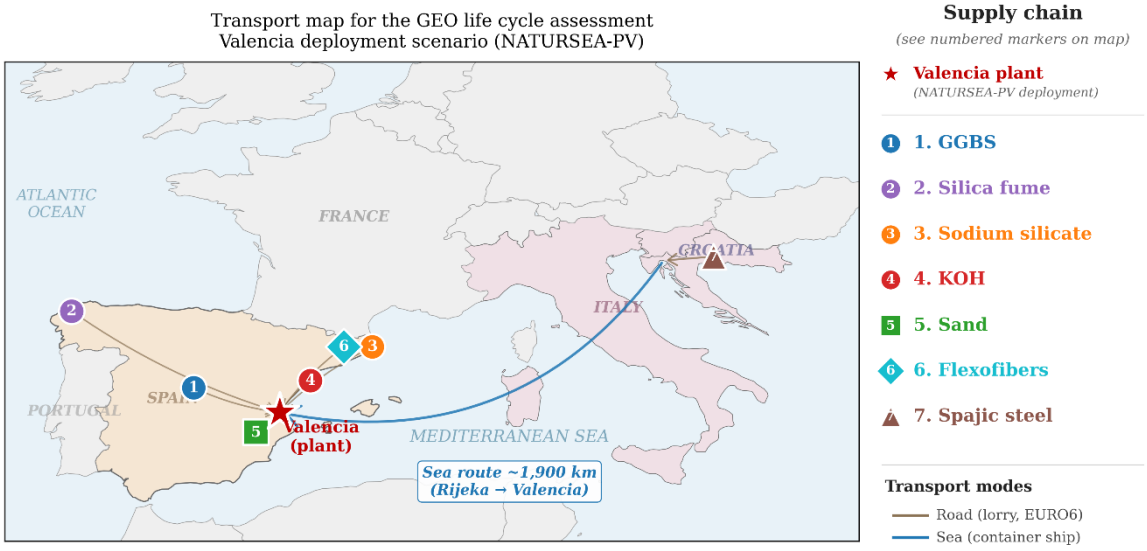

Figure 4-22: Spatial layout of the GEO supply chain for the Valencia deployment scenario.

4.5.4 Data quality

The data-quality rating is computed against the matrix of EN 15804+A2 Annex E, with separate technological, geographical, and temporal scores. The mean rating for the GEO inventory is 1.78, in the very good band and comparable to the 1.67 of the REF-EPD

declaration. The GEO inventory is therefore adequate for the comparison conducted here, with the qualification that it is not intended to support an Environmental Product Declaration for GEO at this stage, since the precursor scores are not third-party verified. The cut-off rule covers more than 99% of the mass of each mix, and all components above 1% of mix mass are inventoried explicitly. The mass-based allocation is applied uniformly to both mixes and is the conservative choice for GEO, assigning GGBS the full upstream burden of blast-furnace operation prorated by mass. The sensitivity of the result to economic allocation, under which GGBS would carry a far lower share, is examined in the sensitivity analysis.

4.6 Impact assessment

This section reports the cradle-to-grave life cycle impact assessment of GEO and REF-EPD under the EF 3.1 method, with an independent cross-check against CML-IA at the end. It is the heart of the life-cycle half of the chapter: it delivers the comparative result, identifies the components and modules that drive it, tests its robustness against the choice of functional unit, and verifies that the conclusion is not an artifact of the method choice. The presentation is figure-driven, with the prose developing the quantitative analysis rather than leaving it to the reader to extract from the figures.

4.6.1 Headline result by EN 15804 module

The cradle-to-grave global warming potential of one m^3 of cured concrete is 693.2 kg CO_2-equivalent for GEO and 1099.6 kg CO_2-equivalent for REF-EPD. GEO delivers a 37% reduction on the deployment-scenario basis, an absolute saving of 406.4 kg CO_2-equivalent per m^3 of concrete placed.

At the project scale this is a saving of order 20 to 24 tons of CO_2-equivalent per typical floater unit (assuming 50 to 60 m^3 of concrete per substructure) and above 200 tons for a representative deployment of 10 substructures, the scale at which the project envisions industrial roll-out. These absolute figures become the basis of the KPI 2.1 verdict in Section 4.9. Figure 4-23 decomposes the total by EN 15804+A2 module, and Table 4-6 reports the same decomposition numerically.

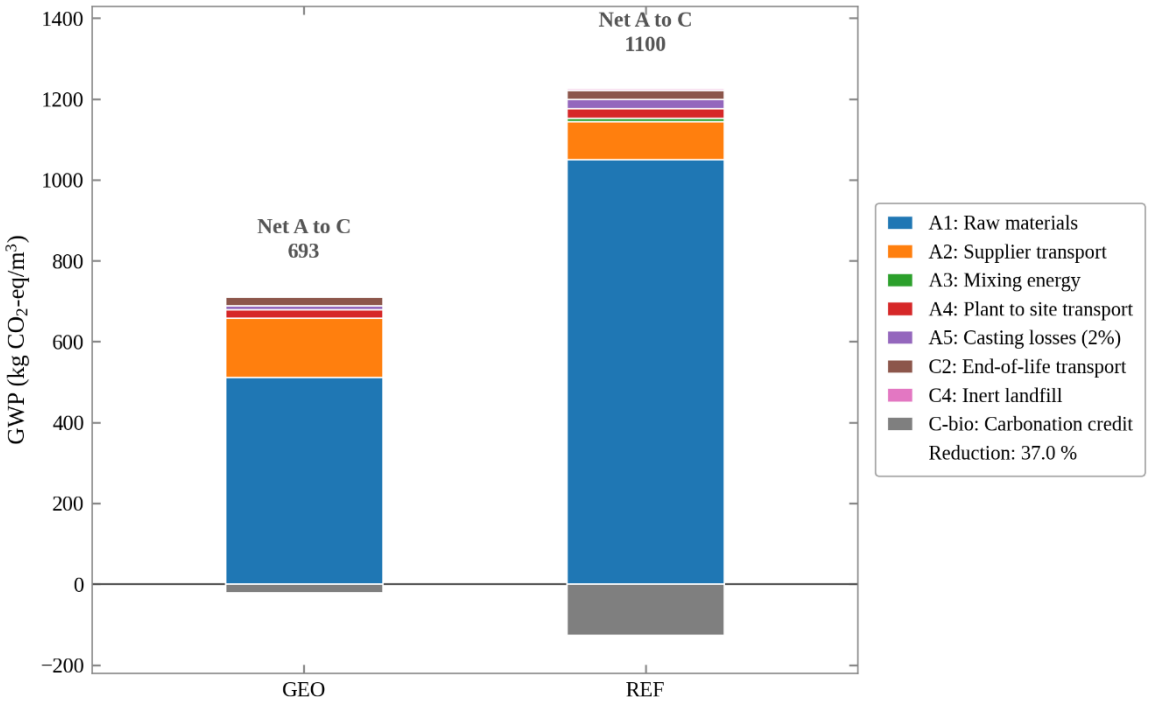

Figure 4-23: Cradle-to-grave global warming potential by EN 15804+A2 module, per m^3.

Table 4-6: Module-by-module cradle-to-grave global warming potential of GEO and REF, in kg CO_2-equivalent per m^3.

EN 15804+A2 module	GEO (kg CO_2-eq/m^3)	REF-EPD (kg CO_2-eq/m^3)	Δ (GEO − REF-EPD)
A1 raw materials	511.4	1050.1	−538.7
A2 supplier transport	146.3	93.7	+52.6
A3 manufacturing	0.3	9.6	−9.3
A4 transport to site (50 km)	21.2	22.8	−1.6
A5 installation (2% losses)	10.2	23.1	−12.9
C2 transport to end-of-life	21.2	22.8	−1.6
C4 inert landfill	3.1	3.4	-0.3
C-bio carbonation credit	−20.5	−126	+105.5
Cradle-to-grave total	693.3	1099.6	−406 (−37%)

Five observations carry forward:

First, the A1 stage accounts for 511.4 kg in GEO and 1050.1 kg in REF-EPD, a difference of 538.7 kg that slightly exceeds the entire cradle-to-grave delta, because the GEO A1 advantage is partly eroded by the other modules. In substitution terms, the GEO advantage is an A1 advantage: the formulation does not produce the clinker-calcination CO_2 that is the dominant burden of any Portland UHPC.

Second, A2 supplier transport is the only module unfavorable to GEO (146.3 against 93.7 kg, a penalty of about 50 kg), the direct cost of the multimodal Spajic microfiber supply, whose Croatia-to-Valencia leg alone contributes about 35% of the GEO A2 burden despite being 1.9% of the mass. This lever is examined in the sensitivity analysis.

Third, manufacturing A3 is an order of magnitude smaller for GEO (0.3 against 9.6 kg) because GEO is ambient-cured while REF-EPD carries the embedded energy of clinker grinding. The absolute difference is small but the qualitative point is structural, ambient-cured geopolymers carry essentially no A3 burden.

Fourth, the construction and end-of-life transport modules are nearly symmetric by the project-symmetric assumptions, and the small GEO advantage there reflects only its lower density, not binder substitution.

Fifth, the carbonation credit is the largest module favorable to REF-EPD (−126.0 against −20.5 kg): Portland binders carry a higher free-calcium reservoir to react with atmospheric CO_2, justifying the 12% A1-stock credit following Souto-Martinez et al. (2018), while geopolymers carbonate more slowly because the calcium is bound in the C-(N,K)-A-S-H phase rather than as free portlandite, justifying the 4% credit following Stripple and Gustafsson (2018). The asymmetry is a real and substantive partial offset, but it does not reverse the comparison.

Two pre-carbonation comparisons frame the role of the credit. On the cradle-to-gate basis A1+A2+A3, the standard EPD-comparable scope with no carbonation credit, GEO emits 658.0 kg against 1153.5 for REF-EPD, a reduction of 42.9%. On the cradle-to-grave basis with no carbonation crediting on either mix, the reduction is 41.7%. The 37% headline value with asymmetric crediting therefore sits below both pre-carbonation values, which is the methodologically conservative position: the credit, which favors REF-EPD, makes the GEO advantage look smaller, not larger, so the headline cannot be accused of flattering the geopolymer.

One boundary of this comparison must be stated at the point where the result is presented. Carbon footprint assessment is a multi-criteria method, and a comparison between two products cannot be settled on a single indicator: a material that improves on global warming potential may worsen on acidification, eutrophication, ecotoxicity, or resource depletion, and any of those could prove the more critical for a given application.

The present assessment quantifies global warming potential alone, for the reasons set out in Section 4.4.1, so what follows is a carbon comparison and not a determination that GEO is environmentally preferable to REF-EPD in the round. The hotspot analysis of Section 4.6.2 indicates where a wider assessment should be directed, since the chlor-alkali production of the potassium hydroxide activator that dominates the GEO carbon burden would be expected to dominate its acidification, eutrophication, and ionizing-radiation profiles as well.

The comparison is made on a declared quantity rather than on a defined function, so the two materials are compared volume for volume and mass for mass rather than at equal structural performance. The two are not exactly interchangeable: GEO reaches 137 MPa at 28 days against a declared 130 MPa for REF-EPD, so a section designed to a given capacity would not require identical volumes of the two. That difference is small relative to the carbon gap and acts in GEO's favor, so the declared-quantity comparison is conservative; the per-strength comparison is reported in Section 4.8 where the cost-to-strength KPI requires it.

4.6.2 Hotspot analysis of the GEO raw-materials stage

Since the delta is driven by A1, the diagnostic value of the assessment lies in where the residual 511 kg of the GEO A1 stage comes from, which determines the priority lever for further reduction and connects the assessment back to the formulation chapters. Figure 4-24 disaggregates the GEO A1 burden by component.

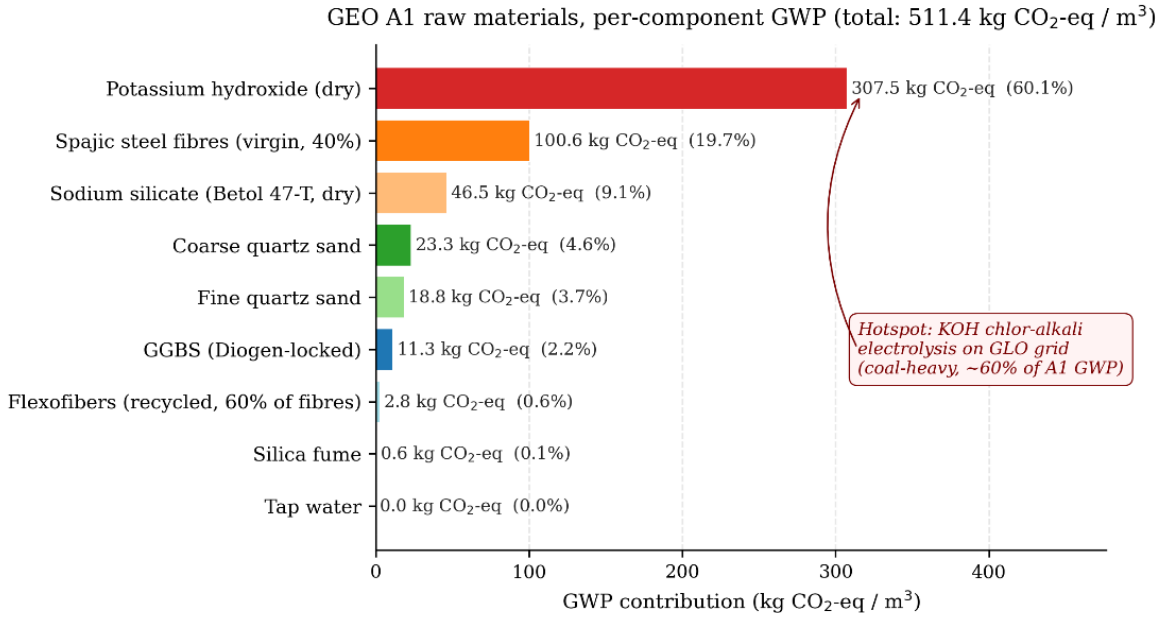

Figure 4-24: Decomposition of the GEO A1 raw-materials stage by component, ranked from largest to smallest.

The dominant contributor is the potassium hydroxide activator, alone 60% of the GEO A1 burden despite being 2.9% of the mass. This concentration of impact in a low-mass component reflects the high specific carbon intensity of chlor-alkali production: the Ecoinvent global-average process places dry KOH at 4.74 kg CO_2-equivalent per kg, against about 0.8 to 0.9 kg per kg for Portland clinker on the same basis. The driver is the electricity of the chlor-alkali cell, and its carbon intensity is grid-dependent: the Ecoinvent global-average grid carries about 480 g CO_2 per kWh, conservative for Europe, where intensity ranges from about 50 g/kWh in France to 700 g/kWh in Poland. The Spanish grid relevant to deployment averaged 175 g/kWh in 2024, so an explicitly modeled Spanish chlor-alkali

supply would lower the KOH contribution materially. This lever is flagged as a follow-up in the General Conclusion.

The second contributor is the virgin steel microfiber at 19.7% of the A1 burden, from 1.9% of the mass, at 2.33 kg CO_2-equivalent per kg of primary hot-rolled steel. The recycled tire-derived fiber, at an equal share of the fiber system by mass, contributes 0.6%, a ratio of more than 50 to 1 between the two fiber routes and the quantitative basis of the recycled-fiber advantage examined in the sensitivity analysis. The sodium silicate adds 9.1%, at a lower specific intensity of 0.65 kg CO_2-equivalent per kg dry since the chlor-alkali step does not enter its route. The activator subsystem therefore accounts for 69% of the GEO A1 burden, inside the 60 to 85% band Habert and Ouellet-Plamondon (2016) report for alkali-activated formulations, confirming that GEO is an activator-dominated rather than precursor-dominated formulation.

By contrast, the GGBS precursor contributes 2.2% of the A1 burden despite being 32% of the mass, and the silica fume 0.1%. The supplier-specific Diogen value of 15.7 kg CO_2-equivalent per t is two orders of magnitude below Portland clinker, and this is the structural reason GEO delivers its reduction: the substitution replaces high-carbon clinker with a near-zero-carbon by-product, and the activator surcharge needed to mobilize that by-product is smaller in absolute terms than the clinker burden it displaces. The quartz sands together contribute 8.3%, and the remaining components below 1% each.

4.6.3 Robustness against the functional unit

On the two units defined in Section 4.4.2, the cradle-to-grave global warming potential is 693.2 against 1099.5 kg CO_2-equivalent per m^3, a reduction of 37%, and 310.8 against 457.6 kg per t, a reduction of 32.1%. The qualitative finding holds on both bases. The difference between them has a clean physical reading: the per-ton basis compresses the advantage because GEO is about 7% less dense, so a m^3 contains about 169 fewer kg and the mass basis does not credit that lightness. The volumetric result therefore combines the binder substitution with the density advantage, while the mass result isolates the substitution alone. Both are above the 30% project threshold.

4.6.4 End-of-life modules and method robustness

The combined C2+C4 end-of-life contribution is 24.3 kg CO_2-equivalent per m^3 for GEO and 27.2 kg for REF-EPD, in both cases below 3% of the cradle-to-grave total. The end-of-life stage is therefore quantitatively minor, a structural feature of inert mineral materials with long service lives, for which most of the burden sits in the A1 stage and end-of-life boundary choices cannot move the headline by more than two or three percentage points. The carbonation credit, the only project-specific module outside the standard set, is the most consequential end-of-life treatment: applied asymmetrically at 12% of the A1 stock

for REF-EPD (Souto-Martinez et al., 2018) and 4% for GEO (Stripple, it reduces the REF-EPD footprint by 11.4% and the GEO footprint by 2.9%, so a no-credit assessment would compute 714.8 against 1225.6 kg CO_2-equivalent per m^3, a 41.7% reduction. The 37% headline with asymmetric crediting is therefore conservative. Removing the credit widens the GEO advantage.

The last methodological lever is the impact-assessment method itself, since the shift from IPCC AR4 to AR6 characterization factors introduces systematic differences of order 5 to 8% in the cradle-to-gate GWP of cement-based products relative to older CML-based studies. Figure 4-25 reports the GEO GWP per module under both EF 3.1 (AR6) and CML-IA (AR4). The cross-check produces a cradle-to-grave GEO GWP of 689.9 kg CO_2-equivalent per m^3 under CML-IA against 693.2 under EF 3.1, a relative difference of 0.48%, inside the 0.5 to 1% band expected on cement-based products (Andrade and Sanjuán, 2018) and confirming that the 37% reduction is method-robust. The REF-EPD declaration reports both methods with a similar sub-0.5% difference, so the method-induced uncertainty on the headline reduction is of order one percentage point, well below the magnitudes examined in the sensitivity analysis.

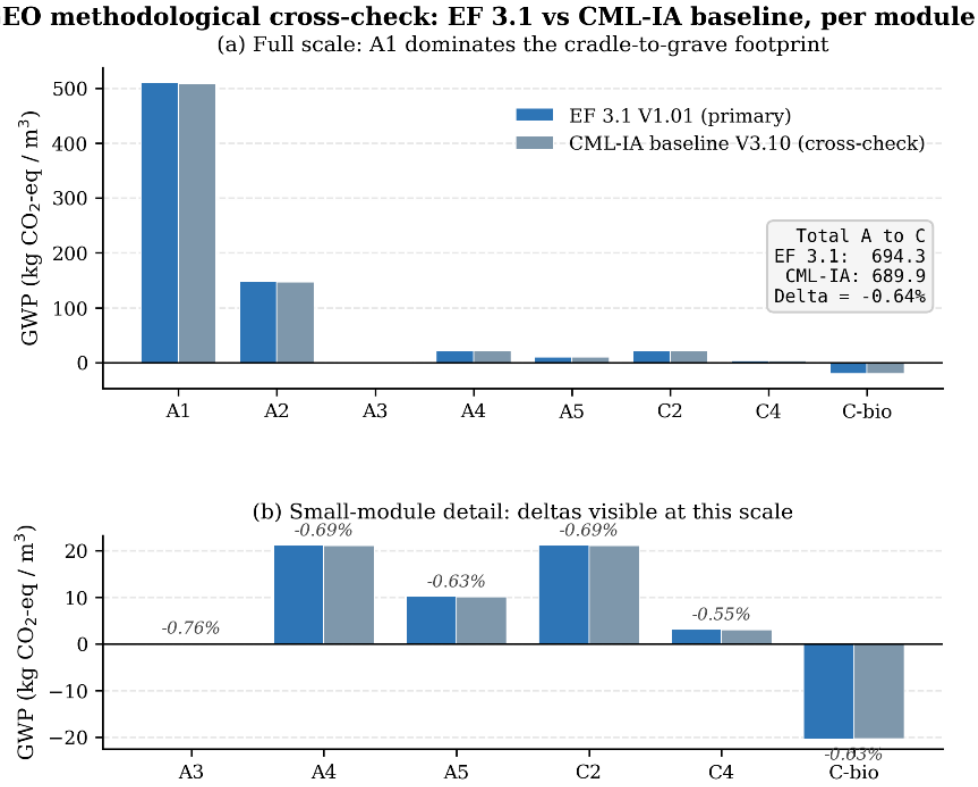

Figure 4-25: Cradle-to-grave global warming potential of GEO decomposed by EN 15804+A2 module under two methods: EF 3.1 V1.01 (IPCC AR6 factors) and CML-IA Baseline V3.10 (IPCC AR4 factors). The two agree within 0.7% on the cradle-to-grave total, inside the expected band for cement-based products.

4.6.5 Summary of the impact assessment

Five findings carry into the remainder of the chapter:

First, GEO reduces the cradle-to-grave global warming potential of one m^3 of UHPC by 37% relative to a verified Portland reference, an absolute saving of 406 kg CO_2-equivalent per m^3, 20 to 24 tons per typical floater at the deployment scale.

Second, the reduction is robust across both functional units, compressing to 32.1% per t, so the verdict does not depend on the functional-unit choice.

Third, the residual GEO A1 burden is dominated by the chlor-alkali chemistry of the KOH activator, the priority lever for further reduction.

Fourth, the assessment quantifies global warming potential only. A comparison across the wider EF 3.1 indicator set was not performed, since the modeling of the GEO inventory on the remaining categories fell outside the scope of the present work, so burden-shifting from carbon to other impact categories cannot be excluded on the basis of the data reported here. The hotspot analysis nevertheless identifies where such a check should be directed: the chlor-alkali production of the potassium hydroxide activator dominates the GEO carbon burden and would be expected to dominate the acidification, eutrophication, and ionizing-radiation profiles as well, so the priority reduction lever for carbon is also the priority target for any wider assessment.

Fifth, the CML-IA cross-check confirms method-robustness to within one percentage point. These set up the sensitivity analysis, which tests the headline against nine perturbations, and the economic analysis, which translates the result into the cost-to-strength metric of the second KPI. One boundary of this assessment should be stated plainly. It quantifies a single impact category, global warming potential, on the ground that the project KPI is expressed in carbon and that the reference declaration provides a verified comparator on that category.

The alkali-activated literature reports cases in which a carbon gain is accompanied by increases in acidification, eutrophication, or ecotoxicity, and the present work does not test for that.

4.7 Sensitivity analysis

4.7.1 Scenario design

The headline reduction of 37% was computed against a single locked combination of inventory values, allocation rules, transport assumptions, and impact-assessment method. Whether that figure is substantive or a contingent artifact of the chosen baseline depends on its robustness against plausible perturbations of each lever.

This section answers that through a structured analysis of nine scenarios, each perturbing one inventory or methodological choice while holding the others at baseline. The

scenarios are not arbitrary: each tests a lever flagged in the preceding sections or in the alkali-activated assessment literature as a documented source of uncertainty (Provis and Deventer, 2014; Habert and Ouellet-Plamondon, 2016), and the set spans both the upside and downside of every lever.

The **nine scenarios** fall into four families. The **first (S1, S2)** probes the sodium silicate inventory: S1 intensifies the Ecoinvent proxy by 15% to test the conservatism of the dry-basis process, S2 substitutes a rice-husk-ash silicate route at −70% intensity to test a future-state sourcing. The **second (S3, S4)** probes transport, multiplying every road and sea segment by 1.5 (S3) and halving every segment (S4), bracketing the supplier-distance uncertainty most often raised against a single-deployment-scenario assessment. The **third (S5, S6)** probes the carbonation credit: S5 doubles it on both mixes for a fully aggressive hundred-year exposure, S6 removes it from both.

The **fourth (S7, S8, S9)** probes the remaining first-order levers: S7 resets the GEO fibers to 100% virgin steel to quantify the recycling advantage, S8 replaces the supplier-specific Diogen GGBS value of 15.7 kg CO_2-equivalent per t, whose magnitude indicates a cut-off treatment in which no ironmaking burden is allocated to the slag, with a value of 130 kg per t, corresponding to a 2% allocation of steel production to the slag as reported by Habert and Ouellet-Plamondon (2016) citing Van den Heede and de Belie, and S9 reroutes the heavy GGBS and silica fume through a multimodal road-and-sea path proposed in the project as a deployment optimization. Table 4-7 summarizes the nine scenarios and the resulting cradle-to-grave delta.

Table 4-7: Sensitivity analysis of the cradle-to-grave GEO advantage against nine one-at-a-time perturbations from the baseline of Section 4.6.

ID	Perturbation	New Δ (GEO/REF-EPD −1)	Shift vs baseline
Baseline	Baseline inventory and EF 3.1 V1.01	−37%	–
S1	Sodium silicate proxy intensified by 15%	−36.2%	+0.7 pp
S2	Sodium silicate from rice-husk-ash route (−70%)	−39.8%	−2.9 pp
S3	All transport distances × 1.5	−32.5%	+4.4 pp
S4	All transport distances halved	−41.8%	−4.9 pp
S5	Carbonation uptake doubled (24% REF-EPD, 8% GEO)	−30.8%	+6.1 pp
S6	No carbonation credit on either mix	−41.7%	−4.8 pp
S7	GEO fibers reset to 100% virgin steel	−23.5%	+13.5 pp

ID	Perturbation	New Δ (GEO/REF-EPD −1)	Shift vs baseline
S8	GGBS at 2% steel allocation (130 vs 15.7 kg CO_2-eq/t)	−29.5%	+7.5 pp (KPI 2.1 not met)
S9	Multimodal transport for GGBS and silica fume	−44.1%	−7.2 pp

4.7.2 Tornado representation and lever ranking

Figure 4-26 presents the sensitivity table as a horizontal tornado plot, scenarios ranked from highest to lowest leverage. Bars extending right widen the GEO advantage relative to baseline. Bars extending left compress it.

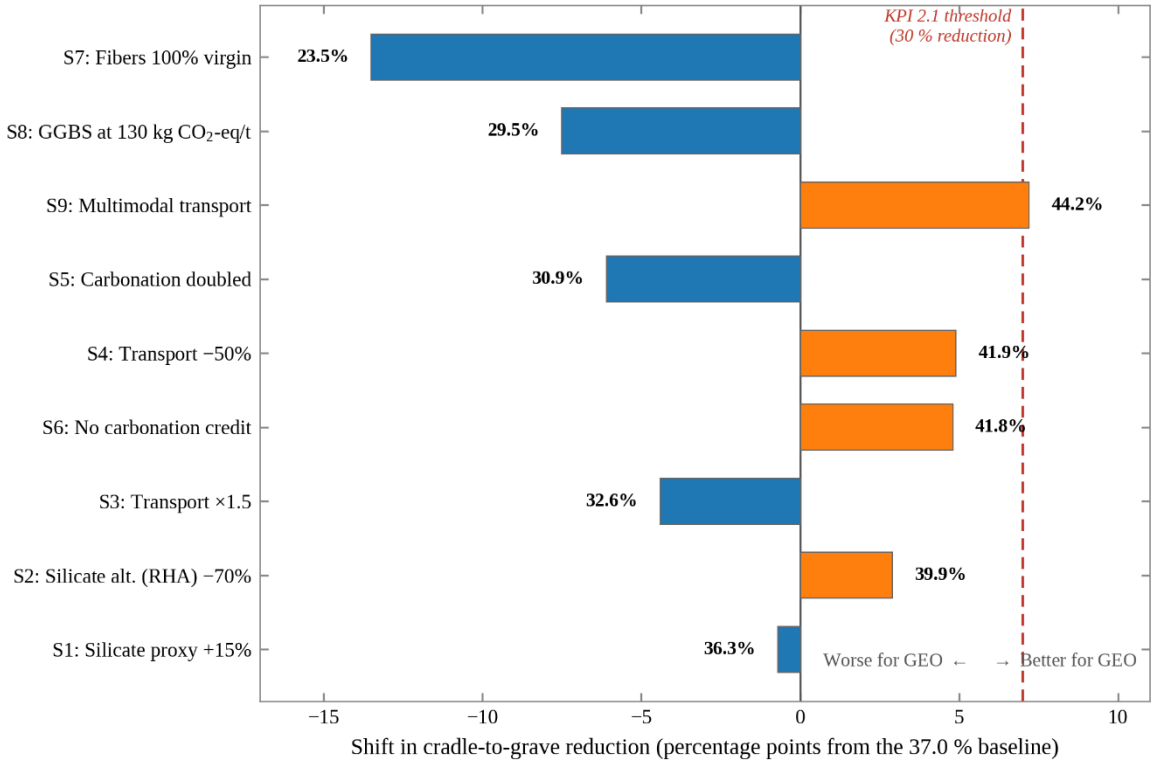

Figure 4-26: Sensitivity tornado plot of the GEO/REF-EPD cradle-to-grave GWP delta under nine one-at-a-time perturbations from the baseline.

The tornado identifies three strata of leverage:

First stratum, dominated by S8 (GGBS at economic allocation), shifts the headline by 7.5 percentage points, from −37% to −29.5%, taking the result below the 30% threshold. This is the accounting choice to which the result is most sensitive, and it does so by reassigning to the GGBS precursor the high upstream burden of primary iron-and-steel production that mass allocation legitimately attributes to the blast furnace's principal products rather than to the slag by-product. The allocation rule for slag is contested. Habert and Ouellet-Plamondon (2016) note that the European end-of-waste directive means blast

furnace slag can no longer be classified as waste but as a by-product, so an allocation is in principle required. The present work adopts the supplier-specific cut-off value, and the target fails for any slag factor above approximately 120 kg CO_2-equivalent per t.

Second stratum, dominated by S7 (fibers reset to 100% virgin), shifts the headline by about 13 percentage points, quantifying the hybrid-fiber recycling advantage as a substantive but secondary lever worth roughly one-third of the cradle-to-grave advantage. S7 is also the only perturbation other than the slag allocation that takes the result below the 30% threshold, at 23.5%. Unlike the slag treatment it is not an accounting convention but a supply condition, so the carbon verdict depends on continued availability of the recycled fiber stream as well as on the accounting rule for slag.

Third stratum shifts the headline by 4 to 7 percentage points each, the transport and carbonation levers, which bracket the headline without changing its direction. S1 and S2 shift it by less than 3 percentage points, confirming the silicate background process is not a first-order lever despite being 5% of the A1 burden. The lever ranking is therefore: GGBS allocation, fiber recycling, transport routing, carbonation crediting, silicate inventory, in decreasing order.

4.7.3 Robustness verdict

The most consequential finding is the lower bound on the GEO advantage. Across the nine scenarios the cradle-to-grave reduction ranges from −23.5% (S7, worst case) to −44.1% (S9, best case), with the baseline at −37%. GEO emits less than REF-EPD in every one of the nine scenarios, but two of them fall below the 30% project threshold, so the qualitative advantage is robust while the KPI verdict is conditional. The two are S7, the virgin-fiber case at −23.5%, and S8, the slag-allocation case at −29.5%. The comparative conclusion is therefore not contingent on any single inventory or methodological choice: the qualitative finding that the GEO formulation reduces the carbon footprint of UHPC relative to a verified Portland reference is robust across the full set of perturbations.

Two qualifications are made explicit, in keeping with the honest reporting standard of this chapter.

First, S8 lowers the reduction by 7.5 percentage points to 29.5%, just below the KPI 2.1 threshold of 30%, and would fail the project's binary verdict if that allocation were the chosen rule. The present work adopts the supplier-specific cut-off factor for the slag and mass allocation for all other flows, consistent with the REF-EPD declaration and with practice in the alkali-activated assessment literature (Habert et al., 2013; Provis and Deventer, 2014). The KPI 2.1 verdict of Section 4.9 is therefore conditional on this allocation rule and is documented as such.

Second, the analysis is a one-at-a-time perturbation that does not capture compounding of two unfavorable levers. A combined stress test (S8 plus S3 plus S5) would

compress the advantage by approximately 18 percentage points relative to baseline, placing the result near −19%, still a GEO advantage but well below the KPI threshold. This combination is not reported as a separate entry because the joint probability of all three unfavorable levers materializing is low, but the reader should treat the one-at-a-time analysis as a lower bound on the methodological uncertainty rather than a full envelope.

4.8 Economic analysis

The environmental case for the GEO mix established in Sections 4.6 and 4.7 is necessary but not sufficient for industrial adoption: the NATURSEA-PV project framework imposes a second binding KPI on the cost-to-strength ratio of the candidate material, set at a reduction above 35% relative to the project reference UHPC (KPI 2.2). This section evaluates the cost-to-strength of the GEO mix on a materials-only basis, following the scope adopted by the predecessor economic study in the same laboratory (Monteiro, 2023): raw material costs at the plant gate, excluding transport, labor, plant overhead, and commercial margin.

In the absence of procurement-stage quotations for every component, each unit price in the inventory is labeled by its evidence basis, ranked from supplier quotation to commodity price index to market estimate, and the result is reported as a documented price envelope rather than a point value. The analysis is anchored on Figure 4-27, which places the GEO envelope and the REF-EPD reference in cost-to-strength versus carbon-to-strength space against the two NATURSEA-PV thresholds.

4.8.1 Price basis, procurement tiers, and evidence quality

Two procurement scales must be distinguished before any cost figure is quoted, because the dominant cost driver of the geopolymer formulation, the alkaline activator, is priced differently by two orders of magnitude depending on the supply channel. The laboratory scale is what was actually paid for the experimental work of Chapters 1 to 4: reagent-grade potassium hydroxide (Sigma-Aldrich P1767 or equivalent laboratory-supply products at comparable price tiers) at 70.50 € per kg, which yields a laboratory materials cost of 4946 € per m^3 of GEO. The premium over industrial supply covers analytical-grade purity certification, small-batch packaging, and the laboratory logistics chain.

The KOH molecule itself is chemically identical in both channels. The laboratory figure is reported for transparency and is excluded from the KPI evaluation, since KPI 2.2 is defined for an industrial deployment scenario and no factory would procure activator chemicals through a laboratory-reagent channel. The industrial scale is the relevant basis for the KPI, and it is priced component by component in Table 4-8.

One component of the industrial inventory is anchored on a formal supplier quotation, and it is the single most consequential line of the cost table. The sodium silicate solution (Betol 47T, 44.5% solids by mass, silica modulus 1.66) was quoted at 1130 € per t EXWORKS in 300 kg drums by the supplier during the experimental campaign. The LCA inventory carries the silicate on a dry-mass basis at 71.2 kg per m^3, which corresponds to 160 kg of solution per m^3 at the declared solids content, so the quoted price applies to 160 kg and contributes 180.8 € per m^3, the largest single line of the GEO materials cost.

The same quotation documents the procurement-tier effect directly: the 30 kg jerrycan tier of the identical product was offered at approximately 2.23 € per kg of material before transport and handling surcharges, so the step from jerrycans to 300 kg drums alone halves the unit price. A further reduction at tanker-scale supply is plausible for a factory consuming of the order of 100 tons of silicate solution per year, but no tanker-tier quotation is in hand, and the drum price is therefore retained as the conservative documented value. The potassium hydroxide, by contrast, has no quotation in hand and is bracketed by two independent commodity price indices: the European bulk-tier index at approximately 0.65 to 0.80 € per kg and the France-specific index for early 2026 at approximately 1.40 to 1.50 € per kg. The two sources span 0.75 to 1.50 € per kg.

In the absence of a supplier quotation for the potassium hydroxide, the arithmetic mean of 1.125 € per kg is carried through the cost table as a single representative value, and the effect of the full range on the verdict is examined below. The remaining components (GGBS, silica fume, sand, the two fiber streams, and water) are priced at single-point market estimates and are labeled as such. Their combined contribution of 294 € per m^3 is dominated by the silica fume and the virgin fiber lines, and none of them individually approaches the leverage of the activator subsystem.

Table 4-8: Materials-only cost inventory of the GEO mix at industrial scale.

Component	Mass (kg/m^3)	Unit price	Cost (€/m^3)	Evidence basis
GGBS	720	65 €/t	46.8	(Youssef et al., 2020)
Silica fume (densified, UHPC grade)	180	750 €/t	135.0	Market estimate, Grade 92 class
Sodium silicate solution (Betol 47T, 44.5% solids)	160	1130 €/t	180.8	Supplier quotation, EXWORKS, 300 kg drums
Potassium hydroxide (dry, technical grade)	64.8	1125 €/t	72.9	Commodity indices, bulk grade
Quartz sand (fine + coarse)	975	15 €/t	14.6	Market estimate

Component	Mass (kg/m^3)	Unit price	Cost (€/m^3)	Evidence basis
Recycled steel fibers (Flexofibers)	64.8	500 €/t	32.4	Market estimate
Virgin drawn steel fibers (Spajic)	43.2	1500 €/t	64.8	Market estimate
Tap water	115.2	2.5 €/m^3	0.3	Estimate
Total, GEO materials	2234	-	548	KOH mean index value of 1.125€/kg

4.8.2 Cost-to-strength against KPI 2.2

The REF-EPD cost is taken from the supplier price sheet at 583 € per m^3 of fresh concrete, a publicly disclosed commercial price alongside the verified EPD. On the declared characteristic strength of 130 MPa, the REF-EPD cost-to-strength is 4.48 € per m^3 per MPa, and the KPI 2.2 threshold of a 35% reduction corresponds to a ceiling of 2.92 € per m^3 per MPa. On the industrial materials basis, with the potassium hydroxide priced at the mean index value of 1.125 € per kg, the GEO mix costs 548 € per m^3, which at the 137 MPa cube strength yields a cost-to-strength of 4.00 € per m^3 per MPa, a reduction of 10.9% relative to REF-EPD. This sits above the KPI 2.2 ceiling of 2.92 € per m^3 per MPa, so the target is not met, with a residual gap of 24 percentage points. The verdict is robust to the potassium hydroxide price uncertainty across the full index range: at the low end of 0.75 € per kg the reduction reaches 14.8%, at the high end of 1.50 € per kg it falls to 6.9%, and at no point does it approach the 35% target.

It is also sensitive to the strength basis, and this should be stated. The comparison above uses the declared characteristic strength of 130 MPa for REF-EPD, which is the performance the commercial price warrants and therefore the coherent pairing with a price sheet. Section 4.4.2 reports a measured mean of 145 MPa for the same material on the same cube geometry and curing regime as the GEO value. On that like-for-like measured basis the two mixes give 4.00 against 4.02 € per m^3 per MPa, a reduction of 0.5%, so essentially the whole of the reported 10.9% derives from comparing a measured GEO mean against a declared REF minimum. Under either basis the KPI is not met, and the residual gap is 24 percentage points on the declared basis and 34.5 on the measured one. Table 4-9 summarizes the comparison and Figure 4-27 places it in the two-dimensional KPI space.

Two qualifications bound this verdict, and they pull in opposite directions, which is precisely why the verdict must remain provisional pending a procurement-stage quotation campaign.

The first qualification is unfavorable to GEO: the comparison is asymmetric, because the REF-EPD figure is a commercial product price that includes plant conversion cost, quality control, and margin, whereas the GEO figure is a raw-materials cost that includes none of these. Adding a plant conversion cost, a commercial margin, and the inbound freight of the raw materials to the deployment-region plant to the GEO side would widen the gap further. The inbound freight is not negligible: the A2 transport inventory of Section 4.5.3 carries of the order of 810 ton-kilometers per m^3, dominated by the GGBS supply, and the same materials-only scope was adopted for the same reason by the predecessor economic study in this laboratory, which estimated the excluded geopolymer freight at 100 to 200 euros against approximately 10 euros for the cement system whose plants sit closer to the port (Monteiro, 2023). The reduction of 10.9% is therefore an upper bound on the product-level advantage rather than a central estimate.

The **second** qualification is favorable to GEO: both activator prices in the envelope are conservative for a true factory scale. The silicate is priced at the 300 kg drum tier although the quotation itself demonstrates that each step up in order volume roughly halves the unit price, and the upper end of the KOH envelope is a single-country monthly spot index rather than a contracted bulk price.

A quotation campaign covering a chlor-alkali producer for the KOH and a tanker-tier silicate supply would resolve both qualifications. It is flagged as the follow-up activity that finalizes the KPI 2.2 verdict, and the present chapter reports the verdict as not met on the documented materials basis.

Table 4-9: Cost-to-strength of the GEO and REF mixes against the KPI 2.2 threshold.

Case	Strength (MPa)	Cost (€/m^3)	Cost-to-strength (€/m^3/MPa)	Δ vs REF-EPD
REF-EPD (declared characteristic)	130	583	4.48	-
REF-EPD, (measured mean)	145	583	4.02	-
GEO industrial materials (KOH at mean index price)	137	548	4.00	−10.9%
KPI 2.2 target (−35% vs REF-EPD)	-	399	2.92	−35% (target)

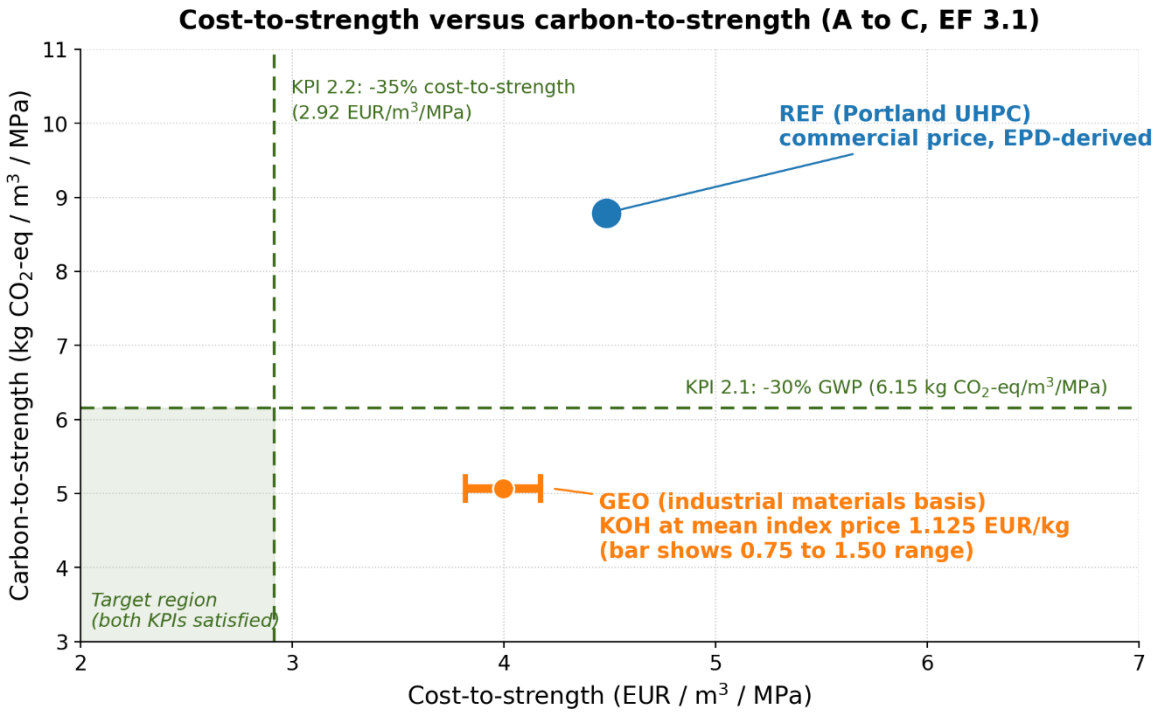

Figure 4-27: KPI dashboard of the REF-EPD and GEO mixes in cost-to-strength versus carbon-to-strength space.

4.8.3 Cost-carbon coupling and the path to the target

The structural finding of this section is not the verdict itself but the location of the residual gap. The activator subsystem (sodium silicate plus potassium hydroxide) carries 44 to 49% of the GEO materials cost across the documented envelope, and the same subsystem carries approximately 69% of the A1 carbon burden established in Section 4.6.2. The cost gap and the carbon hotspot are therefore the same lever, which is consistent with the near-linear coupling between activator dosage, cost, and carbon reported by McLellan and colleagues (McLellan et al., 2011) across 40 published geopolymer formulations.

Two consequences follow. **First,** any reduction of the activator dosage in subsequent formulation work, or a partial substitution of the hydroxide by sodium carbonate along the route demonstrated for strain-hardening UHPGC by Lao and colleagues (Lao et al., 2023), acts on KPI 2.1 and KPI 2.2 in parallel rather than trading one against the other. **Second,** the comparison is sensitive to any future internalization of the carbon cost: the cradle-to-grave gap of 406 kg CO_2-equivalent per m^3 in favor of GEO is an economic asset under any carbon pricing mechanism, and a materials-only comparison at current prices systematically understates the economic position of the low-carbon mix in a decarbonizing regulatory environment.

The chapter therefore closes the economic analysis with a conditional verdict: KPI 2.1 is met, subject to the conditions set out in Section 4.7. KPI 2.2 is not met on the

documented materials basis, and the single lever that closes the residual cost gap is the same activator subsystem that dominates the remaining carbon burden.

The activator dosage is not a free parameter available for cost reduction. Chapter 1 established that the activator-to-binder ratio was optimized downward across Stage 3, from 0.50 through 0.40 to 0.30, and that reducing it more than doubled the 24-hour compressive strength, a gain read as the removal of a passivating silicate barrier on the slag particle surfaces but not isolated from the co-varying water-to-binder ratio.

The deployed formulation sits at 0.38 with a silicate-to-hydroxide ratio of 0.89, selected as the composition satisfying all five acceptance criteria simultaneously. The residual cost and carbon burden of the activator therefore cannot be reduced by lowering the dosage, since the dosage is already at a value determined by the strength and open-time targets rather than by cost. Closing the gap requires either a cheaper hydroxide supply, through contracted bulk procurement rather than spot indices, or partial substitution of the potassium hydroxide by a lower-carbon and lower-cost alkali source.

4.9 Conclusion

The chapter asked whether the distinct binder chemistry of GEO confers net durability advantages over REF under marine-relevant aggression, or whether the gains are offset by losses in thermal performance, and whether the resulting material delivers the carbon and cost-to-strength advantages needed to justify replacing conventional UHPC in offshore floating photovoltaic substructures.

Durability was assessed through sulfate and acid immersion over 52 weeks, residual strength after exposure to 900 °C, rapid chloride penetration, a year of impedance monitoring, and a 10-month marine campaign at the HarshLab floating facility. Environmental and economic performance were assessed through a cradle-to-grave carbon footprint under EN 15804+A2 and a materials-cost comparison, both against the same verified reference declaration. Table 4-10 summarizes the position against the project acceptance envelope; the four verdicts are set out below.

Table 4-10: Position of GEO against the NATURSEA-PV acceptance envelope.

Criterion	Target	GEO	Verdict
24-hour compressive strength	≥ 65 MPa	65 MPa	Met
28-day compressive strength	≥ 130 MPa	137 MPa	Met
Slump flow	200 to 250 mm	208 mm	Met
Open time	≥ 20 min	23 min	Met
Recycled fiber content	≥ 35 wt%	60 wt%	Met

Marine durability	6 months	10 months, full class retained (1 to 3 prisms per group)	Met
Service life	50 years	Not tested directly; Fick estimate about 28 to more than 100 years	Not demonstrated
KPI 2.1, carbon reduction	**> 30%**	**37% per m³, 32.1% per ton**	**Met, conditional**
KPI 2.2, cost-to-strength reduction	**> 35%**	**10.9%** (declared REF strength); 0.5% (measured means)	**Not met**

On durability the answer is affirmative over the exposures tested, and specific to each medium and indicator. GEO shows a clear advantage over REF in sodium sulfate and nitric acid, but it expands by about 0.17% in magnesium sulfate and 0.21% in the combined solution at 52 weeks, above the 0.10% ASTM C1012 screen, and in every aggressive bath its flexural retention falls below its compressive retention, a pattern read as the aggressor reaching the fiber-matrix interface; the magnesium mechanism remains a hypothesis without post-exposure phase analysis. Both binders sit in the UHPC range on chloride, with the charge, apparent diffusion coefficient and resistivity drawn from one measurement. Ten months of real marine exposure supported these laboratory findings, with retained alkalinity, no detectable chloride front, and retention of the mechanical class in every exposure zone, on one to three prisms per group and without same-age unexposed controls. The campaign also carried the two bio-based protective coatings developed within the project. No effect of either coating was resolvable at these replicate counts, where a difference of the order of 10% would not be detected, so a coating effect can be neither demonstrated nor excluded. Its single disadvantage, elevated-temperature strength retention, lies outside the service conditions of a floating substructure.

A one-dimensional Fickian estimate of the time to corrosion initiation, using the uncorrected GEO diffusion coefficient of 6.9×10^{-13} m²/s, a clear cover of 40 to 50 mm, a surface chloride content of 0.5 to 0.8% by mass of binder, and a critical threshold of 0.2 to 0.4%, gives more than 100 years under moderate marine assumptions and approximately 28 years under the most aggressive combination within those ranges. The estimate therefore brackets the fifty-year design life rather than clearing it uniformly. It is not a lifetime prediction, since a constant-coefficient diffusion model with a single ingress mechanism cannot support extrapolation of that length; it indicates only that chloride-induced corrosion initiation is not expected to govern under moderate assumptions, and cannot be excluded as governing under the most aggressive.

On carbon the answer is affirmative (Section 4.6), **subject to two conditions; across the nine sensitivity scenarios of** Section 4.7 **the reduction spans** 23.5 to 44.1%, and two

scenarios fall below the 30% threshold. The first is the accounting treatment of the slag precursor: the baseline adopts a cut-off factor of 15.7 kg CO_2-equivalent per ton, and allocating two percent of steel production to the slag lowers the reduction to 29.5%, the threshold being crossed at approximately 120 kg per ton. The second is the fiber system: replacing the 60 wt% recycled content with virgin drawn steel lowers the reduction to 23.5%. The headline is nonetheless the methodologically conservative position, since the asymmetric carbonation credit it includes favors the reference; removing that credit from both mixes widens the reduction to 41.7%.

On cost the answer is negative (Section 4.8) **as the material is currently costed**, and the gap is not marginal. The verdict is robust to the residual hydroxide price uncertainty across the full index range, from 14.8% at the low end to 6.9% at the high end, and to the strength basis, since on the measured means of both mixes the difference narrows to 0.5%. Two asymmetries bound it in opposite directions: the reference figure is a commercial sold price while the GEO figure excludes conversion cost, margin, and inbound freight, which makes 10.9% an upper bound rather than a central estimate; and both activator prices are conservative for factory-scale procurement, since the silicate is quoted at drum tier and the hydroxide at spot-index rather than contract prices.

The chapter therefore returns a divided answer, and the division is informative rather than incidental: GEO retained its performance over the marine exposures tested and is substantially lower in carbon; it is not, at documented material prices, cheap enough to meet the project cost target. The two residual findings converge on one subsystem: the alkaline activator carries 46% of the material cost and 69% of the production-stage carbon burden, so the remaining cost gap and the remaining carbon burden are not competing objectives but a single lever. That lever is narrower than it appears, because Chapter 1 established that the activator-to-binder ratio was already optimized downward across the formulation stages, from 0.50 through 0.40 to 0.30, with the deployed mix at 0.38 selected as the composition satisfying all five acceptance criteria simultaneously. The dosage is therefore set by the strength and open-time targets rather than by cost, and closing the gap requires a cheaper hydroxide supply or partial substitution of the activator system rather than a reduction in dosage. Subject to that qualification, the evidence supports the central proposition of the thesis on the dimensions that decide technical feasibility: a 100% cement-free, ambient-cured UHPGC can retain its UHPC mechanical class and chemical resistance over the exposures tested here, twelve months of immersion and ten months at sea, at a cradle-to-grave carbon footprint 37% below the conventional Portland UHPC it is intended to replace in the baseline scenario. Whether this durability extends to the fifty-year design life requires longer exposure and an aging model. Whether it can also do so at a competitive cost depends on procurement decisions that lie outside the laboratory.

4.9.1 Limitations and perspectives

- **Durability:** The marine campaign covers ten months against a fifty-year design life, on one to three prisms per group and without same-age unexposed controls, so the retention of mechanical class and the absence of a detectable chloride front are demonstrated over that period and not extrapolated.
- **Carbon, the slag convention:** The accounting treatment of the precursor remains open, since it turns on a convention still in transition, and the verdict is stated as conditional for that reason.
- **Carbon, the fiber supply:** The recycled fiber stream is a procurement channel not yet secured at production scale.
- **Cost:** The comparison is asymmetric in a direction that favors GEO, and both activator prices are conservative for factory scale, so the two asymmetries pull against each other and neither is resolved here.
- **Scope:** The assessment quantifies a single impact category, global warming potential. Burden-shifting to other impact categories was not tested and cannot be excluded on the basis of the data reported here.

A procurement-stage quotation campaign covering a chlor-alkali producer for the hydroxide and a tanker-tier silicate supply would settle the cost verdict by resolving both asymmetries at once. Partial substitution of the potassium hydroxide by a lower-carbon alkali source would act simultaneously on the residual cost gap and the residual carbon burden. And marine exposure beyond ten months would convert the demonstrated durability into a validated service-life prediction.

General Conclusions

Offshore floating photovoltaics require a substructure that survives decades of open-sea service, and the material class that currently meets that envelope, Portland-cement UHPC, carries an embodied carbon near the upper bound of the construction sector. This thesis asked whether the Portland binder can be removed altogether: can a 100% cement-free, ambient-cured UHPGC reach the mechanical and durability performance required to survive harsh marine environments and replace conventional UHPC in offshore floating photovoltaic substructures?

Chapter 1: **Formulation and characterization**

A six-stage, bottleneck-driven optimization was conducted, each stage resolving the limiting factor identified at the previous one. It produced GEO, a binary GGBS and silica fume binder at 900 kg/m^3 activated by sodium silicate and 10 M KOH, reinforced by a 60/40 recycled to virgin steel fiber blend at 12 wt% of binder. The results showed:

- The five NATURSEA-PV criteria met simultaneously under ambient curing: 65 MPa at 24 hours, met exactly and without margin, and 152 ± 5 MPa, 208 mm slump flow, 23 minutes open time, and 60 wt% recycled fiber
- Precursor calcium content rather than the activator as the descriptor controlling the achievable strength regime
- An empirical strength optimum organized by the absolute sodium silicate dosage, in the 160 to 190 kg/m^3 band
- The Na+ to K+ substitution at equal molarity breaking the strength-workability trade-off that constrains NaOH-activated slag (an activation-route comparison in which the water-to-binder ratio co-varies slightly; the cation mechanism is an interpretation)
- A residual 8% gap to REF associated with the absence of an induction period, GEO reaching its exotherm at 5.6 hours against 38.2 and locking in a capillary network of 700 against 6.2 nm dominant pore entry, in a portlandite-free C-(N,K)-A-S-H gel at Ca/Si 0.39 against 1.72

Objective 1 is met. To the author's knowledge this is the first reported UHPGC combining ambient curing, a fly-ash-free binary GGBS and silica fume binder, KOH activation above 130 MPa, and over 60 wt% recycled tire-derived steel fibers in one mix design.

Chapter 2: **Electrochemical impedance spectroscopy**

Electrochemical impedance spectroscopy was applied non-destructively at eight curing ages from 1 to 28 days, from 4 Hz to 5 MHz, with the spectra validated by Kramers-Kronig consistency checks and fitted by complex nonlinear least-squares to physically motivated equivalent circuits. The results showed:

- An impedance magnitude one to two orders lower in GEO than in REF at every age

- A single-stage two-arc topology for GEO, against a stage-dependent topology for REF that adds a third interfacial arc from Day 10
- No interfacial arc resolvable in GEO at any age, consistent with the cohesive fiber-matrix interface identified in Chapter 1
- Binder-specific strength indicators, the gel pore resistance R2 for REF (Pearson r = 0.987 on log axes) and the Warburg coefficient W for GEO (r = 0.983)
- An irregular response of GEO between Days 10 and 21, interpreted as a gel reorganization but not confirmed, two of the five affected observables having fitting causes, which disqualifies R2 in that binder and leaves W robust

These results establish that a cement-free UHPC is open to the same class of electrochemical quality control as conventional UHPC, provided the indicator is calibrated to the binder chemistry. No universal parameter serves both.

Chapter 3: **Acoustic emission and fracture mechanics**

Multi-parameter acoustic emission was recorded under three-point bending on a two-by-two design in binder chemistry and fiber inclusion, at 24 hours and 28 days, with fiber type and volume held constant (120 kg/m³ of virgin fibers, not the deployed 108 kg/m³ recycled-virgin blend) and attenuation calibrated on every specimen. The results showed:

- Two distinct fracture pathways, cross-anchored to the fracture surfaces of Chapter 1, friction-dominated interfacial pull-out in the cementitious composite and cohesive matrix debonding in the geopolymer
- Fiber addition raising the shear fraction of the cementitious composite by 6.8 points at 28 days and lowering that of the geopolymer by 4.7
- Median signal durations of 168 µs in the cementitious composite against 72 µs in the geopolymer
- A toughness crossover, 30.20 against 25.05 J at 24 hours in favor of the geopolymer and 34.98 against 46.67 J at 28 days against it, consistent with frictional capacity growing with the maturing interface while debonding is engaged from the first day
- A continuum-damage model calibrated on the measured flexural response reproducing the peak load to within 1.3% and the crack localization, but not the post-peak branch, which the perfect-bond fiber representation cannot carry

Objective 2 is therefore met on both the electrochemical and the fracture side, the binder difference established in Chapter 1 carrying through to the fracture process itself.

Chapter 4: **Marine durability and carbon footprint assessment**

Twelve months of sulfate and acid immersion, rapid chloride migration and elevated-temperature programs, and a ten-month offshore campaign at HarshLab across atmospheric, splash, and immersed zones were combined with a cradle-to-grave carbon and cost assessment following the module structure of EN 15804+A2. The results showed:

- A GEO advantage over REF in sodium sulfate and nitric acid, interpreted as the absence of portlandite closing the ettringite pathway and a self-limiting surface layer replacing an advancing dissolution front, but an expansion of about 0.17% in magnesium sulfate and 0.21% in the combined solution at 52 weeks, above the 0.10% ASTM C1012 screen, and a flexural retention below the compressive retention in every aggressive bath.
- Chloride resistance in the UHPC range for both binders, all five tested mixes in the negligible corrosion-risk resistivity class, the charge, apparent diffusion coefficient and resistivity being three outputs of one measurement, with retained alkalinity and no chloride or carbonation front detected by colorimetry after real immersion.
- Retention of the UHPC mechanical class in every exposure zone after ten months at sea, on one to three prisms per group and without same-age unexposed controls, with no coating effect resolvable at these replicate counts.
- A single disadvantage, 36% compressive retention at 600 °C against 90% for the one REF specimen that survived intact, lying outside the service envelope, with the integrity ranking reversed.
- A carbon reduction of 37% per m^3 and 32.1% per ton, meeting KPI 2.1 conditionally as a comparative carbon footprint on global warming potential alone, the reduction spanning 23.5 to 44.1% across nine sensitivity scenarios and falling below 30% only under a 2% steel allocation to the slag or a return to virgin fiber.
- A cost-to-strength reduction of 10.9% on the declared REF strength and 0.5% on the measured mean strengths of both mixes, against a 35% target, leaving KPI 2.2 unmet at documented material prices; since the REF figure is a commercial price and the GEO figure a raw-material cost, neither value is a product-level economic advantage.

Objective 3 is met over the exposures tested. Objective 4 is met for carbon, conditionally, and not met for cost.

The answer to the central question is therefore affirmative at the level of a laboratory specification and over the exposures tested, and conditional on the dimension deciding commercial adoption. Meeting the NATURSEA-PV targets is not an engineering validation: a fifty-year service life, shrinkage and drying cracking, cyclic loading, scale effects and production variability remain outside the present demonstration. Both residual burdens converge on a single subsystem, the activator carrying 46% of the material cost and 69% of the production-stage carbon, and since Chapter 1 already drove that ratio from 0.50 to 0.38 under the strength and open-time constraints, the lever is procurement and partial substitution rather than dosage reduction. Four limitations bound the conclusion, none reversing the directional findings but each qualifying the precision of the supporting numbers: single-batch transport and mechanical results, fracture pathways identified on n = 2 cells, a numerical description calibrated on one curve and not independently validated, and an unmeasured formation factor.

Read by strength of evidence, the findings fall into three groups. Measured directly: the five acceptance criteria on laboratory batches, the pore-structure contrast between the

binders, the binder-specific impedance correlations, the acoustic emission descriptors and the toughness crossover, the mass, length and strength responses over 52 weeks of immersion, the retention of mechanical class after ten months at sea, and the carbon and cost figures under the stated inventory and prices. Interpreted, consistent with the data but not isolated: silicate passivation, the cation mechanism behind the Na^{+} to K^{+} substitution, the intermediate-age gel reorganization of GEO, the frictional and cohesive fracture pathways, the fiber-matrix interface as the site reached by the aggressors, and the magnesium mechanism in the sulfate baths. Extrapolated and awaiting validation: a fifty-year service life, production-level compliance with the 24-hour criterion, behavior under shrinkage, cyclic loading and at precast scale, the transfer of the fracture conclusions to the recycled-fiber blend, and the product-level cost position.

Perspectives

The results open several directions, organized along three axes: completing the description of the material, extending its envelope to service conditions that were not tested, and moving from the specimen to the substructure.

- **Completing the description:**

Two extractions would convert two upper bounds into measurements: 29Si MAS NMR or selective dissolution to separate the gel from the unreacted precursor and yield a measured gel content, and a pore-solution extraction to anchor a formation factor and make the transport comparison of Chapter 4 quantitative rather than indicative. Time-resolved in-situ diffraction or nuclear magnetic resonance across Days 10 to 21 would establish whether the irregular response of GEO in that window is a gel reorganization, as inferred from three of the five affected impedance observables, and settle whether the gel pore resistance is recoverable as a GEO indicator outside that window. Completing the EN 15804+A2 indicator set beyond global warming potential, and resolving the slag allocation convention on which the carbon verdict is conditional, would convert the present carbon footprint into a full life cycle assessment. A design of experiments around the selected mix would map its neighborhood and test whether the sequential path converged on a local rather than a global optimum. Direct characterization of the fiber-matrix interface after failure, by SEM-EDS line scans or nanoindentation, would test the frictional and cohesive pathways inferred from acoustic emission. For impedance, a matched-fiber series, a frequency ceiling above 10 MHz, additional batches, and circuit-free analyses of the full spectrum would move from a binder-specific calibration toward a multidimensional maturation signature.

- **Extending the envelope :**

Drying and autogenous shrinkage, and restrained-shrinkage cracking, were not addressed here and are developed more strongly by alkali-activated slag than by Portland systems, and they are the first properties to measure before any thick-section application. Fatigue under cyclic loading representative of wave action, monitored by acoustic emission, would close a gap this manuscript itself opens, since cyclic performance is named in the introduction as a design driver and only monotonic loading was applied. Marine exposure beyond ten months, with alkali leaching and the corrosion state of the fibers quantified on retrieval, would convert a demonstrated durability into a validated service-life prediction. Replacing the perfect-bond fiber representation by an explicit interface law calibrated on single-fiber pull-out would extend the model to the post-peak response and to the recycled fiber system, with a formal mesh-convergence study at the same stage. Flow retention over the open-time window, measured on the complete fiber-reinforced concrete, would turn the setting-based open time into a placement guarantee. The acoustic emission campaign should be repeated on the 60/40 recycled blend and at 90 days and one year, to test whether the

toughness hierarchy observed at 28 days is stable, and single-fiber pull-out on aged recycled fibers would quantify the long-term effect of the rubber residue on bond. Future marine campaigns should include same-age unexposed controls, post-exposure diffraction and chloride titration profiles, and feed an aging model with a time-dependent diffusion coefficient and chloride binding.

- **From specimen to substructure :**

A heat-transfer and shrinkage calculation at the 300 to 500 mm section scale of a floater, fed by the measured release curves, would quantify delayed ettringite risk in REF and thermal-gradient cracking risk in GEO. A procurement campaign at chlor-alkali and tanker tier, together with partial substitution of the hydroxide, acts on the residual cost gap and the residual carbon burden simultaneously rather than trading one against the other. Batch reproducibility at precast scale, with the binder-specific EIS indicators as in-line control and a loaded structural element as its terminus, would also raise the replicate counts that currently bound the single-batch transport results and the n = 2 fracture cells. A lot-to-lot robustness study on several lots of slag, silica fume and recycled fibers, with the 24-hour criterion set on a characteristic value rather than a mean, is the precondition for production. On the activator, the lever is the source rather than the dose: potassium hydroxide from low-carbon chlor-alkali electricity, a silicate from rice-husk ash, or a one-part activator.

References

Abdellatief, M., Elrahman, M., Abadel, A., Wasim, M., Tahwia, A., 2023. Ultra-high performance concrete versus ultra-high performance geopolymer concrete: Mechanical performance, microstructure, and ecological assessment.

Aggelis, D.G., 2011. Classification of cracking mode in concrete by acoustic emission parameters. Mechanics Research Communications 38, 153–157. https://doi.org/10.1016/j.mechrescom.2011.03.007

Aggelis, D.G., Mpalaskas, A.C., Matikas, T.E., 2013a. Acoustic signature of different fracture modes in marble and cementitious materials under flexural load. Mechanics Research Communications 47, 39–43. https://doi.org/10.1016/j.mechrescom.2012.11.007

Aggelis, D.G., Verbruggen, S., Tsangouri, E., Tysmans, T., Van Hemelrijck, D., 2013b. Characterization of mechanical performance of concrete beams with external reinforcement by acoustic emission and digital image correlation. Construction and Building Materials 47, 1037–1045. https://doi.org/10.1016/j.conbuildmat.2013.06.005

Aiello, M.A., Leuzzi, F., Centonze, G., Maffezzoli, A., 2009. Use of steel fibres recovered from waste tyres as reinforcement in concrete: Pull-out behaviour, compressive and flexural strength. Waste Management 29, 1960–1970. https://doi.org/10.1016/j.wasman.2008.12.002

Aiken, T.A., Kwasny, J., Sha, W., Soutsos, M.N., 2018. Effect of slag content and activator dosage on the resistance of fly ash geopolymer binders to sulfuric acid attack. Cement and Concrete Research 111, 23–40. https://doi.org/10.1016/j.cemconres.2018.06.011

Aki, K., 1965. Maximum likelihood estimate of b in the formula log10 N= a-bM and its confidence limits. Bulletin of Earthquake Research 43, 237.

Alameri, M., Joseph, J., Mohamed Ali, M.S., Elchalakani, M., Sheikh, A.H., 2025. Optimising GGBS-based ultra high-performance geopolymer mortar: an orthogonal array approach. Australian Journal of Structural Engineering 26, 95–110. https://doi.org/10.1080/13287982.2024.2375468

Alexander, C.L., 2026. Electrochemical impedance spectroscopy for corrosion diagnosis of reinforced concrete. Current Opinion in Electrochemistry 55, 101790. https://doi.org/10.1016/j.coelec.2025.101790

Alsalman, A., Assi, L.N., Kareem, R.S., Carter, K., Ziehl, P., 2021. Energy and CO2 emission assessments of alkali-activated concrete and Ordinary Portland Cement concrete: A comparative analysis of different grades of concrete. Cleaner Environmental Systems 3, 100047. https://doi.org/10.1016/j.cesys.2021.100047

Ambily, P.S., Umarani, C., Ravisankar, K., Prem, P.R., Bharatkumar, B.H., Iyer, N.R., 2015. Studies on ultra high performance concrete incorporating copper slag as fine aggregate. Construction and Building Materials 77, 233–240. https://doi.org/10.1016/j.conbuildmat.2014.12.092

Amran, M., Huang, S.-S., Onaizi, A.M., Makul, N., Abdelgader, H.S., Ozbakkaloglu, T., 2022. Recent trends in ultra-high performance concrete (UHPC): Current status, challenges, and future prospects. Construction and Building Materials 352, 129029. https://doi.org/10.1016/j.conbuildmat.2022.129029

Andrade, C., 1993. Calculation of chloride diffusion coefficients in concrete from ionic migration measurements. Cement and Concrete Research 23, 724–742. https://doi.org/10.1016/0008-8846(93)90023-3

Andrade, C., Sanjuán, M.Á., 2018. Updating Carbon Storage Capacity of Spanish Cements. Sustainability 10, 4806. https://doi.org/10.3390/su10124806

Angelis, D., Grosse, C., Masayasu, O., Shiotani, T., 2018. Acoustic Emission Testing: Basics for Research-Appllication in Civil Engineering, Springer Tracts in Civil Engineering. Springer. https://doi.org/10.1007/978-3-030-67936-1

Aydın, S., Baradan, B., 2013. The effect of fiber properties on high performance alkali-activated slag/silica fume mortars. Composites Part B: Engineering 45, 63–69. https://doi.org/10.1016/j.compositesb.2012.09.080

Bakharev, T., 2005. Resistance of geopolymer materials to acid attack. Cement and Concrete Research 35, 658–670. https://doi.org/10.1016/j.cemconres.2004.06.005

Barsoukov, E., 2005. Impedance spectroscopy theory, experiment, and applications. Wiley Online Library.

Behnia, A., Chai, H.K., Shiotani, T., 2014. Advanced structural health monitoring of concrete structures with the aid of acoustic emission. Construction and Building Materials 65, 282–302. https://doi.org/10.1016/j.conbuildmat.2014.04.103

Bernal, S.A., Provis, J.L., Walkley, B., San Nicolas, R., Gehman, J.D., Brice, D.G., Kilcullen, A.R., Duxson, P., van Deventer, J.S.J., 2013. Gel nanostructure in alkali-activated binders based on slag and fly ash, and effects of accelerated carbonation. Cement and Concrete Research 53, 127–144. https://doi.org/10.1016/j.cemconres.2013.06.007

Berrocal, C.G., Hornbostel, K., Geiker, M.R., Löfgren, I., Lundgren, K., Bekas, D.G., 2018. Electrical resistivity measurements in steel fibre reinforced cementitious materials. Cement and Concrete Composites 89, 216–229. https://doi.org/10.1016/j.cemconcomp.2018.03.015

Biondi, L., Perry, M., Vlachakis, C., Wu, Z., Hamilton, A., McAlorum, J., 2019. Ambient cured fly ash geopolymer coatings for concrete. Materials 12, 923.

Bonen, D., Cohen, M.D., 1992. Magnesium sulfate attack on portland cement paste — II. Chemical and mineralogical analyses. Cement and Concrete Research 22, 707–718. https://doi.org/10.1016/0008-8846(92)90023-O

Boukamp, B.A., 1995. A linear Kronig-Kramers transform test for immittance data validation. Journal of the electrochemical society 142, 1885–1894.

Broomfield, J.P., 2023. Corrosion of steel in concrete: understanding, investigation and repair. Crc Press.

Brug, G.J., van den Eeden, A.L., Sluyters-Rehbach, M., Sluyters, J.H., 1984. The analysis of electrode impedances complicated by the presence of a constant phase element. Journal of electroanalytical chemistry and interfacial electrochemistry 176, 275–295.

Cabeza, M., Merino, P., Miranda, A., Nóvoa, X.R., Sanchez, I., 2002. Impedance spectroscopy study of hardened Portland cement paste. Cement and Concrete Research 32, 881–891.

Caggiano, A., Folino, P., Lima, C., Martinelli, E., Pepe, M., 2017. On the mechanical response of Hybrid Fiber Reinforced Concrete with Recycled and Industrial Steel

Fibers. Construction and Building Materials 147, 286–295. https://doi.org/10.1016/j.conbuildmat.2017.04.160

Caggiano, A., Xargay, H., Folino, P., Martinelli, E., 2015. Experimental and numerical characterization of the bond behavior of steel fibers recovered from waste tires embedded in cementitious matrices. Cement and Concrete Composites 62, 146–155. https://doi.org/10.1016/j.cemconcomp.2015.04.015

Cai, R., Ye, H., 2021. Clinkerless ultra-high strength concrete based on alkali-activated slag at high temperatures. Cement and Concrete Research 145, 106465. https://doi.org/10.1016/j.cemconres.2021.106465

Camacho Torregrosa, E.E., 2013. Dosage optimization and bolted connections for UHPFRC ties. Universitat Politècnica de València, Valencia (Spain). https://doi.org/10.4995/Thesis/10251/34790

Carpinteri, A., Lacidogna, G., Accornero, F., Mpalaskas, A.C., Matikas, T.E., Aggelis, D.G., 2013. Influence of damage in the acoustic emission parameters. Cement and Concrete Composites 44, 9–16. https://doi.org/10.1016/j.cemconcomp.2013.08.001

Caruso, M.C., Pascale, C., Camacho, E., Ferrara, L., 2022. Comparative environmental and social life cycle assessments of off-shore aquaculture rafts made in ultra-high performance concrete (UHPC). Int J Life Cycle Assess 27, 281–300. https://doi.org/10.1007/s11367-021-02017-6

Centonze, G., Leone, M., Aiello, M.A., 2012. Steel fibers from waste tires as reinforcement in concrete: A mechanical characterization. Construction and Building Materials 36, 46–57. https://doi.org/10.1016/j.conbuildmat.2012.04.088

Chen, C., Chen, X., Ning, Y., 2022. Identification of fracture damage characteristics in ultra-high performance cement-based composite using digital image correlation and acoustic emission techniques. Composite Structures 291, 115612. https://doi.org/10.1016/j.compstruct.2022.115612

Chen, M., Kang, X., Chen, Y., Chen, R., 2025. Unveiling the synergistic effects of stray current and high hydraulic pressure on chloride transport in ultra-high-performance concrete. Cement and Concrete Composites 157, 105957. https://doi.org/10.1016/j.cemconcomp.2025.105957

Chi, L., Wang, Z., Lu, S., Zhao, D., Yao, Y., 2019. Development of mathematical models for predicting the compressive strength and hydration process using the EIS impedance of cementitious materials. Construction and Building Materials 208, 659–668. https://doi.org/10.1016/j.conbuildmat.2019.03.056

Christensen, B.J., Coverdale, T., Olson, R.A., Ford, S.J., Garboczi, E.J., Jennings, H.M., Mason, T.O., 1994. Impedance Spectroscopy of Hydrating Cement-Based Materials: Measurement, Interpretation, and Application. Journal of the American Ceramic Society 77, 2789–2804. https://doi.org/10.1111/j.1151-2916.1994.tb04507.x

Christensen, B.J., Mason, T.O., Jennings, H.M., 1996. Comparison of measured and calculated permeabilities for hardened cement pastes. Cement and Concrete Research 26, 1325–1334. https://doi.org/10.1016/0008-8846(96)00130-5

CO2 costs in cement Some calculations, n.d.

COMMUNICATION FROM THE COMMISSION TO THE EUROPEAN PARLIAMENT, THE COUNCIL, THE EUROPEAN ECONOMIC AND SOCIAL COMMITTEE AND THE COMMITTEE OF THE REGIONS An EU Strategy to harness the potential of offshore renewable energy for a climate neutral future, 2020.

COMMUNICATION FROM THE COMMISSION TO THE EUROPEAN PARLIAMENT, THE EUROPEAN COUNCIL, THE COUNCIL, THE EUROPEAN ECONOMIC AND SOCIAL COMMITTEE AND THE COMMITTEE OF THE REGIONS The European Green Deal, 2019.

Cosoli, G., Mobili, A., Tittarelli, F., Revel, G.M., Chiariotti, P., 2020. Electrical Resistivity and Electrical Impedance Measurement in Mortar and Concrete Elements: A Systematic Review. Applied Sciences 10, 9152. https://doi.org/10.3390/app10249152

Criado, M., Fernández-Jiménez, A., Palomo, A., 2010. Alkali activation of fly ash. Part III: Effect of curing conditions on reaction and its graphical description. Fuel 89, 3185–3192. https://doi.org/10.1016/j.fuel.2010.03.051

Cuenca, E., Monte, F.L., Moro, M., Schiona, A., Ferrara, L., 2021. Effects of Autogenous and Stimulated Self-Healing on Durability and Mechanical Performance of UHPFRC: Validation of Tailored Test Method through Multi-Performance Healing-Induced Recovery Indices. Sustainability 13. https://doi.org/10.3390/su132011386

Davidovits, J., 2005. Geopolymers: Inorganic polymeric new materials. Journal of Thermal Analysis and Calorimetry 37, 1633–1656. https://doi.org/10.1007/bf01912193

Davidovits, J., 1993. Geopolymer cements to minimize carbon dioxide greenhouse warming. Ceram. Trans. 37, 165–182.

Davidovits, J., 1991. Geopolymers: inorganic polymeric new materials. Journal of Thermal Analysis and calorimetry 37, 1633–1656.

Design of steel fibre reinforced concrete using the σ-w method: principles and applications, 2002. . Mat. Struct. 35, 262–278. https://doi.org/10.1007/BF02482132

Diard, J.P., Le Gorrec, B., Montella, C., 2008. Diffusion Impedances. Hosted by Bio-Logic@ http://biologic. info.

Dong, B., Qiu, Q., Xiang, J., Huang, C., Sun, H., Xing, F., Liu, W., 2015. Electrochemical impedance interpretation of the carbonation behavior for fly ash–slag–cement materials. Construction and Building Materials 93, 933–942. https://doi.org/10.1016/j.conbuildmat.2015.05.066

Dotelli, G., Mari, C.M., 2001. The evolution of cement paste hydration process by impedance spectroscopy. Materials Science and Engineering: A 303, 54–59. https://doi.org/10.1016/S0921-5093(00)01886-4

Duxson, P., Provis, J.L., Lukey, G.C., Mallicoat, S.W., Kriven, W.M., van Deventer, J.S.J., 2005. Understanding the relationship between geopolymer composition, microstructure and mechanical properties. Colloids and Surfaces A: Physicochemical and Engineering Aspects 269, 47–58. https://doi.org/10.1016/j.colsurfa.2005.06.060

Fehling, E., Schmidt, M., Walraven, J., Leutbecher, T., Fröhlich, S. (Eds.), 2014. Ultra-High Performance Concrete UHPC, 1st ed. Wiley. https://doi.org/10.1002/9783433604076

Ferdiansyah, T., Turatsinze, A., Balayssac, J.-P., 2018. Design and characterization of self-sensing steel fiber reinforced concrete. MATEC Web Conf. 199, 11008. https://doi.org/10.1051/matecconf/201819911008

Fernández-Jiménez, A., Palomo, A., 2005. Composition and microstructure of alkali activated fly ash binder: Effect of the activator. Cement and Concrete Research 35, 1984–1992. https://doi.org/10.1016/j.cemconres.2005.03.003

Gao, S., Tian, M., 2025. Flexural damage characterization of lightweight ultra-high performance concrete by recycled powder revealed based on acoustic emission technology. Journal of Building Engineering 114, 114260. https://doi.org/10.1016/j.jobe.2025.114260

Garcia-Lodeiro, I., Palomo, A., Fernández-Jiménez, A., Macphee, D.E., 2011. Compatibility studies between N-A-S-H and C-A-S-H gels. Study in the ternary diagram Na2O–CaO–Al2O3–SiO2–H2O. Cement and Concrete Research 41, 923–931. https://doi.org/10.1016/j.cemconres.2011.05.006

Ghosh, P., Hammond, A., Tikalsky, P.J., 2011. Prediction of Equivalent Steady-State Chloride Diffusion Coefficients. ACI Materials Journal 108.

Graybeal, B., Davis, M., 2008. Cylinder or cube: strength testing of 80 to 200 MPa (11.6 to 29 ksi) ultra-high-performance fiber-reinforced concrete. ACI Materials Journal 105, 603.

Graybeal, B., Tanesi, J., 2007. Durability of an Ultrahigh-Performance Concrete. Journal of Materials in Civil Engineering 19, 848–854. https://doi.org/10.1061/(ASCE)0899-1561(2007)19:10(848)

Graybeal, B.A., 2006. Material property characterization of ultra-high performance concrete. United States. Federal Highway Administration. Office of Infrastructure ….

Grosse, C.U., Ohtsu, M., Aggelis, D.G., Shiotani, T., 2021. Acoustic emission testing: Basics for research–applications in engineering. Springer Nature.

Gu, P., Xie, P., Beaudoin, J.J., Brousseau, R., 1993. AC impedance spectroscopy (II): Microstructural characterization of hydrating cement-silica fume systems. Cement and Concrete Research 23, 157–168.

Gu, P., Xie, P., Beaudoin, J.J., Brousseau, R., 1992. AC impedance spectroscopy (I): A new equivalent circuit model for hydrated portland cement paste. Cement and Concrete Research 22, 833–840.

Gu, P., Xie, P., Fu, Y., Beaudoin, J.J., 1994. A.C impedance phenomena in hydrating cement systems; The drying-rewetting process. Cement and Concrete Research 24, 89–91. https://doi.org/10.1016/0008-8846(94)90087-6

Guerrieri, M., Sanjayan, J.G., 2010. Behavior of combined fly ash/slag-based geopolymers when exposed to high temperatures. Fire and Materials 34, 163–175. https://doi.org/10.1002/fam.1014

Habert, G., Denarié, E., Šajna, A., Rossi, P., 2013. Lowering the global warming impact of bridge rehabilitations by using Ultra High Performance Fibre Reinforced Concretes. Cement and Concrete Composites 38, 1–11.

Habert, G., Ouellet-Plamondon, C., 2016. Recent update on the environmental impact of geopolymers. RILEM Technical Letters 1, 17–23. https://doi.org/10.21809/rilemtechlett.2016.6

Haha, M.B., Lothenbach, B., Le Saout, G., Winnefeld, F., 2011. Influence of slag chemistry on the hydration of alkali-activated blast-furnace slag — Part I: Effect of MgO. Cement and Concrete Research 41, 955–963. https://doi.org/10.1016/j.cemconres.2011.05.002

Hajimohammadi, A., Provis, J.L., van Deventer, J.S.J., 2011. The effect of silica availability on the mechanism of geopolymerisation. Cement and Concrete Research 41, 210–216. https://doi.org/10.1016/j.cemconres.2011.02.001

Hasan, T.M., Allena, S., Gilbert, L., 2024. Rapid chloride penetration test: An evaluation of corrosion resistance in ultra-high performance concrete. Journal of Building Engineering 82, 108317. https://doi.org/10.1016/j.jobe.2023.108317

Hassan, A.M.T., Jones, S.W., 2012. Non-destructive testing of ultra high performance fibre reinforced concrete (UHPFRC): A feasibility study for using ultrasonic and resonant frequency testing techniques. Construction and Building Materials 35, 361–367.

HSU, N., FR, B., 1981. CHARACTERIZATION AND CALIBRATION OF ACOUSTIC EMISSION SENSORS. CHARACTERIZATION AND CALIBRATION OF ACOUSTIC EMISSION SENSORS.

Hu, H., Papastergiou, P., Angelakopoulos, H., Guadagnini, M., Pilakoutas, K., 2018. Mechanical properties of SFRC using blended manufactured and recycled tyre steel fibres. Construction and Building Materials 163, 376–389. https://doi.org/10.1016/j.conbuildmat.2017.12.116

Isa, M.N., Pilakoutas, K., Guadagnini, M., 2021. Determination of tensile characteristics and design of eco-efficient UHPC. Structures 32, 2174–2194. https://doi.org/10.1016/j.istruc.2021.03.114

Isa, M.N., Pilakoutas, K., Guadagnini, M., Angelakopoulos, H., 2020. Mechanical performance of affordable and eco-efficient ultra-high performance concrete (UHPC) containing recycled tyre steel fibres. Construction and Building Materials 255, 119272.

Ismail, I., Bernal, S.A., Provis, J.L., San Nicolas, R., Hamdan, S., van Deventer, J.S.J., 2014. Modification of phase evolution in alkali-activated blast furnace slag by the incorporation of fly ash. Cement and Concrete Composites 45, 125–135. https://doi.org/10.1016/j.cemconcomp.2013.09.006

Joshi, R., Chatterji, S., Achari, G., Mackie, P., 2000. Reexamination of ASTM C 1202—Standard Test Method for Electrical Indication of Concrete's Ability to Resist Chloride Ion Penetration. J. Test. Eval. 28, 59–61. https://doi.org/10.1520/JTE12075J

Julio-Betancourt, G.A., Hooton, R.D., 2004. Study of the Joule effect on rapid chloride permeability values and evaluation of related electrical properties of concretes. Cement and Concrete Research 34, 1007–1015. https://doi.org/10.1016/j.cemconres.2003.11.012

Keddam, M., Takenouti, H., Nóvoa, X.R., Andrade, C., Alonso, C., 1997. Impedance measurements on cement paste. Cement and Concrete Research 27, 1191–1201. https://doi.org/10.1016/S0008-8846(97)00117-8

Kim, T., Kang, C., 2021. Investigation of the Effect of Mixing Time on the Mechanical Properties of Alkali-Activated Cement Mixed with Fly Ash and Slag. Materials 14. https://doi.org/10.3390/ma14092301

Kim, Y.J., Choi, S., Oh, S.R., 2024. The Effects of Ester and Ether Polycarboxylate Superplasticizers on the Fluidity and Setting Behavior of Alkali-Activated Slag Paste. Materials 17, 4951. https://doi.org/10.3390/ma17204951

Komljenović, M., Baščarević, Z., Marjanović, N., Nikolić, V., 2013. External sulfate attack on alkali-activated slag. Construction and Building Materials 49, 31–39. https://doi.org/10.1016/j.conbuildmat.2013.08.013

Kong, D.L.Y., Sanjayan, J.G., 2010. Effect of elevated temperatures on geopolymer paste, mortar and concrete. Cement and Concrete Research 40, 334–339. https://doi.org/10.1016/j.cemconres.2009.10.017

Korniejenko, K., Figiela, B., Ziejewska, C., Marczyk, J., Bazan, P., Hebda, M., Choińska, M., Lin, W.-T., 2022. Fracture Behavior of Long Fiber Reinforced Geopolymer Composites at Different Operating Temperatures. Materials (Basel) 15, 482. https://doi.org/10.3390/ma15020482

Krizan, D., Zivanovic, B., 2002. Effects of dosage and modulus of water glass on early hydration of alkali–slag cements. Cement and Concrete Research 32, 1181–1188. https://doi.org/10.1016/S0008-8846(01)00717-7

Kushwaha, M., Shankar, S., Goel, D., Singh, S., Rahul, J., Rachna, K., Singh, J., 2024. Microplastics pollution in the marine environment: A review of sources, impacts and mitigation. Marine Pollution Bulletin 209, 117109. https://doi.org/10.1016/j.marpolbul.2024.117109

Kusumawardaningsih, Y., Fehling, E., Ismail, M., 2015. UHPC compressive strength test specimens: Cylinder or cube? Procedia Engineering 125, 1076–1080.

Lahoti, M., Wong, K.K., Tan, K.H., Yang, E.-H., 2018. Effect of alkali cation type on strength endurance of fly ash geopolymers subject to high temperature exposure. Materials & Design 154, 8–19. https://doi.org/10.1016/j.matdes.2018.05.023

Landis, E., Baillon, L., 2002. Experiments to Relate Acoustic Emission Energy to Fracture Energy of Concrete. Journal of Engineering Mechanics-asce - J ENG MECH-ASCE 128. https://doi.org/10.1061/(ASCE)0733-9399(2002)128:6(698)

Lao, J.-C., Xu, L.-Y., Huang, B.-T., Dai, J.-G., Shah, S.P., 2022. Strain-hardening Ultra-High-Performance Geopolymer Concrete (UHPGC): Matrix design and effect of steel fibers. Composites Communications 30, 101081. https://doi.org/10.1016/j.coco.2022.101081

Lao, J.-C., Xu, L.-Y., Huang, B.-T., Zhu, J.-X., Khan, M., Dai, J.-G., 2023. Utilization of sodium carbonate activator in strain-hardening ultra-high-performance geopolymer concrete (SH-UHPGC). Frontiers in Materials 10, 1142237.

Li, B., Yu, S., Yang, L., Zhu, W., Xue, Y., Feng, D., Wang, C., Chen, Y., 2022. Multiscale fracture characteristics and failure mechanism quantification method of cracked rock under true triaxial compression. Engineering Fracture Mechanics 262, 108257. https://doi.org/10.1016/j.engfracmech.2022.108257

Li, J., Wu, Z., Shi, C., Yuan, Q., Zhang, Z., 2020. Durability of ultra-high performance concrete – A review. Construction and Building Materials 255, 119296. https://doi.org/10.1016/j.conbuildmat.2020.119296

Li, S., Zhang, L., Guo, P., Zhang, P., Wang, C., Sun, W., Han, S., 2021. Characteristic analysis of acoustic emission monitoring parameters for crack propagation in UHPC-NC composite beam under bending test. Construction and Building Materials 278, 122401. https://doi.org/10.1016/j.conbuildmat.2021.122401

Liu, G., Guo, J., Peng, H., Ping, H., Ma, Q., 2024. Review of Recent Offshore Floating Photovoltaic Systems. Journal of Marine Science and Engineering 12. https://doi.org/10.3390/jmse12111942

Liu, Y., Shi, C., Zhang, Z., Li, N., Shi, D., 2020a. Mechanical and fracture properties of ultra-high performance geopolymer concrete: Effects of steel fiber and silica fume. Cement and Concrete Composites 112, 103665. https://doi.org/10.1016/j.cemconcomp.2020.103665

Liu, Y., Zhang, Z., Shi, C., Zhu, D., Li, N., Deng, Y., 2020b. Development of ultra-high performance geopolymer concrete (UHPGC): Influence of steel fiber on mechanical properties. Cement and Concrete Composites 112, 103670. https://doi.org/10.1016/j.cemconcomp.2020.103670

Lloyd, R.R., Provis, J.L., van Deventer, J.S.J., 2012. Acid resistance of inorganic polymer binders. 1. Corrosion rate. Mater Struct 45, 1–14. https://doi.org/10.1617/s11527-011-9744-7

Lothenbach, B., Scrivener, K., Hooton, R.D., 2011. Supplementary cementitious materials. Cement and Concrete Research 41, 1244–1256. https://doi.org/10.1016/j.cemconres.2010.12.001

Macdonald, D.D., 2006. Reflections on the history of electrochemical impedance spectroscopy. Electrochimica acta 51, 1376–1388.

Macdonald, J.R., Johnson, W.B., 2005. Fundamentals of Impedance Spectroscopy, in: Impedance Spectroscopy. John Wiley & Sons, Ltd, pp. 1–26. https://doi.org/10.1002/0471716243.ch1

Malhotra, V.M., Carino, N.J., 2003. Handbook on nondestructive testing of concrete. CRC press.

Martinelli, E., Caggiano, A., Xargay, H., 2015. An experimental study on the post-cracking behaviour of Hybrid Industrial/Recycled Steel Fibre-Reinforced Concrete. Construction and Building Materials 94, 290–298. https://doi.org/10.1016/j.conbuildmat.2015.07.007

McCarter, W.J., Brousseau, R., 1990. The AC response of hardened cement paste. Cement and Concrete Research 20, 891–900.

McCarter, W.J., Chrisp, T.M., Starrs, G., Blewett, J., 2003. Characterization and monitoring of cement-based systems using intrinsic electrical property measurements. Cement and Concrete Research, Papers presented at the Fall 2001 Materials Research Society Symposium on Design, Characteristics and Properties of Cementitious Materials 33, 197–206. https://doi.org/10.1016/S0008-8846(02)00824-4

McLellan, B.C., Williams, R.P., Lay, J., van Riessen, A., Corder, G.D., 2011. Costs and carbon emissions for geopolymer pastes in comparison to ordinary portland cement. Journal of Cleaner Production 19, 1080–1090. https://doi.org/10.1016/j.jclepro.2011.02.010

Mehta, P.K., 1983. Mechanism of sulfate attack on portland cement concrete — Another look. Cement and Concrete Research 13, 401–406. https://doi.org/10.1016/0008-8846(83)90040-6

Meng, W., Valipour, M., Khayat, K.H., 2017. Optimization and performance of cost-effective ultra-high performance concrete. Mater Struct 50, 29. https://doi.org/10.1617/s11527-016-0896-3

Midhin, M.A.K., Wong, L.S., Ahmed, A.N., Jasim, A.M.D.A., Paul, S.C., 2023. Strength and Chemical Characterization of Ultra High-Performance Geopolymer Concrete: A Coherent Evaluation. Civ Eng J 9, 3254–3277. https://doi.org/10.28991/CEJ-2023-09-12-020

Monteiro, L., 2023. Valorisation des sédiments de Nouvelle-Aquitaine non-traités dans un composite géopolymérisé : étude mécanique, microscopique et environnementale (Theses). Université de Bordeaux.

Muralidhara, S., Prasad, B.K.R., Eskandari, H., Karihaloo, B.L., 2010. Fracture process zone size and true fracture energy of concrete using acoustic emission. Construction and Building Materials 24, 479–486. https://doi.org/10.1016/j.conbuildmat.2009.10.014

Myers, R.J., Bernal, S.A., San Nicolas, R., Provis, J.L., 2013. Generalized Structural Description of Calcium–Sodium Aluminosilicate Hydrate Gels: The Cross-Linked Substituted Tobermorite Model. Langmuir 29, 5294–5306. https://doi.org/10.1021/la4000473

Nasir, M., Mahmood, A.H., Bahraq, A.A., 2024. History, recent progress, and future challenges of alkali-activated binders – An overview. Construction and Building Materials 426, 136141. https://doi.org/10.1016/j.conbuildmat.2024.136141

Neville, A.M., 1963. Properties of concrete. Pearson Education India.

Nóvoa, X.R., 2026. Electrochemical impedance spectroscopy to characterise plain and fibre-reinforced cementitious mixes. Current Opinion in Electrochemistry 55, 101802. https://doi.org/10.1016/j.coelec.2025.101802

Ohno, K., Ohtsu, M., 2010. Crack classification in concrete based on acoustic emission. Construction and Building Materials, Special Issue on Fracture, Acoustic Emission and NDE in Concrete (KIFA-5) 24, 2339–2346. https://doi.org/10.1016/j.conbuildmat.2010.05.004

Ohtsu, M., Isoda, T., Tomoda, Y., n.d. Acoustic Emission Techniques Standardized for Concrete Structures.

Olson, R.A., Christensen, B.J., Coverdale, R.T., Ford, S.J., Moss, G.M., Jennings, H.M., Mason, T.O., Garboczi, E.J., 1995. Interpretation of the impedance spectroscopy of cement paste via computer modelling: Part III Microstructural analysis of frozen cement paste. Journal of Materials Science 30, 5078–5086.

Orazem, M.E., 2008. Electrochemical impedance spectroscopy. Hoboken, N.J. : Wiley.

Ospitia, N., Korda, E., Kalteremidou, K.-A., Lefever, G., Tsangouri, E., Aggelis, D.G., 2023. Recent developments in acoustic emission for better performance of structural materials. Developments in the Built Environment 13, 100106. https://doi.org/10.1016/j.dibe.2022.100106

Pacheco-Torgal, F., Castro-Gomes, J., Jalali, S., 2008. Alkali-activated binders: A review: Part 1. Historical background, terminology, reaction mechanisms and hydration products. Construction and Building Materials 22, 1305–1314. https://doi.org/10.1016/j.conbuildmat.2007.10.015

Palacios, M., Puertas, F., 2005. Effect of superplasticizer and shrinkage-reducing admixtures on alkali-activated slag pastes and mortars. Cement and Concrete Research 35, 1358–1367. https://doi.org/10.1016/j.cemconres.2004.10.014

Palomo, A., Grutzeck, M.W., Blanco, M.T., 1999. Alkali-activated fly ashes. Cement and Concrete Research 29, 1323–1329. https://doi.org/10.1016/S0008-8846(98)00243-9

Pan, Z., Sanjayan, J.G., Rangan, B.V., 2011. Fracture properties of geopolymer paste and concrete. Magazine of concrete research 63, 763–771.

Park, J., Song, H., Choi, H., 2022. Estimation of water-to-cement ratio in cementitious materials using electrochemical impedance spectroscopy and artificial neural

networks. Construction and Building Materials 350, 128843. https://doi.org/10.1016/j.conbuildmat.2022.128843

Phair, J.W., Van Deventer, J.S.J., 2001. Effect of silicate activator pH on the leaching and material characteristics of waste-based inorganic polymers. Minerals Engineering 14, 289–304. https://doi.org/10.1016/S0892-6875(01)00002-4

Pilakoutas, K., Neocleous, K., Tlemat, H., 2004. Reuse of tyre steel fibres as concrete reinforcement. Proceedings of the Institution of Civil Engineers - Engineering Sustainability 157, 131–138. https://doi.org/10.1680/ensu.2004.157.3.131

Pontes, C.V., Réus, G.C., Araújo, E.C., Medeiros, M.H.F., 2021. Silver nitrate colorimetric method to detect chloride penetration in carbonated concrete: How to prevent false positives. Journal of Building Engineering 34, 101860. https://doi.org/10.1016/j.jobe.2020.101860

Pouhet, R., Cyr, M., 2016. Carbonation in the pore solution of metakaolin-based geopolymer. Cement and Concrete Research 88, 227–235.

Provis, J., Deventer, J., 2014. Alkali Activated Materials: State-of-the-Art Report, RILEM TC 224-AAM. https://doi.org/10.1007/978-94-007-7672-2

Provis, J.L., 2018. Alkali-activated materials. Cement and Concrete Research, Report of UNEP SBCI WORKING GROUP ON LOW-CO2 ECO-EFFICIENT CEMENT-BASED MATERIALS 114, 40–48. https://doi.org/10.1016/j.cemconres.2017.02.009

Provis, J.L., Bernal, S.A., 2014. Geopolymers and Related Alkali-Activated Materials. Annual Review of Materials Research 44, 299–327. https://doi.org/10.1146/annurev-matsci-070813-113515

Provis, J.L., Myers, R.J., White, C.E., Rose, V., van Deventer, J.S.J., 2012. X-ray microtomography shows pore structure and tortuosity in alkali-activated binders. Cement and Concrete Research 42, 855–864. https://doi.org/10.1016/j.cemconres.2012.03.004

Provis, J.L., Palomo, A., Shi, C., 2015. Advances in understanding alkali-activated materials. Cement and Concrete Research 78, 110–125.

Puertas, F., Palacios, M., Manzano, H., Dolado, J.S., Rico, A., Rodríguez, J., 2011. A model for the C-A-S-H gel formed in alkali-activated slag cements. Journal of the European Ceramic Society 31, 2043–2056. https://doi.org/10.1016/j.jeurceramsoc.2011.04.036

Rajabipour, F., Weiss, J., 2007. Electrical conductivity of drying cement paste. Materials and Structures 40, 1143–1160.

Randl, N., Steiner, T., Ofner, S., Baumgartner, E., Mészöly, T., 2014. Development of UHPC mixtures from an ecological point of view. Construction and Building Materials 67, 373–378.

Ranjbar, N., Talebian, S., Mehrali, M., Kuenzel, C., Metselaar, H.S.C., Jumaat, M.Z., 2016. Mechanisms of interfacial bond in steel and polypropylene fiber reinforced geopolymer composites. Composites Science and Technology 122, 73–81.

Rashad, A.M., 2014. A comprehensive overview about the influence of different admixtures and additives on the properties of alkali-activated fly ash. Materials & Design 53, 1005–1025. https://doi.org/10.1016/j.matdes.2013.07.074

Regulation (EU) 2021/1119 of the European Parliament and of the Council of 30 June 2021 establishing the framework for achieving climate neutrality and amending Regulations (EC) No 401/2009 and (EU) 2018/1999 ('European Climate Law'), 2021. , OJ L.

Richard, P., Cheyrezy, M., 1995. Composition of reactive powder concretes. Cement and Concrete Research 25, 1501–1511. https://doi.org/10.1016/0008-8846(95)00144-2

RILEM, n.d. 212-ACD : Acoustic emission and related NDE techniques for crack detection and damage evaluation in concrete [WWW Document]. URL https://www.rilem.net/groupe/212-acd-acoustic-emission-and-related-nde-techniques-for-crack-detection-and-damage-evaluation-in-concrete-209/page/presentation (accessed 5.17.26).

Roy, D.M., 1999. Alkali-activated cements Opportunities and challenges. Cement and Concrete Research 29, 249–254. https://doi.org/10.1016/S0008-8846(98)00093-3

Sameer, H., Weber, V., Mostert, C., Bringezu, S., Fehling, E., Wetzel, A., 2019. Environmental assessment of ultra-high-performance concrete using carbon, material, and water footprint. Materials 12, 851.

Sánchez, I., Nóvoa, X.R., de Vera, G., Climent, M.A., 2008. Microstructural modifications in Portland cement concrete due to forced ionic migration tests. Study by impedance spectroscopy. Cement and Concrete Research 38, 1015–1025. https://doi.org/10.1016/j.cemconres.2008.03.012

Sant, G., Rajabipour, F., Weiss, J., 2008. The influence of temperature on electrical conductivity measurements and maturity predictions in cementitious materials during hydration.

SAVIC, L., n.d. EC Library Guides: EU Sources and Information: EU Statistics and Data [WWW Document]. URL https://ec-europa-eu.libguides.com/EU_sources/statistics-and-data (accessed 5.15.26).

Schechinger, B., Vogel, T., 2007. Acoustic emission for monitoring a reinforced concrete beam subject to four-point-bending. Construction and Building Materials, Fracture, Acoustic Emission and NDE in Concrete (KIFA-4) 21, 483–490. https://doi.org/10.1016/j.conbuildmat.2006.04.003

Schönleber, M., Klotz, D., Ivers-Tiffée, E., 2014. A method for improving the robustness of linear Kramers-Kronig validity tests. Electrochimica Acta 131, 20–27.

Shi, C., Day, R.L., 1995. A calorimetric study of early hydration of alkali-slag cements. Cement and Concrete Research 25, 1333–1346. https://doi.org/10.1016/0008-8846(95)00126-W

Shi, C., Jiménez, A.F., Palomo, A., 2011. New cements for the 21st century: The pursuit of an alternative to Portland cement. Cement and Concrete Research, Special Issue: 13th International Congress on the Chemistry of Cement 41, 750–763. https://doi.org/10.1016/j.cemconres.2011.03.016

Shi, C., Wu, Z., Xiao, J., Wang, D., Huang, Z., Fang, Z., 2015. A review on ultra high performance concrete: Part I. Raw materials and mixture design. Construction and Building Materials 101, 741–751.

Shiotani, T., Ohtsu, M., Ikeda, K., 2001. Detection and evaluation of AE waves due to rock deformation. Construction and Building Materials, Fracture Mechanics and Acoustic Emmission 15, 235–246. https://doi.org/10.1016/S0950-0618(00)00073-8

Sindhunata, Van Deventer, J.S.J., Lukey, G.C., Xu, H., 2006. Effect of Curing Temperature and Silicate Concentration on Fly-Ash-Based Geopolymerization. Ind. Eng. Chem. Res. 45, 3559–3568. https://doi.org/10.1021/ie051251p

Singh, B., Ishwarya, G., Gupta, M., Bhattacharyya, S.K., 2015. Geopolymer concrete: A review of some recent developments. Construction and Building Materials 85, 78–90. https://doi.org/10.1016/j.conbuildmat.2015.03.036

Snyder, K.A., Ferraris, C., Martys, N.S., Garboczi, E.J., 2000. Using Impedance Spectroscopy to Assess the Viability of the Rapid Chloride Test for Determining Concrete Conductivity. J Res Natl Inst Stand Technol 105, 497–509. https://doi.org/10.6028/jres.105.040

Song, G., 2000. Equivalent circuit model for AC electrochemical impedance spectroscopy of concrete. Cement and Concrete Research 30, 1723–1730. https://doi.org/10.1016/S0008-8846(00)00400-2

Song, H.-W., Saraswathy, V., 2007. Corrosion Monitoring of Reinforced Concrete Structures – A Review. International Journal of Electrochemical Science 2, 1–28. https://doi.org/10.1016/S1452-3981(23)17049-0

Souto-Martinez, A., Arehart, J.H., Srubar, W.V., 2018. Cradle-to-gate CO2e emissions vs. *in situ* CO2 sequestration of structural concrete elements. Energy and Buildings 167, 301–311. https://doi.org/10.1016/j.enbuild.2018.02.042

Spragg, R., Villani, C., Snyder, K., Bentz, D., Bullard, J.W., Weiss, J., 2013. Factors that Influence Electrical Resistivity Measurements in Cementitious Systems. Transportation Research Record: Journal of the Transportation Research Board 2342, 90–98. https://doi.org/10.3141/2342-11

Stengel, T., Schießl, P., 2014. Life cycle assessment (LCA) of ultra high performance concrete (UHPC) structures, in: Eco-Efficient Construction and Building Materials. Elsevier, pp. 528–564.

Stripple, H., Gustafsson, T., 2018. CO2 uptake in cement-containing products-Background and calculation models for IPCC implementation.

Suryanto, B., McCarter, W.J., Starrs, G., Ludford-Jones, G.V., 2016. Electrochemical immittance spectroscopy applied to a hybrid PVA/steel fiber engineered cementitious composite. Materials & Design 105, 179–189.

Suryavanshi, A.K., Scantlebury, J.D., Lyon, S.B., 1996. Mechanism of Friedel's salt formation in cements rich in tri-calcium aluminate. Cement and Concrete Research 26, 717–727. https://doi.org/10.1016/S0008-8846(96)85009-5

Tafraoui, A., Escadeillas, G., Vidal, T., 2016. Durability of the Ultra High Performances Concrete containing metakaolin. Construction and Building Materials 112, 980–987. https://doi.org/10.1016/j.conbuildmat.2016.02.169

Taylor, H.F., 1997. Cement chemistry. Thomas Telford.

Taylor, H.F.W., Famy, C., Scrivener, K.L., 2001. Delayed ettringite formation. Cement and Concrete Research 31, 683–693. https://doi.org/10.1016/S0008-8846(01)00466-5

Torrents, J.M., Mason, T.O., Garboczi, E.J., 2000. Impedance spectra of fiber-reinforced cement-based composites: a modeling approach. Cement and Concrete Research 30, 585–592.

Vafaei, M., Allahverdi, A., Dong, P., Bassim, N., 2018. Acid attack on geopolymer cement mortar based on waste-glass powder and calcium aluminate cement at mild

concentration. Construction and Building Materials 193, 363–372. https://doi.org/10.1016/j.conbuildmat.2018.10.203

Van Jaarsveld, J.G.S., Van Deventer, J.S.J., 1999. Effect of the Alkali Metal Activator on the Properties of Fly Ash-Based Geopolymers. Ind. Eng. Chem. Res. 38, 3932–3941. https://doi.org/10.1021/ie980804b

Van Westing, E.P.M., Ferrari, G.M., De Wit, J.H.W., 1994. The determination of coating performance with impedance measurements—II. Water uptake of coatings. Corrosion Science 36, 957–977.

Walkley, B., San Nicolas, R., Sani, M.-A., Rees, G.J., Hanna, J.V., Van Deventer, J.S.J., Provis, J.L., 2016. Phase evolution of C-(N)-A-S-H/N-A-S-H gel blends investigated via alkali-activation of synthetic calcium aluminosilicate precursors. Cement and Concrete Research 89, 120–135. https://doi.org/10.1016/j.cemconres.2016.08.010

Wang, A., Zheng, Y., Zhang, Z., Liu, K., Li, Y., Shi, L., Sun, D., 2020. The Durability of Alkali-Activated Materials in Comparison with Ordinary Portland Cements and Concretes: A Review. Engineering 6, 695–706. https://doi.org/10.1016/j.eng.2019.08.019

Wang, D., Zhang, Z., Shi, C., Wang, Y., Ren, Q., Ning, C., Liu, X., Jiang, Z., 2025. Comparison study of ultra-high performance geopolymer concrete (UHPGC) and ultra-high performance concrete (UHPC): mechanical properties, durability and carbon emissions. Composites Part B: Engineering 307, 112903. https://doi.org/10.1016/j.compositesb.2025.112903

Wang, J., Lund, P.D., 2022. Review of Recent Offshore Photovoltaics Development. Energies 15. https://doi.org/10.3390/en15207462

Wang, S.-D., Scrivener, K.L., 1995. Hydration products of alkali activated slag cement. Cement and Concrete research 25, 561–571.

Wang, S.-D., Scrivener, K.L., Pratt, P.L., 1994. Factors affecting the strength of alkali-activated slag. Cement and Concrete Research 24, 1033–1043. https://doi.org/10.1016/0008-8846(94)90026-4

Wetzel, A., Middendorf, B., 2019. Influence of silica fume on properties of fresh and hardened ultra-high performance concrete based on alkali-activated slag. Cement and Concrete Composites 100, 53–59. https://doi.org/10.1016/j.cemconcomp.2019.03.023

Wille, K., Naaman, A.E., Parra-Montesinos, G.J., 2011. Ultra-high performance concrete with compressive strength exceeding 150 MPa (22 ksi): a simpler way. ACI materials journal 108.

Wu, Z., Shi, C., He, W., Wu, L., 2016. Effects of steel fiber content and shape on mechanical properties of ultra high performance concrete. Construction and building materials 103, 8–14.

Xu, H., Van Deventer, J.S.J., 2000. The geopolymerisation of alumino-silicate minerals. International Journal of Mineral Processing 59, 247–266. https://doi.org/10.1016/S0301-7516(99)00074-5

Yang, K., Li, D., He, Z., Zhou, H., Li, J., 2021. Study on Acoustic Emission Characteristics of Low-Temperature Asphalt Concrete Cracking Damage. Materials 14, 881. https://doi.org/10.3390/ma14040881

Yang, K., Long, G., Tang, Z., Ma, G., Zhao, H., He, J., Cheng, Z., Xie, Y., 2023. Insight into the flexural characteristics of rapid hardening ultra-high performance concrete (RH-UHPC) incorporating C-S-H seeds using acoustic emission technology. Construction and Building Materials 408, 133632. https://doi.org/10.1016/j.conbuildmat.2023.133632

Yazıcı, H., Yiğiter, H., Karabulut, A.Ş., Baradan, B., 2008. Utilization of fly ash and ground granulated blast furnace slag as an alternative silica source in reactive powder concrete. Fuel 87, 2401–2407. https://doi.org/10.1016/j.fuel.2008.03.005

Yip, C.K., Van Deventer, J.S.J., 2003. Microanalysis of calcium silicate hydrate gel formed within a geopolymeric binder. Journal of Materials Science 38, 3851–3860. https://doi.org/10.1023/A:1025904905176

Yoo, D.-Y., Banthia, N., 2016. Mechanical properties of ultra-high-performance fiber-reinforced concrete: A review. Cement and Concrete Composites 73, 267–280. https://doi.org/10.1016/j.cemconcomp.2016.08.001

Youssef, N., Lafhaj, Z., Chapiseau, C., 2020. Economic Analysis of Geopolymer Brick Manufacturing: A French Case Study. Sustainability 12, 7403. https://doi.org/10.3390/su12187403

Yu, R., Spiesz, P., Brouwers, H.J.H., 2015. Development of an eco-friendly Ultra-High Performance Concrete (UHPC) with efficient cement and mineral admixtures uses. Cement and Concrete Composites 55, 383–394.

Zhang, J., Heath, A., Ball, R.J., Paine, K., 2022. Effect of fibre loading on the microstructural, electrical, and mechanical properties of carbon fibre incorporated smart cement-based composites. Front. Mater. 9. https://doi.org/10.3389/fmats.2022.1055796

Synthèse en langue française

Introduction générale

Énergies marines renouvelables et opportunité du photovoltaïque flottant en mer

L'Union européenne s'est engagée à atteindre la neutralité climatique en 2050. Cet objectif a d'abord été formulé dans le Pacte vert pour l'Europe (The European Green Deal, 2019), puis rendu juridiquement contraignant par la loi européenne sur le climat (Règlement (UE) 2021/1119), qui engage les États membres vers la neutralité des émissions de gaz à effet de serre en 2050 et vers une réduction d'au moins 55 % par rapport aux niveaux de 1990 à l'horizon 2030 (European Climate Law, 2021). Atteindre ces cibles suppose une décarbonation quasi complète du secteur électrique et une expansion substantielle de la production totale, la stratégie consistant à électrifier les transports, le chauffage et les procédés industriels aujourd'hui alimentés par des combustibles fossiles. L'éolien, l'hydroélectricité, la géothermie et le solaire doivent tous y contribuer. Aucune technologie isolée ne suffit à l'échelle et au rythme requis. La communication COM (2020) 741 de la Commission européenne, « Une stratégie de l'UE pour exploiter le potentiel des énergies renouvelables en mer en vue d'un avenir neutre pour le climat », identifie les renouvelables en mer comme essentielles à cette trajectoire (European Commission, 2020).

Le photovoltaïque (PV) solaire se heurte à une contrainte de surface qui devient déterminante à l'échelle continentale. Dans les conditions climatiques européennes actuelles, 1 km2 de capacité PV installée produit environ 100 GWh par an. La consommation électrique totale de l'UE en 2019 s'élevait à 2900 TWh (SAVIC). Si cette demande était intégralement satisfaite par le PV, une surface d'installation d'environ 29000 km2 serait nécessaire, comparable à la superficie de la Belgique. Le scénario tout-PV relève de l'expérience de pensée plutôt que de la proposition politique, mais il fixe une borne supérieure utile de ce que le PV au sol peut absorber à l'échelle de l'UE. Le déploiement terrestre entre en concurrence directe avec l'agriculture, l'urbanisation et les écosystèmes protégés, et la surface disponible pour de nouvelles installations en Europe est intrinsèquement limitée par la densité de population et les priorités de biodiversité. Avec 71 % de la surface terrestre couverte par l'eau, et l'UE bordée sur trois côtés par la mer, le solaire en mer représente l'extension naturelle de la frontière de déploiement.

Le photovoltaïque flottant (FPV) sur les plans d'eau intérieurs a désormais atteint la maturité commerciale. Réservoirs, lacs de barrage et plans d'eau de carrière accueillent des centaines d'installations dans le monde, généralement avec des flotteurs en polyéthylène haute densité (PEHD). Le FPV en mer, en revanche, demeure à un stade précoce de

recherche et de développement (European Commission, 2020 ; Wang and Lund, 2022 ; Liu et al., 2024). Le plus grand déploiement en mer rapporté à ce jour est une centrale de 5 MW dans le détroit de Johor (Sunseap Group, Singapour). Des installations pilotes ont été déployées dans les eaux norvégiennes (Ocean Sun, membrane PEHD hydro-élastique tendue sur un tube circulaire), en mer du Nord néerlandaise (Oceans of Energy, plateformes modulaires interconnectées), ainsi qu'à IJzendoorn aux Pays-Bas et en mer du Nord (SolarDuck, plateformes semi-submersibles triangulaires à poutres d'aluminium supportées par trois cylindres verticaux en acier) (Wang and Lund, 2022 ; Liu et al., 2024). Chacune fonctionne à l'échelle du kilowatt au mégawatt faible, et chacune a rapporté des limitations propres à sa conception : faible extensibilité des membranes souples en raison de la complexité de l'ancrage et de la salissure biologique, fragilité structurelle sous chargement de houle prolongé, et coûts d'installation par m² qui ont jusqu'ici empêché un déploiement à l'échelle commerciale (Liu et al., 2024). L'écart d'ordre de grandeur entre le déploiement actuel du FPV en mer et le niveau requis pour une contribution significative à l'approvisionnement électrique de l'UE demeure large de plusieurs décennies. La Figure 0-1 présente les quatre principales lignes technologiques actuellement en validation sur site, y compris les flotteurs en béton fibré à ultra hautes performances (BFUP) testés et installés par PREF dans le réservoir d'Alqueva. La réduction de cet écart est moins contrainte par les modules photovoltaïques eux-mêmes, qui sont essentiellement les mêmes unités que celles employées à terre, que par ce qui les maintient au-dessus de l'eau. La structure porteuse doit survivre aux conditions de haute mer sur une durée de vie de plusieurs décennies, à un coût actualisé de l'électricité (LCOE) compatible avec les cibles fixées par la stratégie européenne pour les renouvelables en mer (European Commission, 2020). C'est le verrou technique sur lequel la présente thèse est ancrée.

Le problème de la structure porteuse : du PEHD au BFUP

Les structures porteuses du FPV intérieur sont dominées par le PEHD. Le matériau est peu coûteux, facile à mouler en flotteurs modulaires, et entièrement adéquat pour les régimes de houle calmes des réservoirs et des lacs. Ses limites apparaissent en mer. L'exploitation en haute mer exige des matériaux capables de résister à des vitesses de vent supérieures à 25 m/s, des courants supérieurs à 1,2 m/s et des hauteurs de vague dépassant 14 m (European Commission, 2020). Le PEHD ne possède ni la rigidité nécessaire au maintien de la stabilité géométrique sous un tel chargement, ni la résistance à long terme à l'exposition ultraviolette, à l'oxydation et à la salissure biologique qu'exige un service en mer à l'échelle décennale. Sa dégradation en conditions marines génère en outre une pollution par microplastiques, aux impacts mesurables sur l'écosystème aquatique environnant (Kushwaha et al., 2024).

Les alternatives structurelles à l'échelle de la haute mer sont limitées. L'acier peut supporter les charges mais requiert une maintenance périodique pour prévenir la corrosion, ce qui accroît les dépenses d'exploitation (OPEX) et réduit la fiabilité. L'aluminium, déployé dans le pilote SolarDuck, se heurte à des coûts de protection contre la corrosion comparables et à une performance en fatigue limitée sous chargement cyclique de houle. Le polyester renforcé de fibres de verre, utilisé dans les installations historiques de fermes mytilicoles du bassin atlantique, manque de la rigidité requise à l'échelle d'une plateforme de plusieurs mégawatts (Caruso et al., 2022). Le candidat restant est le béton, mais le béton armé conventionnel ne peut atteindre le rapport résistance sur masse requis pour un service flottant.

Le BFUP, en revanche, satisfait l'enveloppe structurelle. Le BFUP est environ 40 fois plus rigide que le PEHD et 5 fois plus résistant (European Commission, 2020). Sa résistance à la compression dépasse couramment 150 MPa avec une résistance en traction d'environ 10 MPa, obtenue par une compacité granulaire optimisée, un faible rapport eau sur liant (0,16 à 0,24), une teneur élevée en ciment, l'ajout de fumée de silice et un renforcement par microfibres d'acier à environ 2 % en volume (Richard and Cheyrezy, 1995 ; Shi et al., 2015). La combinaison d'une résistance en traction élevée et d'une faible perméabilité permet la production d'éléments précontraints élancés sans le risque de corrosion des armatures que présente le béton conventionnel en milieu marin. Le BFUP présente en outre une réponse écrouissante en traction, dans laquelle la charge post-fissuration est transférée au réseau de fibres et la contrainte dissipée par de multiples microfissures plutôt que par une macrofissure unique (Yoo and Banthia, 2016). L'auto-cicatrisation autogène des ouvertures de fissures jusqu'à environ 50 µm sous exposition marine prolonge encore la durée de vie (Cuenca et al., 2021). La performance mécanique par unité de masse étant élevée, le volume de matériau requis pour une fonction structurelle donnée est d'autant plus faible : une structure en BFUP bien conçue peut être réalisée avec 50 % à 70 % de matériau en moins que son équivalent en béton ordinaire (European Commission, 2020). La légèreté réduit à son tour la demande de flottabilité, la complexité de l'ancrage et le coût d'installation par m², qui se cumulent tous en un LCOE plus faible.

La transition de la recherche au déploiement est documentée. Des composants préfabriqués en BFUP sont utilisés dans des installations aquacoles en mer depuis 2018, en remplacement des flotteurs en polyester renforcé de fibres de verre des structures de fermes mytilicoles exposées à des vagues atteignant 4 m (Caruso et al., 2022). En janvier 2022, 1450 m2 de flotteurs en BFUP ont été installés dans une centrale FPV de 5 MW sur le réservoir d'Alqueva (Portugal), premier usage industriel rapporté du BFUP dans des structures porteuses FPV de classe marine, avec une production annuelle d'environ 7 GWh (European Commission, 2020). La faisabilité mécanique, la durabilité et la viabilité

économique du BFUP pour le FPV en mer ne constituent donc pas une hypothèse de recherche mais une référence opérationnelle.

La barrière restante est environnementale. La caractéristique même qui confère au BFUP son avantage mécanique, sa teneur élevée en ciment, entraîne une empreinte carbone incorporée incompatible avec le contexte de décarbonation de la stratégie européenne pour les renouvelables en mer. La Section 0.3 quantifie cette incompatibilité.

Le problème carbone du BFUP conventionnel

La production de ciment Portland représente environ 8 % des émissions anthropiques mondiales de dioxyde de carbone (Habert et al., 2013 ; Sameer et al., 2019). L'essentiel de cette empreinte provient de la calcination du calcaire à 1450 °C, qui libère du CO2 à la fois par le combustible brûlé et par la décomposition chimique de la matière première carbonatée. Le BFUP concentre le problème : les teneurs en ciment des formulations commerciales de BFUP atteignent jusqu'à 1000 kg/m3, le ciment de type I à fort taux de clinker représentant typiquement jusqu'à 50 % de la masse totale du système liant (Wille et al., 2011 ; European Commission, 2020). Le carbone incorporé du BFUP est proportionnellement élevé. Les évaluations du berceau à la porte rapportent des valeurs comprises entre 600 et 1300 kg CO2-eq/m3 selon la teneur en ciment, l'origine de la fumée de silice et la provenance des fibres d'acier (Yu et al., 2015). Le BFUP commercial de référence utilisé dans le projet NATURSEA-PV, désigné ci-après « le BFUP de référence du projet », rapporte une valeur d'environ 930 kg CO2-eq/m3, proche de la borne supérieure de cet intervalle (European Commission, 2020).

Cette empreinte évolue défavorablement selon la trajectoire du Pacte vert européen. D'après les estimations de CEMBUREAU, les émissions de CO2 représentent déjà environ 10 % du coût du ciment, sous l'effet d'une augmentation d'environ 350 % du prix des quotas de CO2 en 2021 (CO2 costs in cement Some calculations). À mesure que le mécanisme de tarification du carbone se resserre sur le reste de la décennie, la pénalité de coût sur les systèmes structurels à forte intensité de ciment se cumulera. Une structure porteuse FPV destinée à fournir des décennies d'électricité bas carbone ne peut reposer sur un matériau structurel dont l'intensité carbone propre se situe dans le haut du secteur de la construction. La contradiction est structurelle : le levier de décarbonation du PV en mer, s'il était mis à l'échelle avec des structures porteuses en BFUP conventionnel, générerait une dette de CO2 à la construction qui éroderait une partie du bénéfice climatique opérationnel qu'il est censé délivrer.

Découpler la performance mécanique du BFUP de son empreinte carbone dictée par le ciment constitue donc une condition préalable au déploiement industriel du FPV en mer à l'échelle qu'exigent les objectifs climatiques de l'UE. La question est de savoir si un liant reconçu, à teneur en clinker fortement réduite ou entièrement éliminée, peut délivrer

l'enveloppe mécanique et de durabilité du BFUP. Deux voies sont ouvertes : le BFUP éco-cimentaire, dans lequel le clinker est partiellement substitué par des sous-produits industriels tels que le laitier granulé de haut fourneau moulu ou les cendres volantes au sein d'un liant à base de Portland, et le béton géopolymère à ultra hautes performances (BFUP géopolymère), dans lequel le ciment Portland est entièrement supprimé et remplacé par un liant aluminosilicaté activé alcalinement. Les deux voies sont poursuivies en parallèle au sein du projet européen qui encadre ce travail, décrit à la Section 0.4.

Le cadre du projet NATURSEA-PV

NATURSEA-PV vise à développer de nouveaux matériaux et composants éco-cimentaires qui augmentent la durée de vie, la fiabilité et la maintenabilité des structures porteuses FPV en mer, et réduisent ainsi leur taux de dégradation, le risque d'investissement et le LCOE, tout en poursuivant le démantèlement, le réemploi et la recyclabilité en fin de service. Le travail rapporté dans cette thèse est mené au sein de ce projet, financé par le programme Horizon Europe au titre de l'appel HORIZON-CL5-2021-D3-03 « Sustainable, secure and competitive energy supply », convention de subvention numéro 101084348, sous le titre complet « Novel eco-cementitious materials and components for durable, competitive, and bio-inspired offshore FPV substructures ». Le consortium réunit 10 partenaires répartis dans 6 pays :

- Fundación Tecnalia Research and Innovation (TEC, Espagne, coordinateur)
- Stichting Maritiem Research Instituut Nederland (MAR, Pays-Bas)
- Université de Bordeaux (UBX, France)
- University College Cork (UCC, Irlande)
- Technical University of Darmstadt (TUD, Allemagne)
- Universidad del País Vasco (EHU, Espagne)
- Consejo Superior de Investigaciones Científicas (CSIC, Espagne)
- Warrant Hub (WH, Italie)
- Prefabricados Supplier S.L. (PREF, Espagne)
- Research and Development Concretes S.L. (RDC, Espagne)

Le travail technique est organisé en cinq lots de travaux, comme le montre la Figure 0-2.

- Le WP1 couvre la conception conceptuelle et structurelle de la structure porteuse, dont la géométrie bio-inspirée, dérivée de l'architecture à nervures radiales de la feuille de Victoria amazonica et validée par des essais sur modèle en bassin peu profond, fixe la cible structurelle que les matériaux du WP2 doivent atteindre (Figure 0-3).
- Le WP2 développe les nouveaux matériaux circulaires et poursuit le volet matériaux du projet selon deux voies de liant parallèles : une voie BFUP éco-cimentaire, pilotée

par TEC, dans laquelle le liant est un ciment Portland à fort taux de substitution du clinker par des sous-produits industriels (laitier granulé de haut fourneau moulu, type CEM III), et une voie BFUP géopolymère activée alcalinement et entièrement sans ciment, pilotée par UBX, dans laquelle le liant est constitué de laitier granulé de haut fourneau moulu et de fumée de silice activés par solution alcaline. Les deux voies sont évaluées au regard des mêmes indicateurs de performance limitants, détaillés au troisième paragraphe de la Section 0.4, et comparées au BFUP de référence du projet, la campagne d'exposition en mer à HarshLab servant d'environnement de validation commun. Le WP2 développe également des revêtements protecteurs biosourcés, pilotés par EHU.

- Le WP3 développe les outils de calcul prédictifs, dans lesquels UBX livre le modèle mécanique qui alimente le modèle de transport de pénétration des chlorures et de durabilité mis en œuvre par TUD.
- Le WP4 couvre les essais et la validation des matériaux et composants, y compris la validation en mer à HarshLab. UBX pilote le WP4.
- Le WP5 traite l'analyse de cycle de vie, l'acceptabilité sociale et les questions réglementaires (European Commission, 2020).

Le rôle d'UBX est donc réparti sur les volets matériaux, modélisation et validation, assurant une continuité directe entre formulation, caractérisation, durabilité et simulation structurelle. Les deux voies de liant au sein du WP2 sont encadrées par un ensemble de cibles mécaniques, rhéologiques, de durabilité et environnementales dérivées de la Description of Action du projet et de documents internes de jalons.

Les cibles mécaniques et rhéologiques spécifient une résistance à la compression à 24 heures d'au moins 65 MPa, une résistance à la compression à 28 jours d'au moins 130 MPa, un étalement compris entre 200 et 250 mm selon ASTM C1856, et un temps ouvert d'au moins 20 minutes. Les cibles de soutenabilité spécifient une teneur en fibres recyclées d'au moins 35 % en masse, une réduction de l'empreinte carbone d'au moins 30 %, et une réduction du coût rapporté à la résistance d'au moins 35 % par rapport au BFUP de référence du projet. Les cibles de durabilité spécifient une validation à HarshLab sur au moins 6 mois, et une durée de vie de 50 ans (European Commission, 2020). Ces cibles définissent ensemble l'enveloppe d'acceptation de tout matériau développé au sein du WP2. La présente thèse les démontre pour la voie BFUP géopolymère (formulation GEO) dans le périmètre UBX des WP2 et WP4.

La validation marine est conduite à HarshLab, un laboratoire flottant en mer exploité par TEC et ancré en 2018 sur la Biscay Marine Platform (BiMEP), à 1,6 mille de la côte basque dans le golfe de Gascogne (Espagne), à une profondeur d'eau de 65 m en haute mer non abritée, exposée aux houles atlantiques (European Commission, 2020). La mise à niveau de 2022 a porté la plateforme à 8,5 m de diamètre et 7 m de hauteur, avec 120 m2 de pont et

une capacité de plus de 2000 éprouvettes réparties entre les zones atmosphérique, de marnage et d'immersion (Figure 0-4). Au sein de NATURSEA-PV, les matériaux sont exposés pendant 10 mois et évalués par inspection visuelle, essais mécaniques résiduels sur carottes extraites et analyse de la profondeur de pénétration des chlorures par indication AgNO3/phénolphtaléine.

Des deux voies de liant encadrées par cette enveloppe d'acceptation, la présente thèse traite la voie géopolymère sans ciment. La Section 0.5 expose la chimie de l'activation alcaline, passe en revue les niveaux de résistance atteints dans la littérature publiée sur les géopolymères à ultra hautes performances, et identifie les questions qui demeurent ouvertes au niveau de la formulation.

Le BFUP géopolymère comme voie sans ciment

La géopolymérisation, formalisée pour la première fois par Davidovits en 1975 (Davidovits, 1991), remplace la chimie d'hydratation du ciment Portland par l'activation alcaline de précurseurs aluminosilicatés. Le processus se déroule en trois étapes couplées (Shi et al., 2011 ; Provis and Deventer, 2014) :

1. Dissolution de la surface du précurseur dans l'activateur alcalin
2. Réorganisation des espèces aluminate et silicate dissoutes
3. Polycondensation en un réseau aluminosilicaté tridimensionnel

Les précurseurs employés dans les systèmes de substitution du ciment sont majoritairement des sous-produits industriels : laitier granulé de haut fourneau moulu (GGBS), cendres volantes (FA) et fumée de silice (SF), valorisés à faible coût énergétique par rapport à la production de clinker (Davidovits, 1993). Les activateurs sont des solutions alcalines d'hydroxyde de sodium ou de potassium combinées à des silicates solubles (Singh et al., 2015).

La chimie du gel liant qui en résulte dépend de la teneur en calcium du système précurseur. Les systèmes à faible teneur en calcium à base de cendres volantes et de métakaolin forment des gels d'aluminosilicate de sodium hydraté (N-A-S-H), tandis que les systèmes à forte teneur en calcium à base de laitier forment des gels d'aluminosilicate de calcium hydraté qui incorporent des ions alcalins et sont désignés C-(K)-A-S-H ou C-(N)-A-S-H selon le cation de l'activateur (Garcia-Lodeiro et al., 2011 ; Bernal et al., 2013). La formulation riche en laitier et activée par KOH développée dans cette thèse relève de la seconde catégorie et est ancrée mécanistiquement sur un gel C-(N,K)-A-S-H, distinct à la fois du système C-S-H plus portlandite du BFUP Portland et du gel N-A-S-H des géopolymères à faible teneur en calcium. Correctement formulé, un BFUP géopolymère égale ou dépasse la performance mécanique du BFUP Portland tout en réduisant le carbone incorporé de 50 % à 80 % (Yu et al., 2015 ; Cai and Ye, 2021).

Des travaux récents ont progressivement repoussé la résistance et la soutenabilité atteignables des BFUP géopolymère. Wetzel and Middendorf (2019) ont atteint 178,6 MPa avec une teneur en fumée de silice optimisée dans un système de laitier activé alcalinement sous cure thermique. Lao et al. (2022, 2023) ont produit des BFUP géopolymère écrouissants atteignant 186 à 220 MPa en utilisant des activateurs Na2CO3/Na2SiO3 avec renforcement par fibres d'acier. Liu et al. (2020b) ont montré que l'optimisation de la teneur en fumée de silice peut réduire la consommation de fibres d'acier tout en préservant la performance mécanique. Plus récemment, (Wang et al., 2025) ont rapporté une comparaison directe BFUP géopolymère contre BFUP avec une résistance à la compression supérieure de 25,7 % à 61,6 % entre 28 et 84 jours, et des émissions de CO2 normalisées par la résistance inférieures de 64,7 % à 86,0 %, confirmant le BFUP géopolymère comme une alternative viable et environnementalement supérieure.

Malgré ces progrès, quatre questions demeurent ouvertes au niveau de la formulation pour un BFUP géopolymère de qualité marine et définissent le périmètre que cette thèse doit traiter. Premièrement, la plupart des études sur les BFUP géopolymère optimisent une ou deux propriétés isolément, alors que le déploiement structurel, en particulier la préfabrication dans des coffrages complexes, exige que la résistance, l'écoulement autoplaçant et le temps ouvert soient contrôlés simultanément (Midhin et al., 2023 ; Alameri et al., 2025). Deuxièmement, le rôle du cation alcalin aux niveaux de résistance des BFUP géopolymère est essentiellement inexploré. Les systèmes activés par KOH produisent des structures de gel et des cinétiques de réaction différentes de celles activées par NaOH, et les géopolymères conventionnels (20 à 60 MPa) montrent des effets Na+/K+ mesurables (Duxson et al., 2005 ; Sindhunata et al., 2006), mais aucune comparaison directe au-delà de 130 MPa n'a été rapportée. Troisièmement, le comportement du rapport silicate de sodium sur hydroxyde à la faible teneur en eau sur liant caractéristique des BFUP géopolymère est mal documenté. Quatrièmement, les fibres d'acier utilisées dans les formulations de BFUP géopolymère publiées sont majoritairement vierges, alors que les fibres représentent une part significative du coût et du carbone incorporé du matériau final. Les fibres d'acier issues de pneus recyclés offrent une alternative de seconde vie crédible mais leur intégration dans des matrices denses n'a pas été optimisée systématiquement (Ferdiansyah et al., 2018). Aucune des formulations de BFUP géopolymère publiées n'est simultanément sans ciment, à cure ambiante, porteuse de fibres recyclées et validée en conditions de durabilité marine à des niveaux de résistance supérieurs à 130 MPa. C'est le verrou que cette thèse traite, dans le cadre plus large de l'investigation NATURSEA-PV sur les liants éco-cimentaires et géopolymères pour un service marin durable.

Objectifs de la thèse et question de recherche centrale

La présente thèse développe, caractérise, modélise et évalue un BFUP géopolymère 100 % sans ciment et à cure ambiante, désigné GEO, destiné à se substituer au BFUP de

référence du projet dans les structures porteuses FPV en mer au sein du cadre NATURSEA-PV. Un BFUP au ciment Portland de classe mécanique équivalente, désigné REF, sert de référence interne pour toutes les comparaisons. La voie parallèle du BFUP éco-cimentaire, poursuivie dans le même cadre WP2 par TEC et comparée au même BFUP de référence du projet, est mentionnée pour le contexte lorsqu'elle éclaire l'interprétation mais se situe hors du périmètre de cette thèse. Les comparaisons dans le présent manuscrit sont restreintes à GEO contre REF. Quatre objectifs spécifiques structurent le travail et correspondent directement aux chapitres du manuscrit :

Objectif 1. Développer et caractériser un BFUP géopolymère 100 % sans ciment et à cure ambiante à base de laitier granulé de haut fourneau moulu, de fumée de silice et d'une activation KOH/silicate de sodium, incorporant des fibres d'acier issues de pneus recyclés, qui satisfasse simultanément les cibles mécaniques et rhéologiques de NATURSEA-PV. Traité au Chapitre 1.

Objectif 2. Établir les signatures multi-échelles et non destructives des liants GEO et REF par spectroscopie d'impédance électrochimique (réseau poreux et chimie de la solution interstitielle, Chapitre 2) et par suivi d'émission acoustique en flexion trois points (amorçage, propagation et dissipation d'énergie de la fissuration, Chapitre 3), afin de fournir des outils méthodologiques pour la surveillance de l'état de santé structurel des éléments en BFUP géopolymère en service.

Objectif 3. Quantifier la durabilité à long terme du GEO sous agressions chimique et thermique pertinentes en milieu marin (sulfates, acide, chlorures, température élevée) et valider les résultats à l'échelle du laboratoire en conditions marines réelles à HarshLab, afin de déterminer si la chimie du gel C-(N,K)-A-S-H confère un avantage net sur le système C-S-H plus portlandite du REF. Traité au Chapitre 4.

Objectif 4. Évaluer la performance environnementale et économique du berceau à la tombe du GEO face au BFUP de référence du projet par évaluation de l'empreinte carbone, en identifiant les scénarios (distance de transport, contenu recyclé, mix électrique) dans lesquels le système GEO satisfait les cibles environnementales et économiques de NATURSEA-PV et ceux dans lesquels l'avantage se dégrade. Traité au Chapitre 4.

Les quatre objectifs s'enchaînent en un argument unique, et les chapitres suivent cet enchaînement plutôt que l'ordre dans lequel les campagnes ont été menées. Le Chapitre 1 doit réussir d'abord, car sans une formulation satisfaisant les critères d'acceptation il n'y a rien à caractériser. La microstructure qu'il établit détermine ensuite ce que les chapitres suivants peuvent mesurer. Le réseau poreux du GEO est 100 fois plus grossier que celui du REF en taille de pore dominante, 700 nm contre 6,2 nm, et sa solution interstitielle est dominée par des espèces résiduelles K^+ et silicatées plutôt que par le couple Ca^{2+} et OH^- d'un système Portland tamponné par la portlandite. Les deux différences se situent dans la

résolution de la spectroscopie d'impédance électrochimique, ce qui explique que le Chapitre 2 suive.

Le Chapitre 2 caractérise le matériau au repos : la réponse en impédance est intégrative et moyennée en volume, rendant compte de l'état net de la matrice sans résoudre les événements discrets par lesquels elle accumule et libère l'énergie mécanique. L'application en structure porteuse marine soumet le matériau à un chargement plutôt qu'aux conditions de quasi-équilibre de la cure, de sorte que le Chapitre 3 observe directement l'interface fibre-matrice en flexion, la population de fibres étant maintenue constante afin que la comparaison isole le liant.

Les Chapitres 1 à 3 établissent ensemble le GEO comme un système distinct, mécaniquement, électrochimiquement et dans son chemin de rupture, mais aucun d'entre eux ne détermine si ce système survit à des mois d'exposition marine ni si son bilan carbone et économique justifie le remplacement de la référence.

Le Chapitre 4 clôt les deux questions, et le bilan de durabilité et environnemental qu'il établit doit se vérifier pour que le déploiement à l'échelle industrielle soit justifié.

La question fédératrice qui organise cet argument est la question de recherche centrale de la thèse :

Un BFUP géopolymère 100 % sans ciment et à cure ambiante peut-il atteindre la performance mécanique et de durabilité nécessaire pour survivre en environnement marin sévère et remplacer le BFUP conventionnel dans les structures porteuses FPV en mer surveillées par SHM ?

Structure de la thèse

Le manuscrit répond à cette question centrale à travers quatre chapitres en séquence linéaire. Chaque chapitre s'ouvre sur un état de l'art ciblé sur son propre périmètre, est ancré par sa propre question de recherche énoncée explicitement dans le paragraphe d'ouverture du chapitre et à laquelle répond la conclusion du chapitre, et se termine par une transition qui transmet le résultat du chapitre au suivant. Les questions de recherche des chapitres ne sont pas des reformulations parallèles de la question centrale. Elles la décomposent en les problèmes spécifiques que les mesures du chapitre sondent effectivement, de sorte qu'aucun chapitre n'excède ce que ses propres données permettent d'étayer.

Chapitre 1, Formulation et caractérisation, établit la formulation GEO par une optimisation en six étapes pilotée par les verrous et démontre que les cibles mécaniques et rhéologiques de NATURSEA-PV peuvent être atteintes sous cure ambiante avec des fibres d'acier issues de pneus recyclés. La formulation retenue satisfait les cinq critères d'acceptation simultanément : 65 MPa à 24 heures, 137 MPa à 28 jours sur cubes de 100 mm et 152 ± 5 MPa sur demi-prismes, soit 92 % des 165 ± 4 MPa obtenus par le REF sur

géométrie appariée, un étalement de 208 mm, un temps ouvert de 23 minutes et une teneur en fibres recyclées de 60 % en masse. Trois résultats se transposent au-delà de cette formulation : la teneur en calcium du précurseur plutôt que l'activateur contrôle le régime de résistance atteignable, le dosage absolu en silicate organise un optimum de résistance, et la substitution de Na+ par K+ à molarité égale rompt le compromis résistance-ouvrabilité qui contraint le laitier activé par NaOH. Les points clés du chapitre sont résumés à la Figure 0-5.

Chapitre 2, Spectroscopie d'impédance électrochimique, caractérise le réseau poreux et la chimie de la solution interstitielle du REF et du GEO de 1 à 28 jours et teste si l'impédance globale peut servir d'indicateur non destructif du développement de la résistance. Les deux liants se révèlent électrochimiquement distincts sur chaque axe résolu, et l'indicateur de résistance lui-même se révèle propre au liant : la résistance des pores du gel R2 suit le REF (r de Pearson = 0,987 en axes logarithmiques) tandis que le coefficient de Warburg suit le GEO (r = 0,983), et aucun des deux paramètres ne convient à l'autre liant. Un BFUP sans ciment est donc ouvert à la même classe de contrôle qualité électrochimique que le BFUP conventionnel, à condition que l'indicateur soit calibré sur le liant. Les points clés du chapitre sont résumés à la Figure 0-6.

Chapitre 3, Émission acoustique et mécanique de la rupture, caractérise l'amorçage, la propagation et la dissipation d'énergie de la fissuration dans le REF et le GEO, non fibrés et fibrés, le type et le dosage des fibres d'acier étant maintenus constants. Deux chemins distincts émergent : l'énergie est dissipée par arrachement frictionnel des fibres le long de la zone de transition interfaciale dans le composite cimentaire et par décohésion cohésive de la matrice dans le géopolymère. Les deux mûrissent sur des échelles de temps différentes et produisent un croisement de ténacité, le composite géopolymère dissipant 30,20 contre 25,05 J à 24 heures et 34,98 contre 46,67 J à 28 jours. Un modèle d'endommagement continu calé sur la réponse en flexion mesurée reproduit la charge au pic à 2,3 % près et la localisation de la fissure, mais non la branche post-pic. Les points clés du chapitre sont résumés à la Figure 0-7.

Chapitre 4, Durabilité et évaluation de l'empreinte carbone, évalue la résistance du REF et du GEO sous exposition aux sulfates, à l'acide, aux chlorures et à température élevée sur 12 mois, avec un suivi par spectroscopie d'impédance électrochimique dans toutes les solutions, et rapporte la campagne d'exposition en mer de 10 mois à HarshLab. Le GEO détient un avantage décisif sous attaque sulfatique et acide, égale la référence sur les chlorures au niveau qui gouverne le service marin, et conserve l'intégralité de sa classe mécanique dans les trois zones d'exposition après immersion réelle, avec un unique désavantage à température élevée, 36 % de conservation en compression à 600 °C contre 90 % pour le REF. L'évaluation du berceau à la tombe retourne une réduction carbone de 37 % par m3 et de 32,1 % par tonne, satisfaisant la cible carbone du projet, tandis que la réduction

du coût rapporté à la résistance atteint 10,9 % pour une exigence de 35 % et ne la satisfait donc pas. Les points clés du chapitre sont résumés à la Figure 0-8.

L'architecture du manuscrit et l'enchaînement des questions de recherche sont résumés à la Figure 0-9. À travers les quatre chapitres, les systèmes géopolymère et de référence apparaissent sous des désignations propres à chaque chapitre, dont les systèmes de fibres diffèrent par conception et sont précisés dans chaque chapitre. Le BFUP de référence du projet de l'analyse d'empreinte carbone est un matériau distinct, commercialement confidentiel, et est répertorié séparément.

Résumé étendu

Contexte et positionnement du problème

Le photovoltaïque flottant en mer exige une structure porteuse capable de survivre à plusieurs décennies de service en haute mer. La classe de matériau qui satisfait aujourd'hui cette enveloppe, le béton fibré à ultra hautes performances (BFUP) au ciment Portland, porte un carbone incorporé situé près de la borne supérieure du secteur de la construction, de l'ordre de 930 kg CO2-eq/m3 pour le BFUP de référence du projet. La contradiction est structurelle : un levier de décarbonation de la production électrique construit avec un matériau à forte intensité carbone érode une partie du bénéfice climatique qu'il est censé délivrer.

Cette thèse a posé la question de savoir si le liant Portland peut être entièrement supprimé. Elle développe, caractérise, modélise et évalue un béton géopolymère à ultra hautes performances (BFUP géopolymère) 100 % sans ciment et à cure ambiante, désigné GEO, comme candidat au remplacement du BFUP de référence du projet dans le cadre du projet Horizon Europe NATURSEA-PV. Un BFUP au ciment Portland de classe mécanique équivalente, désigné REF, sert de référence interne pour toutes les comparaisons.

Chapitre 1. Formulation et caractérisation

Une optimisation en six étapes pilotée par les verrous a été conduite, chaque étape résolvant le facteur limitant identifié à la précédente. Elle a produit le GEO, un liant binaire de laitier granulé de haut fourneau moulu et de fumée de silice à 900 kg/m3, activé par silicate de sodium et KOH 10 M, renforcé par un mélange de fibres d'acier recyclées et vierges dans un rapport 60/40 à 12 % en masse de liant.

Les cinq critères d'acceptation de NATURSEA-PV sont satisfaits simultanément sous cure ambiante : 65 MPa à 24 heures, atteint exactement et sans marge, 152 ± 5 MPa à 28 jours sur demi-prismes, 208 mm d'étalement, 23 minutes de temps ouvert et 60 % en masse de fibres recyclées. Cette valeur à 28 jours représente 92 % du témoin REF, à 165 ±

4 MPa sur géométrie appariée. Trois résultats se transposent au-delà de cette formulation : la teneur en calcium du précurseur, plutôt que l'activateur, constitue le descripteur qui contrôle le régime de résistance atteignable ; un optimum empirique de résistance est organisé par le dosage absolu en silicate de sodium, dans la bande de 160 à 190 kg/m3 ; et la substitution de Na+ par K+ à molarité égale rompt le compromis résistance-ouvrabilité qui contraint le laitier activé par NaOH.

L'écart résiduel de 8 % au REF est traçable à l'absence de période d'induction, le GEO atteignant son exotherme à 5,6 heures contre 38,2, et verrouillant un réseau capillaire de 700 nm contre 6,2 nm en taille de pore dominante, dans un gel C-(N,K)-A-S-H exempt de portlandite à un rapport Ca/Si de 0,39 contre 1,72. À la connaissance de l'auteur, il s'agit du premier BFUP géopolymère rapporté combinant en une seule formulation la cure ambiante, un liant binaire laitier et fumée de silice sans cendres volantes, une activation par KOH au-delà de 130 MPa et plus de 60 % en masse de fibres d'acier issues de pneus recyclés.

Chapitre 2. Spectroscopie d'impédance électrochimique

La spectroscopie d'impédance électrochimique a été appliquée de manière non destructive à huit âges de cure de 1 à 28 jours, de 4 Hz à 5 MHz, les spectres étant validés par des contrôles de cohérence de Kramers-Kronig et ajustés par moindres carrés non linéaires complexes sur des circuits équivalents physiquement motivés.

Le module d'impédance du GEO est inférieur d'un à deux ordres de grandeur à celui du REF à tous les âges. Le GEO présente une topologie à deux arcs en une seule étape, contre une topologie dépendante du stade pour le REF, qui ajoute un troisième arc interfacial à partir du jour 10. Aucun arc interfacial n'est résoluble dans le GEO à quelque âge que ce soit, ce qui est cohérent avec l'interface fibre-matrice cohésive identifiée au Chapitre 1.

Les indicateurs de résistance se révèlent propres au liant : la résistance des pores du gel R2 pour le REF (r de Pearson = 0,987 en axes logarithmiques) et le coefficient de Warburg W pour le GEO (r = 0,983). Un événement de réorganisation est enregistré dans le GEO entre les jours 14 et 21 par cinq observables indépendantes, qui disqualifie R2 dans ce liant et laisse W robuste. Ces résultats établissent qu'un BFUP sans ciment est ouvert à la même classe de contrôle qualité électrochimique que le BFUP conventionnel, à condition que l'indicateur soit calibré sur la chimie du liant. Aucun paramètre universel ne convient aux deux.

Chapitre 3. Émission acoustique et mécanique de la rupture

Une émission acoustique multiparamétrique a été enregistrée en flexion trois points sur un plan factoriel deux par deux en chimie de liant et en présence de fibres, à 24 heures et 28 jours, le type et le volume de fibres étant maintenus constants et l'atténuation calibrée sur chaque éprouvette.

Deux chemins de rupture distincts émergent, croisés avec les surfaces de rupture du Chapitre 1 : un arrachement interfacial dominé par le frottement dans le composite cimentaire et une décohésion cohésive de la matrice dans le géopolymère. L'ajout de fibres élève la fraction de cisaillement du composite cimentaire de 6,8 points à 28 jours et abaisse celle du géopolymère de 4,7. Les durées médianes de signal s'établissent à 168 µs dans le composite cimentaire contre 72 µs dans le géopolymère.

Un croisement de ténacité est observé, 30,20 contre 25,05 J à 24 heures en faveur du géopolymère et 34,98 contre 46,67 J à 28 jours à son détriment, parce que la capacité frictionnelle croît avec la maturation de l'interface tandis que la décohésion est engagée dès le premier jour. Un modèle d'endommagement continu calé sur la réponse en flexion mesurée reproduit la charge au pic à 2,3 % près ainsi que la localisation de la fissure, mais non la branche post-pic, que la représentation des fibres à liaison parfaite ne peut porter.

Chapitre 4. Durabilité marine et empreinte carbone

Douze mois d'immersion sulfatique et acide, des programmes de migration rapide des chlorures et d'exposition à température élevée, ainsi qu'une campagne en mer de dix mois à HarshLab couvrant les zones atmosphérique, de marnage et immergée, ont été combinés à une évaluation carbone et économique du berceau à la tombe suivant la structure modulaire de l'EN 15804+A2.

Le GEO détient un avantage décisif sous attaque sulfatique et acide, où l'absence de portlandite ferme la voie de l'ettringite et où une couche de surface autolimitante remplace un front de dissolution progressant. La parité avec la référence est établie sur les chlorures au niveau qui gouverne le service marin, avec une alcalinité conservée et aucun front de chlorures ni de carbonatation après immersion réelle. La classe mécanique est intégralement conservée dans chaque zone d'exposition, aucun des revêtements biosourcés ne conférant d'avantage mesurable, de sorte que la durabilité repose sur le liant lui-même plutôt que sur une barrière de surface.

Un unique désavantage est relevé : 36 % de conservation en compression à 600 °C contre 90 % pour la seule éprouvette REF ayant survécu intacte, condition qui se situe hors de l'enveloppe de service et pour laquelle le classement d'intégrité est inversé.

L'évaluation retourne une réduction carbone de 37 % par m3 et de 32,1 % par tonne, satisfaisant conditionnellement le KPI 2.1, la réduction s'étendant de 23,5 à 44,1 % sur neuf scénarios de sensibilité et ne tombant sous 30 % que sous une allocation de 2 % de l'acier au laitier ou un retour aux fibres vierges. La réduction du coût rapporté à la résistance atteint 10,9 % pour une cible de 35 %, laissant le KPI 2.2 non satisfait aux prix de matériaux documentés.

Réponse à la question centrale

La réponse est affirmative sur les dimensions qui décident de la faisabilité technique, et conditionnelle sur celle qui décide de l'adoption commerciale. Les deux charges résiduelles convergent sur un seul sous-système, l'activateur portant 46 % du coût matériau et 69 % du carbone de l'étape de production. Le Chapitre 1 ayant déjà ramené ce rapport de 0,50 à 0,38 sous les contraintes de résistance et de temps ouvert, le levier relève de l'approvisionnement et de la substitution partielle plutôt que de la réduction du dosage.

Quatre limitations encadrent la conclusion, aucune n'inversant les résultats directionnels mais chacune qualifiant la précision des valeurs qui les étayent : des résultats de transport et mécaniques issus d'un lot unique, des chemins de rupture identifiés sur des cellules à n = 2, une description numérique calée sur une seule courbe et non validée indépendamment, et un facteur de formation non mesuré.

Conclusion générale et perspectives

Le photovoltaïque flottant en mer exige une structure porteuse qui survive à des décennies de service en haute mer, et la classe de matériau qui satisfait actuellement cette enveloppe, le BFUP au ciment Portland, porte un carbone incorporé proche de la borne supérieure du secteur de la construction. Cette thèse a posé la question de savoir si le liant Portland peut être entièrement supprimé : un BFUP géopolymère 100 % sans ciment et à cure ambiante peut-il atteindre la performance mécanique et de durabilité requise pour survivre en environnements marins sévères et remplacer le BFUP conventionnel dans les structures porteuses photovoltaïques flottantes en mer ?

Chapitre 1 : Formulation et caractérisation

Une optimisation en six étapes pilotée par les verrous a été conduite, chaque étape résolvant le facteur limitant identifié à la précédente. Elle a produit le GEO, un liant binaire de laitier granulé de haut fourneau moulu et de fumée de silice à 900 kg/m3, activé par silicate de sodium et KOH 10 M, renforcé par un mélange de fibres d'acier recyclées et vierges dans un rapport 60/40 à 12 % en masse de liant. Les résultats ont montré :

- Les cinq critères NATURSEA-PV satisfaits simultanément sous cure ambiante : 65 MPa à 24 heures, atteint exactement et sans marge, et 152 ± 5 MPa, 208 mm d'étalement, 23 minutes de temps ouvert et 60 % en masse de fibres recyclées
- La teneur en calcium du précurseur plutôt que l'activateur comme descripteur contrôlant le régime de résistance atteignable
- Un optimum empirique de résistance organisé par le dosage absolu en silicate de sodium, dans la bande de 160 à 190 kg/m3
- La substitution de Na+ par K+ à molarité égale rompant le compromis résistance-ouvrabilité qui contraint le laitier activé par NaOH

- Un écart résiduel de 8 % au REF traçable à l'absence de période d'induction, le GEO atteignant son exotherme à 5,6 heures contre 38,2 et verrouillant un réseau capillaire de 700 contre 6,2 nm en entrée de pore dominante, dans un gel C-(N,K)-A-S-H exempt de portlandite à Ca/Si 0,39 contre 1,72

L'objectif 1 est atteint. À la connaissance de l'auteur, il s'agit du premier BFUP géopolymère rapporté combinant la cure ambiante, un liant binaire laitier et fumée de silice sans cendres volantes, une activation par KOH au-delà de 130 MPa et plus de 60 % en masse de fibres d'acier issues de pneus recyclés dans une seule formulation.

Chapitre 2 : Spectroscopie d'impédance électrochimique

La spectroscopie d'impédance électrochimique a été appliquée de manière non destructive à huit âges de cure de 1 à 28 jours, de 4 Hz à 5 MHz, les spectres étant validés par des contrôles de cohérence de Kramers-Kronig et ajustés par moindres carrés non linéaires complexes sur des circuits équivalents physiquement motivés. Les résultats ont montré :

- Un module d'impédance inférieur d'un à deux ordres de grandeur dans le GEO par rapport au REF à tous les âges
- Une topologie à deux arcs en une seule étape pour le GEO, contre une topologie dépendante du stade pour le REF qui ajoute un troisième arc interfacial à partir du jour 10
- Aucun arc interfacial résoluble dans le GEO à quelque âge que ce soit, en cohérence avec l'interface fibre-matrice cohésive identifiée au Chapitre 1
- Des indicateurs de résistance propres au liant, la résistance des pores du gel R2 pour le REF (r de Pearson = 0,987 en axes logarithmiques) et le coefficient de Warburg W pour le GEO (r = 0,983)
- Un événement de réorganisation dans le GEO entre les jours 14 et 21, enregistré par cinq observables indépendantes, qui disqualifie R2 dans ce liant et laisse W robuste

Ces résultats établissent qu'un BFUP sans ciment est ouvert à la même classe de contrôle qualité électrochimique que le BFUP conventionnel, à condition que l'indicateur soit calibré sur la chimie du liant. Aucun paramètre universel ne convient aux deux.

Chapitre 3 : Émission acoustique et mécanique de la rupture

Une émission acoustique multiparamétrique a été enregistrée en flexion trois points sur un plan factoriel deux par deux en chimie de liant et en présence de fibres, à 24 heures et 28 jours, le type et le volume de fibres étant maintenus constants et l'atténuation calibrée sur chaque éprouvette. Les résultats ont montré :

- Deux chemins de rupture distincts, croisés avec les surfaces de rupture du Chapitre 1, un arrachement interfacial dominé par le frottement dans le composite cimentaire et une décohésion cohésive de la matrice dans le géopolymère

- L'ajout de fibres élevant la fraction de cisaillement du composite cimentaire de 6,8 points à 28 jours et abaissant celle du géopolymère de 4,7
- Des durées médianes de signal de 168 µs dans le composite cimentaire contre 72 µs dans le géopolymère
- Un croisement de ténacité, 30,20 contre 25,05 J à 24 heures en faveur du géopolymère et 34,98 contre 46,67 J à 28 jours à son détriment, parce que la capacité frictionnelle croît avec la maturation de l'interface tandis que la décohésion est engagée dès le premier jour
- Un modèle d'endommagement continu calé sur la réponse en flexion mesurée reproduisant la charge au pic à 2,3 % près et la localisation de la fissure, mais non la branche post-pic, que la représentation des fibres à liaison parfaite ne peut porter

L'objectif 2 est donc atteint tant du côté électrochimique que du côté de la rupture, la différence de liant établie au Chapitre 1 se propageant jusqu'au processus de rupture lui-même.

Chapitre 4 : Durabilité marine et évaluation de l'empreinte carbone

Douze mois d'immersion sulfatique et acide, des programmes de migration rapide des chlorures et d'exposition à température élevée, ainsi qu'une campagne en mer de dix mois à HarshLab couvrant les zones atmosphérique, de marnage et immergée, ont été combinés à une évaluation carbone et économique du berceau à la tombe suivant la structure modulaire de l'EN 15804+A2. Les résultats ont montré :

- Un avantage décisif du GEO sous attaque sulfatique et acide, où l'absence de portlandite ferme la voie de l'ettringite et où une couche de surface autolimitante remplace un front de dissolution progressant.
- La parité avec la référence sur les chlorures au niveau qui gouverne le service marin, avec une alcalinité conservée et aucun front de chlorures ni de carbonatation après immersion réelle.
- La conservation intégrale de la classe mécanique dans chaque zone d'exposition, aucun des revêtements biosourcés ne conférant d'avantage mesurable, de sorte que la durabilité repose sur le liant lui-même plutôt que sur une barrière de surface.
- Un unique désavantage, 36 % de conservation en compression à 600 °C contre 90 % pour la seule éprouvette REF ayant survécu intacte, condition située hors de l'enveloppe de service, avec le classement d'intégrité inversé.
- Une réduction carbone de 37 % par m3 et de 32,1 % par tonne, satisfaisant conditionnellement le KPI 2.1, la réduction s'étendant de 23,5 à 44,1 % sur neuf scénarios de sensibilité et ne tombant sous 30 % que sous une allocation de 2 % de l'acier au laitier ou un retour aux fibres vierges.
- Une réduction du coût rapporté à la résistance de 10,9 % pour une cible de 35 %, laissant le KPI 2.2 non satisfait aux prix de matériaux documentés.

Les objectifs 3 et 4 sont atteints, le quatrième conditionnellement.

La réponse à la question centrale est donc affirmative sur les dimensions qui décident de la faisabilité technique et conditionnelle sur celle qui décide de l'adoption commerciale. Les deux charges résiduelles convergent sur un seul sous-système, l'activateur portant 46 % du coût matériau et 69 % du carbone de l'étape de production, et puisque le Chapitre 1 a déjà ramené ce rapport de 0,50 à 0,38 sous les contraintes de résistance et de temps ouvert, le levier relève de l'approvisionnement et de la substitution partielle plutôt que de la réduction du dosage. Quatre limitations encadrent la conclusion, aucune n'inversant les résultats directionnels mais chacune qualifiant la précision des valeurs qui les étayent : des résultats de transport et mécaniques issus d'un lot unique, des chemins de rupture identifiés sur des cellules à n = 2, une description numérique calée sur une seule courbe et non validée indépendamment, et un facteur de formation non mesuré.